Lipophilic and Cationic Gallium-68 Complexes for the Detection of Mitochondrial Dysfunction

By

Bradley Edward Osborne

A thesis submitted in partial fulfilment of the requirements for the degree of

Doctor of Philosophy in Chemistry

November 2022

Department of Chemistry

Imperial College London

Statement of Originality

The work reported in this thesis was completed between October 2018 and November 2022 at the Department of Chemistry, Imperial College London or the Division of Imaging Sciences and Biomedical Engineering, King's College London. The work reported is entirely my own, unless otherwise stated through cited reference or acknowledgement and has never been previously submitted for a degree at this or any other university.

Copyright Declaration

Abstract

This thesis gives an account of the synthesis of macrocyclic and acyclic ligands for radiolabelling with gallium-68 to afford lipophilic and cationic radiotracers to report on mitochondrial dysfunction. These radiotracers are designed to be lipophilic enough to ensure the successful permeation of lipid bilayer membranes, and to also possess a cationic charge in order to be attracted into the mitochondria in a manner dependent on the mitochondrial membrane potential.

The synthesis of novel macrocyclic chelators for gallium-68 labelling is described in chapter 2. The synthesis of three sets of macrocyclic compounds are discussed, beginning with a focus on triarylphosphonium functionalisation to afford lipophilic and cationic compounds.

All three sets of compounds described in chapter 2 were successfully radiolabelled with generator-produced gallium-68. Chapter 3 describes this radiolabelling, starting with the optimisation of radiochemical yields through a series of altering reaction condition experiments. Initial screening of these radiolabelled compounds was performed through the measurement of their log *D* values. RadioHPLC analysis was used to investigate the purity of the reaction mixture and assess the presence of speciation.

Chapter 4 described the candidate radiotracer's behaviour in a preclinical model. The cardiac uptake and retention of the candidate radiotracer was determined using the *ex vivo* Langendorff isolated perfused heart model in both healthy and depolarised mitochondria, with MIBI used as a baseline for this model. This work provides the foundation for additional, more thorough, biological evaluation of such radiotracers, as well as informing on the design and development of future lipophilic and cationic gallium-68 radiotracers.

As well as macrocyclic ligands discussed in chapter 2, several acyclic ligand families were also synthesised. These series of acyclic ligands are described in chapter 5, including a focus on bis(salicylaldimine) compounds and some phosphinic acid functionalised analogues, two series of tridentate ligands which have been shown to selectively form 2:1 complexes with metals in the oxidation state of +3, and a final series of bis(semicarbazone) chelates with a focus on triarylphosphonium functionalisation to yield lipophilic and cationic compounds.

Chapter 6 summarises the conclusions of this thesis and ideas for future work of this research. Chapter 7 summarises the experimental procedures for the synthetic chemistry and radiochemistry. Chapter 8 contains an Appendix for NMR, MS and DFT data.

Publications Arising From This Thesis

DO2A-Based Ligands for Gallium-68 Chelation: Synthesis, Radiochemistry and *Ex Vivo* Cardiac Uptake; Adam J. Smith, Bradley E. Osborne, George P. Keeling, Philip J. Blower, Richard Southworth, Nicholas J. Long. *Dalton Transactions*, 2020, doi: 10.1039/C9DT02354B.

Synthesis and *Ex Vivo* Biological Evaluation of Gallium-68 Labelled NODAGA Chelates Assessing Cardiac Uptake and Retention; Bradley E. Osborne, Thomas T. C. Yue, Edward C. T. Waters, Friedrich Baark, Richard Southworth, Nicholas J. Long. *Dalton Transactions*, 2021, doi: 10.1039/D1DT02224E.

Table of Contents

Acknowledgements

First and foremost, I would like to thank my supervisors Prof. Nicholas Long and Dr Richard Southworth for your invaluable help, guidance and support throughout this project. Nick, thank you for always being available for a chat. All your advice has been invaluable, your encouragement has kept my morale high throughout this project. Your competitive streak certainly turns up during the Long Group socials, especially for the cricket and golf. Hopefully we'll see Bristol Rovers in the Premier League one day, West Ham deserve a trophy by now and we may even see QPR win promotion in person if the discounted tickets are still available.

Thank you to Rick for introducing me to the biological aspect of this project. Thank you for taking the time to integrate me into the world of biology, without your advice and guidance it would have been far more difficult to understand. Thanks to the Southworth Group, with a special mention going to Ed and Fred for your training and company on those long days in the NMR lab. A big thank you to Dr Peter Gawne and Dr George Keeling for all the help with getting me started in the hot lab and learning the trade of a radiochemist. I am hugely grateful to the staff and students at BMEIS for all the support I have received during my PhD research.

Thank you to all the staff in the Department of Chemistry for their help in completing my PhD research. Special thanks to Pete Haycock for help with NMR, and Dr Lisa Haigh for Mass Spectrometry analysis of my compounds.

To all members of the Long Group, thank you for always being full of laughs, support and making both the lab and office lovely places to be. You truly are amazing people. It would take far too long to list all the friends I've made during my time in the Long Group, but I'm going to anyway. To Sammy, thank you for always being on hand for a quick quiz in the afternoons. Tamara, thanks for all your help and advice on amide couplings. Thank you Luke for being a part of the re-creation of THAT iconic photo. To Marie, thank you for enlightening me in the ways of a Waste Tzar. To Rhiannon, I don't think I will ever again meet anyone who could consistently write 10,000 words per day. To Steph, thank you for also enlightening me on being a Waste Tzar and your advice about anhydrous THF. To Tom, thank you for being my lab and desk neighbour for the best part of 2 years, I am still awaiting news of your entrance into the realm of politics. Thank you Megan, for being the 'mother' of the group, always looking after everyone and acting as a sounding board when things were frustrating. You are the Long Group's best fullback. I'm sure Oxford is treating you well. Troy, hopefully Coventry City and

Scunthorpe United will have as successful football campaigns as they have under your leadership on the gaming console. Ed, I hope West Ham have success like Leicester have had in recent years, maybe Maddison will get a call up eventually. Thanks for all of your help in the lab, we will keep the Rick Astley and Rasputin tradition going forever. Angelo, you will forever be the barbecue head chef. To Saul, I truly think this project would not have been as successful without your unlimited knowledge of chemistry. Thank you for allowing me to regain my love of strategy boardgames and inviting me into your lovely home, and also allowing me to totally annihilate the fellowship in my first taste of War of the Ring. A special mention to my first Long Group friend, Chloe. Thank you for igniting my passion for running, and always being there for me when times were tough. Shane, thank you for sharing the best birthday, please teach me how to master FPL. Jin, if I ever need any radiochemistry advice, I know who to contact. Tom Yue, if I need advice about camping in the wilderness, I know who to call, I'll forgive you for being a Chelsea supporter. Ben, your knowledge of Belgian beer is second to none. William, you never know, Arsenal may win a trophy this year. Katharine, you are 'weally' weird. To the latest additions to the Long Group, Poppy and Titan, you are in good hands.

Thank you to all my family and friends, without you this would not have been possible. A special thank you to my mum, dad and brother Jason, you are the strongest people I have ever known. Thank you for always being a phone call away and providing me with your unwavering support. Mum, I could not have asked for a better role model in life. You have an incredible ability to deal with whatever life throws your way. Jason, although you have had much to deal with in your 21 years, I have never seen you have such confidence and joy in your life as you currently do. Long may it continue. To dad, I know life has dealt you a difficult hand recently, but your recovery could not be better. You may not see it, but we all do. Your motivation to push yourself could not be greater and I'm sure you will keep going no matter the challenge. I will say, if you ever want me to spend an October half-term holiday clearing out bushes and large plants for a new pond, I will be charging more than £20.

To my dearest Tasha, I could not have asked for a more loving, supporting and caring partner. Nearly 10 years and you haven't called it quits. I must be worth it. I promise the proposal is on its way. It's now in writing. I don't think there is a better cook and cleaner duo in the universe. In the words written by J.R.R Tolkien and spoken by Gandalf "All we have to decide is what to do with the time that is given to us". My time is yours.

Abbreviations

[^{18}F]FDG	[^{18}F]fluorodeoxyglucose
a.u.	Arbitrary Unit
AAPA	Arylaldiminophosphinic Acid
ADP	Adenosine Diphosphate
Ar	Aryl
ATP	Adenosine Triphosphate
ATSM	Diacetyl-bis(*N*^{4}-methylsemicarbazone)
BAPDMEN	*N,N*′-Bis(3-aminopropyl)-*N,N*′-dimethylethylenediamine
BAPEN	*N,N*′-Bis(3-aminopropyl)ethylenediamine
BDMAPEN	*N,N*′-Bis(dimethyl)(3-aminopropyl)ethylenediamine
Bn	Benzyl
BnTP	Benzyl-triphenylphosphonium
bpm	Beats Per Minute
CAD	Coronary Artery Disease
CB-DO2A	4,10-Bis(carboxymethyl)-1,4,7,10-tetraazabicyclo[5.5.2]tetradecane
CCCP	Carbonyl Cyanide *m*-Chlorophenyl Hydrazone
CoQ	Ubiquinone
cyclen	1,4,7,10-Tetraazacyclododecane
DCC	Dicyclohexylcarbodiimide
DCM	Dichloromethane
DCU	Dicyclohexylurea
DIPEA	*N,N*′-Diisopropylethylamine
DME	Dimethoxyethane
DMF	Dimethyl Formamide
DMSO	Dimethyl Sulfoxide
DNA	Deoxyribonucleic Acid
DO2A	1,4,7,10-Tetraazacyclododecane-1,7-diacetic Acid
DO3A	1,4,7,10-Tetraazacyclododecane-1,4,7-triacetic Acid
DOTA	1,4,7,10- Tetraazacyclododecane-1,4,7,10-tetraacetic Acid
DOX	Doxorubicin
DPPA	Diphenylphosphorylazide

DTPA	Diethylenetriamine Pentaacetate
EC	Electron Capture
EDTA	Ethylenediaminetetraacetic Acid
EG	Ethylene Glycol
E_m	Membrane Potential
ENBDMPI	(1,2-Ethylenediamino-bis[1-{(phenyl-2-ate)methyleneamino-2,2-dimethyl}-propane]) Iodide
ESI	Electrospray Ionization
Et	Ethyl
ETC	Electron Transport Chain
F	Faraday constant (9.649×10^4 C mol^{-1})
FAD	Flavin Adenine Dinucleotide
FDA	Food and Drug Administration
FT-IR	Fourier Transform Infrared Spectroscopy
H_2dedpa	1,2-((6-Carboxy-pyridin-2-yl)-methylamino)ethane
H_4bsc	Bis(semicarbazone)
H_4btsc	Bis(thiosemicarbazone)
HAPI	(*E*)-*N*′-(1-(2-Hydroxyphenyl)ethylidene)isonicotinohydrazide
HBED	*N,N*′-Di-(2-hydroxybenzoyl)-ethylenediamine-*N,N*′-diacetic acid
HFMA	*N,N*′-[Bis-(2-hydroxy-3-formyl-5-methylbenzyl)(dimethyl)] ethylenediamine
HMBC	Heteronuclear Multiple Bond Correlation
HMQC	Heteronuclear Multiple Quantum Coherence
HMTA	Hexamethylenetetramine
HPLC	High-Performance Liquid Chromatography
HR	Heart Rate
HRMS	High-Resolution Mass Spectrometry
i.p.	Intraperitoneal
^{i}Pr	*Iso*-propyl
iTLC	Instant Thin Layer Chromatography
IU	International Unit
JC-1	1,1′,3,3′-Tetraethyl-5,5′,6,6′-tetrachloroimidacarbocyanine Iodide
LC	Liquid Chromatography

log *D*	Distribution Coefficient
LVDP	Left Ventricular Diastolic Pressure
LVEDP	Left Ventricular End Diastolic Pressure
LVEF	Left Ventricular Ejection Fraction
MALDI	Matrix-Assisted Laser Desorption/Ionization
Me	Methyl
MIBI	[^{99m}Tc]Tc-Sestamibi
mKHB	Modified Krebs-Henseleit Buffer
MRI	Magnetic Resonance Imaging
MS	Mass Spectrometry
MUGA	Multigated Acquisition
NAD	Nicotinamide Adenine Dinucleotide
NBS	*N*-Bromosuccinimide
NMR	Nuclear Magnetic Resonance Spectroscopy
NOC	1-Nal3-octreotide
NODAGA	1,4,7-Triazacyclononane,1-glutaric acid-4,7-acetic Acid
NOET	Bis(*N*-ethoxy,*N*-ethyl Dithiocarbamato) Nitrido
NOTA	1,4,7- Triazacyclononane-1,4,7-triacetic Acid
ORTEP	Oak Ridge Thermal-Ellipsoid Plot Program
p.i.	Post Injection
PBS	Phosphate-Buffered Saline
PET	Positron Emission Tomography
P_i	Inorganic Phosphate
PP	Perfusion Pressure
ppm	Parts Per Million
PSMA	Prostate-Specific Membrane Antigen
PTSM	Pyruvaldehyde Bis(N^4-methylthiosemicarbazone)
QC	Quality Control
R	Ideal Gas Constant (8.314 J mol^{-1} K^{-1})
RCP	Radiochemical Purity
RCY	Radiochemical Yield
R_f	Retention Factor
ROS	Reactive Oxygen Species

rt	Room Temperature
SC	Semicarbazide
SD	Standard Deviation
SIH	Salicylaldehyde Isonicotinoyl Hydrazone
SPECT	Single Photon Emission Computed Tomography
SSR	Somatostatin Receptor
T	Temperature
t	Time
TACN	1,4,7-Triazacyclononane
TAEP	Triaryletherphosphonium
TAP	Triarylphosphonium
TATE	[Tyr3]-Octreotate
TDiMeOPP	Tri-*m*,*m*′-dimethoxyphenylphosphonium
TEA	Triethylamine
TETA	1,4,8,11-Tetraazacyclotetradecane-*N*,*N*′,*N*″,*N*‴-tetraacetic Acid
TEtOPP	Tri-*p*-ethoxyphenylphosphonium
TFA	Trifluoroacetic Acid
THF	Tetrahydrofuran
THP	Tris(hydroxypyridinone)
TLC	Thin Layer Chromatography
TMeOPP	Tri-*p*-methoxyphenylphosphonium
TMRE	Tetramethylrhodamine, Ethyl Ester
TOC	[Tyr3]-Octreotide
TOF	Time of Flight
TOM	Translocase of the Outer Membrane
TPMP	Methyltriphenylphosphonium
TPP	Triphenylphosphonium
TRAP	3,3′,3”-(((1,4,7-triazonane-1,4,7-triyl)tris(methylene)) tris(hydroxyphosphoryl))tripropanoic Acid
tRNA	Transfer Ribonucleic Acid
TTP	Tritolylphosphonium
TXP	Trixylylphosphonium
UCP	Mitochondrial Uncoupling Protein

UV	Ultraviolet
xy	Xylyl
z	Charge
$\Delta\Psi_m$	Mitochondrial Membrane Potential
$\Delta\Psi_p$	Plasma Membrane Potential

Index of New Compounds

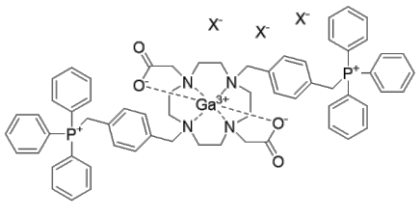

Ga-DO2A(-xy-TPP)$_2$
Ga1a
(X = NO_3^-, Cl^-, TFA^-)

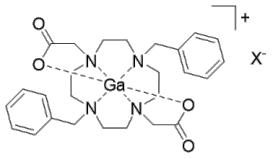

Ga-DO2A-Bn$_2$
Ga1b
(X = NO_3^-, Cl^-, TFA^-)

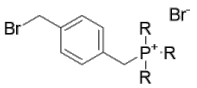

Br-xy-TAEP
4d-f

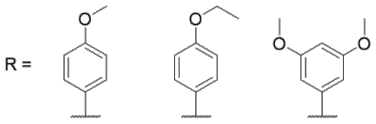

(d) TMeOPP (e) TEtOPP (f) TDiMeOPP

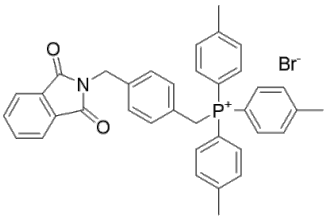

Phth-xy-TTP
5b

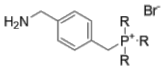

NH_2-xy-TAP/TAEP
6a-f

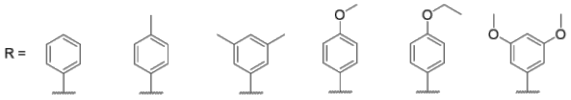

(a) TPP (b) TTP (c) TXP (d) TMeOPP (e) TEtOPP (f) TDiMeOPP

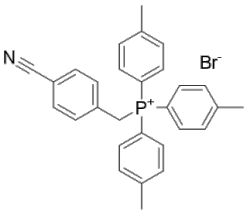

CN-xy-TTP
8b

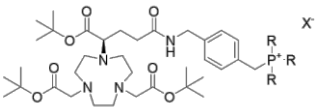

NODAGA(^{t}Bu)$_3$-xy-TAP/TAEP
9a-f
(X = Br^-, TFA^-)

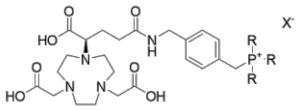

NODAGA-xy-TAP/TAEP
10a-f
(X = Br^-, TFA^-)

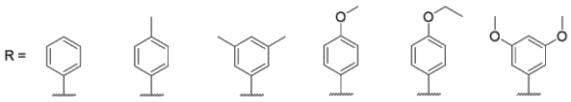

(a) TPP (b) TTP (c) TXP (d) TMeOPP (e) TEtOPP (f) TDiMeOPP

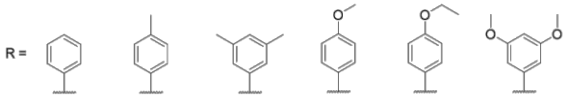

(a) TPP (b) TTP (c) TXP (d) TMeOPP (e) TEtOPP (f) TDiMeOPP

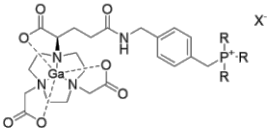

Ga-NODAGA-xy-TAP/TAEP
Ga10a-f
(X = Br^-, TFA^-, NO_3^-)

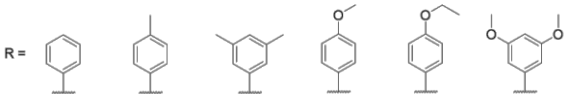

(a) TPP (b) TTP (c) TXP (d) TMeOPP (e) TEtOPP (f) TDiMeOPP

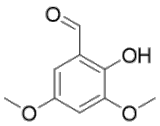

2-Hydroxy-3,5-dimethoxybenzaldehyde
14a

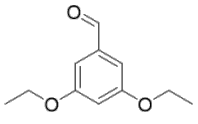

3,5-Diethoxybenzaldehyde
15b

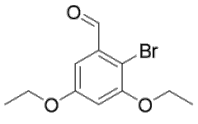

2-Bromo-3,5-diethoxybenzaldehyde
16b

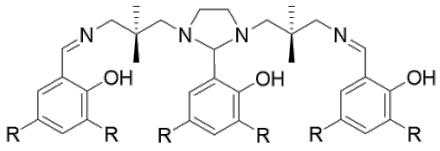

(3,5-Dialkoxysalicylaldehyde)$_2$BDMAPEN
18a-c
R = OMe (a), OEt (b), O^{i}Pr (c)

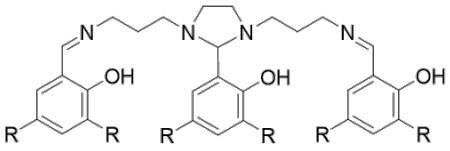

Bis(3,5-dialkoxysalicylaldehyde)BAPEN
19a-c
R = OMe (a), OEt (b), O^{i}Pr (c)

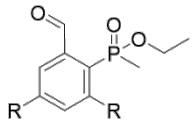

2-Ethyl(methyl)phosphinate-3,5-dialkoxybenzaldehyde
23a-c
R = OMe (a), OEt (b), O^{i}Pr (c)

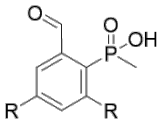

2-Methylphosphinic acid-3,5-dialkoxybenzaldehyde
24a-c
R = OMe (a), OEt (b), O^{i}Pr (c)

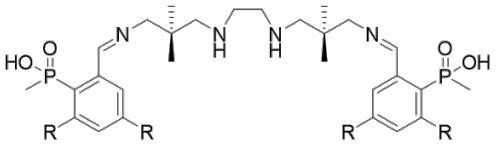

Bis(AAPA)BDMAPEN
25a-c
R = OMe (a), OEt (b), O^{i}Pr (c)

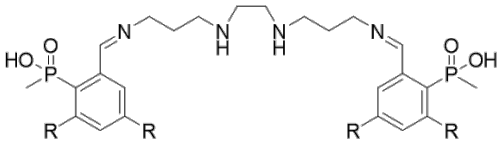

Bis(AAPA)BAPEN
26a-c
R = OMe (a), OEt (b), O^{i}Pr (c)

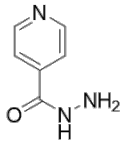

Isonicotinohydrazide
28

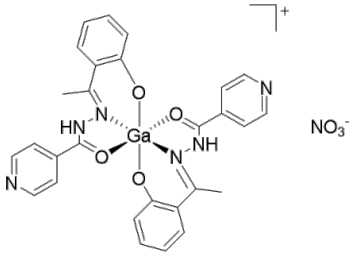

[Ga(HAPI)$_2$][NO$_3$]
30

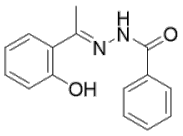

(E)-*N'*-(1-(2-hydroxyphenyl)ethylidene)benzohydrazide
32

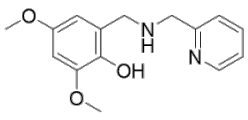

L^{DiOMe}
34

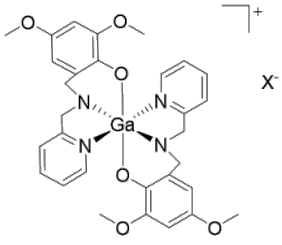

[Ga(L^{DiOMe})$_2$][X]
Ga34
(X = NO$_3^-$, ClO$_4^-$)

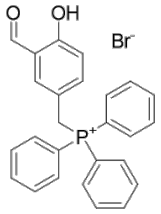

(5-TPPmethyl)-2-hydroxybenzaldehyde bromide
36

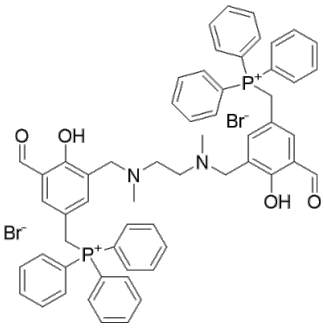

Salan-(2-formyl-4-methylTPP)$_2$ dibromide
37

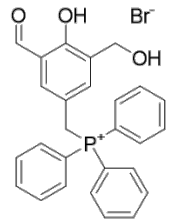

(3-(Hydroxymethyl)-5-formyl-4-hydroxybenzyl)TPP bromide
40

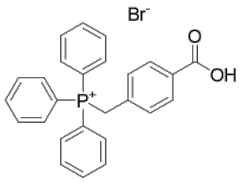

(4-Carboxybenzyl)TPP bromide
41

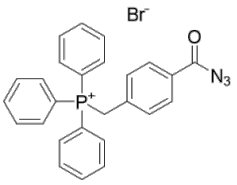

(4-Azidocarboxybenzyl)TPP bromide
42

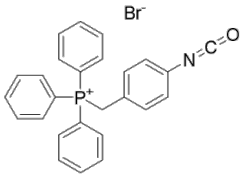

(4-Isocyanatobenzyl)TPP bromide
43

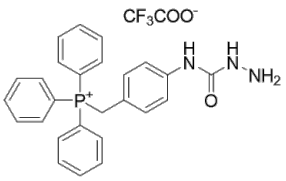

SC_BnTPP
44

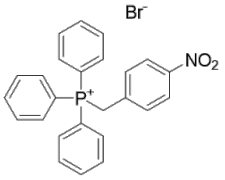

Nitro-benzylTPP
45

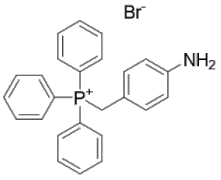

Amino-benzylTPP
46

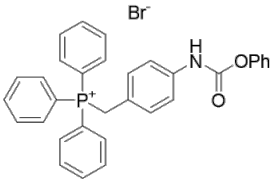

Phenylcarbamate-benzylTPP
47

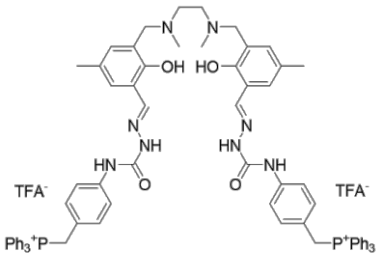

H$_4$bsc-(TPP)$_2$
48

Index of Known Compounds

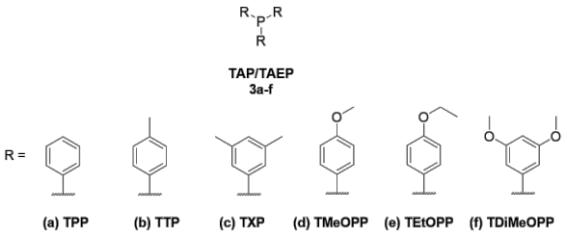

TAP/TAEP
3a-f

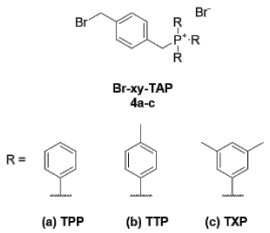

Br-xy-TAP
4a-c

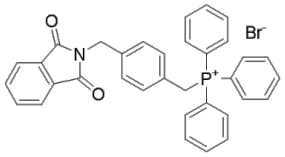

Phth-xy-TPP
5a

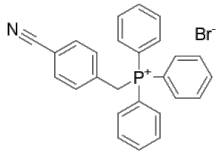

CN-xy-TPP
8a

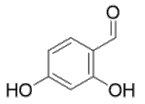

2,4-Dihydroxybenzaldehyde
11

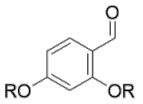

2,4-Dialkoxybenzaldehyde
12a-b
(R = Me, Et)

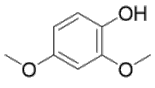

2,4-Dimethoxyphenol
13a

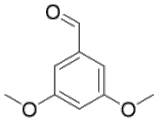

3,5-Dimethoxybenzaldehyde
15a

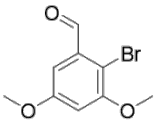

2-Bromo-3,5-dimethoxybenzaldehyde
16a

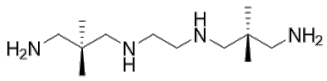

Bis(*N*,*N*'-amino-2,2-dimethylpropane)ethylenediamine
17

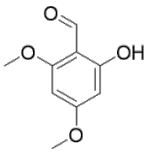

2-Hydroxy-4,6-dimethoxybenzaldehyde
20

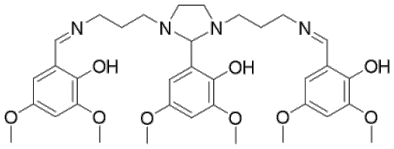

$(4,6(MeO)_2sal)_2BAPEN$
21

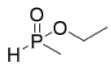

Ethyl methylphosphinate
22

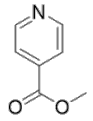

Methyl isonicotinate
27

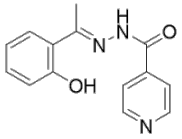

HAPI
29

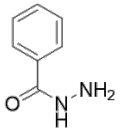

Benzohydrazide
31

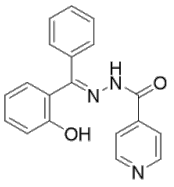

33

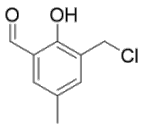

(3-Chloromethyl)-2-hydroxy-5-methylbenzaldehyde
38

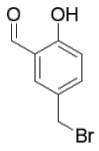

(5-Bromomethyl)-2-hydroxybenzaldehyde
35

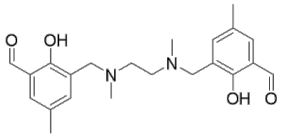

HFMA
39

CHAPTER 1 - INTRODUCTION

1. Introduction

This thesis describes research carried out in a joint project between Imperial College London and King's College London. The research focuses on the development of novel lipophilic and cationic gallium-68 radiotracers for imaging mitochondrial function and dysfunction. The tendency for the radiotracer to be retained in the mitochondria can give an indication of the membrane potential and mitochondrial disease state. This chapter aims to provide an introduction to the range of research topics involved in this work, first, with an overview of the biology of the mitochondria, including the mitochondrial membrane potential and disease states arising from mitochondrial function or dysfunction, with a focus on anthracycline-induced cardiotoxicity. Secondly, nuclear imaging techniques single-photon emission computed tomography (SPECT) and positron emission tomography (PET) will be outlined, leading to a detailed discussion of the coordination chemistry and radiochemistry of gallium-68. Finally, the current uses of lipophilic and cationic radiotracers for mitochondrial imaging will be discussed.

1.1 Mitochondria

Mitochondria are membrane bound organelles that are found in the majority of eukaryotic cells, these are multi-component cells which make up all multi cellular organisms and are commonly referred to as the building blocks of complex life.[1] The primary role of the mitochondria is the synthesis of adenosine triphosphate (ATP) from adenosine diphosphate (ADP) and inorganic phosphate (P_i) via a series of biochemical steps. This process is required to provide energy to a vast range of biological processes throughout the organism. Mitochondria are also responsible for multiple other processes, such as cellular growth, as well as providing a platform for cell signalling and cell death. The vast list of processes the mitochondria are responsible for emphasises how fundamental they are for cell life and death.[2,3]

1.1.1 Mitochondrial Structure

The structure of the mitochondria, shown in **Figure 1.1**, highlights the components which make up this organelle. Mitochondria are separated from the cytoplasm by two phospholipid bilayers, the outer and inner mitochondrial membranes. The outer membrane encloses the mitochondrion which is freely permeable, and this allows free passage of ions and small, uncharged molecules through pore-forming membrane proteins (porins).[4] Porins are one of two

different types of transport protein which are integrated into the membrane, with translocase of the outer membrane (TOM) being the second type. Proteins with a mass of less than 6 kD enter the organelle by diffusion with the assistance of porins, whereas larger proteins require TOM for passage through the outer membrane.[5]

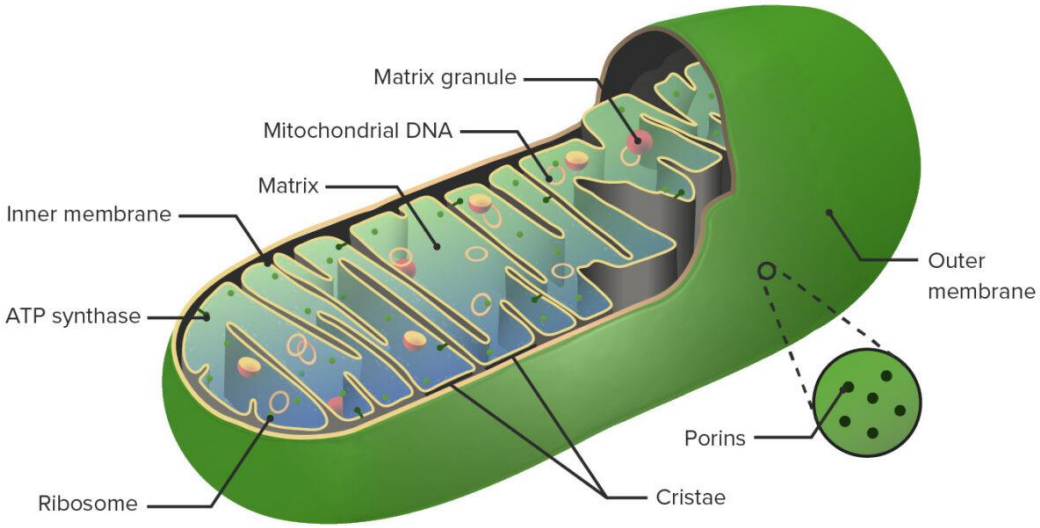

Figure 1.1 Cartoon image of the structure of the mitochondria, highlighting the major components. Image taken from www.lecturio.com.[6]

The inner membrane is more complex than the outer membrane. It separates the intermembrane space and the matrix, and small molecules such as carbon dioxide, oxygen and water can freely diffuse through the inner membrane. A variety of specialised proteins and phospholipids are contained within the inner membrane, including the complexes of the electron transport chain and ATP synthase, along with transport proteins which cause the membrane to be selectively permeable to small molecules that are required by enzymes situated in the matrix. In contrast to this, the inner membrane is highly impermeable to most other molecules including ions, which require active transport. High impermeability to ions is likely due to the high proportion of 'double' phospholipid *cardiolipin* situated in the membrane.[7]

The intermembrane space lies between the outer and inner membrane, and acts as the bridge between these two membranes. The permeable outer membrane means that small molecules can freely enter the intermembrane space, thus the concentration of small molecules internally is the same as that in the cytosol. Larger molecules, however, require active transport by membrane-bound proteins to enter the intermembrane space. Folding of the inner membrane forms compartments in the mitochondria, known as the cristae. The large surface area of the cristae means they are ideal locations for chemical processes to occur, and as such contain

enzymes such as ATP synthase and cytochromes, therefore they are the main sites of mitochondrial energy conversion.

The matrix is the space encapsulated by the inner mitochondrial membrane and contains a highly concentrated mixture of compounds vital to the mitochondria, including tRNA, special mitochondrial ribosomes, enzymes and mitochondrial DNA. The matrix is the production area for ATP and contains mitochondrial enzymes required for the oxidation of pyruvate and fatty acids, alongside enzymes carrying out the citric acid cycle involving the reduction of NAD^+ to NADH.

1.1.2 ATP Synthase and the Electron Transport Chain

ATP is used as an energy source for most cellular processes, as the conversion of ATP from ADP and P_i releases a large amount of energy. The consequence of this is that a considerable amount of energy is needed to reform ATP via oxidative phosphorylation so it can be reused for other cellular processes. ATP synthase is the universal enzyme that produces ATP from ADP and P_i through oxidative phosphorylation, shown in **Figure 1.2**.[8]

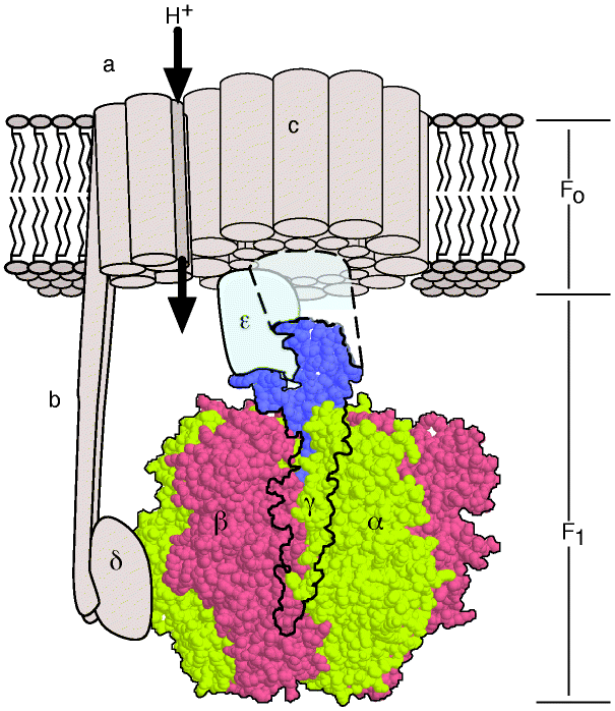

Figure 1.2 Illustration of ATP Synthase, showing the transmembrane component (F_0), and the soluble portion (F_1), along with the flow direction of protons through the enzyme. Reprinted with permission from Wang *et al*.[8] Nature © Macmillan Publishers Ltd 1998.

ATP synthase consists of two parts, a rotating soluble component (F_1) which contains the catalytic sites, and a static membrane-spanning component (F_0) comprised of the proton channel. The flow of protons through the proton channels situated in F_0 generate an electrostatic torque which is transmitted to F_1 by an asymmetrical shaft, known as the γ-subunit. The generated torque drives the rotor and stator in opposite directions. The assembly consisting of a, b, δ and the F_1 hexamer is defined as the 'stator', with components c, γ and ε being defined as the 'rotor'. As the γ-subunit rotates, the three active catalytic sites contained in F_1 undergo conformational changes facilitating the uptake of ADP and P_i, the synthesis of ATP and the release of synthesised ATP from the enzyme. The free-energy difference across the inner mitochondrial membrane is adequate for ATP synthase to produce three ATP molecules for every twelve protons passing through the enzyme.[9]

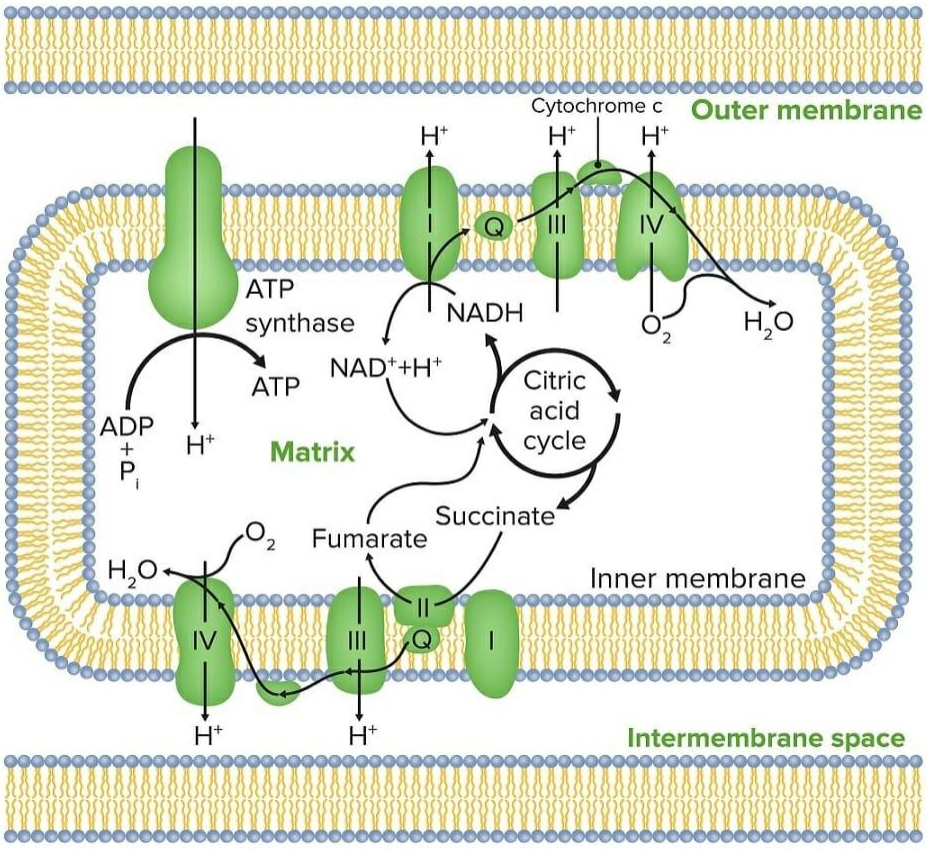

Figure 1.3 Diagram of the electron transport chain (ETC), including ATP synthase, key proteins within the inner mitochondrial membrane and the citric acid cycle. Image taken from www.lecturio.com.[6]

The electron transport chain (ETC) consists of a series of four protein complexes that couple redox reactions, leading to an electrochemical gradient across the inner mitochondrial membrane that results in the generation of ATP.[10,11] The ETC is linked to the effective function

of ATP synthase due to its dependency on the proton gradient to create ATP. As depicted in **Figure 1.3**, the transfer of electrons from electron donors to electron acceptors leads to protons being pumped from the mitochondrial matrix to the intermembrane space, creating a proton gradient.[6,10] The breakdown of glucose by glycolysis and the citric acid cycle yield the electron carriers NADH and $FADH_2$. Electrons from NADH and $FADH_2$ are transferred to O_2 leading to large amounts of energy being released from these redox reactions, which are used to drive the formation of ATP via oxidative phosphorylation.[12] Electrons from NADH enter the ETC through the reduction of NADH to NAD+ at complex I. In complex I, a series of reduction and oxidation reactions occur, leading to a release of energy and the pumping of protons from the mitochondrial matrix to the intermembrane space. In complex II, electrons are transferred to $FADH_2$, instead of NADH, and then to ubiquinone (CoQ). A lower energy barrier is associated with the transfer of electrons from $FADH_2$ to CoQ, meaning less energy is released and complex II cannot pump protons across the inner membrane.

CoQ functions as an electron carrier, and transfers electrons through the membrane to complex III, also known as cytochrome c reductase, in its fully reduced form, $CoQH_2$. The movement of electrons through complex III is associated with a second proton being pumped across the inner membrane, before cytochrome c, an electron carrier protein, transfers the electrons to complex IV (cytochrome c oxidase). Two important functions are performed by complex IV; first, a third proton is pumped out of the matrix and secondly, four electrons are used to reduce one molecule of O_2, which then accepts protons in the matrix to generate two molecules of H_2O.

1.1.3 Membrane Potentials of Living Cells

The coupling of the electron transport chain (ETC) and oxidative phosphorylation results in a proton gradient existing across the inner mitochondrial membrane. As shown in **Figure 1.4**, a higher concentration of protons exists in the intermembrane space compared to the matrix, and this helps to drive the activity of ATP synthase. In healthy functioning mitochondria, the mitochondrial membrane potential ($\Delta\Psi_m$) is between 150-180 mV, with this value being negative inside the matrix.[13] Lipophilic and cationic substrates can pass easily through lipid bilayer membranes because their positive charge is dispersed over a large surface area and the electrostatic gradient drives their accumulation into the matrix. As well as the $\Delta\Psi_m$, a plasma membrane potential ($\Delta\Psi_p$) exists in eukaryotic cells across the cell membrane. The $\Delta\Psi_p$ arises from the distribution of ions across the membrane, with Na^+, Ca^{2+} and Cl^- ions having higher

extracellular concentrations, and K^+ cations at high concentrations in the intracellular compartment (in the cytosol).

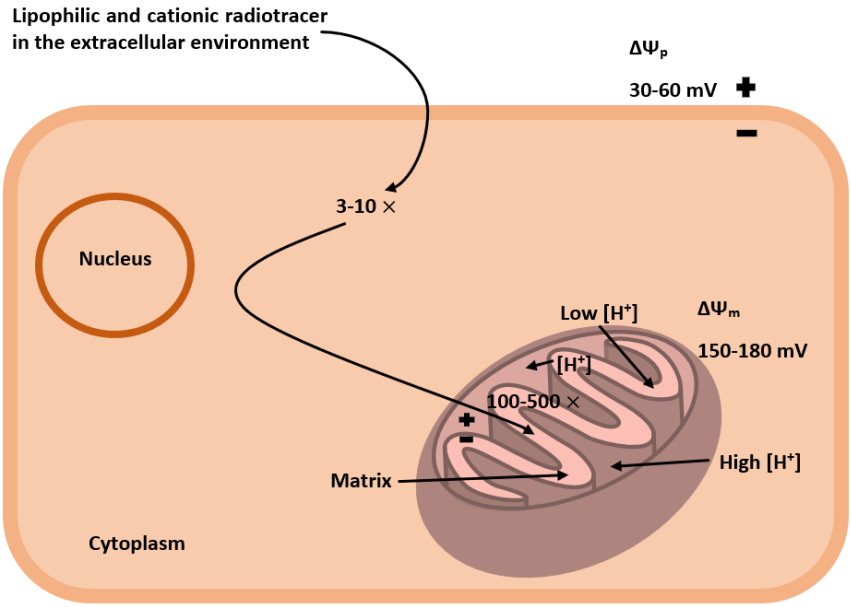

Figure 1.4 A schematic showing the uptake of cationic substrates into the cytoplasm from the extracellular environment, driven by the plasma membrane potential ($\Delta\Psi_p$) that exists across the cell membrane. The cationic substrate is then further accumulated into the mitochondria from the cytoplasm, driven by the mitochondrial membrane potential ($\Delta\Psi_m$) that exists across the inner mitochondrial membrane. Schematic adaptation from Murphy *et al.*[13]

Hydrophilic ion channels that span the cell membrane allow the plasma membrane to be fully permeable to K^+, Na^+ and Cl^- ions. The membrane-bound enzyme, Na^+/K^+-ATPase, maintains the $\Delta\Psi_p$ by pumping Na^+ and K^+ cations against their respective concentration gradients. In normally functioning cells, the $\Delta\Psi_p$ is between 30-60 mV.[14] Cardiac cells exhibit a significantly greater range of $\Delta\Psi_p$ values compared to other eukaryotic cells. This wider range of $\Delta\Psi_p$ values is due to a process called the excitation-contraction coupling, which enables the chambers of the heart to contract and relax.[15] Ca^{2+} cations are considered the most crucial ions in this process, due to their role as the direct activator of cardiac myofilaments, which cause contraction. Contraction is dependent on the concentration of Ca^{2+} cations ($[Ca^{2+}]$), among other factors, which varies throughout the cardiac cycle and results in $\Delta\Psi_p$ values between -90 and +40 mV.

1.1.4 Mitochondrial Uptake of Cations: Biophysical Rationale

The $\Delta\Psi_m$ is substantially greater than any other membrane potential in eukaryotic cells, including $\Delta\Psi_p$, which results in cations being selectively attracted into the mitochondrial matrix from the extracellular environment.[14,16] In order to reach and accumulate in the mitochondrial matrix, cations are attracted across the cell membrane into the cytoplasm by $\Delta\Psi_p$, before being attracted into the matrix by $\Delta\Psi_m$. At equilibrium, the concentrations of the ion on both sides of the membrane can be described by the Nernst equation:

$$E_m = \frac{RT}{zF} ln\left(\frac{[out]}{[in]}\right) \quad \textbf{(Equation 1.1)}$$

where: R is the universal gas constant (8.314 J mol^{-1} K^{-1}), T is the temperature (K), z is the valence of the charged species, F is the Faraday constant (9.649×10^4 C mol^{-1}), [out] and [in] are the concentrations of the charged species outside and inside the membrane respectively, and E_m is the membrane potential being studied. For a mono-cationic species being attracted across a membrane with a potential E_m, which is negative inside, positive outside and at the temperature of 37 °C, known values can be substituted in **Equation 1.1** to give **Equation 1.2**.[14,16–18]

$$E_m(mV) = 61.5 \times log_{10}\left(\frac{[out]}{[in]}\right) \quad \textbf{(Equation 1.2)}$$

Equation 1.2 shows that any increase in E_m also results in an increase in the charged species concentration inside the membrane and the mitochondrial matrix. As illustrated in **Figure 1.4**, in healthy functioning mitochondrion, the $\Delta\Psi_p$, typically 30-60 mV, leads to a 3-5 fold increase in cation uptake compared to the extracellular environment. The $\Delta\Psi_m$ exhibits a typical range of 120-180 mV and leads to further increases in cation uptake by a factor of 100-500 in the matrix.[13]

1.1.5 Exploiting Membrane Potentials to Target Mitochondria

The $\Delta\Psi_m$ reflects the functional status of the mitochondria and can be correlated with several different cellular pathologies. This heterogeneity of $\Delta\Psi_m$ means the uptake of lipophilic cations can be related to various disease states, with one such example being tumour cells, which exhibit a significant increase in $\Delta\Psi_m$ when compared to healthy cells.[19–22] Numerous studies have described carcinoma-derived cells, such as breast cancer, prostate cancer and melanomas, as possessing $\Delta\Psi_m$ values of at least 60 mV above that exhibited by normal epithelial cells. A

number of explanations have been proposed to explain the origin of this hyperpolarisation. The first explanation is that hyperpolarisation is a result of increased metabolism rates that occur in tumour cells, leading to an increase in the rate of production of ATP by ATP synthase. However, this explanation presents complications, with one being that at $\Delta\Psi_m$ = ~-120 mV, ATP synthase functions optimally compared to in hyperpolarised conditions. Cancer cells also use glycolysis more readily as a metabolic pathway for energy metabolism, meaning cancer cells should be less dependent on ATP for energy, therefore less dependent on mitochondria as an energy source.

A secondary explanation for the hyperpolarisation of $\Delta\Psi_m$ in tumour mitochondria involves the underexpression of mitochondrial uncoupling proteins (UCPs) in cancer stem cells.[22] In 2006, Derdak *et al*. reported that UCP2-knockout mice developed more colon tumours than UCP2-expressing littermates.[23] Considering that UCPs primary function is to dissipate $\Delta\Psi_m$ as heat, their underexpression in tumour cells gives rise to higher $\Delta\Psi_m$ values. Additionally, mitochondrial hyperpolarisation may correlate with tumorigenic properties of cancer stem cells, such as their resistance to apoptosis. A higher $\Delta\Psi_m$ value may prove protective against tumour cell death, since the dissipation of $\Delta\Psi_m$ is proposed to be an important step in apoptosis.[24,25]

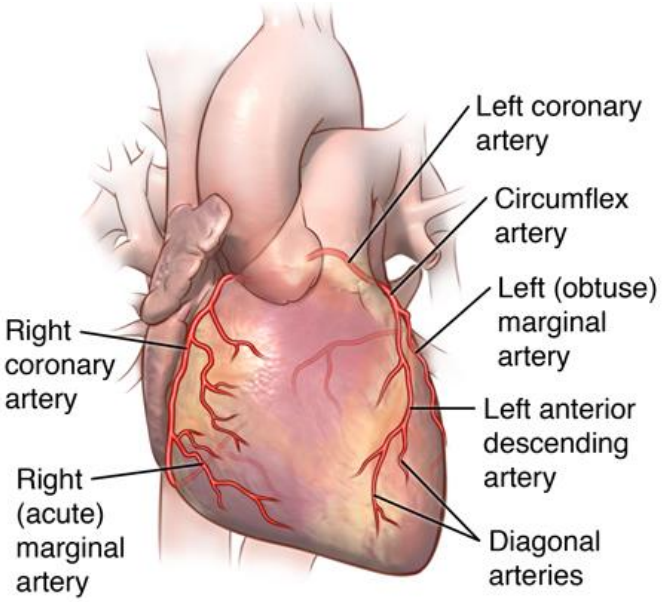

Figure 1.5 Diagram showing the coronary arteries of the heart. Picture taken from www.hopkinsmedicine.org.[26]

The heart synthesizes approximately 30 kg of ATP per day, which means that the heart is under a constant high workload. Cardiomyocytes, the cells responsible for generating the contractile force in the heart, each contain 5000 mitochondria to maintain the high workload and synthesize the significant amount of ATP per day.[27] Like all eukaryotic cells, cardiomyocytes require oxygen to function efficiently. This oxygen is provided by oxygenated blood in the coronary arteries, shown in **Figure 1.5**, that perfuse the myocardium. When cardiomyocytes are no longer supplied with oxygen, the ETC can no longer function efficiently due to no oxygen being available to accept the electron at the end of the chain, shown in **Figure 1.3**. Cardiomyocytes may not be supplied with oxygen if there is an arterial blockage or rupture, to name two examples. Healthy cardiac mitochondria have relatively low $\Delta\Psi_m$ values of 100-140 mV, whereas hearts suffering from ischemia/reperfusion injury exhibit increases in $\Delta\Psi_m$ values of up to 200 mV when under such stress. The $\Delta\Psi_m$ values gradually reach zero as the mitochondria begin to degrade and cease to function.[28] This leads to a reduction in the uptake of mitochondrial cations in damaged heart tissue.

1.1.5.1 Detection of Anthracycline-Induced Cardiotoxicity

Anthracyclines are the most studied anticancer drugs with established cardiotoxic effects, which drastically affect the magnitude of the mitochondrial membrane potential.[29] Anthracyclines are a primary chemotherapeutic employed to treat a variety of malignancies, including breast, gastric and lung carcinoma.[30,31] However, they are highly toxic to the heart, and may induce coronary and valvular heart disease, cardiomyopathy and heart failure.[32–34] The primary clinical focus in oncology is on the treatment of the cancer, with the cardiovascular outcome being the secondary concern, and as such, cardiovascular disease is the leading non-malignant cause of death in cancer.[35] The possibility of anthracycline-induced cardiac injury is generally dose-dependent, with the risk increasing dramatically when higher cumulative doses are administered for treatment of the malignancy.[36] As well as being dose-dependent, anthracycline-induced cardiac injury depends on a number of factors such as age, gender, pre- and/or co-existing disease, and the rate and frequency of drug administration.[37–42] The timeline of cardiotoxicity development can vary from weeks to years following administration of the chemotherapy, meaning that clinical presentation may occur years after the initial damage.[36] A delay in the development of symptoms creates a significant challenge for treating cardiotoxic effects, especially when such a vast number of variables need to be considered in order to provide a personalized chemotherapeutic dosage whilst minimizing cardiac injury. Although

the precise mechanism of anthracycline cardiotoxicity is unclear, proposed mechanisms involve the generation of reactive oxygen species (ROS), mitochondrial iron accumulation, disruption of mitochondrial biogenesis, alteration of cell survival and cell death pathways.[43–48]

Cardiotoxicity is routinely monitored by clinicians using echocardiography or multigated acquisition (MUGA) scanning.[49,50] It is typically defined as an asymptomatic loss of more than 10 % of the left ventricular ejection fraction (LVEF), however the intra-observer variability by echocardiography itself is 10 %, meaning the technique is at its limit of sensitivity.[51,52] The loss of contractile function is a late and irreversible event, and significant injury is evident in biopsies, long before contractile changes are identifiable. Cardiotoxicity is initiated at the subcellular level, analogous with changes in $\Delta\Psi_m$ and ROS generation, therefore by the time contractile dysfunction is detectable, the window for effective intervention has probably passed.[53] Being able to detect the evolution of cardiac injury at the subcellular level using non-invasive molecular imaging techniques, before contractile dysfunction occurs would be hugely clinically favourable for earlier cardioprotective intervention and could possibly accelerate cardioprotective drug development.

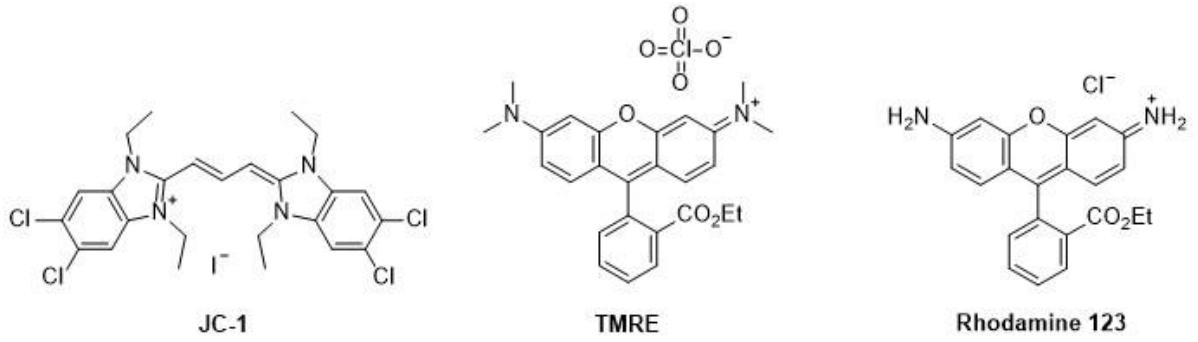

Figure 1.6 The structures of fluorescent lipophilic cations (JC-1[54], TMRE[55] and Rhodamine 123[56]), widely used to report on mitochondrial function *in vitro*.

Fluorescent lipophilic cations such as JC-1, TMRE and Rhodamine 123, shown in **Figure 1.6**, are widely used to measure $\Delta\Psi_m$, through accumulation by passive diffusion through cell membranes of mitochondria, in an *in vitro* context.[54–56] However, due to poor depth penetration and lack of whole body scanning, these fluorescent probes have minimal usefulness *in vivo*. The Southworth Group at King's College London have previously demonstrated the promise of utilising radiolabelled lipophilic cations to report on anthracycline-induced mitochondrial dysfunction. First, a well-established fluorine-18-based ROS probe was repurposed for the direct detection of superoxide *in vivo*.[57] Secondly, the SPECT imaging agent

[^{99m}Tc]Tc-sestamibi (MIBI), shown in **Figure 1.16**, which is routinely used in myocardial perfusion imaging, is dependent on both $\Delta\Psi_m$ and regional perfusion for its mitochondrial uptake. The cardiac retention of MIBI was corrected for variations in perfusion using [^{99m}Tc]Tc-NOET, the uptake of which is $\Delta\Psi_m$-independent, in order to repurpose MIBI to specifically report on $\Delta\Psi_m$ as a readout of mitochondrial cardiotoxicity.[58] By developing a PET 'equivalent', an approach to report on mitochondrial dysfunction with higher resolution imaging could be obtained and would facilitate the beneficial application of pharmacokinetic modelling.

1.1.6 Lipophilicity Contributions to Mitochondrial Uptake

Lipophilicity is an important property that governs a tracer's ability to permeate lipid bilayer membranes in order to reach the target cells. The uptake of cationic species through the intermembrane space into the mitochondrial matrix is therefore governed by its lipophilicity as well as the extent of its delocalised positive charge. Both cellular and mitochondrial membranes are formed of phospholipid bilayers, which consist of a hydrophobic 'tail' made up of two fatty acid chains and a hydrophilic phosphate 'head'. A hydrophobic region therefore exists in the membrane, meaning a targeted probe must be lipophilic enough to cross the intermembrane space. However, if the probe is too lipophilic, it will not fully permeate the phospholipid bilayer membrane and remain trapped inside the hydrophobic region. The ideal lipophilicity for uptake into the mitochondria is still an ongoing debate. Successful lipophilic and cationic radiotracers MIBI and [^{18}F]FBnTP, which exhibit mean distribution coefficients (log *D*) values of 1.29 and -0.38 respectively epitomise this.[59,60] Developing a radiotracer that exhibits 'optimal' lipophilicity and while maintaining a delocalised positive charge is the key challenge and focus at present in this area of tracer development.

1.2 SPECT Imaging

There are a number of non-invasive imaging modalities, summarised in **Table 1.1**, that can be employed for imaging mitochondrial function.[61] The focus in this thesis will be on two of the most common nuclear imaging modalities, Single Photon Emission Computed Tomography (SPECT) and Positron Emission Tomography (PET). As illustrated in **Table 1.1**, no individual molecular imaging modality can be utilised for every purpose. For example, to effectively image mitochondrial function, an imaging modality with superior cell penetration, as seen with contrast agents for Magnetic Resonance Imaging (MRI), and optimal depth penetration of

signal would be required to image the intracellular organelle. Due to the significant increase of mitochondrial targeted tracers from the extracellular environment to the mitochondrial matrix, an imaging technique that requires a high concentration of tracer to be administered, could be toxic for the mitochondria. Using this brief, the nuclear imaging techniques PET and SPECT have the most suitable properties to image and report on mitochondrial function.

Table 1.1 Qualitative summary of non-invasive molecular imaging modalities.[61]

Modality	Resolution	Depth Penetration	Sensitivity	Ionising Radiation	Tracer Quantities
Optical	Variable	Low (cm)	High	No	High
MRI	Moderate (μm)	No Limit	Low	No	High (mM)
Ultrasound	Moderate (μm)	Moderate (mm-cm)	Moderate	No	High
SPECT	Low (mm)	No Limit	High	Yes	Low (pM)
PET	Low (mm)	No Limit	High	Yes	Low (pM)

Both nuclear imaging modalities generate images through the detection of high energy gamma (γ) photons, and with low tissue interaction, have superior depth penetration and very high sensitivity. This means that very low quantities of tracer are needed to produce quality images for clinical use. However, the exposure to ionising radiation does put patients at greater risk of harm compared to other techniques and the source of ionising radiation is typically very expensive. Generators that are used as sources for SPECT-based radioisotopes are widely available, leading to SPECT being much less expensive than PET, which frequently requires a cyclotron for radioisotope production. Cyclotrons are considerably expensive to operate and maintain. However, PET is significantly more sensitive compared to SPECT, along with providing greater spatial resolution, resulting in higher quality images which can be used to determine accurate pharmacokinetic profiles of tracers.[62,63]

1.2.1 Principles of SPECT Imaging

Since its initial demonstration by Kuhl and Edwards in 1963, SPECT has undergone major development to reach the stage of being clinically applicable and commercially available.[64] SPECT involves the emission of a single γ-ray per nuclear disintegration produced by radionuclides, as they relax from their excited daughter nuclei, which are produced by parent nuclei that have undergone α- or β-emission. A great number of singular γ-rays are detected by rotating gamma cameras, which consist of three basic layers. As shown in **Figure 1.7**, γ-rays

enter the camera through a collimator, which is a special lens that only allows entry of γ-rays that are perpendicular to the plane of the camera. Collinear γ-rays collide with a scintillator, producing an electron that passes through a photomultiplier tube, which concentrates the presence of electrons in the tube and increases the sensitivity of the gamma camera.

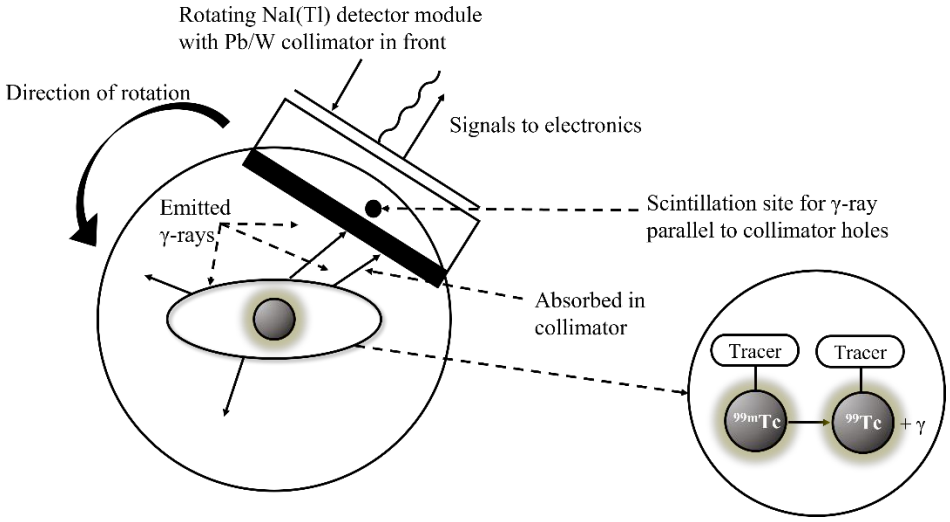

Figure 1.7 Schematic diagram showing the basic principles of SPECT. Schematic adapted from Long and Wong.[61]

The gamma camera contains a crystal, typically a thallium-activated sodium iodide [NaI(Tl)] crystal, which absorbs γ-rays and scintillates to generate a light signal which is detected. The gamma detector is made up of a few cameras which are diametrically opposed to one another to form a cylindrical detector, allowing for movement around the patient. By using multiple cameras, the cylindrical detector only needs to rotate 120-180 degrees to accurately collect enough data to generate an image of the entire body. Different techniques are used to build up 2D and 3D cross-sectional images, with the most common reconstruction method being the back-projection method, which produces 2D cross-sectional images of activity from a slice within the detected area using projection profiles for the slice of interest. However, this leads to poorer spatial resolution than the raw 2D images. Direct Fourier transform reconstruction is an algorithmic technique used to improve the decreased spatial resolution. Filtered back-projection is a desirable analytical reconstruction method for data reconstruction, and can be utilised to visualise 3D biodistribution profiles of radiotracers.[61]

1.2.2 Technetium-99m (^{99m}Tc)

The most widely used SPECT radioisotope is technetium-99m (^{99m}Tc), accounting for approximately 85 % of all radiopharmaceutical diagnostic scans, and equates to around 30 million patient examinations worldwide every year.[65] The decay profile of molybdenum-99 (^{99}Mo) via ^{99m}Tc is shown below in **Figure 1.8**, and begins with ^{99}Mo undergoing β-decay with a half-life ($T_{1/2}$) of 66 hours to form a metastable nuclear isomer of ^{99}Tc, ^{99m}Tc. Technetium-99m is known as a metastable isomer because it is more energetically excited compared to ^{99}Tc. This metastable nuclear isomer undergoes isomeric transition with a half-life of 6.01 hours to ^{99}Tc, resulting in emission of a γ-photon at 0.14 MeV.

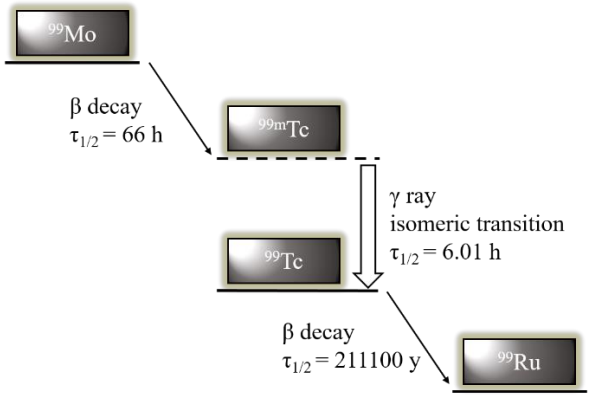

Figure 1.8 A schematic for the decay profile of molybdenum-99 (^{99}Mo) via ^{99m}Tc. Schematic adapted from Long and Wong.[61]

The vast majority of radioisotopes are produced using a cyclotron, but the infrastructure to maintain a laboratory on the site of a cyclotron is not always feasible. A generator provides the means of on-site production and extraction of radioisotopes, such as ^{99m}Tc.[66] The half-life of ^{99}Mo, means a generator can be used for approximately 2 weeks, and consists of an alumina (Al_2O_3) anion exchange column which adsorbs ^{99}Mo in the form of the molybdate dianion, $[^{99}Mo][MoO_4]^{2-}$. As ^{99}Mo decays it forms pertechnetate, $[^{99m}Tc][TcO_4]^-$ which is not as strongly bound to the alumina column due to its monoanionic charge. As a saline solution is passed through the column, the chloride and pertechnetate ions undergo ionic exchange, resulting in sodium pertechnetate, $[^{99m}Tc]NaTcO_4$, being eluted from the column.[67] A sterile solution of sodium pertechnetate has its own clinical use without any need for further manipulation, with applications in thyroid and tumour diagnostics.[68] Owing to its multiple oxidation states, ^{99m}Tc has a versatile coordination chemistry, making it possible to produce a wide range of complexes with desirable characteristics for diagnostic purposes.

Technetium-99m radiopharmaceuticals are generally formulated from labelling kits. A kit typically contains the ligand for ^{99m}Tc complexation, a reducing agent, buffer for pH adjustment of labelling conditions and stabilizing agents. The major advantage of such kits is that they are prepared in a freeze-dried form resulting in a considerably long shelf life.

1.2.3 A Brief Overview of Other Commonly Used SPECT Radioisotopes

Whilst ^{99m}Tc-based imaging agents are classed as the mainstay in nuclear medical imaging globally, due to their production using commercially available labelling kits, there are a number of other SPECT-based radioisotopes that are currently also being used in the clinical setting.[69] Where ^{99m}Tc requires the development of a chelating agent to allow its incorporation into a molecule without hindering the target site binding, an alternative SPECT radioisotope, iodine-123 (^{123}I), can directly substitute a hydrogen atom of a compound, making its incorporation into a small molecule facile.[70] However, ^{123}I requires a cyclotron, a particle accelerator which accelerates charged particles towards a target, to be produced.[71] On the other hand, ^{123}I has a half-life of 13 hours which means it can be transported to a hospital site and distributed over large distances. A cyclotron propels charged particles via an alternating electric field in a constant magnetic field until these particles have accumulated enough kinetic energy to annihilate a target and produce the desired radioisotope.

Indium-111 (^{111}In) has a half-life of 67 hours and was the first radionuclide to be commercially and clinically established in imaging applications.[69] The long half-life of ^{111}In lends itself for use in monoclonal antibody targeting, along with white blood cell imaging, which localise in tissue over a long period of time.[72,73] Thallium-201 (^{201}Tl) is another SPECT radionuclide, and has a half-life of 73 hours. It is known as the radioactive analogue of potassium because it can mimic potassium in biological systems. As such, the cation $^{201}Tl^{+}$ can be transported into the myocardium via the Na^{+}/K^{+}-ATPase, and has played a major role in myocardial perfusion imaging since the early 1970's.[74] Gallium-67 (^{67}Ga) is a cyclotron-produced SPECT radionuclide with a half-life of 3.3 days and has been used in nuclear medicine for many decades. The two clinical roles ^{67}Ga has mainly been employed for is the imaging of infections and lymphomas.[75,76] Uptake of ^{67}Ga, in its citrate form ([^{67}Ga]Ga-citrate), in lymphoma is mediated through iron-binding sites of the iron transport protein, transferrin, highlighting the mimicry of ^{67}Ga as iron in biological systems. The introduction of [^{18}F]fluorodeoxyglucose ([^{18}F]FDG) which is a positron emitter for PET (vide infra), and a non-specific metabolic indicator using glucose metabolism, for oncological imaging, has mostly replaced

[^{67}Ga]Ga-citrate. This is mainly due to [^{18}F]FDG imaging using PET, which has considerably greater specificity and sensitivity compared to [^{67}Ga]Ga-citrate imaging.[77]

1.3 PET Imaging

Since the early 1970s, when the first PET scan was performed, all aspects of PET imaging have undergone rapid improvement and innovation, in order to provide higher levels of patient care, including the vast improvement of diagnosis and prognosis in all areas of nuclear medicine.[78] Whilst innovation has pervaded the PET imaging field, the basic principles have remained constant throughout. In the same manner that SPECT imaging is dependent on the detection of γ rays produced by the interaction of radiation with matter, PET imaging relies on this process too. However, the production of γ rays arises from a different source in PET imaging.[62]

1.3.1 Principles of PET Imaging

PET imaging uses positron-emitting radioisotopes (β^+) to produce a signal that can be detected to generate an image. When the radioisotope decays by positron emission, the emitted β^+, known as the antiparticle of the electron (β^-), travels ~1 mm in tissue before undergoing an annihilation event with an β^- which produces two coincident γ photons with identical energies of 511 keV, illustrated in **Figure 1.9**.[79]

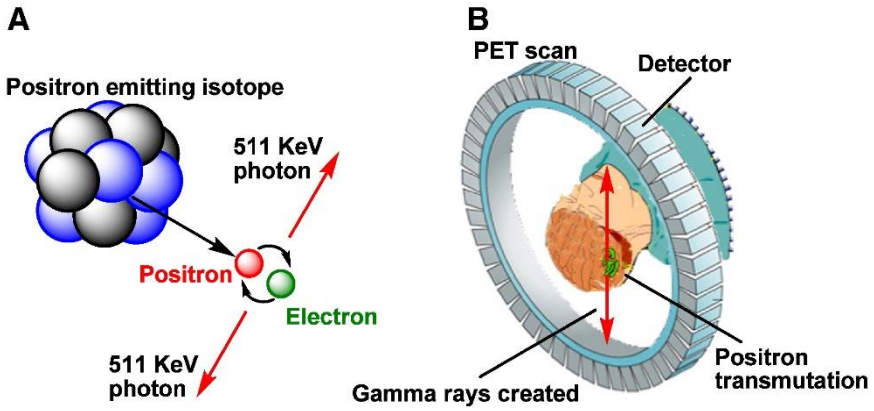

Figure 1.9 A schematic showing **(A)** a positron (β^+) and an electron (β^-) annihilating to produce two antiparallel 511 keV photons and **(B)** the 511 keV photon being detected by the gamma camera. Picture reproduced with permission by Li *et al.*[79]

These high energy γ photons are then detected by a 360 ° array of gamma cameras, leading to a 3D image being reconstructed by determining the localisation of the decay event.[80] The co-detection of γ photons from the same annihilation event means that fewer decay events are

undetected and with the generation of 3D images, PET boasts a number of key advantages over SPECT imaging. The use of the 360 º array of gamma cameras for PET imaging, improves the viability of whole-body imaging greatly compared to SPECT imaging, where the gamma camera gantry must rotate around the entire patient. Nevertheless, SPECT does have advantages over PET, with SPECT radioisotopes being cheaper to produce and handle, whilst also having longer half-lives, and are more clinically widespread. The distance a β^+ can travel before it annihilates with an β^- is determined by its energy, the higher the energy, the further the β^+ is likely to travel before the annihilation event, leading to greater ambiguity between the location of annihilation and the radioisotopes definitive position, reducing the resolution of PET as an imaging technique. A beneficial advantage SPECT imaging has over PET, is that multiple radioisotopes can be used to simultaneously image, due to the difference in γ photon emission energies of different SPECT radioisotopes. Multiple PET radioisotopes cannot be employed for such a use, due to the annihilation event always producing γ photons with energies of 511 keV.

1.3.2 PET Radioisotopes for the Clinic and Biomedical Research

The variety of PET radioisotopes widely used for clinical and research-based applications has expanded greatly due to the imaging techniques evolution over recent decades. The evolution of PET imaging has resulted in all areas of the periodic table being represented in this technique, with the evolution of the aforementioned applications to improve the efficiency of production and use of radioisotopes through their radiological and chemical properties.[69]

1.3.2.1 Cyclotron Produced PET Radioisotopes

Table 1.2 A summary of the properties of a selection of cyclotron produced PET radioisotopes.[81–85]

PET Radioisotope	Half-life ($T_{1/2}$)	Proportion of β^+ Decay/ %	Max β^+ Energy/ MeV
Carbon-11	20.4 min	100	0.96
Nitrogen-13	9.9 min	100	1.20
Oxygen-15	2.2 min	100	1.72
Fluorine-18	109.8 min	97	0.63
Copper-64	12.7 h	19	0.65
Zirconium-89	3.3 days	23	0.90

Commonly used PET radioisotopes, shown in **Table 1.2**, are produced using a cyclotron, the process of which was described above in section 1.2.3. The first radiological property to be

discussed is half-life, which governs the time a radioisotope can be chemically manipulated and administered before its activity becomes too depleted to generate useful images. The caveat to this, is that a longer half-life radioisotope will increase the radiation dose a patient receives and potentially cause the patient unnecessary harm. Extremely short-lived radioisotopes such as carbon-11 (^{11}C), nitrogen-13 (^{13}N) and oxygen-15 (^{15}O) require the time from cyclotron to patient administration to be very short, therefore limiting the extent of chemical manipulation that can be performed. Oxygen-15 is commonly used for blood flow imaging, in specific for regional myocardial flow measurements, because it is freely diffusible in its water form, [^{15}O]H_2O, and also lends itself to multiple imaging sessions in quick succession because of its half-life of 2.2 minutes.[86] Longer-lived radioisotopes such as copper-64 (^{64}Cu) and zirconium-89 (^{89}Zr) will, as mentioned before, lead to a higher patient dose, but they are well suited for imaging systems that also have a long biological half-life. For example, ^{89}Zr with its half-life of 3.3 days is a perfect match for antibody-based PET (immunoPET) imaging, as the circulation half-life of antibodies is multiple days.[87]

The second radiological property is the proportion of β^+-decay that occurs for a specific radioisotope, with a greater percentage of β^+-decay leading to a lower amount of radioactivity needed for administration to achieve the same number of β^+-emitted signals. The radioisotopes ^{11}C, ^{13}N and ^{15}O all undergo 100 % β^+-decay, whereas ^{18}F undergoes electron capture (EC) decay 3 % of the time.[85] [64]Cu undergoes other decay pathways, β^+-emission 19 % of the time, β^--emission 38 % of the time, and γ-emission 43 % of the time.[84] Both β^-- and γ-emissions will increase the radioactive dose to a patient, as well as increasing noise observed in the image.

The final radiological property is the maximum energy of the β^+ particles emitted, which ultimately governs the resolution of the image produced. As explained previously, the higher the energy of the β^+ emitted, the greater the distance the particle can travel from its actual decay site before annihilating with a β^-, therefore decreasing the resolution of the image produced. High energy β^+-emitting radioisotopes such as ^{15}O typically produce lower resolution images compared to ^{18}F, which emits significantly lower energy β^+ particles.

Radiological properties are important to consider in imaging agent efficacy, but chemical properties must also be scrutinised, as it is the chemistry of the radioisotope that will dictate the compounds and complexes they can be incorporated into. Direct replacement of atoms present in a molecule with ^{11}C is a routine radiosynthetic strategy for producing ^{11}C-based

radiotracers, such as L-[^{11}C]methyl-methionine (**Figure 1.10**), where the thiomethyl group is formed with ^{11}C to form the radiotracer.[88]

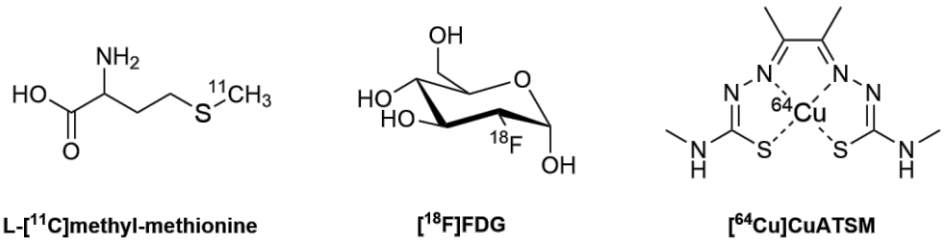

L-[^{11}C]methyl-methionine [^{18}F]FDG [^{64}Cu]CuATSM

Figure 1.10 Three examples of radiotracers containing radioisotopes shown in **Table 1.2**.[88–90]

As mentioned in section 1.2.3, [^{18}F]FDG (**Figure 1.10**) is a glucose mimic with one hydroxyl group substituted with ^{18}F. The major route ^{18}F is incorporated into radiotracers, is through the formation of carbon-fluorine bonds.[89] Being a mimic of glucose means [^{18}F]FDG can enter the glycolysis pathway, but the presence of the fluorine atom means it does not complete the glycolysis pathway and instead localizes in the body, which can be used to quantify the rate of metabolism. The increased rate of metabolism exhibited by tumour cells compared to healthy cells, means that [^{18}F]FDG can be used in oncology imaging as it will be preferentially taken up into tumour cells.[91] Organic radionuclides are considered simple in terms of compound incorporation, whereas inorganic radionuclides have significantly diverse chemical properties, resulting in a wide-range of applicable imaging targets.[69] The range of accessible redox states of copper means that ^{64}Cu can be utilised in targeting biological oxidative processes, such as hypoxia. [^{64}Cu]CuATSM (**Figure 1.10**) utilises its highly conjugated ligand system to easily pass through the lipid bilayer membrane before the copper is reduced in the hypoxic region, meaning it becomes trapped in myocardial tissue, allowing the detection of ROS generation to be possible.[90]

1.3.2.2 Generator Produced PET Radioisotopes

Table 1.3 A summary of the properties of generator produced PET radioisotopes.[92–94]

PET Radioisotope	Half-life ($T_{1/2}$)	Proportion of β^+ Decay/ %	Max β^+ Energy/ MeV
Rubidium-82	1.25 min	100	3.15
Copper-62	9.7 min	98	2.90
Gallium-68	68 min	89	1.92

Generator-produced PET radioisotopes, some examples shown in **Table 1.3**, offer somewhat fewer options for PET imaging than cyclotron produced alternatives. However, the more cost-

effective properties of generators compared to cyclotrons has generated a lot of interest in their use. Rubidium-82 (^{82}Rb) is produced by a strontium-82 (^{82}Sr) generator, which has a half-life of 25.6 days, and consists of an ion-exchange column that can elute ^{82}Rb with a 0.9 % saline solution. The ionic radius of monocationic rubidium-82 ($^{82}Rb^{+}$) is comparable with monocationic potassium, along with its kinetics, meaning it has been widely implemented as a myocardial perfusion imaging agent. The short half-life of ^{82}Rb (1.25 min) means it needs to be administered to patients immediately after elution as $^{82}Rb^{+}$ where it is taken up into cardiomyocytes as a potassium mimic.[92] Copper-62 (^{62}Cu) is also a fairly short-lived radioisotope (half-life of 9.7 min) and is produced by a generator consisting of zinc-62 (^{62}Zn, half-life of 9.3 h), meaning the generator will only last from a few days to one week. The ^{62}Zn generator consists of an anion exchange column, which will elute ^{62}Cu with 2 M HCl.[93] As with ^{82}Rb, the relatively short half-life of ^{62}Cu means imaging with it is limited to less than one hour post-injection, but does allow for repeated scanning in quick succession. ^{62}Cu is used in relatively small imaging agents that exhibit fast kinetics, such as [^{62}Cu]CuATSM (**Figure 1.10**) and [^{62}Cu]CuPTSM, used for hypoxia and blood flow imaging.[90,95]

1.4 Gallium-68 (^{68}Ga)

Gallium-68 (^{68}Ga), shown in **Table 1.3**, is the radioisotope of interest in this project, and as such will be the main focal point for the remainder of this thesis. Over recent years, ^{68}Ga has gained considerable interest for PET imaging, with one of its key benefits being its production via a ^{68}Ge/^{68}Ga generator, which has recently been granted clinical approval. Radioisotopes such as carbon-11 and fluorine-18, require a cyclotron to be produced, which limits their use to radiopharmaceutical sites with the necessary infrastructure and financial capability.[96] The convenient half-life of ^{68}Ga (68 min), has resulted in a significant wave of interest for its use in various disease states, with new ^{68}Ga-labelled imaging agents currently in the preclinical and clinical pipelines. This increase in clinical demand for ^{68}Ga-based PET-imaging shows the impact this interest has caused, with the focus now turning towards the formulation of ^{68}Ga-labelling kits, a procedure similar to well-established kit-based ^{99m}Tc chemistry, in order to further improve the feasibility and widespread use of ^{68}Ga in radiopharmaceutical diagnostics.[97]

1.4.1 Gallium-68 Production and Decay Profile

Germanium-68 (^{68}Ge) decays by EC 100 % of the time to generate the daughter isotope, ^{68}Ga, shown in **Figure 1.11**. ^{68}Ge is produced in a high energy cyclotron from the stable gallium-69 isotope (^{69}Ga(p,2n)^{68}Ge).[98] Compared to the approximate 2 week shelf-life afforded by ^{99}Mo/^{99m}Tc generators, ^{68}Ge/^{68}Ga generators have a more clinically beneficial shelf-life of roughly 1 year, which results from the conveniently long half-life (271 days) of the parent isotope, ^{68}Ge.

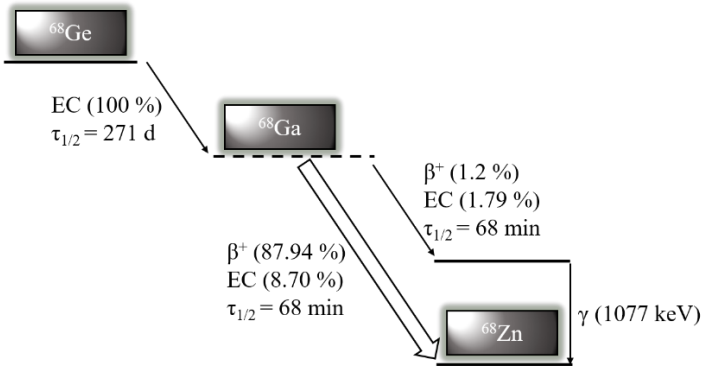

Figure 1.11 A schematic of the decay pathway of germanium-68 via gallium-68. Schematic reproduced from da Silva *et al*.[99]

Once ^{68}Ge decays by EC to ^{68}Ga, the daughter isotope then decays to zinc-68 (^{68}Zn) with a half-life of 68 minutes, undergoing 90 % β^+-decay and 10 % EC decay. ^{68}Ga nuclei do have a 3 % probability of decaying into a higher-energy state of ^{68}Zn, which undergoes γ-decay to form the ground-state ^{68}Zn.[98,99]

1.4.2 Germanium-68/Gallium-68 Generators

The introduction of ^{68}Ga for medical use was proposed in 1960 by Gleason, but its application was not possible due to the absence of a primary generator design.[100] An initial design for a ^{68}Ge/^{68}Ga generator was developed and presented, just a year later, by Greene *et al* in 1961, just a few years after the first ^{99}Mo/^{99m}Tc generators were produced.[101] Both generators operate in a similar way, consisting of a parent isotope impregnated stationary phase, which decays to produce the daughter isotope which can be eluted from the column. The parent isotope, ^{68}Ge, naturally exists in the +4 oxidation state, once it has undergone EC decay the ^{68}Ga daughter isotope exists in the +3 oxidation state. The decrease in positive valency results in the isotope

being more weakly bound to the stationary phase, therefore ^{68}Ga can be eluted from the generator.

Initial ^{68}Ge/^{68}Ga generators relied on a liquid/liquid extraction process, but this extraction process was quickly replaced solid/liquid extraction via an ion exchange resin.[100–102] The solid/liquid extraction process involves the isotope impregnated stationary phase described above. Both ^{68}Ge/^{68}Ge generators developed by Greene *et al*. and Yano *et al*. (in 1964) used alumina stationary phases, with the alumina later being found to bind $^{68}Ga^{3+}$ too strongly for successful elution to occur.[101,102] The chelating ligand ethylenediaminetetraacetic acid (EDTA) was used in a solution to bind ^{68}Ga to solve the elution problem, however the resulting [^{68}Ga]Ga-EDTA complex is highly stable due to its hexadentate character meaning the desired [^{68}Ga]Ga(III) could not be removed for complexation with the ligand of interest.[101,102] Generators which utilised hydrochloric acid as the mobile phase were developed in 1975 by Malyshev *et al*. and in 1980 by Loc'h *et al*., which contained titanium dioxide and stannic oxide stationary phases respectively.[103,104] The success of elution with solutions of hydrochloric acid meant there was no risk of complexation with ^{68}Ga compared to using a solution of a chelating mobile phase, such as EDTA. Lewis *et al*. designed a generator in 1981, consisting of an alumina stationary phase and a sodium hydroxide mobile phase.[105] Schumacher *et al*. investigated the use of organic resin stationary phases as a means to prevent the leaching of undesired metal contaminants from the generator and improve elution quality.[106]

Table 1.4 Clinically approved and commercially available ^{68}Ge/^{68}Ga generators in use today.[97]

Type	GalliaPharm®	GalliAd®	GeGrant®
Supplier	Eckert & Ziegler AG, Berlin, Germany	IRE Elit, Fleurus, Belgium	ITG, Garching, Germany
Column	TiO_2	TiO_2	SiO_2
Eluant	0.1 M HCl	0.1 M HCl	0.05 M HCl

This early generation of ^{68}Ge/^{68}Ga generators all displayed a wide range of problems for clinical use. A large volume of mobile phase required for acceptable ^{68}Ga activity, means that the concentration of ^{68}Ga is low and the concentration of acidic protons, [H^+], is high. The breakthrough of ^{68}Ge and other metallic impurities, such as ^{68}Zn, raised a number of concerns, including lower activity of ^{68}Ga, competition with impurities for chelation and toxicity issues. Various pre-elution procedures and post-processing methods, such as eluate fractionation, anion exchange, cation exchange, and a combination of these techniques have been implemented to mitigate these problems.[98,105,107,108] Currently there are two TiO_2-based

$^{68}Ge/^{68}Ga$ generators approved for clinical use in humans, GalliaPharm® and GalliAd®, shown in **Table 1.4**. The GeGrant® generator of ITG has recently been granted approval for review and sale of the generator. All three of these generators can generate ^{68}Ga to a standard that complies with pharmacopoeia, and therefore in use clinically, without the need for any post-processing techniques.

1.4.3 Coordination Chemistry of Gallium

Gallium is a group 13 metal, and its most stable oxidation state is +3. The trivalent cation, Ga^{3+}, is a hard Lewis acid, due to its high cation density and small ionic radius (62 pm), with similar coordination chemistry, ionic radius (65 pm) and the same valency as Fe^{3+}.[109] In its +3 oxidation state, the metal centre adopts a highly stable electronic configuration $[Ar]3d^{10}4s^{0}4p^{0}$, meaning it can adopt a range of coordination spheres (4, 5 and 6), with a coordination number of 6 being most favourable. Ga^{3+} preferentially coordinates with hard Lewis bases, containing nitrogen and oxygen donor atoms, and sulphur, to a smaller extent, in order to form thermodynamically stable complexes.[110] Ga^{3+} is not afforded any stabilisation through ligand field stabilisation energy upon complexation, due to its closed-shell electronic structure, and instead favours complexation with multidentate ligands for stabilisation through chelate and macrocyclic effects. In its trivalent form, Ga^{3+} is stable in media below pH 3, above pH 3 it begins to associate with hydroxide ions. At pH 3-7, a colloidal species forms, $[Ga(OH)_3]$, which is highly insoluble and the metal can no longer undergo complexation. At basic pH >7, the gallate ion, $[Ga(OH)_4]^-$, which is soluble but Ga^{3+} still cannot undergo complexation.[111] The formation of insoluble hydroxide species remain a problem in the preparation of ^{68}Ga imaging agents, however the use of weak and stabilizing ligands such as citrate have alleviated this problem.[112]

The complexation of radiometals takes advantage of excess ligand concentration, compared to the radiometal concentration, to improve the efficiency of the labelling process. Standard protocols for ^{68}Ga labelling typically involve nanomolar concentrations of ^{68}Ga and micromolar concentrations of ligand, resulting in the ligand always being in excess.[113] The excess of ligand promotes the formation of the desired complex, as indicated by Le Chatelier's Principle. The large excess of ligand tends to improve the yield in radiometal complexation compared to their non-radioactive analogues, because the same ratio of excess ligand is not obtainable in the 'cold' context, which would likely require tens of grams of ligand to be in the same ratio of excess compared to the 'hot' context. The trade-off that dominates the

radiochemical field involves the kinetics and thermodynamics of complexation. Faster radiolabelling kinetics allow for shorter radiolabelling times and milder conditions, resulting in higher amounts of activity being available for patient administration, with higher quality images generally being obtained. However, thermodynamically stable radiometal complexes require more energy to overcome the frequently higher activation energy barrier, meaning their formation is more difficult to achieve under mild conditions, but they exhibit superior *in vivo* stability, with transchelation of the radiometal being more preventable. As a 'rule of thumb', a PET-based imaging agent should be available for clinical use within three half-lives of the initial production of the radioisotope.[114] This emphasises that ^{68}Ga radiopharmaceuticals should be thermodynamically stable for upwards of 3 hours *in vivo*, and fast radiolabelling kinetics are considered crucial to help ensure the stability of ^{68}Ga complexes for the desired 3 hour duration.

1.4.4 A Survey of Gallium(III) Chelators

The chemistry of six-coordinate Ga(III) complexes has been extensively investigated and reviewed.[115] In 2014, Price *et al*. surveyed a vast range of chelators for a plethora of radiometals used in the clinic and in research.[116] The efficiency of these chelators for ^{68}Ga chelation were reviewed and categorised from being the 'best' to 'poorest' match, as shown in **Figure 1.12**. In terms of thermodynamic stability, azamacrocycle-based chelators such as 1,4,7-triazacyclononane-1,4,7-triacetic acid (NOTA) and 3,3′,3"-(((1,4,7-triazonane-1,4,7-triyl)tris(methylene))tris(hydroxyphosphoryl))tripropanoic acid (TRAP) excel, with the triazacyclic ring being a convenient size match for Ga(III) cations, as well as satisfying the stable hexadentate geometry. A problem NOTA possesses is that if all carboxylate arms are coordinated to the Ga(III) centre, then there is no availability for functionalisation. If one arm is used for functionalisation, then the thermodynamic stability of the complex is compromised as the optimal coordination sphere of 6 is no longer satisfied. In order to preserve the denticity of NOTA, carbon-functionalised derivatives have been designed.[117] Derivatives of NOTA functionalised with phosphinic and phosphonic acid arms such as 1,4,7-Triazacyclononane-1,4,7-tri(methylenephosphonic acid) (NOTP), 3-(((4,7-bis((hydroxy(hydroxymethyl)phosphoryl)methyl)-1,4,7-triazonan-1-yl)methyl)(hydroxy)phosphoryl)propanoic acid (NOPO) and TRAP, are further examples of bifunctional chelators for ^{68}Ga, forming thermodynamically stable complexes.[118–120] In the case of TRAP, chelation of ^{68}Ga is coordinated through the phosphinic hydroxyl groups, allowing

for functionalisation of the terminal carboxylate groups. Whilst macrocyclic chelating agents are more inert than acyclic chelating agents of comparable stability, they do not exhibit higher complexation kinetics. Considering ^{68}Ga imaging agents need only resist metal leaching for 3 hours *in vivo* to allow for imaging, high complexation kinetics are favoured, with acyclic chelating agents being preferred. The acyclic chelator 1,2-((6-carboxy-pyridin-2-yl)-methylamino)ethane (H_2dedpa) is a very good ^{68}Ga ligand, with quantitative radiolabelling being obtained within 10 minutes at room temperature at nanomolar concentrations of ligand.[121]

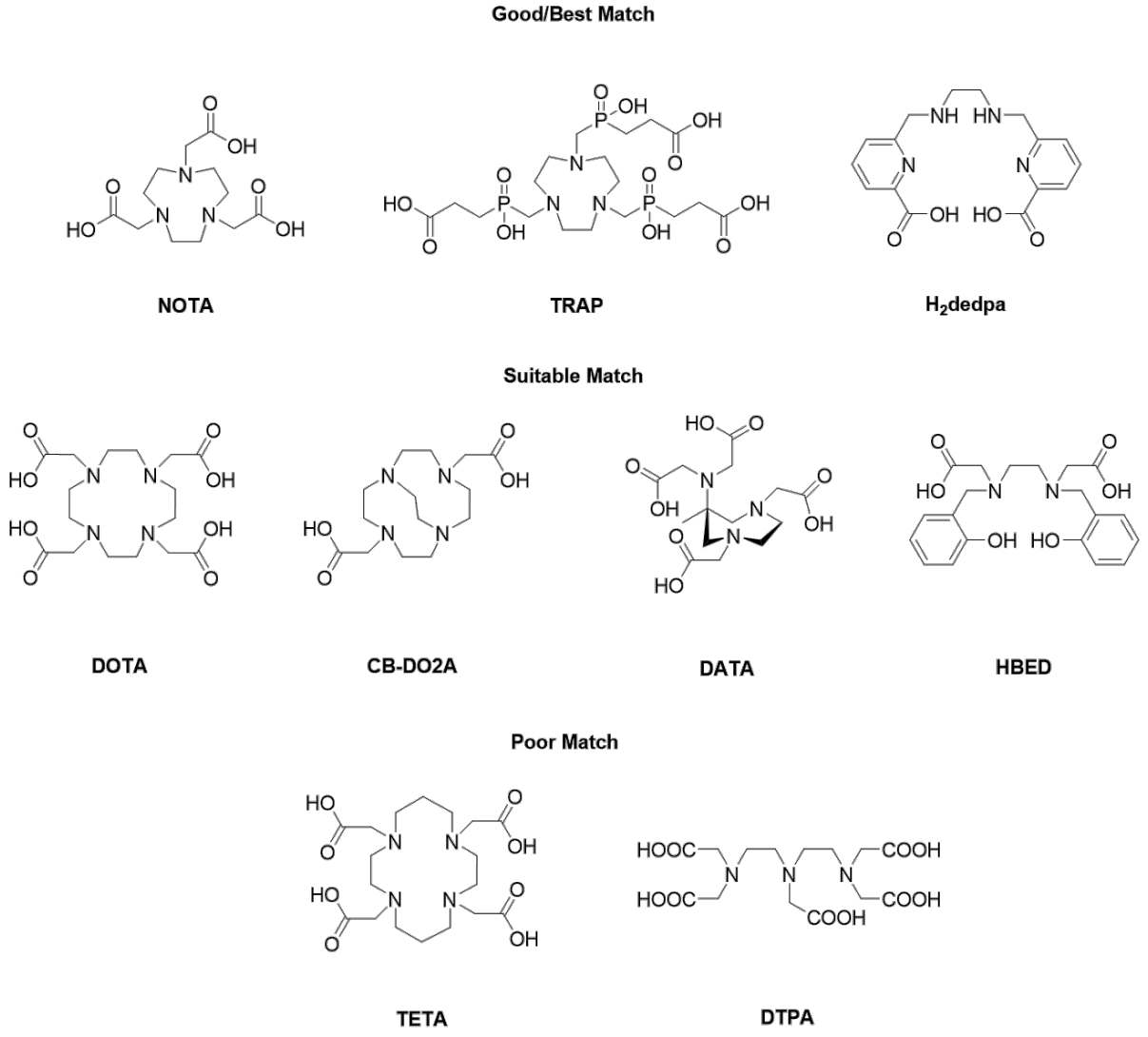

Figure 1.12 Summary of the chelators reviewed by Price *et al*. outlining the individual preference for ^{68}Ga complexation.[116]

In 2017, Tsionou *et al*. performed a quantitative comparison of ^{68}Ga chelators by reacting generator produced ^{68}Ga with chelators for 10 minutes before assessing their ^{68}Ga-labelling

efficiency by iTLC.[113] At 25 ºC and pH 3.5, a 5 μM solution of NOTA achieved a radiochemical yield (RCY) of 93 %, surprisingly lower than the RCY achieved at 90 ºC. This is thought to be due to thermodynamically favoured complexation of non-radioactive trace metals in the generator eluate, facilitated by the higher temperature. Both NOTA and TRAP exhibited promising RCY values of < 89 % at pH 6.5, showing that their ^{68}Ga chelation is fairly pH independent. Chelators 1,4,8,11-tetraazacyclotetradecane-N,N′,N″,N‴-tetraacetic acid (TETA) and diethylenetriamine pentaacetate (DTPA), not included in the study by Tsionou *et al*., are deemed as a 'poor' match for chelation with ^{68}Ga. TETA was shown to have a very low affinity with Ga(III), with ^{68}Ga-labelling of DTPA at 90 ºC taking 1 hour.[122,123] Compared to the convenient size match between the cavity of NOTA and Ga(III), TETA and DTPA provide a much larger ligand cavity, leading to a greater size mismatch with Ga(III) and less stable complexes being formed.

The third tier of chelators put forward by Price *et al*, are those that are a 'suitable' match for ^{68}Ga chelation. They are deemed to be not as appropriate for ^{68}Ga complexation as NOTA, TRAP and H_2dedpa due to their slow radiolabelling kinetics. For example, 1,4,7,10-tetraazacyclododecane-1,4,7,10-tetraacetic acid (DOTA), a macrocyclic chelator widely used for chelating large metal centres such as gadolinium(III) (Gd(III)) owing to its large cavity size, is used to some effect for ^{68}Ga chelation.[124] Only two of DOTAs carboxylate arms contribute in complexation, with one of the free carboxylate arms being functionalised for bioconjugation or even removed to yield an unfunctionalized nitrogen atom, which can convert DOTA into a bifunctional chelator. DOTA is very kinetically inert, meaning it undergoes slow complexation formation, with radiolabelling methods stating that heating above 90 ºC is required to achieve RCY values > 90 %.[110] Many derivatives of DOTA have been developed to address the issues exhibited by this chelator, such as 4,10-bis(carboxymethyl)-1,4,7,10-tetraazabicyclo[5.5.2]tetradecane (CB-DO2A) which is a bridged cyclen chelator and improves ligand preorganisation, leading to higher complex stability.[125]

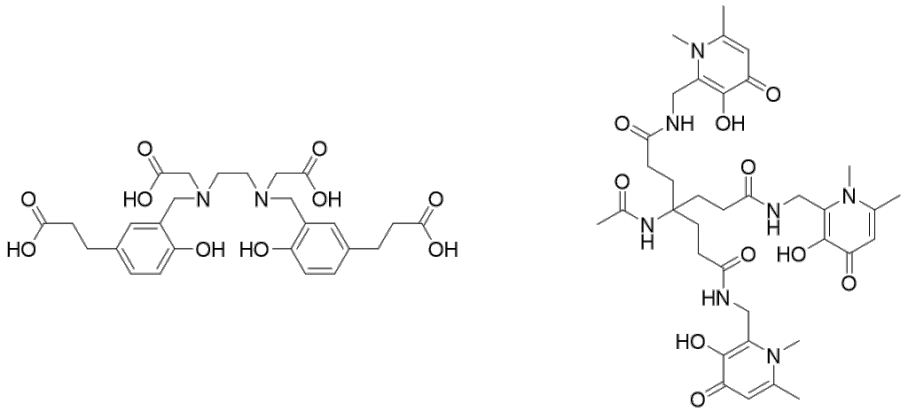

Figure 1.13 HBED-CC, a bifunctional chelator analogue of HBED, and CP256, an example of THP ligands originally synthesised for iron chelation.[126,127]

The chelator N,N′-di-(2-hydroxybenzoyl)-ethylenediamine-N,N′-diacetic acid (HBED), shown in **Figure 1.12**, is currently considered as one of the most superior acyclic chelating agents, with rapid radiolabelling kinetics due to its acyclic nature and high Ga(III) affinity. The comparative study conducted by Tsionou *et al*. found that at 0.5 μM ligand concentration at pH 6.5, an RCY value of 86 % was obtained. Its stability in serum is also comparable to that of NOTA, setting it apart from other acyclic chelating agents. The unfunctionalised form of HBED, does however, lead to the formation of isomers upon complexation with Ga(III). Among its functionalised derivatives, N,N′-bis-(2-hydroxy-5-(carboxyethyl)benzyl)ethylenediamine-N,N′-diacetic acid (HBED-CC) (**Figure 1.13**) was developed to transform HBED into a bifunctional chelator, consisting of two pendant carboxylate arms ready for functionalisation with targeting vectors.[126,128]

Tripodal compounds, such as tris(hydroxypyridinone) (THP), an example of which is shown in **Figure 1.13** (CP256), are also very promising chelators for ^{68}Ga, however they were originally developed as iron chelating agents but due to the similarity in ionic radii of Ga(III) and Fe(III), they were translated into ^{68}Ga radiopharmaceuticals.[127,129] THP allows for radiolabelling of ^{68}Ga at room temperature in 5 minutes at ligand concentrations as low as 0.5 μM, and has exhibited such high affinity of Ga(III) it is able to sequester the metal from serum *in vitro*.[130] Conversion of THP ligands into bifunctional chelators is facilitated through the amide functionality, located on the central quaternary carbon atom, with these promising ^{68}Ga chelating agents demonstrate rapid radiolabelling kinetics and high thermodynamic stability *in vivo*.

1.4.5 Current Clinical Applications

1.4.5.1 Neuroendocrine Tumour Imaging

A significant branch of ^{68}Ga-based imaging involves the use of bifunctional chelators consisting of a DO3A chelating moiety attached to an octreotate peptide, [^{68}Ga]Ga-DOTA-TATE, or an octreotide peptide, [^{68}Ga]Ga-DOTA-TOC and [^{68}Ga]Ga-DOTA-NOC, shown in **Figure 1.14**. These examples have shown to be particularly useful for neuroendocrine tumour imaging, with both [^{68}Ga]Ga-DOTA-TOC and [^{68}Ga]Ga-DOTA-TATE being approved for gastro-entero-pancreatic neuroendocrine tumour imaging.[131] Octreotate and octreotide act as somatostatin receptor (SSR) antagonists, meaning the three aforementioned ^{68}Ga bifunctional chelators accumulate in regions where SSRs are overexpressed, such as in malignant tumours found in breast, lung and lymphatic tissue, as well as neuroendocrine tumours. Neuroendocrine tumours do not consume glucose, meaning [^{18}F]FDG cannot effectively image this tumour type, paving the way for the use of DOTA-TATE, DOTA-TOC and DOTA-NOC to image these tumours.[131] Once bound to the transmembrane receptors of the target tumour cells, the bifunctional chelator undergoes active transport in to the cell via endocytosis, with the trapping of the radiolabelled chelator serving to increase the contrast of ^{68}Ga imaging.[132]

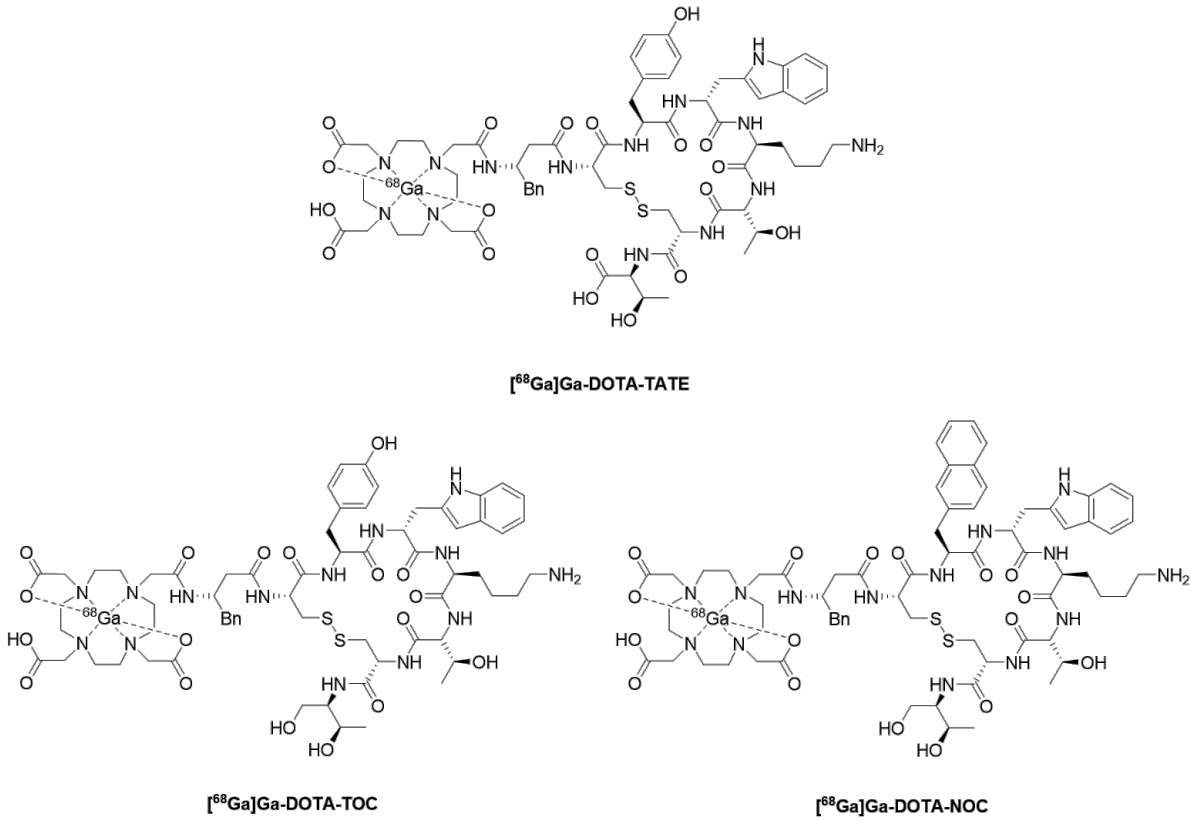

Figure 1.14 [^{68}Ga]Ga-DOTA-TATE, [^{68}Ga]Ga-DOTA-TOC and [^{68}Ga]Ga-DOTA-NOC, bifunctional chelators with a DO3A chelating component attached to octreotate and octreotide peptides for tumour imaging.[131]

As mentioned previously, ^{68}Ga radiolabelling with DOTA peptides requires heating at > 90 ºC, as such it needs very harsh conditions to achieve DOTA-based ^{68}Ga radiotracers within a reasonable timeframe. To achieve rapid radiolabelling kinetics under mild conditions, other chelators have been proposed, such as a THP analogue. [^{68}Ga]Ga-THP-TATE can achieve radiolabelling with ^{68}Ga in 2 minutes at room temperature with a RCY of > 95 %.[133]

1.4.5.2 Prostate Cancer Imaging

Another clinical use of ^{68}Ga in nuclear medicine is currently in prostate-specific membrane antigen (PSMA) imaging. PSMA is a transmembrane protein located on the surface of cancer cells, which is overexpressed in high-grade tumours, such as malignant prostate tumour cells, making PSMA an ideal target for imaging prostate cancer. Small molecule PSMA inhibitors such as Glu-Urea-Lys, shown in **Figure 1.15**, have been conjugated with several chelators for ^{68}Ga complexation.[134] Urea-based inhibitors have shown great affinity and specificity for PSMA, as well as fast internalisation into tumour cells.[135]

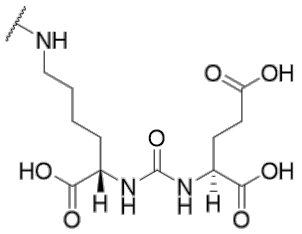

Figure 1.15 Glu-Urea-Lys, a small molecule PSMA inhibitor, which can be used as a targeting vector for imaging as part of a bifunctional chelator.[134]

In 2010, Banerjee *et al*. published a DO3A PSMA targeting ^{68}Ga radiotracer, which successfully delineated *in vivo* tumours, compared to the ^{99m}Tc based radiotracers from their previous work, which is thought to be a result of the higher resolution afforded by PET over SPECT.[136] In 2012, Eder *et al*. reported on the development of a HBED-CC PSMA targeting ^{68}Ga radiotracer, [^{68}Ga]Ga-HBED-CC-PSMA-11, which was shown to be a very effective imaging agent, and has recently become the first FDA-approved ^{68}Ga-radiopharmaceutical for clinical use of PET-based prostate cancer imaging.[137–139] Comparative studies have been performed to assess the effect changing the chelating moiety will have on the uptake and retention of imaging agents in healthy and cancerous cells. A comparison of three PSMA imaging agents with DOTA, NOTA and HBED-CC chelating moieties showed that the HBED radiotracer exhibited the highest uptake and retention in healthy tissue, but the NOTA-based radiotracer showed the highest retention in cancerous tissue and the fastest clearance from healthy tissue, therefore highlighting the NOTA-based imaging agent as the more effective for PSMA imaging.[134] Another derivative of PSMA, based on THP, has also been reported, with much of the attention being gained from its facile radiolabelling of ^{68}Ga. This facile radiolabelling has resulted in the development of a single-vial kit formulation, with complete radiolabelling occurring in 5 minutes at room temperature. *In vivo* experiments were performed for the THP PSMA derivative, showing similar biological characteristics to HBED-based radiotracers.[140] Due to the positive results this THP radiotracer has shown, a phase II clinical trial has been approved and is currently ongoing.[141]

1.5 Examples of Lipophilic and Cationic Radiotracers

The uptake and retention of lipophilic and cationic imaging agents are related to mitochondrial function by $\Delta\Psi_m$ (**Figure 1.4**, **Equations 1.1** and **1.2**). Non-invasive imaging modalities have been outlined (**Table 1.1**), with a focus on nuclear imaging techniques and how they provide

the means to image molecular processes *in vivo*. In this section both SPECT- and PET-based radiotracers will be discussed, focusing on their application for imaging mitochondrial function through the use of lipophilic cations.

1.5.1 Thallium-201 Chloride ([^{201}Tl]TlCl)

Thallium(I) has the same electron valence as K^+ and a similar ionic radius, prompting its use as a potassium mimic for myocardial perfusion imaging in 1979, with its uptake into the myocardium facilitated via the Na^+/K^+-ATPase. ^{201}Tl is a gamma emitting isotope with a half-life of 73 hours, meaning the effective dose to patients remains very high. The first assessment of [^{201}Tl]TlCl for myocardial perfusion imaging by Bodenheimer *et al*., found it improved sensitivity and had good specificity in the diagnosis of coronary heart disease (CAD), compared to electrocardiography.[142]

1.5.2 [^{99m}Tc]Tc-Sestamibi and [^{99m}Tc]Tc-Tetrofosmin

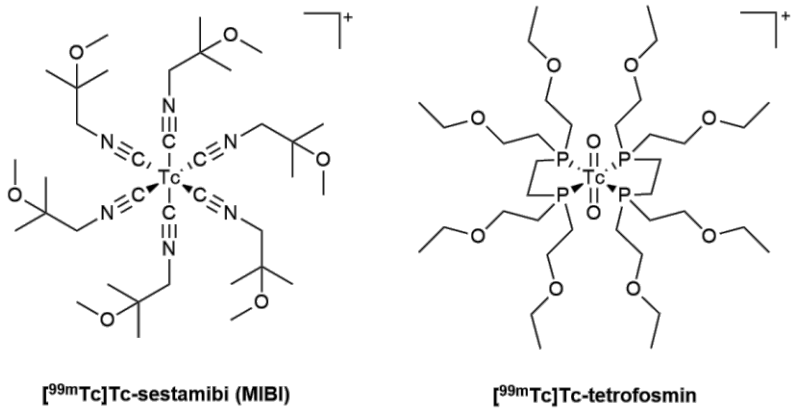

Figure 1.16 Two examples of ^{99m}Tc radiolabelled lipophilic cations, [^{99m}Tc]Tc-MIBI and [^{99m}Tc]Tc-tetrofosmin, used for mitochondrial imaging and myocardial perfusion imaging.[143,144]

In the 1990s, ^{99m}Tc complexes superseded ^{201}Tl as the gold-standard radioisotope for mitochondrial imaging and myocardial perfusion imaging. Compared to the long half-life of ^{201}Tl, ^{99m}Tc has a half-life of 6 hours, resulting in a lower radiation dose to the patient. Another advantage of ^{99m}Tc is the longer half-life of the ^{99}Mo parent isotope, compared to the parent isotope of ^{201}Tl, ^{201}Pb, therefore ^{99}Mo generators are usable for much longer than their ^{201}Pb analogue. Two gold-standard ^{99m}Tc lipophilic cations are [^{99m}Tc]Tc-MIBI and [^{99m}Tc]Tc-tetrofosmin (**Figure 1.16**), with both consisting of a cationic technetium core, Tc(I) for MIBI and Tc(V) for tetrofosmin.[143,144] The metal Tc^+ cores are shielded from hydrophilic

interactions through the protection afforded by the surrounding alkoxy ligands, leading to the improvement of lipophilicity of the radiotracer. [^{99m}Tc]Tc-MIBI was designed as part of a study looking into the potential of hexakis(alkylisonitrile)Tc(I) complexes to effectively image the myocardium. The *tert*-butyl isonitrile derivative was found to be the most effective myocardial imaging agent, owing to its high lipophilicity.[143] In 1990, MIBI had undergone a transformation into the 2-methoxy isobutyl isonitrile ligand system shown in **Figure 1.16**, which showed effective detection of disease in coronary arteries.[145]

[^{99m}Tc]Tc-tetrofosmin is a trans-dioxo-bis(diphosphine)Tc(V) cation that was developed by Kelly *et al*. in 1993, which shows an increased clearance rate from non-target tissue, such as blood and liver, as well as being stable for 8 hours after room temperature reconstitution.[144] Both ^{99m}Tc-based imaging agents are used for clinical myocardial perfusion imaging and are available in radiolabelling kits, removing the need for any complex radiosynthesis, easing patient administration.[146] Recent work by the Southworth Group focusses on the preclinical assessment of the effect of anthracycline-based anti-cancer pharmaceuticals, such as doxorubicin on the function of the heart. The aim of these studies is to detect changes in $\Delta\Psi_m$ related to cardiac dysfunction before it is detectable by echocardiography, and beyond the point of clinical intervention.[58]

1.5.3 PET-Based Triarylphosphonium Salts

The advantages of higher resolution images and the capacity for 3D pharmacokinetic modelling afforded by PET imaging, has resulted in a shift of focus in research from SPECT-based techniques, commonly used in the clinic, towards the development of PET-based lipophilic and cationic imaging agents for imaging mitochondrial function. Organic-based PET radioisotopes, the most common of which are ^{11}C and ^{18}F, do not rely on a lipophilic coordination sphere as ^{99m}Tc does. Instead, mitochondrial targeting is typically achieved through the addition of a triphenylphosphonium (TPP) group, via an S_N2 reaction of the phosphorus-centred lone pair on a primary (1^o) carbon atom and a leaving group such as a halide, mesylate or tosylate.[147–149] The high lipophilicity of the TPP moiety is facilitated through electronic resonance, with the positive charge easily delocalised across the surface area of the three aromatic rings (**Scheme 1.1**).

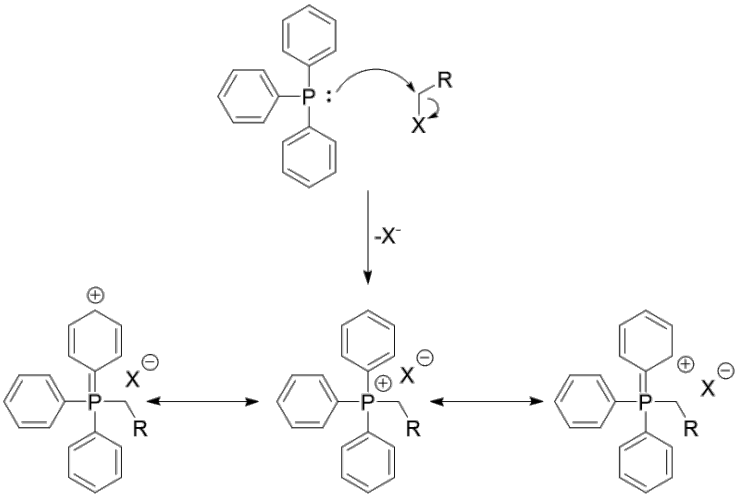

Scheme 1.1 The formation of a quaternary TPP cation via an S_N2 reaction, including resonance forms allowing for the delocalisation of the positive charge across the aromatic rings. X = counter ion.

In 2017, Zielonka *et al*. reviewed the capacity of TPP-functionalised compounds to target the mitochondria.[16] A generic structure for TPP-conjugated compounds was proposed, consisting of three parts: a functional moiety, a linker and a targeting moiety (**Figure 1.17**). With this project in mind, the functional moiety (blue) represents the imaging moiety, in specific the metal chelating ligand.

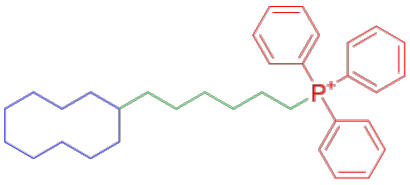

Figure 1.17 Generic mitochondrial targeting compound described by Zielonka *et al*., consisting of a functional moiety (blue), a linker (green) and a targeting moiety (red).[16]

The imaging moiety is connected to the targeting moiety, TPP, through a linking functionality, which can help to distance the functional moiety, if hydrophilic, from the lipophilic TPP group to promote mitochondrial uptake. An example of this is Mito-Gd-DOTA, which has a ten-carbon long chain distancing Gd-DOTA from TPP.

1.5.3.1 [^{11}C]C-TPMP

The first PET-based TPP containing probe was developed by Fukuda *et al*. in 1986, consisting of a TPP group methylated with [^{11}C]methyl iodide. The radiotracer, [^{11}C]C-TPMP, showed preferential uptake in the myocardium, where it was retained for 60 minutes.[150] [^{11}C]C-TPMP

was implemented in a canine brain tumour model, which utilised a combination of histology and PET imaging to indicate enhanced uptake and retention in brain tumours.[151]

1.5.3.2 ^{18}F-Labelled TAP Radiotracers

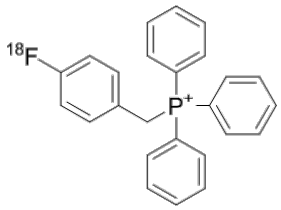

Figure 1.18 [^{18}F]F-BnTP, the incipient ^{18}F-labelled phosphonium cation radiotracer for mitochondrial imaging.[152]

The short physical half-life of ^{11}C (20 min) limits its use in PET imaging, with the length and complexity of the chemistry being restricted. The longer half-life of ^{18}F (110 min) quickly turned the focus of PET-based TPP radiotracers towards utilising ^{18}F, most notably [^{18}F]F-BnTP (**Figure 1.18**), synthesised by Ravert *et al*. in 2004.[152] Initial *in vivo* studies by Madar *et al*. showed notable uptake and retention in the myocardium, at 60 minutes post-injection (p.i.) the anatomy of the heart was clearly delineated from the blood, lungs and liver.[153] The promise of [^{18}F]F-BnTP in its initial *in vivo* study has led to its comparison, using *ex vivo* ischemia experiments, with [^{99m}Tc]Tc-tetrofosmin and [^{201}Tl]Tl.[154,155] [^{18}F]F-BnTP exhibited better accuracy in determining stenosis compared to [^{99m}Tc]Tc-tetrofosmin, and showed clear delineation of the ischemic area of interest compared to [^{201}Tl]Tl. The primary limitation of [^{18}F]F-BnTP was its radiosynthesis, initially reported as involving four reaction steps taking 82 minutes, giving an RCY of just 6 %.[153] However, in 2016, Zhang *et al*. reported a one-step synthesis using a pinacolyl arylboronate precursor with an RCY of over 60 %, followed by Waldmann *et al* designing an automated route in 2018.[156,157]

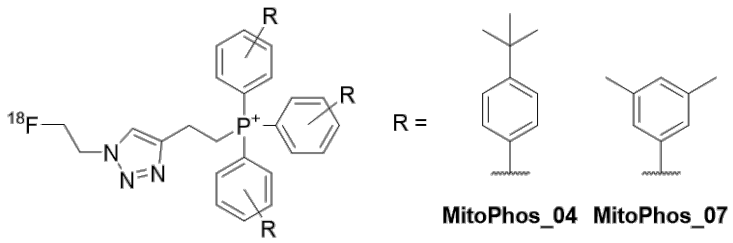

Figure 1.19 [^{18}F]F-MitoPhos_04 and _07, synthesised by Haslop *et al*.[158,159] These radiotracers consist of a 'click' chemistry motif to facilitate radiosynthesis and different alkyl functionalisation motifs to alter their mitochondrial uptake.

Kim *et al*. prepared a series of [^{18}F]F-BnTP derivatives, with each analogue consisting of a different linker group, such as ethoxyethyl and hexyl linkers, between the ^{18}F moiety and the TPP cation, to assess differences in uptake and retention in the myocardium.[160,161] In line with studies by Kim *et al*., Haslop *et al*. developed a series of radiofluorinated TPP cations, the MitoPhos series (**Figure 1.19**), which incorporated alkyl-functionalisation on triarylphosphonium (TAP) moieties to assess their differences in lipophilicity, therefore how readily these radiotracers can permeate lipid bilayer membranes for successful mitochondrial uptake.[158,159] The differing lipophilicities of these MitoPhos compounds results in a change of their retention times by HPLC, which led to Haslop *et al*. synthesising all of the MitoPhos compounds in 'one-pot' and isolating them by HPLC once the reaction was complete. In 2019, McCluskey *et al*. assessed the cardiac uptake and retention in depolarised mitochondria of [^{18}F]F-MitoPhos_07 (**Figure 1.19**) compared to [^{99m}Tc]Tc-MIBI, using isolated perfused rat hearts.[162] The pharmacokinetic profiles of [^{18}F]F-MitoPhos_07 and [^{18}F]F-BnTP and their response to acute doxorubicin-induced cardiotoxicity were assessed *in vivo*. [^{18}F]F-MitoPhos_07 was found to exhibit more than double retention in the myocardium, compared to [^{99m}Tc]Tc-MIBI, and also showed promising *in vivo* biodistribution properties, with fast washout from blood and liver, and stable retention in the myocardium. The most significant finding of this study was a notable dose-dependent decrease of cardiac retention of [^{18}F]F-MitoPhos_07 was observed before biomarker alterations were detected, highlighting its promise for imaging chemotherapy-induced cardiotoxicity.

1.5.3.3 ^{64}Cu-Labelled TAP Radiotracers

In 2007, Wang *et al*. utilised the radiometal ^{64}Cu through the use of a DO3A chelator linked to a variety of TAP motifs with a xylyl bridging group, shown in **Figure 1.20**.[163] Unlike radioisotopes such as ^{11}C and ^{18}F, ^{64}Cu and other radiometals require a chelator to connect the imaging moiety with the TAP targeting moiety. Wang *et al*. synthesised a range of ^{64}Cu-labelled imaging agents, including *para*-methoxy functionalisation of the phenyl groups and replacing the phosphorus cation centre with an arsenic cation. Despite low log *D* values exhibited for these radiotracers, tumour mitochondria were still targeted effectively, with the methoxy analogue showing a tumour/heart uptake ratio 40 times greater than [^{99m}Tc]Tc-MIBI at 120 minutes post-injection.

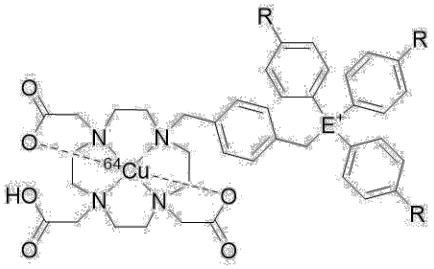

Figure 1.20 Generic structure of ^{64}Cu-labelled DO3A probes developed by Wang *et al*., R = H, OMe; E = P, As.[163]

In 2011, Zhou *et al*. reviewed ^{64}Cu-chelation of TAP-functionalised DO3A ligands, including a range of phosphonium cations, including mono-TPP and bis-TPP functionalised DO2A chelators. The review also surveyed different linking groups, including propyl and butyl groups, along with the generic xylyl linker.[164] The final aspect of the review discussed different synthetic methodologies, with a focus on functionalising a DO3A or NOTA chelator with a thiocyanate group and connecting the TPP cation through its functionalisation with an amine group.

1.5.4 $^{67/68}$Ga-Labelled Lipophilic and Cationic Radiotracers

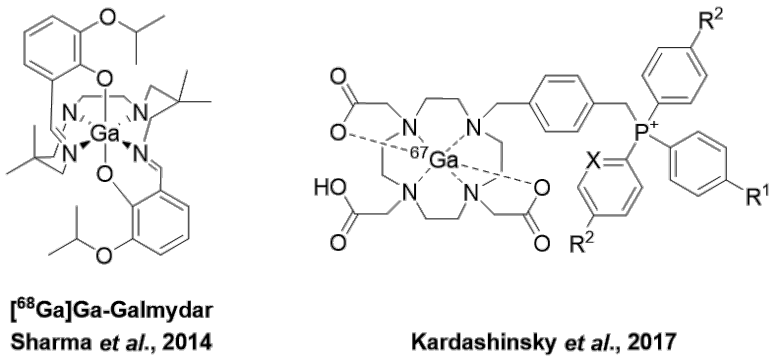

Figure 1.21 Two examples of $^{67/68}$Ga-labelled lipophilic cations. [^{68}Ga]Ga-Galmydar, developed by Sharma *et al*. in 2014 (*left)*.[165] ^{67}Ga-labelled DO3A compounds developed by Kardashinsky *et al*. in 2017 (*right*). R^1 = I, H, Me, OMe; R^2 = H, Me, OMe; X = CH, N.[166]

In 2014, Sharma *et al*. designed the first reported ^{68}Ga-labelled lipophilic cation for PET myocardial perfusion imaging, later named [^{68}Ga]Ga-Galmydar (**Figure 1.21**).[165] [^{68}Ga]Ga-Galmydar consists of a gallium-68 metal core surrounded by aromatic and isopropoxide groups as a means to improve the lipophilicity of the complex, as is the case for [^{99m}Tc]Tc-MIBI which is surrounded by alkoxy ligands which protect the Tc^+ from hydrophilic interactions. Biological experiments were performed using ^{67}Ga, owing to its longer half-life.

For ^{68}Ga radiosynthesis of the compound, the [^{68}Ga]$GaCl_3$ generator eluate is converted into [^{68}Ga][$Ga(acac)_3$] before labelling begins, since a low affinity of the ligand is required to counter the energy needed to remove the protecting group of the chelator upon radiolabelling.

Despite the radiosynthetic problem, the radiotracer demonstrated good uptake in *in vitro* assays, and *in vivo* studies showed significant heart/blood uptake after 120 minutes, but also showed a very low heart/liver activity ratio, confirming significant liver uptake of the radiotracer. In 2019, Sivapackiam *et al*. assessed [^{68}Ga]Ga-Galmydar for its use in reporting on doxorubicin-induced cardiotoxicity.[167] *In vivo* experiments showed a near 2-fold decrease in cardiac retention of doxorubicin treated rats compared with their control vehicle-treated counterparts. These results demonstrate the sensitivity of [^{68}Ga]Ga-Galmydar towards changes in $\Delta\Psi_m$, and therefore its use in monitoring the mitochondrial function of cardiac tissue after anthracycline treatment *in vivo*.

The second family of compounds to be discussed were synthesised by Kardashinsky *et al*. in 2017, where a series of TAP-functionalised DO3A compounds were developed for ^{67}Ga-labelling, shown in **Figure 1.21**.[166] This series of compounds included methyl and methoxy aryl-functionalisation, as well as mono-iodo and pyridyl asymmetric analogues, with functionalisation of the TAP motif allowing for the tuning of radiotracer lipophilicity, therefore modifying radiotracer pharmacokinetics and their capacity to penetrate cellular membranes. In a similar manner as the initial study by Sharma *et al*., Kardashinksy *et al*. focussed on radiolabelling with ^{67}Ga to utilise its longer half-life. The radiosynthetic procedure required pH adjustments, along with two purification steps which would not be suitable for ^{68}Ga-labelling due to its shorter half-life. All four complexes studied were stable in PBS, but did show metabolic degradation after 24 hours in human serum.

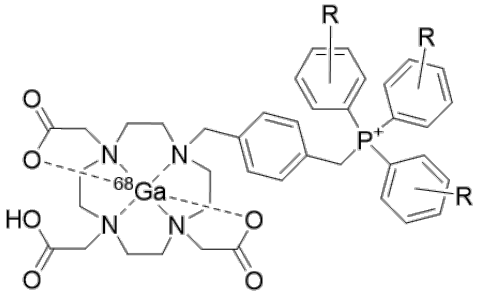

Figure 1.22 General structure of ^{68}Ga-labelled TAP-functionalised DO3A complexes synthesised by Smith *et al*., R = H, *p*-Me and *m*,*m'*-Me.[168]

This degradation was thought not to be issue on the timescale afforded by the half-life of ^{68}Ga, and led to the development of a series of TAP-functionalised DO3A complexes for ^{68}Ga-chelation by Smith *et al*. in 2018 (**Figure 1.22**).[168] The design of these chelators originated from the rationale of combining DO3A-xy-TAP chelators used for ^{67}Ga, shown in **Figure 1.21**, and the tuneable lipophilicity afforded by alkyl-functionalised TAP cations.[159,166] As anticipated for ^{68}Ga-chelation of DO3A chelators, successful radiolabelling required heating at 100 ºC for 30 minutes, with RCY values of 98 %, 100 % and 97 % obtained for triphenylphosphonium (TPP), tritolylphosphonium (TTP) and trixylylphosphonium (TXP) derivatives respectively. The major advantage of these high RCY values, meant no post-labelling purification was needed before biological experiments were performed. The capacity of these compounds to report on $\Delta\Psi_m$ was assessed *in vitro* in cultured tumour cells, showing a three-fold increase in uptake compared to free [^{68}Ga]Ga(III). However, *ex vivo* assessment of the TXP analogue in isolated perfused rat hearts showed less than 1 % retention in healthy cardiac tissue, compared to approximately 40 % uptake typically observed for [^{99m}Tc]Tc-MIBI.[58] The retention was not significantly diminished by mitochondrial depolarisation with the ionophore carbonyl cyanide *m*-chlorophenyl hydrazone (CCCP), which was explained by the insufficient lipophilicity exhibited by this family of radiotracers (log $D_{7.4}$ between -3.12 and -1.81) to successfully penetrate cell membranes to reach the mitochondria. The research outlined in this thesis will begin with a series of DO2A-based ligands with bisTAP- and bisaryl-functionalisation, aimed at providing a more uniform positive charge distribution across the overall complex, whilst also increasing the lipophilicity of such complexes to improve their mitochondrial uptake and retention. Radiosynthetic and biological studies performed on such radiotracers will advise future designs of ^{68}Ga-based lipophilic cations discussed in this thesis. The following section briefly outlines the aims and objectives of the work in this thesis, including an overview of the content involved in each chapter.

1.6 Aims of the Project

The primary aim of this PhD project has been to develop new ligand systems to form lipophilic and cationic complexes with gallium-68, for the purpose of assessing their mitochondrial uptake and retention in pre-clinical studies. In order to achieve this, new ligands are synthesised, characterised and subsequently radiochemical experiments are performed, with a view to optimise their radiochemistry to produce ^{68}Ga-based radiotracers with high radiochemical purity and yield. To assess each radiotracers lipophilicity, log *D* measurements

will be performed to gain an insight into their viability as mitochondrially-targeted radiotracers. Those radiotracers that exhibit desirable log *D* values will be explored further through an initial biological assessment. The *ex vivo* Langendorff isolated perfused heart model is used to assess the myocardial uptake and retention of the radiotracers in both healthy and compromised hearts.[169] This initial biological assessment will aide in determining if further biological studies are warranted, as well as informing on the design of future families of ligands.

Chapter 2 explores the chemical synthesis of a range of macrocyclic-based ligand families for gallium-68 chelation, with a modular approach employed to provide ligand sets with tuneable lipophilicities.

Chapter 3 explores the radiolabelling of the aforementioned macrocyclic-based ligands with gallium-68. To assess the lipophilicities of these radiotracers, log *D* measurements will be taken, including analysis by HPLC to identify the degree of speciation in the radiolabelled complexes. Ligand radiolabelling optimisation will be investigated if required.

Chapter 4 discusses the initial biological assessment of the most promising radiotracers from *chapters 2* and *3*. The first biological assessment undertaken is the Langendorff isolated perfused heart model. This *ex vivo* study provides a direct readout for the ability of a chosen radiotracer to report on mitochondrial dysfunction.

Chapter 5 looks at the chemical synthesis of several acyclic-based ligand sets for gallium-68, and as with macrocyclic ligand sets in *chapter 2*, a modular approach is used to give ligand families with tuneable lipophilicities.

Chapter 6 looks at the conclusions drawn from this project, outlining the outlook and future work of the project, in relation to the radiolabelling of acyclic ligand sets with gallium-68, and the generation of future series of ligands for gallium-68 chelation.

Chapter 7 includes experimental procedures for synthetic chemistry (*chapters 2* and *5*), gallium-68 radiochemistry (*chapter 3*) and initial pre-clinical biological studies (*chapter 4*).

Chapter 8 includes NMR, MS and DFT data.

1.7 References for Chapter 1

1 M. R. Duchen, *Mol. Aspects Med.*, 2004, **25**, 365–451.

2 J. F. Tait, *J. Nucl. Med.*, 2008, **49**, 1573–1576.

3 D. R. Green and G. Kroemer, *Science.*, 2004, **305**, 626–629.

4 W. Kühlbrandt, *BMC Biol.*, 2015, **13**, 89.

5 M. P. Murphy and R. A. . Smith, *Adv. Drug Deliv. Rev.*, 2000, **41**, 235–250.

6 S. Oiseth, L. Jones and E. Maza, Electron Transport Chain (ETC), https://www.lecturio.com/concepts/electron-transport-chain-etc/, (accessed 21 February 2022).

7 B. Alberts, A. Johnson and J. Lewis, *Molecular Biology of the Cell*, Garland Science, New York, 4th edn., 2002.

8 H. Wang and G. Oster, *Nature*, 1998, **396**, 279–282.

9 T. Elston, H. Wang and G. Oster, *Nature*, 1998, **391**, 510–513.

10 M. Ahmad, A. Wolberg and C. I. Kahwaji, *Biochemistry, Electron Transport Chain*, StatPearls Publishing, Treasure Island (FL), 2021.

11 A. Kumari, in *Sweet Biochemistry*, ed. A. Kumari, Academic Press, 2018, pp. 13–16.

12 G. M. Cooper, *The Cell: A Molecular Approach*, Sinauer Associates, Sunderland (MA), 2nd edn., 2000.

13 M. P. Murphy, *Biochim. Biophys. Acta - Bioenerg.*, 2008, **1777**, 1028–1031.

14 M. P. Murphy, *Trends Biotechnol.*, 1997, **15**, 326–330.

15 D. M. Bers, *Nature*, 2002, **415**, 198–205.

16 J. Zielonka, J. Joseph, A. Sikora, M. Hardy, O. Ouari, J. Vasquez-Vivar, G. Cheng, M. Lopez and B. Kalyanaraman, *Chem. Rev.*, 2017, **117**, 10043–10120.

17 G. F. Azzone, D. Pietrobon and M. Zoratti, in *Current Topics in Bioenergetics*, ed. C. P. Lee, Elsevier, 1984, vol. 13, pp. 1–77.

18 L. D. Zorova, V. A. Popkov, E. Y. Plotnikov, D. N. Silachev, I. B. Pevzner, S. S. Jankauskas, V. A. Babenko, S. D. Zorov, A. V Balakireva, M. Juhaszova, S. J. Sollott and D. B. Zorov, *Anal. Biochem.*, 2018, **552**, 50–59.

19 L. B. Chen, *Annu. Rev. Cell Biol.*, 1988, **4**, 155–181.

20 D. M. Hockenbery, *Cancer Cell*, 2002, **2**, 1–2.

21 G. Kroemer and J. Pouyssegur, *Cancer Cell*, 2008, **13**, 472–482.

22 B. Zhang, D. Wang, F. Guo and C. Xuan, *Fam. Cancer*, 2015, **14**, 19–23.

23 Z. Derdák, P. Fülöp, E. Sabo, R. Tavares, E. P. Berthiaume, M. B. Resnick, G. Paragh, J. R. Wands and G. Baffy, *Carcinogenesis*, 2006, **27**, 956–961.

24 C. Brenner and G. Kroemer, *Science.*, 2000, **289**, 1150–1151.

25 B. G. Heerdt, M. A. Houston, A. J. Wilson and L. H. Augenlicht, *Cancer Res.*, 2003, **63**, 6311–9.

26 J. Hopkins, Anatomy and Function of the Coronary Arteries, https://www.hopkinsmedicine.org/health/conditions-and-diseases/anatomy-and-function-of-the-coronary-arteries, (accessed 11 May 2022).

27 H. Lemieux and C. L. Hoppel, *J. Bioenerg. Biomembr.*, 2009, **41**, 99–106.

28 B. Kadenbach, R. Ramzan, R. Moosdorf and S. Vogt, *Mitochondrion*, 2011, **11**, 700–706.

29 E. T. H. Yeh, A. T. Tong, D. J. Lenihan, S. W. Yusuf, J. Swafford, C. Champion, J.-B. Durand, H. Gibbs, A. A. Zafarmand and M. S. Ewer, *Circulation*, 2004, **109**, 3122–3131.

30 S. E. Lipshultz, R. Karnik, P. Sambatakos, V. I. Franco, S. W. Ross and T. L. Miller, *Curr. Opin. Cardiol.*, 2014, **29**, 103–112.

31 R. Kizek, V. Adam, J. Hrabeta, T. Eckschlager, S. Smutny, J. V Burda, E. Frei and M. Stiborova, *Pharmacol. Ther.*, 2012, **133**, 26–39.

32 D. J. Cutter, M. Schaapveld, S. C. Darby, M. Hauptmann, F. A. van Nimwegen, A. D. G. Krol, C. P. M. Janus, F. E. van Leeuwen and B. M. P. Aleman, *JNCI J. Natl. Cancer Inst.*, 2015, **107**, 1–9.

33 F. A. van Nimwegen, M. Schaapveld, C. P. M. Janus, A. D. G. Krol, E. J. Petersen, J. M. M. Raemaekers, W. E. M. Kok, B. M. P. Aleman and F. E. van Leeuwen, *JAMA Intern. Med.*, 2015, **175**, 1007.

34 H. S. Haugnes, T. Wethal, N. Aass, O. Dahl, O. Klepp, C. W. Langberg, T. Wilsgaard, R. M. Bremnes and S. D. Fosså, *J. Clin. Oncol.*, 2010, **28**, 4649–4657.

35 J. V McGowan, R. Chung, A. Maulik, I. Piotrowska, J. M. Walker and D. M. Yellon, *Cardiovasc. Drugs Ther.*, 2017, **31**, 63–75.

36 D. Cardinale, F. Iacopo and C. M. Cipolla, *Front. Cardiovasc. Med.*, 2020, **7**, 26.

37 S. M. Swain, F. S. Whaley and M. S. Ewer, *Cancer*, 2003, **97**, 2869–2879.

38 D. L. Hershman, R. B. McBride, A. Eisenberger, W. Y. Tsai, V. R. Grann and J. S. Jacobson, *J. Clin. Oncol.*, 2008, **26**, 3159–3165.

39 M. Moulin, J. Piquereau, P. Mateo, D. Fortin, C. Rucker-Martin, M. Gressette, F. Lefebvre, M. Gresikova, A. Solgadi, V. Veksler, A. Garnier and R. Ventura-Clapier, *Circ. Hear. Fail.*, 2015, **8**, 98–108.

40 P. J. Barrett-Lee, J. M. Dixon, C. Farrell, A. Jones, R. Leonard, N. Murray, C. Palmieri, C. J. Plummer, A. Stanley and M. W. Verrill, *Ann. Oncol.*, 2009, **20**, 816–827.

41 L. W. Jones, M. J. Haykowsky, J. J. Swartz, P. S. Douglas and J. R. Mackey, *J. Am. Coll. Cardiol.*, 2007, **50**, 1435–1441.

42 D. Wadhwa, N. Fallah-Rad, D. Grenier, M. Krahn, T. Fang, R. Ahmadie, J. R. Walker, D. Lister, R. C. Arora, I. Barac, A. Morris and D. S. Jassal, *Breast Cancer Res. Treat.*, 2009, **117**, 357–364.

43 E. D. Brookins Danz, J. Skramsted, N. Henry, J. A. Bennett and R. S. Keller, *Free Radic. Biol. Med.*, 2009, **46**, 1589–1597.

44 P. S. Green and C. Leeuwenburgh, *Biochim. Biophys. Acta*, 2002, **1588**, 94–101.

45 Y. Ichikawa, M. Ghanefar, M. Bayeva, R. Wu, A. Khechaduri, S. V. N. Prasad, R. K. Mutharasan, T. J. Naik and H. Ardehali, *J. Clin. Invest.*, 2014, **124**, 617–630.

46 T. Simůnek, M. Stérba, O. Popelová, M. Adamcová, R. Hrdina and V. Gersl, *Pharmacol. Rep.*, 2009, **61**, 154–171.

47 X. Xu, H. L. Persson and D. R. Richardson, *Mol. Pharmacol.*, 2005, **68**, 261–271.

48 K. T. Sawicki, V. Sala, L. Prever, E. Hirsch, H. Ardehali and A. Ghigo, *Annu. Rev. Pharmacol. Toxicol.*, 2021, **61**, 309–332.

49 T. C. Tan and M. Scherrer-Crosbie, *Curr. Cardiovasc. Imaging Rep.*, 2012, **5**, 403–409.

50 M. Martín, F. J. Esteva, E. Alba, B. Khandheria, L. Pérez-Isla, J. Á. García-Sáenz, A. Márquez, P. Sengupta and J. Zamorano, *Oncologist*, 2009, **14**, 1–11.

51 T. Paaladinesh, G. A. D., N. Tomoko, P. J. Carlos, P. Z. B. and M. T. H., *J. Am. Coll. Cardiol.*, 2013, **61**, 77–84.

52 M. S. Ewer and D. J. Lenihan, *J. Clin. Oncol.*, 2008, **26**, 1201–1203.

53 G. J. Yoon, M. L. Telli, D. P. Kao, K. Y. Matsuda, R. W. Carlson and R. M. Witteles, *J. Am. Coll. Cardiol.*, 2010, **56**, 1644–1650.

54 S. T. Smiley, M. Reers, C. Mottola-Hartshorn, M. Lin, A. Chen, T. W. Smith, G. D. J. Steele and L. B. Chen, *Proc. Natl. Acad. Sci. U. S. A.*, 1991, **88**, 3671–3675.

55 B. Ehrenberg, V. Montana, M. D. Wei, J. P. Wuskell and L. M. Loew, *Biophys. J.*, 1988, **53**, 785–794.

56 R. K. Emaus, R. Grunwald and J. J. Lemasters, *Biochim. Biophys. Acta - Bioenerg.*, 1986, **850**, 436–448.

57 E. C. T. Waters, F. Baark, Z. Yu, F. Mota, T. R. Eykyn, R. Yan and R. Southworth, *Mol. Imaging Biol.*, 2022, **24**, 377–383.

58 Z. M. Safee, F. Baark, E. C. T. Waters, M. Veronese, V. R. Pell, J. E. Clark, F. Mota, L. Livieratos, T. R. Eykyn, P. J. Blower and R. Southworth, *Sci. Rep.*, 2019, **9**, 216.

59 Y.-S. Kim, Z. He, W.-Y. Hsieh and S. Liu, *Bioconjug. Chem.*, 2007, **18**, 929–936.

60 T. Tominaga, H. Ito, Y. Ishikawa, R. Iwata, K. Ishiwata and S. Furumoto, *J. Label. Compd. Radiopharm.*, 2016, **59**, 117–123.

61 G. L. Law and W. T. Wong, in *The Chemistry of Molecular Imaging*, ed. N. J. Long and W. T. Wong, John Wiley & Sons, Inc., Hobken New Jersey, 1st edn., 2014, ch. 1, pp. 1-24.

62 A. Rahmim and H. Zaidi, *Nucl. Med. Commun.*, 2008, **29**, 193–207.

63 G. R. Small, R. G. Wells, T. Schindler, B. J. W. Chow and T. D. Ruddy, *Can. J. Cardiol.*, 2013, 29, 275–284.

64 D. E. Kuhl and R. Q. Edwards, *Radiology*, 1963, **80**, 653–662.

65 OECD and Nuclear Energy Agency, in *The Supply of Medical Isotopes*, 2019, pp. 42–47.

66 R. Gupta and M. F. Hashmi, *Mo99 - Tc99m Generator*, Treasure Island (FL), 2022.

67 S. Hasan and M. A. Prelas, *SN Appl. Sci.*, 2020, **2**, 1782.

68 H. A. Parmar, M. Ibrahim, M. Arabi and S. K. Mukherji, in *Oncologic Imaging: A Multidisciplinary Approach*, ed. P. Silverman, W.B. Saunders, Philadelphia, 2012, pp. 621–631.

69 P. J. Blower, *Dalton. Trans.*, 2015, **44**, 4819–4844.

70 S. L. Pimlott and A. Sutherland, *Chem. Soc. Rev.*, 2011, **40**, 149–162.

71 A. P. Wolf and W. B. Jones, *Radiochim. Acta*, 1983, **34**, 1–8.

72 J. Nairne, P. B. Iveson and A. Meijer, in *Progress in Medicinal Chemistry*, eds. G. Lawton and D. Witty, Elsevier, 2015, vol. 54, pp. 231–280.

73 L. K. Petrovich and E. S. Pretorius, in *Radiology Secrets Plus*, eds. E. S. Pretorius and J. Solomon, Elsevier, Philadelphia, 2011, pp. 19–22.

74 K. M. Osytek, P. J. Blower, I. M. Costa, G. E. Smith, V. Abbate and S. Y. A. Terry, *EJNMMI Res.*, 2021, **11**, 63.

75 S. J. Goldsmith and S. Vallabhajosula, *Semin. Nucl. Med.*, 2009, **39**, 2–10.

76 A. Draisma, L. Maffioli, M. Gasparini, G. Savelli, E. Pauwels and E. Bombardieri, *Tumori*, 1998, **84**, 434–41.

77 M. Okada, N. Sato, K. Ishii, K. Matsumura, M. Hosono and T. Murakami, *RadioGraphics*, 2010, **30**, 939–957.

78 G. B. Saha, *Basics of PET Imaging*, Springer Cham, Cleveland, 2016.

79 Z. Li and P. S. Conti, *Adv. Drug Deliv. Rev.*, 2010, **62 11**, 1031–1051.

80 D. L. Bailey, D. W. Townsend, P. E. Valk and M. N. Maisey, *Positron Emission Tomography: Basic Sciences*, Springer London, 2005.

81 M. Rudin, *Molecular Imaging*, Imperial College Press, Zurich, 2nd edn., 2013.

82 A. K. Shukla and U. Kumar, *J. Med. Phys.*, 2006, **31**, 13–21.

83 G. W. Severin, J. W. Engle, T. E. Barnhart and R. J. Nickles, *Med. Chem.*, 2011, **7**, 389–394.

84 A. Niccoli Asabella, G. L. Cascini, C. Altini, D. Paparella, A. Notaristefano and G. Rubini, *Biomed Res. Int.*, 2014, **2014**, 1–9.

85 R. W. P. Drever, A. Moljk and J. Scobie, *Philos. Mag. A J. Theor. Exp. Appl. Phys.*, 1956, **1**, 942–948.

86 H. A. Ziessman, J. P. O'Malley and J. Thrall, Eds., in *Nuclear Medicine*, W.B. Saunders, Philadelphia, 4th edn., 2014, pp. 378–423.

87 F. C. J. van de Watering, M. Rijpkema, L. Perk, U. Brinkmann, W. J. G. Oyen and O. C. Boerman, *Biomed Res. Int.*, 2014, **2014**, 1–13.

88 J. Hatazawa, K. Ishiwata, M. Itoh, M. Kameyama, K. Kubota, T. Ido, T. Matsuzawa, T. Yoshimoto, S. Watanuki and S. Seo, *J. Nucl. Med.*, 1989, **30**, 1809–13.

89 T. Ido, C.-N. Wan, V. Casella, J. S. Fowler, A. P. Wolf, M. Reivich and D. E. Kuhl, *J. Label. Compd. Radiopharm.*, 1978, **14**, 175–183.

90 J. Y. Kim, H. Park, J. C. Lee, K. M. Kim, K. C. Lee, H. J. Ha, T. H. Choi, G. Il An and G. J. Cheon, *Appl. Radiat. Isot.*, 2009, **67**, 1190–1194.

91 T. Belhocine, K. Spaepen, M. Dusart, C. Castaigne, K. Muylle, P. Bourgeois, D. Bourgeois, L. Dierickx and P. Flamen, *Int. J. Oncol.*, 2006, **28**, 1249–1261.

92 K. Yoshinaga, R. Klein and N. Tamaki, *J. Cardiol.*, 2010, **55**, 163–173.

93 J. Pijarowska-Kruszyna, M. Pocięgiel and R. Mikołajczak, in *Reference Module in Biomedical Sciences*, Elsevier, 2021.

94 M. Benešová and G. Reischl, in *Reference Module in Biomedical Sciences*, Elsevier, 2021.

95 K. Matsumoto, Y. Fujibayashi, Y. Yonekura, K. Wada, Y. Takemura, J. Konishi and A. Yokoyama, *Int. J. Radiat. Appl. Instrumentation. Part B. Nucl. Med. Biol.*, 1992, **19**, 39–44.

96 S. R. Banerjee and M. G. Pomper, *Appl. Radiat. Isot.*, 2013, **76**, 2–13.

97 N. Lepareur, *Front. Med.*, 2022, **9**, 812050.

98 I. Velikyan, *Molecules*, 2015, **20**, 12913–12943.

99 C. J. da Silva, P. A. L. da Cruz, A. Iwahara, E. M. de Oliveira, J. dos S. Loureiro, L. Tauhata, R. L. da Silva, R. Poledna and R. T. Lopes, *Appl. Radiat. Isot.*, 2018, **134**, 307–311.

100 G. I. Gleason, *Int. J. Appl. Radiat. Isot.*, 1960, **8**, 90–94.

101 M. W. Greene and W. D. Tucker, *Int. J. Appl. Radiat. Isot.*, 1961, **12**, 62–63.

102 Y. Yano and H. O. Anger, *J. Nucl. Med.*, 1964, **5**, 484–487.

103 K. V Malyshev and V. V Smirnov, *Radiokhimiya*, 1975, **17**, 137–140.

104 C. Loc'h, B. Mazièré and D. Comar, *J. Nucl. Med.*, 1980, **21**, 171–3.

105 F. Rösch, *Appl. Radiat. Isot.*, 2013, **76**, 24–30.

106 J. Schuhmacher and W. Maier-Borst, *Int. J. Appl. Radiat. Isot.*, 1981, **32**, 31–36.

107 K. P. Zhernosekov, D. V Filosofov, R. P. Baum, P. Aschoff, H. Bihl, A. A. Razbash, M. Jahn, M. Jennewein and F. Rösch, *J. Nucl. Med.*, 2007, **48**, 1741–1748.

108 F. Roesch, *Curr. Radiopharm.*, 2012, **5**, 202–211.

109 L. E. McInnes, S. E. Rudd and P. S. Donnelly, *Coord. Chem. Rev.*, 2017, **352**, 499–516.

110 M. D. Bartholomä, A. S. Louie, J. F. Valliant and J. Zubieta, *Chem. Rev.*, 2010, **110**, 2903–2920.

111 S. Kulprathipanja and D. J. Hnatowich, *Int. J. Appl. Radiat. Isot.*, 1977, **28**, 229–233.

112 M. Bauwens, R. Chekol, H. Vanbilloen, G. Bormans and A. Verbruggen, *Nucl. Med. Commun.*, 2010, **31**, 753–758.

113 M. I. Tsionou, C. E. Knapp, C. A. Foley, C. R. Munteanu, A. Cakebread, C. Imberti, T. R. Eykyn, J. D. Young, B. M. Paterson, P. J. Blower and M. T. Ma, *RSC Adv.*, 2017, **7**, 49586–49599.

114 P. M. Matthews, E. A. Rabiner, J. Passchier and R. N. Gunn, *Br. J. Clin. Pharmacol.*, 2012, **73**, 175–186.

115 G. Bandoli, A. Dolmella, F. Tisato, M. Porchia and F. Refosco, *Coord. Chem. Rev.*, 2009, **253**, 56–77.

116 E. W. Price and C. Orvig, *Chem. Soc. Rev.*, 2014, **43**, 260–290.

117 T. J. McMurry, M. Brechbiel, K. Kumar and O. A. Gansow, *Bioconjug. Chem.*, 1992, **3**, 108–117.

118 J. Šimeček, M. Schulz, J. Notni, J. Plutnar, V. Kubíček, J. Havlíčková and P. Hermann, *Inorg. Chem.*, 2012, **51**, 577–590.

119 M. I. M. Prata, A. C. Santos, C. F. G. C. Geraldes and J. J. P. de Lima, *J. Inorg. Biochem.*, 2000, **79**, 359–363.

120 J. Notni, J. Šimeček and H.-J. Wester, *ChemMedChem*, 2014, **9**, 1107–1115.

121 E. Boros, C. L. Ferreira, J. F. Cawthray, E. W. Price, B. O. Patrick, D. W. Wester, M. J. Adam and C. Orvig, *J. Am. Chem. Soc.*, 2010, **132**, 15726–15733.

122 E. T. Clarke and A. E. Martell, *Inorganica Chim. Acta*, 1991, **190**, 37–46.

123 Y. Sun, C. J. Anderson, T. S. Pajeau, D. E. Reichert, R. D. Hancock, R. J. Motekaitis, A. E. Martell and M. J. Welch, *J. Med. Chem.*, 1996, **39**, 458–470.

124 D. Meyer, M. Schaefer and B. Bonnemain, *Invest. Radiol.*, 1988, **23**, 232–235.

125 W. Niu, E. H. Wong, G. R. Weisman, Y. Peng, C. J. Anderson, L. N. Zakharov, J. A. Golen and A. L. Rheingold, *Eur. J. Inorg. Chem.*, 2004, **2004**, 3310–3315.

126 M. Zöller, J. Schuhmacher, J. Reed, W. Maier-Borst and S. Matzku, *J. Nucl. Med.*, 1992, **33**, 1366–1372.

127 T. Zhou, H. Neubert, D. Y. Liu, Z. D. Liu, Y. M. Ma, X. Le Kong, W. Luo, S. Mark and R. C. Hider, *J. Med. Chem.*, 2006, **49**, 4171–4182.

128 C. H. Taliaferro and A. Martell, *Inorganica Chim. Acta*, 1984, **85**, 9–15.

129 R. Cusnir, C. Imberti, R. C. Hider, P. J. Blower and M. T. Ma, *Int. J. Mol. Sci.* , 2017, 18.

130 D. J. Berry, Y. Ma, J. R. Ballinger, R. Tavaré, A. Koers, K. Sunassee, T. Zhou, S. Nawaz, G. E. D. Mullen, R. C. Hider and P. J. Blower, *Chem. Commun.*, 2011, **47**, 7068–7070.

131 I. Virgolini, V. Ambrosini, J. B. Bomanji, R. P. Baum, S. Fanti, M. Gabriel, N. D. Papathanasiou, G. Pepe, W. Oyen, C. De Cristoforo and A. Chiti, *Eur. J. Nucl. Med. Mol. Imaging*, 2010, **37**, 2004–2010.

132 E. Pauwels, F. Cleeren, G. Bormans and C. M. Deroose, *Am. J. Nucl. Med. Mol. Imaging*, 2018, **8**, 311–331.

133 M. T. Ma, C. Cullinane, K. Waldeck, P. Roselt, R. J. Hicks and P. J. Blower, *EJNMMI Res.*, 2015, **5**, 52.

134 S. Ray Banerjee, Z. Chen, M. Pullambhatla, A. Lisok, J. Chen, R. C. Mease and M. G. Pomper, *Bioconjug. Chem.*, 2016, **27**, 1447–1455.

135 T. Maurer, M. Eiber, M. Schwaiger and J. E. Gschwend, *Nat. Rev. Urol.*, 2016, **13**, 226–235.

136 S. R. Banerjee, M. Pullambhatla, Y. Byun, S. Nimmagadda, G. Green, J. J. Fox, A. Horti, R. C. Mease and M. G. Pomper, *J. Med. Chem.*, 2010, **53**, 5333–5341.

137 M. Eder, M. Schäfer, U. Bauder-Wüst, W.-E. Hull, C. Wängler, W. Mier, U. Haberkorn and M. Eisenhut, *Bioconjug. Chem.*, 2012, **23**, 688–697.

138 M. Eder, O. Neels, M. Müller, U. Bauder-Wüst, Y. Remde, M. Schäfer, U. Hennrich, M. Eisenhut, A. Afshar-Oromieh, U. Haberkorn and K. Kopka, *Pharmaceuticals*, 2014, **7**, 779–796.

139 U. Hennrich and M. Eder, *Pharmaceuticals*, 2021, **14**, 713.

140 J. D. Young, V. Abbate, C. Imberti, L. K. Meszaros, M. T. Ma, S. Y. A. Terry, R. C. Hider, G. E. Mullen and P. J. Blower, *J. Nucl. Med.*, 2017, **58**, 1270–1277.

141 M. Kulkarni, S. Hughes, A. Mallia, V. Gibson, J. Young, A. Aggarwal, S. Morris, B. Challacombe, R. Popert, C. Brown, P. Cathcart, P. Dasgupta, V. S. Warbey and G. J. R. Cook, *Eur. J. Nucl. Med. Mol. Imaging*, 2020, **47**, 674–686.

142 M. B. Bodenheimer, V. S. Banka, C. M. Fooshee and R. H. Helfant, *Arch. Intern. Med.*, 1979, **139**, 630–634.

143 A. G. Jones, M. J. Abrams, A. Davison, J. W. Brodack, A. K. Toothaker, S. J. Adelstein and A. I. Kassis, *Int. J. Nucl. Med. Biol.*, 1984, **11**, 225–234.

144 J. D. Kelly, A. M. Forster, B. Higley, C. M. Archer, F. S. Booker, L. R. Canning, K. W. Chiu, B. Edwards, H. K. Gill and M. McPartlin, *J. Nucl. Med.*, 1993, **34**, 222–7.

145 J. Maddahi, H. Kiat, K. F. Van Train, F. Prigent, J. Friedman, E. V Garcia, N. Alazraki, E. G. DePuey, K. Nichols and D. S. Berman, *Am. J. Cardiol.*, 1990, **66**, 55–62.

146 A. S. Arbab, K. Koizumi, K. Toyama, T. Arai and T. Araki, *J. Nucl. Med.*, 1998, **39**, 266.

147 R. J. Burns, R. A. J. Smith and M. P. Murphy, *Arch. Biochem. Biophys.*, 1995, **322**, 60–68.

148 S. E. Brown, M. F. Ross, A. Sanjuan-Pla, A.-R. B. Manas, R. A. J. Smith and M. P. Murphy, *Free Radic. Biol. Med.*, 2007, **42**, 1766–1780.

149 G. F. Kelso, C. M. Porteous, C. V Coulter, G. Hughes, W. K. Porteous, E. C. Ledgerwood, R. A. J. Smith and M. P. Murphy, *J. Biol. Chem.*, 2001, **276**, 4588–4596.

150 H. Fukuda, A. Syrota, P. Charbonneau, J. Vallois, M. Crouzel, C. Prenant, J. Sastre and C. Crouzel, *Eur. J. Nucl. Med.*, 1986, **11**, 478–483.

151 I. Madar, J. H. Anderson, Z. Szabo, U. Scheffel, P.-F. Kao, H. T. Ravert and R. F. Dannals, *J. Nucl. Med.*, 1999, **40**, 1180.

152 H. T. Ravert, I. Madar and R. F. Dannals, *J. Label. Compd. Radiopharm.*, 2004, **47**, 469–476.

153 I. Madar, H. T. Ravert, Y. Du, J. Hilton, L. Volokh, R. F. Dannals, J. J. Frost and J. M. Hare, *J. Nucl. Med.*, 2006, **47**, 1359.

154 I. Madar, H. Ravert, A. DiPaula, Y. Du, R. F. Dannals and L. Becker, *J. Nucl. Med.*, 2007, **48**, 1021.

155 T. Higuchi, K. Fukushima, C. Rischpler, T. Isoda, M. S. Javadi, H. Ravert, D. P. Holt, R. F. Dannals, I. Madar and F. M. Bengel, *J. Nucl. Med.*, 2011, **52**, 965.

156 Z. Zhang, C. Zhang, J. Lau, N. Colpo, F. Bénard and K.-S. Lin, *J. Label. Compd. Radiopharm.*, 2016, **59**, 467–471.

157 C. M. Waldmann, A. Gomez, P. Marchis, S. T. Bailey, M. Momcilovic, A. E. Jones, D. B. Shackelford and S. Sadeghi, *Mol. Imaging Biol.*, 2018, **20**, 205–212.

158 A. Haslop, A. Gee, C. Plisson and N. Long, *J. Label. Compd. Radiopharm.*, 2013, **56**, 313–316.

159 A. Haslop, L. Wells, A. Gee, C. Plisson and N. Long, *Mol. Pharm.*, 2014, **11**, 3818–3822.

160 D. Y. Kim, K. H. Yu, H.-S. Bom and J.-J. Min, *Nucl. Med. Mol. Imaging.*, 2007, **41**, 561–565.

161 D.-Y. Kim, H.-J. Kim, K.-H. Yu and J.-J. Min, *Nucl. Med. Biol.*, 2012, **39**, 1093–1098.

162 S. P. McCluskey, A. Haslop, C. Coello, R. N. Gunn, E. W. Tate, R. Southworth, C. Plisson, N. J. Long and L. A. Wells, *J. Nucl. Med.*, 2019, **60**, 1750–1756.

163 J. Wang, C.-T. T. Yang, Y.-S. S. Kim, S. G. Sreerama, Q. Cao, Z.-B. B. Li, Z. He, X. Chen and S. Liu, *J. Med. Chem.*, 2007, **50**, 5057–5069.

164 Y. Zhou and S. Liu, *Bioconjug. Chem.*, 2011, **22**, 1459–1472.

165 V. Sharma, J. Sivapackiam, S. E. Harpstrite, J. L. Prior, H. Gu, N. P. Rath and D. Piwnica-Worms, *PLoS One*, 2014, **9**, e109361.

166 M. Kardashinsky, N. Lengkeek and L. M. Rendina, *J. Label. Compd. Radiopharm.*, 2017, **60**, 4–11.

167 J. Sivapackiam, S. Kabra, S. Speidel, M. Sharma, R. Laforest, A. Salter, M. P. Rettig and V. Sharma, *PLoS One*, 2019, **14**, e0215579.

168 A. J. Smith, P. J. Gawne, M. T. Ma, P. J. Blower, R. Southworth and N. J. Long, *Dalton. Trans.*, 2018, **47**, 15448–15457.

169 O. Langendorff, *Arch. für die gesamte Physiol. des Menschen und der Tiere*, 1895, **61**, 291–332.

CHAPTER 2 – SYNTHESIS OF LIPOPHILIC AND CATIONIC MACROCYCLIC LIGANDS FOR GALLIUM-68

2. Synthesis of Lipophilic and Cationic Macrocyclic Ligands for Gallium-68

The design and synthesis of chelators that bind $[^{68}Ga]Ga^{3+}$ effectively, whilst maintaining an overall positive charge and desirable lipophilicity, is the first stage in the development of ^{68}Ga-based lipophilic and cationic radiotracers. The design of such chelators, as are relevant to this thesis, as well as their synthesis and characterisation are discussed in the chapter. Further radiolabelling and biological experiments of these chelators also helped to inform the development of subsequent ligands for ^{68}Ga-labelling, but will be discussed in chapter 3 and chapter 4.

2.1 DO2A-Based Chelators

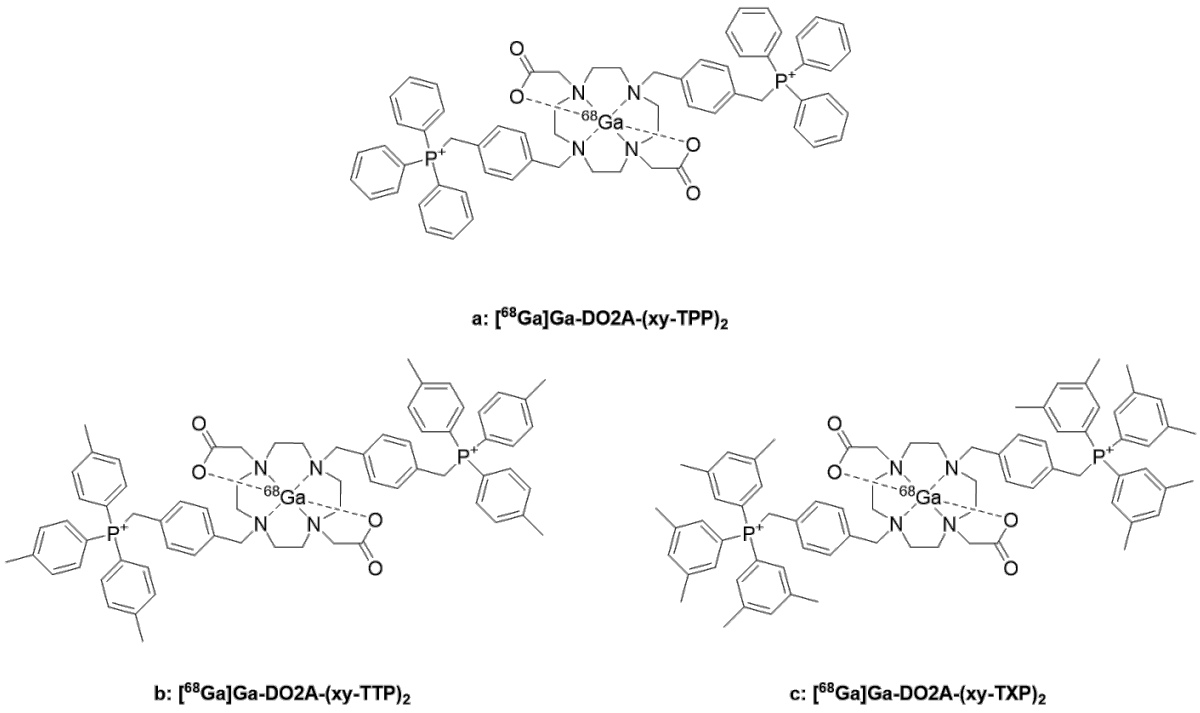

Figure 2.1 Three target DO2A-(xy-TAP)$_2$ chelators developed by Smith *et al*. in 2020, consisting of a DO2A chelating moiety and two xylyl linking groups, functionalised with TPP (**a**), TTP (**b**) or TXP (**c**) cations.[1] For clarity, counterions have been omitted.

The chelation of Ga(III) with DO3A results in one of the carboxylate arms being unbound, leading to the potential for hydrophilic interactions, and decreasing the overall lipophilicity of the radiotracer. This has been demonstrated by work published by Smith *et al*. in 2018.[2] In order to alleviate the problem posed by the presence of an unbound carboxylate arm, we

synthesised a series of 1,4,7,10-tetraazacyclododecane-1,7-diacetic acid (DO2A) compounds.[1] DO2A exhibits the appropriate hexadentate coordination environment for Ga(III), with no unbound carboxylate arm present upon binding and also providing a site for further functionalisation to improve the lipophilicity of the desired radiotracers. Following on from the previous work using the DO3A-xy-TAP chelators, the initial synthetic target was DO2A-(xy-TAP)$_2$, which contain triphenylphosphonium (TPP, **Figure 2.1a**), tritolylphosphonium (TTP, **Figure 2.1b**), and trixylylphosphonium (TXP, **Figure 2.1c**) functionalisation.

Initial synthesis of DO2A-(xy-TAP)$_2$ chelators and preliminary radiolabelling experiments with ^{68}Ga showed that replacing one of the carboxylate arms with a TAP-functionalised xylyl group, led to an increase in the overall charge of the radiotracer and an increase in mitochondrial uptake, in accordance with the Nernst equation.[3] However, in agreement with the Born equation, an increase in charge will result in a higher degree of hydrophilic interactions with aqueous solvents. The potential of increased hydrophilic interactions with aqueous solvents of the three [^{68}Ga]Ga-DO2A-(xy-TAP)$_2$ compounds, owing to the increased cationic charge, could lead to a decrease in lipophilicity. The steric bulk generated by the two large TAP groups was also thought to hinder the passage of the radiotracers through the lipid bilayer membranes. Consequentially, two DO2A-Ar$_2$ chelators (**Figure 2.2**) were also synthesised, exhibiting only a monocationic charge and being smaller in size compared to the DO2A-(xy-TAP)$_2$ analogues.

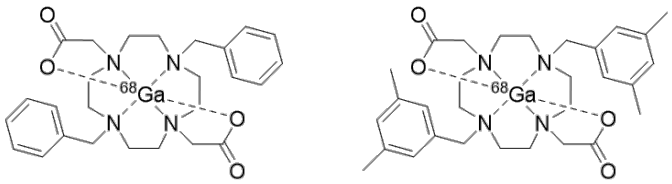

a: [^{68}Ga]Ga-DO2A-Bn$_2$ **b: [^{68}Ga]Ga-DO2A-Xy$_2$**

Figure 2.2 Two target DO2A-Ar$_2$ compounds, consisting of a DO2A chelating moiety, functionalised with two benzyl (**a**) or *m*,*m*′-xylyl (**b**) groups.[1]

Alkylation of the aromatic groups provided the means for tuneable lipophilicities, with phenyl (**Figure 2.2a**) and *m*,*m*′-xylyl (**Figure 2.2b**) analogues being synthesised. Unfunctionalised phenyl groups were chosen due to their lipophilicity and their use as a base scaffold for further functionalisation to yield future DO2A-Ar$_2$ derivatives. Functionalisation with xylyl groups is known to improve the overall lipophilicity of compounds, therefore a dixylyl derivative was

also synthesised.[2,4] This thesis describes the author's subsequent synthetic contribution towards this work that entailed the synthesis of non-radioactive Ga(III) analogues of DO2A-(xy-TPP)$_2$ (**1a**) and DO2A-Bn$_2$ (**1b**), as shown in **Scheme 2.1**, to be used as reference compounds for the radiolabelled compounds. Both sets of DO2A-based radiotracers were observed to form speciation upon chelation with [^{68}Ga]Ga(III), and could be visualised and separated by radioHPLC and will be discussed in a later section of this thesis. The synthesis of non-radioactive Ga(III) analogues would support the proposed rationale of speciation.

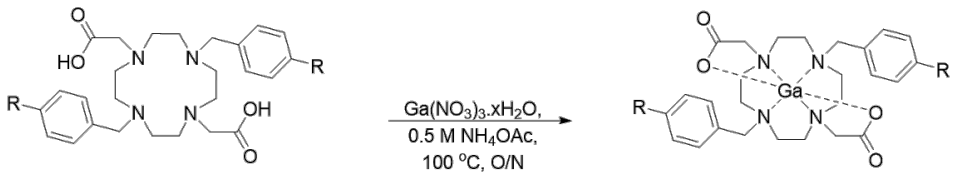

1a: DO2A-(xy-TPP)$_2$
1b: DO2A-Bn$_2$

Ga1a: Ga-DO2A-(xy-TPP)$_2$ (58 %)
Ga1b: Ga-DO2A-Bn$_2$ (11 %)

Scheme 2.1 The synthesis of Ga-DO2A-based compounds **Ga1a** and **Ga1b**. R = CH$_2$-TPP, H.

The synthetic work of Dr Smith meant that compounds DO2A-(xy-TPP)$_2$ (**1a**) and DO2A-Bn$_2$ (**1b**) were readily available for complexation with Ga(III). The source of Ga(III) came in the nitrate hydrate form, Ga(NO$_3$)$_3$.xH$_2$O, and using 0.5 M ammonium acetate, NH$_4$OAc, as the buffer of choice. Reverse-phase chromatography was used as the purification technique due to the analogous HPLC technique being ideal for assessing their radiolabelled counterparts.

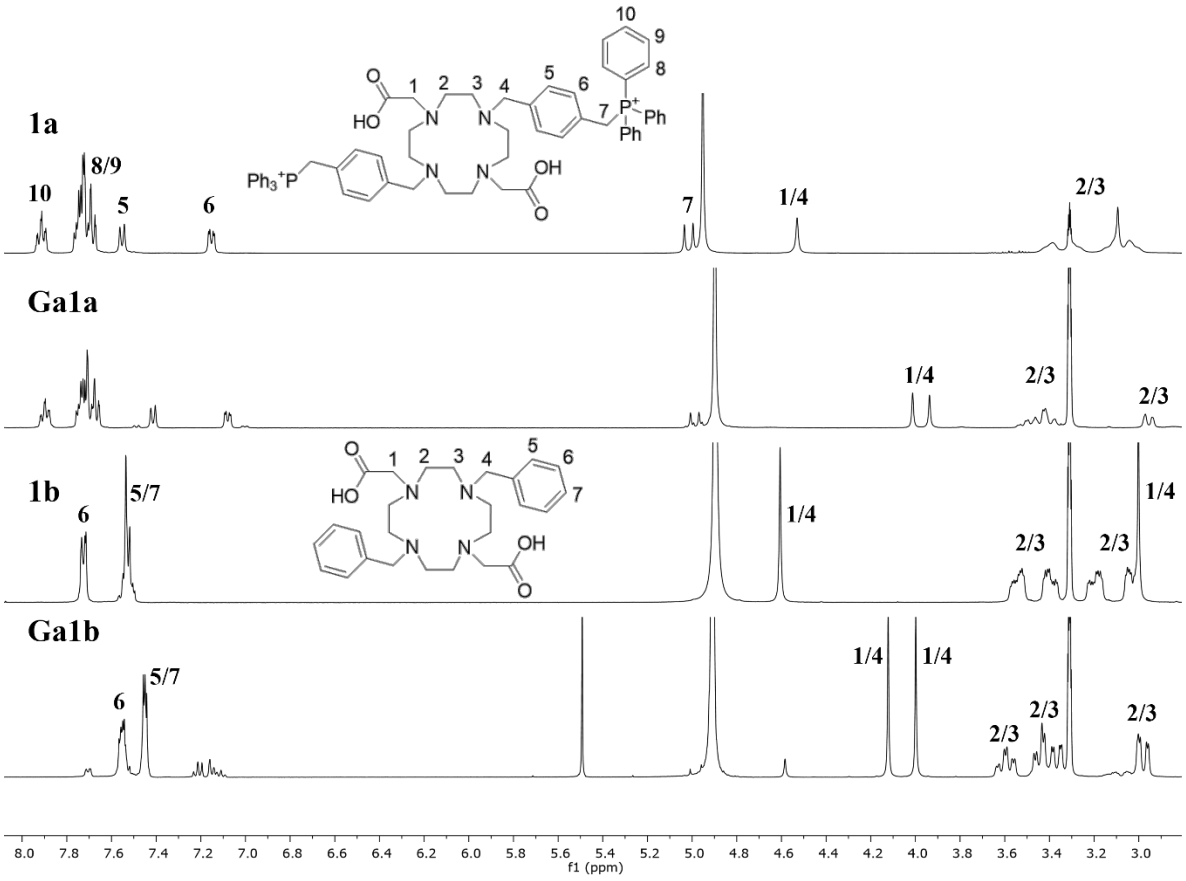

Figure 2.3 ^{1}H NMR spectra of DO2A-based ligands and their Ga-complexed analogues (CD_3OD, 400 MHz, 298 K). From top to bottom: DO2A-(xy-TPP)$_2$ (**1a**), Ga-DO2A-(xy-TPP)$_2$ (**Ga1a**), DO2A-Bn$_2$ (**1b**), Ga-DO2A-Bn$_2$ (**Ga1b**).

Characterisation of **Ga1a** and **Ga1b** was initially performed by ^{1}H NMR spectroscopy, the spectrum of both compounds shown in **Figure 2.3**. Several common features of the ^{1}H NMR spectrum of **1a** include a doublet at 5.02 ppm, arising from geminal proton phosphorus coupling, and very broad peaks referring to the protons of the ethylene bridges in the macrocyclic ring. Complexation of **1a** with Ga(III) to form complex **Ga1a** was initially confirmed by ^{1}H NMR spectroscopy, firstly the singlet at 4.60 ppm, referring to the methylene bridge protons of the pendant acetate arms and xylyl groups, shifts to 4.01 and 3.94 ppm as two singlets, representing the effect the Ga(III) core has on these two proton environments. Secondly the broad multiplet at 3.20 ppm referring to the macrocyclic protons becomes two multiplets at 3.45 and 2.95 ppm once **1a** coordinates the Ga(III) cation. Similar observations were made for the chelation of the benzyl derivative (**1b**) with Ga(III), with a shift in the aryl proton environments also seen. The ^{31}P{^{1}H} NMR spectrum was not as conclusive in identifying the formation of **Ga1a** compared to ^{1}H NMR, with the chelation of Ga(III) having

little effect on the chemical shift of the phosphorus centre, however one phosphorus-containing species was still observed.

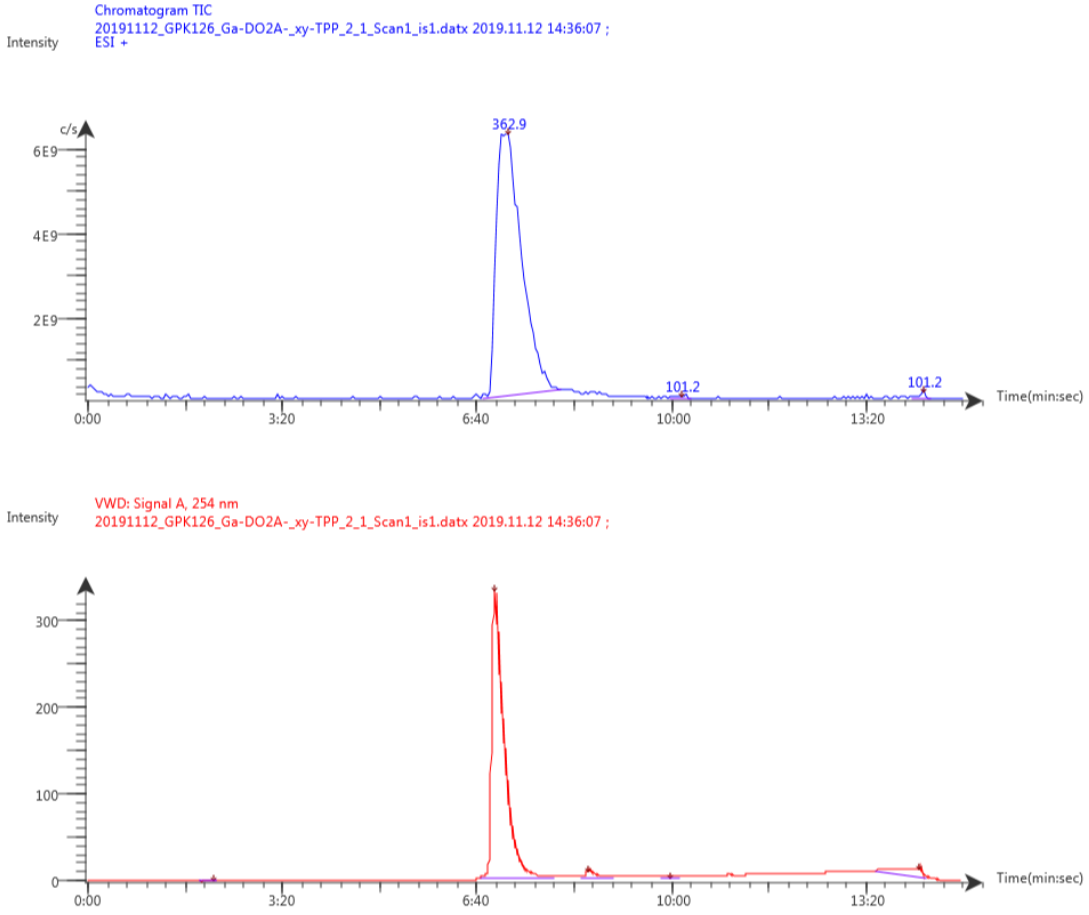

Figure 2.4 LCMS spectra of **Ga1a**, including ESI+-MS (*top*) and UV traces (*bottom*).

Additionally, a single peak was in both the ESI+-MS and UV traces (**Figure 2.4**) of **Ga1a**, and a *m/z* value of 362.9 was found, indicating the tricationic species had formed. Both non-radioactive Ga(III) analogues were used further to elucidate the speciation observed for the ^{68}Ga-labelled compounds and will be discussed in detail in chapter 3.

2.2 NODAGA-Based Chelators

In 2018, Smith *et al*. designed and developed a series of DO3A-based chelators containing a DO3A chelating moiety, a *p*-xylyl linker and a triarylphosphonium (TAP) group, shown in **Figure 2.5**.[2] Three different TAP groups were utilised, including TPP, TTP and TXP functionalities aimed at altering the lipophilicities of the ^{68}Ga-labelled radiotracers. The inspiration for this work originated from the study published by Haslop *et al*., who synthesised

the MitoPhos series of compounds functionalised with a range of TAP groups in order to provide radiotracers with tuneable lipophilicities.[4]

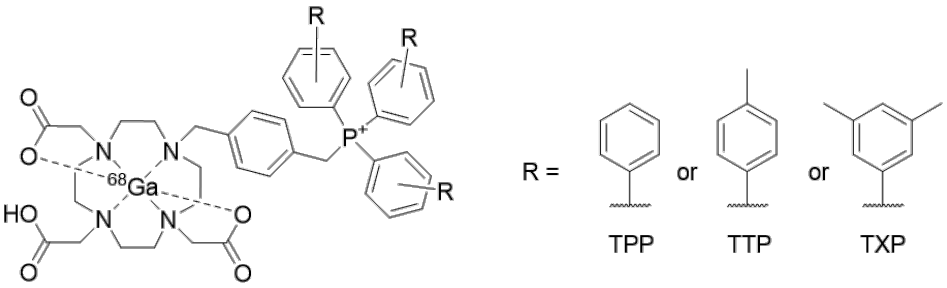

Figure 2.5 ^{68}Ga-labelled DO3A-xy-TAP compounds developed by Smith *et al*. R = H (TPP), *p*-Me (TTP) and *m,m'*-diMe (TXP).[2]

Owing to the trianionic charge afforded by the three carboxylic acid arms cancelling out the tricationic charge of the Ga(III) metal centre, the monocationic charge provided by the TAP group resulted in an overall charge of +1 for each compound in the DO3A-xy-TAP series. Smith *et al*. showed in this series of compounds that increasing the degree of alkyl functionalisation increased the log *D* values of these compounds.[2] This family of radiotracers exhibited log *D* values between -3.12 and -1.81, with the most lipophilic tracer being the xylyl variant, [^{68}Ga]Ga-DO3A-xy-TXP, and as such, was assessed *ex vivo* in isolated perfused rat hearts for its capacity to report on $\Delta\Psi_m$. Less than 1 % retention in healthy hearts was observed, compared to approximately 40 % retention typically observed with [^{99m}Tc]Tc-MIBI.[5] This was not significantly diminished in hearts treated with the ionophore carbonyl *m*-chlorophenyl hydrazone (CCCP), to induce mitochondrial depolarisation, which suggested that the radiotracer was not lipophilic enough to successfully penetrate cell membranes to reach the mitochondria.

A review in 2014 by Price and Orvig described DOTA as a 'suitable match' for Ga(III) complexation and labelling conditions have been reported between 37 and 90 °C for 10 to 30 minutes.[6] Smith *et al*. reported successful labelling of gallium-68 at 100 °C for 30 minutes with the series of DO3A-xy-TAP compounds, highlighting the need for high temperatures and longer radiolabelling times for successful chelation of gallium-68.[2] DO3A-based chelates are thought to require harsh radiolabelling conditions for successful ^{68}Ga-labelling due to the size mismatch between the macrocyclic ring and the Ga(III) cation. The unbound carboxylic acid arm present in the DO3A-based radiotracers led to an increase in hydrophilic interactions,

therefore increasing the overall hydrophilicity of these complexes, further confirmed by the low log *D* values measured for this series of compounds.

In the same review article by Price and Orvig, NOTA, a hexadentate N_3O_3 chelator, and its derivatives are considered to be the "gold standard" for Ga(III) chelation.[6] Specifically, the NODAGA chelator, containing a glutamic acid arm, was of interest as it can be conjugated with targeting moieties, whilst still maintaining three carboxylic acid arms available for chelating Ga(III). The three carboxylic acid arms, along with the three amine sites, satisfy the preference of Ga(III) for a coordination number of 6. NOTA and its bifunctional derivatives were also described as possessing very favourable ^{68}Ga radiolabelling conditions, room temperature for 30-60 minutes, including excellent *in vivo* stability.[6] The more favourable radiolabelling conditions for successful ^{68}Ga-labelling of NODAGA-based chelators compared to DO3A-based chelates is a result of the better size match between Ga(III) and the cavity size provided by the macrocyclic ring of NODAGA. This chelator does not have an unbound carboxylic acid arm once complexed with Ga(III), reducing the possibility of hydrophilic interactions, therefore improving the overall lipophilicity of the final radiotracer.

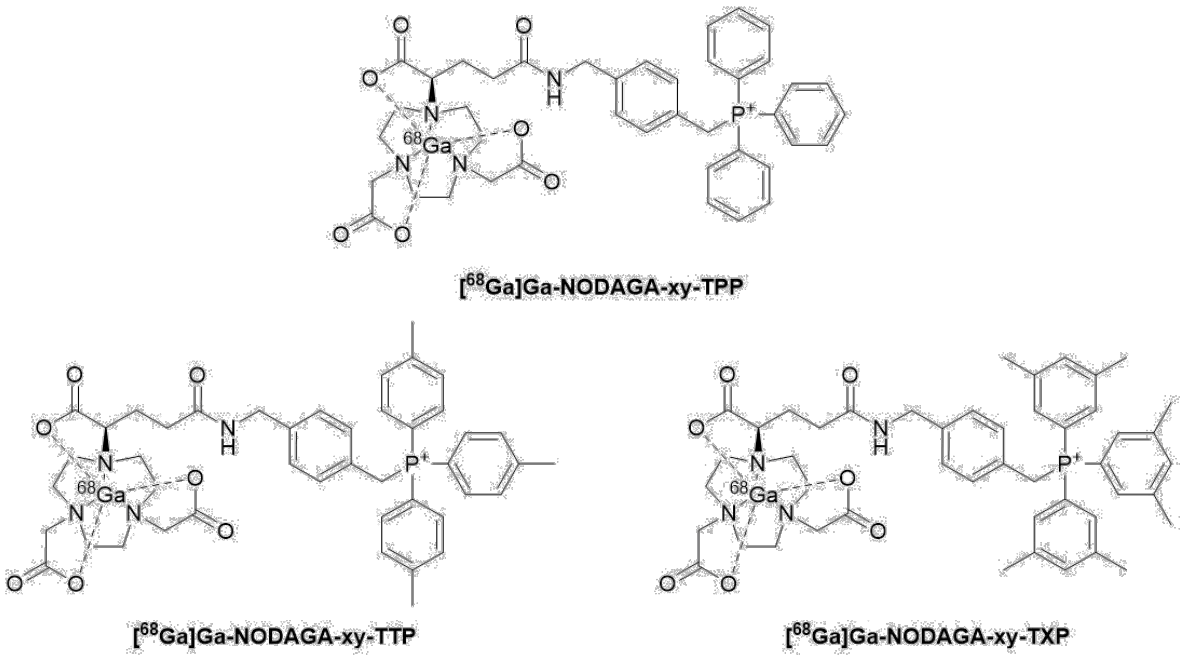

Figure 2.6 The three initial target NODAGA-based compounds investigated in this thesis, consisting of a NODAGA moiety capable of chelating [^{68}Ga]Ga(III), a xylyl linking group, and a TPP, TTP or TXP cation designed to provide a cationic charge and lipophilic character to the overall compound.

This rationale provided the foundation for the first family of lipophilic and cationic ^{68}Ga-based radiotracers developed in this project. The first analogous series of target compounds, shown

in **Figure 2.6**, consist of a NODAGA chelating moiety, a *p*-xylyl linker, and a TPP, TTP or TXP group affording tuneable lipophilicities of the final radiolabelled tracers.

2.2.1 Synthesis of Triarylphosphines

The development of NODAGA-xy-TAP compounds began with the synthesis of triarylphosphines (**3**), shown in **Scheme 2.2**, providing the means for the incorporation of triarylphosphonium cations for the final tracers. The first step, originally developed by Haslop *et al*. and further utilised by Smith *et al*., involved the *in situ* formation of Grignard reagents through the reaction between magnesium turnings and aryl bromides (**2**). Subsequent addition of phosphorus trichloride formed the desired triarylphosphines (**3**).[1,2,4]

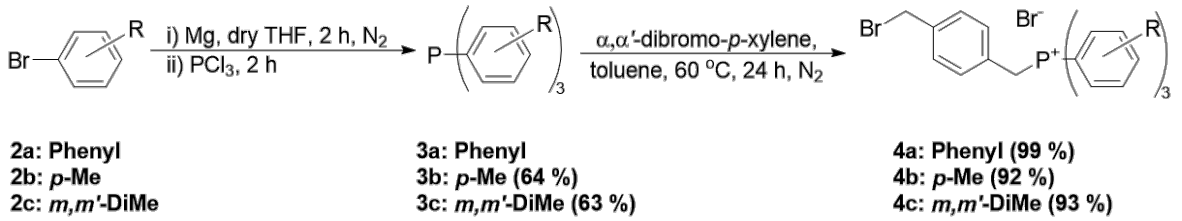

Scheme 2.2 The first two steps towards the synthesis of NODAGA-xy-TAP compounds. Procedures described by Haslop *et al*. and Smith *et al*.[1,2,4]

Triphenylphosphine is known to have a ^{31}P NMR shift of −4.7 ppm, meaning the desired products **3a-c** could be assigned using proton-decoupled phosphorus-31 ($^{31}P\{^{1}H\}$) NMR spectroscopy, as shown in **Figure 2.7**.[7] Both variants show two peaks, with the negative chemical shift species corresponding to the product, and the peak at approximately 30 ppm corresponding to the oxidised form of the product. The oxidation of the phosphorus atom arises from quenching with oxygenated water to eliminate excess Grignard reagent. In all cases, less than 10 % of the oxidised impurity was measured following the integration of the peaks in **Figure 2.7**, and as such **3b-c** were carried forward without further purification.

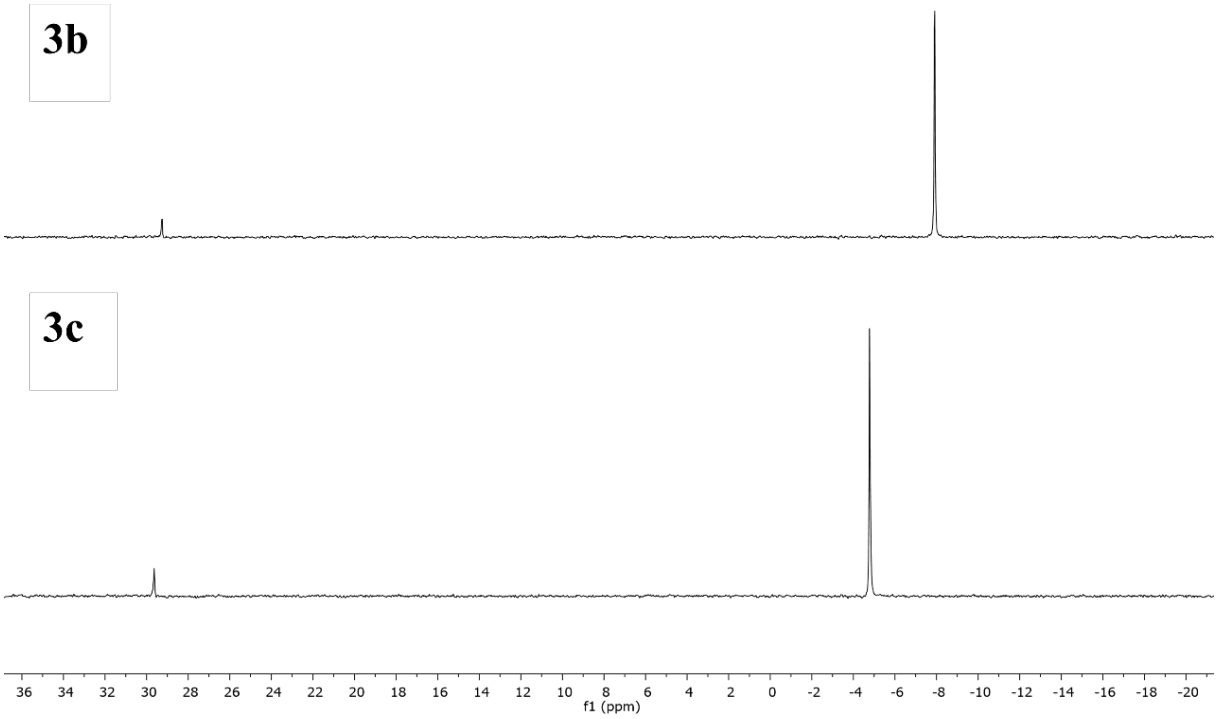

Figure 2.7 $^{31}P\{^{1}H\}$ NMR spectra of triarylphosphines **3b-c** (162 MHz, 298 K, $CDCl_3$).

Owing to the absence of an internal phosphorus-containing standard in the NMR samples of **3b** and **3c**, the difference in chemical shift of the phosphorus atoms could not be directly compared.

2.2.2 Formation of Bromoxylene-Triarylphosphonium Cations

The second step of this synthesis involved the formation of triarylphosphonium cations (**Scheme 2.2**). Nucleophilic substitution of triarylphosphines **3a**, **3b** and **3c** with α,α′-dibromo-*p*-xylene provides the TAP cation with a xylyl linking group, as well as an alkyl bromide for further functionalisation. The nucleophilic substitution is initiated through the phosphorus-centred lone pair, not present in the oxidised form of the triarylphosphines, and as such the oxidised impurity is inert in this reaction and can be carried through with no parallel activity. As described by Smith *et al*., heating triarylphosphines **3a-c** and α,α′-dibromo-*p*-xylene at 60 °C in toluene allows the reaction to proceed and the TAP-functionalised bromoxylene products **4a-c** to precipitate out of solution, a result of the low solubility cationic species exhibit in toluene.[2] This temperature was chosen as it was the minimum temperature required to dissolve the α,α′-dibromo-*p*-xylene starting material, with **3a-c** being fully soluble in toluene at room temperature.

The TPP-functionalised bromoxylene **4a** was synthesised according to the methodology reported by Smith *et al*. in quantitative yields, however the use of more electron donating TAP groups, such as **3b** and **3c**, led to small amounts of impurities, depicted in **Figure 2.8**.[2] For example, the TXP variant **4c** was characterized by NMR and mass spectrometry, with the latter showing two peaks at *m/z* = 529 and 398 corresponding to the monosubstituted product **4c** and the disubstituted impurity (**TXP-xy-TXP**) respectively.

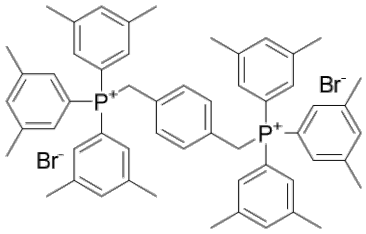

Figure 2.8 Structure of the disubstituted impurity, **TXP-xy-TXP**, confirmed by mass spectrometry.

However, by exploiting the decrease in solubility of the monosubstituted product in toluene at 60 °C, the mono-cationic species precipitated out of solution and did not react further. The product was isolated through the use of filtration, followed by purification of the product which was washed with toluene and diethyl ether.

2.2.3 Synthesis of Aminoxylene-Triarylphosphonium Cations

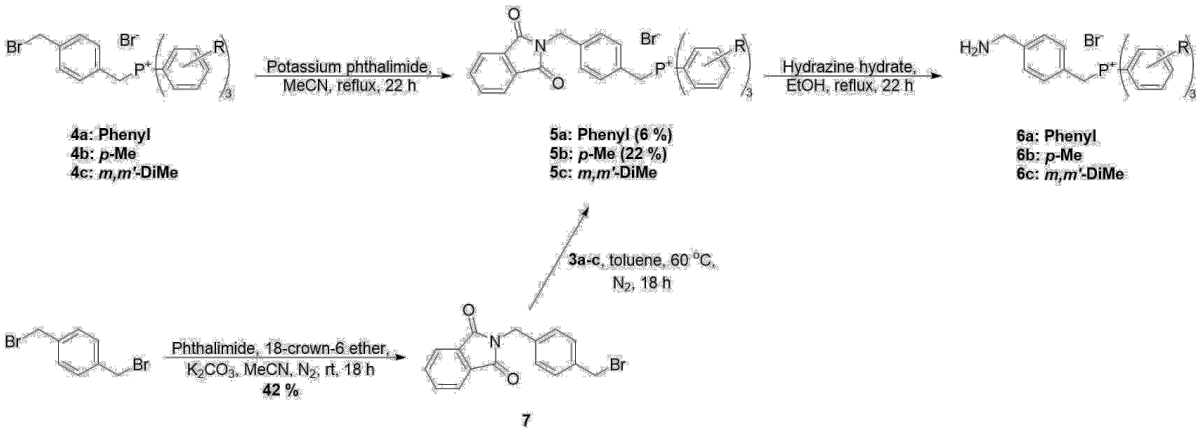

Scheme 2.3 The initial synthetic route performed for the formation of aminoxylene-TAP compounds **6a-c**. The synthesis of aminoxylene analogues **6a-c** via phthalimide intermediates **5a-c** from compounds **4a-c** was performed using an adapted procedure described by Kim *et al*.[8] The alternative route for the synthesis of the phthalimido-xylene-TAP compounds was performed as described by Škopić *et al*., and a modification of the methodology developed by Smith *et al*.[2,9]

In order to functionalise the TAP moieties with the chosen macrocycle NODAGA, the TAP-functionalised bromoxylenes need to be converted to their respective amino analogue, providing a primary amine which could be coupled with the free carboxylic acid pendant arm of NODAGA, forming an inert amide linkage. The initial focus for the synthesis of TAP-functionalised aminoxylenes started with the Gabriel synthesis, as shown in **Scheme 2.3**. This classical procedure is useful and involves the transformation of primary alkyl halides into primary amines via a phthalimide intermediate. To obtain the phthalimide intermediates **5a-c**, bromoxylene TAP cations were dissolved in hot acetonitrile before addition of potassium phthalimide to the solution. The potassium phthalimide salt is used instead of phthalimide, due to the greater nucleophilicity afforded by the negatively charged nitrogen of the potassium salt. In 2008, Kim *et al*. synthesised the aminoxylene-triphenylphosphonium variant using the Gabriel synthesis, providing an effective methodology to follow for the tolyl and xylyl (**6b-c**) analogues.[8] Following the addition of potassium phthalimide to the solution of **4a-c** in acetonitrile, the mixture was heated at reflux. A white precipitate formed overnight, corresponding to the formation of the potassium bromide by-product and confirmed that the reaction was proceeding.

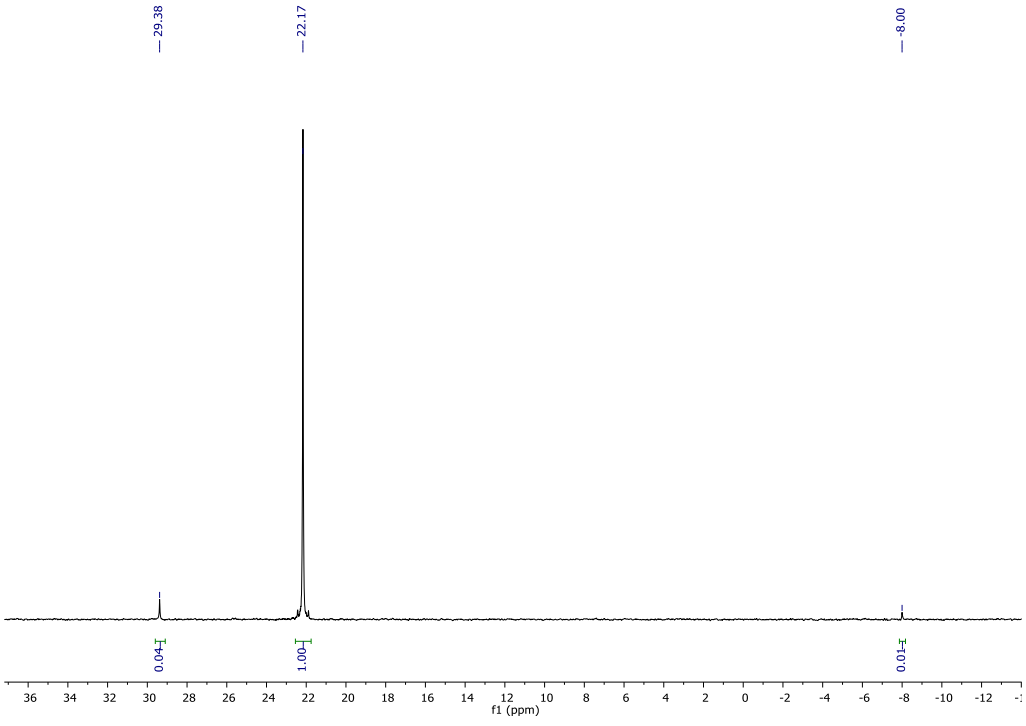

Figure 2.9 $^{31}P\{^{1}H\}$ NMR spectrum of phthalimidoxylene-TTP **5b** (162 MHz, 298 K, $CDCl_3$).

The by-product was removed by filtration and the crude product obtained from removing the filtrate solvent under reduced pressure was recrystallised from a methanol/ether mixture.

However, compared to the 44 % yield achieved by Kim *et al*. for **5a**, we report a yield of just 6 %. This was not greatly improved with the *p*-tolyl analogue **5b**. The white solid obtained from the recrystallisation of the crude phthalimidoxylene-TTP, **5b**, was characterised using $^{31}P\{^{1}H\}$ NMR, shown in **Figure 2.9**. This elucidated, to some extent, the low yields being obtained for the synthesis of **5a** and **5b**. The major peak at 22.2 ppm corresponds to the desired phthalimide intermediate, the peak at -8.00 ppm corresponds to tri-*p*-tolylphosphine and its oxidised form is represented by the peak at 29.4 ppm. It appears that the triarylphosphonium substituent acts as a leaving group during the substitution, leading to the generation of tri-*p*-tolylphosphine (**3b**) and its subsequent oxidation over time. Triphenylphosphine is a weak base, suggesting that it could act as a good leaving group, and this could lend itself to aryl-functionalised derivatives of triphenylphosphine such as tri-*p*-tolylphosphine. However, the extent of this occurring appears to be low in this reaction due to the integration of peaks corresponding to **3b** and its oxidised form accounting for a combined 5 %, compared to the peak corresponding to **5b**.

In an effort to improve the yield for the synthesis of phthalimidoxylene-TAP compounds, we employed an alternative strategy which involved the generation of a bromoxylene-phthalimide precursor **7** using methods described by Škopić *et al*.[9] This then allowed for a simple substitution with triarylphosphines **3a-c** using a modification of the methodology reported by Smith *et al*.[2] To somewhat circumvent the difficulties previously described, the phthalimidoxylene-TAP analogues were not isolated using this method, and instead an aliquot of the crude material was analysed by ^{1}H and $^{31}P\{^{1}H\}$ NMR to confirm the generation of the phthalimide intermediates **5a-c** before commencing the following step. Intermediates **5a-c** were dissolved in ethanol and an excess of hydrazine hydrate was added to the solution before heating at reflux overnight. Due to the cationic nature of these compounds, column chromatography could not be used as a purification technique as the compounds would interact strongly with the silica stationary phase, adhering to the stationary phase, making elution of the compounds no longer possible. Doping the solvent system with between 0.1 and 10 % of various bases, such as triethylamine and ammonium hydroxide, did not aide purification. An aliquot of crude **6b** was successfully analysed by LCMS, which indicated that the product could potentially be purified by reverse-phase flash chromatography using a C18 column.

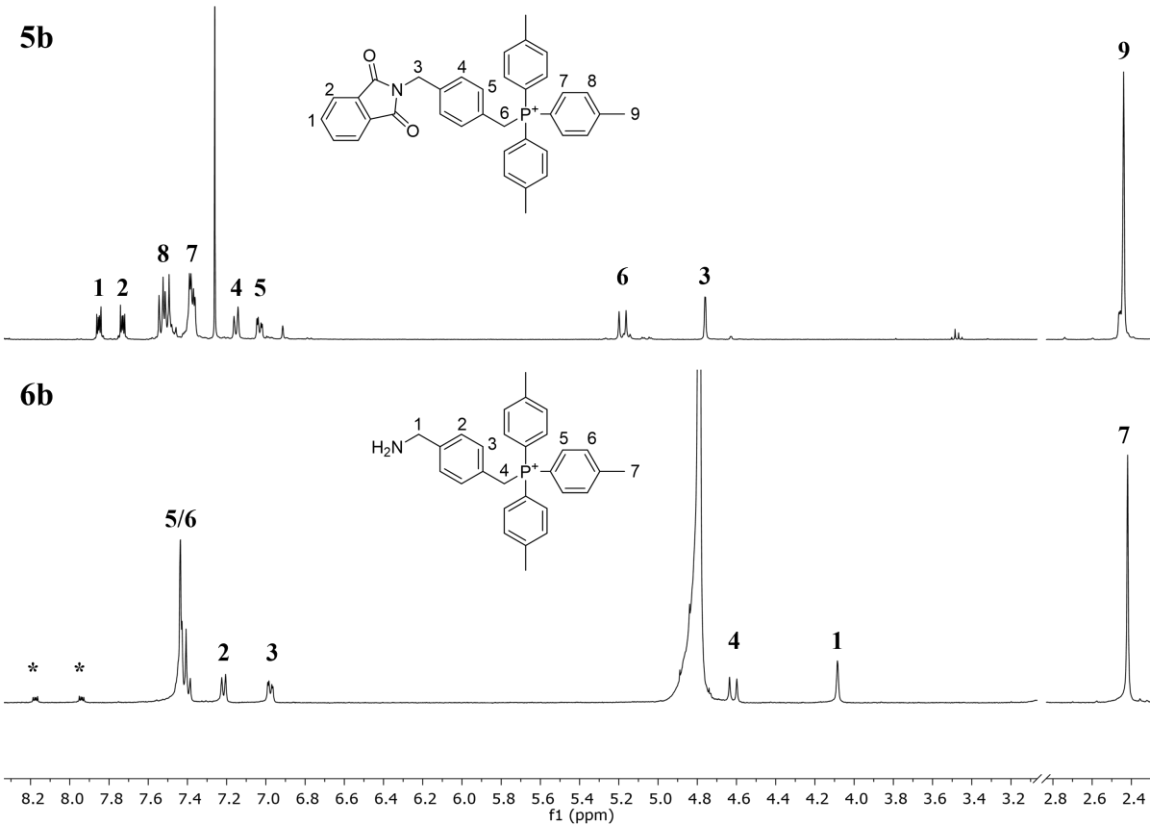

Figure 2.10 ^{1}H NMR spectra of phthalimidoxylene-TTP (**5b**) ($CDCl_3$, 400 MHz, 298 K) and aminoxylene-TTP (**6b**) (D_2O, 400 MHz, 298 K). The aromatic phthalhydrazide proton peaks are denoted by asterisks (*). Some peaks have been truncated for clarity.

A standard solvent system was used for the reverse-phase purification of **6b**, consisting of acetonitrile doped with 0.1 % TFA in water doped with 0.1 % TFA. The product eluted in 20 % acetonitrile and was obtained as a white solid. Analysis of the white solid with ^{1}H NMR, shown in **Figure 2.10**, showed the presence of the phthalhydrazide product, which was not removed with further purifications. The following step was envisioned as an amide coupling of the aminoxylene-TAP compounds with the chelator NODAGA(^{t}Bu)$_3$. The product would likely require purification by reverse-phase column chromatography, and the phthalhydrazide impurity could still be present in the product sample if co-elution occurred again. Therefore, this was not considered an optimal synthetic route.

We instead explored the synthesis of cyanoxylene-TAP analogues **8a-c** in which the nitrile group could be reduced to produce the desired aminoxylene-TAP compounds, shown in **Scheme 2.4**. As described by Nomura *et al*., cyanoxylene-bromide was suspended in anhydrous acetonitrile before triphenylphosphine **3a** was added to the suspension, and the

mixture was heated at reflux.[10] As noted previously, phosphonium salts are not soluble in non-polar solvents and as such the crude material obtained from removal of acetonitrile under reduced pressure was added to toluene to promote the precipitation of the phosphonium product. The phenyl variant **8a** was synthesised in near quantitative yields. The tolyl variant **8b** was also synthesised using the same method in a good 71 % yield.

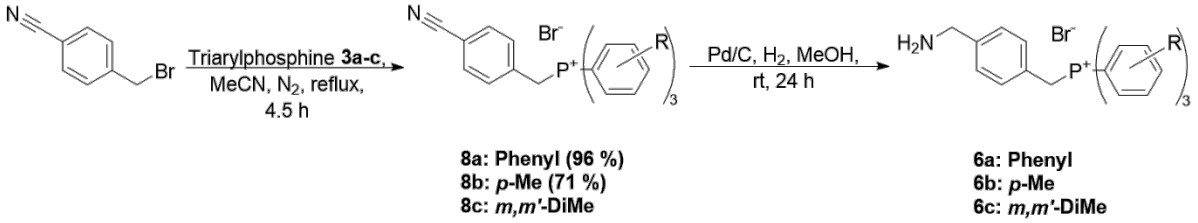

Scheme 2.4 Synthesis of aminoxylene-TAP compounds **6a-c** via cyanoxylene-TAP intermediates **8a-c**. The synthesis of cyanoxylene-TAP intermediates was performed using a modification of the methodology by Nomura *et al*.[10]

The reduction of the nitrile groups in **8a-b** using hydrogen gas in the presence of a palladium on carbon catalyst were not successful. This was attributed to the steric bulk of the triarylphosphonium moiety preventing the carbon-nitrogen triple bond from adsorbing effectively onto the palladium catalyst surface. Hydrogenation of nitrile compounds are usually carried out in high pressure environments, which was not possible at the time of synthesis, and could also explain the lack of reactivity observed.[11] The reduction of nitriles to primary amines is typically performed using the strong reducing agent lithium aluminium hydride. This route was not explored due to concerns about the strong nucleophilicity of the hydride anion causing the cyanoxylene-TAP species to break down. An example of this would involve the hydride attacking the α-carbon respective to the phosphorus centre, resulting in the cleavage of triphenylphosphine. The harsh conditions afforded by this nitrile reduction method were therefore not attempted with the cyanoxylene-TAP precursors.

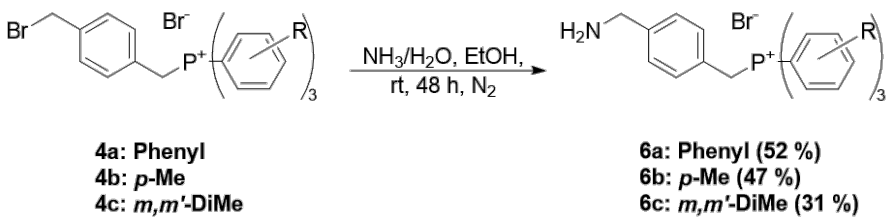

Scheme 2.5 The alkylation of ammonia with bromoxylene-TAP cations **4a-c** to generate TAP-functionalised aminoxylenes **6a-c**.

Alternatively, the reaction between bromoxylene-TAP cations **4a-c** and ammonia was explored to directly generate aminoxylene analogues **6a-c**, shown in **Scheme 2.5**. To promote the formation of the desired mono-alkylated amines, and in turn hinder the formation of di- and tri-alkylated amines, a 200-fold excess of ammonia was used. Compared to the aforementioned Gabriel synthesis and nitrile reduction methods for the synthesis of **6a-c**, the reaction of ammonia with **4a-c** did not require an intermediary species to be generated before the respective amines could be formed. The use of aqueous ammonia and ethanol at room temperature also provided more favourable, milder conditions. The direct *N*-alkylation of ammonia with alkyl halides is typically performed in a sealed reaction vessel, to avoid the loss of gaseous ammonia as it evaporates over time, and from heating.[12] Accordingly, aminoxylenes **6a-c** bearing triphenylphosphonium (**6a**), tri-*p*-tolylphosphonium (**6b**) and tri-*m*,*m*′-xylylphosphonium (**6c**) functionalisation were synthesised in high purity and with yields of 52 %, 47 % and 31 % respectively on a 2 g scale.

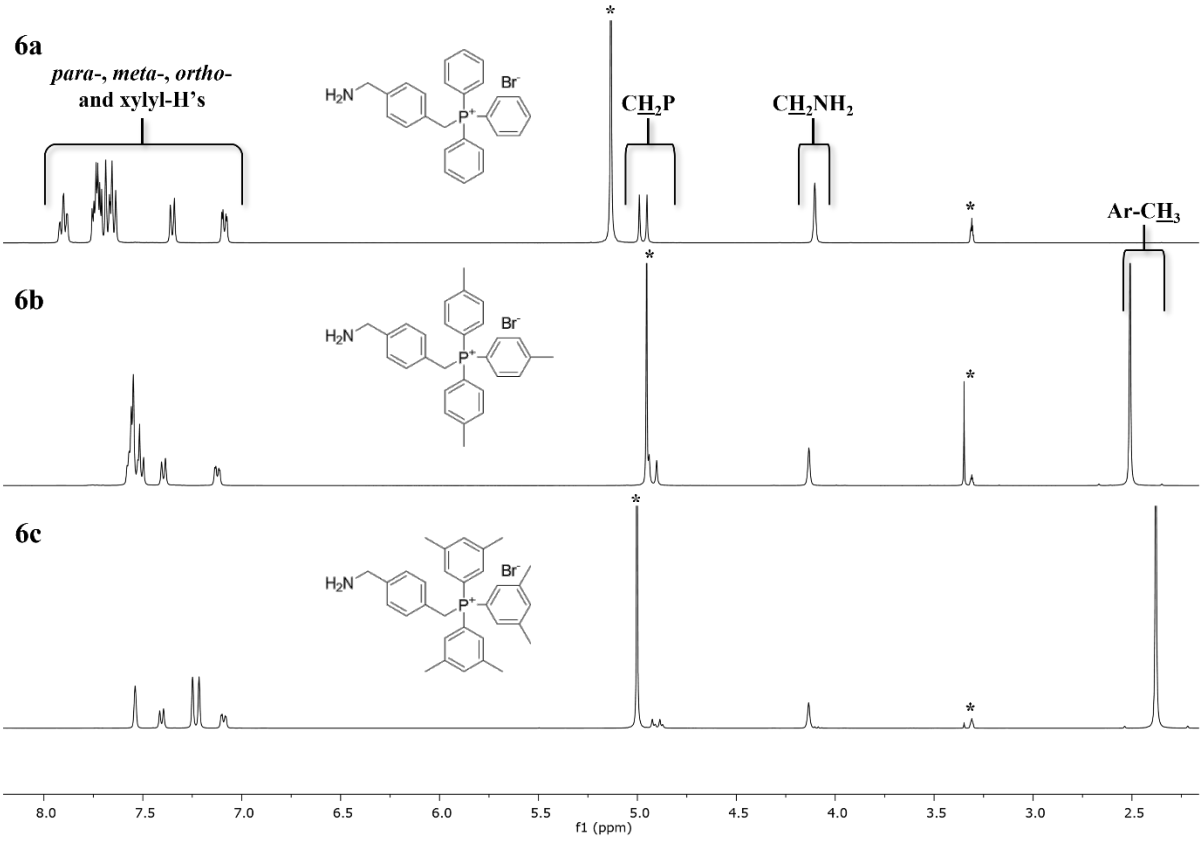

Figure 2.11 ^{1}H NMR spectra of TAP-functionalised aminoxylenes **6a-c** (CD_3OD, 400 MHz, 298 K). Water and methanol solvent peaks are indicated with asterisks (*).

The ^{1}H NMR spectra of compounds **6a-c** are shown in **Figure 2.11**. In addition, mass spectrometry was employed for further confirmation that **6a-c** had been synthesised, and showed peaks at *m/z* = 382, 424 and 466 corresponding to the TPP, TTP and TXP aminoxylene analogues respectively. All three TAP-functionalised aminoxylenes **6a-c** were used for macrocycle functionalisation.

2.2.4 Amide Coupling of Aminoxylene-TAP Cations to NODAGA

(R)-NODAGAtri-*tert*-butylester ((R)-NODAGA(^{t}Bu)$_3$) was synthesised in high purity but low overall yield according to Eisenwiener *et al*.[13,14] Scalability problems caused by the low yielding synthesis resulted in the commercial sourcing of the R-isomer of NODAGAtri-*tert*-butylester to aide in the continuation of the synthetic route.

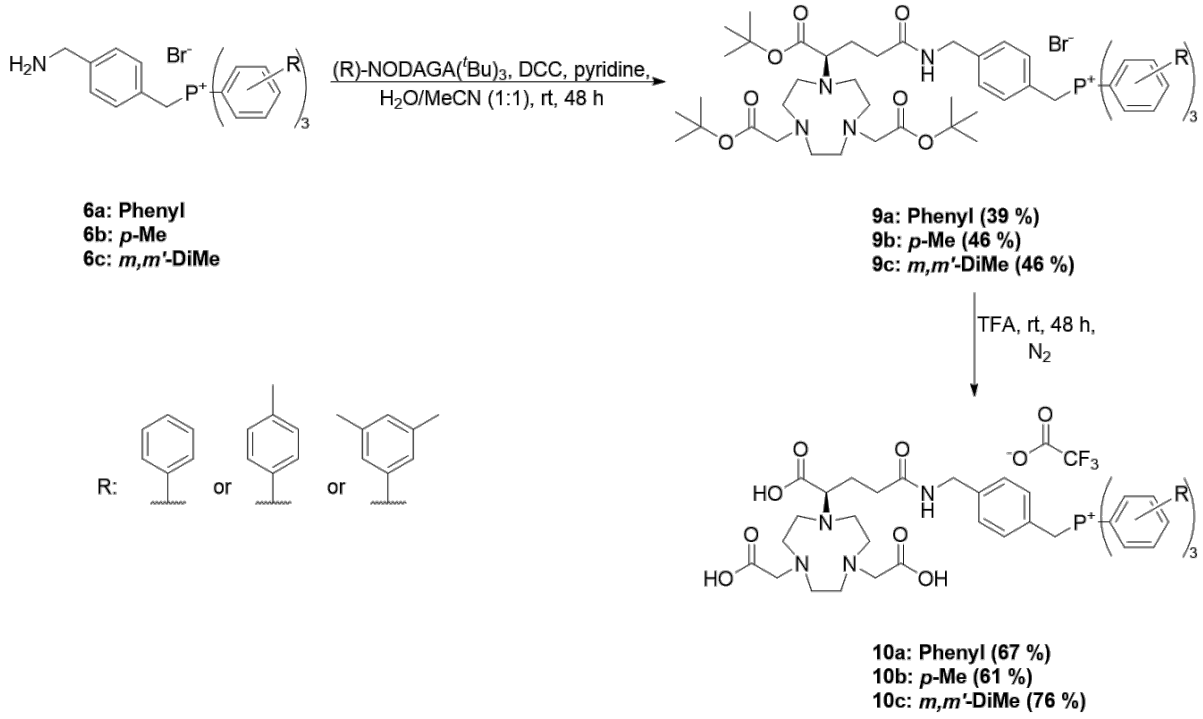

Scheme 2.6 Synthesis of the (R)-NODAGA-xy-TAP series of compounds from the TAP-functionalised aminoxylenes **6a-c**. The amide coupling of compounds **6a-c** and (R)-NODAGA(^{t}Bu)$_3$ was performed as a modification of the procedure according to Schirrmacher *et al*.[15]

TAP-functionalised aminoxylenes **6a-c** were coupled to commercially sourced (R)-NODAGAtri-*tert*-butylester in the presence of the coupling reagent dicyclohexylcarbodiimide (DCC). The methodology was a modification of the procedure described by Schirrmacher *et al*., who coupled NODAGAtri-*tert*-butylester to a S-trityl-mercapto-protected ethylamine substrate for conjugation with a protein-based targeting

vector.[15] DCC was deemed the preferred coupling reagent due to the facile removal of the dicyclohexylurea (DCU) by-product. DCU is insoluble in most organic solvents, and as such, prompted the addition of acetonitrile to the crude material once the reaction mixture had been concentrated under reduced pressure. Concentration under reduced pressure aided in the removal of pyridine, and the subsequent addition of acetonitrile causing the precipitation of DCU, which was removed by filtration. Any trace amounts of DCU and pyridine remaining in the crude material was removed by reverse-phase C18 chromatography. The purified *tert*-butyl-protected compounds **9a-c** were then deprotected in trifluoroacetic acid to give the NODAGA-xy-TAP ligands **10a-c** in moderate total yields of between 20 and 35 %, shown above in **Scheme 2.6**.

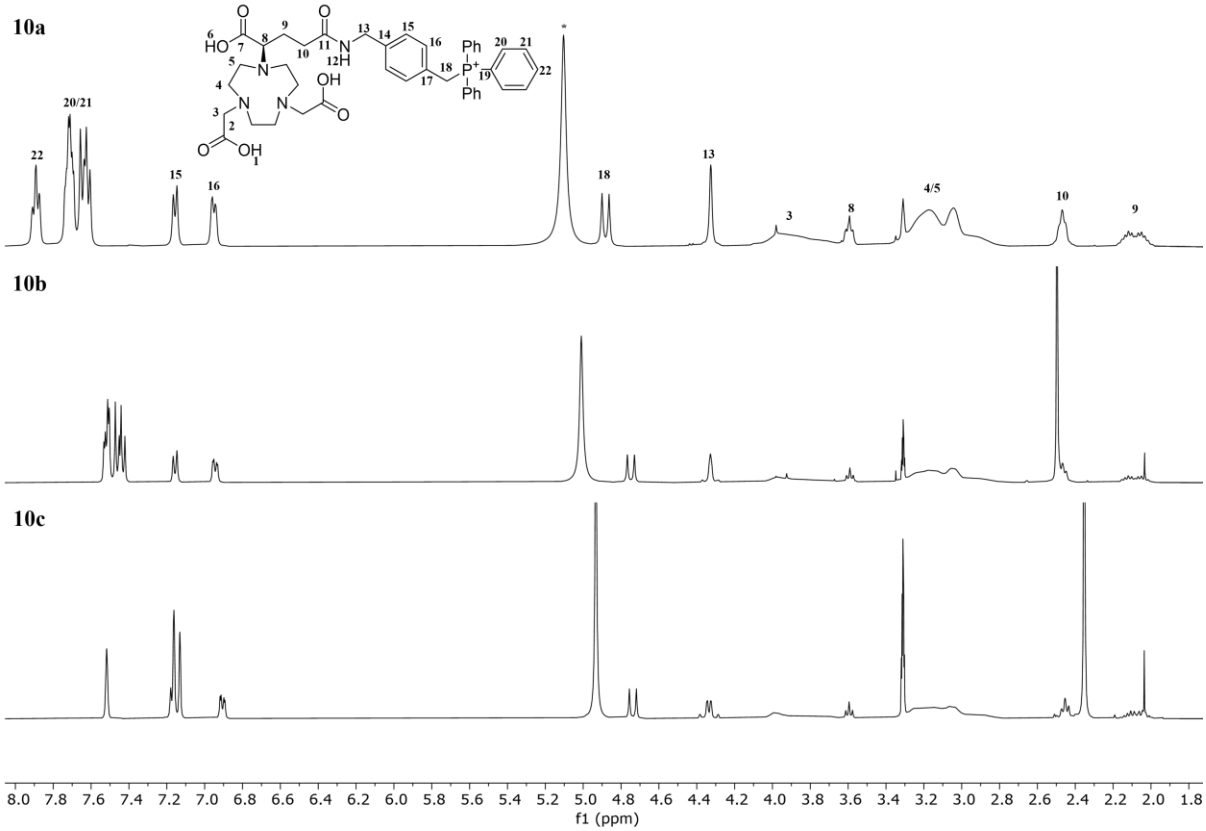

Figure 2.12 ^{1}H NMR spectra of the deprotected (R)-NODAGA-xy-TAP ligands (CD_3OD, 400 MHz, 298 K). From top to bottom: (R)-NODAGA-xy-TPP (**10a**), (R)-NODAGA-xy-TTP (**10b**), (R)-NODAGA-xy-TXP (**10c**). The labelled structure of **10a** and NMR spectroscopy characterisation is also included. Water solvent peak labelled with an asterisk (*).

These novel ligands **10a-c** were initially characterised by ^{1}H NMR spectroscopy and the resultant spectra are shown in **Figure 2.12**. As expected, each ligand displays several common features including the doublet at 4.88 ppm arising from geminal proton phosphorus coupling,

and a large broad peak at 3.11 ppm referring to the macrocyclic protons. Comparing these ^{1}H NMR spectra highlights a simplification in the aromatic region, afforded by the increase in alkyl functionalisation removing the occurrence of appreciable vicinal coupling between the aryl hydrogens. The methyl proton peaks also increase in intensity as they become more numerous in these compounds. ^{31}P{^{1}H} NMR spectroscopic analysis of compounds **10a-c** confirmed the presence of a single phosphorus-containing species, and ^{19}F{^{1}H} NMR gave one peak at -77 ppm, which indicates the presence of trifluoroacetate as the counter-anion in each compound. ^{13}C{^{1}H} NMR spectra were also assigned, with doublets observed in the spectrum due to carbon-phosphorus coupling. HMQC and HMBC NMR spectroscopic techniques were used to assign multiple peaks through comparison with the ^{1}H NMR spectra. Remaining peaks were assigned using the theory that coupling constants decrease as the number of bonds increases, with one-bond coupling constants of $^{1}J_{HP}$ = 87 and 48 Hz observed, and five-bond couplings were also observed. Mass spectrometry was also used to characterise these ligands, with *m*/*z* values of $[M\text{-}CF_3CO_2]^+$ = 739, 781 and 823 observed for **10a**, **10b** and **10c** respectively, and UV traces obtained through LCMS confirmed one UV active species.

After the purification of **10a-c** by reverse-phase C18 chromatography, the products were lyophilised and stored at -18 °C until they were required to be used in order to prevent the gradual decomposition observed in solution at room temperature. When the ligands were required for the preparation of a stock solution of radiotracer, the ligands were dissolved in 3.6 M sodium acetate buffer to form the necessary solution immediately before use and prepared fresh for each experiment.

2.2.5 Synthesis and Characterisation of Non-Radioactive Reference Ga-(R)-NODAGA-xy-TAP Compounds

There is a significant emphasis in radiochemistry to synthesise a non-radioactive analogue of the respective radiotracer whenever possible to act as an isostructural reference compound. Since radiolabelled complexes are in low concentration and constantly undergoing radioactive decay, they cannot be analysed by standard analytical chemistry techniques, such as NMR and mass spectrometry, thus a non-radioactive analogue is required for full characterisation. Once fully characterised, the non-radioactive analogue is analysed by the same HPLC method as the radiolabelled analogue, and if both analogues have identical retention times, it confirms that the radiolabelled compound is highly likely to possess the same structure as the fully characterised non-radioactive compound.

The synthesis of non-radioactive gallium(III) TAP-functionalised macrocycles have been outlined previously in the group.[1,2] Extensive analysis on the effect of radiolabelling buffer on radiochemical yield (RCY) performed by Smith *et al*. concluded that using sodium acetate buffer for radiolabelling, compared to ammonium acetate buffer, greatly improved RCY values.[1] We translated these findings towards the synthesis of the non-radioactive Ga-NODAGA analogues shown in **Scheme 2.7**, and increased the concentration of NaOAc from 0.2 M to 3.6 M, as this is the concentration of clinical grade NaOAc buffer and will improve the clinical translatability of this series of compounds.

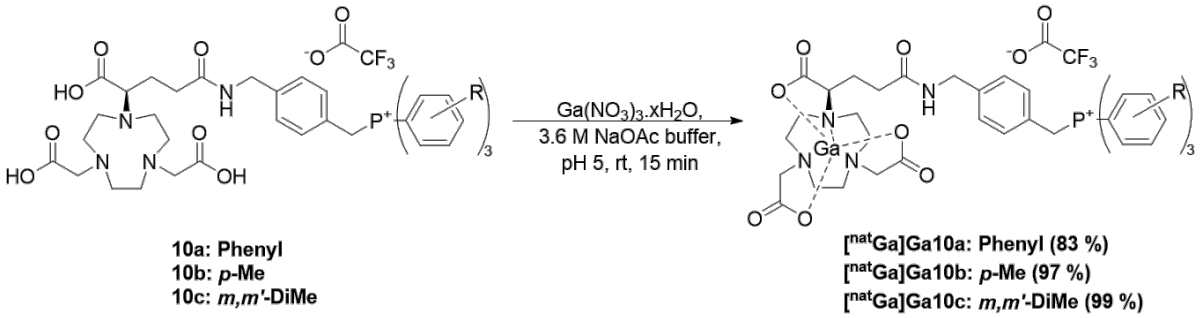

Scheme 2.7 Protocol for the complexation of (R)-NODAGA-xy-TAP ligands with $Ga(NO_3)_3.xH_2O$ in 3.6 M NaOAc buffer at pH 5.

The previously synthesised non-radioactive Ga-DO3A-xy-TPP, described by Kardashinsky *et al*. used gallium trichloride in aqueous solvent as the source of Ga(III).[16] However, gallium trichloride is highly unstable and rapidly forms insoluble gallium hydroxide species, which are very stable, and as such would prevent the binding of gallium to the ligand. Instead, we used the more stable gallium trisnitrate as the source of Ga(III), in accordance with previous work in the group.[1,2] Although the use of nitrate counter-anion does not exactly reflect the radiolabelling conditions used with the gallium-68 generator eluate, the presence of other counter-anions such as trifluoroacetate in the HPLC likely leads to counterion exchange and means the identity of the final complex counter-anion will not be identified in any case.

The NaOAc buffer was adjusted to pH 5 using acetic acid, and the complexation was carried out at this pH. A 1.5-fold excess of gallium trisnitrate was used to promote the chelation of Ga(III) with ligands **10a-c**. After stirring at room temperature over 15 minutes, the mixture was concentrated to give the crude product, which was purified using reverse-phase C18 chromatography. Unreacted gallium precursor was easily isolated as its elution coincides with the solvent front, 100 % H_2O (doped with 0.1 % TFA). The non-radioactive analogues **Ga10a-c** were synthesised in very good yields, 83 – 99 %. Considering these yields were achieved

over 15 minutes with no heating required, this highlights that these novel NODAGA ligands possess fast chelation kinetics, with the macrocyclic framework imparting a high degree of stability.

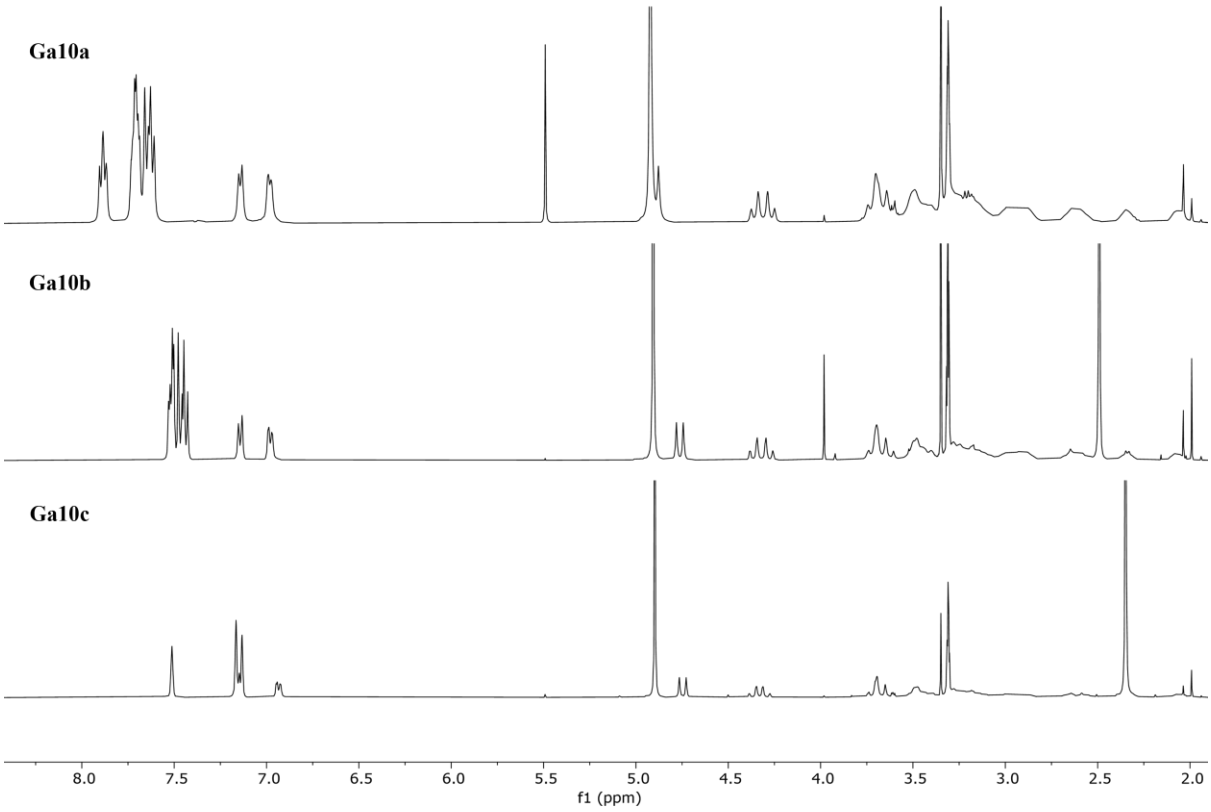

Figure 2.13 ^{1}H NMR spectra obtained for the non-radioactive complexes **Ga-(R)-NODAGA-xy-TPP** (**Ga10a**), **Ga-(R)-NODAGA-xy-TTP** (**Ga10b**) and **Ga-(R)-NODAGA-xy-TXP** (**Ga10c**) (400 MHz, 298 K, CD_3OD).

This complexation process produced the ^{1}H NMR spectra shown above in **Figure 2.13**, which show several common features including an upfield shift of the multiplet at 3.67 ppm, referring to the methylene bridge protons of the acetate arms, from 3.97 ppm shown in **Figure 2.12** for the ^{1}H NMR spectrum of **10a**. This upfield shift can be explained through the deprotonation of the carboxylic acid groups to bind Ga(III), which removes the capacity for hydrogen bonding and therefore an increase in shielding was observed for these methylene bridge protons. The presence of the Ga(III) metal centre was confirmed by mass spectrometry.

2.2.5.1 HPLC Analysis of Ga-(R)-NODAGA-xy-TAP Complexes

The HPLC traces of the three Ga-NODAGA-xy-TAP complexes can be found in **Figure 2.14a**. Importantly, each complex shows one peak, highlighting the purity of the Ga(III)-chelated

reference complexes along with an absence of isomerisation and speciation. The difference between retention times of the unchelated ligands and the Ga(III) complexes of all three NODAGA-xy-TPP, -TTP and -TXP analogues are summarised in **Table 2.1**.

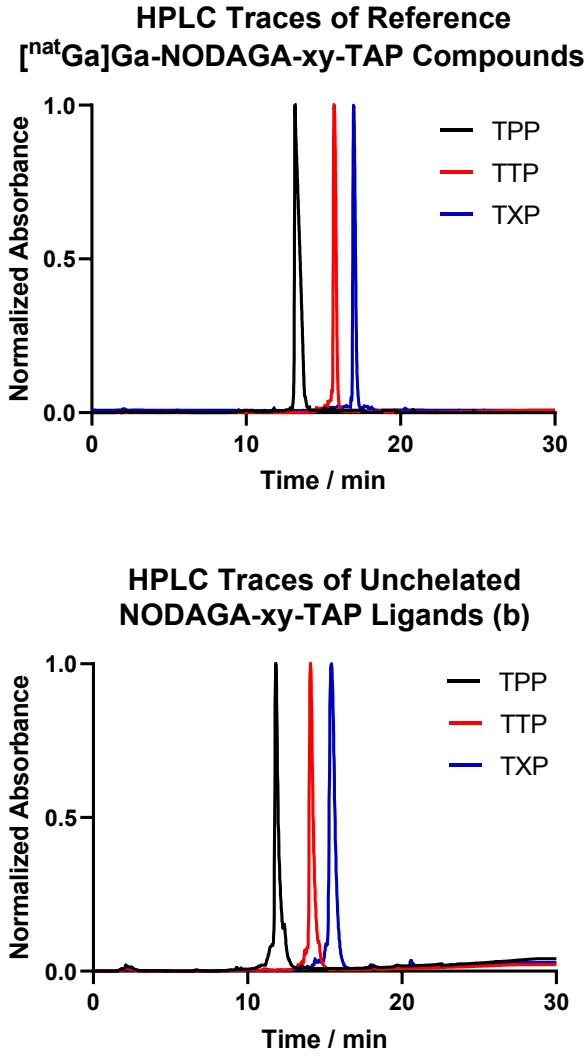

Figure 2.14 HPLC traces of **(a)** the non-radioactive reference Ga-NODAGA-xy-TAP compounds and **(b)** the corresponding HPLC traces of the unchelated ligands, included for reference. Eluent gradient: 95 % A for 5 min; 0–95 % B in A for 20 min; 95 % B in A for 5 min at a flow rate of 1 mL min^{-1} (λ_{ex} = 254 nm). All traces have been normalised so that the maximum absorbance measured for each compound is equal to 1.

Table 2.1 Summary of the data represented in the HPLC traces in **Figure 2.14**.

	Retention Time / min		
	TPP	**TTP**	**TXP**
Unchelated Ligand	11.8	14.1	15.4
Ga-Complex	13.2	15.7	17.0

The difference in retention time between the Ga-NODAGA-xy-TAP compounds indicates a change in their lipophilicities relative to each other, with the TXP analogue exhibiting a longer retention time and therefore a higher degree of lipophilicity. In order to ensure the HPLC traces obtained in **Figure 2.14a** did not correspond to the unchelated ligand, HPLC traces were also obtained for the unchelated ligands, shown in **Figure 2.14b** and summarised in **Table 2.1**. As shown by the retention times in **Table 2.1**, Ga(III) complexation causes a significant decrease in retention time, confirming the HPLC traces in **Figure 2.14a** do refer to the Ga(III) complexes, and demonstrates an increase in lipophilicity upon chelation with Ga(III). This results from a reduction in in hydrophilic interactions afforded by the carboxylate arms, once they are bound with Ga(III). These three non-radioactive complexes are now ready to be compared to their ^{68}Ga-labelled analogues in chapter 3.

2.3 Ether-Functionalised NODAGA-xy-TAEP Chelates

The introduction of ether groups into the chemical structures of lipophilic and cationic technetium-99m radiotracers has been extensively explored, with the aim to modulate the lipophilicity of the final radiotracer.[17–19] This has also been investigated to a lesser extent with cationic gallium(III) complexes.[20] It seemed natural for the next set of compounds to be synthesised to be based on the same NODAGA-xy-TAP compounds, but with the aryl phosphonium groups functionalised with ether groups instead of alkyl substituents. The three ether-functionalised (R)-NODAGA-xy-TAEP compounds to be synthesised are shown in **Figure 2.15** and are considered analogous to the TAP-functionalised NODAGA-based compounds shown in **Figure 2.6**.

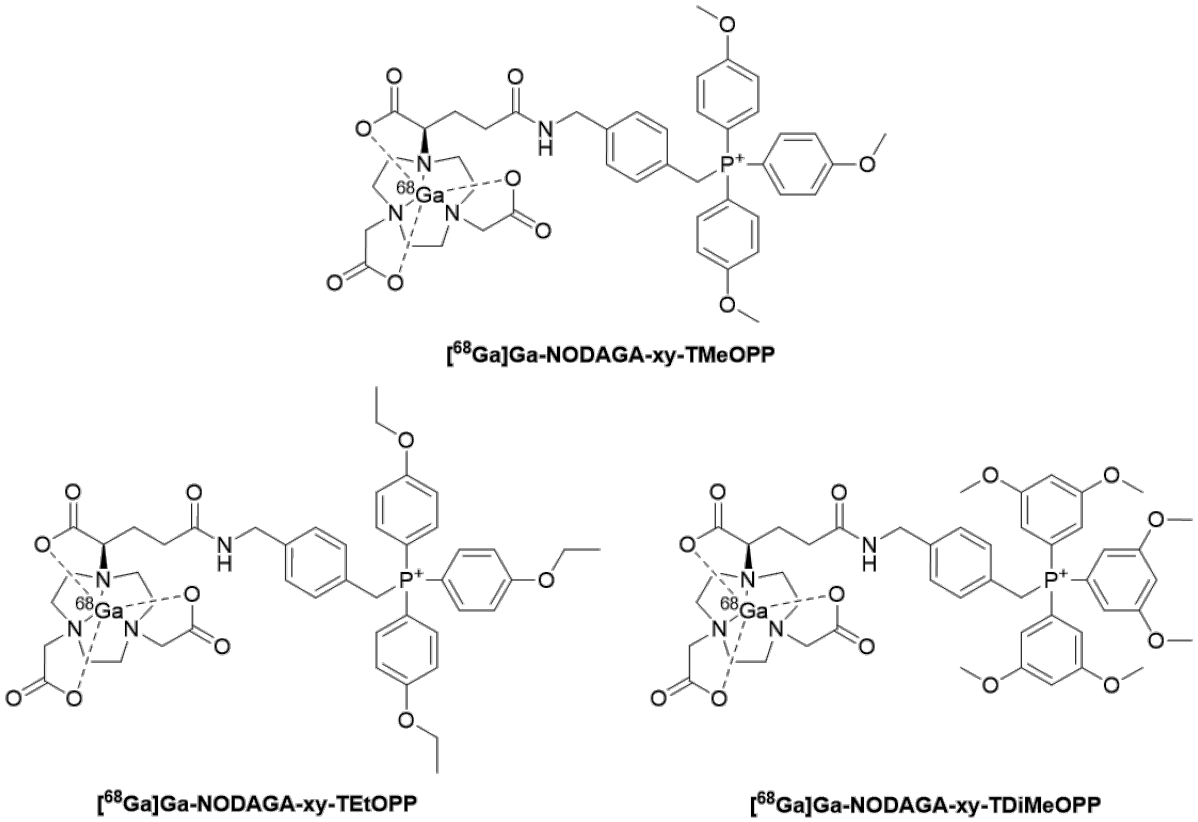

Figure 2.15 The three target NODAGA-xy-TAEP compounds investigated in this project. These consist of a (R)-NODAGA chelating moiety capable of chelating [^{68}Ga]Ga(III), a xylyl linking group and a TMeOPP, TEtOPP or TDiMeOPP cation respectively.

The introduction of a *para*-methoxy group on each aryl unit provides a direct comparison of the effect of this substituent on the final radiotracers lipophilicity, compared to the alkyl-functionalised *para*-methyl (TTP) analogue of the previous series of compounds. We also investigated how radiotracer lipophilicity could be modulated by increasing the alkyl chain-length of the ether moiety, through the synthesis of a tris-*p*-ethoxy variant. The final derivative of this family, tris(*m*,*m'*-dimethoxy), will assess how increasing the number of ether groups on each aromatic ring effects radiotracer lipophilicity and can also serve as a comparison to both the TXP and tri-*p*-methoxy analogues.

2.3.1 Synthesis of TAEP-Functionalised Aminoxylenes

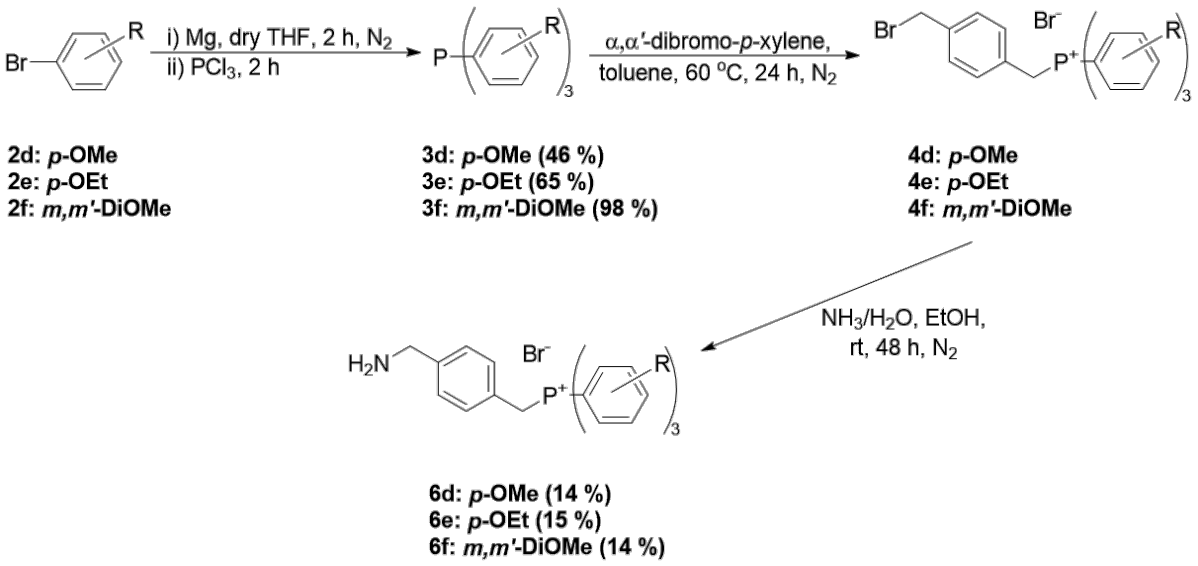

Scheme 2.8 The synthetic route employed for the preparation of TAEP-functionalised aminoxylenes **6d-f**. The synthesis of **6d-f** was performed analogously to **6a-c**. Triarylphosphines **3d-f** and TAEP-functionalised bromoxylenes were generated using an adapted method described by Smith *et al*.[2]

Analogous methods used for the preparation of TAP-functionalised aminoxylenes **6a-c** were employed for the synthesis of ether-functionalised derivatives **6d-f**, as shown in **Scheme 2.8**.[2] The $^{31}P\{^{1}H\}$ NMR spectra of the triarylphosphines **3d-f** are shown in **Figure 2.16**, with the same two peaks observed for **3d-e** as for **3a-c**. The negative chemical shift peak at approximately -10 ppm indicates the presence of the desired triarylphosphine, and the peak at approximately 30 ppm refers to the oxidised phosphine impurity. A higher, more rapid degree of oxidation was observed for these ether-functionalised triarylphosphines **3d-e**, which can be attributed to the increased nucleophilicity of the phosphorus-centred lone pair arising from the mesomeric electron donation from the oxygen atoms. This led to a decrease in yield for the synthesis of **3d**. The synthesis of **3f** was repeated with the product maintained under an inert atmosphere from its generation until its use for the synthesis of its bromoxylene-TAEP counterpart. Instead of quenching the reaction with water, the inorganic impurities were removed by cannula filtration and the mixture was then concentrated under reduced pressure using an in-line trap. The recrystallisation step was performed using anhydrous ethanol under a nitrogen atmosphere. These steps were performed in the work-up stage of **3f** to prevent the generation of impurities and maximise the yield of **3f**.

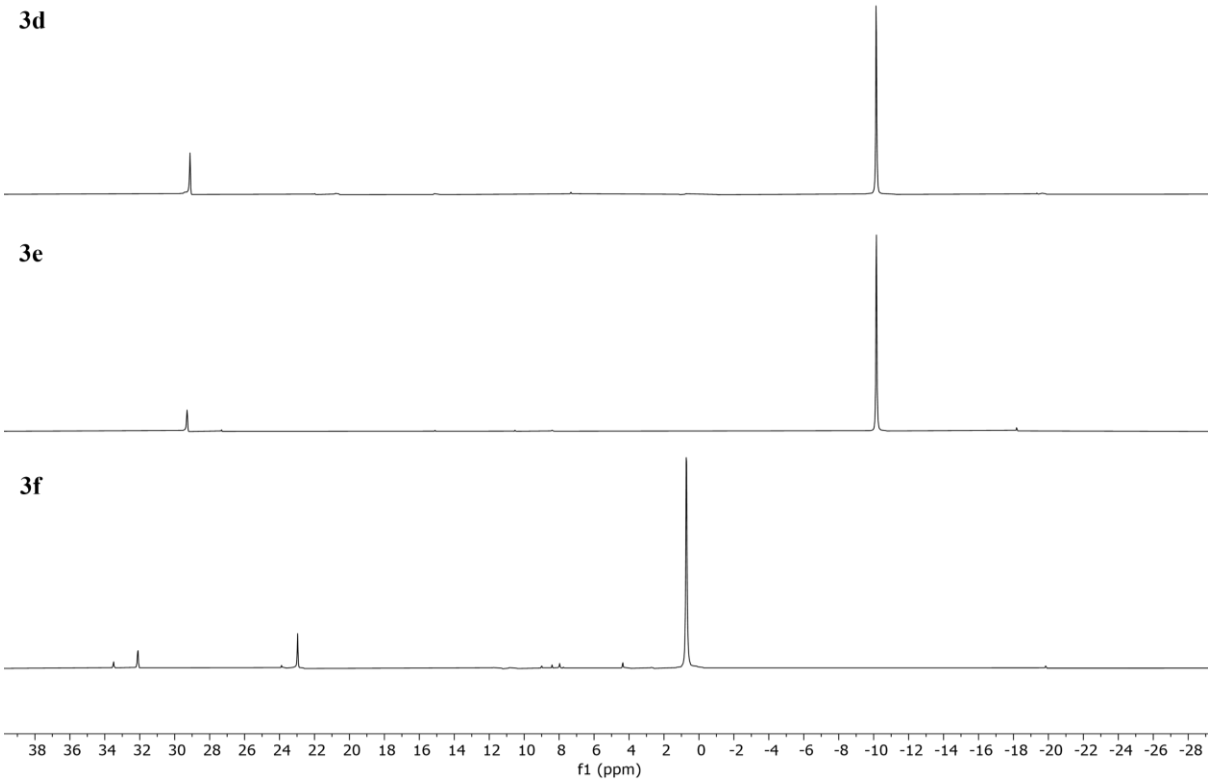

Figure 2.16 $^{31}P\{^{1}H\}$ NMR spectra of crude triarylphosphines **3d-f** (162 MHz, 298 K, $CDCl_3$).

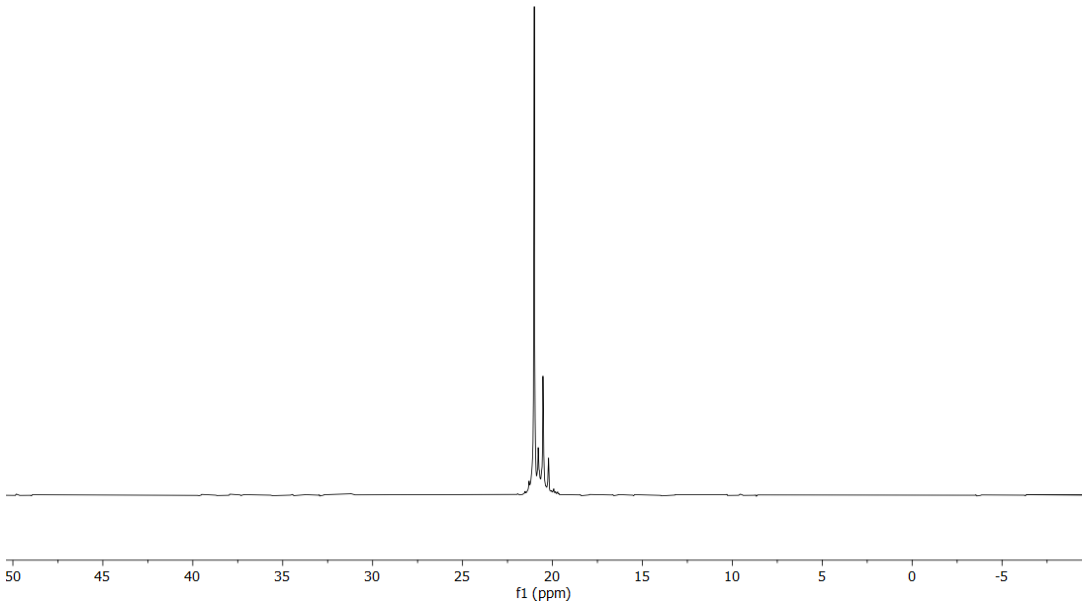

Figure 2.17 $^{31}P\{^{1}H\}$ NMR spectrum of crude bromoxylene-TMeOPP **4d** (162 MHz, 298 K, $CDCl_3$).

The increased nucleophilicity of the phosphorus-centred lone pair resulted in a lack of control and regioselectivity for the reaction between α,α′-dibromo-*p*-xylene and **3d-f**, highlighted by the $^{31}P\{^{1}H\}$ NMR spectrum of **4d** shown in **Figure 2.17**, in which four peaks at 21.0 ppm were observed. The same observations were made for the ethoxy-substituted variant **4e**. The

dimethoxy-substituted variant **3f** proved insoluble in toluene, even at elevated temperatures, but it was found to be soluble in acetonitrile at elevated temperatures and this solvent was subsequently used for the synthesis of **4f**. Purification by silica flash chromatography of **4f** was used as an alternative to toluene and diethyl ether washes to assess its viability in removing the impurities observed by $^{31}P\{^{1}H\}$ NMR. Some impurities were successfully removed, but two peaks were present in the $^{31}P\{^{1}H\}$ NMR of **4f**. ^{1}H NMR elucidated the major phosphorus-containing species as the desired product, however the second peak in the $^{31}P\{^{1}H\}$ NMR accounted for nearly forty percent of the sample collected by column chromatography, which confirmed this method of purification was of limited success.

Regardless, the following reaction involving the generation of the TAEP-functionalised aminoxylenes **6d-f** involved reverse-phase column chromatography, which was deemed a sufficient technique to remove impurities if the crude bromoxylenes **4d-f** were carried forward with impurities present. Compared to the TAP-functionalised aminoxylenes **6a-c**, analogues **6d-f** were obtained in lower yields, but sufficient product material was collected for all three compounds to perform subsequent macrocycle functionalisation.

2.3.2 Amide Coupling of Aminoxylene-TAEP Cations to (R)-NODAGA

For the synthesis of (R)-NODAGAtri-*tert*-butylester-xylene-TAEP compounds **9d-f** shown in **Scheme 2.9**, commercially sourced (R)-NODAGA(^{t}Bu)$_3$ was coupled with aminoxylenes **6d-f** using the same methodology employed for the synthesis of compounds **9a-c**.[15] The methoxy- and dimethoxy-substituted variants gave considerably good yields compared to **9a-c**, with the latter giving quantitative yields. Compared to the other analogues **9a-e** which were isolated as solids, **9f** was obtained as a pale-yellow oil. This family of compounds were noted as being relatively hygroscopic, with the solids initially obtained gradually becoming oils if they were not freeze-dried and stored at -18 °C until they were required. However, the dimethoxy-substituted variant once freeze-dried would form a glassy foam which would immediately form an oil. Therefore, the reported 100 % yield for the synthesis **9f** is used very loosely as there is expected to be a degree of water present, which could not be quantified using NMR spectroscopy due to the use of deuterated methanol for this analysis, which already contained a residual amount of water.

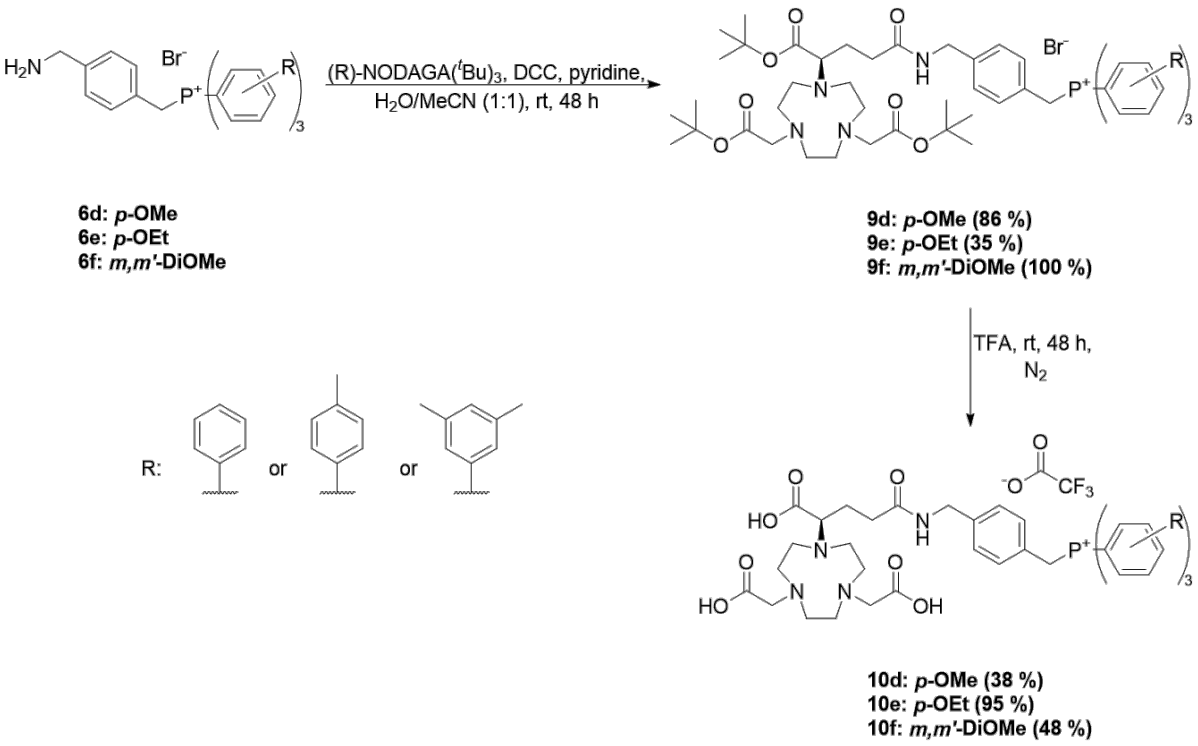

Scheme 2.9 Synthesis of (R)-NODAGA-xy-TAEP compounds **10d-f** from the TAEP-functionalised aminoxylenes **6d-f**. The amide coupling of **6d-f** to (R)-NODAGA(^{t}Bu)$_3$ was performed using an adapted procedure developed by Schirrmacher *et al*.[15]

The TFA-assisted deprotection of **9d-f** resulted in range of chemical yields, with the ethoxy-substituted analogue **10e** obtained in a 95 % yield, compared to 38 % and 48 % for compounds **10d** and **10f** respectively. The lower yields obtained for **10d** and **10f** were attributed to the cleavage of the methoxy groups arising from their acid-lability, whereas the ethoxy groups present in **10e** are base-labile and would not cleave in the acidic conditions afforded by TFA. The formation of carboxylic acid groups, including the UV activity afforded by the aromatic rings, make these compounds ideal for purification by reverse-phase C-18 chromatography.

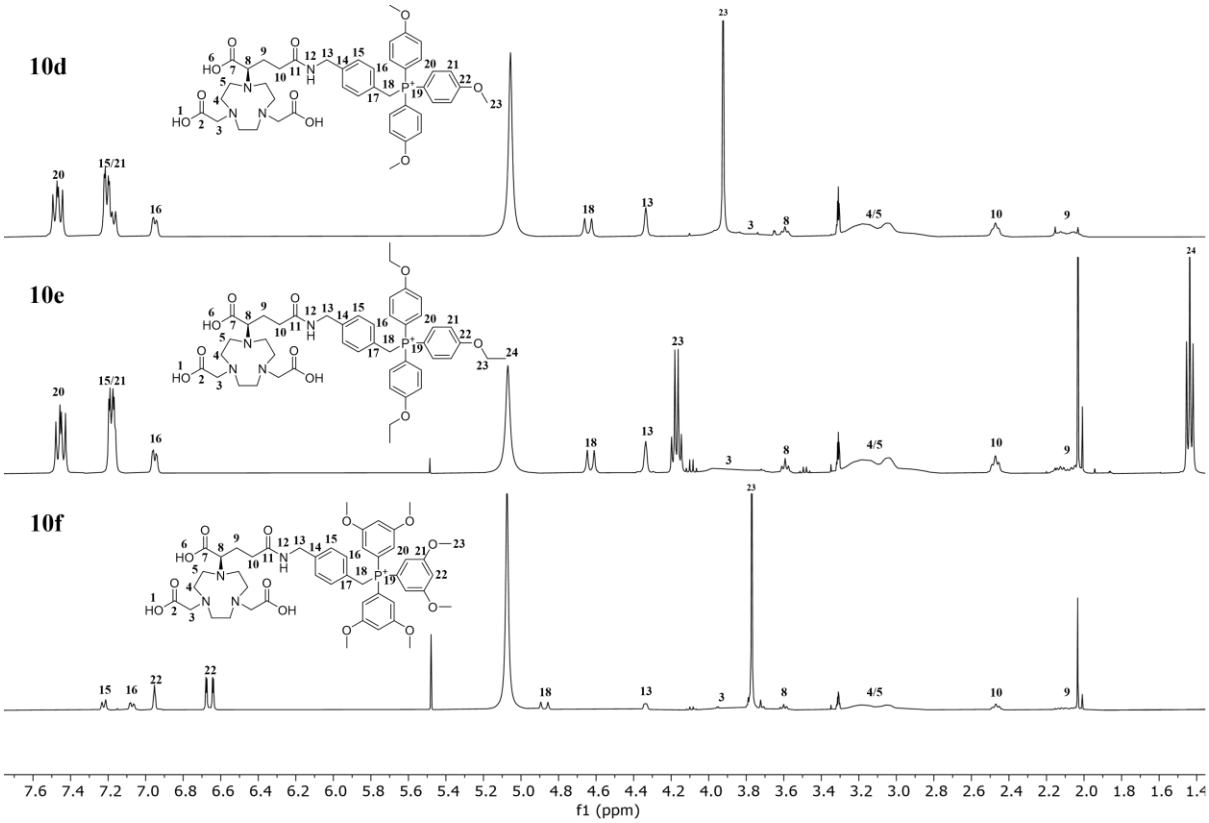

Figure 2.18 ^{1}H NMR spectra of the deprotected (R)-NODAGA-xy-TAEP ligands (CD_3OD, 400 MHz, 298 K). From top to bottom: (R)-NODAGA-xy-TMeOPP (**10d**), (R)-NODAGA-xy-TEtOPP (**10e**), (R)-NODAGA-xy-TDiMeOPP (**10f**). The labelled structures of **10d-f** and NMR characterisation are also included.

The ^{1}H NMR spectra of these three compounds are shown in **Figure 2.18**, with a single peak observed in the $^{31}P\{^{1}H\}$ NMR spectra for all three compounds. Mass spectrometry also showed a single peak in the LC-MS spectrum, confirming one UV active species was present in the case for all three analogues, with *m*/*z* values of 829, 871 and 919 observed for **10d**, **10e** and **10f** respectively. Compounds **10d-f** were stored at -18 °C to prevent decomposition, as was the case for **10a-c** in section 2.2.4.

2.3.3 Synthesis and Characterisation of Non-Radioactive Reference Ga-(R) NODAGA-xy-TAEP Compounds

As explained in section 2.2.5, the synthesis of a non-radioactive analogue is required for full characterisation by analytical techniques, such as NMR spectroscopy and mass spectrometry, and can also be analysed by the same HPLC method as the radiolabelled analogue. The synthesis of non-radioactive Ga(III) TAEP-functionalised NODAGA complexes were

performed analogously to NODAGA-xy-TAP analogues prepared in section 2.2.5, and shown in **Scheme 2.10**.

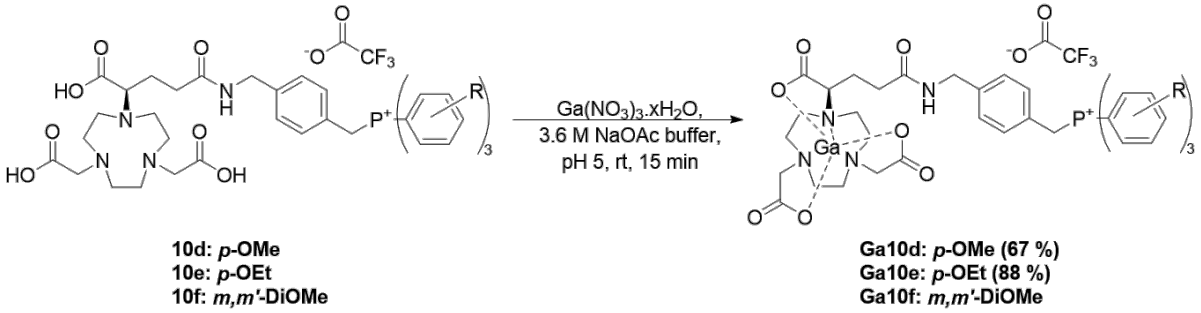

Scheme 2.10 Protocol for the complexation of (R)-NODAGA-xy-TAEP ligands with Ga(III) trisnitrate in 3.6 M NaOAc buffer at pH 5, as shown in **Scheme 2.7**.

Using 1.5 equivalents of Ga(III) trisnitrate and 3.6 M NaOAc buffer, the ligand **10d-f** was stirred at room temperature for 15 minutes to give the non-radioactive analogues **Ga10d-f** were prepared. All three compounds were characterised by NMR spectroscopy, mass spectrometry and HPLC.

2.3.3.1 HPLC Analysis of Ga-(R)-NODAGA-xy-TAP Complexes

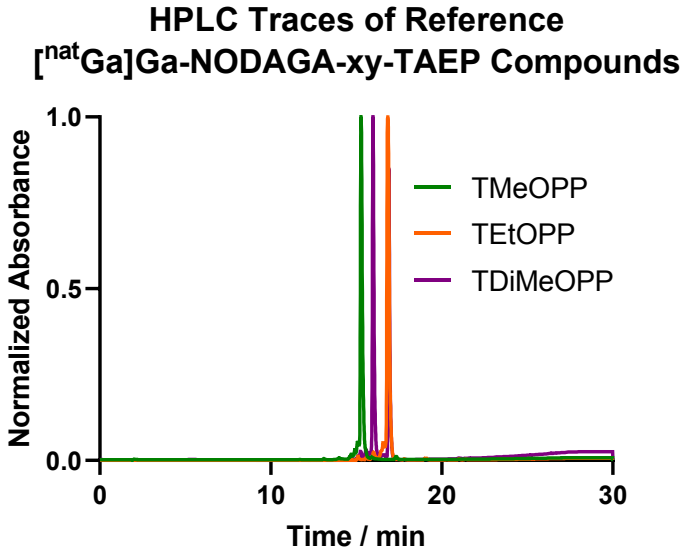

Figure 2.19 The HPLC traces of the non-radioactive reference Ga-NODAGA-xy-TAEP compounds. Eluent gradient as described in **Figure 2.14**. All traces have been normalised so that the maximum absorbance measured for each compound is equal to 1.

The HPLC traces of the three Ga-NODAGA-xy-TAEP complexes can be found in **Figure 2.19**. Importantly, each complex shows one peak, highlighting the purity of the Ga(III)-chelated

reference complexes along with an absence of isomerisation and speciation. The difference in retention time between the Ga-NODAGA-xy-TAEP compounds indicates a change in their lipophilicities relative to each other, with the TEtOPP analogue exhibiting a longer retention time and therefore a higher degree of lipophilicity. These three non-radioactive complexes are now ready to be compared to their ^{68}Ga-labelled analogues in chapter 3.

2.4 Concluding Remarks

This chapter outlines the synthesis of a series of macrocyclic ligands for the formation of lipophilic and cationic gallium-68 complexes. First, we explored the synthesis of triarylphosphonium-functionalised aminoxylenes, through the preparation of bromoxylenes developed by Smith *et al*.[2] We also exploited the tuning of lipophilicity described by Haslop *et al*. for this strategy.[4] Functionalisation of (R)-NODAGA-tris-*tert*-butylester with the aminoxylenes afforded the protected (R)-NODAGA(^{t}Bu)$_3$-xy-TAP compounds using an adapted method described by Schirrmacher *et al*.[15] These compounds were subsequently deprotected using trifluoroacetic acid to give a novel analogues series of ligands in good yields. Non-radioactive reference complexes were prepared using gallium nitrate as the Ga(III) source due to the instability of gallium chloride, along with clinical grade sodium acetate buffer to improve the clinical translatability of this series of complexes. HPLC experiments on the non-radioactive reference compounds, including radiochemical and biological experiments discussed in the proceeding chapters, highlighted that a change in TAP functionalisation had the desired effect on lipophilicity, demonstrated by the increase in retention time as the extent of alkyl functionalisation increased.

Following on from the synthesis of TAP-functionalised NODAGA chelates, triaryletherphosphonium (TAEP)-functionalised NODAGA ligands were synthesised to investigate the effect of ether groups on the lipophilicity of the final complexes. This second series of compounds were synthesised in an analogous fashion to the NODAGA-xy-TAP analogues. The non-radioactive reference complexes were prepared using the same methodology for the synthesis of Ga-(R)-NODAGA-xy-TAP complexes. HPLC experiments on non-radioactive reference compounds, using the same methodology for NODAGA-xy-TAP compounds, also indicated that altering TAEP functionalisation had a significant effect on retention time, therefore an effect on lipophilicity.

2.5 References for Chapter 2

1 A. J. Smith, B. E. Osborne, G. P. Keeling, P. J. Blower, R. Southworth and N. J. Long, *Dalton Trans.*, 2020, **49**, 1097–1106.

2 A. J. Smith, P. J. Gawne, M. T. Ma, P. J. Blower, R. Southworth and N. J. Long, *Dalton Trans.*, 2018, **47**, 15448–15457.

3 A. J. Smith, Imperial College London, 2019.

4 A. Haslop, L. Wells, A. Gee, C. Plisson and N. Long, *Mol. Pharm.*, 2014, **11**, 3818–3822.

5 Z. M. Safee, F. Baark, E. C. T. Waters, M. Veronese, V. R. Pell, J. E. Clark, F. Mota, L. Livieratos, T. R. Eykyn, P. J. Blower and R. Southworth, *Sci. Rep.*, 2019, **9**, 216.

6 E. W. Price and C. Orvig, *Chem. Soc. Rev.*, 2014, **43**, 260–290.

7 J. Schraml, M. Čapka and V. Blechta, *Magn. Reson. Chem.*, 1992, **30**, 544–547.

8 Y.-S. Kim, C.-T. Yang, J. Wang, L. Wang, Z.-B. Li, X. Chen and S. Liu, *J. Med. Chem.*, 2008, **51**, 2971–2984.

9 M. Klika Škopić, S. Willems, B. Wagner, J. Schieven, N. Krause and A. Brunschweiger, *Org. Biomol. Chem.*, 2017, **15**, 8648–8654.

10 S. Nomura, K. Endo-Umeda, A. Aoyama, M. Makishima, Y. Hashimoto and M. Ishikawa, *ACS Med. Chem. Lett.*, 2015, **6**, 902–907.

11 J. Volf and J. Pašek, in *Catalytic Hydrogenation*, ed. L. B. T.-S. in S. S. and C. Cerveny, Elsevier, 1986, vol. 27, pp. 105–144.

12 P. Roose, K. Eller, E. Henkes, R. Rossbacher and H. Höke, in *Ullmann's Encyclopedia of Industrial Chemistry*, Wiley-VCH Verlag GmbH & Co. KGaA, Weinheim, Germany, 2015, pp. 1–55.

13 K.-P. Eisenwiener, P. Powell and H. R. Mäcke, *Bioorg. Med. Chem. Lett.*, 2000, **10**, 2133–2135.

14 K.-P. Eisenwiener, M. I. M. Prata, I. Buschmann, H.-W. Zhang, A. C. Santos, S. Wenger, J. C. Reubi and H. R. Mäcke, *Bioconjug. Chem.*, 2002, **13**, 530–541.

15 World Intellectual Property Organization, WO 2010/066051 A1, 2010, 1–35.

16 M. Kardashinsky, N. Lengkeek and L. M. Rendina, *J. Label. Compd. Radiopharm.*, 2017, **60**, 4–11.

17 N. Salvarese, D. Carta, C. Marzano, G. Gerardi, L. Melendez-Alafort and C. Bolzati, *J. Med. Chem.*, 2018, **61**, 11114–11126.

18 C. Bolzati, M. Cavazza-Ceccato, S. Agostini, F. Refosco, Y. Yamamichi, S. Tokunaga, D. Carta, N. Salvarese, D. Bernardini and G. Bandoli, *Bioconjug. Chem.*, 2010, **21**, 928–939.

19 A. Boschi, L. Uccelli, L. Marvelli, C. Cittanti, M. Giganti and P. Martini, *Molecules*, 2022, **27**, 1188.

20 B. W. Tsang, C. J. Mathias, P. E. Fanwick and M. A. Green, *J. Med. Chem.*, 1994, **37**, 4400–4406.

CHAPTER 3 – RADIOLABELLING OF LIPOPHILIC AND CATIONIC MACROCYCLIC LIGANDS WITH GALLIUM-68

3. Radiolabelling of Lipophilic and Cationic Macrocyclic Ligands with Gallium-68

In chapter 2, the synthesis of potentially lipophilic and cationic ligands for gallium-68 was discussed. Chapter 3 will investigate the radiolabelling properties of these macrocyclic ligands with gallium-68. Once effective radiolabelling strategies for such ligands had been identified, their log *D* values were calculated as an initial readout of their potential for mitochondrial uptake in myocardial tissue.

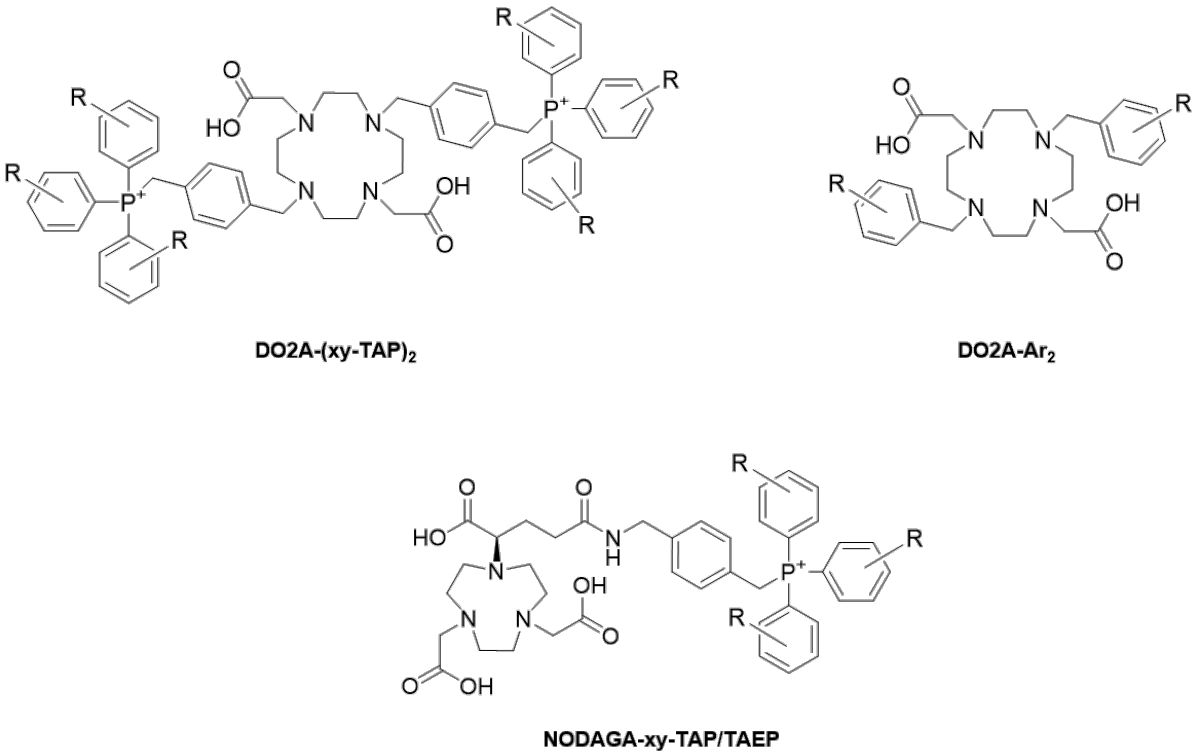

Figure 3.1 The general structures of macrocyclic ligands discussed in chapter 2, ready for ^{68}Ga-labelling. R = H, *p*-Me, *m*,*m*′-diMe, *p*-OMe, *p*-OEt, *m*,*m*′-diOMe.

As discussed in chapter 2, four macrocycle-based series of compounds, shown in **Figure 3.1**, were synthesised and made ready for ^{68}Ga-labelling. In the following sections of this chapter, the ^{68}Ga-labelling of these compounds will be discussed, and ultimately led to two publications.[1,2]

3.1 [^{68}Ga]Ga-DO2A-(xy-TAP)$_2$ and [^{68}Ga]Ga-DO2A-Ar$_2$

The first set of compounds to be assessed for their gallium-68 radiolabelling properties was the DO2A-based chelates, including triarylphosphonium (TAP) and aryl functionalisation. Preliminary radiochemical work showed evidence of kinetic/thermodynamic speciation upon chelation with gallium-68. The individual species could be visualised and separated by radioHPLC.[1,3] This speciation was observed consistently for all five analogues, TPP-, TTP-, TXP-, Bn- and Xy-functionalised DO2A compounds.

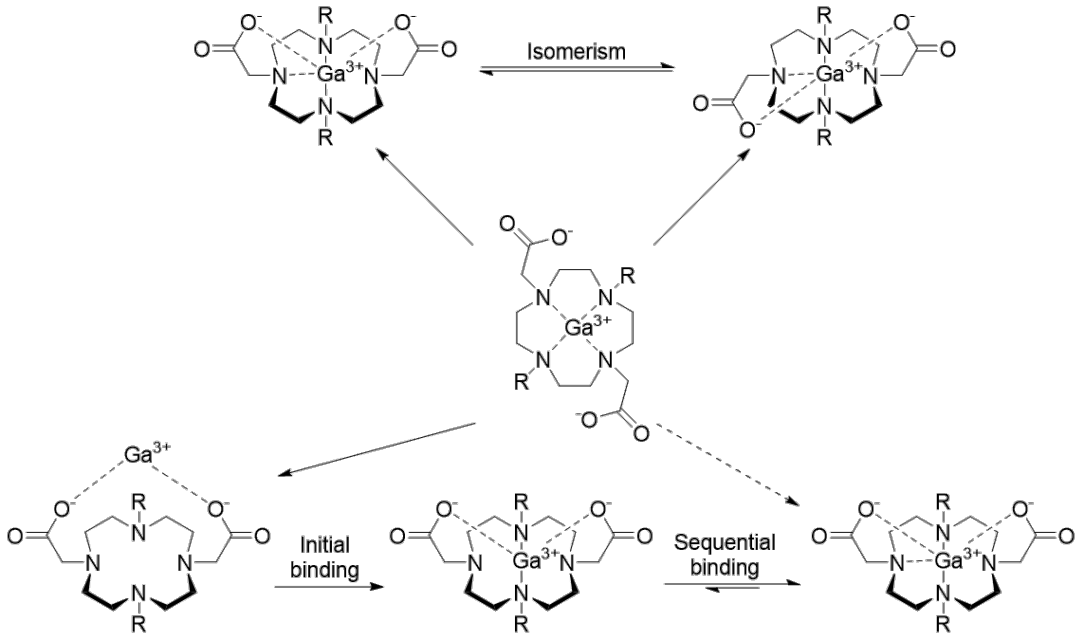

Figure 3.2 Schematic proposing two explanations for the speciation seen in [^{68}Ga]Ga-DO2A complexes, shown in section 2.1. Either the complex formation involves binding of the two carboxylate arms in *cis*/*trans* conformations, or sequential binding of the carboxylate arms to the metal centre. R = non-chelating group, such as the TAP moiety. Adapted from Smith.[3]

Two possible explanations were proposed for the observed speciation (**Figure 3.2**). The first of which outlined the possibility of *cis*/*trans* isomerism existing in the complex, which was dependent on which face of the macrocycle the two carboxylate arms bind to metal ions.[3] It was thought that both isomers would be interconvertible, as well as existing as a pair of kinetic/thermodynamic products. The second explanation was that the binding of the two carboxylate arms could occur sequentially. The proposed rationale for this explanation is shown in **Figure 3.2**, beginning with an initial binding step to the two carboxylate oxygens forming the expected 'out-of-cage' complex, followed by binding to the four cyclen nitrogens.[4] Binding of the four cyclen nitrogen atoms to the Ga(III) metal centre occurs in a sequential

manner, with the unbound nitrogen atom present in the intermediate responsible for an increase in hydrophilicity, leading to a reduction in retention time by reverse-phase HPLC.

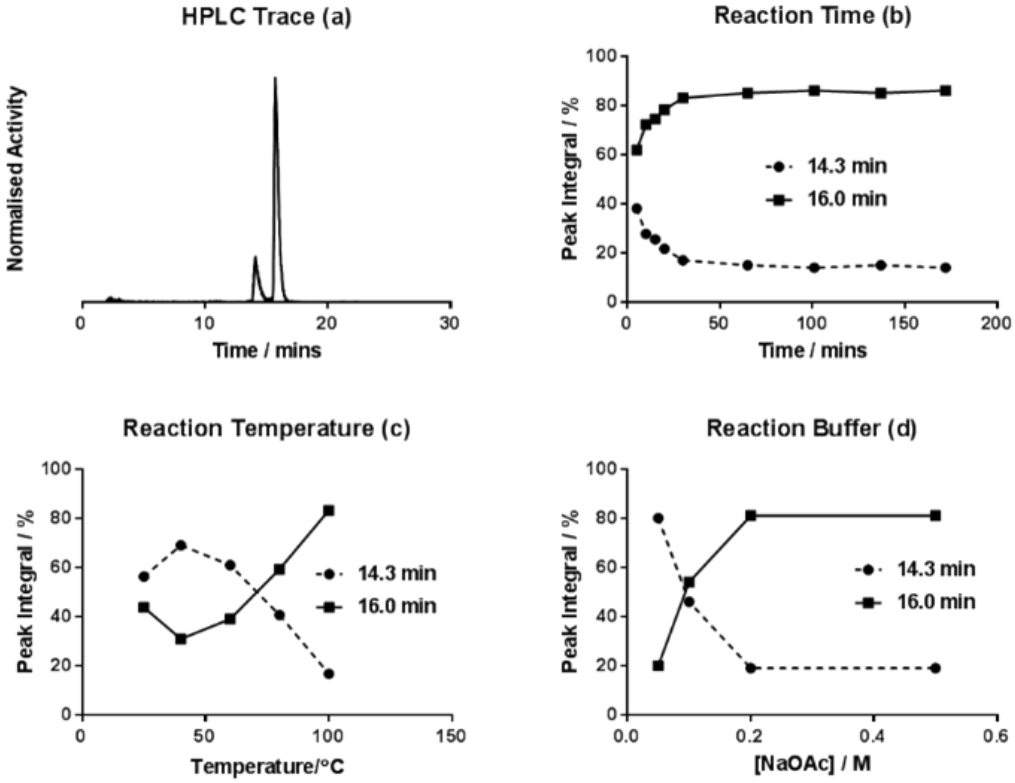

Figure 3.3 (a) RadioHPLC trace of [^{68}Ga]Ga-DO2A-(xy-TPP)$_2$, **[^{68}Ga]Ga1a** (eluent gradient: 100 % A for 5 min, 0–100 % B in A for 20 min, 100 % B for 5 min; flow rate 1 mL min^{-1}). Peaks are observed at 14.3 min and 16.0 min. **(b)–(d)** Summaries of the speciation analysis experiments, reporting how the relative integrals of the two peaks in **(a)** change with changing reaction time **(b)**, temperature **(c)** and buffer concentration **(d)**. Reprinted with permission from Smith *et al*.[1]

The first possibility concerning *cis*/*trans* isomerism was discounted due to the lack of evidence in the literature supporting the presence of any macrocyclic chelate binding a metal ion with carboxylate arms in a *trans* configuration, with respect to each other. It is known that for the binding of DOTA-based chelates with pendant carboxylate arms with metal ions, the metal ion is pulled into the macrocycle cavity by both carboxylate arms on the same face. As described previously, it would not be possible for both carboxylate arms to occupy *trans* geometries.[4]

Initial radiolabelling experiments focused on the effect of different buffers, such as NH_4OAc and NaOAc, and their concentrations on the radiochemical yield (RCY).[1] It was determined that 0.2 M NaOAc buffer gave the best RCY values. Summarised in **Figure 3.3** are three other

parameters that can be altered to try to improve the RCY: ligand concentration, temperature, and time. Due to the simplicity of the chemical structure of the TPP analogue compared to its derivatives, **1a** was used to probe these phenomena further. Using a basic protocol of 500 μM ligand concentration, 0.2 M NaOAc buffer and 30 min of heating at 100 °C, aliquots of the reaction mixture were taken at specific time points and analysed by iTLC and radioHPLC. Heating the reaction mixture at 100 °C for the first 30 min showed that the integral of the 16.0 min peak (**Figure 3.3a**) increases, indicating that it corresponds to the thermodynamic product of the reaction. In comparison, the integral of the 14.3 min peak (**Figure 3.3a**) decreases over the course of the reaction, meaning it corresponds to the kinetic product, summarised in **Figure *3.3*b**. After 30 min, an 80:20 ratio is established and maintained between both peaks, indicating that an equilibrium exists between the two products. After 60 min, the speciation remained unchanged, even with prolonged heating, resulting in the thermodynamic product having an approximate 85 % abundance in the reaction mixture.

Studying this radiolabelling process at varying temperatures helped to establish whether the two species did form a kinetic/thermodynamic product pairing, and the data obtained from these experiments are outlined in **Figure 3.3c**. Radiolabelling was performed at room temperature, as it was thought that lowering the temperature would slow the interconversion of any isomerism, further confirming the theory proposed in the 100 °C experiments. However, the radiolabelling at room temperature was not as effective as at 100 °C, highlighted by the large activity peak at 2 min referring to unchelated [^{68}Ga]Ga(III).[3] The peak at 14.3 min peak was more intense than the 16.0 min peak, corroborating the findings drawn from **Figure 3.3b**, with the 14.3 min peak being the kinetic product as it is formed more readily at room temperature due to the lower activation energy of its formation. Nevertheless, the purpose of this experiment was to determine whether labelling at room temperature, slowing the kinetics of the complexation, would lead to the formation of a single species, which it does not. Data from the experiments summarised in **Figure 3.3c** showed that as the reaction temperature is increased, the prevalence of the 16.0 min peak also increased, confirming that the peak refers to a thermodynamically favoured product. These observations further validate the kinetic/thermodynamic product formation rationale.

The final set of experiments involved altering the concentration of the NaOAc buffer. The data from these experiments is summarised in **Figure 3.3d**.[1] Lowering the NaOAc buffer concentration would lead to a decrease in pH, with the more acidic radiolabelling conditions hindering the necessary deprotonation of cyclen amine and carboxylate groups to bind the

Ga(III) ion in its full hexadentate coordination. The pKa of the cyclen amine groups are higher than that of the carboxylate groups.[5] This means that the amine sites would prove to be more difficult to deprotonate at lower pH to bind the metal centre, highlighting the deprotonation of these groups are the important factors in the sequential binding pathway proposed. At low pH values, the 14.3 min peak dominated, whilst at higher pH values the 16.0 min peak dominated, corroborating the sequential binding event, as higher pH values would promote deprotonation of the binding groups, allowing for the binding of the Ga(III) centre. At 0.5 M NaOAc buffer concentration, the 80:20 peak ratio is maintained, indicating that the equilibrium of this process is maintained between 0.2 M and 0.5 M NaOAc concentration.[1]

To probe this rationale further, after 30 min of heating at 100 °C the two peaks at 14.3 min and 16.0 min were isolated by radioHPLC. The 14.3 min peak was separated into two reaction vessels, one was heated at 100 °C for an additional 35 min and the second was left to stand at room temperature for an additional 70 min, the radioHPLC traces of these data are shown in **Figure 3.4**. Heating the 14.3 min peak for an additional 35 min did show some conversion to the 16.0 min peak, establishing a 40:60 peak ratio. Leaving the 14.3 min peak product at room temperature for a further 70 min showed a lesser degree of conversion to the 16.0 min peak in a 55:45 peak ratio, confirming that an equilibrium exists between the two species and lower temperatures favour the kinetic product. Heating the isolated 16.0 min peak for an additional 35 min gave the same radioHPLC trace, implying this peak does refer to the thermodynamic product.

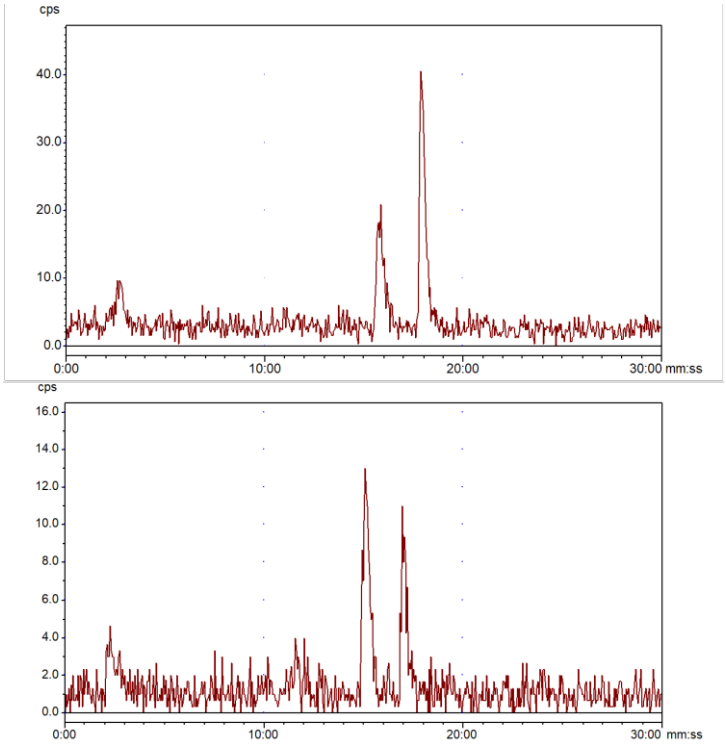

Figure 3.4 RadioHPLC traces of the experiments on the isolated kinetic peak species of **[^{68}Ga]Ga1a**. 100 °C, 65 min, 0.2 M NaOAc (*top*), and 25 °C, 100 min, 0.2 M NaOAc (*bottom*). Eluent gradient as described for **Figure 3.3a**. Reprinted with permission from Smith *et al*.[1]

As discussed in section 2.1, a non-radioactive analogue of **[^{68}Ga]Ga1a**, **Ga1a**, was synthesised to further analyse the observed speciation on the macroscopic level. Characterisation by NMR of **Ga1a** shown in **Figure 2.3** did not indicate the presence of two different species.

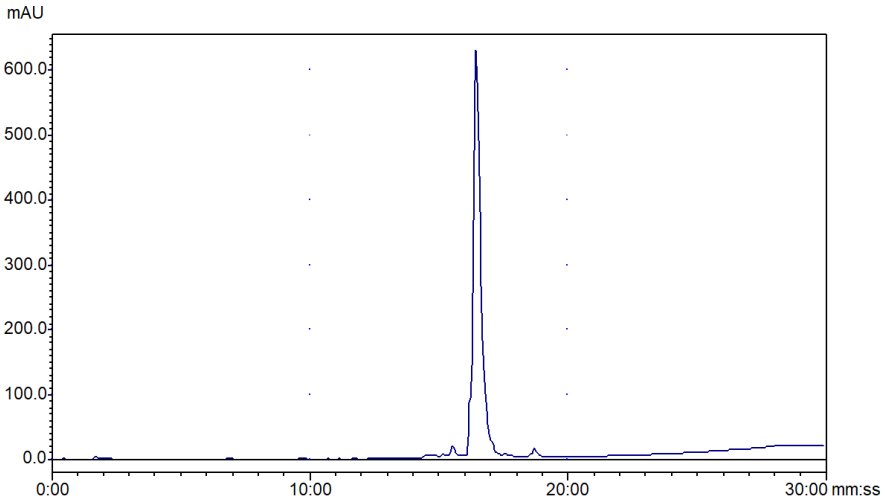

Figure 3.5 HPLC trace of **Ga1a** trisnitrate. Eluent gradient as described for **Figure 3.3a**. Reprinted with permission from Smith *et al*.[1]

The HPLC of the non-radioactive analogue **Ga1a** trisnitrate, shown in **Figure 3.5**, corresponded to the radioHPLC 16.0 min peak of the thermodynamic product. Due to the complexation of Ga(III) with **1a** involving heating at 100 °C overnight, the 16.0 min peak was expected to be the only, if not dominant, species in the HPLC trace, as longer heating times would promote the formation of the thermodynamic product.[1]

Another explanation of the speciation observed by radioHPLC could be the involvement of counter ions and solvent molecules in the coordination sphere. Therefore, generating competition for the Ga^{3+} centre between counter ions, solvent molecules, pendant carboxylate arms and amine donor sites. One or more of the coordination sites could be occupied by various monodentate ligands, such as chloride, water, or hydroxide ions, instead of the expected pendant carboxylate arms and an interchange between these species could occur.[16,17] Since the radiolabelling was performed in the presence of chloride ions, from the generator eluent, it could be assumed that one of the coordination sites was occupied by a chloride ion. However, such a minor change in structure or polarity occurring with this interchange would not be expected to give a near 2-minute difference in retention time by radioHPLC.

3.2 [^{68}Ga]Ga-NODAGA-xy-TAP

Analogues of NODAGA-xy-TAP, containing DO3A and DO2A macrocyclic chelates, exist in the literature, with appropriate gallium-68 radiolabelling strategies established for these literature radiotracers.[1,6] Therefore, it seemed like an ideal starting point to investigate the gallium-68 radiolabelling properties of these NODAGA-based chelates.[1,6] The radiolabelling protocol, adapted from gallium-68 labelled DO3A-xy-TAP compounds demonstrated by Smith *et al*., outlined in **Scheme 3.1**, was employed for preliminary radiolabelling studies of NODAGA-xy-TAP compounds.

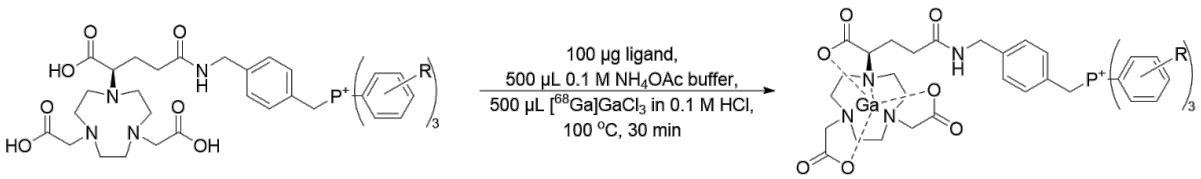

10a: NODAGA-xy-TPP
10b: NODAGA-xy-TTP
10c: NODAGA-xy-TXP

[^{68}Ga]Ga10a: [^{68}Ga]Ga-NODAGA-xy-TPP
[^{68}Ga]Ga10b: [^{68}Ga]Ga-NODAGA-xy-TTP
[^{68}Ga]Ga10c: [^{68}Ga]Ga-NODAGA-xy-TXP

Scheme 3.1 Protocol for the preliminary radiolabelling of NODAGA-xy-TAP compounds with generator-produced [^{68}Ga]$GaCl_3$, adapted from the literature protocol by Smith *et al*.[6]

It was expected that these conditions would lead to near quantitative RCYs of the NODAGA-based radiotracers **[^{68}Ga]Ga10a-c**, due to the more favourable ^{68}Ga-labelling conditions afforded by NODAGA compared to DO3A analogues, discussed in section 2.2.[7] First, 100 µg of ligand was dissolved in 500 µL of 0.1 M NH_4OAc buffer to give an average initial ligand concentration of 220 µM. A concentration of 0.1 M NH_4OAc was chosen as it would be equimolar to the 0.1 M HCl used to elute the generator.

The Eckert & Ziegler gallium-68 generator used in the radiolabelling experiments of this project, similar to that shown in **Figure 3.6a**, functions in a similar way to the technetium-99m generator shown in **Figure 3.6b**, and is susceptible to a high degree of variability in the properties of the [^{68}Ga]$GaCl_3$ solution eluted from the generator.

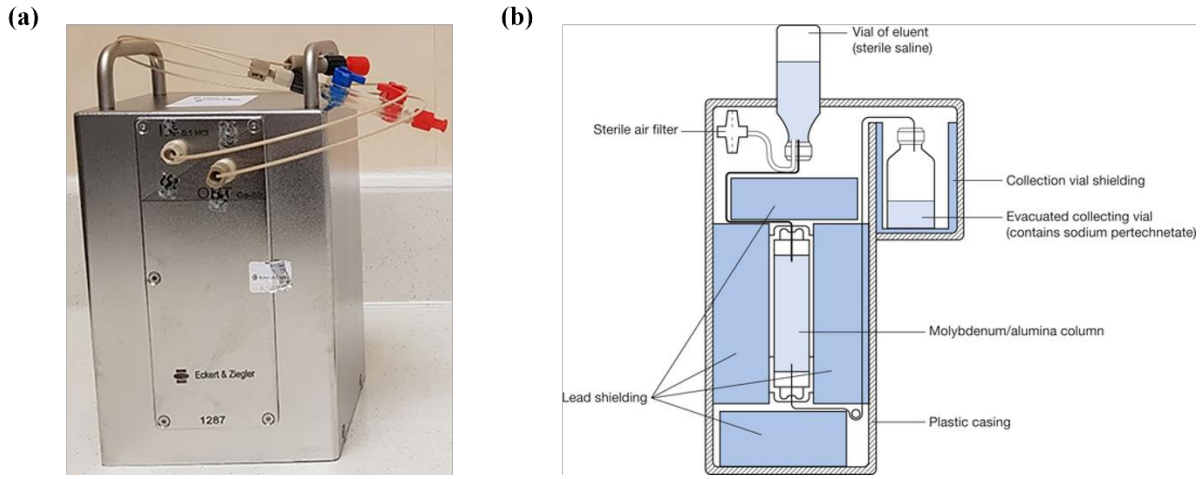

Figure 3.6 (a) Eckert & Ziegler Gallium-68 Generator, similar to the one used in this project. Adapted from Lepareur *et al*.[8] **(b)** Schematic of a technetium-99m generator. Taken from www.radiologykey.com.[9]

First, gallium-68 generators used in research have an approximate functional lifetime of one year, due to the parent germanium-68 isotope having a half-life of 271 days. A gallium-68 generator is typically dedicated towards clinical use whilst it is at its most radioactive before being transferred for use in research. Once the generator is designated for research, it is capable of producing more than 400 MBq of [^{68}Ga]$GaCl_3$ in 5 mL eluate. However, after one year, it only produces 200 MBq of radioactivity in the same volume. In order to maximise the radioactivity of the eluate, if a generator has been eluted for 24 hours, a pre-elution is performed to remove excess non-radioactive zinc-68, which competes for chelation with gallium-68, resulting in a lowering of RCYs obtained. It is considered to be completely regenerated three

hours post-elution, due to the rates of formation and decay of gallium-68 being equal at this time point.

The generator is eluted with 5 mL of 0.1 M HCl into five 1.5 mL Eppendorf tubes, in the order of 0.5 mL, 1.5 mL, 1.0 mL, 1.0 mL and 1.0 mL. Careful administration and collection of the eluate ensures that the majority of radioactivity can be collected in the second fraction (the 1.5 mL of eluate in the 1.5 mL Eppendorf tube), meaning between 50 and 100 MBq can be used in each 500 µL aliquot of [^{68}Ga]GaCl$_3$.

3.2.1 RadioHPLC Analysis

The gallium-68 radiolabelling effectiveness of NODAGA-xy-TAP compounds were initially assessed by radioHPLC. Generally, in radioHPLC, the standard UV detector used by most HPLC systems is followed by a gamma detector to detect radioactivity. The gamma detector is surrounded by lead shielding, aiding in reducing the detection of background radiation. In addition, a lead collimator is also used to focus the detection over a thin cross-section of the HPLC outlet tubing. The distance of tubing between the UV and gamma detectors results in an approximate 30 second time-lapse for the eluate to pass between both detectors. However, from a practical perspective, the low concentration of radiolabelled compounds means that it is not typically detected by the UV detector.

3.2.1.1 RadioHPLC Method Development

To assess the purity of the obtained [^{68}Ga]Ga-NODAGA-xy-TAP radiocomplexes, the reaction mixtures for all three radiolabelled compounds were analysed by radioHPLC, shown in **Figure 3.7**. Following radioHPLC methodologies described by Smith *et al*. for TAP-functionalised DO3A analogues, a mobile phase of water doped with 0.1 % TFA (A) and acetonitrile doped with 0.1 % TFA (B) was implemented for the use of analytical C-18 reverse-phase HPLC.[3,6]

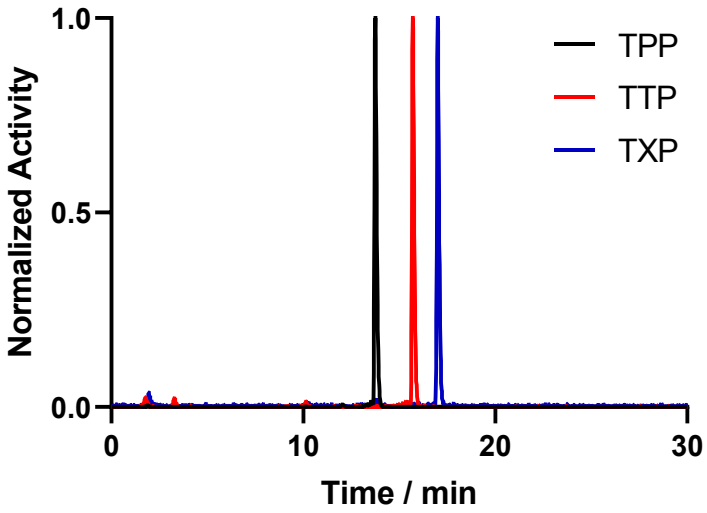

Figure 3.7 RadioHPLC traces of the three labelled [^{68}Ga]Ga-NODAGA-xy-TAP complexes. Eluent gradient: 5 % B in A for 5 min; 5–95 % B in A for 20 min; 95 % B in A for 5 min; flow rate 1 mL min^{-1}. All traces have been normalised such that the maximum activity measured for each complex is equal to 1.

The traces in **Figure 3.7** used a gradient of 5 % B in A for 5 min, followed by a gradient increase from 5–95 % B in A for 20 min, finishing with 95 % B in A for 5 min. After each HPLC experiment, the HPLC column was equilibrated with 100 % A. Analysis of the traces in **Figure 3.7** allowed for an estimation of RCY, due to unchelated [^{68}Ga]Ga(III) eluting with the solvent front with a retention time of two min. RadioHPLC traces also allow for confirmation of radiochemical purity (RCP), with a single peak implying the formation of a single radiolabelled compound. As demonstrated in **Figure 3.7**, unlike the phenomena outlined in section 3.1, all three radiolabelled compounds showed no evidence of any of isomerism. The retention times of the three radiocomplexes **[^{68}Ga]Ga10a-c** can also be used to provide a qualitative assessment of their respective lipophilicities. Since a reverse-phase column consisting of C-18 functionalised silica stationary phase, compounds with a greater degree of lipophilic character will adhere to the column more effectively, resulting in a longer retention time. **Figure 3.7** illustrates this trend very clearly, as the degree of alkyl functionalisation increases the retention time increases, indicating an increase in lipophilicity, with retention times determined to be 13.8 min, 15.7 min and 17.0 min for TPP, TTP and TXP radio-analogues respectively. This provided an initial indication that the alkyl functionalisation was having the desired effect, with the addition of three methyl groups leading to an increase in retention time of approximately two min.

3.2.1.2 Comparison with Non-Radioactive Reference Compounds

The radiolabelled species observed by radioHPLC, shown in **Figure 3.7**, were compared to their respective non-radioactive analogues, synthesised and characterised in section 2.2.5, by comparing their retention times, shown in **Figure 3.8**. The retention times for the non-radioactive reference and ^{68}Ga-labelled compounds are summarised in **Table 3.1**, and can be compared directly since the same HPLC instrument and gradient was used to analyse all sets of compounds. For the all three radiolabelled compounds, the retention times match-up with the non-radioactive reference analogues, meaning that it is highly likely that the observed radioactive species' are [^{68}Ga]Ga-NODAGA-xy-TPP, [^{68}Ga]Ga-NODAGA-xy-TTP and [^{68}Ga]Ga-NODAGA-xy-TXP.

As discussed in section 2.2.5.1, an increase in alkyl functionalisation leads to a longer HPLC retention time. The same trend was seen in analogous HPLC traces of the unchelated ligands **10a-c** (**Figure 3.8c**). The unchelated ligands also show shorter HPLC retention times than their radiolabelled analogues, demonstrating an increase in lipophilicity upon chelation with ^{68}Ga. This is a direct result of a reduction in hydrophilic interactions afforded by the carboxylate pendant arms upon binding the Ga(III) metal centre.

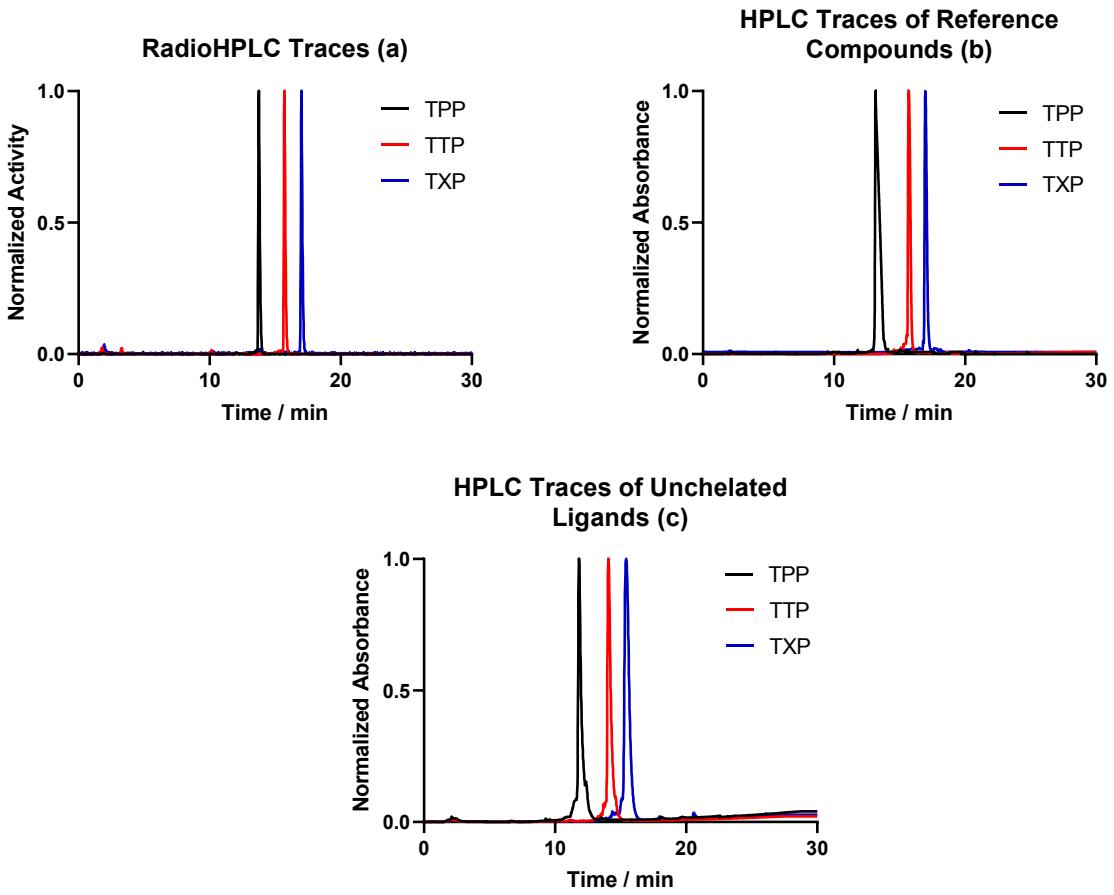

Figure 3.8 (a) RadioHPLC traces of the three radiolabelled [^{68}Ga]Ga-NODAGA-xy-TAP compounds. **(b)** HPLC traces of all three non-radioactive reference compounds, and **(c)** HPLC traces of the unchelated ligands. Eluent gradient as described in **Figure 3.7**. All traces have been normalised so that the maximum activity/absorbance measured for each compound is equal to 1.

Table 3.1 Summary of the data represented in the HPLC traces of **Figure 3.8**.

	Retention Time / min		
	TPP (a)	**TTP (b)**	**TXP (c)**
Unchelated Ligands 10a-c	11.8	14.1	15.4
Ga-Complex	13.2	15.7	17.0
[^{68}Ga]Ga-Complex	13.8	15.7	17.0

3.2.2 iTLC Quality Control Development

Whilst the use of radioHPLC in the analysis of radiolabelling experiments is very powerful, due to its high sensitivity and resolution, the technique does also have some drawbacks. One of these drawbacks is that calculating RCY values by HPLC is difficult since only compounds that are successfully eluted from the column are detected, meaning that any radioactive species

that does not elute from the column is not taken into account in the calculation of the RCYs. On a more practical perspective, HPLC runs are typically performed using a 30-minute method. Therefore, when pairing this with the time taken to successfully radiolabel and characterise the radiotracer, nearly one half-life of gallium-68 would have passed. Lowering the amount of radioactivity available for subsequent biological experiments. For these reasons, the primary quality control (QC) technique used in radiochemistry with metal radioisotopes is instant thin-layer chromatography (iTLC). Whilst iTLC does present its own drawbacks, including a general lower resolution compared to HPLC and traditional TLC, iTLC can be performed in approximately two min. When coupled with a radioTLC plate reader, this allows for rapid confirmation of radiolabelling efficiency. Compared to HPLC, iTLC provides a more accurate measurement of RCY, as all radiolabelled species applied on the baseline of the iTLC plate will be identified by the detector.

3.2.2.1 Determination of Appropriate Mobile Phases

The primary factor in ensuring the use of iTLC as a QC method in radiochemistry is effective, is determining the appropriate mobile phases to give good separation of radiolabelled species and any unchelated [^{68}Ga]Ga(III). In the literature, iTLC methods almost exclusively use aqueous mobile phases to assess ^{68}Ga-labelling efficiency.[10] Even though the target radiotracers in this project are intended to be lipophilic, the cationic charge they exhibit means they adhere to the polar silica gel of the iTLC plate very strongly.

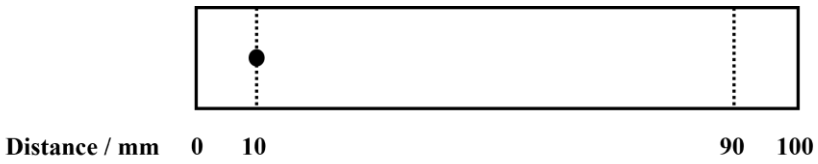

Figure 3.9 A diagram of the iTLC method used in this project. In this method, a 100 mm length iTLC plate is used, where the radiotracer is spotted on the baseline which is located 10 mm from the bottom of the plate. The mobile phase is run to a distance of 90 mm.

Initially, iTLC methods used to visualise the radiolabelled compounds in this project, illustrated in **Figure 3.9**, were designed to keep the desired radiolabelled compound on the baseline, and move the unchelated [^{68}Ga]Ga(III) to the solvent front. One such chelating mobile phase, identified and used by Smith *et al*. for the radiolabelling of TAP-functionalised DO3A and DO2A analogues with gallium-68, was a 0.1 M solution of disodium ethylenediaminetetraacetic acid (EDTA), which binds any free [^{68}Ga]Ga(III).[1,6] An aliquot of

the reaction mixture was spotted 10 mm from the bottom of the iTLC plate and the mobile phase was run up to 90 mm. The use of 0.1 M EDTA as the mobile phase for the QC method was assessed using [^{68}Ga]Ga-NODAGA-xy-TPP and a control experiment of unchelated [^{68}Ga]Ga(III). The iTLC traces of these experiments are shown in **Figure 3.10**.

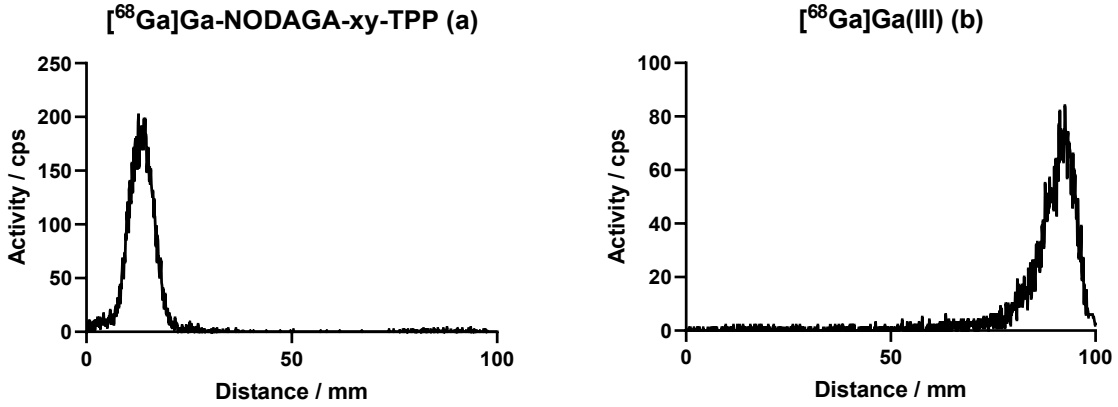

Figure 3.10 The iTLC-based QC method for assessing the radiolabelling efficiency of [^{68}Ga]Ga-NODAGA-xy-TPP (**a**) and a comparison to the control experiment involving unchelated [^{68}Ga]Ga(III) (**b**), using a mobile phase of 0.1 M EDTA. The iTLC plates were scanned using the method illustrated in **Figure 3.9** and a gamma detector.

As shown in **Figure 3.10a**, the major radioactive species remaining on the baseline refers to the radiolabelled compound [^{68}Ga]Ga-NODAGA-xy-TPP, and unchelated [^{68}Ga]Ga(III) travels with the solvent front. The trace obtained for the control experiment, shown in **Figure 3.10b**, shows that whilst some activity remains on the baseline, there is an increase in activity towards the solvent front which refers to the unchelated [^{68}Ga]Ga(III), indicating the 0.1 M EDTA mobile phase does cause separation. The activity that remained on the baseline for the control experiment refers to insoluble [^{68}Ga]Ga(OH)$_3$ that forms when Ga(III) is in aqueous solution.

Due to the observed colloidal gallium species, [^{68}Ga]Ga(OH)$_3$, remaining on the baseline in the control experiment, it cannot be concluded that the radiolabelled species on the baseline for the radiolabelling experiment in **Figure 3.10a** is entirely the radiolabelled compound, as some colloidal gallium may also be present. A second mobile phase system was used to co-validate the observations for the iTLC experiments which used a mobile phase of 0.1 M EDTA. The second mobile phase was designed to move the desired radiolabelled compound with the solvent front and the unchelated [^{68}Ga]Ga(III), including [^{68}Ga]Ga(OH)$_3$, would remain on the baseline. Work by Fuscaldi *et al*. determined that a mixture of ammonium acetate and methanol

in a 1-to-1 ratio moved the desired ^{68}Ga-labelled compound with the solvent front (R_f = 0.9–1.0), whereas unchelated [^{68}Ga]Ga(III) remained on the baseline (R_f = 0.1–0.2).[11] The subsequent iTLC traces for [^{68}Ga]Ga-NODAGA-xy-TPP and the control experiment of unchelated [^{68}Ga]Ga(III) are shown in **Figure 3.9**.

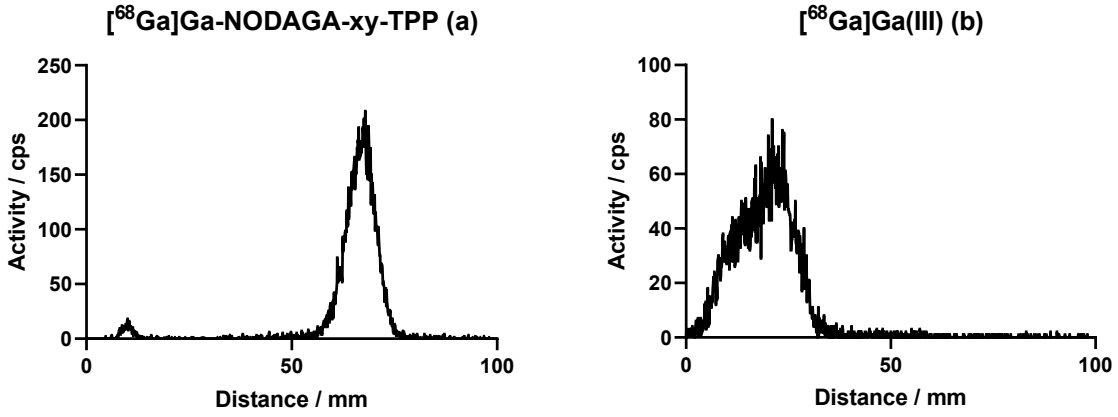

Figure 3.11 The iTLC traces obtained for [^{68}Ga]Ga-NODAGA-xy-TPP (**a**) and a comparison to the control experiment involving unchelated [^{68}Ga]Ga(III) (**b**), using a mobile phase of 2.0 M NH_4OAc/MeOH (1:1). The iTLC plates were scanned using the method illustrated in **Figure 3.9** and a gamma detector.

Using a mobile phase of 2.0 M NH_4OAc and methanol in a 1-to-1 mixture, clear separation was achieved between the desired radiolabelled compound and unchelated [^{68}Ga]Ga(III). As shown by **Figure 3.11a**, the radiolabelled compound [^{68}Ga]Ga-NODAGA-xy-TPP moves with the solvent front (R_f = 0.6–0.7) and unchelated [^{68}Ga]Ga(III) remains on the baseline (R_f < 0.1). This was confirmed by the control experiment shown in **Figure 3.11b**.

3.2.3 Temperature Alteration Experiments for the Optimization of Gallium-68 Radiolabelling

Having performed experiments at 100 °C in 0.1 M NH_4OAc buffer, using methodology by Smith *et al*., the next set of experiments involved reducing the temperature to 50 °C and monitoring the reaction between 10 and 30 min by iTLC. The obtained iTLC traces were visualised using a phosphorimager for clarity, shown in **Figure 3.12**.[6] All three analogues were radiolabelled for this set of experiments, with the TTP analogue data being shown in this instance.

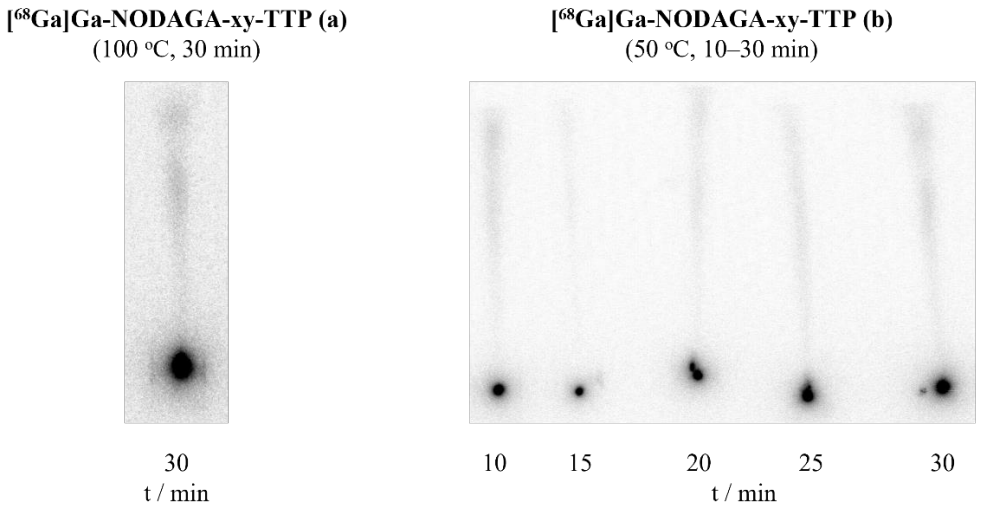

Figure 3.12 The iTLC traces of temperature alteration experiments of [^{68}Ga]Ga-NODAGA-xy-TTP, visualised by phosphorimager. A mobile phase of 0.1 M EDTA was used.

As shown in **Figure 3.12b**, an aliquot of the reaction mixture was spotted on the iTLC plate in 5-minute intervals between 10 and 30 min of heating at 50 °C in 0.1 M NH_4OAc. For comparability, the same ligand concentration, buffer volume and volume of [^{68}Ga]$GaCl_3$ were used in these experiments as described previously in this section. As expected, when using a mobile phase of 0.1 M EDTA, the majority of activity remains on the baseline referring to the radiotracer [^{68}Ga]Ga-NODAGA-xy-TTP, and unchelated [^{68}Ga]Ga(III) runs with the solvent front. This agreed with the iTLC trace obtained for the original radiolabelling conditions, shown in **Figure 3.12a**, which involved heating the ligand NODAGA-xy-TTP at 100 °C for 30 min. The key result in this set of experiments was that ^{68}Ga-labelling occurs near quantitatively when heated at 50 °C for 10 min.

3.2.4 Buffer Alteration Experiments with Varying Reaction Temperatures

Previous work by Smith *et al*., assessed the effect radiolabelling buffer and its concentration has on RCYs.[1,3] It was concluded that the best RCY values for ^{68}Ga-labelling were obtained when using 0.2 M NaOAc buffer, compared to 0.2 M NH_4OAc buffer amongst a range of alternative buffer concentrations. It was postulated that the protons in the ammonium cation serve to protonate the ligand lone pairs and inhibit radiolabelling. Therefore, radiolabelling experiments from this point in the project were performed using NaOAc as the radiolabelling buffer. Knowing that successful radiolabelling could be obtained at 50 °C for 10 min, these conditions were repeated for the TTP analogue using 0.2 M NaOAc buffer. This was also compared to the same radiolabelling procedure performed at room temperature, and had the

main purpose of determining if the reaction would proceed at all at room temperature. If the radiolabelling could be performed successfully at room temperature, it means no heating equipment is required to perform the radiolabelling and the reaction mixture does not need to cool down before it can be administered to the patient in a clinical setting.

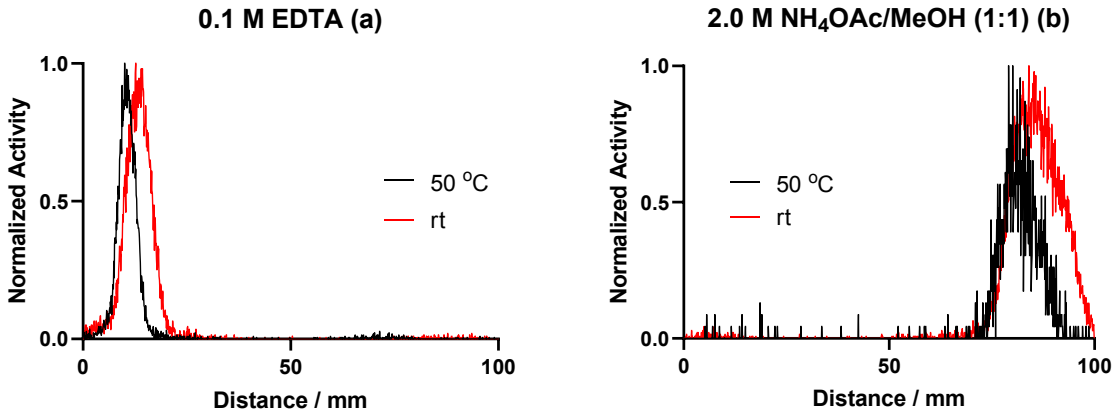

Figure 3.13 The iTLC traces obtained for [^{68}Ga]Ga-NODAGA-xy-TTP when the reaction was heated at 50 °C (black) or stirred at room temperature (red) in 0.2 M NaOAc buffer. Mobile phases used were 0.1 M disodium EDTA (**a**) and 2.0 M NH_4OAc/MeOH (1:1) (**b**). The iTLC plates were scanned using the method illustrated in **Figure 3.9** and a gamma detector.

The iTLC traces obtained for radiolabelling 100 µg of ligand with [^{68}Ga]$GaCl_3$ (0.1 M HCl, 500 µL) in 500 µL of 0.2 M NaOAc buffer, with heating at 50 °C or no heating for 15 min are illustrated in **Figure 3.13**. Successful separation of the product and unchelated [^{68}Ga]Ga(III) was achieved using both mobile phases, 0.1 M EDTA (**Figure 3.13a**) and 2.0 M NH_4OAc/MeOH (1:1) (**Figure 3.13b**). Both heating at 50 °C and leaving the reaction at room temperature resulted in near quantitative RCYs of over 99 %, calculated in both mobile phase systems.

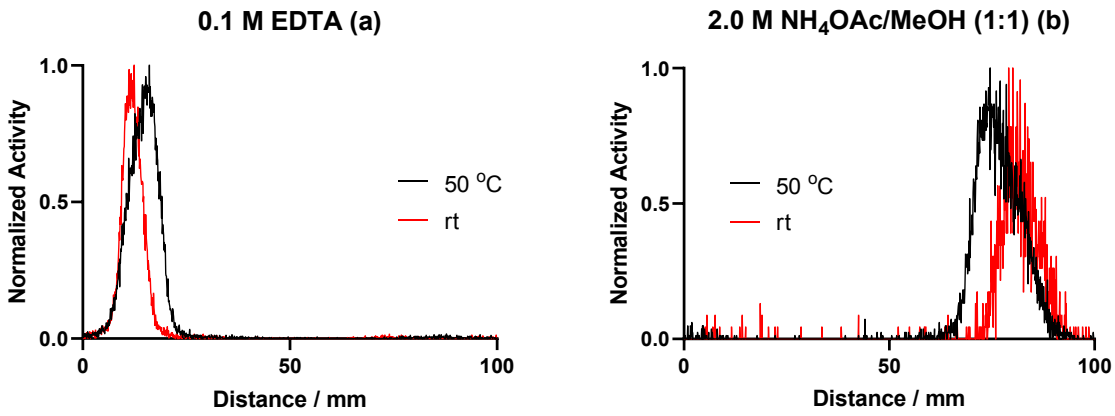

Figure 3.14 The iTLC traces obtained for [^{68}Ga]Ga-NODAGA-xy-TTP when the reaction was heated at 50 °C (black) or stirred at room temperature (red) in 3.6 M NaOAc buffer. Mobile phases used were 0.1 M disodium EDTA (**a**) and 2.0 M NH_4OAc/MeOH (1:1) (**b**). The iTLC plates were scanned using the method illustrated in **Figure 3.9** and a gamma detector.

Following on from radiolabelling experiments using 0.2 M NaOAc, a more clinical grade concentration of NaOAc buffer, 3.6 M, was utilised to improve the clinical translatability of this ^{68}Ga-labelling protocol. Instead of using 500 µL of buffer, as was the case for radiolabelling experiments using 0.2 M NaOAc, using just 42 µL of 3.6 M NaOAc buffer gave a pH of 5 for the reaction mixture. This meant a 100 mL stock solution of 3.6 M NaOAc buffer would last for over 2000 individual radiolabelling experiments, making it an incredibly efficient buffer system. The iTLC traces obtained for experiments using 3.6 M NaOAc at 50 °C and at room temperature for 15 min are shown in **Figure 3.14**. These iTLC traces correspond with the observations made in **Figure 3.13**, and also gave RCYs of over 99 %. Furthermore, this highlighted that near quantitative radiolabelling of these novel TAP-functionalised NODAGA ligands with gallium-68 could be achieved at room temperature over a period of 15 min using clinical grade NaOAc buffer.

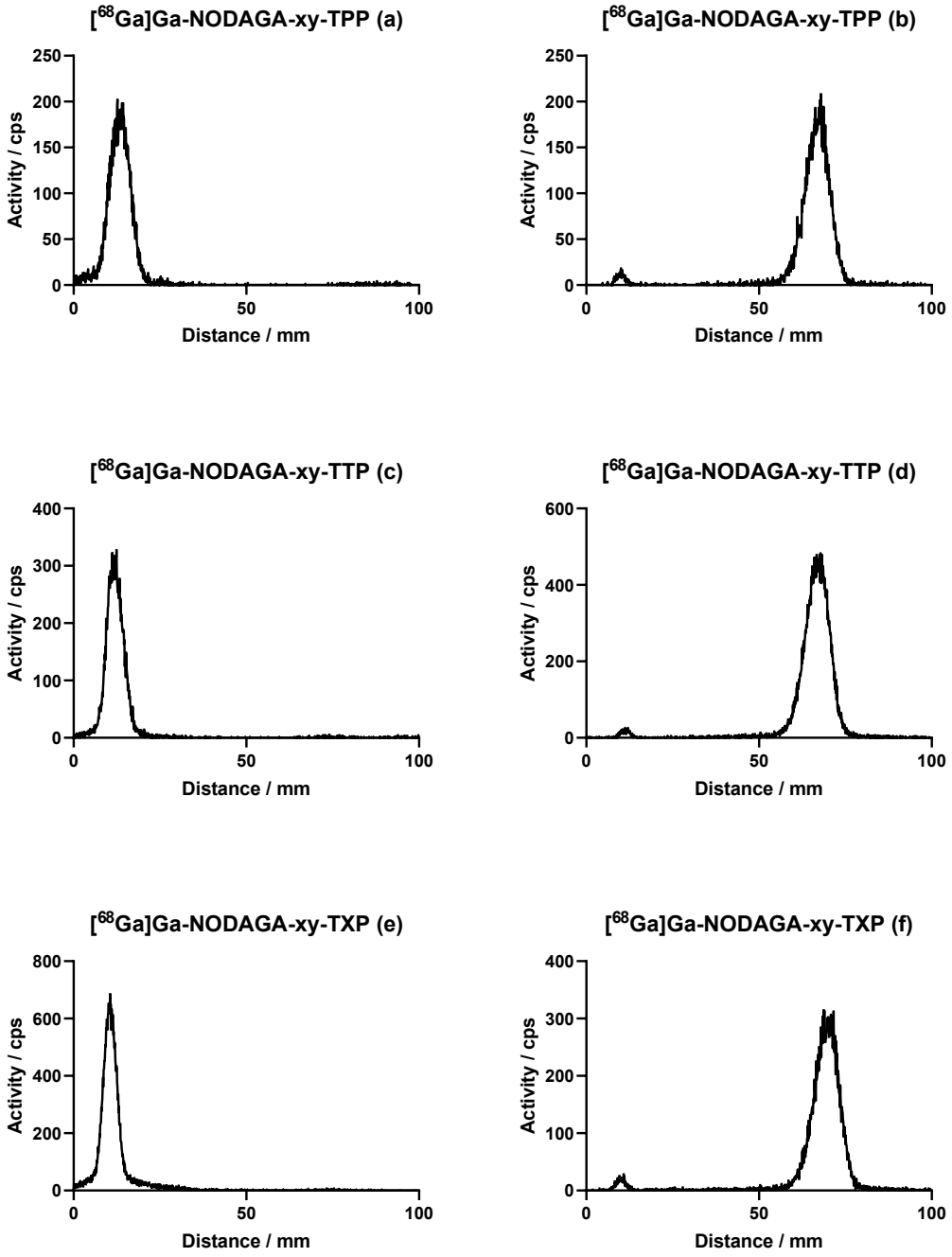

Figure 3.15 The iTLC traces of the [^{68}Ga]Ga-NODAGA-xy-TAP series of compounds having been labelled with a 3.6 M NaOAc buffer. Mobile phases of 0.1 M EDTA (**a,c,e**) and 2.0 M NH_4OAc/MeOH (**b,d,f**) were used. The iTLC plates were scanned using the method illustrated in **Figure 3.9** and a gamma detector.

The HPLC traces obtained for the TPP, TTP and TXP analogues, using the new radiolabelling conditions were the same as those shown in **Figure 3.7**, and the obtained iTLC traces are shown in **Figure 3.15**, further supporting the formation of the desired [^{68}Ga]Ga-NODAGA-xy-TAP compounds. These conditions were used for all subsequent radiolabelling experiments in this project.

3.2.5 Assessment of ^{68}Ga-Labelling Efficiency through Ligand Concentration Alteration Experiments

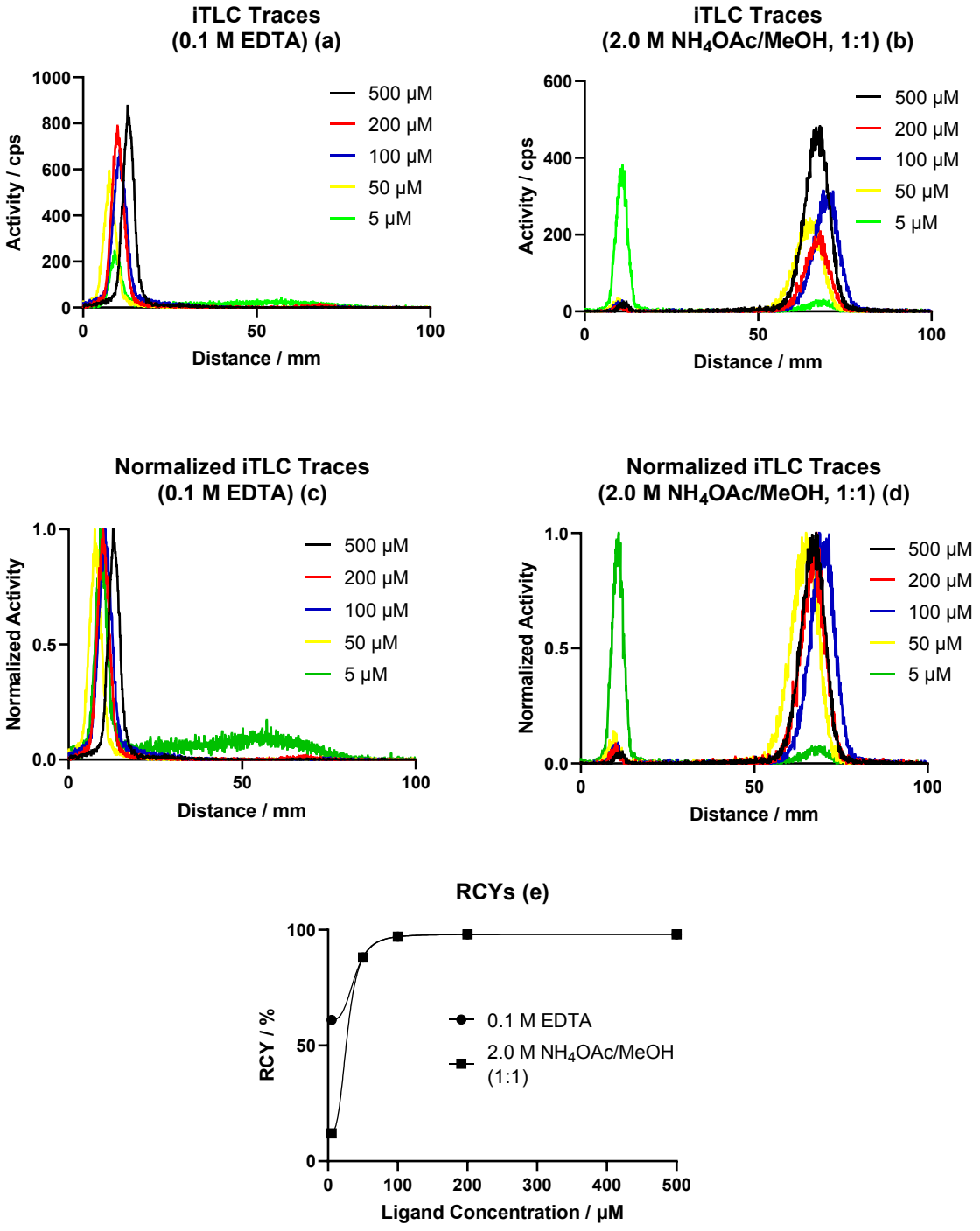

Figure 3.16 iTLC traces of concentration alteration experiments for [^{68}Ga]Ga-NODAGA-xy-TXP, including the actual activity in counts per second (cps) (**a-b**) and normalized activity (**c-d**). A summary of the RCY values from the iTLC traces shown in **Figure 3.16a-d** (**e**). Data are fitted using a sigmoidal curve. The iTLC plates were scanned using the method illustrated in **Figure 3.9** and a gamma detector.

In order to determine the efficiency of ^{68}Ga-labelling this series of NODAGA-xy-TAP compounds possess, a series of experiments were undertaken in which the [^{68}Ga]Ga(III) eluate was added to a solution of ligand in 3.6 M NaOAc (42 μL) to give a final ligand concentration of 5–500 μM. Parity was maintained with previous NODAGA radiolabelling experiments by allowing the mixture to stir at room temperature for 15 min. As shown in **Figure 3.16a-d** and summarised in **Figure 3.16e**, final ligand concentrations of 500, 200 and 100 μM gave quantitative RCYs of 98, 98 and 97 % respectively. The 50 μM concentration experiment gave a slightly lower RCY of 88 %, still demonstrating near quantitative RCY values at this ligand concentration. At 5 μM there is a significant decrease in RCY, determined to be 61 % using 0.1 M EDTA and 12 % using 2.0 M NH_4OAc/MeOH. The difference in RCY values obtained for each mobile phase method is thought to be due to the presence of [^{68}Ga]$Ga(OH)_3$. In 0.1 M EDTA, both [^{68}Ga]$Ga(OH)_3$ and [^{68}Ga]Ga-NODAGA-xy-TAP remain on the baseline, whereas in NH_4OAc/MeOH, [^{68}Ga]$Ga(OH)_3$ remains on the baseline with unchelated [^{68}Ga]Ga(III) and [^{68}Ga]Ga-NODAGA-xy-TAP moves with the solvent front. This results in a distortion of the observed RCY value for both mobile phase methods. Regardless, a 100 μM ligand concentration can be used rather than the 500 μM concentration normally used to achieve quantitative RCYs, potentially increasing the number of radiolabelling experiments which can be performed with a single batch of ligand by 5 times.

Table 3.2 Maximum RCYs obtained for the three [^{68}Ga]Ga-NODAGA-xy-TAP compounds, using a final ligand concentration of 100 μM.

[^{68}Ga]Ga-NODAGA-xy-TAP	TPP	TTP	TXP
RCY / %	97	98	97
RCP / %	97	98	97

Using 500 μL of [^{68}Ga]$GaCl_3$ (0.1 M HCl), 42 μL of 3.6 M NaOAc buffer and ligand with a final concentration of 100 μM, all three [^{68}Ga]Ga-NODAGA-xy-TAP compounds were obtained in RCYs of over 97 %, reported in **Table 3.2**, when labelling is performed at room temperature for 15 min. Quantitative RCY values are expected for biological imaging studies, as this limits the amount of activity non-specific to the radiotracer, and therefore to parts of the body that are not relevant to diagnosis.

3.2.6 Measurements of Log *D* Values

As a thorough readout of the lipophilicity of this series of radiotracers, octanol/phosphate-buffered saline (PBS) distribution coefficients (log *D* values) were measured and determined. Log *D* values are calculated by taking a 1:1 mixture of *n*-octanol and PBS, chosen to mimic the physiological pH of 7.4, and adding an aliquot of the radiotracer to this mixture. The mixture is then mixed vigorously to allow the radiotracer to be thoroughly distributed according to its solubility. The more lipophilic a radiotracer is the more soluble it will be in octanol and will therefore favour the octanol layer. The reverse is the case for more hydrophilic radiotracers, which favour the PBS layer. After the mixture is centrifuged to separate the two immiscible layers, samples of identical volume were taken from each layer and the activity of each sample was measured. Log *D* values were calculated using **Equation 3.1**.

$$\text{Log } D_{7.4} = \log_{10}\left(\frac{\text{A}_{\text{octanol}}}{\text{A}_{\text{PBS}}}\right)$$

(Equation 3.1)

Where $A_{octanol}$ is the activity measured in the *n*-octanol layer, and A_{PBS} is the activity measured in the PBS layer.

Although log *D* is defined as a concentration ratio, the equation can be derived due to equal volumes of sample being taken, meaning the volume terms cancel out one another. To obtain an accurate log *D* value of a compound, six replicate values were measured and the log *D* is reported as the mean ± standard deviation (SD). Since lipophilic compounds favour being dissolved in the non-polar octanol layer, compounds with higher lipophilicities exhibit higher log *D* values.

Along with lipophilicity, a number of other factors are used as a rule of thumb to determine a chemical compounds pharmacological and biological activity for its use as an orally active drug/radiotracer.[14] These factors are known as Lipinski's Rule of Five, which states that an orally active drug should have no more than 5 hydrogen bond donors, no more than 10 hydrogen bond acceptors, a molecular weight of less than 500 g/mol and a partition coefficient, log *P*, of less than 5. The rule describes the molecular properties important for the pharmacokinetics of a drug in the body, including their absorption, distribution, metabolism and excretion (ADME).[15] The lipophilicity of compounds discussed in this thesis was

prioritised over other factors in the rule, but these should still be considered when developing a drug.

The log *D* values for the [^{68}Ga]Ga-NODAGA-xy-TAP series of compounds are shown below in **Figure 3.17**, with a control value of unchelated [^{68}Ga]Ga(III) and a literature log *D* value for the clinically used SPECT-based lipophilic cation MIBI, as obtained by Kim *et al*.[12]

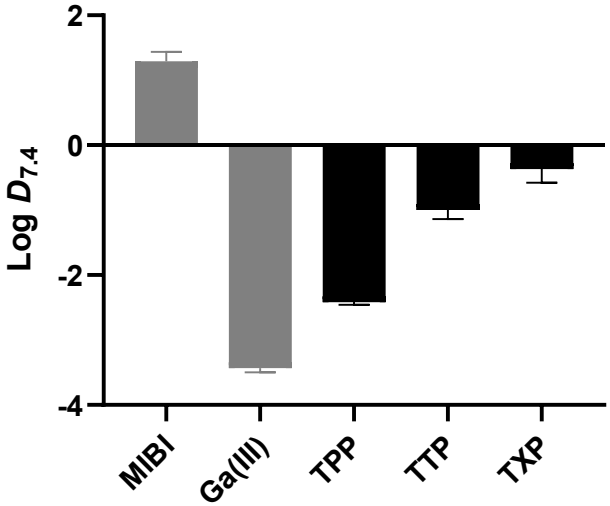

Figure 3.17 Log *D* values obtained for the [^{68}Ga]Ga-NODAGA-xy-TAP series of compounds (black), compared to the control experiments of unchelated [^{68}Ga]Ga(III), and the literature log *D* value of MIBI obtained by Kim *et al*.[12] (grey). Data are mean ± SD (n = 6 for all compounds except for MIBI, where n = 3).

Table 3.3 Summary of the data represented in **Figure 3.17**.[2]

	Log $D_{7.4}$ Values		
	TPP	**TTP**	**TXP**
[^{68}Ga]Ga-NODAGA-xy-TAP	-2.43 ± 0.07	-1.00 ± 0.14	-0.37 ± 0.21

Unchelated [^{68}Ga]Ga(III) gave a log *D* value of -3.43 ± 0.07, indicating that it preferentially dissolves in PBS, but still has a very small tendency to dissolve in octanol. Kim *et al*. reported MIBI as having a log *D* value of 1.29 ± 0.15, which acts as a positive control, and a target log *D* value for ^{68}Ga-labelled compounds to exhibit. The log *D* values were determined to be -2.43 ± 0.07, -1.00 ± 0.14 and 0.37 ± 0.21 for [^{68}Ga]Ga-NODAGA-xy-TPP, TTP and TXP respectively. These results indicated that increasing the level of alkyl-functionalisation of the TAP moiety causes an increase in log *D* value, and therefore an increase in the overall lipophilicity of the compound. This trend was studied and shown previously.[1,6,13] As shown in

Table 3.3, the log *D* values for the [^{68}Ga]Ga-NODAGA-xy-TAP compounds are higher than those observed for the DO3A analogues studied previously.[6] This provides confirmation that removing the unbound carboxylate arm, present in the DO3A analogues, decreases hydrophilic interactions and improves the overall lipophilicity of the [^{68}Ga]Ga-NODAGA-xy-TAP compounds.

An important characteristic exhibited by these compounds is that a small change, such as the addition of three methyl groups to the TPP group, has a significant effect (1.4 unit difference) on the log *D* value, even when attached to a hydrophilic macrocyclic ring such as NODAGA. This effect was also observed upon the addition of three more methyl groups to the TTP group, resulting in a 0.6 unit difference between the TTP and TXP-functionalised compounds. As with other ^{68}Ga-labelled lipophilic cations studied previously in our group, the log *D* values of these compounds are low compared to the log *D* value of MIBI. However, since there is precedent of lipophilic cations with low log *D* values successfully crossing lipid bilayer membranes, the most lipophilic radiotracer of this family [^{68}Ga]Ga-NODAGA-xy-TXP was assessed for its ability to report on mitochondrial dysfunction by *ex vivo* experimentation (section 4.5.2).

3.3 [^{68}Ga]Ga-NODAGA-xy-TAEP

The next family to be assessed was the NODAGA-xy-TAEP series of compounds, to examine how ether-functionalisation influenced the lipophilicity of these compounds. Tri-*para*-methoxy (TMeOPP) and Tri-*m*,*m*′-methoxy (TDiMeOPP) compounds were synthesised as ether derivatives of TTP and TXP analogues, giving a direct comparison between ether- and alkyl-functionalised variants in terms of their lipophilicities. The third member of this family is the tri-*para*-ethoxy (TEtOPP) analogue, providing an assessment on how extending the alkyl chain length affects the tracer lipophilicity.

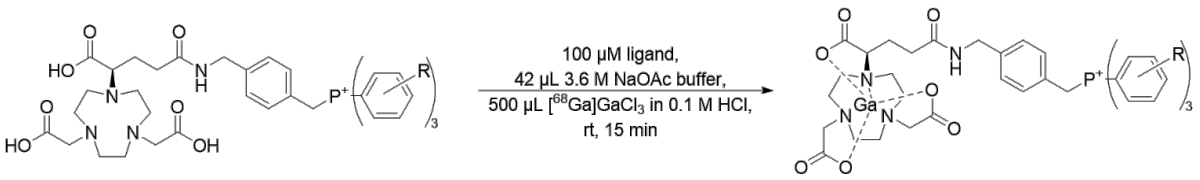

10d: NODAGA-xy-TMeOPP
10e: NODAGA-xy-TEtOPP
10f: NODAGA-xy-TDiMeOPP

[^{68}Ga]Ga10d: [^{68}Ga]Ga-NODAGA-xy-TMeOPP
[^{68}Ga]Ga10e: [^{68}Ga]Ga-NODAGA-xy-TEtOPP
[^{68}Ga]Ga10f: [^{68}Ga]Ga-NODAGA-xy-TDiMeOPP

Scheme 3.2 Protocol for the radiolabelling of NODAGA-xy-TAEP ligands, using generator produced [^{68}Ga]$GaCl_3$. R = *p*-OMe, *p*-OEt, *m*,*m*′-diOMe.

Using the labelling conditions outlined in section 3.2.5, the NODAGA-xy-TAEP series of compounds were radiolabelled with ^{68}Ga, shown in **Scheme 3.2**. To assess the purity of the three radiolabelled compounds, aliquots of the reaction mixtures were taken for radioHPLC analysis, shown in **Figure 3.18**.

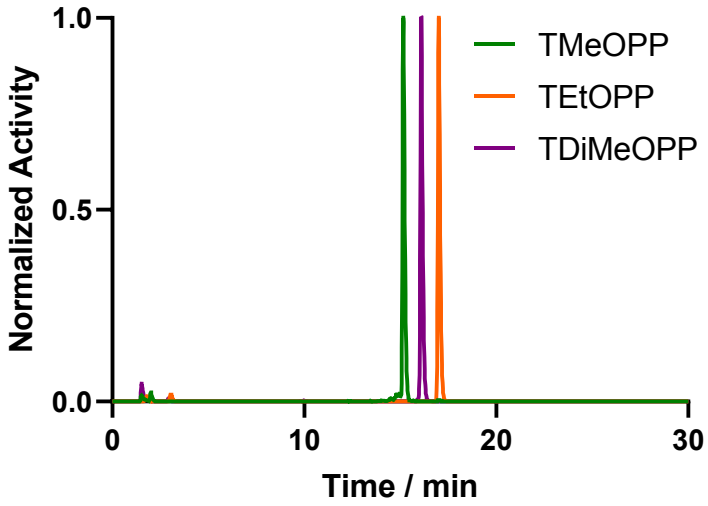

Figure 3.18 RadioHPLC traces obtained for radiolabelled [^{68}Ga]Ga-NODAGA-xy-TAEP compounds. Eluent gradient as described for **Figure 3.7**. All traces have been normalised such that the maximum activity measured for each complex is equal to 1.

As explained in sections 3.2.1 and 3.2.2, radioHPLC is a radioanalytical technique that allows for confirmation of RCP but is not accurate at determining RCY values due to the lack of all radiolabelled species eluting from the HPLC column. All three radiolabelled compounds were obtained in more than 99 % RCP with retention times of 13.7, 15.6 and 15.4 min for [^{68}Ga]Ga-NODAGA-TMeOPP, TEtOPP and TDiMeOPP respectively. The retention time of the three radiolabelled compounds can also be used as a qualitative assessment of their respective lipophilicities. As discussed previously, the greater degree of lipophilic character exhibited by a compound, the more it adheres to the column, resulting in a longer retention time. In addition, increasing the alkyl chain length of the ether group from a methyl group to an ethyl group leads to an increase in retention time of 1.9 min, and the addition of three extra methoxy groups on the TMeOPP derivative leads to a 1.7 min increase in retention time (**Figure 3.18**). Importantly, it appears that increasing the alkyl chain length appended to the ether oxygen atom increases lipophilicity of the final compound to a greater extent than introducing an additional methoxy group on each aromatic ring.

3.3.1.1 Comparison with Non-Radioactive Compounds

The radiolabelled species observed by radioHPLC, shown in **Figure 3.18**, were compared to their respective non-radioactive analogues, synthesised and characterised in section 2.3.3, by comparing their retention times, shown in **Figure 3.19**. The retention times for the non-radioactive reference and ^{68}Ga-labelled compounds are summarised in **Table 3.4**, and can be compared directly since the same HPLC instrument and gradient was used to analyse both sets of compounds.

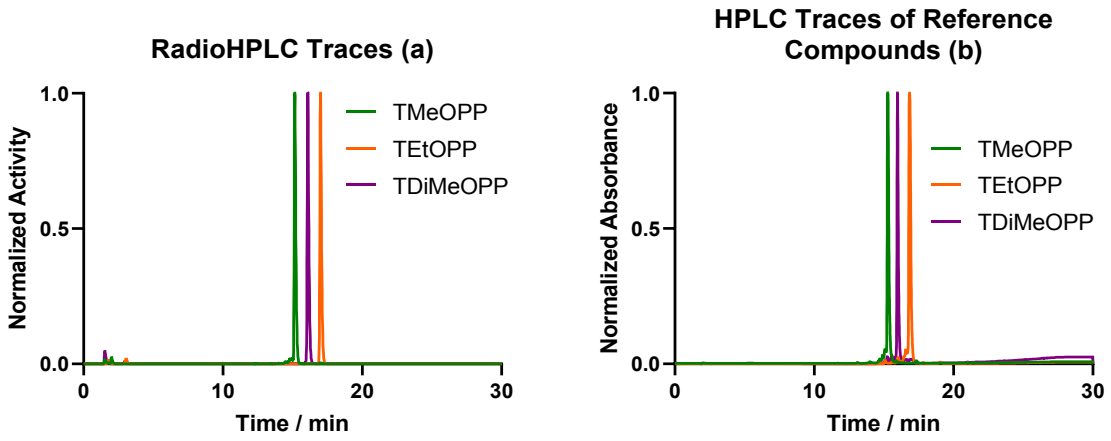

Figure 3.19 (a) RadioHPLC traces of the three radiolabelled [^{68}Ga]Ga-NODAGA-xy-TAEP compounds. **(b)** HPLC traces of the non-radioactive reference compounds. Eluent gradient as described in **Figure 3.7**. All traces have been normalised such that the maximum activity measured for each complex is equal to 1.

Table 3.4 Summary of the data represented in the HPLC traces of **Figure 3.19**.

	Retention Time / min		
	TMeOPP (d)	**TEtOPP (e)**	**TDiMeOPP (f)**
Ga10d-f	15.3	16.8	16.0
[^{68}Ga]Ga-10d-f	15.2	17.0	16.1

For all three compounds, there is approximately a 9 second difference between the retention times of the reference and radiolabelled compounds, meaning that it is highly likely that the observed radioactive species are the desired complexes; [^{68}Ga]Ga-NODAGA-xy-TMeOPP, [^{68}Ga]Ga-NODAGA-xy-TEtOPP and [^{68}Ga]Ga-NODAGA-xy-TDiMeOPP.

3.3.2 iTLC Assessment for RCY Values

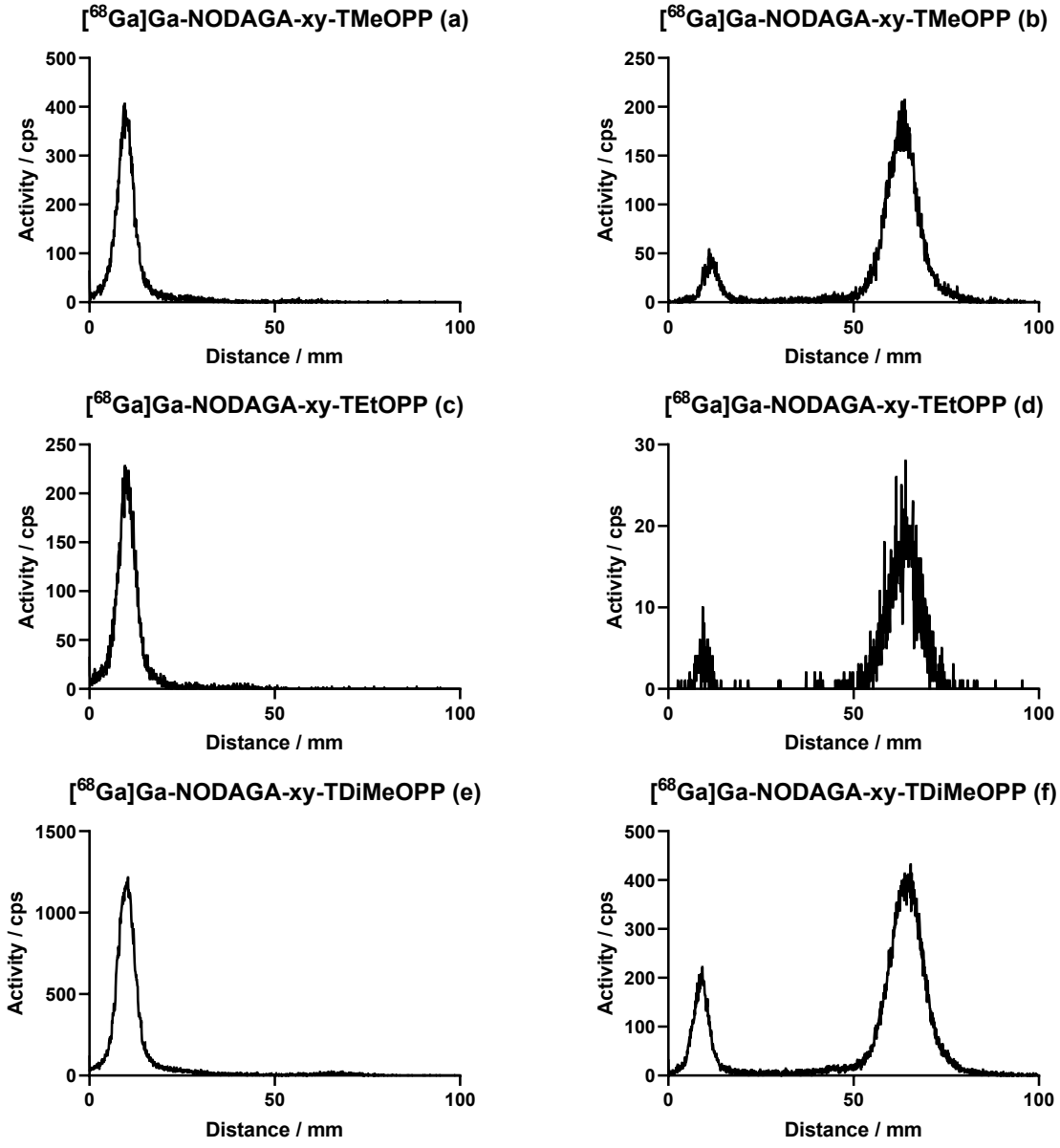

Figure 3.20 The iTLC traces of the [^{68}Ga]Ga-NODAGA-xy-TAEP series of compounds having been labelled with a 3.6 M NaOAc buffer. Mobile phases of 0.1 M EDTA (**a,c,e**) and 2.0 M NH_4OAc/MeOH (**b,d,f**) were used. The iTLC plates were scanned using the method illustrated in **Figure 3.9** and a gamma detector.

As explained in section 3.2.2, iTLC provides a more accurate measurement of RCY than HPLC, as all radiolabelled species applied on the baseline of the iTLC plate will be identified by the detector. Mobile phases determined in section 3.2.2.1 for the successful separation of unchelated [^{68}Ga]Ga(III) and radiolabelled [^{68}Ga]Ga-NODAGA-xy-TAP compounds were implemented for the NODAGA-xy-TAEP series of compounds. As shown in **Figure 3.20**, all

three radiolabelled compounds were successfully separated from unchelated [^{68}Ga]Ga(III) using mobile phases of 0.1 M EDTA and 2.0 M NH_4OAc/MeOH. Using a mobile phase of 0.1 M EDTA results in the radiolabelled compound remaining on the baseline and unchelated [^{68}Ga]Ga(III) moving with the solvent front, shown in **Figure 3.20a,c,e**. Whereas, a mobile phase of 2.0 M NH_4OAc/MeOH (1:1) leads to unchelated [^{68}Ga]Ga(III) remaining on the baseline, and the radiolabelled compound moving with the solvent front, shown in **Figure 3.20b,d,f**.

Table 3.5 Maximum RCYs obtained for the three [^{68}Ga]Ga-NODAGA-xy-TAEP compounds, using a final ligand concentration of 100 μM.

		[^{68}Ga]Ga-NODAGA-xy-TAEP		
	Mobile Phase	**TMeOPP**	**TEtOPP**	**TDiMeOPP**
RCY / %	0.1 M EDTA	99	99	97
	2.0 M NH_4OAc/MeOH	90	93	82

The RCY values obtained for the radiolabelling of all three [^{68}Ga]Ga-NODAGA-xy-TAEP compounds are summarised in **Table 3.5**, with high to quantitative yields achieved.

3.3.3 Log *D* Measurements

In order to determine the lipophilicity of this series of compound, the log *D* values were measured using a conventional 'shake-flask' method, described in section 3.2.6. The log *D* values, illustrated in **Figure 3.21**, were determined to be -1.47 ± 0.26, 0.01 ± 0.04 and -0.44 ± 0.08 for [^{68}Ga]Ga-NODAGA-xy-TMeOPP, TEtOPP and TDiMeOPP respectively.

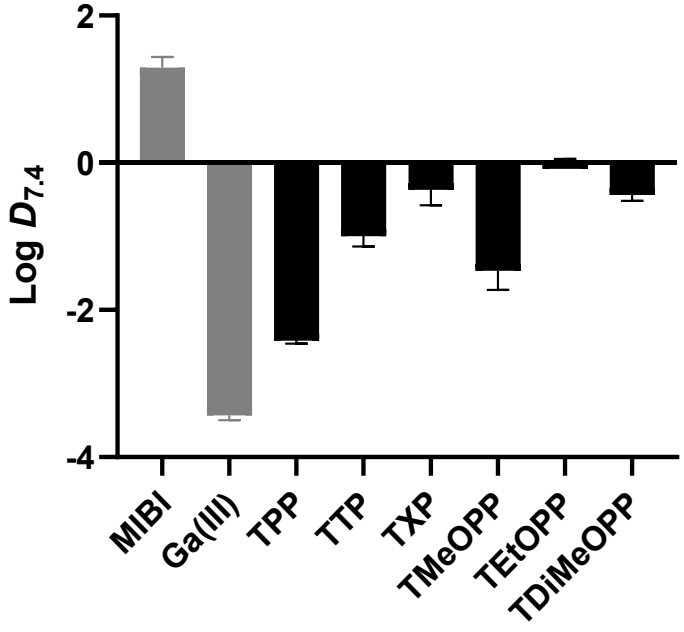

Figure 3.21 Log *D* values obtained for [^{68}Ga]Ga-NODAGA-xy-TAEP compounds (black), compared to [^{68}Ga]Ga-NODAGA-xy-TAP compounds (black), control experiment of unchelated [^{68}Ga]Ga(III), and the literature log *D* value of MIBI obtained by Kim *et al*., shown in **Figure 3.17**.[12] (grey). Data are mean ± SD (n = 6 for all compounds except for MIBI, where n = 3).

The results displayed in **Figure 3.21** indicated that increasing the alkyl chain length of the ether functionality from methyl to ethyl groups leads to a greater increase in lipophilicity (1.5 unit difference) than the incorporation of three additional methoxy groups (1.0 unit difference). Upon comparison with the log *D* values of [^{68}Ga]Ga-NODAGA-xy-TAP compounds, unchelated [^{68}Ga]Ga(III) and MIBI, a number of conclusions could be drawn. First, replacing *para*-methyl groups (TTP analogue), with *para*-methoxy groups (TMeOPP analogue) did not have the desired effect of increasing lipophilicity, instead the result was a 0.5 unit decrease in log *D* value. Secondly, replacing the *m*,*m*′-dimethyl groups (TXP analogue) with *m*,*m*′-dimethoxy groups (TDiMeOPP), resulted in a negligible decrease in log *D* value.

The replacement of methyl groups with methoxy groups did not have the desired effect of increasing the lipophilicity of the final compound. However, unexpectedly, extending the alkyl chain length significantly increased the overall lipophilic character of the final compound. As with the [^{68}Ga]Ga-NODAGA-xy-TAP series, the log *D* values of these compounds are still low compared to the log *D* value of MIBI. Even though the log *D* value of [^{68}Ga]Ga-NODAGA-xy-TEtOPP was the most positive for both NODAGA-based series, it is still too low compared to MIBI. Due to the findings of the *ex vivo* studies discussed in chapter 4, the TEtOPP-functionalised tracer was not assessed for its cardiac uptake and retention.

3.4 Concluding Remarks

This chapter outlines the radiolabelling of three analogous series of chelators with generator-produced ^{68}Ga. The first series of ligands investigated were the DO2A-(xy-TAP)$_2$ compounds, with initial work on this series performed by Smith *et al*.[1,3] HPLC studies of these complexes indicated the presence of multiple species upon ^{68}Ga-radiolabelling. Originally, two explanations were proposed for this observation: the chelator was not binding completely to the Ga(III) centre, or that a *cis*/*trans* isomer pair was forming. The latter explanation was discounted after DFT analysis confirmed the inability of the complex to form a *trans* isomer, due to its mode of binding. Through a series of altering reaction condition experiments, it was established that the two species existed as a kinetic/thermodynamic product pair.

The second series of ligands studied were the NODAGA-xy-TAP compounds.[2] Initial ^{68}Ga-radiolabelling experiments confirmed quantitative RCY values were achieved using high temperature conditions developed by Smith *et al*.[1,6] Through a series of reaction optimisation experiments, near quantitative radiolabelling was achieved at room temperature over a period of 15 min in clinical grade NaOAc buffer. One radiolabelled product was observed by HPLC in each reaction mixture which correlated to the non-radioactive reference compounds. Two iTLC QC methods were developed for RCY calculations of the radiolabelled compounds. However, the compounds discussed in this chapter did show low log *D* values compared to the 'gold' standard SPECT imaging agent MIBI.

Following on from the NODAGA-xy-TAP analogues, a second series of NODAGA-based complexes, [^{68}Ga]Ga-NODAGA-xy-TAEP compounds, were assessed. The primary focus of this family of compounds was to assess the effect that replacing alkyl groups with ether groups had on the lipophilicity of the final compounds. Using radiolabelling conditions developed for

the analogous NODAGA-xy-TAP series, the three radiolabelled [^{68}Ga]Ga-NODAGA-xy-TAEP complexes were obtained in high to near quantitative RCYs. One radiolabelled product was also observed in each reaction mixture which referred to the non-radioactive reference compounds by HPLC. Interestingly, the incorporation of ether groups on the TAP moiety did not have the desired effect on the lipophilicity of the radiotracers. However, increasing the alkyl chain length of the methyl groups did significantly increase the log *D* value, therefore increasing the overall lipophilicity of the final radiotracer.

3.5 References for Chapter 3

1 A. J. Smith, B. E. Osborne, G. P. Keeling, P. J. Blower, R. Southworth and N. J. Long, *Dalton Trans.*, 2020, **49**, 1097–1106.

2 B. E. Osborne, T. T. C. Yue, E. C. T. Waters, F. Baark, R. Southworth and N. J. Long, *Dalton Trans.*, 2021, **50**, 14695–14705.

3 A. J. Smith, *PhD Thesis*, Imperial College London, 2019.

4 S. Procházková, V. Kubíček, Z. Böhmová, K. Holá, J. Kotek and P. Hermann, *Dalton Trans.*, 2017, **46**, 10484–10497.

5 V. Kubíček, J. Havlíčková, J. Kotek, G. Tircsó, P. Hermann, É. Tóth and I. Lukeš, *Inorg. Chem.*, 2010, **49**, 10960–10969.

6 A. J. Smith, P. J. Gawne, M. T. Ma, P. J. Blower, R. Southworth and N. J. Long, *Dalton Trans.*, 2018, **47**, 15448–15457.

7 E. W. Price and C. Orvig, *Chem. Soc. Rev.*, 2014, **43**, 260–290.

8 N. Lepareur, *Front. Med.*, 2022, **9**, 812050.

9 Radiology Key, *Radionuclide Imaging - Radiology Key*, 2016, https://radiologykey.com/radionuclide-imaging-2/

10 M. I. Tsionou, C. E. Knapp, C. A. Foley, C. R. Munteanu, A. Cakebread, C. Imberti, T. R. Eykyn, J. D. Young, B. M. Paterson, P. J. Blower and M. T. Ma, *RSC Adv.*, 2017, **7**, 49586–49599.

11 L. L. Fuscaldi, D. V Sobral, A. C. R. Durante, F. F. Mendonça, A. C. C. Miranda, M. L. da Cunha, L. Malavolta, J. Mejia and M. F. de Barboza, *Pharmaceuticals*, 2021, 14.

12 Y.-S. Kim, Z. He, W.-Y. Hsieh and S. Liu, *Bioconjug. Chem.*, 2007, **18**, 929–936.

13 A. Haslop, L. Wells, A. Gee, C. Plisson and N. Long, *Mol. Pharm.*, 2014, **11**, 3818–3822.

14 C. A. Lipinski, F. Lombardo, B. W. Dominy and P. J. Feeney, *Adv. Drug Deliv. Rev.*, 2001, **46**, 3–26.

15 T. I. Oprea, A. M. Davis, S. J. Teague and P. D. Leeson, *J. Chem. Inf. Comput. Sci.*, 2001, **41**, 1308–1315.

16 A. Schmidtke, T. Läppchen, C. Weinmann, L. Bier-Schorr, M. Keller, Y. Kiefer, J. P. Holland and M. D. Bartholomä, *Inorg. Chem.*, 2017, **56**, 9097–9110.

17 J. P. Holland, *Inorg. Chem.*, 2020, **59**, 2070–2082.

CHAPTER 4 – BIOLOGICAL EVALUATION OF LIPOPHILIC AND CATIONIC GALLIUM-68 COMPLEXES

4. Biological Evaluation of Lipophilic and Cationic Gallium-68 Complexes

Following on from the synthesis of lipophilic and cationic Ga(III) complexes (chapter 2), with their radiochemical properties analysed with ^{68}Ga (chapter 3), a potential candidate was identified for biological evaluation, shown in **Figure 4.1**.

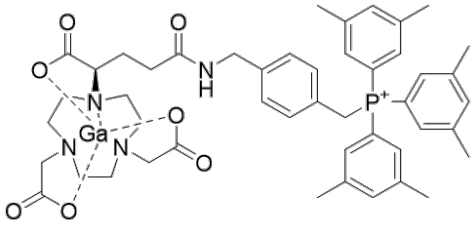

[^{68}Ga]Ga-NODAGA-xy-TXP

Figure 4.1 The ^{68}Ga-labelled complex, [^{68}Ga]Ga-NODAGA-xy-TXP, proposed for biological evaluation.

In order to determine whether this complex exhibited $\Delta\Psi_m$-dependant uptake and retention in the mitochondria, it was assessed using the *ex vivo* Langendorff isolated perfused heart model. The heart perfusion model is ideal for investigating the kinetics of radiotracer uptake, retention and washout in intact beating myocardial tissue, with the ability to modify perfusion and/or workload (to model ischaemia), buffer oxygenation (to model hypoxia), acidosis, energy substrate composition etc.[1,2] Previous work in the Southworth group has shown that the model is fast, simple and highly reproducible.[3–6]

4.1 Coronary Circulation Process *In Vivo*

To ensure the Langendorff perfusion model apparatus can be fully understood, the basic biology of the heart must be re-examined. The heart consists of four muscle-encased chambers, illustrated in **Figure 4.2**, in which blood flows. Each chamber contains an inlet and outlet valve, which increase circulation and prevent the backflow of blood. When these chambers contract, the pressure increases, leading to the shutting of the inlet valves and the opening of the outlet valves. This causes the blood to be pumped around the circulatory system, with this process being named systole. The opposite process to systole, diastole, occurs when the chambers of

the heart relax, leading to a decrease in internal heart pressure, which causes the inlet valves to open and heart refills with blood.

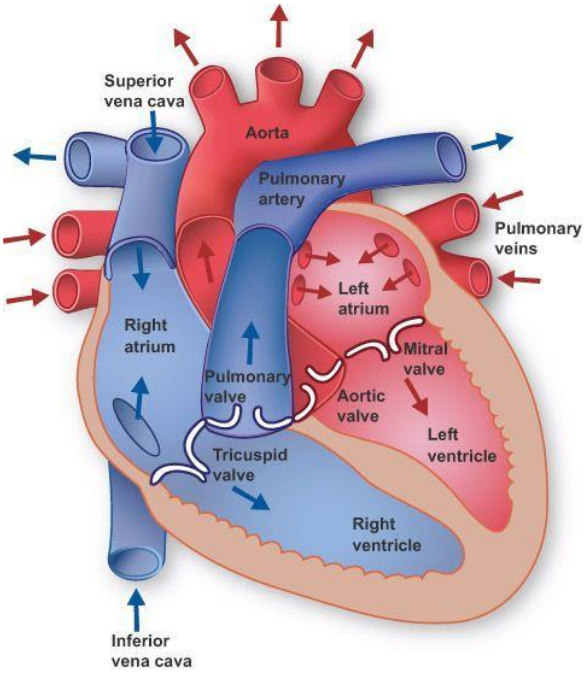

Figure 4.2 A schematic of the heart, showing the direction of blood flow through the four chambers. Picture taken from https://biomedical-laboratory.blogspot.com.[7]

These two processes, systole and diastole, form the crux of the cardiac cycle. The cardiac cycle begins with the return of deoxygenated blood from systemic circulation to the right atrium via the venae cavae. Blood then flows through the tricuspid valve into the right ventricle, which is then pumped through the pulmonary valve to the lungs via the pulmonary artery. Oxygenated blood returns from the lungs via the pulmonary veins to the left atrium of the heart, where it is pumped through the mitral valve into the left ventricle. The left ventricle then pumps this oxygenated blood through the aortic valve into the aorta and onward to the systemic circulation. As the left ventricle begins to relax at the end of systole, the high residual blood pressure in the aorta forces the aortic valve shut (preventing the left ventricle from refilling with the blood it has just pumped out), and the blood in the aortic root is diverted into the two coronary ostia above the aortic valve. These coronary ostia feed the coronary arteries, which perfuse the myocardium with oxygenated blood, which then drains back into the right atrium, primarily through the coronary sinus.[8]

4.2 Langendorff Isolated Perfused Heart Model

The Langendorff isolated perfused heart model exploits coronary circulation through cannulation of the aorta to provide a physiologically relevant and controllable model for a range of cardiovascular research applications, shown in **Figure 4.3**.

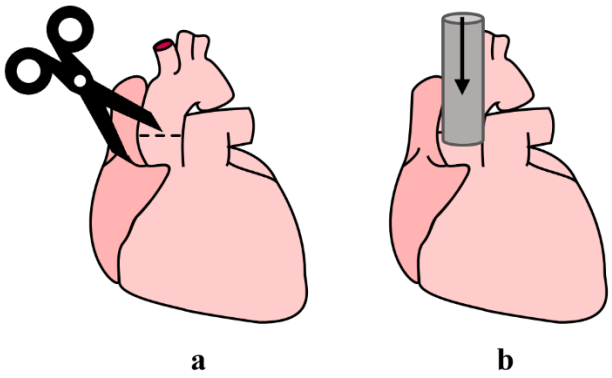

Figure 4.3 Cartoon schematic illustrating **(a)** the incision of the aorta to allow Langendorff mode perfusion, shown by the dashed line, and **(b)** insertion of the cannula through which Krebs-Henseleit buffer is perfused.

By cannulating the descending aorta, it is possible to perfuse the heart in a retrograde manner (**Figure 4.3a**), by inserting a cannula to a point just above the coronary ostia (**Figure 4.3b**). Due to the pressure in the aorta, the aortic valve is forced shut, which prevents the backflow of perfusate into the left ventricle. An incision is made at the base of the pulmonary artery to allow perfusate to flow freely through the coronary vasculature. The incision allows the perfusate to be pumped out of the heart via the right ventricle. *In vivo*, the left ventricle is full of blood and functions normally, however, in Langendorff mode perfusion, the left ventricle is empty which means the physiological workload on the ventricle is reduced. The workload can be simulated through the removal of the left atrium, followed by insertion of a water-filled balloon into the left ventricle through the mitral valve. The balloon is then connected to a pressure transducer which allows for a readout of left ventricular pressure. The final step of the Langendorff perfused heart experiment involves the implementation of external electrical pacing, which provides a means to keep the heart rate consistent throughout the experiment. Ensuring a consistent heart rate is maintained, keeps the energetic demand of the heart consistent, therefore improving the overall reproducibility of the model. To achieve the electrical pacing, a silver wire is hooked through the right atrium near the sinoatrial node, with the other end of the circuit

connected to the metal cannula. The circuit is connected to a pacing unit to allow tuneability of the pacing frequency and voltage.

4.3 Carbonyl Cyanide *m*-Chlorophenyl Hydrazone (CCCP)

Due to the nature of the buffer used to keep the heart functioning normally, chemical agents/drugs can be investigated directly on the heart, providing an advantage over *in vitro* and *in vivo* models. Often in these studies carbonyl cyanide *m*-chlorophenyl hydrazone (CCCP) is usedas a chemical inhibitor of oxidative phosphorylation, and acts as a protonophore with a high degree of lipophilicity. It is commonly used in isolated perfused heart studies as a pharmacological intervention, capable of shuttling protons across the inner mitochondrial membrane at a faster rate than ATP synthase uses them. This means that ATP production is halted, along with uncoupling of the proton gradient which reduces the magnitude of $\Delta\Psi_m$ in a dose-dependent manner.

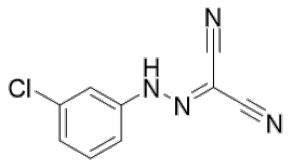

Figure 4.4 CCCP, a chemical inhibitor of oxidative phosphorylation, causing uncoupling of the proton gradient in mitochondria, which reduces $\Delta\Psi_m$ to zero.

Since the uptake of lipophilic cations in myocardial tissue is dependent on the magnitude of $\Delta\Psi_m$, its intervention can be exploited to determine the relative contribution of the active retention of radiotracers within the mitochondria in a $\Delta\Psi_m$-dependent manner, compared to their passive, non-selective, trapping in cell membranes due to their lipophilicity.[9] The use of CCCP as a method of assessing radiotracer uptake and retention in hearts, in which $\Delta\Psi_m$ has been compromised, has been explored by Safee *et al*.[10] In the work by Safee *et al*., the clinical SPECT radiopharmaceutical, MIBI, was used as a validation, finding that a 600 nM solution of CCCP was optimal to effect complete $\Delta\Psi_m$ depolarisation.

4.4 Materials and Methods

4.4.1 Isolated Perfused Heart Apparatus

A schematic representation of the isolated perfused heart apparatus is shown in **Figure 4.5**. All glassware used, including the buffer reservoir and heated cup were jacketed with warm-circulating water at approximately 40 °C, allowing the temperature of the heart to be maintained between 37.0 and 37.4 °C, confirmed using a thermocouple. The system was operated using the constant flow method rather than the constant pressure method. Constant flow perfusion at physiologically appropriate perfusion pressure was chosen over the more traditional constant perfusion pressure approach because changes in coronary flow would potentially affect the measured pharmacokinetic properties of the radiotracers under investigation.

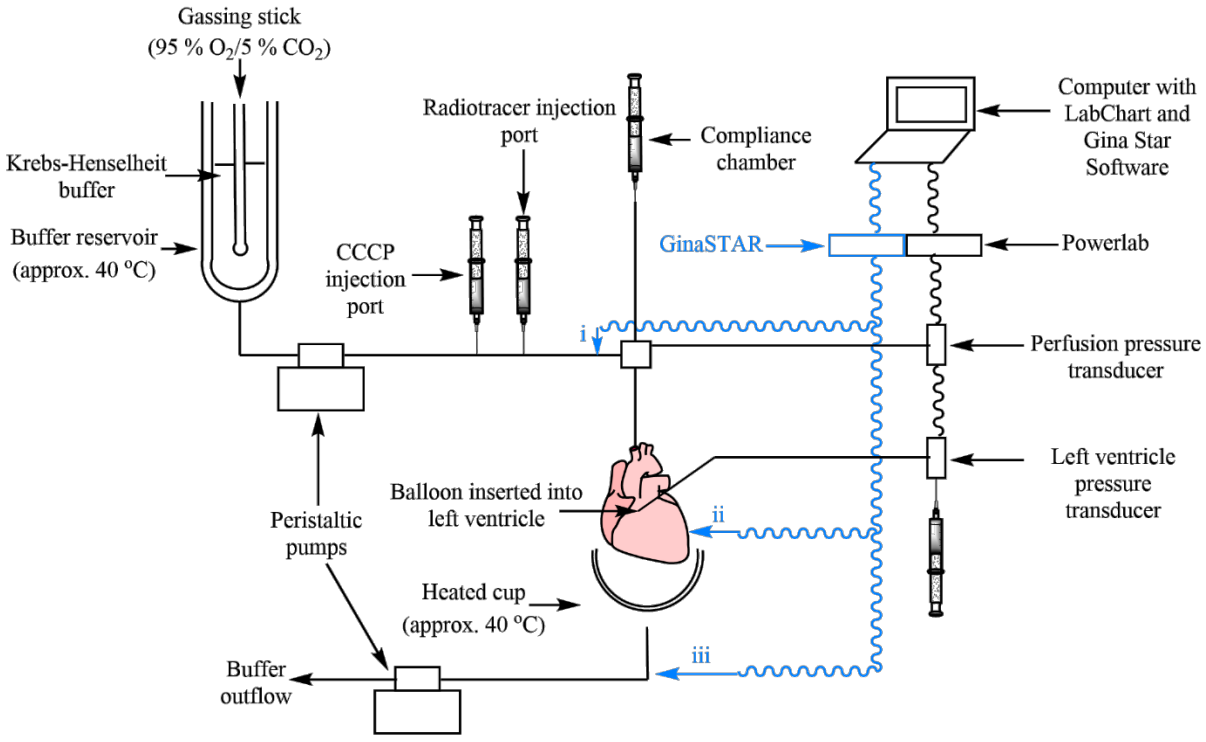

Figure 4.5 Schematic representation of the Langendorff isolated perfused heart apparatus, showing the triple gamma detector system in blue.

A constant flow was maintained by peristaltic pumps (Gilson, USA). The buffer outflow was removed by using a second peristaltic pump which is attached to the heated cup.

4.4.1.1 Krebs-Henseleit Buffer and Gas Mixture

The use of synthetic solutions, such as Krebs-Henseleit Buffer (KHB), in perfusion experiments instead of fresh oxygenated blood has been proven to be much less technically challenging and advantageous. The perfusate fluid used in these experiments was a phosphorus-free modified KHB (mKHB), consisting of NaCl (118 mM), KCl (5.90 mM), $MgSO_4$ (2.30 mM), $NaHCO_3$ (25.0 mM), disodium EDTA (0.65 mM), glucose (11.1 mM) and $CaCl_2$ (2.50 mM), which is freshly prepared and filtered before use. The buffer was warmed in the reservoir at approximately 40 °C in order to maintain the temperature of the perfusate at the cannula between 37.0 and 37.4 °C. The buffer is also gassed with 95 % O_2 / 5% CO_2.

4.4.1.2 Temperature, Pressure and Flow Rate Measurements

The temperature of the mKHB at the cannula was confirmed using a thermocouple thermometer into the cannula, with adjustment to the circulator temperature if necessary. Pressure transducers were used to obtain pressure measurements, which were connected to a PowerLab/4SP data acquisition system running LabChart 7 (version 7.3.3, AD Instruments, UK.) and a sphygmomanometer was used to calibrate the pressure transducers before experiments were started. Constant flow rate of the perfusate was controlled through the speed of the peristaltic pump, thereby standardising the rate of radiotracer delivery, simplifying the pharmacokinetic modelling. A constant flow rate of 14 mL min^{-1} of mKHB through the cannula was obtained through manual calibration of the peristaltic pump speed before experiments were started. A blood-perfused rat heart typically has a flow rate of 3 mL min^{-1}, however due to the lower oxygen carrying capacity of mKHB, flow rates of 12–16 mL min^{-1} are required to achieve comparable perfusion pressures. Therefore, 14 mL min^{-1} was the selected flow rate for the experiments detailed in this thesis, which reliably induced a perfusion pressure of 60 mmHg, comparable to that *in vivo*.

4.4.1.3 Functional Data Acquisition

Perfusion pressure (PP) was measured using a pressure transducer, inserted into the arterial line near the cannula. A liquid-filled intraventricular balloon was used to monitor cardiac contractile function. The left atrial appendage was removed and a deflated PVC balloon, connected to a pressure transducer, was inserted into the left ventricle via the hole made when the left atrial appendage was removed. The balloon was inflated with water until an end-diastolic pressure between 5−12 mmHg was measured by LabChart. The left ventricular

pressure measurement, Left Ventricular End Diastolic Pressure (LVEDP) was calculated as the lowest pressure recorded in each heartbeat cycle. The Left Ventricular Diastolic Pressure (LVDP) was calculated as the maximum pressure developed over the LVEDP in each heartbeat cycle, and the heart rate (HR) was calculated as the frequency of heartbeat cycles.

4.4.1.4 Protocol for Heart Preparation and Perfusion

Adult male Wistar rats (250−300 g) were anaesthetised with sodium pentobarbital and heparin sodium (200 mg kg^{-1} and 200 IU kg^{-1} respectively, intraperitoneal (i.p)). Hearts were excised in a rapid manner and placed in ice-cold mKHB. After removal of excess lung tissue, trachea, thymus and connective tissue, the heart was cannulated via the aorta with a very low flow of buffer (1−2 drops per second). The aorta was securely tied with a suture, followed by a small incision into the pulmonary artery to allow outflow of the buffer. The buffer flow rate was increased to 14 mL min^{-1}. After insertion of the left ventricular balloon, mentioned previously, the heart was externally paced using a Harvard student stimulator pacing unit. One terminal was connected to the heart through the right atrium using a silver wire, with the other terminal connected to the metal cannula. A HR of 340 bpm was achieved by setting the frequency to 5.7 Hz, and after the HR dropped consistently below 320 bpm, the voltage of the stimulator was slowly increased until the HR increased to 340 bpm.

4.4.1.5 Exclusion Criteria

In order to demonstrate a high degree of competence in isolated heart perfusion, a series of stability studies were undertaken to determine the duration of heart stability post-preparation, including the establishment of exclusion criteria for all future experiments performed in this project. If a preparation did not match the exclusion criteria within 10 minutes of the cannulation of the heart, the experiment would be aborted, and another preparation was performed. Isolated rat hearts were excised, cannulated, paced and perfused as described previously. The haemodynamic parameters: PP, LVEDP, HR and LVDP were monitored and recorded for 60 minutes. The average haemodynamic parameters 10 minutes post-cannulation from 6 hearts, recorded as capable of developing > 100 mmHg LVDP 60 minutes post-cannulation, were used as the exclusion criteria for all future experiments.

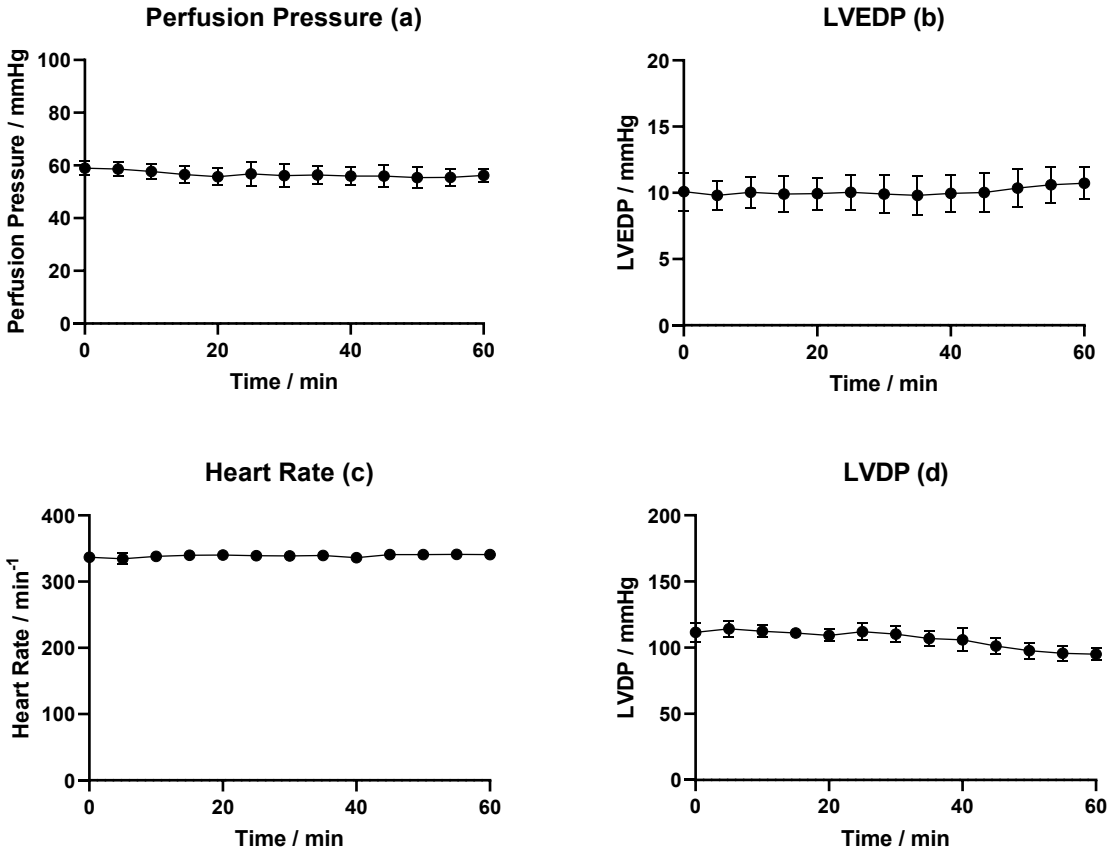

Figure 4.6 Stability study for the cardiac function of isolated perfused hearts. **(a)** Perfusion pressure, **(b)** LVEDP, **(c)** HR, and **(d)** LVDP. Data are mean ± SD (n = 6).

The data from the stability study are summarised in **Figure 4.6**, with the exclusion criteria determined from these data shown in **Table 3.1**.

Table 4.1 Exclusion criteria for the measured haemodynamic parameters at t = 10 minutes, obtained from the stability study data summarised in **Figure 4.6**.

Parameter	Acceptable Values at t = 10 min	
	Minimum	Maximum
Perfusion Pressure / mmHg	54	60
LVEDP / mmHg	9	12
Heart Rate / bpm	335	341
LVDP / mmHg	107	117

The values stated are ± SD of the mean values from the stability study. In following experiments, hearts which do not meet these levels of function at t = 10 minutes will not be used for uptake and retention experiments, due to the fact the effective function of the heart cannot be guaranteed at the end of the experiment.

4.4.2 Radiotracer Kinetics Measurements in Isolated Perfused Hearts

The basic Langendorff heart perfusion apparatus was coupled with a triple γ-detector system, previously developed and utilised in the Southworth group.[5] This system is illustrated in blue in **Figure 4.5**, and shown below in **Figure 4.7** and **Figure 4.8**.

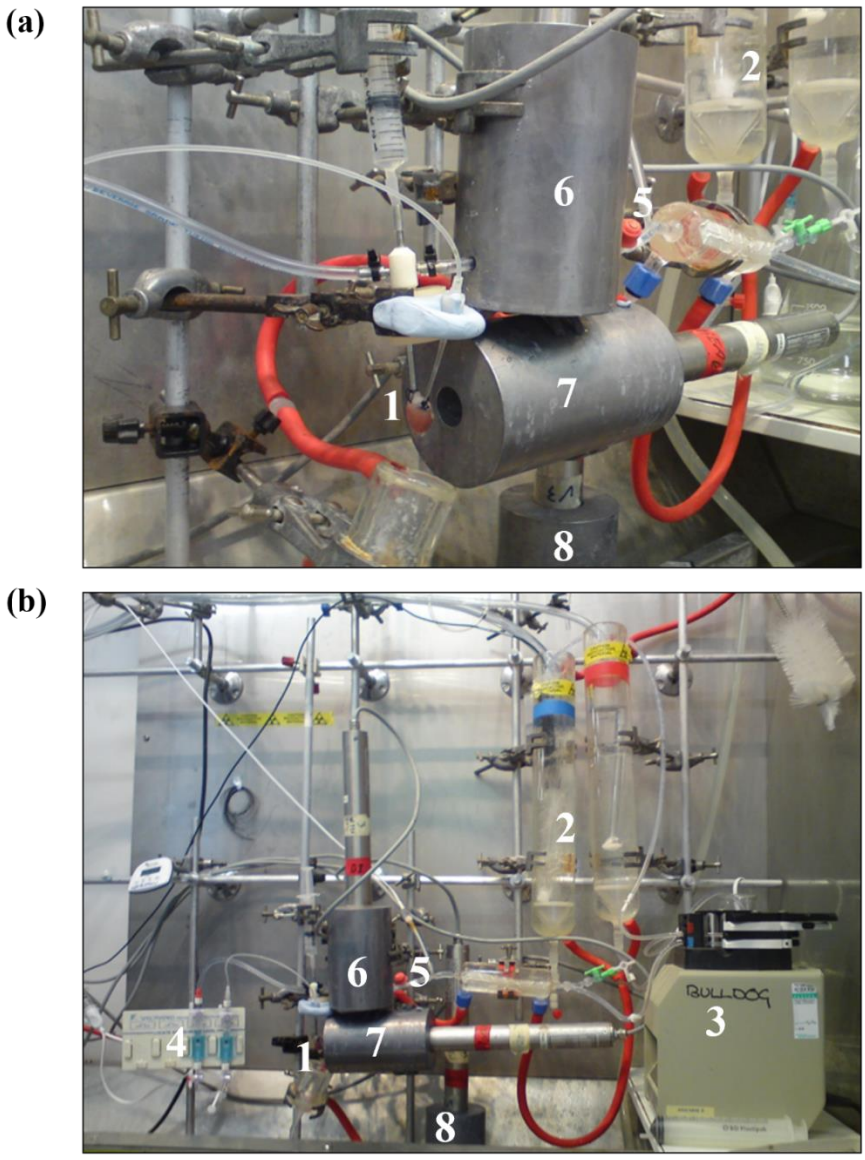

Figure 4.7 The triple γ-detector system for monitoring radiotracer uptake and retention in isolated perfused hearts. Hearts were cannulated **(1)**, perfused with mKHB contained in reservoirs maintained at 37 °C **(2)**. Coronary flow was maintained constantly, and venous outflow was removed via the heated cup connected to a peristaltic pump **(3)**. Cardiac haemodynamic parameters were monitored by two pressure transducers **(4)**. Radiotracer bolus injections were administered via the injection port **(5)**, and the passage through the perfusion system and the heart were monitored by three Na/I detectors located on the arterial line **(6)**, the heart **(7)** and venous outflow line **(8)**.

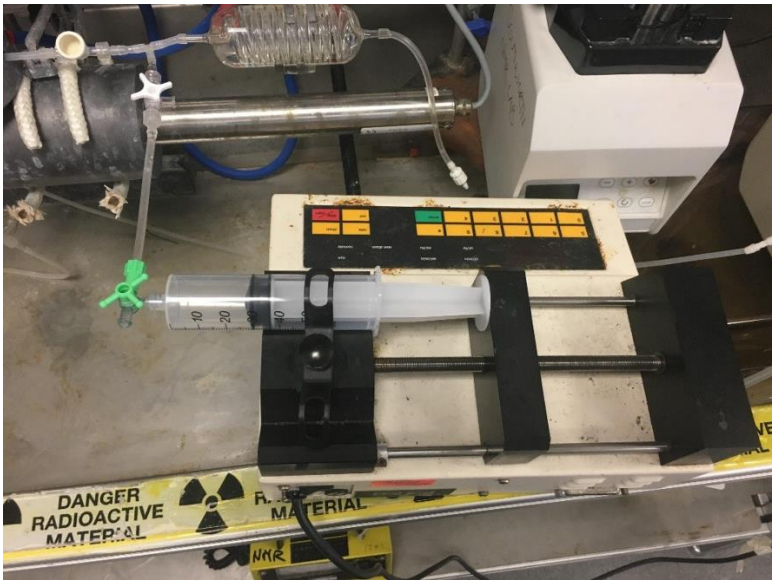

Figure 4.8 The syringe pump attached to the Langendorff perfusion system, used to administer CCCP into the arterial line.

4.4.2.1 Gina Star™ Data Acquisition System and Na/I γ-Detector Array

Radiotracer uptake, retention and washout through the Langendorff isolated perfused heart model was monitored using a unique triple γ-detector incorporated into the perfusion apparatus. Three Na/I γ-detectors were positioned, as shown in **Figure 4.7**, on the arterial line above the heart cannula **(6)**, directly opposite the perfused heart **(7)**, and the coronary effluent line **(8)**. The detection system was controlled by a modified Gina Star radioHPLC system, controlled by Gina Star data acquisition software.

4.4.2.2 Time-Activity Curve Uptake, Retention and Clearance Assessment

The kinetic profiles of radiotracers moving through the heart and perfusion system are shown in **Figure 4.9**. The radiochromatogram shown in **Figure 4.9a** represents the time-activity curves obtained for the arterial line, corresponding to the injection of the radiotracer into the system via the injection port. **Figure 4.9b** shows the retention and washout of the radiotracer by the heart, and **Figure 4.9c** shows the washout of the radiotracer in the coronary effluent line. Whilst attempts have been made to use the radiochromatogram generated from **Figure 4.9a** as a pharmacokinetic modelling input function of the radiotracer retention in **Figure 4.9b**, this has proved challenging, therefore only results shown in **Figure 4.9b** are shown and analysed in the rest of this thesis.[11] All data sets were corrected for radioactive decay.

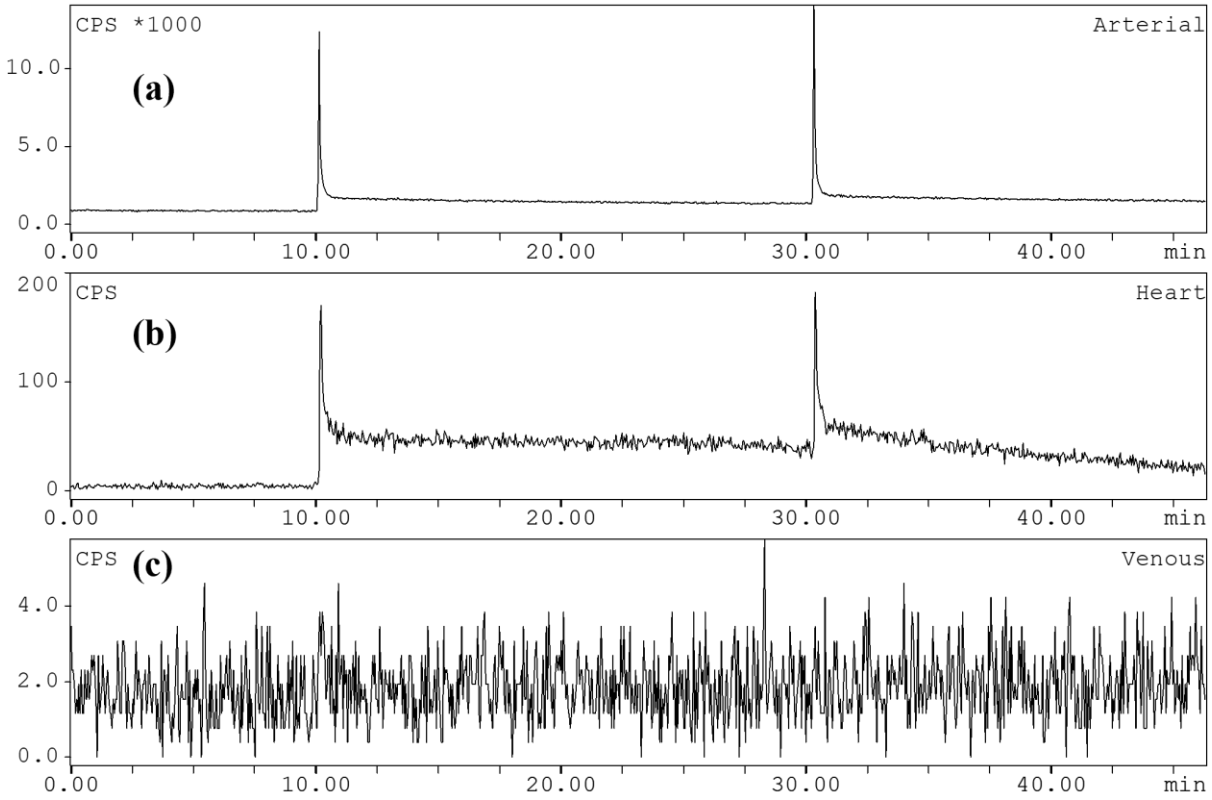

Figure 4.9 Representative time-activity curves demonstrating MIBI uptake, retention and washout in the arterial flow **(a)**, heart **(b)** and venous outflow **(c)**. The first injection is into a healthy heart, and the second into a heart infused with 600 nM CCCP, discussed later.

4.4.2.3 Analysis of Radiotracer Retention

In order to calculate reproducible values of cardiac retention of radiotracers in perfusion experiments, the data shown in **Figure 4.9b** was exported as a .csv file, before it is decay corrected. The retention of the radiotracer is recorded between 14–15 minutes post-injection as a fraction of the average background-corrected value at this time point divided by the average background-corrected value of the highest recorded activity at approximately 0 minutes post-injection.

4.4.2.4 Preparation of Radiopharmaceuticals

MIBI was prepared and supplied by the Radiopharmacy at St. Thomas' Hospital. The ^{68}Ga-labelled radiotracer [^{68}Ga]Ga-NODAGA-xy-TXP was prepared as described in the previous chapter. Upon being given a start time, the radionuclide half-life used for the generation of the radiotracer being studied, including the initial volume and activity of the radiopharmaceutical preparation were processed to give the aliquot volume required to obtain

1 MBq activity of radiotracer for injection. The aliquot volume required inevitably increases throughout the day as the radionuclide decays. Using this method allows for consistent 1 MBq boluses of radiotracer to be administered over the course of a day of perfusion experiments.

4.4.3 Protocols for Biological Experiments

4.4.3.1 *Ex Vivo* Heart Uptake and Retention Study Using a Two-Injection Protocol

Rat hearts were excised, cannulated and perfused according to the methodologies described in section 5.4.1.4. Hearts were perfused with mKHB buffer gassed with 95 % O_2 and 5 % CO_2. Hearts were allowed to stabilise for 20 minutes, during this time cardiac haemodynamic parameters were monitored to ensure the exclusion criteria were met, summarised in **Figure 4.6** and **Table 3.1**. After the stabilisation period, the first 1 MBq bolus of radiotracer was administered into the arterial line of the perfusion apparatus.

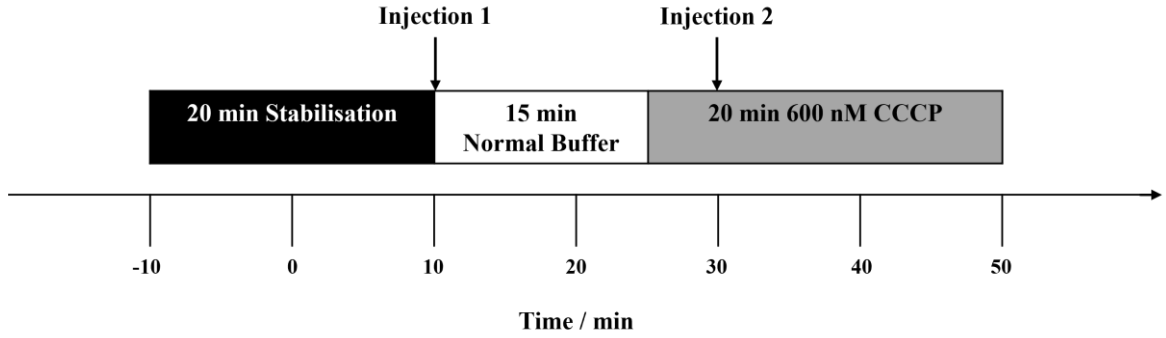

Figure 4.10 Representation of the experimental protocol for the two-injection protocol, assessing radiotracer uptake and retention in isolated perfused rat hearts. Radiotracer injections are indicated by black arrows.

The kinetics of the radiotracer were monitored for 15 minutes, before a 600 nM solution of CCCP in mKHB, heated to 37 °C, was infused via the arterial line at 1.4 mL min^{-1} (10 % of the coronary flow), whilst the flow rate at the peristaltic pump was reduced by 10 % to accommodate this infusion, and maintain the same perfusate flow rate to the heart. After 5 minutes of 600 nM CCCP infusion, an additional 1 MBq bolus of radiotracer was administered. This two-injection protocol is illustrated in **Figure 4.10**. Radiotracer uptake and retention after both injections was calculated using the methodology described in section 5.4.2.3, with statistical significance between the two values established using Student's t-test.

All experimental procedures were approved by King's College London's local Animal Care and Ethics Committee, and carried out in accordance with Home Office regulations as detailed in the Guidance on the Operation of Animals (Scientific Procedures) Act 1986.

4.5 Results

4.5.1 [^{99m}Tc]Tc-sestaMIBI (MIBI)

4.5.1.1 Cardiac Uptake and Retention of MIBI in Control and CCCP-Infused Hearts

As described in section 5.4.3.1, the two-injection experimental protocol was followed using the clinical 'gold-standard' SPECT-based lipophilic and cationic radiotracer MIBI.

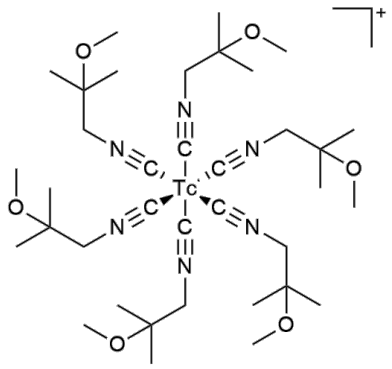

Figure 4.11 The chemical structure of the SPECT-based lipophilic cation MIBI.

These experiments provided a means to ensure that the model was valid for this study. As shown by the time-activity curves in **Figure 4.9**, and summarised in **Figure 4.12**, MIBI exhibits a cardiac retention of 25.4 ± 1.92 % (n = 3 separate hearts) 15 minutes post-injection in healthy hearts (polarised mitochondria). Whereas, in 600 nM CCCP-infused hearts (depolarised mitochondria) MIBI demonstrates a cardiac retention of 0.00 ± 8.12 % (n = 3 separate hearts, $P < 0.05$) 15 minutes post-injection. This observed negative retention corresponds to retained radiotracer in the heart from the first injection leaching out of the mitochondria as it is depolarised.

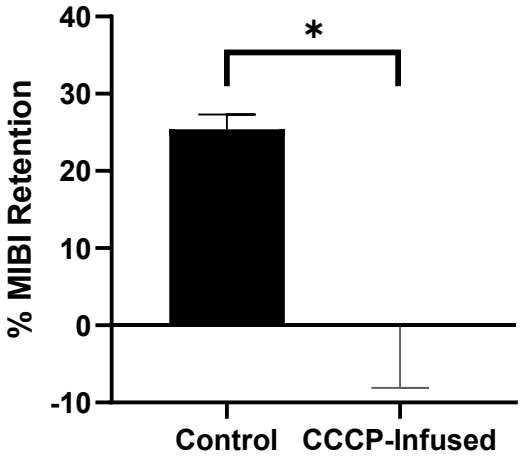

Figure 4.12 The retention values calculated using the two-injection protocol 15 minutes post-injection for MIBI. Control data were obtained from the injection before the infusion of CCCP, and CCCP data were obtained during 600 nM CCCP infusion. Data are mean ± SD (n = 3 separate hearts). * = $P < 0.05$.

4.5.1.2 Cardiac Haemodynamic Parameters in Hearts Infused with 600 nM CCCP

The cardiac haemodynamic parameters observed throughout the same protocol compared to those obtained from the stability study, shown in **Figure 4.6**, can be seen in **Figure 4.13**.

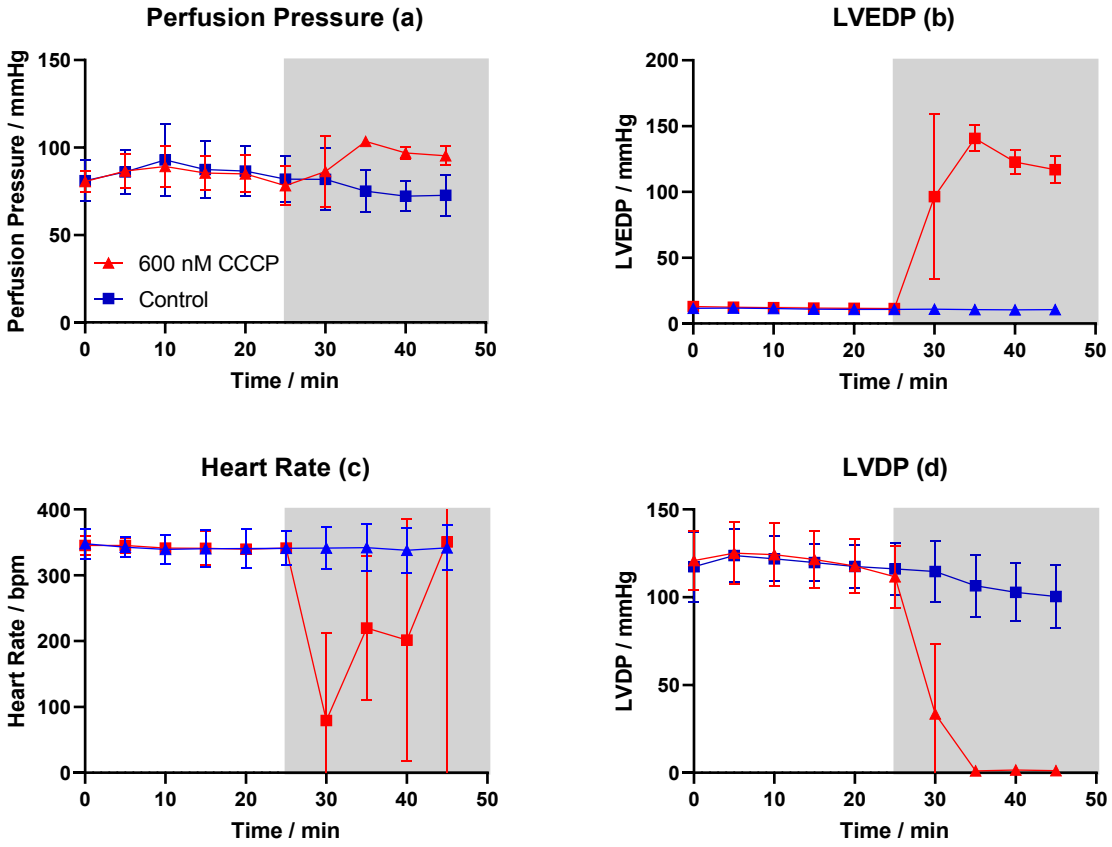

Figure 4.13 Cardiac haemodynamic parameters for control hearts undergoing normal (healthy) function for 45 minutes (n = 6, blue) and hearts undergoing normal function for 25 minutes, followed by 600 nM CCCP infusion for 20 minutes (n = 6, red). **(a)** Perfusion pressure, **(b)** LVEDP, **(c)** HR, **(d)** LVDP. Data represents mean ± SD.

It is important to note that there is no difference in cardiac haemodynamic parameters between both sets of experiments before hearts were infused with 600 nM CCCP at 25 minutes. In the stability study, after 35 minutes of normal function, the perfusion pressure was measured as 75.0 ± 12.2 mmHg, whereas at the same time-point (10 minutes post-CCCP infusion) the perfusion pressure increased to 103.5 ± 2.63 mmHg. After 20 minutes of CCCP infusion, the perfusion pressure was measured as 95.3 ± 5.34 mmHg. LVEDP increases significantly from 11.4 ± 0.97 mmHg at the beginning of CCCP infusion to 140.6 ± 9.83 mmHg within 10 minutes, before falling to 116.9 ± 10.4 mmHg after 20 minutes of CCCP infusion. The opposite trend was observed for LVDP, which dramatically decreased from 111.6 ± 17.7 mmHg at the

start of CCCP infusion to 1.10 ± 0.50 mmHg and remained at around this value for the duration of the experiment. The heart rate grew considerably more erratic once CCCP infusion was commenced, with mean values of 79.5–350.6 bpm observed. Interestingly, the standard deviation increases from an average of 13.8 bpm before CCCP infusion to 212.6 bpm after CCCP infusion.

4.5.2 [^{68}Ga]Ga-NODAGA-xy-TXP

Following the protocol described in section 5.4.3.1, the most lipophilic derivative of the NODAGA-xy-TAP series of compounds, [^{68}Ga]Ga-NODAGA-xy-TXP (log *D* = -0.37), was assessed for its cardiac uptake and retention in healthy and 600 nM CCCP infused isolated rat hearts.

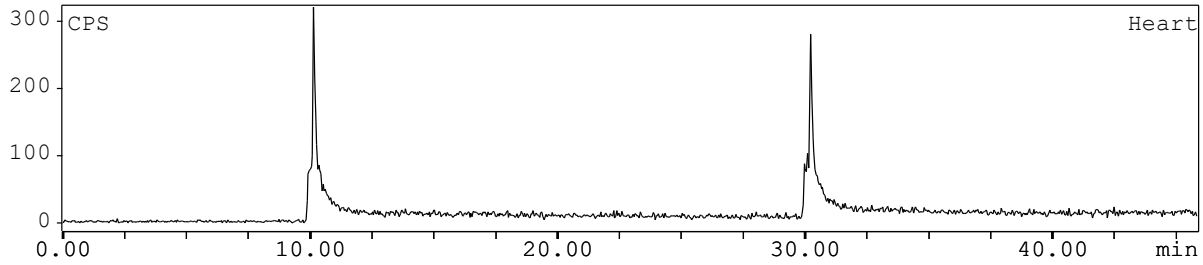

Figure 4.14 Representative time-activity curves demonstrating injections of [^{68}Ga]Ga-NODAGA-xy-TXP into healthy (first injection at 10 minutes) and 600 nM CCCP infused hearts (second injection at 30 minutes).

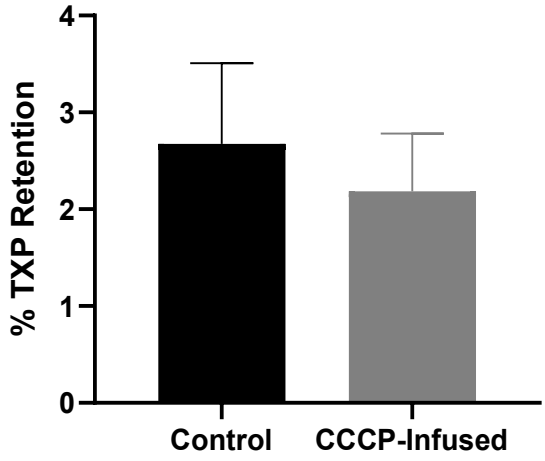

Figure 4.15 Retention values calculated using the two-injection protocol 15 minutes post-injection for [^{68}Ga]Ga-NODAGA-xy-TXP. Control experimental data was calculated from the injection before CCCP infusion, and CCCP data was calculated during infusion with 600 nM CCCP. Data are mean ± SD.

As shown in **Figure 4.14** and summarised in **Figure 4.15**, [^{68}Ga]Ga-NODAGA-xy-TXP exhibits 2.67 ± 0.83 % (n = 3 separate hearts) retention 15 minutes post-injection in hearts under normal conditions, whereas upon 600 nM CCCP infusion, the retention of [^{68}Ga]Ga-NODAGA-xy-TXP was not significantly diminished 15 minutes post-injection, falling to 2.19 ± 0.60 % (n = 3 separate hearts). Furthermore, [^{68}Ga]Ga-NODAGA-xy-TXP demonstrates a near 10-fold decrease in uptake and retention in control hearts than MIBI under the same conditions. Compared to [^{68}Ga]Ga-DO2A-(xy-TXP)$_2$, the uptake and retention of which was investigated by Smith *et al*. using the same two-injection protocol, [^{68}Ga]Ga-NODAGA-xy-TXP shows less cardiac uptake and retention in both healthy and CCCP-infused hearts.[12,13] However, [^{68}Ga]Ga-NODAGA-xy-TXP does show a near 2-fold increase in cardiac uptake and retention in healthy and CCCP-infused hearts compared to [^{68}Ga]Ga-DO3A-xy-TXP, assessed by Smith *et al*.[14]

4.6 Discussion

4.6.1 Analysis of the Two-Injection Protocol Using MIBI

Previous Langendorff isolated perfused heart studies utilising the triple-gamma detector to investigate radiotracer uptake and retention kinetics typically use three-injection protocols.[3,5] However, Smith *et al*. developed a two-injection protocol to limit the drawbacks of the three-injection protocols.[12–14] The main drawback of the three-injection protocols is that the experiment is performed over a 75 minute period, which creates a notable time constraint on short-lived radionuclides such as ^{68}Ga. Smith *et al*., developed a protocol which reduced the experiment time from 75 minutes to 45 minutes, helping the translation of this protocol with short-lived radioisotopes and providing the means to give reliable, reproducible results for cardiac uptake and retention in three experiments.[13] This method also allows each perfused heart to act as its own control experiment, due to any defects present in the heart affecting both radiotracer injections.

Smith *et al*. highlighted that the major drawback of the two-injection protocol was the lack of a time-matched control experiment, involving the injection of two boluses of radiotracer at the same timepoints into a heart which did not receive infusion with CCCP.[13] To circumvent this problem in this project, a control experiment was performed involving two injections of radiotracer at the usual timepoints for each CCCP-infused heart experiment. This allows for a more accurate comparison between injections. The two-injection protocol provides a highly

controllable, physiologically relevant tool for the initial screening of novel lipophilic and cationic radiotracers.

Another reason that these experiments were undertaken was to establish the effect 600 nM CCCP has on the heart, and importantly the rate at which these effects manifest. The most considerable changes were observed for LVEDP and LVDP. Upon infusion of CCCP, the heart begins to stop beating efficiently and eventually beating ceases entirely, leading to a rapid increase in LVEDP, which confirmed that CCCP infusion causes the contraction of myocardial muscles, meaning the heart no longer relaxes. As the heart ceases to beat, LVDP also undergoes a rapid decrease, most notably within 5 minutes, as a lack of contractile function means no pressure is developed in the heart. Perfusion pressure also increases, albeit not as dramatically as LVEDP, due to the perfusate flow, governed by the coronary vasculature at diastole, no longer functioning normally since the coronary arteries are constricted when the heart contracts. Due to the irreversible contraction of myocardial muscles upon CCCP infusion, the buffer flow experiences an increased resistance, leading to a backpressure building up in the arterial line. Even though the heart rate ceases to beat upon CCCP infusion, the heart rate was recorded as becoming erratic during these depolarising conditions, which was put down to the software attempting to fit a beating pattern between changes in left ventricular pressure, despite this pressure becoming effectively constant. Therefore, upon CCCP infusion the heart rate is not seen as a viable marker for heart functionality. For all cardiac haemodynamic parameters, a functional change was observed within 5 minutes of CCCP infusion, meaning that the mitochondria have been depolarised and changes in radiotracer uptake and retention will reflect these changes.

Using the two-injection protocol, experiments with the clinically used MIBI showed, as expected, exceptional $\Delta\Psi_m$-dependent uptake and retention in hearts, highlighting this protocol as being powerful enough to screen novel lipophilic and cationic radiotracers for their uptake and retention in hearts. This series of experiments also enabled the development of the analysis protocol on real experimental data, such as using the minimum value as the activity measured 1–2 minutes before the radiotracer injection. This was to allow for instances of radiotracer leaching out of the mitochondria upon depolarisation, from the original radiotracer injection.

4.6.2 Comparison of Cardiac Uptake and Retention of [^{68}Ga]Ga-NODAGA-xy-TXP

By establishing the two-injection protocol, with the MIBI experiments, as a high efficacy model for assessing lipophilic and cationic radiotracer kinetics, the cardiac uptake and retention of [^{68}Ga]Ga-NODAGA-xy-TXP was studied. Unfortunately, this ^{68}Ga-based tracer showed low uptake and retention in normally functioning cardiac mitochondria, which was not significantly diminished in depolarised cardiac mitochondria. The lower cardiac uptake and retention compared to MIBI (log D = 1.29 ± 0.15) is likely due to the lower lipophilicity of [^{68}Ga]Ga-NODAGA-xy-TXP (log D = -0.37 ± 0.21) hindering passage through the lipid bilayer membrane. As a result of its increased lipophilicity, [^{68}Ga]Ga-NODAGA-xy-TXP does demonstrate a 2-fold increase in uptake and retention in healthy cardiac mitochondria compared to DO3A analogues, such as [^{68}Ga]Ga-DO3A-xy-TXP (log D = -1.81 ± 0.02) studied previously.[14] However, in depolarised cardiac mitochondria, both NODAGA and DO3A analogues exhibited no statistically significant difference in retention compared to in healthy cardiac mitochondria.

4.6.2.1 Effect of Charge Distribution on the Cardiac Uptake and Retention of [^{68}Ga]Ga-NODAGA-xy-TXP

It is possible that whilst the net positive charge and gross lipophilicity may make radiotracers more amenable to crossing cell membranes and being retained within the mitochondria, compared to previous DO3A analogues, the distribution of the positive charge across the surface area of the molecule also plays a key role. If the positive charge distribution of the complex is uneven, such that there may be an amplified polarity within the molecule, this may hinder its capacity to enter the cell. In effect, it is possible that whilst the lipophilic "head" of the molecule may penetrate cell membranes, the cationic "tail" cannot. This effective polarity rationale is further supported by the uptake and retention obtained for the DO2A analogue, [^{68}Ga]Ga-DO2A-(xy-TXP)$_2$, which demonstrated the importance of charge distribution in terms of $\Delta\Psi_m$-dependent uptake and retention.[12]

Based on initial analysis of molecular electrostatic potential (MEP) mapping of the DFT optimised structures of [Ga-NODAGA-xy-TXP]$^+$ and its DO2A counterpart, performed by Thomas Yue, [Ga-DO2A-(xy-TXP)$_2$]$^{3+}$ shown in **Figure 4.16**, a more symmetrical charge distribution can be seen for the DO2A analogue, along with a greater distribution of positive

charge across the entire molecule compared to [Ga-NODAGA-xy-TXP]$^{+}$. A more substantial and symmetrical positive charge distribution would lead to greater uptake and retention in healthy mitochondria, which was observed in the case of [^{68}Ga]Ga-DO2A-(xy-TXP)$_2$, resulting in a significant difference in retention when the membrane potential is no longer present, compared to [^{68}Ga]Ga-NODAGA-xy-TXP.

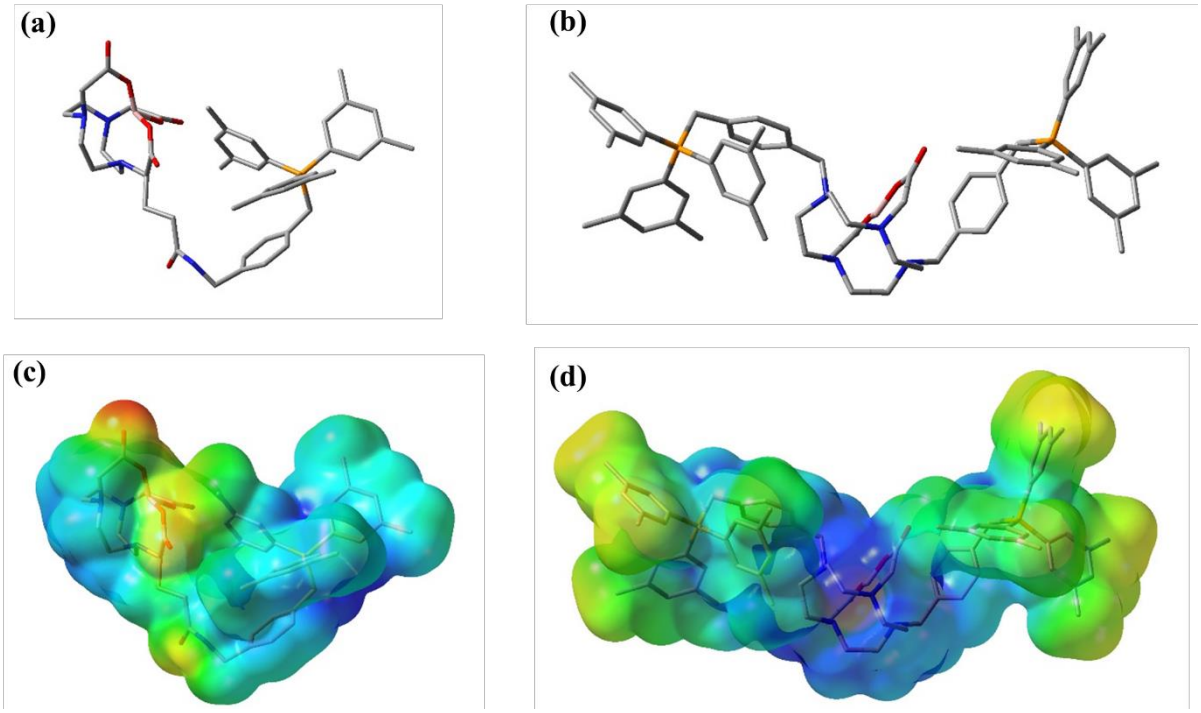

Figure 4.16 DFT optimised structures of **(a)** [Ga-NODAGA-xy-TXP]$^{+}$ and **(b)** [Ga-DO2A-(xy-TXP)$_2$]$^{3+}$ with hexacoordinated metal centres (Ga(III)). Mapping of the electrostatic potentials of **(c)** [Ga-NODAGA-xy-TXP]$^{+}$ and **(d)** [Ga-DO2A-(xy-TXP)$_2$]$^{3+}$ onto electron density surface; the MEP of **(c)** represents a maximum potential of 0.12 a.u. and minimum of -0.03 a.u. while the MEP of **(d)** represents a maximum potential of 0.25 a.u. and minimum of 0.10 a.u. (red to blue = negative to positive).

Although [^{68}Ga]Ga-NODAGA-xy-TXP does not exhibit superior $\Delta\Psi_m$-dependent uptake and retention in cardiac cells compared to previous [^{68}Ga]Ga-cationic tracers, this work does expand our understanding of the structure/activity relationship for refining the employed synthetic strategy, providing a basis for further functionalisation to improve these characteristics.

All calculations were performed using the Gaussian 16 package (Revision C.01).[15] Full geometry optimisations were performed using the ωB97X-D functional[16] in aqueous solution using the polarisable continuum model (PCM),[17] with the LANL2DZ basis set and effective

core potentials for Ga, and 6-311+G** for all other atoms.[18] Frequency analysis of the optimised structures confirmed a true minimum energy structure by the absence of imaginary frequencies.

4.7 Concluding Remarks

Outlined in this chapter was the cardiac uptake and retention of a novel ^{68}Ga-labelled complex, [^{68}Ga]Ga-NODAGA-xy-TXP, which was assessed using the Langendorff isolated perfused heart model. This novel radiotracer was compared to the 'gold' standard clinically used radiotracer, MIBI. As an initial index on radiotracer lipophilicity, log *D* values were utilised to inform on the potential cardiac uptake and retention in isolated perfused rat hearts. However, this work has established a non-linear relationship between log *D* and the effectiveness of a radiotracer for reporting on mitochondrial dysfunction. In fact, many factors play a role in determining how effective a radiotracer's cardiac uptake and retention is in hearts. One major factor briefly investigated in this chapter was the effect the charge distribution across the surface area of the entire molecule has on the cardiac uptake and retention kinetics. Unfortunately, the novel ^{68}Ga complex investigated did not come close to the uptake, retention and washout kinetics demonstrated by MIBI. Nevertheless, this initial study will inform on the development of future ^{68}Ga-based lipophilic and cationic radiotracers to report on mitochondrial dysfunction.

4.8 References for Chapter 4

1 R. M. Bell, M. M. Mocanu and D. M. Yellon, *J. Mol. Cell. Cardiol.*, 2011, **50**, 940–950.

2 M. Skrzypiec-Spring, B. Grotthus, A. Szelag and R. Schulz, *J. Pharmacol. Toxicol. Methods*, 2007, **55**, 113–126.

3 E. Mariotti, M. Veronese, J. T. Dunn, R. A. Medina, P. J. Blower, R. Southworth and T. R. Eykyn, *EJNMMI Res.*, 2013, **3**, 74.

4 F. Shaughnessy, E. Mariotti, K. P. Shaw, T. R. Eykyn, P. J. Blower, R. Siow and R. Southworth, *EJNMMI Res.*, 2014, **4**, 1–10.

5 M. G. Handley, R. A. Medina, E. Mariotti, G. D. Kenny, K. P. Shaw, R. Yan, T. R. Eykyn, P. J. Blower and R. Southworth, *J. Nucl. Med.*, 2014, **55**, 488–494.

6 R. A. Medina, E. Mariotti, D. Pavlovic, K. P. Shaw, T. R. Eykyn, P. J. Blower and R. Southworth, *J. Nucl. Med.*, 2015, **56**, 921–926.

7 Biomedical Laboratory Science, https://biomedical-laboratory.blogspot.com/%0D, (accessed 12 April 2020).

8 P. A. Iaizzo, Ed., *Handbook of Cardiac Anatomy, Physiology, and Devices*, Springer International Publishing, Cham, 3rd edn., 2015.

9 R. L. Gallo, J. N. Finkelstein and R. H. Notter, *Biochim. Biophys. Acta*, 1984, **771**, 217–27.

10 Z. M. Safee, F. Baark, E. C. T. Waters, M. Veronese, V. R. Pell, J. E. Clark, F. Mota, L. Livieratos, T. R. Eykyn, P. J. Blower and R. Southworth, *Sci. Rep.*, 2019, **9**, 216.

11 Z. M. Safee, *PhD Thesis*, King's College London, 2015.

12 A. J. Smith, B. E. Osborne, G. P. Keeling, P. J. Blower, R. Southworth and N. J. Long, *Dalton Trans.*, 2020, **49**, 1097–1106.

13 A. J. Smith, *PhD Thesis*, Imperial College London, 2019.

14 A. J. Smith, P. J. Gawne, M. T. Ma, P. J. Blower, R. Southworth and N. J. Long, *Dalton Trans.*, 2018, **47**, 15448–15457.

15 M. J. Frisch, G. W. Trucks, H. B. Schlegel, G. E. Scuseria, M. a. Robb, J. R. Cheeseman, G. Scalmani, V. Barone, G. a. Petersson, H. Nakatsuji, X. Li, M. Caricato, a. V. Marenich, J. Bloino, B. G. Janesko, R. Gomperts, B. Mennucci, H. P. Hratchian, J. V. Ortiz, a. F. Izmaylov, J. L. Sonnenberg, Williams, F. Ding, F. Lipparini, F. Egidi, J. Goings, B. Peng, A. Petrone, T. Henderson, D. Ranasinghe, V. G. Zakrzewski, J. Gao, N. Rega, G. Zheng, W. Liang, M. Hada, M. Ehara, K. Toyota, R. Fukuda, J. Hasegawa, M. Ishida, T. Nakajima, Y. Honda, O. Kitao, H. Nakai, T. Vreven, K. Throssell, J. a. Montgomery Jr., J. E. Peralta, F. Ogliaro, M. J. Bearpark, J. J. Heyd, E. N. Brothers, K. N. Kudin, V. N. Staroverov, T. a. Keith, R. Kobayashi, J. Normand, K. Raghavachari, a. P. Rendell, J. C. Burant, S. S. Iyengar, J. Tomasi, M. Cossi, J. M. Millam, M. Klene, C. Adamo, R. Cammi, J. W. Ochterski, R. L. Martin, K. Morokuma, O. Farkas, J. B.

Foresman and D. J. Fox, 2016, Gaussian 16, Revision C.01, Gaussian, Inc., Wallin.

16 J.-D. Chai and M. Head-Gordon, *Phys. Chem. Chem. Phys.*, 2008, **10**, 6615.

17 G. Scalmani and M. J. Frisch, *J. Chem. Phys.*, 2010, **132**, 114110.

18 W. R. Wadt and P. J. Hay, *J. Chem. Phys.*, 1985, **82**, 284–298.

CHAPTER 5 – SYNTHESIS OF ACYCLIC LIGANDS FOR THE GENERATION OF LIPOPHILIC AND CATIONIC GALLIUM-68 COMPLEXES

5. Synthesis of Acyclic Ligands for the Generation of Lipophilic and Cationic Gallium-68 Complexes

As outlined in chapter 2, the design of chelators that maintain an overall positive charge and desirable lipophilicity, whilst binding $[^{68}Ga]^{3+}$ effectively, is the first stage in the development of ^{68}Ga-based lipophilic and cationic radiotracers. Chapter 2 described the synthesis and characterisation of some macrocyclic chelators. Macrocycle-based chelating agents are typically more inert than acyclic chelators of a similar stability, but generally do not exhibit superior complexation kinetics. However, ^{68}Ga imaging agents only need to resist metal leaching for 3 hours *in vivo* to allow for imaging, meaning high complexation kinetics are favoured and acyclic chelators are preferred.[1] In this chapter we discuss the synthesis and characterisation of novel acyclic ligands for the formation of ^{68}Ga complexes.

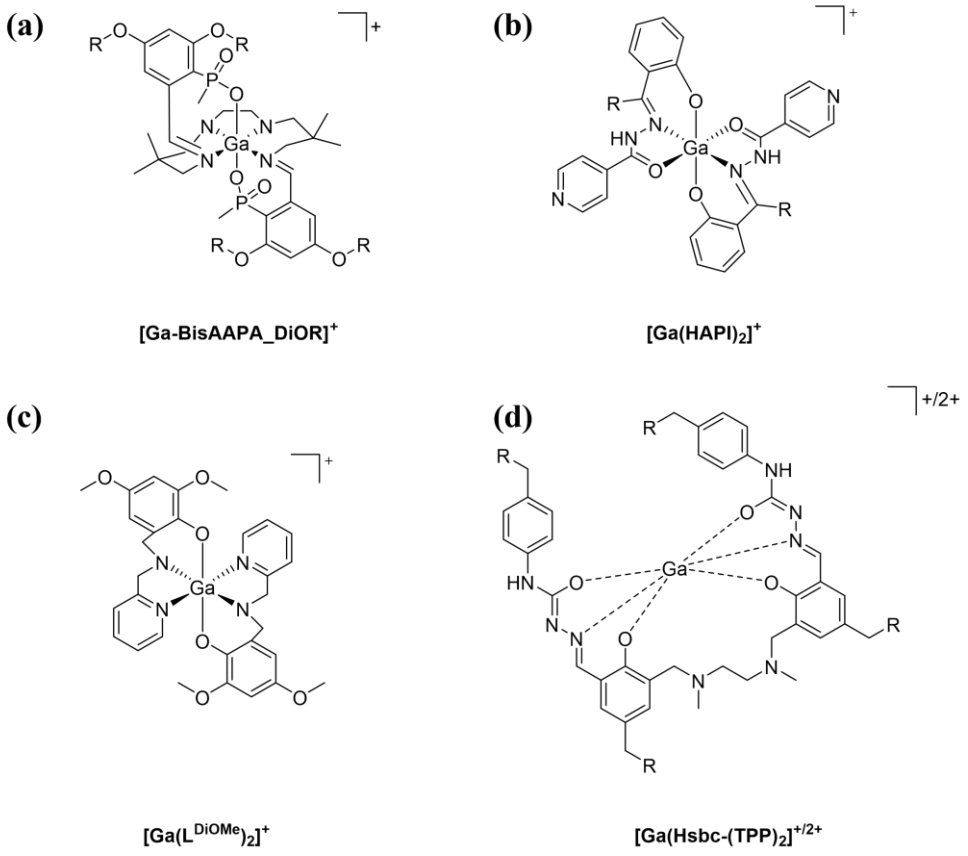

Figure 5.1 The general structures of the four series of compounds **(a)-(d)** discussed in this chapter.

5.1 Bis(Arylaldiminophosphinic Acid) (BisAAPA) Ligands

Gallium(III) complexes of selected Schiff-base phenolic ligands have shown significant promise as radiopharmaceuticals for use in targeting and imaging mitochondria.[2–7] The first of these cationic ^{68}Ga complexes of hexadentate $N_4O_2^{2-}$ Schiff-base ligands that were shown to possess heart-specific accumulation was [^{68}Ga][Ga-bis(4,6-dimethoxysalicylaldimino)-*N,N′*-bis(3-aminopropyl)ethylenediamine]$^+$ ([^{68}Ga][Ga(4,6-MeO$_2$sal)$_2$BAPEN]$^+$), shown in **Figure *5.2*a**.[2] The mechanism of its myocardial uptake is thought to be similar to that of [^{99m}Tc]Tc-sestaMIBI because both radiotracers are lipophilic and mono-cationic.[8]

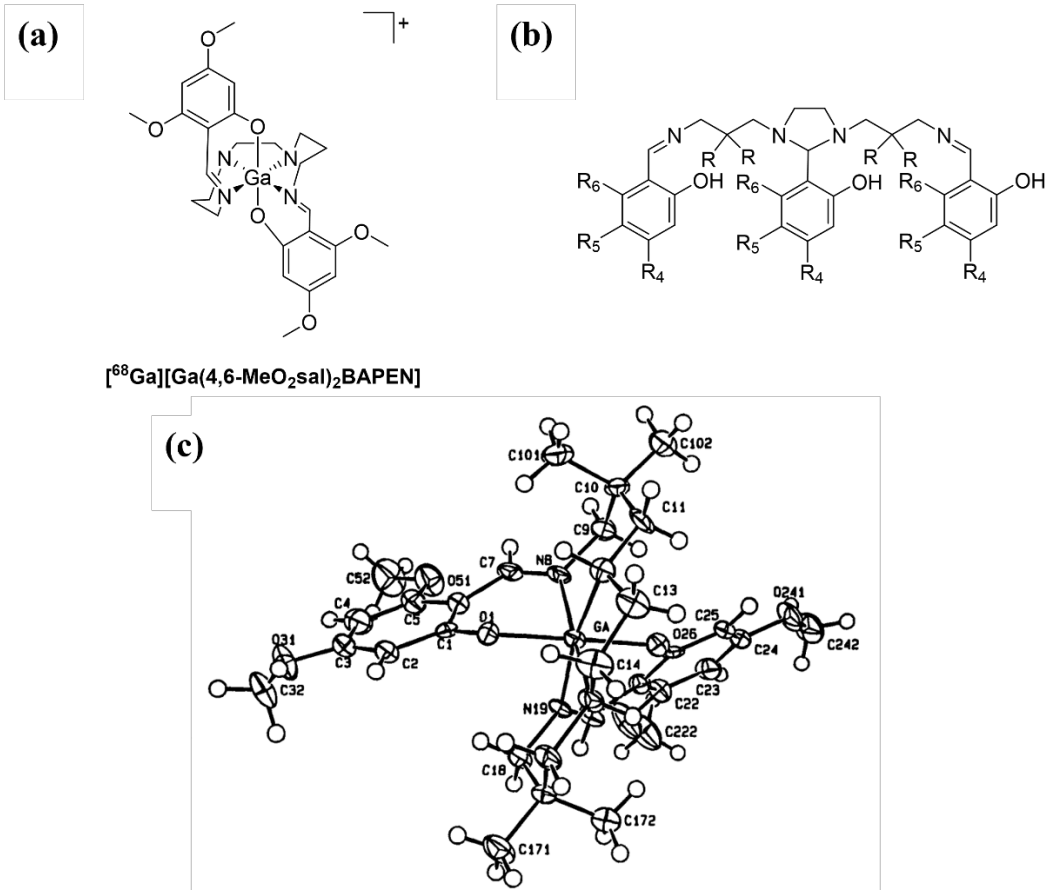

Figure 5.2 (a) The structure of [^{68}Ga][Ga(4,6-MeO$_2$sal)$_2$BAPEN]$^+$.[2] **(b)** General structural formula for bis(salicylaldimine)ligands.[4] R = H, Me; R_4 = H, OMe, OEt, NEt_2; R_5 = H, Me, OMe, *i*-Pr; R_6 = H, Me, OMe. **(c)** ORTEP drawing of the molecular structure of [^{68}Ga][Ga(4,6-MeO$_2$sal)$_2$Me$_4$BAPEN]$^+$ illustrating the *trans* configuration of the phenolic oxygens around the Ga(III) metal centre.[4] Reprinted with permission from Tsang *et al*.[4]

While this compound exhibited significant myocardial uptake and indefinite tracer retention in the myocardium, the net uptake remained less than ideal. For example, in 1994 Tsang *et al*.

investigated the derivatization of $[Ga(4,6\text{-}MeO_2sal)_2BAPEN]^+$ to identify related compounds that exhibit improved myocardial uptake, whilst maintaining desired myocardial retention in the myocardium.[4] Tsang *et al*. developed a series of ten lipophilic mono-cationic Ga(III) complexes of the general structural formula shown in **Figure 5.2b**, which contain alkoxy, alkyl, and/or alkylamino substituents on the aromatic rings of the ligand.[4] Interestingly, the reaction of these tris(salicylaldimine) compounds with the Ga(III) precursor resulted in the hydrolytic cleavage of the bridging imino group to form the desired Ga(III) bis(salicylaldimine) complexes, which have been widely reported in the literature.[4,9,10]

As shown in X-ray crystallographic characterisation of $[^{68}Ga][Ga(4,6\text{-}MeO_2sal)_2Me_4BAPEN]^+ I^-$, shown in **Figure 5.2c**, Ga(III) centres display a preference for hexadentate coordination with a distorted octahedral geometry.[4] The phenolic oxygens (shown by O1 and O26 in **Figure 5.2c**) are shown to be coordinated in a *trans* configuration, which contrasts with the *cis* arrangement observed for the Fe(III) complexes of similar bis(salicylaldimino)triethylenetetraamine compounds.[11] Alongside these complexes being cationic, their lipophilicity is also a key component that dictates their myocardial uptake and retention, with log *P* values ranging from 0.8 to 3.0.[4] The lipophilicity of these compounds increased with increasing alkyl functionalisation, of either the tetraamine backbone or the aromatic rings, and this was also found to depend on the position of the alkyl or alkoxy substituents on the aromatic rings. A methoxy group in position 5 of the aromatic ring was found to have no effect on log *P*, whilst a methoxy group in position 4 increased log *P* by 0.26. A methyl group in position 5 of the aromatic ring increased log *P* by 0.50, and a methyl group in position 6 increased log *P* by 1.02.[4]

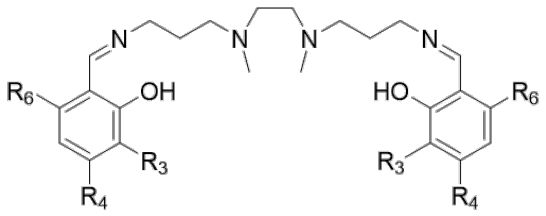

Figure 5.3 The general structural formula for hexadentate bis(salicylaldimine) ligands derived from BAPDMEN. R_3, R_4 and R_6 = H, OMe.[5]

Despite these modifications made to the structure of the lead compound $[^{68}Ga][Ga(4,6\text{-}MeO_2sal)_2BAPEN]^+$ resulting in similar favourable characteristics in

biodistribution studies, none of the modifications lead to a significant improvement of biological properties on the lead compound.

In 2009, Hsiao *et al*. reported the synthesis and biodistribution of a related series of five Ga(III) bis(salicylaldimine) radiotracers derived from *N,N′*-bis(3-aminopropyl)-*N,N′*-dimethylethylenediamine (BAPDMEN), which involve the addition of methyl groups on each of the two nitrogen atoms of the central ethylenediamine fragment of the BAPEN ligands, shown in **Figure 5.3**.[5] X-ray crystallographic characterisation of the 4,6-dimethoxy BAPDMEN analogue, confirmed that these ligands retain their ability to bind the Ga(III) centre in a hexadentate fashion with a distorted octahedral geometry, with the phenolic oxygen atoms adopting a *trans* geometry. The five BAPDMEN ligands were radiolabelled with ^{67}Ga and their lipophilicities were assessed using their octanol/water partition coefficients, giving log *P* values of 1.4 to 3.0. As expected, each additional *N*-methyl substituent of the BAPDMEN backbone increased log *P* by approximately 0.4. Using their rat model, Hsiao *et al*. assessed the myocardial uptake and retention of the ^{68}Ga-labelled BAPDMEN radiotracers, and it was found that these tracers exceeded the uptake of [^{99m}Tc]Tc-sestaMIBI after 1-min post-injection, including their prolonged retention in the myocardium for 2 h. Particularly desirable characteristics were exhibited by the 3-methoxy derivative [$^{67/68}$Ga][Ga(3-MeOsal)$_2$BAPDMEN]$^+$ compared to the previously reported BAPEN analogues.[2,5]

In 2014, Sharma *et al*. reported a novel lipophilic mono-cationic Ga(III) complex, [$^{67/68}$Ga][Ga-3-isopropoxy-ENBDMPI]$^+$ which was later renamed ^{68}Ga-Galmydar and is shown in **Figure 5.4a**.[7,12] As expected, this ligand coordinates the Ga(III) centre in a hexadentate manner with a distorted octahedral geometry, confirmed by X-ray crystallography (**Figure 5.4b**).

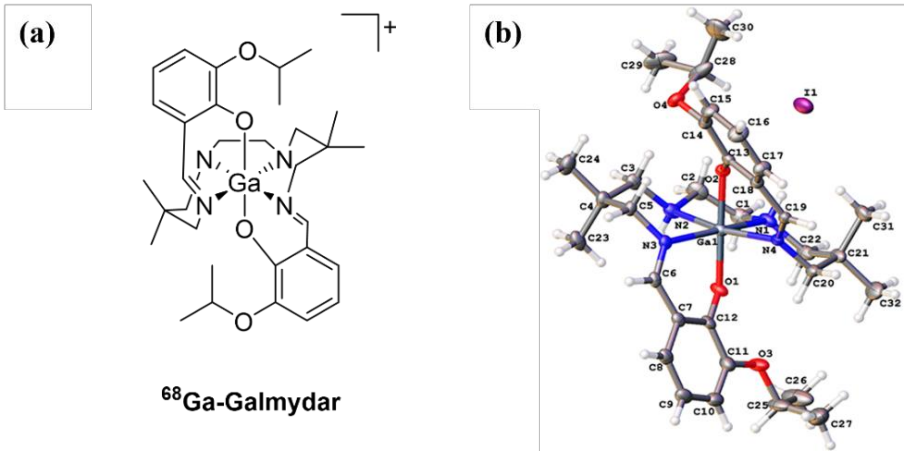

Figure 5.4 (a) The chemical structure of ^{68}Ga-Galmydar. **(b)** The crystal structure of ^{nat}Ga-Galmydar.[12] Reprinted with permission from *PLoS One*, 2019, **14**, e0215579.

As discussed in section 1.5.1.1, anthracyclines are inherently used in cancer therapy, but exhibit cardiotoxic effects, which includes a drastic change of the mitochondrial membrane potential.[13] As such, the use of anthracyclines, such as doxorubicin (DOX), in animal models to induce mitochondrial dysfunction and evaluate anthracycline-induced cardiotoxicity has gained much interest in recent years.[12,14–16] In 2019, Sivapackiam *et al*. assessed the potential of ^{68}Ga-Galmydar to report on DOX-induced cardiotoxicity *in vivo*, which showed an approximate 2-fold decrease in retention in hearts of DOX-treated hearts compared to their vehicle-treated counterparts.[12] Galmydar (λ_{ex} = 375 nm, λ_{em} = 485 nm) was also found to be a mildly fluorescent compound, which was shown to localize in the mitochondria in a similar manner to Mitotracker5^{TM} red using live-cell imaging.[12] Live-cell imaging indicated a decrease in cellular uptake and retention of Galmydar in DOX-treated cells compared to untreated cells, confirming the uptake and retention of the probe in mitochondria is dependent on the mitochondrial membrane potential.[12]

The success of this class of bis(salicylaldimine) ligands for gallium-68 chelation and reporting on mitochondrial dysfunction provided the basis for the first family of acyclic ligands for the formation of lipophilic and cationic gallium-68 complexes developed in this project. In 2015, Máté *et al*. investigated the influence of carboxylate and phosphinate pendant arms in 1,4,7-triazacyclononane(TACN)-based chelators on their gallium-68 labelling properties.[17] The phosphinate-containing analogues showed higher labelling efficiency, binding with lower ligand excess, over a wide range of temperatures compared to their respective carboxylate counterparts.[17] Indeed, Notni *et al*. had similar findings for their TACN-based

phosphinate-containing radiotracers, noting efficient ^{68}Ga complexation at 10-30-fold lower concentrations than carboxylate-containing derivatives.[18]

The proton affinity constants of chelators can be very useful in predicting the ability of a chelator to coordinate Ga(III). The lower the pKa value, the more easily deprotonation will occur, leading to greater metal binding efficiency. Protonation constants of TACN-based chelates containing phenolate, carboxylate or phosphinate pendant arms confirmed the phosphinate derivatives gave the lowest pKa values, meaning they should bind Ga(III) more efficiently, further supporting the observations by Máté *et al*. and Notni *et al*.[17–20] It therefore seemed natural to begin with replacing the hydroxyl coordinating groups of bis(salicylaldimine) ligands with phosphinate donors to assess ^{68}Ga-labelling efficiency, and we also investigated the effect of alkoxy-functionalisation, in the 3- and 5-positions of the aromatic rings, on the lipophilicities of the final radiotracers. Using the rationale discussed in chapter 2, we attempted the synthesis of methoxy, ethoxy and *iso*-propoxy analogues, shown in **Figure 5.5**, in order to modulate the lipophilicity of the final radiotracers.

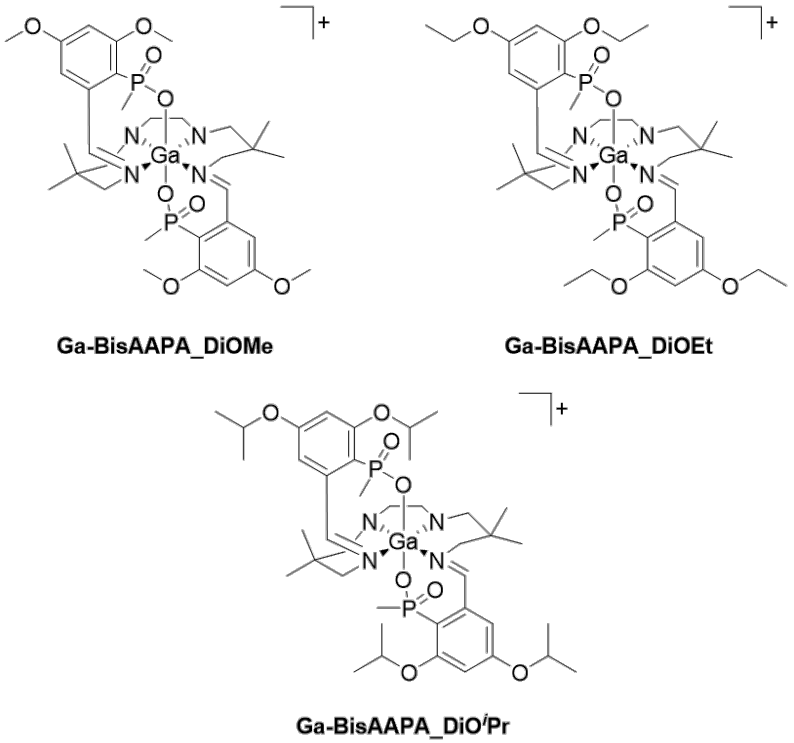

Figure 5.5 The three target Ga(III) BisAAPA complexes investigated in this thesis, consisting of a N_4O_2 donor core capable of chelating Ga(III) utilising two phosphinate pendant arms, and either 3,5-dimethoxy-, 3,5-diethoxy- or 3,5-di-*iso*-propoxy functionalisation of the aromatic rings, providing lipophilic and cationic complexes to target mitochondrial function.

5.1.1 Synthesis of Bis(Salicylaldimine) Analogues

In order to accurately determine the effect phosphinate pendant arms have on gallium-68 chelation efficiency, compared to hydroxyl binding groups present in the BAPEN-based complexes discussed previously, the synthesis of hydroxyl-containing bisAAPA derivatives, shown in **Figure 5.6**, was performed.[4,5,7]

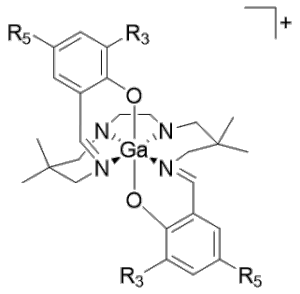

Figure 5.6 The general structural formula of Ga(III) bis(salicylaldimine) compounds, $(3,5\text{-}R_2sal)_2BDMAPEN$. R_3 and R_5 = OMe, OEt and O^{i}Pr.

The first four steps towards the synthesis of $(3,5\text{-}R_2sal)_2BDMAPEN$ compounds are shown in **Scheme 5.1**. The synthetic route of the dimethoxy-variant started with 2,4-dimethoxybenzaldehyde **12a**, because of its commercial availability. For diethoxy **b** and di-*iso*-propoxy **c** variants, the synthetic route began with Vilsmeier-Haack formylation of resorcinol to give 2,4-dihydroxybenzaldehyde **11**.[21] This was followed by *o*-alkylation of **11** using the respective alkyl iodide to synthesise 2,4-dialkoxybenzaldehydes **12b-c**, using an adaptation of the procedure reported by Gudipudi *et al*.[21] Upon addition of two equivalents of ethyl iodide to a mixture of **11** and potassium carbonate in acetone, the mixture was stirred overnight at room temperature. Purification of the crude product by silica flash chromatography gave three individual UV-active bands which were originally expected to be the starting material **11**, the mono-substituted derivative and the desired di-substituted product **12b**. However, analysis of each band by ^{1}H NMR spectroscopy identified one band as **11** and the other two bands as the two possible mono-substituted derivatives, with the alkylation occurring on the 2-position or 4-position. Increasing the equivalents of ethyl iodide unfortunately did not promote the desired di-substitution. As a result, a change of focus was adopted towards alternative synthetic routes.

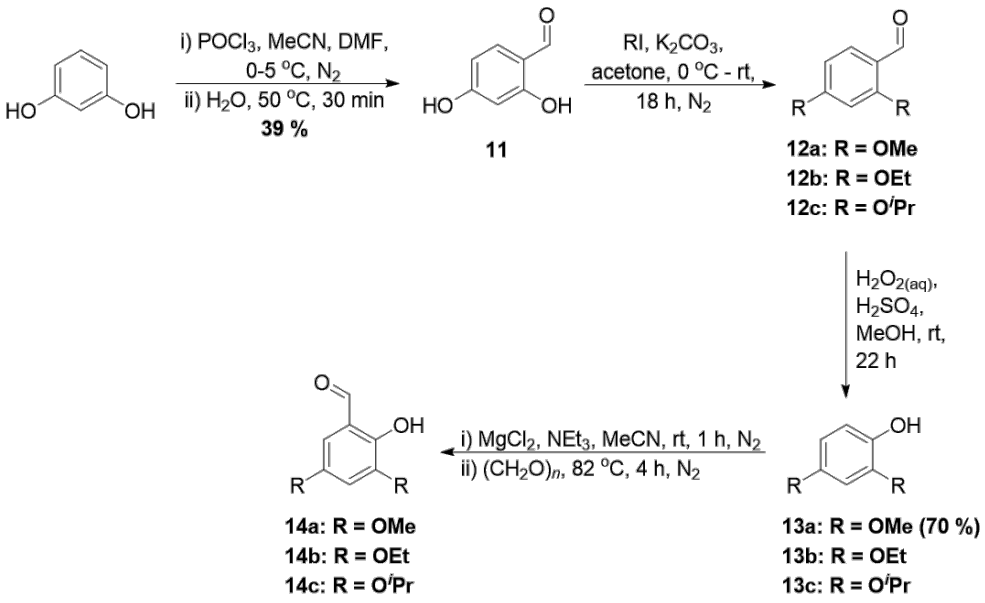

Scheme 5.1 The first four steps towards the synthesis of (3,5-R_2sal)$_2$BDMAPEN ligands. The synthesis of 2,4-dihydroxybenzaldehyde **11** and 2,4-dialkoxybenzaldehyde derivatives **12a-c** was performed as a modification of the procedure reported by Gudipudi *et al*.[21] 2-Hydroxy-3,5-dialkoxybenzaldehydes **14a-c** were synthesised via the reduction of **12a-c** to form 2,4-dialkoxyphenols **13a-c**, which underwent *ortho*-formylation using $MgCl_2$ following modifications of procedures reported by Azevedo *et al*. and Sharma *et al*.[7,22]

Regardless of these synthetic issues observed in the synthesis of **12b**, the commercial availability of 2,4-dimethoxybenzaldehyde **12a** meant that the synthetic route for the dimethoxy variant could begin two steps ahead of the other two variants. The oxidation of benzaldehydes to phenols can be achieved through the Dakin reaction.[23] The acid-catalysed Dakin oxidation of benzaldehydes with hydrogen peroxide and acidic methanol was shown to be highly selective towards the generation of the respective phenol compared to the methyl benzoate by-product. The conversion of 2,4-dimethoxybenzaldehyde **12a** to 2,4-dimethoxyphenol **13a** was performed using the procedure reported by Azevedo *et al*.[22] The work-up described by Azevedo *et al*. involved concentration of the mixture under reduced pressure and the crude residue was partitioned between DCM and distilled water.[22] However, upon addition of both solvents, an opaque black solution formed, and the two layers could not be accurately delineated. Instead, the solvent was removed under reduced pressure and the crude residue was immediately purified by column chromatography to give the pure product **13a** as a yellow oil in a 70 % yield.

The Casnati-Skattebøl *ortho*-formylation method by which phenols are converted to salicylaldehydes was employed for the formation of 3,5-dialkoxysalicylaldehhydes **14a-c** from 2,4-dialkoxyphenols **13a-c**.[7,24] The reaction utilises a combination of a $MgCl_2$-Et_3N base system to convert the phenol to its magnesium salt and its subsequent reaction with paraformaldehyde to afford the desired salicylaldehyde **14a-c**. In 2014, Sharma *et al*. synthesised 3-*iso*-propoxysalicylaldehyde using the Casnati-Skattebøl reaction, for the generation of Galmydar, shown in **Figure 5.4**.[7] For the synthesis of the dimethoxy analogue **14a**, the formation of the magnesium salt of **13a** proceeded through stirring **13a** with $MgCl_2$ and Et_3N in large excesses in anhydrous acetonitrile at room temperature for 1 hour. This was followed by the addition of paraformaldehyde, also in a large excess, and subsequent refluxing of the mixture to promote the formation of the desired salicylaldehyde **14a**.

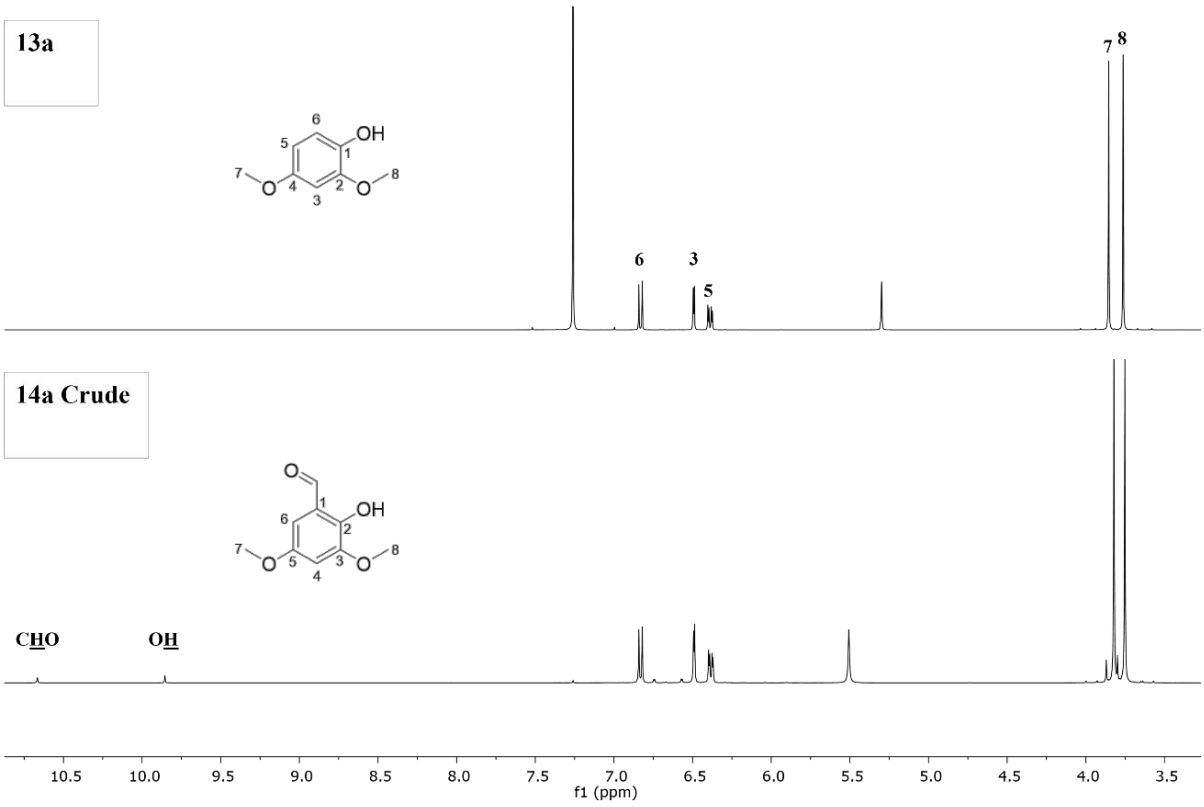

Figure 5.7 ^1H NMR spectra of the phenol and salicylaldehyde of the dimethoxy variant ($CDCl_3$, 400 MHz, 298 K). From top to bottom: 2,4-dimethoxyphenol **13a**, crude 2-hydroxy-3,5-dimethoxybenzaldehyde **14a**. The labelled structures of **13a** and **14a**, including NMR spectroscopic characterisation of **13a** are shown.

After the recommended 4 hours of heating at reflux, an aliquot of the mixture was used to monitor the progress of the reaction via TLC analysis and NMR spectroscopy. A comparison

of the ^{1}H NMR spectrum of the crude aliquot of **14a** and the ^{1}H NMR spectrum of **13a**, shown in **Figure 5.7**, highlighting a lack of reactivity, confirmed by the presence of two small peaks at 10.67 ppm and 9.85 ppm corresponding to the aldehyde and hydroxyl protons of **14a** respectively.

Integration of these two peaks confirmed a 6 % conversion to the salicylaldehyde product **14a**, with the degree of conversion not significantly increasing after stirring the reaction mixture for a further 48 hours. The lack of reactivity was initially attributed to the electron-donating methoxy groups, deactivating the *meta*-position (1-position) on the aromatic ring. However, the 3-*iso*-propoxy salicylaldehyde synthesised by Sharma *et al*. similarly contained an electron-donating group in the 3-position, and the formylation reaction was not significantly hindered.

Instead, a second strategy involving the dialkylation of 3,5-dihydroxybenzaldehyde, N-bromosuccinimide (NBS)-assisted bromination and subsequent hydroxylation to synthesise 3,5-dialkoxysalicylaldehydes **14a-c**, shown in **Scheme 5.2**, was investigated.[25,26]

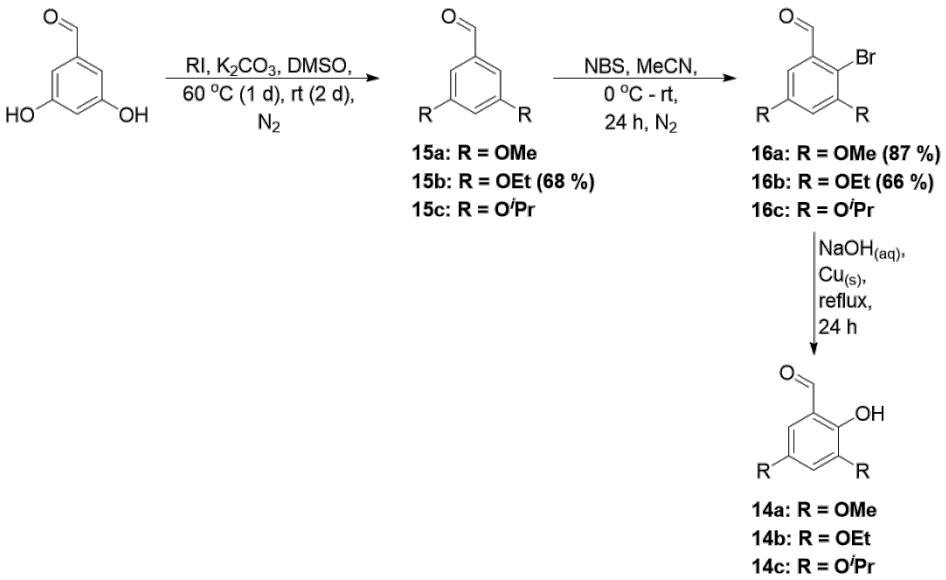

Scheme 5.2 Alternative synthetic route towards the synthesis of 3,5-dialkoxysalicylaldehyde compounds **14a-c**. *O*-alkylation of 3,5-dihydroxybenzaldehyde to synthesise 3,5-dialkoxybenzaldehydes **15a-c** was performed using a modification of the procedure reported by Döerwald *et al*.[25] NBS-assisted bromination of **15a-c** and subsequent substitution of the bromide group with a hydroxyl group to generate the desired salicylaldehydes **14a-c** was performed using an adaptation to the procedure described by Liao *et al*.[26]

Compared to the alkylation conditions reported by Gudipudi *et al*., heating one equivalent of 3,5-dihydroxybenzaldehyde in DMSO with K_2CO_3 and 3 equivalents of alkyl iodide for 24 hours, followed by stirring at room temperature for 48 hours gave the desired diethoxy variant 3,5-diethoxybenzaldehyde **15b** in a good yield.[21,25] The 68 % yield achieved for the synthesis of **15b** was obtained via a simple aqueous wash and organic extraction work-up, with further purification by silica flash chromatography not being required. As was the case for 2,4-dimethoxybenzaldehyde **12a**, 3,5-dimethoxybenzaldehyde **15a** could be commercially sourced and therefore the synthesis of the dimethoxy variant could begin at this stage of the synthetic route. Benzylic bromination of 3,5-dialkoxybenzaldehydes **15a-b** was performed using NBS, following an adaptation of the procedure described by Liao *et al*.[26] NBS was chosen as the brominating agent for the synthesis of compounds **16a-c**, because diatomic bromine (Br_2) typically reacts with double bonds to form dibromides, whereas NBS provides a lower concentration of bromine, making it more selective towards mono-bromination. In order to prevent multiple bromination reactions occurring on the aromatic ring, NBS was added to a solution of the starting material **16a-b** in acetonitrile at 0 °C. The mixture was allowed to warm to room temperature overnight with stirring. Similarly to **15a-b**, pure products were obtained in good yield by a simple organic extraction work-up.

The following step, illustrated in **Scheme 5.2**, involved a copper-catalysed base hydroxylation of 2-bromo-3,5-dialkoxybenzaldehydes **16a-c** to generate the target salicylaldehyde compounds **14a-c**.[26] This step of the synthetic route was attempted with the dimethoxy analogue **16a** following a modified procedure reported by Liao *et al*.[26] The hydroxylation of **16a** was carried out using an 8 % aqueous solution of sodium hydroxide and copper powder, which was heated at reflux overnight with monitoring by TLC. After 24 hours the starting material was no longer present by TLC and the reaction was deemed complete. Following the addition of sodium bicarbonate to quench the remaining copper powder, the product was extracted using ethyl acetate, and the crude material afforded from the work-up was recrystallised from toluene. An aliquot of the material was taken for analysis by ^{1}H NMR spectroscopy, shown in **Figure 5.8**, and was compared to the ^{1}H NMR spectrum of the bromobenzaldehyde precursor **16a**. Upon comparison, the presence of both aromatic protons seen at 7.04 and 6.71 ppm, corresponding to H_6 and H_4 respectively, and both methyl proton environments at 3.91 and 3.85 ppm, referring to H_8 and H_7 respectively, were confirmed. The key finding by NMR spectroscopic analysis was the disappearance of the aldehyde proton, observed at 10.42 ppm for **16a**.

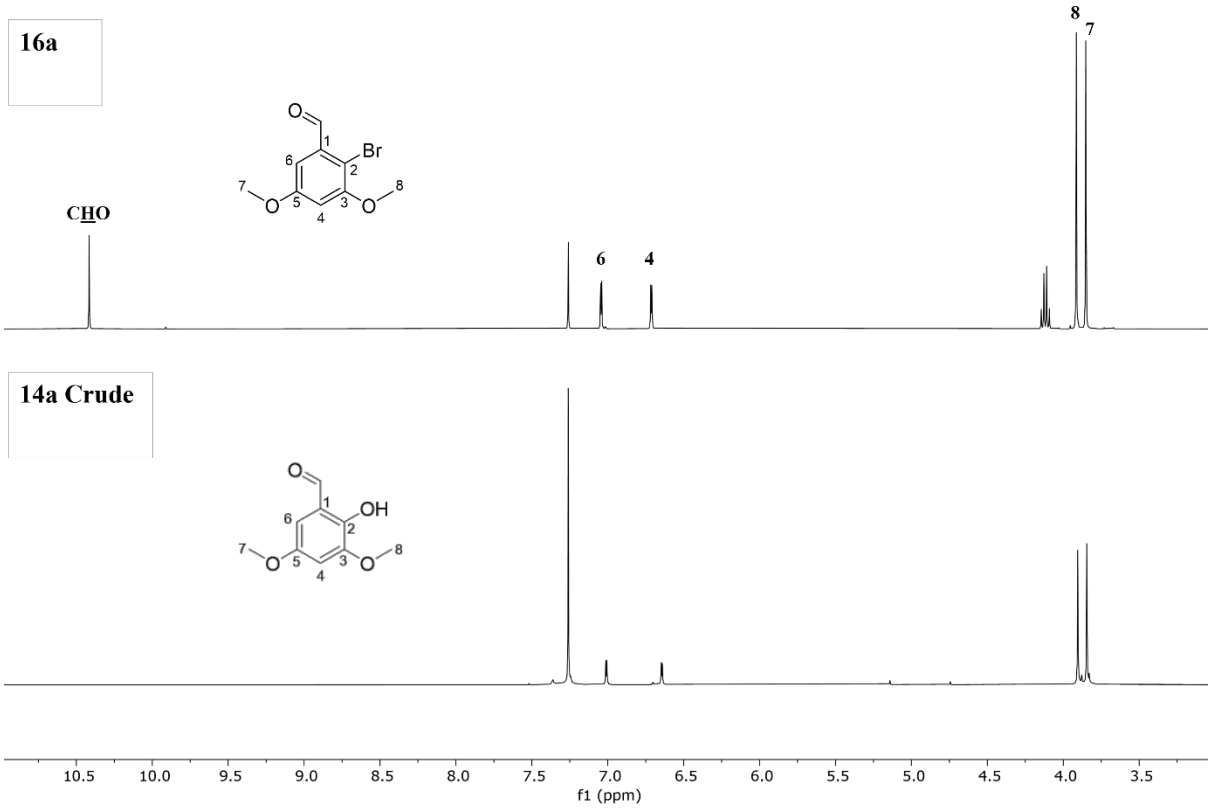

Figure 5.8 ^{1}H NMR spectra of 2-bromo-3,5-dimethoxybenzaldehyde **16a** and crude material obtained via recrystallisation from toluene for the synthesis of **14a** ($CDCl_3$, 400 MHz, 298 K). From top to bottom: 2-bromo-3,5-dimethoxybenzaldehyde **16a**, crude recrystallisation material of **14a**. The labelled structures of **16a** and **14a**, including NMR spectroscopic characterisation of **16a** are shown.

The disappearance of the aldehyde proton suggests a reaction occurred at this functional group. Ellis *et al*. reported that the lack of a hydroxyl group in the 4-position of the aromatic ring led to the aldehyde group undergoing the Cannizzaro reaction to give the benzoic acid analogue.[27] However, the procedure by Liao *et al*. contradicts this explanation by Ellis *et al*., as the 2-bromo-3,5-dimethoxybenzaldehyde **16a** reagent does not contain a 4-hydroxyl group but the reaction is still reported to proceed successfully, achieving a yield of 80 %.[26]

In 2021, Zhang *et al*. reported the successful synthesis of 2-hydroxy-3,5-dimethoxybenzaldehyde **14a** from the hexamine aromatic formylation of 2,4-dimethoxyphenol **13a**, known as the Duff reaction.[28] The Duff reaction is a formylation reaction that uses phenol derivatives, hexamethylenetetramine (HMTA), TFA and a dilute acid to synthesise *ortho*-substituted aromatic aldehydes. However, the Duff reaction is typically low yielding.[29] Following the procedure reported by Zhang *et al*., 2,4-dimethoxyphenol **13a** and an excess of HMTA were refluxed in neat TFA overnight, shown in **Scheme 5.3**. After refluxing

overnight an iminium intermediate forms which is subsequently hydrolysed by water in acidic media in the final step to give the desired salicylaldehyde product **14a**.

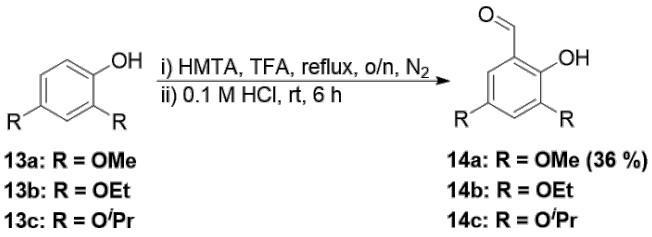

Scheme 5.3 The Duff formylation of 2,4-dialkoxyphenols **13a-c** to generate *ortho*-substituted aromatic aldehydes **14a-c**, using a modification of the procedure developed by Zhang *et al*.[28]

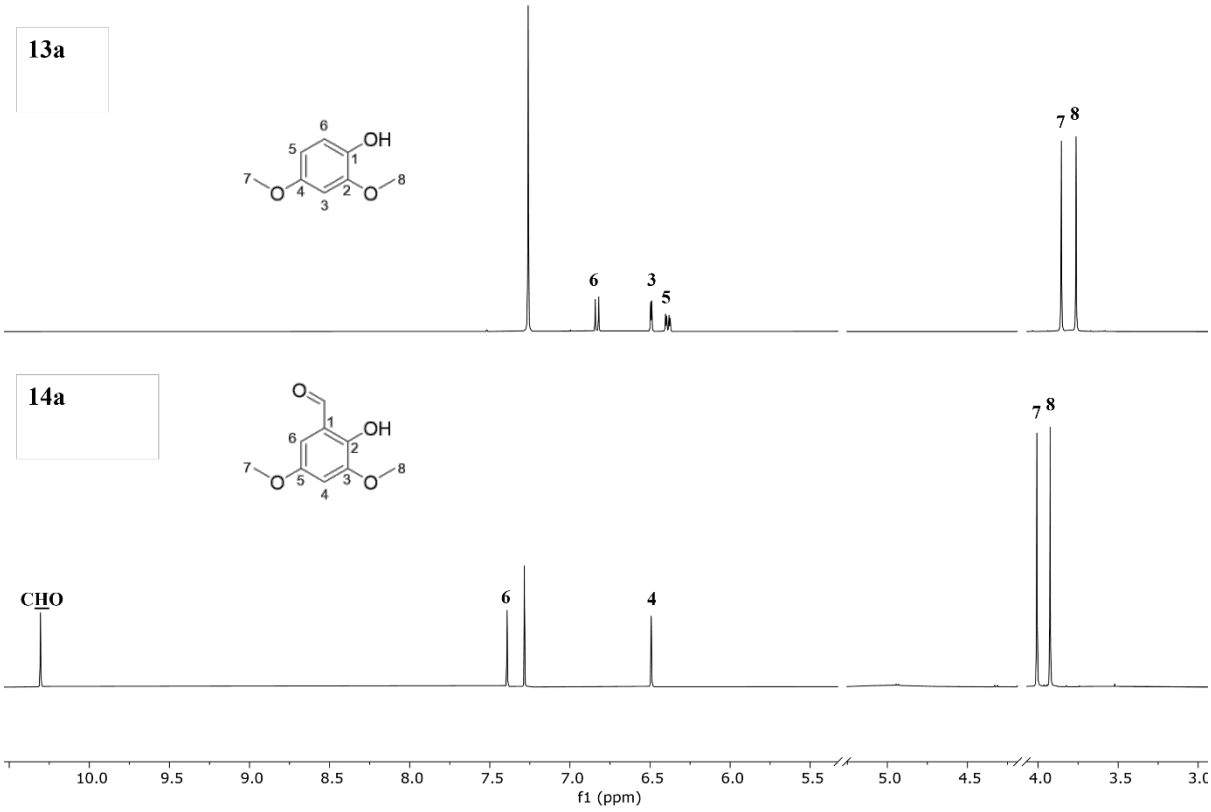

Figure 5.9 ^{1}H NMR spectra of 2,4-dimethoxyphenol **13a** (top) and 2-hydroxy-3,5-dimethoxybenzaldehyde **14a** (bottom) ($CDCl_3$, 400 MHz, 298 K). Ethyl acetate and DCM solvent peaks have been truncated for clarity. The labelled structures of **13a** and **14a**, including NMR spectroscopic characterisation for both compounds, are shown.

The crude product was purified by silica column chromatography to give the pure product as an off-white solid in 17 % yield. Pure **14a** was analysed by ^{1}H NMR spectroscopy, depicted in **Figure 5.9**, confirmed the presence of the expected aldehyde proton as a singlet at 10.27 ppm, including the upfield shift of the aromatic proton on the 6-position (formerly the 5-position for

13a) to 7.36 ppm due to the aldehyde group decreasing the electron density of the nucleus, resulting in a larger chemical shift. The removal of vicinal coupling observed for the aromatic protons H_6 and H_4 also aided in identifying weaker interactions between themselves resulting in two singlets at 7.36 and 6.46 ppm respectively, which would be expected compared to the starting material **13a**. Mass spectrometry was also used to characterise **14a**, with a mass peak at *m*/*z* value of 183.

Initially, according to the procedure by Zhang *et al*., 0.1 M HCl was added to the reaction mixture to initiate the acid hydrolysis of the iminium ion intermediate, which was stirred at room temperature for 1 hour.[28] This gave pure **14a** in a 17 % yield, as mentioned in the preceding paragraph. Increasing the duration of the acid hydrolysis from 1 hour to 6 hours resulted in a significant improvement in chemical yield, with a yield of 36 % achieved for the synthesis of **14a**. The dimethoxy salicylaldehyde analogue **14a** was carried forward to undergo a condensation reaction with a linear tetraamine, discussed below, and once a successful synthetic route had been identified for the target (3,5-R_2sal)$_2$BDMAPEN ligands, the diethoxy and di-*iso*-propoxy variants **b** and **c** could be synthesised analogously.

Following the methodology reported by Harpstrite *et al*. in 2010, the synthesis of a linear tetraamine backbone **17**, illustrated in **Scheme 5.4**, was performed.[7,30] The nucleophilic substitution of 1,2-dibromoethane proceeded via its addition to a suspension of potassium hydroxide in acetonitrile. An excess of 2,2-dimethylpropane-1,3-diamine was then added to initiate the substitution.

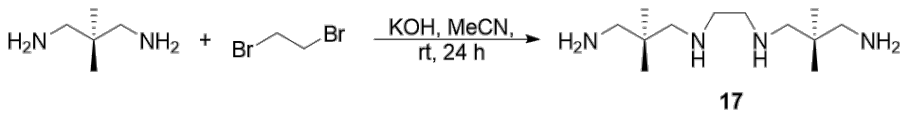

17

Scheme 5.4 Formation of the linear tetraamine backbone, Bis(*N*,*N*′-amino-2,2-dimethylpropane)ethylenediamine **17**, synthesised according to the methodology reported by Harpstrite *et al*.[31]

Typically, reactions with primary amines and alkyl bromides are not selective, leading to a range of substitution products being formed, including secondary amines, tertiary amines, and longer chain amine compounds. The crude residue obtained from the reaction was purified by vacuum distillation, according to Harpstrite *et al*.[31] Multiple attempts performing vacuum distillation on the crude **17** did not yield the pure compound. Analysis of the colourless oil obtained from the distillation by ^{1}H NMR spectroscopy showed extra peaks in the aliphatic

region and presence of the desired compound could not be deduced. Mass spectrometry was also employed to help identify whether **17** had formed, the spectrum is shown in **Figure 5.10**.

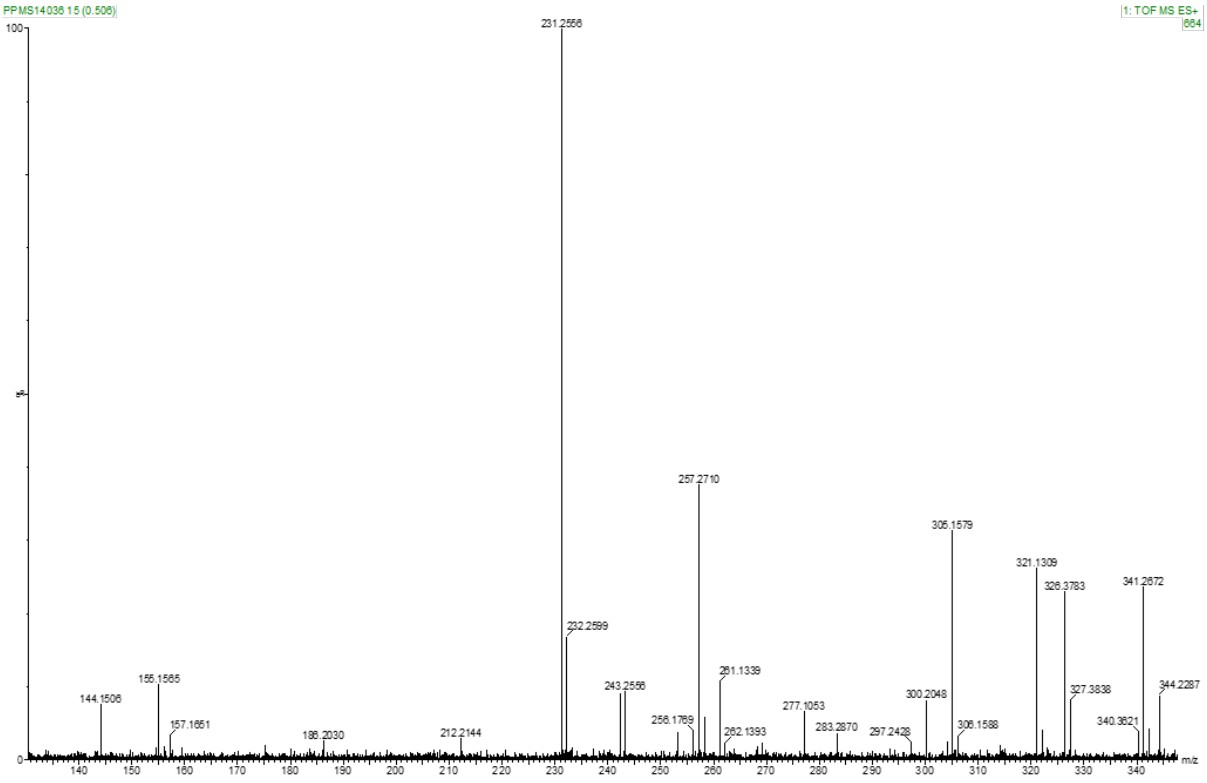

Figure 5.10 The ESI-MS spectrum of the material obtained from the distillation of crude **17**.

The major peak shown by the MS spectrum with a *m*/*z* value of 231, corresponded to the target product **17**. However, a range of other minor peaks were also seen at higher *m*/*z* values, suggesting that further substitution may have occurred. Regardless, compound **17** does appear to be the major species formed, therefore it was carried forward for the condensation reaction with salicylaldehydes **14a-c**.

The condensation of the linear tetraamine **17** and salicylaldehyde compounds **14a-c** was initially performed according to the method described by Tsang *et al*.[4] Using the prepared dimethoxy derivative, three equivalents of **14a** and one equivalent of **17** were dissolved in anhydrous methanol, and molecular sieves were added before the mixture was heated at reflux for 20 minutes, shown in **Scheme 5.5**.

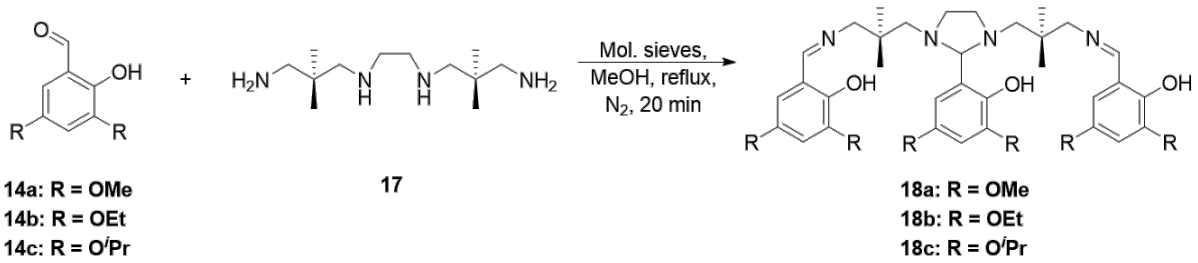

14a: R = OMe
14b: R = OEt
14c: R = O^{i}Pr

17

18a: R = OMe
18b: R = OEt
18c: R = O^{i}Pr

Scheme 5.5 Imine condensation of salicylaldehydes **14a-c** and linear tetraamine **17** for the formation of (3,5-dialkoxysalicylaldehyde)$_2$BDMAPEN ligands **18a-c**. Prepared according to an adaptation of the method reported by Tsang *et al*.[4]

After 20 minutes the mixture was cooled to room temperature, concentrated under reduced pressure and dissolved in diethyl ether. This caused instant precipitation to occur, reported as to be the salicylaldehyde precursor by Tsang *et al*., which was removed by filtration.

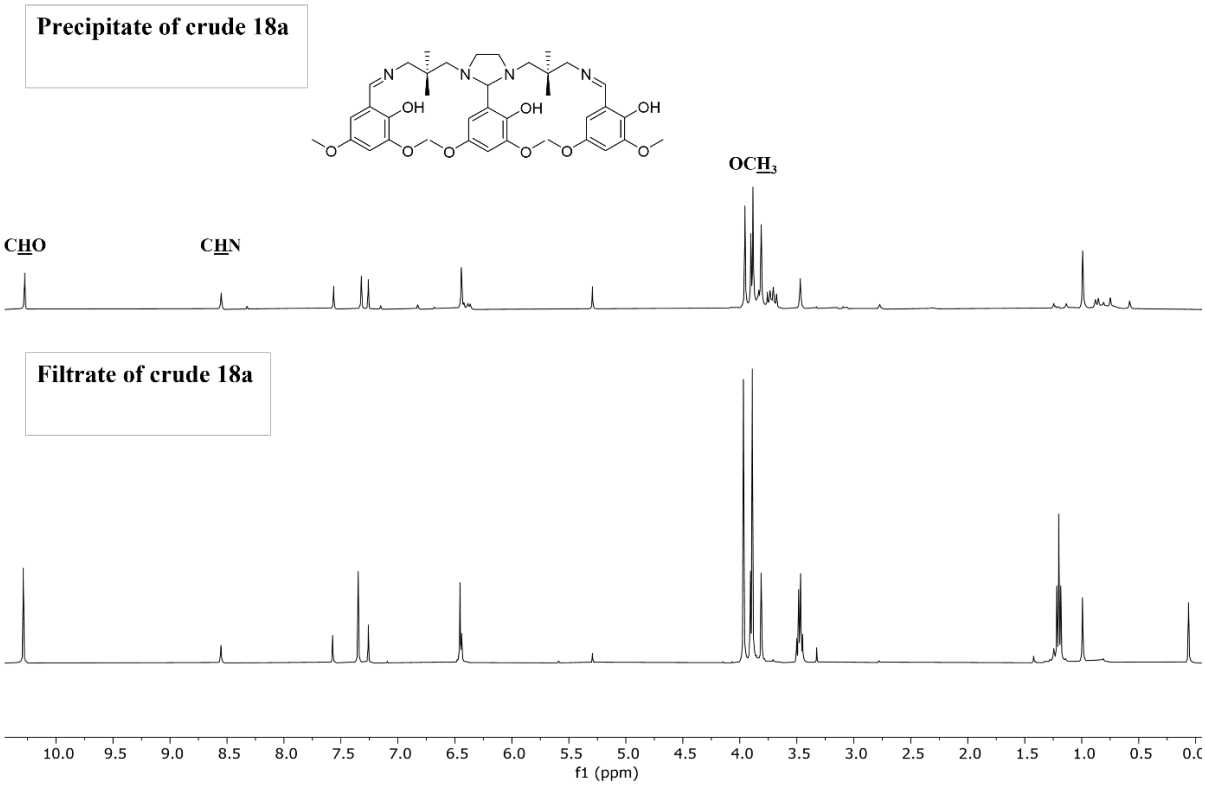

Figure 5.11 ^{1}H NMR spectra of the precipitate (top) collected upon addition of diethyl ether for the synthesis of **18a**, and the filtrate (bottom) ($CDCl_3$, 400 MHz, 298 K).

Leaving the collected filtrate at 4 °C overnight should have resulted in the formation of another precipitate, corresponding to the target tris(salicylaldimine) ligand, however this was not the case for the synthesis of **18a**.[4] Due to the absence of a second precipitate, the filtrate was concentrated under reduced pressure and analysed by ^{1}H NMR spectroscopy, shown in

Figure 5.11, along with the first precipitate, assumed to be the salicylaldehyde precursor **14a**. The spectra of both the precipitate and filtrate highlighted the presence of both **14a**, confirmed by the singlet at 10.29 ppm corresponding to the aldehyde proton, and the imine product **18a**, confirmed by the singlet at 8.55 ppm referring to the imine protons. This elucidated the precipitation induced by the addition of diethyl ether was not successful in separating the aldehyde precursor and the imine product. The methoxy protons of the aromatic rings were also observed and showed two distinct sets of singlets at approximately 3.90 ppm, one set was originally thought to correspond to the methoxy protons of the aryl units located on the two outer imine groups, and the second set belonging to the methoxy protons of the aryl unit bound to the central bridging imino group. However, the presence of the aldehyde proton signal at 10.29 ppm proved this could not be the case, instead one set of singlets at 3.90 ppm belonged to the unreacted **14a** methoxy groups.

Integration of the imine proton peaks compared to the aldehyde proton peaks established that the reaction had undergone an approximate 20 % conversion, not significantly different from the literature findings.[4,7] Extending the duration of the condensation had no significant effect on the degree of conversion. The low conversion was also attributed to the impurities present in compound **17** leading to a range of imine complexes, and if these consist of chemically similar linear amines to **17**, the resulting imine compounds may not be distinguishable by NMR spectroscopy.

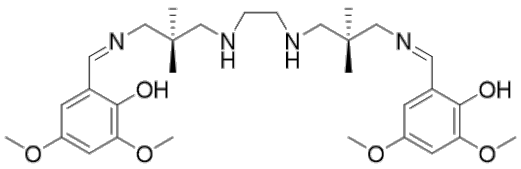

Figure 5.12 Potential side product of the condensation of **14a** and **17**, displaying the absence of the bridging imino group expected for the ligand **18a**.

One possible side product is a variant of the tris(salicylaldimine) **18a**, illustrated in **Figure 5.12**, consisting of two free central amines instead of a bridging imino group. The presence of this side product in the complexation reaction of Ga(III) was deemed feasible due to the hydrolytic cleavage of the bridging imino group, mentioned previously, observed for literature complexations of this ligand type.[4,7] This would ultimately lead to the transformation of ligand **18a** to the hexadentate side product shown in **Figure 5.12**, which is the ligand species that complexes with the Ga(III) metal centre.

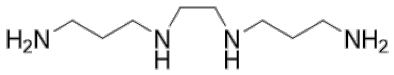

Figure 5.13 The chemical structure of the commercially available linear tetraamine bis(3-aminopropyl)ethylenediamine.

Due to the potential lack of control for the imine condensation presented by the questionable purity of the linear tetraamine **17**, a commercially available linear tetraamine bis(3-aminopropyl)ethylenediamine, displayed in **Figure 5.13**, was used for the imine condensation with **14a** to synthesise alternative bis(salicylaldimine) ligands **19a-c**, shown in **Figure 5.14**.

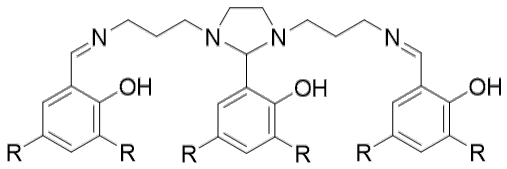

Figure 5.14 The general structure of bis(3,5-dialkoxysalicylaldehyde)BAPEN ligands **19a-c**. R = OMe (**a**), OEt (**b**), O^{i}Pr (**c**).

The difference between this linear tetraamine and **17** is the lack of two methyl groups on the central carbon atom of the propyl chain. The change in structure of the tetraamine backbone has been shown to not affect the subsequent imine condensation and complexation steps to achieve the desired Ga(III) complexes.[4]

The same procedure used for the attempted synthesis of **18a** was employed for the synthesis of bis(salicylaldimine) ligands **19a-c**.[4] This time the linear tetraamine precursor was known to be higher in purity than **17**, therefore the imine condensation of **14a** and bis(3-aminopropyl)ethylenediamine was expected to improve the degree of conversion towards the imine product, along with a smaller amount of impurities. As for the synthesis of **18a**, an aliquot of the reaction mixture of crude **19a** was taken after 20 minutes, and was analysed by ^{1}H NMR spectroscopy. The ^{1}H NMR spectrum of crude **19a** was compared to the aldehyde **14a** and amine starting materials, displayed in **Figure 5.15**, to assess the progression of the condensation reaction.

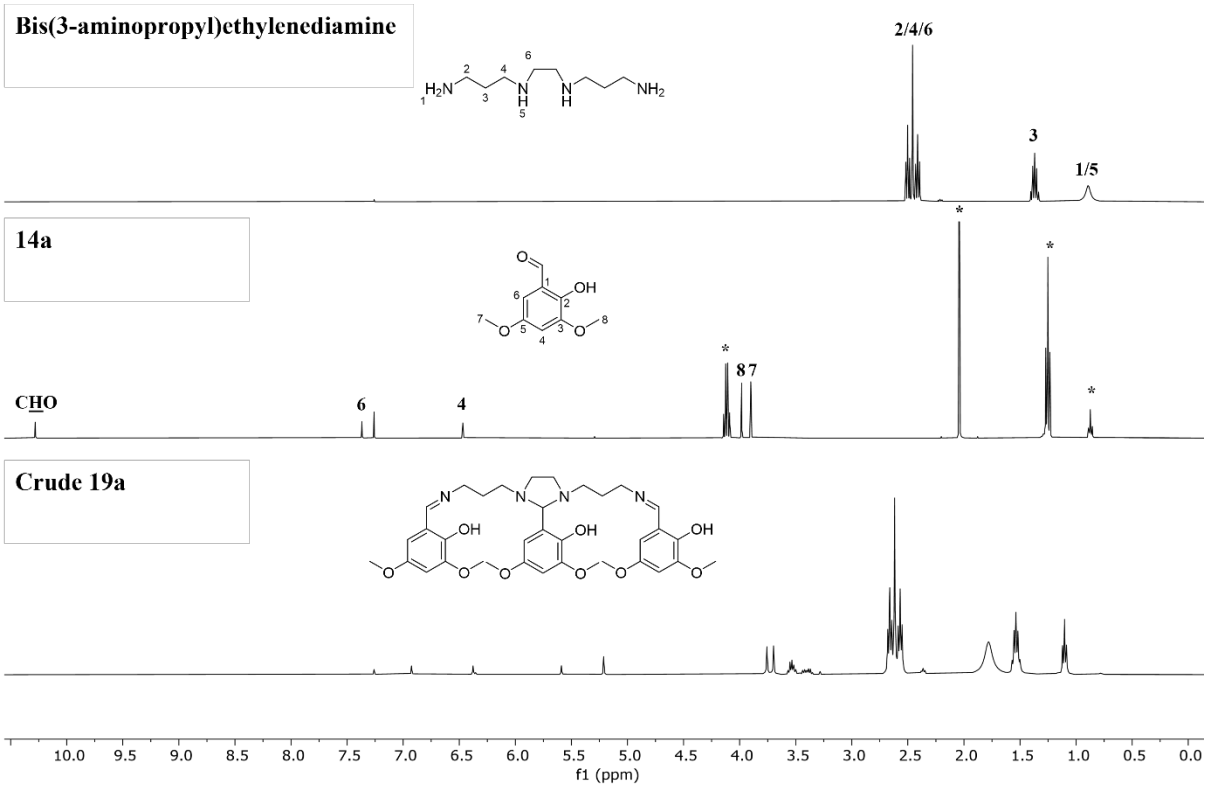

Figure 5.15 ^{1}H NMR spectra of crude **19a**, including both aldehyde **14a** and amine starting materials ($CDCl_3$, 400 MHz, 298 K). From top to bottom: bis(3-aminopropyl)ethylenediamine, **14a** and crude **19a**. Solvent impurities, such as hexane and ethyl acetate, have been denoted with an asterisk (*).

The lack of a singlet at approximately 10.30 ppm, corresponding to the aldehyde proton of **14a**, and a singlet in the expected imine proton range, was the key finding observed in the ^{1}H NMR spectrum of **19a**. Interestingly, the appearance of new peaks in the aliphatic region does suggest reactivity of the tetraamine backbone. For example, a 0.2 ppm upfield shift of the quintet to 1.54 ppm, corresponding to H_3 of the amine precursor, does infer a chemical change of the structure. The broad singlet at 0.89 ppm, representing the amine protons H_1/H_5, also shifted upfield to 1.78 ppm, however the presence of this singlet confirmed that some of the amine sites had not undergone condensation with **14a**. The multiplet at 2.45 ppm for the amine precursor, corresponding to proton environments $H_2/H_4/H_6$, was observed in the spectrum of crude **19a**, with its integration highlighting an 8-fold excess compared to the expected integration value. Regardless of the suggestion that reactions had occurred, due to the lack of any imine species being identified, the synthesis of **19a** was deemed unsuccessful.

To assess the viability of the imine condensation reaction, the synthesis of the literature bis(salicylaldimine) ligand (4,6-$(MeO)_2$sal)$_2$BAPEN, shown in **Figure 5.16**, was

investigated.[2,4] The change in position of the methoxy groups from the 3- and 5-positions, to the 4- and 6-positions on the aromatic ring, meant the effect of the position of directing groups on the rate of condensation could also be assessed.

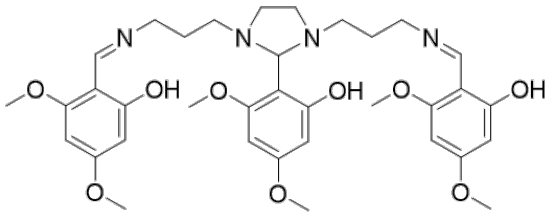

Figure 5.16 The chemical structure of (4,6-(MeO)$_2$sal)$_2$BAPEN, synthesised by Tsang *et al*.[2,4]

A much simpler two-step method could be employed for the synthesis of (4,6-(MeO)$_2$sal)$_2$BAPEN, shown in **Scheme 5.6**, involving mono-demethylation of 2,4,6-trimethoxybenzaldehyde and condensation to give the desired ligand.

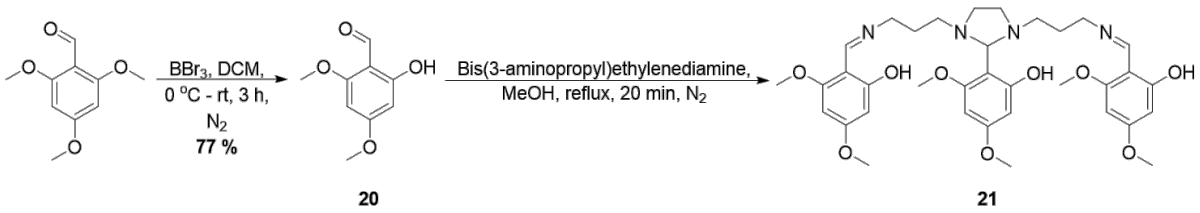

Scheme 5.6 The two-step synthesis of (4,6(MeO)$_2$sal)$_2$BAPEN **21**. Synthesis of 2-hydroxy-4,6-dimethoxybenzaldehyde **20** was carried out using the procedure reported by Janse van Rensburg *et al*., and the imine condensation of **20** with bis(3-aminopropyl)ethylenediamine was performed as reported by Tsang *et al*.[2,4,32]

The mono-demethylation of 2,4,6-trimethoxybenzaldehyde to generate 2-hydroxy-4,6-dimethoxybenzaldehyde **20** was performed following the methodology by Janse van Rensburg.[33] The salicylaldehyde analogue **20** was then reacted with bis(3-aminopropyl)ethylenediamine, in an analogous manner to the syntheses of **18a** and **19a**.[2,4] The crude material, collected from concentrating the reaction mixture under vacuum, was subjected to the addition of diethyl ether which caused a white precipitate to immediately form. This was found to be the expected salicylaldehyde starting material **20** by NMR spectroscopy. The filtrate was left to stand at 4 °C overnight, yielding a second precipitate, yellow in colour. The yellow precipitate was isolated by filtration and analysed by NMR spectroscopy to assess the product conversion rate.

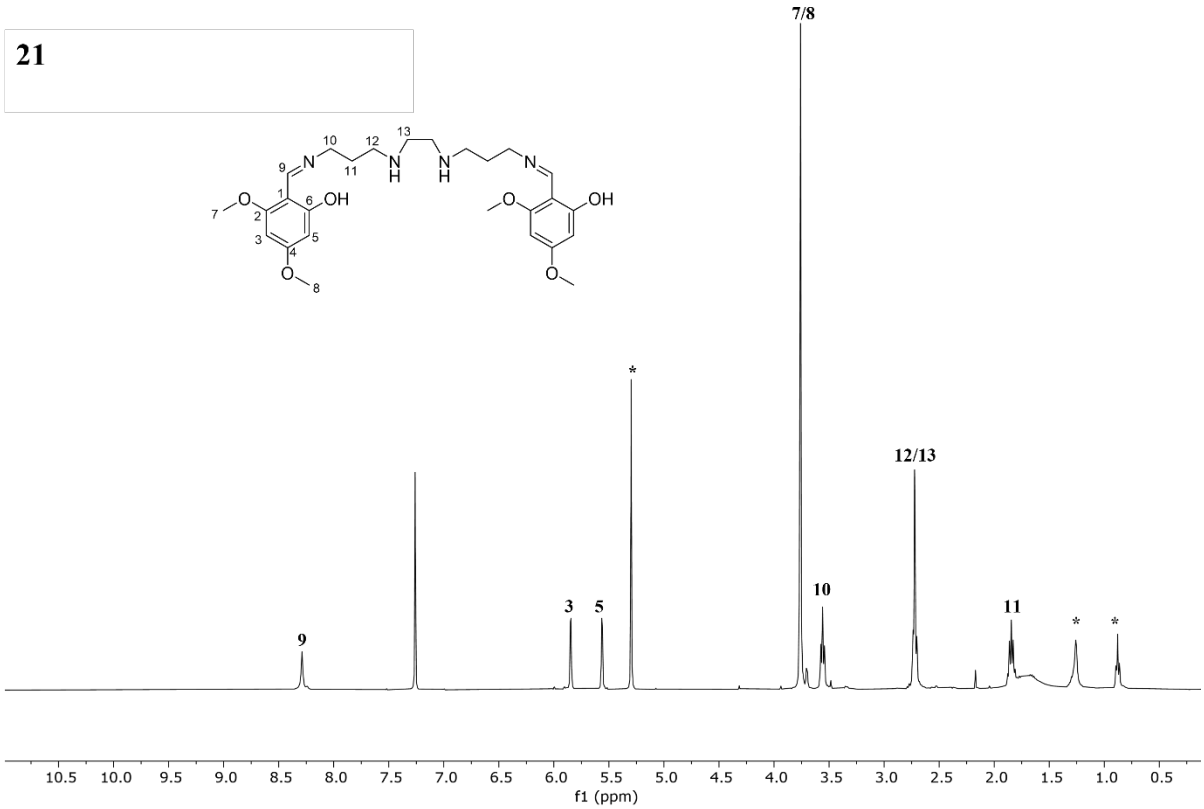

Figure 5.17 ^{1}H NMR spectrum of (4,6-(MeO)$_2$sal)$_2$BAPEN ($CDCl_3$, 400 MHz, 298 K). Includes the labelled structure of **21** and NMR spectroscopic characterisation. Hexane and DCM solvent impurities have been highlighted with an asterisk (*).

As shown in **Figure 5.17**, the ^{1}H NMR spectrum of the second precipitate collected for the synthesis of **21** proved to be clean, with no NMR active impurities observed. Interestingly, the expected imino bridge proton signal reported at 4.32 ppm was not seen, and following integration of the assigned peaks, it was confirmed that the bis(salicylaldimine) ligand had formed without the imino bridge and central aryl unit. As discussed earlier, this would not lead to difficulties with future complexations with Ga(III). As expected, this ligand displays several common features including a singlet at 8.29 ppm referring to the imine protons H_9, two singlets at 5.85 ppm and 5.56 ppm corresponding to the aromatic protons H_3 and H_5, and a singlet at 3.76 ppm referring to the methoxy protons H_7 and H_8. Mass spectrometry was also used to characterise compound **21**, with a *m*/*z* value of 503 for $[M+H]^+$, and also highlighted the presence of a minor species with a *m*/*z* value of 667 corresponding to the tris(salicylaldimine) product. Due to the success of the synthesis of the literature ligand **21**, we can surmise that the position of alkoxy groups on the aromatic ring do have an influence on the condensation of the linear tetraamine and salicylaldehyde precursors. Unfortunately, due to time constraints, investigations into the bis(3,5-dialkoxysalicylaldehyde)BDMAPEN,

bis(3,5-dialkoxysalicylaldehyde)BAPEN ligands, including chelation experiments with Ga(III) could not be explored further.

5.1.2 Synthesis of Bis(Arylaldiminophosphinic Acid) (BisAAPA) Ligands

Alongside synthesising bis(salicylaldimine) ligands, efforts into the synthesis of phosphinic acid functionalised analogues were also investigated. First, we explored the synthesis of 3,5-dialkoxy-functionalised bis(AAPA)BDMAPEN compounds, consisting of the BDMAPEN tetraamine backbone, shown in **Figure 5.18**.

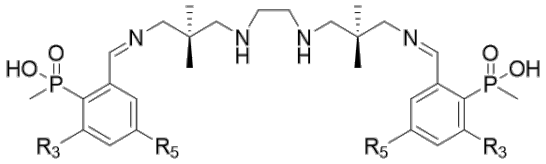

Figure 5.18 General structure of bisAAPA ligands, consisting of the BDMAPEN backbone, bis(AAPA)BDMAPEN ligands. R_3 and R_5 = OMe, OEt, and O^{i}Pr.

Incorporation of the phosphinate group on the aromatic ring required the synthesis of the *H*-phosphinate ester, ethyl methylphosphinate **22**, which could be cross-coupled with 2-bromo-3,5-dialkoxybenzaldehyde compounds **16a-c**, discussed previously, shown in **Scheme 5.7**.

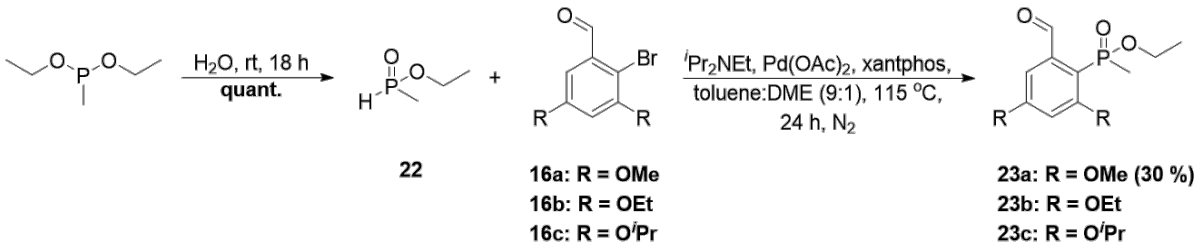

Scheme 5.7 The synthesis of 2-ethyl(methyl)phosphinate-3,5-dialkoxybenzaldehyde analogues **23a-c**. Hydrolysis of diethyl methylphosphonite was performed using the procedure reported by Walter *et al*.[34] Cross-coupling of ethyl methylphosphinate **22** and 2-bromo-3,5-dialkoxybenzaldehyde **16a-c** was performed as an adaptation of the method by Gavara *et al*.[35]

Hydrolysis of diethyl methylphosphonite with one equivalent of water led to ethyl methylphosphinate **22** in a quantitative yield, using the method described by Walter *et al*.[34] Compound **22** was formed with one equivalent of ethanol, as a by-product, and was used *in situ* in the following step without any additional purification. The subsequent step involved the

cross-coupling of **22** and 2-bromo-3,5-dialkoxybenzaldehyde derivatives **16a-c**, synthesised previously, to generate the target phosphinate-functionalised benzaldehyde compounds **23a-c**.

A variety of metal-catalysed cross-coupling reactions have been developed for the formation of P-C bonds, but only a few have been applied to aryl halides, such as the work reported by Deal *et al*. and Gavara *et al*.[35,36] A possible mechanism for *H*-phosphinate coupling was described in 2011 by Deal *et al*., with the catalytic cycle shown in **Scheme 5.8**.

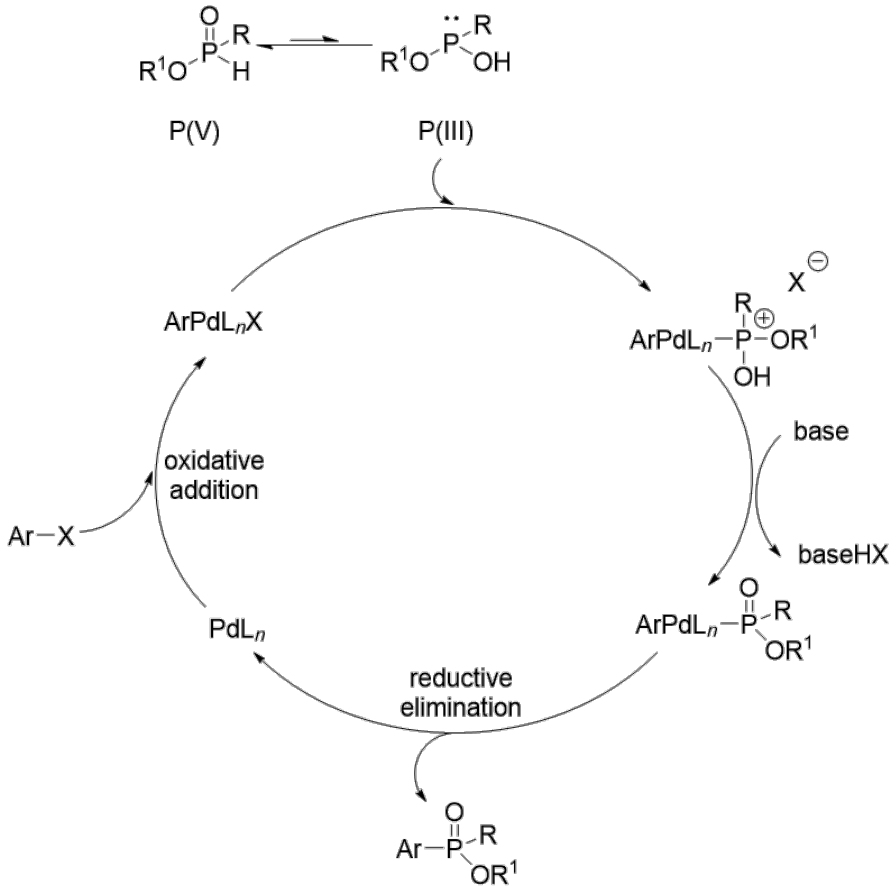

Scheme 5.8 The postulated catalytic cycle of cross-coupling of *H*-phosphinate esters with aryl halides, proposed by Deal *et al*.[36] Schematic adapted from Deal *et al*.[36]

Key to the reaction is the availability of the P(III) nucleophile through tautomerization of the P(V) species. Deal *et al*. reported the usefulness of additives, such as ethylene glycol (EG) and 1,2-dimethoxyethane (DME), to promote the tautomerization of P(V) *H*-phosphinates into the reactive P(III) form.[36] However, the mode of EG's and DME's action could only be speculated at this stage. It was found that 1.5 equivalents of aryl halide, 1.3 equivalents of *i*-Pr$_2$NEt, Pd(OAc)$_2$ (2 mol %), xantphos (2.2 mol %), toluene/EG (9:1, v/v), 110 °C were the best reaction conditions, with the conditions tried on a range of *H*-phosphinate esters and aryl

halides achieving yields of 47−86 %.[36] In 2012, Gavara *et al*. adapted these conditions, utilising the DME additive over EG for the cross-coupling of a *H*-phosphinate ester with ethyl-2-bromobenzoate.[35] These conditions were applied for the cross-coupling of ethyl methylphosphinate **22** and bromobenzaldehyde compounds **16a-c**, shown in **Scheme 5.7**. The reaction was first attempted with the dimethoxy analogue **16a**, heating at reflux over a period of 48 hours. Upon concentration of the reaction mixture under reduced pressure, the crude material was purified by silica column chromatography yielding a yellow solid, achieved in a 30 % yield. Synthesis of the diethoxy analogue **23b** was performed analogously, however the solid obtained post-purification contained multiple phosphorus-containing impurities, as seen by $^{31}P\{^{1}H\}$ NMR spectroscopy, the spectra of **23a** and post-purification **23b** are shown in **Figure 5.19**.

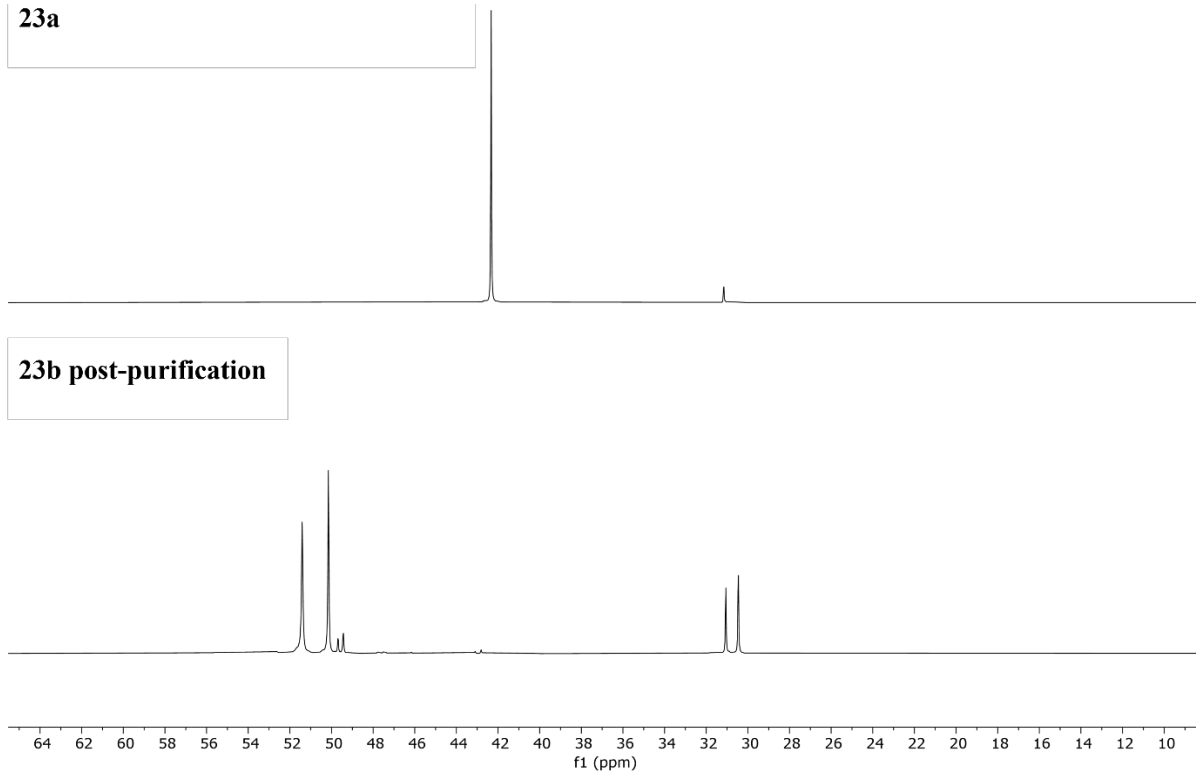

Figure 5.19 $^{31}P\{^{1}H\}$ NMR spectra of 2-ethyl(methyl)phosphinate-3,5-dialkoxybenzaldehydes **23a-b** ($CDCl_3$, 162 MHz, 298 K).

Aryl-phosphinate esters are known to have ^{31}P NMR shifts between 40 ppm and 50 ppm, meaning the desired products **23a-c** could be assigned using $^{31}P\{^{1}H\}$ NMR spectroscopy.[35,36] For the dimethoxy variant, two peaks were observed at 42.33 ppm and 31.16 ppm, corresponding to the product **23a** and a minor impurity respectively. The minor impurity was measured at less than 5 % of the overall sample and was deemed feasible to carry forward

without further purification. The diethoxy variant showed multiple peaks at 50 ppm and 30 ppm which could not be identified, nevertheless it was confirmed that the reaction did not yield the expected aryl-phosphinate.

Aryl-phosphinate **23a** was carried forward onto the synthesis of bis(AAPA)BDMAPEN compounds, shown in **Scheme 5.9**. Once a successful synthetic route has been established with the dimethoxy variant **a**, both diethoxy **b** and di-*iso*-propoxy **c** variants will be synthesised analogously. Due to the susceptibility of imine groups to hydrolyse in aqueous conditions, the deprotection of the aryl-phosphinate ester group was performed prior to the imine condensation reaction of **23a-c** and BDMAPEN **17**.

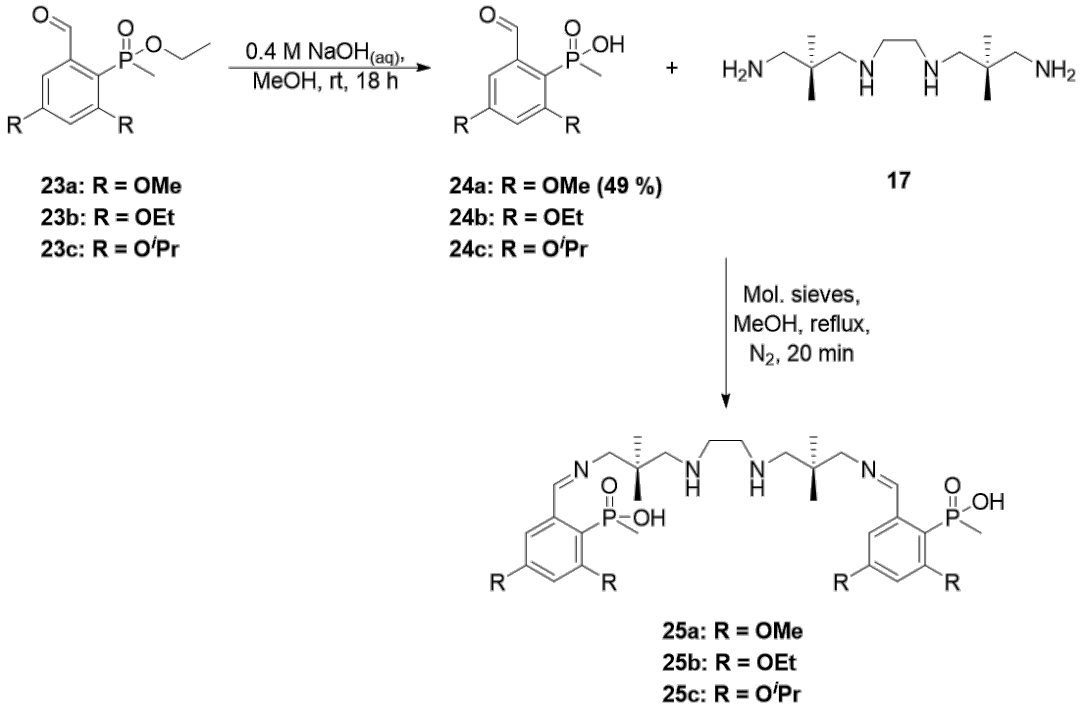

Scheme 5.9 Synthesis of bis(AAPA)BDMAPEN ligands **25a-c**. Aryl-phosphinate compounds **23a-c** were deprotected to give the respective aryl-phosphinic acid compounds **24a-c** using an adaptation of the method developed by Walter *et al*.[34] Imine condensation of **24a-c** and **17** was performed as a modification of the method reported by Tsang *et al*.[2,4]

Deprotection of the ethyl-protected phosphinate ester group of **23a** was performed using 0.4 M sodium hydroxide in water and methanol.[34] The reaction was monitored by TLC and $^{31}P\{^{1}H\}$ NMR spectroscopy. A downfield shift of the peak observed by $^{31}P\{^{1}H\}$ NMR spectroscopy was expected, using previous results in the literature, as a result of the conversion of the phosphinate group to the target phosphinic acid.[34] After stirring at room temperature for

18 hours, solvent was removed under vacuum and the crude residue was purified by reverse-phase chromatography to give the pure product as a yellow oil in a 49 % yield. Compound **24a** was characterised by ^{1}H and $^{31}P\{^{1}H\}$ NMR (**Figure 5.20**) spectroscopy, which showed a broad peak at 29.5 ppm with some sharp shoulders, and mass spectrometry showed a *m*/*z* value of 245 for the $[M+H]^{+}$ adduct. Regardless of the presence of the sharp shoulder peaks in the $^{31}P\{^{1}H\}$ NMR spectrum, this observation taken with the ^{1}H NMR spectrum and mass spectrometry confirm the synthesis of **24a** was successful.

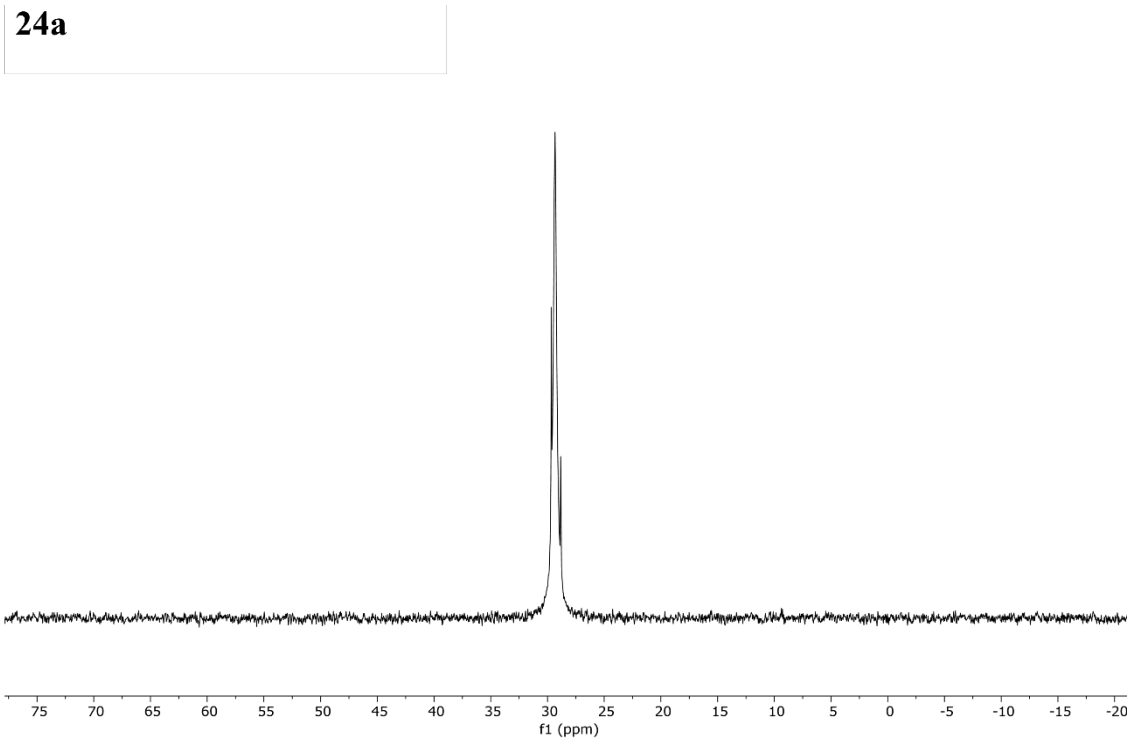

Figure 5.20 $^{31}P\{^{1}H\}$ NMR spectrum of **24a** (CD_3OD, 162 MHz, 298 K).

The next step in the synthetic route involved the condensation reaction between benzaldehyde-phosphinic acid analogue **24a** and the linear tetraamine **17** using methods discussed in section 5.1.1.[2,4,7] After refluxing **24a** and **17** in anhydrous methanol with molecular sieves for 3 hours, the reaction was deemed complete by ^{1}H NMR spectroscopy, due to the broad singlet at 10.95 ppm corresponding to the aldehyde proton of **24a**, no longer being observed. Upon addition of diethyl ether, a precipitate formed instantly, expected to be the aldehyde precursor **24a**, but could not be due to the disappearance of this resonance in the ^{1}H NMR spectrum, as discussed above. The filtrate was left to stand in the fridge overnight but did not result in the expected formation of a second precipitate. The first precipitate and filtrate were analysed by ^{1}H and $^{31}P\{^{1}H\}$ NMR spectroscopy. The ^{1}H NMR spectra of both the precipitate and filtrate confirmed no aldehyde species was present, however, no imine proton

peak could be identified either. The aromatic and aliphatic proton regions for both were complex and the product could not be identified accurately. The $^{31}P\{^{1}H\}$ NMR spectra of the filtrate showed that no phosphorus-containing species was present, whereas the precipitate confirmed a number of species with chemical shifts between 29 ppm and 30 ppm. Due to the potential hydrolysis of the imine groups in acidic/basic/aqueous conditions, as mentioned earlier, purification by column chromatography was not seen as a viable option.

Instead, the condensation of benzaldehyde-phosphinic acid compounds **24a-c** and the commercially available linear tetraamine bis(3-aminopropyl)ethylenediamine was investigated, using a modification of the method reported by Sharma *et al*., resulting in the synthesis of bis(AAPA)BAPEN ligands **26a-c**, shown in **Figure 5.21**.[7]

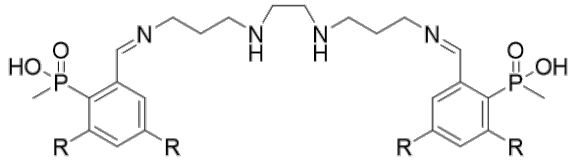

Figure 5.21 The general structure of bis(AAPA)BAPEN compounds **26a-c**, consisting of the BAPEN backbone. R = OMe, OEt, ^{i}OPr.

As mentioned in section 5.1.1, the purification of the linear tetraamine **17** involved vacuum distillation which did not yield a clean ^{1}H NMR spectrum, and instead the product was confirmed by mass spectrometry. The concern of compound **17**'s purity, led to the use of the commercially available bis(3-aminopropyl)ethylenediamine for the subsequent condensation reactions. The same strategy was applied for the bisAAPA ligands. Refluxing **24a** and bis(3-aminopropyl)ethylene diamine in anhydrous ethanol was monitored by ^{1}H and $^{31}P\{^{1}H\}$ NMR spectroscopy. Interestingly, allowing the reaction to proceed over a longer time period led to an increase in the number of imine proton peaks and phosphorus-containing species, identified by ^{1}H and $^{31}P\{^{1}H\}$ NMR spectroscopy respectively. A repeat of the reaction involved refluxing for 2 hours before the reaction was halted and worked up. Addition of diethyl ether to the crude material of **26a** caused instant precipitation, as expected, which was analysed by ^{1}H and $^{31}P\{^{1}H\}$ NMR spectroscopy. The NMR spectroscopic experiments confirmed the presence of phosphinic acid containing species, with imine protons also observed. It is thought that due to the increase in polarity from the hydroxyl to phosphinic acid group, the solubility of the imine product has changed, with the product no longer precipitating over an extended period of time at low temperatures. Instead, the potential imine product rapidly precipitates in

diethyl ether. Mass spectrometry was also used to identify the product **26a**, which was observed as a minor peak with a *m*/*z* value of 627 for the $[M+H]^+$ adduct. However, major impurities were also observed. Ideally, the final ligand, before complexation with Ga(III), should be pure and this could not be achieved without subjecting the imine compounds to conditions which could result in its hydrolysis. Due to time constraints, further investigations into the purification of this ligand type could not be completed but will instead provide a clear platform for any future work involving this ligand class.

5.2 Diaroylhydrazone Ligands as Gallium(III) Chelators

Salicylaldehyde isonicotinoyl hydrazone (SIH) is a tridentate ligand, which selectively form 2:1 complexes with Fe(III).[37] Aroylhydrazone-based Fe(III) chelators represent an interesting group of biologically active molecules.[38] The low molecular weight and optimal lipophilicity of SIH generated significant interest in its use for chelating Fe(III) cations, subsequently blocking the production of reactive oxygen species (ROS), linked to mitochondrial function.[39–41] In addition, SIH has also been shown to efficiently protect against cardiotoxic effects of anthracycline-based drugs, both in vitro and in vivo.[42,43] Despite its promise, SIH exhibits poor plasma stability, due to its labile hydrazone bond making the molecule prone to hydrolysis.[44]

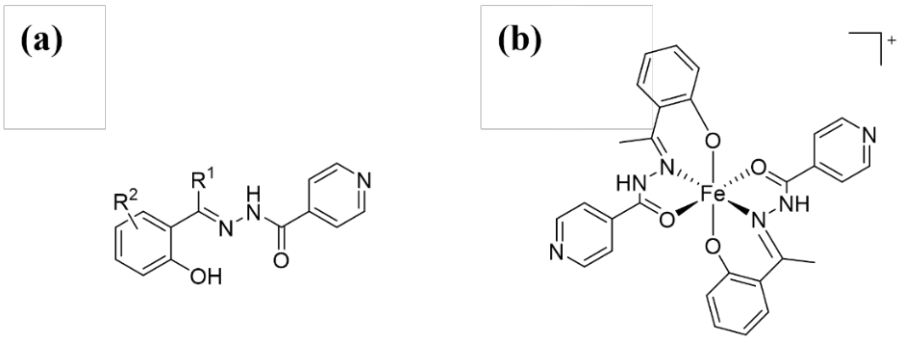

Figure 5.22 (a) General structure of HAPI derivatives.[44] R^1 = H, Me, Et; R^2 = H, 4-OH, 6-OH, 4-OMe, 5-Cl, 5-NO_2, 5-COMe. **(b)** The structure of $[Fe(HAPI)_2]^+$.[45]

In 2011, Hruskova *et al*. developed a series of (*E*)-*N*′-(1-(2-hydroxyphenyl)ethylidene)isonicotinohydrazide (HAPI) compounds, analogous to SIH, involving the substitution of salicylaldehyde by methyl- and ethyl-ketone with various electron donors and acceptors in the phenyl ring, shown in **Figure 5.22a**, with an aim to improve the stability of the hydrazone bond.[44] The formation of the 2:1 Fe(III) HAPI complexes exhibited an overall charge of +1, shown in **Figure 5.22b**.[45] Given that iron in its

+3 oxidation state is similar to Ga(III), in terms of charge, ionic radii (Fe^{3+} = 0.65 Å, Ga^{3+} = 0.62 Å), preferred coordination number (CN = 6), and chemical behaviour (both hard Lewis acids), these tridentate ligands could be used for Ga(III) chelation, and therefore have the potential to be used as ^{68}Ga-based radiotracers.[46]

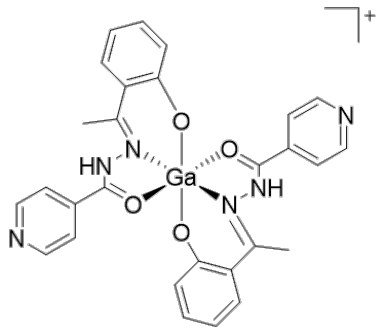

Figure 5.23 The structure of the Ga(III) complex $[Ga(HAPI)_2]^+$, consisting of a Ga(III) metal centre and two tridentate HAPI ligands.

Due to the Fe(III) complex, $[Fe(HAPI)_2]^+$, possessing an overall charge of +1, synthesising the HAPI ligand and generating the Ga(III) complex, $[Ga(HAPI)_2]^+$ shown in **Figure 5.23**, seemed obvious as the first step in the development of the second acyclic ligand set in this project.

5.2.1 Synthesis of the HAPI Ligand

The first step in the synthetic route to obtain the ligand, HAPI, **29** involved the methyl esterification of isonicotinic acid using methanol.[47] After the formation of the intermediate acyl chloride using a catalytic amount of DMF and one equivalent of oxalyl chloride, the mixture was cooled to 0 °C and methanol was added in a dropwise manner to initiate esterification. After stirring overnight, the reaction was quenched with sodium bicarbonate and pure methyl isonicotinate **27** was obtained as a colourless oil in a 97 % yield, after organic extraction work-up.

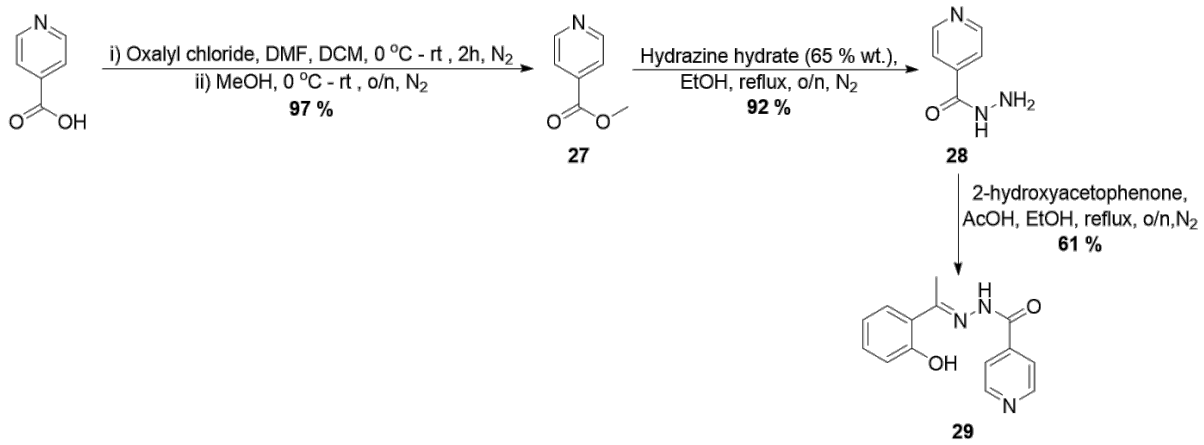

Scheme 5.10 The synthetic route to obtain HAPI **29**. Esterification of isonicotinic acid was performed according to Classen-Houben *et al*.[47] Isonicotinohydrazide **28** was synthesised using the an adaptation of the method reported by Cardoso *et al*.[48] HAPI was generated from the condensation reaction of **28** and 2-acetophenone according to Hruskova *et al*.[44]

The second step was to prepare the hydrazide analogue **28** by reacting the methyl ester **27** and hydrazine hydrate with refluxing in ethanol, which was performed as a modification of the procedure described by Cardoso *et al*.[48] Isonicotinohydrazide **28** was synthesised in an excellent yield of 92 %. The hydrazide **28** was then reacted with 2-hydroxyacetophenone in the presence of acetic acid to form the condensation product HAPI **29**, according to the methodology described by Hruskova *et al*.[44] The 3-step synthesis of HAPI **29** from isonicotinic acid was achieved in a total yield of 83 %. The ligand HAPI was characterised using NMR spectroscopy and mass spectrometry, with the findings in agreement with the literature.[44]

5.2.2 Non-Radioactive Reference $[Ga(HAPI)_2]^+$ Compound – Attempted Synthesis

As mentioned in section 2.2.5, synthesising a non-radioactive analogue of the respective radiotracer, to act as an isostructural reference compound, enables full characterisation including NMR spectroscopy and mass spectrometry, which is not possible with the radiolabelled complex. Following the procedure employed to synthesise the literature Fe(III) complex, $[Fe(HAPI)_2]^+$, the synthesis of $[Ga(HAPI)_2]^+$ **30**, shown in **Figure 5.24**, was attempted.[44] Iron trichloride was used as the source of Fe(III) to generate $[Fe(HAPI)_2]^+$ by Hruskova *et al*.[44] However, due to the reasons explained in section 2.2.5, including the instability and rapid formation of very stable, insoluble gallium hydroxide species, gallium trichloride was not used for the complexation of the HAPI ligand **29**.

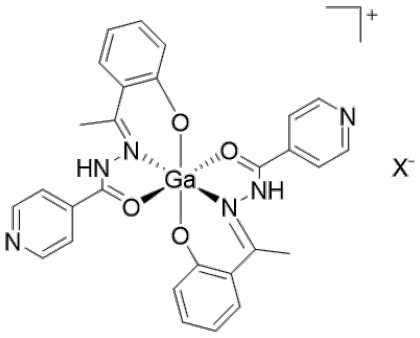

Figure 5.24 The structure of $[Ga(HAPI)_2]^+$ **30**, with the counter-ion denoted by X. X = $(acac)^-$, $(NO_3)^-$.

Instead, we used the more stable gallium trisacetylacetonate precursor as the source of Ga(III). One equivalent of $Ga(acac)_3$ and two equivalents of HAPI **29** were refluxed for one hour, resulting in the formation of an orange precipitate. The orange precipitate was isolated by filtration and characterised by NMR spectroscopy and mass spectrometry. NMR spectroscopy did not aid in elucidating the formation of the Ga(III) complex, however mass spectrometry showed two peaks at m/z = 256 and 577 corresponding to the ligand **29** and the complex **30** respectively. The major peak by mass spectrometry referred to the ligand **29** and the minor peak referred to the complex **30**. The ligand **29** was thought to be observed due to possible fragmentation of the complex **30**. To confirm this, analysis of the orange precipitate by LCMS was desirable to see if one UV active species could be observed. However, due to complex **30** being insoluble in water and acetonitrile, characterisation by LCMS could not be carried out. Complex **30** was found to be soluble in DMSO, but this was not ideal when considering its translation into the radiochemical and biological setting.

To assess the effect of the counter-ion on the solubility of the overall complex **30**, preparation of the Ga(III) complex using an alternative Ga(III) precursor, gallium trisnitrate was performed, leading to a nitrate anion as the counter-ion of **30** instead of acetylacetonate. Using a modification of the procedure reported by Pocrnić *et al*.[49] Two equivalents of **29** were dissolved in anhydrous ethanol, followed by the addition of gallium trisnitrate, immediately leading to a colour change from yellow to orange and precipitation occurred. After refluxing overnight, the orange precipitate was isolated by filtration and analysed by NMR spectroscopy (**Figure 5.25**) and mass spectrometry.

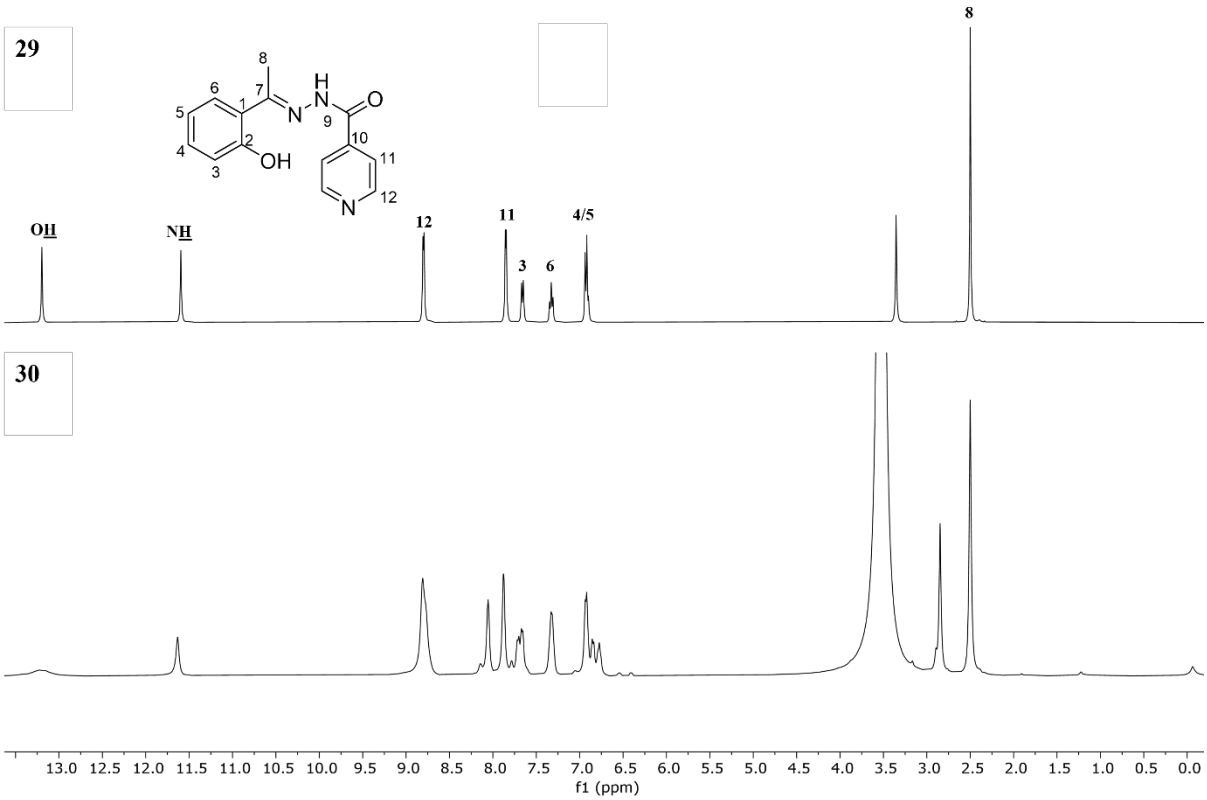

Figure 5.25 ^{1}H NMR spectra of HAPI **29** (top) and the orange precipitate obtained for the synthesis of [Ga(HAPI)$_2$][NO$_3$] **30** (DMSO-d_6, 400 MHz, 298 K).

The ^{1}H NMR spectrum of the orange precipitate showed a number of indicative peaks associated with the HAPI ligand, including a broad singlet at approximately 13.15 ppm referring to the salicylaldimine hydroxyl proton, and a singlet at approximately 11.60 ppm corresponding to amine proton of the hydrazone group. Interestingly, we still observed the hydroxyl protons suggesting complexation with Ga(III) had not occurred. In the aromatic region, a change in multiplicity for a number of proton environments was observed, namely H_{11}, H_4 and H_5 shown in **Figure 5.25** for ligand **29**. Nevertheless, deducing the formation of the Ga(III) complex **30** by NMR spectroscopy proved unfruitful. Further characterisation was attempted using mass spectrometry, including ESI-MS, LC-MS and MALDI-MS. As observed for the triacetylacetonate counter-ion analogue of **30**, the ESI-MS spectrum (**Figure 5.26**) showed two peaks, the major peak at m/z = 256 corresponding to the ligand **29**, and a minor peak at m/z = 577 corresponding to the complex **30**.

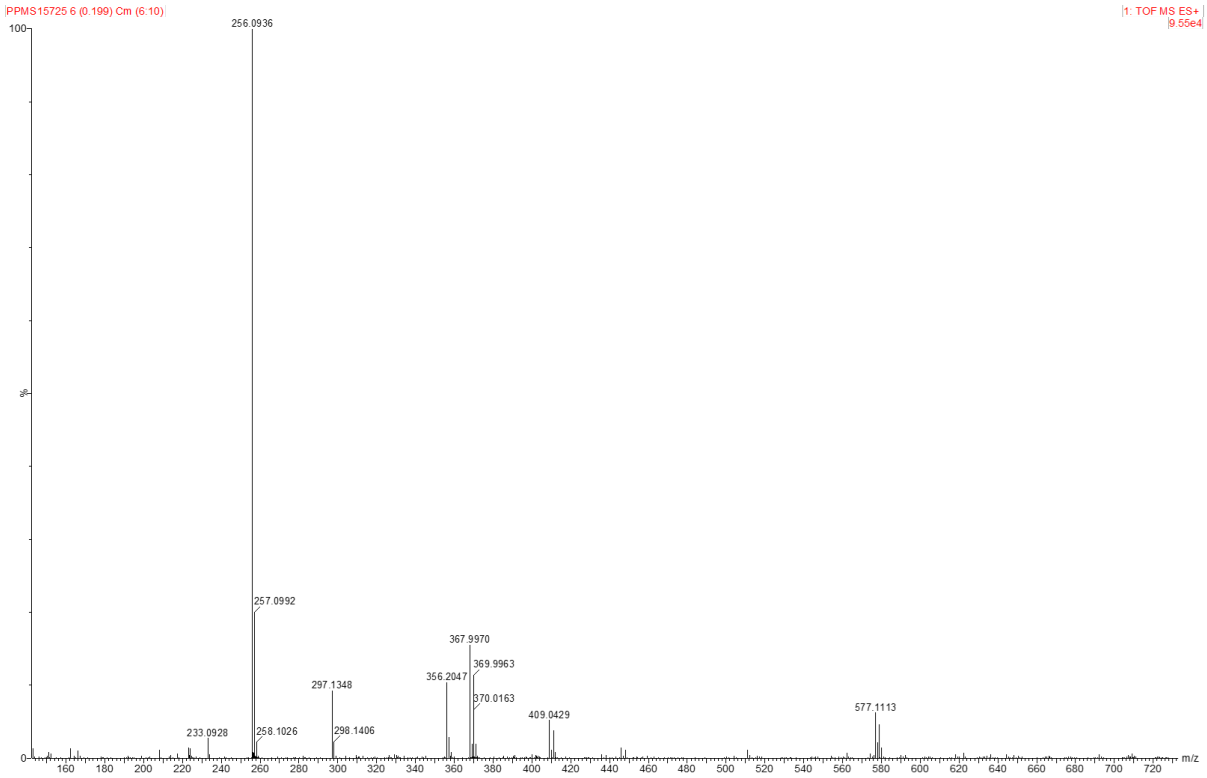

Figure 5.26 ESI-MS spectrum of the orange precipitate obtained from reaction forming the trisnitrate analogue of **30**.

The LC-MS spectrum of **30** showed one UV peak, however this corresponded to a *m*/*z* value of 256 for the precursor **29**. It is thought that the complex **30** could be degrading on the LC-MS column, or its solubility in water and acetonitrile, leading to the expected *m*/*z* value being absent. Analysis of the MALDI-MS spectrum of **30**, shown in **Figure 5.27**, confirmed the presence of the Ga(III) complex, but due to the low molecular weight of the ligand **29**, comparison of the ligand and complex was not feasible. Regardless of the compound **30** being confirmed by mass spectrometry, the solubility of the complex still proved to be problematic. Therefore, alterations of the chemical structure of the HAPI ligand **29** were explored to improve the solubility of the final Ga(III) complex to aid characterisation.

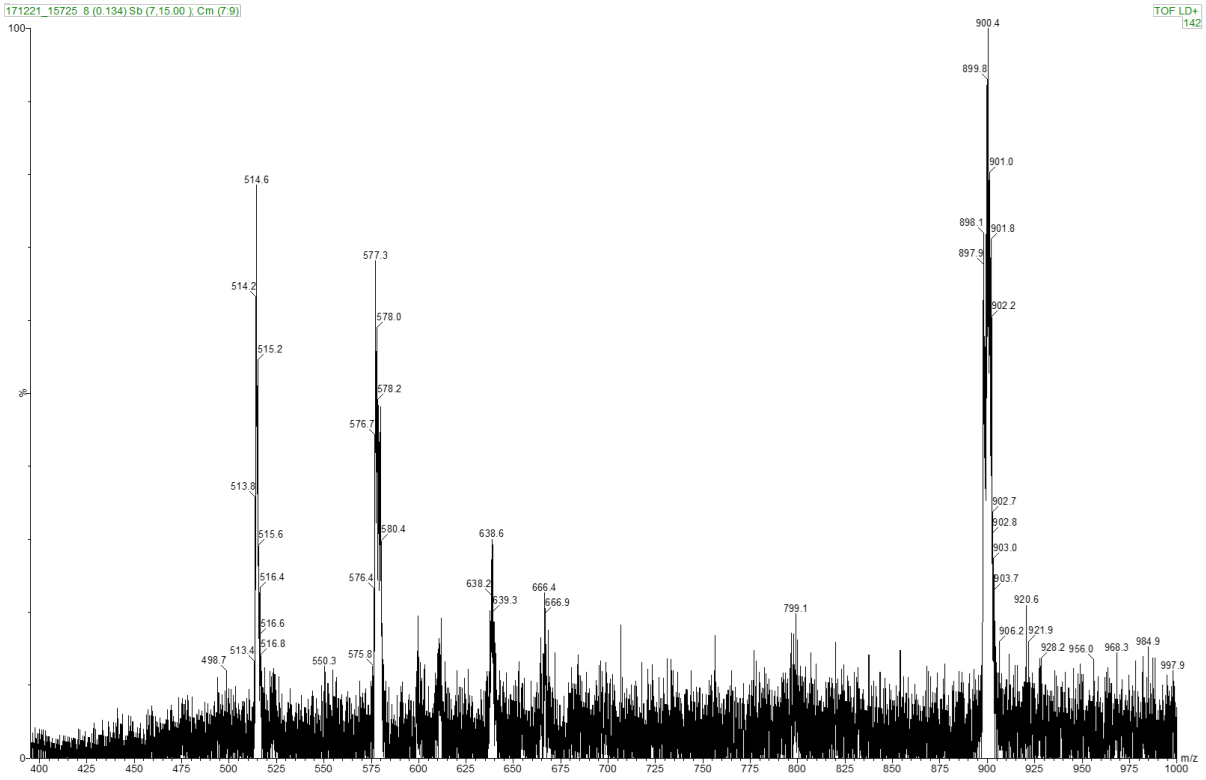

Figure 5.27 MALDI-MS spectrum of the **30** trisnitrate analogue.

Replacing the methyl group attached to the imine α-carbon with a phenyl group, and replacing the pyridyl moiety with a phenyl group was investigated to assess the solubility of the final Ga(III) complex. These HAPI analogues are shown below, in **Scheme 5.11**, and were synthesised analogously to compound **29**.

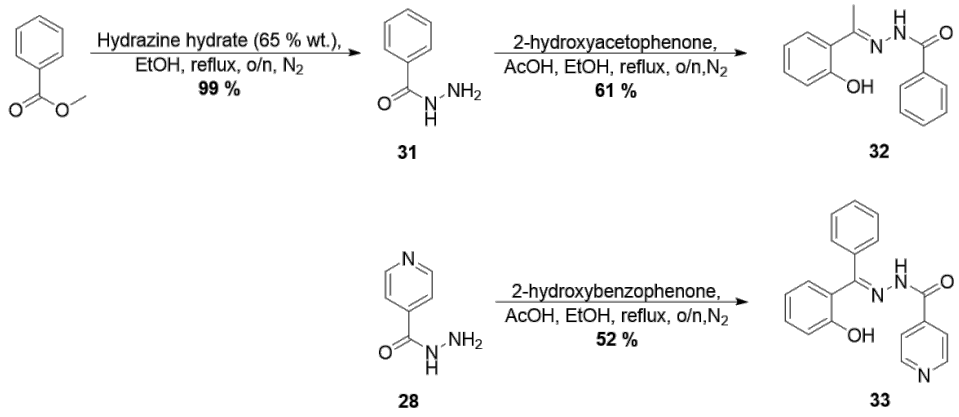

Scheme 5.11 Synthetic pathway of HAPI derivatives **32** and **33**, synthesised analogously to HAPI **29**.[44,48]

Both HAPI analogues were synthesised accordingly, in average yields.[44,48] Complexation of Ga(III) with compound **32** was performed using a modification of the method reported by

Pocrnić *et al*.[49] However, upon isolation of the formed precipitate, analysis by mass spectrometry showed no peak at the expected *m*/*z* value of 575. The mass spectrum of the filtrate did not display a peak corresponding to the product **Ga32** as well. As was seen for $[Ga(HAPI)_2]^+$ **30**, analysis by ^{1}H NMR spectroscopy was inconclusive. Spectroscopic analysis of **Ga33** was likewise not conclusive. Regardless of this, due to the insolubility of this family of compounds in all solvents, excluding DMSO, this work was not explored further. Efforts were directed towards the synthesis of alternative, more soluble, classes of ligands instead.

5.3 Asymmetric Ligands Containing Pyridine and Phenol Pendant-Arms for Gallium(III) Chelation

The use of [NN′O] ligands containing pyridine and phenol binding groups was explored to generate archetypical $[Fe^{III}(L^{NN'O})_2]^+$ complexes. This would help to better understand the geometric, electronic and redox properties of these complexes.[50] These ligands have previously been utilised for the synthesis of cobalt(III) complexes, also assessing their geometric, electronic and redox properties.[51] In 2006, five 2:1 Ga(III) [NN′O] complexes of this nature, shown in **Figure 5.28**, were reported by Shakya *et al*., and were tested for growth-inhibition activity on cisplatin-resistant human neuroblastoma cells.[52]

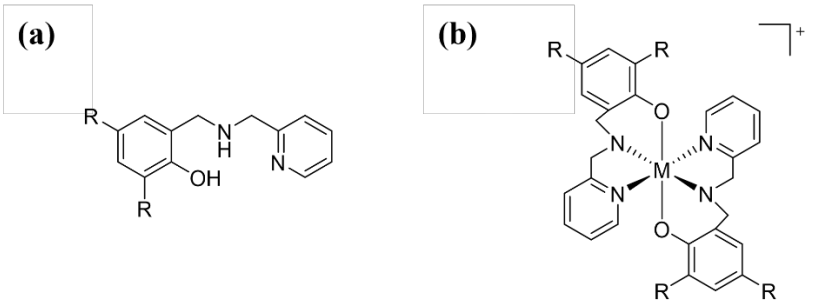

Figure 5.28 (a) The general structure of [NN′O] ligands. **(b)** Structure of 2:1 M(III) [NN′O] complexes, $[M^{III}(L^{NN'O})_2]^+$.[52–54] M = Fe(III), Co(III), Ga(III); R = H, *t*-Bu, OMe, NO_2, Cl, Br, I.

The structures of these Ga(III) complexes were determined by X-ray crystallography, which confirmed the Ga(III) ion was coordinated by two deprotonated ligands containing $N_{am}N_{py}O_{phen}$ sets of donors.[52] Both ligands are facially coordinated with two pyridine and two phenolate rings, and the two imine groups are arranged *trans* to each other, giving rise to a pseudo-octahedral geometry.[52] Since the publication of this article by Shakya *et al*. over a

decade ago, further investigations of these $[Ga^{III}(L^{NN'O})_2]ClO_4$ complexes have not been reported.[52]

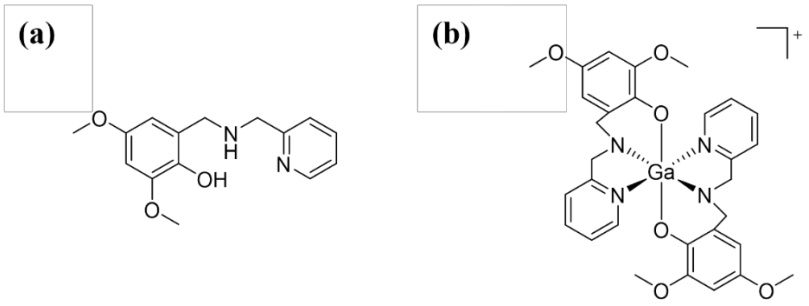

Figure 5.29 (a) Structure of the methoxy analogue of [NN′O] ligands. **(b)** Structure of $[Ga(L^{DiOMe})_2]^+$.

Replacing the insoluble hydrazone functionality of the compounds discussed in section 3.2 with more a more water-soluble secondary amine bridging group between the phenol and pyridine groups seemed to be the next logical step in synthesising a new family of Ga(III) complexes, an example is shown in **Figure 5.29**.

5.3.1 Synthesis of Asymmetric [NN′O] Ligands

The synthesis of the ligand L^{DiOMe} **34**, was achieved by condensation of salicylaldehyde **14a** with 2-picolylamine, followed by in situ reduction of the resulting imine species with sodium borohydride, shown in **Scheme 5.12** below.

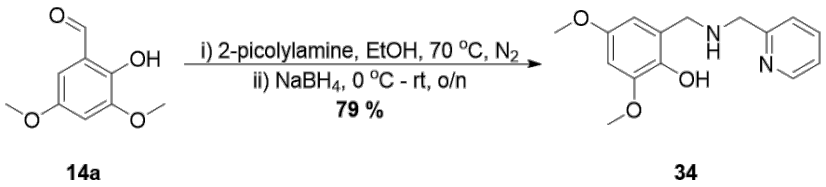

Scheme 5.12 The synthesis of ligand L^{DiOMe} **34**, achieved via the condensation and subsequent $NaBH_4$-assisted reduction of compound **14a** and 2-picolylamine. Performed as an adaptation of the method described by Shakya *et al*.[54]

The investigation of a 3,5-dimethoxy salicylaldehyde variant for this ligand-type has not been reported in the literature. It seemed obvious to begin exploring this family of compounds with the previously-accessed 3,5-dimethoxysalicylaldehyde precursor **14a**, before additional variants could be analogously synthesised. This allowed for the in situ condensation and reduction to generate the desired product **34**. Using an adaptation of the procedure described by Shakya *et al*., compound **14a** and 2-picolylamine in equimolar amounts were added to

anhydrous ethanol and the mixture was heated at 70 °C for six hours.[54] Following the generation of the imine intermediate, the reaction mixture was cooled to 0 °C and sodium borohydride was added in a portion wise manner. Once the addition was complete, the mixture was stirred at room temperature overnight, and the resulting crude residue was purified by silica flash chromatography to give the pure ligand **34** in a good yield.

5.3.2 Non-Radioactive Reference $[Ga(L^{DiOMe})_2]^+$ Compound – Attempted Synthesis

As mentioned in section 2.2.5, synthesising a non-radioactive analogue of the respective radiotracer, to act as an isostructural reference compound, enables full characterisation including NMR spectroscopy and mass spectrometry, which is not possible with the radiolabelled complex. Complexation of the Ga(III) metal ion with two equivalents of ligand **34** to give the complex **$[Ga(34)_2]^+$**, shown in **Figure 5.29**, was carried out using a modification of the protocol according to Shakya *et al*.[52] Shakya *et al*. reported the use of $GaCl_3$ for their experiments as the source of Ga(III). For reasons given previously, the more stable gallium trisnitrate was used instead. The solvent of choice in the literature was anhydrous methanol, however in order to assess the viability of the complexation reaction in buffer, a 1-to-1 mixture of water and methanol was used initially. This also elucidated whether the Ga(III) chelation could occur in normal atmospheric conditions. Therefore, gallium trisnitrate and two equivalents of **34** were added to a 1-to-1 mixture of water and methanol in the presence of triethylamine. The mixture was stirred at rt overnight. Two aliquots, one at the 1-hour time point and another after 18 hours were submitted for LC-MS analysis.

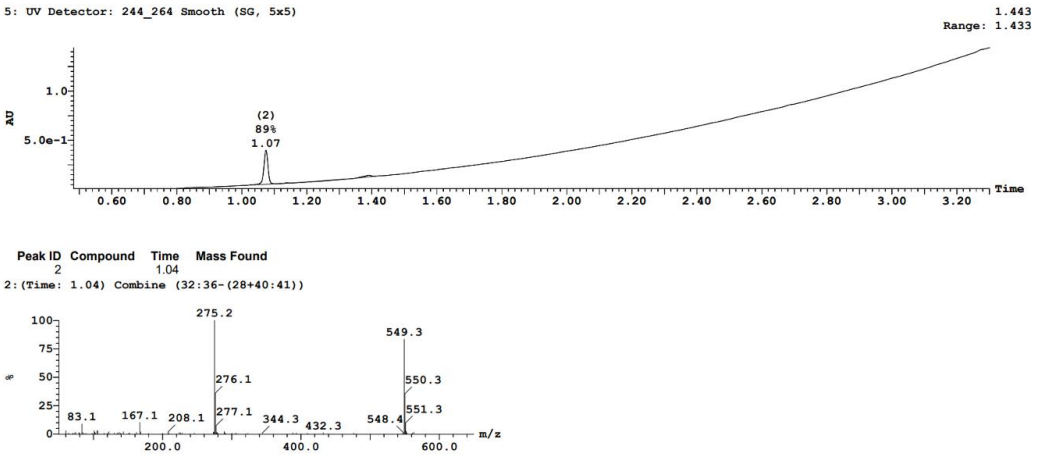

Figure 5.30 LC-MS spectrum of the sample taken at a reaction time of 18 hours for the synthesis of **$[Ga(34)_2]^+$**.

There was no significant change in the LC-MS spectra of the aliquots taken at reaction times 1 hour and 18 hours (**Figure 5.30**). Interestingly, in both samples a single UV active species was seen at 1.07 minutes, which corresponded to the ligand **34** with a *m*/*z* value of 275 and a dimerised version of **34** with a *m*/*z* value of 549. This was thought to be due to a hydrogen-bonding framework or π-stacking system. The expected *m*/*z* value of 613 for the Ga(III) complex was not observed.

Following the literature procedure by Shakya *et al*., anhydrous methanol was used as the solvent and the addition of sodium perchlorate after one hour was conducted. The addition of one equivalent of sodium perchlorate would promote the formation of the cationic 2:1 Ga(III) complex with the perchlorate anion as the counter-ion.[52] After 24 hours the crude material was analysed by LC-MS, but the same spectrum was recorded. Due to time constraints, successfully synthesising the Ga(III) complex $[Ga(L^{DiOMe})_2]^+$ was not investigated further.

5.4 Bis(Semicarbazone-Phosphonium) Chelates

The use of semicarbazones and thiosemicarbazones as chelators for metal ions has been widely explored in the literature, showing a variety of complex coordination modes for different applications.[55] These semicarbazone and thiosemicarbazone chelators, along with their derivatives, have been shown to possess promising pharmacological and biological properties, leading to significant interest in their medicinal applications.[56] Importantly, these ligand-types have been extensively investigated for the development of metal-based radiopharmaceuticals, some examples are shown below in **Figure 5.31**, and their exhibited versatility provides a basis for further structural manipulations to design new radiopharmaceuticals for diagnostic and therapeutic purposes.[57–63]

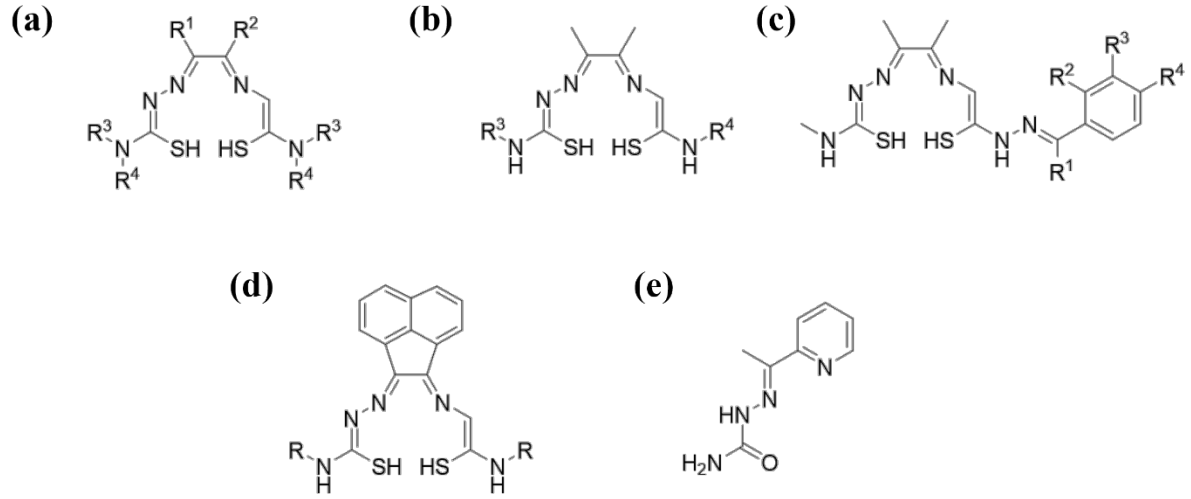

Figure 5.31 (a) General structure of bis(thiosemicarbazone) ligands developed by Dearling *et al*.[57] R^1 = H, Me, Et; R^2 = H, Me, Et; R^3 = H, Me, Et; R^4 = H, Me. **(b)** Structure of bis(thiosemicarbazone) ligands synthesised by Holland *et al*.[58] R^3 = Me, Et, Ph, Allyl; R^4 = Me, Et, NH_2. **(c)** Chemical structure of bis(thiosemicarbazone) ligands reported by Bonnitcha *et al*.[59] R^1 = H, Me; R^2 = H, OH; R^3 = H, NO_2; R^4 = H, NO_2, MeImidazoleNO_2. **(d)** Structure of bis(thiosemicarbazones) with aromatic backbone developed by Arrowsmith *et al*.[60] R = Me, Allyl. **(e)** 2-Acetylpyridine semicarbazone synthesised by Al-Hokbany *et al*.[62]

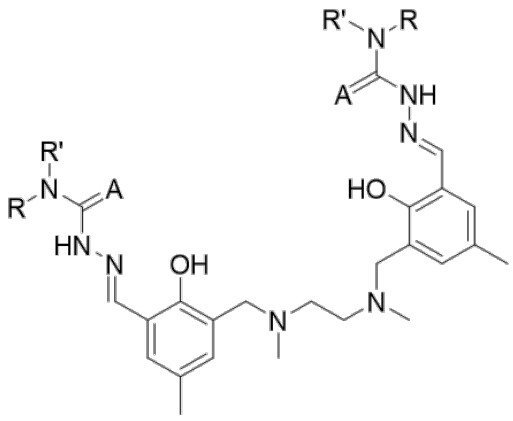

Figure 5.32 General chemical structure of bis(semicarbazone) (H_4bsc) and bis(thiosemicarbazone) (H_4btsc) chelates for Ga(III) and In(III) complexation respectively, synthesised by Prado *et al*.[64] H_4bsc: R = Ph; R′ = H; A = O. H_4btsc: R = Me; R′ = Me; A = S.

More recently, Prado *et al*. reported the synthesis of two novel hexadentate chelates shown in **Figure 5.32**, a bis(semicarbazone) (H_4bsc) and a bis(thiosemicarbazone) (H_4btsc), for the coordination of Ga(III) and In(III) respectively.[64] Both non-radioactive reference compounds, Ga(Hbsc) and In(Hbtsc), were prepared and characterised by FT-IR, NMR spectroscopy, mass spectrometry and single crystal X-ray diffraction analysis. Radiotracers, [^{67}Ga]Ga(Hbsc) and

[^{111}In]In(Hbtsc), were synthesised in high radiochemical yield and purity, confirmed by HPLC and iTLC analyses. Lipophilicity measurements of [^{67}Ga]Ga(Hbsc) gave a log *P* value of 1.40, which indicates that this radiocomplexes lipophilicity is already in the ideal range for developing lipophilic and cationic compounds to target mitochondrial dysfunction. Biodistribution experiments in CD-1 mice showed high uptake of both radiotracers in the liver and intestine, with [^{67}Ga]Ga(Hbsc) exhibiting higher retention. In vitro and in vivo studies also showed a higher stability of the ^{67}Ga-based complex compared to the ^{111}In-based complex, notably in blood. It was concluded that the ^{67}Ga-radiocomplex was a promising candidate warranting further investigation due to its radiolabelling efficiency (RCY > 95 %) at ambient temperature, and a fast reaction time (15 minutes).[64]

Interestingly, X-ray characterisation of Ga(Hbsc) showed that the complex was obtained as a zwitterion following the deprotonation of both phenolic oxygens and both nitrogen atoms of the carbazone groups upon coordination of the ligand to the Ga(III) metal centre. Three of the released protons were found to be transferred to the acetylacetonate (acac) ligands, and the fourth proton was transferred to one of the nitrogen atoms of the ligand *N*,*N*′-dimethylethylenediamine bridge.[64] This results in the final complex having an overall neutral charge.

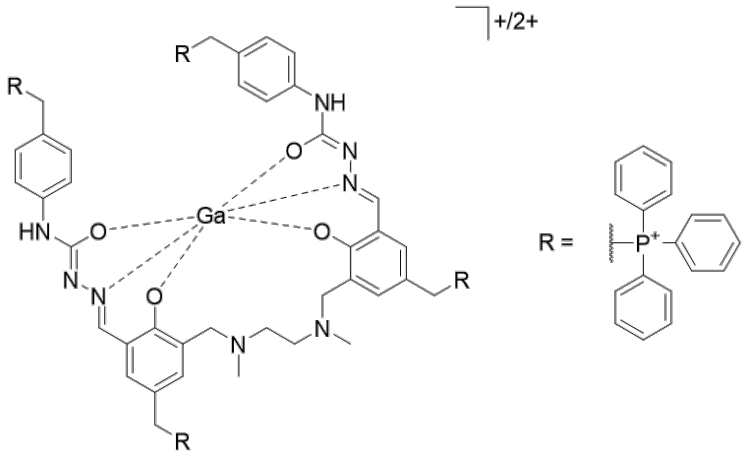

Figure 5.33 Structure of the target [Ga(Hbsc-(TPP)$_2$] complex. R = H or TPP.

Functionalisation of the H$_4$bsc ligand scaffold with triarylphosphonium (TAP) cations to generate a mitochondrial-targeted cationic and lipophilic ^{68}Ga-bis(semicarbazone) complex seemed like the obvious place to start in exploiting this promising class of compounds. At first the aim was to functionalise the literature compound H$_4$bsc with the triphenylphosphonium (TPP) cation, shown in **Figure 5.33**, and once a viable synthetic route is established, other

triarylphosphonium (TAP) groups will be synthesised analogously. Two sites of the chemical structure were identified for TAP-functionalisation, the first involved functionalisation of the *para*-methyl groups of the salen aryl units, and the second was to functionalise the phenyl groups of the semicarbazone units.

5.4.1 Synthesis of Salan-(2-Formyl-4-MethylTPP)$_2$

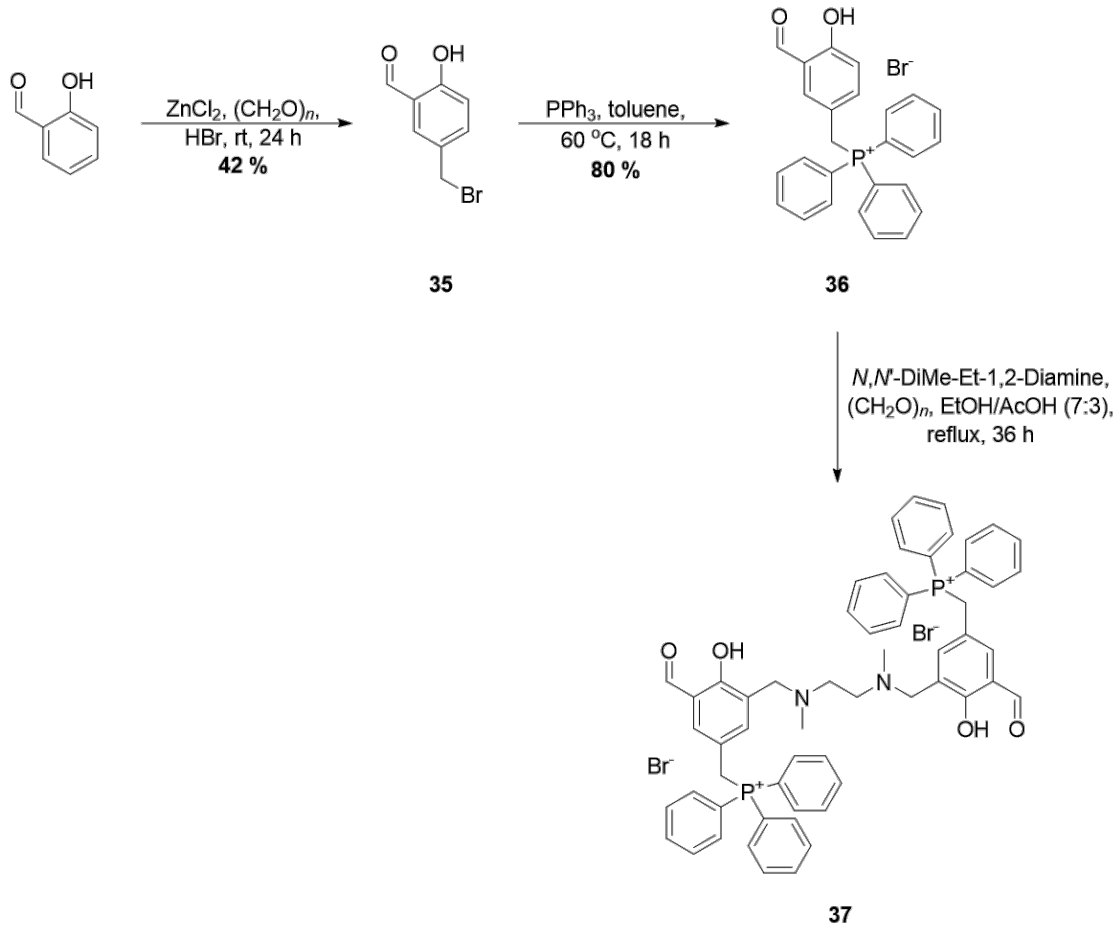

Scheme 5.13 The synthetic pathway to generate salan-(2-formyl-4-methylTPP)$_2$ dibromide **37**. Compound **35** was prepared according to Zhang *et al*.[65] Sal-MeTPP **36** was synthesised using a modification of the procedure by Smith *et al*.[66] Salan-(2-formyl-4-MeTPP)$_2$ **37** was obtained using a modification of the protocol by Thilagar *et al*.[67]

First, the functionalisation of the *para*-methyl groups of the salen aromatic rings was investigated. The first three synthetic steps to synthesise the target ligand H$_4$bsc-(TPP)$_2$ are shown in **Scheme 5.13**. The first step involved the formylation of salicylaldehyde using zinc chloride and paraformaldehyde, before reacting with hydrobromic acid to give (5-bromomethyl)-2-hydroxybenzaldehyde **35**.[65] The second step was to substitute compound

35 with triphenylphosphine to give the phosphonium salt (5-TPPmethyl)-2-hydroxybenzaldehyde **36** using conditions discussed in section 2.2.1.[66] The in situ condensation, imine reduction and formylation of *N*,*N*′-dimethylethylene-1,2-diamine and 3-/4-substituted salicylaldehyde compounds is documented in the literature.[67] These conditions were employed for the synthesis of **37**. Thilagar *et al*. purified their salan compounds with a simple recrystallisation from chloroform, this however was unsuccessful for **37**.[67] Purification by column chromatography also proved ineffective. The reported success of this reaction with 5-bromo-2-hydroxybenzaldehyde led to attempts using compound **35**. TPP-substitution could be performed after the salan product was formed. However, this did not work for compound **35** either.

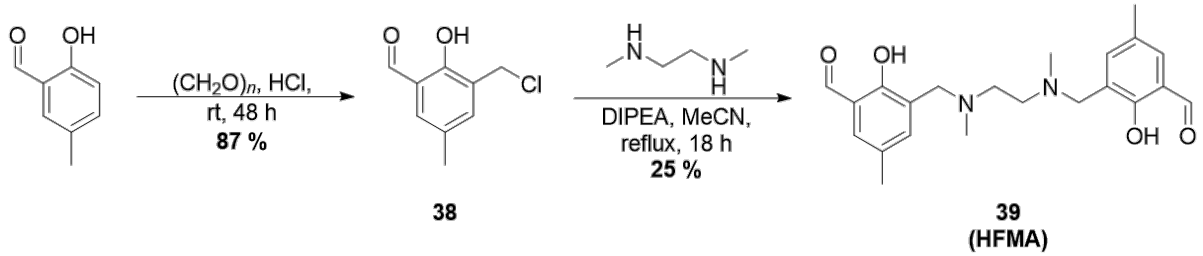

Scheme 5.14 Synthesis of the literature compound HFMA **39**. The precursor **38** was prepared according to the procedure by Akutsu-Suyama *et al*.[68] HFMA was synthesised using standard nucleophilic substitution conditions.

The literature salan compound HFMA shown in **Scheme 5.14**, used in the development of the H_4bsc ligand, is synthesised via simple nucleophilic substitution of *N*,*N*′-dimethylethylene-1,2-diamine and two equivalents of 3-(chloromethyl)-2-hydroxy-5-methylbenzaldehyde, however, reagents and conditions for this reaction have not been documented in literature. Standard substitution reaction conditions, refluxing reagents in the presence of a weak base in acetonitrile, afforded the literature compound HFMA.

Applying this strategy to the target bisTPP-functionalised salan compound, HFMA$(TPP)_2$ **37**, led to the preparation of a 3-substituted analogue of compound **36**. This would afford a methyl halide group in the 3-position to allow for the nucleophilic substitution of the diamine bridge precursor. This was attempted using paraformaldehyde and a strong acid, such as hydrochloric acid or hydrobromic acid, to give the respective methyl halide product, illustrated in **Scheme 5.15**.

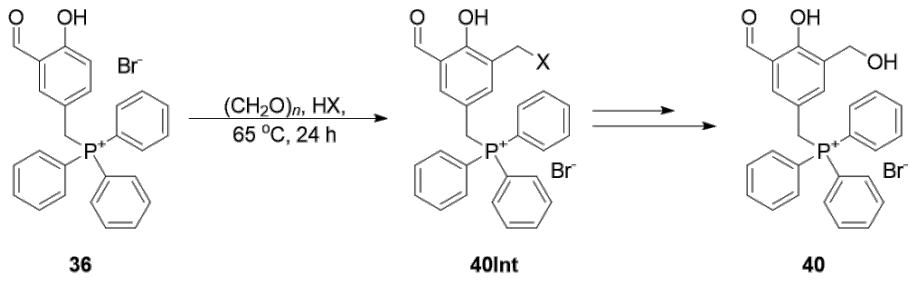

Scheme 5.15 Synthesis of a 3-methyl halide substituted analogue of **36**, **40Int**. The target compound **40Int** was generated using paraformaldehyde and a strong acid with heating. X = Cl, Br.

After heating at 65 °C for 24 hours, the product was extracted into DCM and concentrated under reduced pressure to give the product as an off-white solid in a near quantitative yield. Characterisation of the off-white solid by ^{1}H NMR spectroscopy showed all the expected peaks, which were fully assigned, shown in **Figure 5.34**.

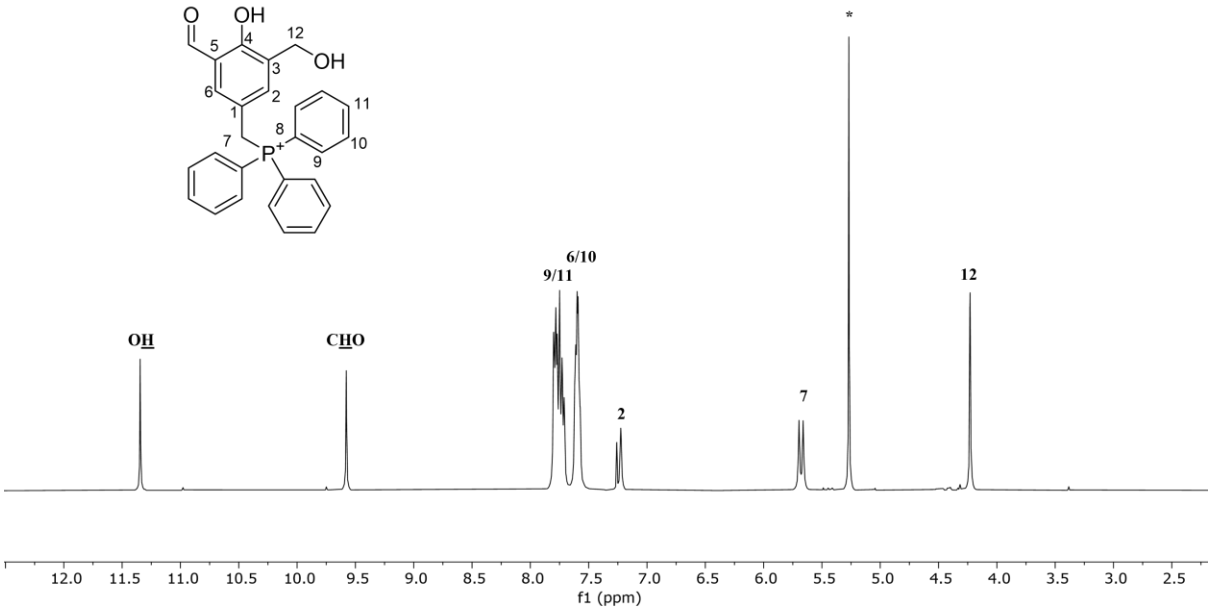

Figure 5.34 The ^{1}H NMR spectrum of **40** ($CDCl_3$, 400 MHz, 298 K), including the labelled structure and NMR characterisation. Solvent impurities, such as DCM, are denoted with an asterisk (*).

Analysis of **40Int** by $^{31}P\{^{1}H\}$ NMR spectroscopy also showed a singlet at 23.2 ppm corresponding to one phosphorus-containing species being present. However, LC-MS analysis showed one UV active species was present with a *m*/*z* value of 427 corresponding to a hydroxylated variant of **40Int**, compound **40**, and not the expected *m*/*z* values of 445 and 489 for the chloro- and bromo-analogues respectively. Attempts were made to convert **40** back to the respective bromo-analogue **40Int**, but once the hydroxylated-analogue **40** had formed it

became chemically inert. Even refluxing in concentrated hydrobromic acid for 4 days did not yield the desired product.[69]

5.4.2 Synthesis of a TPP-Benzyl-Functionalised Semicarbazide

As mentioned in section 3.4, two sites for TPP-functionalisation of the literature compound H_4bsc were identified. The first, mentioned in section 3.4.1, involved functionalising the methyl groups of the salen aromatic rings. The second, incorporates a TPP moiety on each semicarbazone unit, and was performed alongside the first strategy in tandem. In order to achieve this, a TPP-functionalised aromatic semicarbazide was prepared first, the schematic of which is shown below in **Scheme 5.16**.

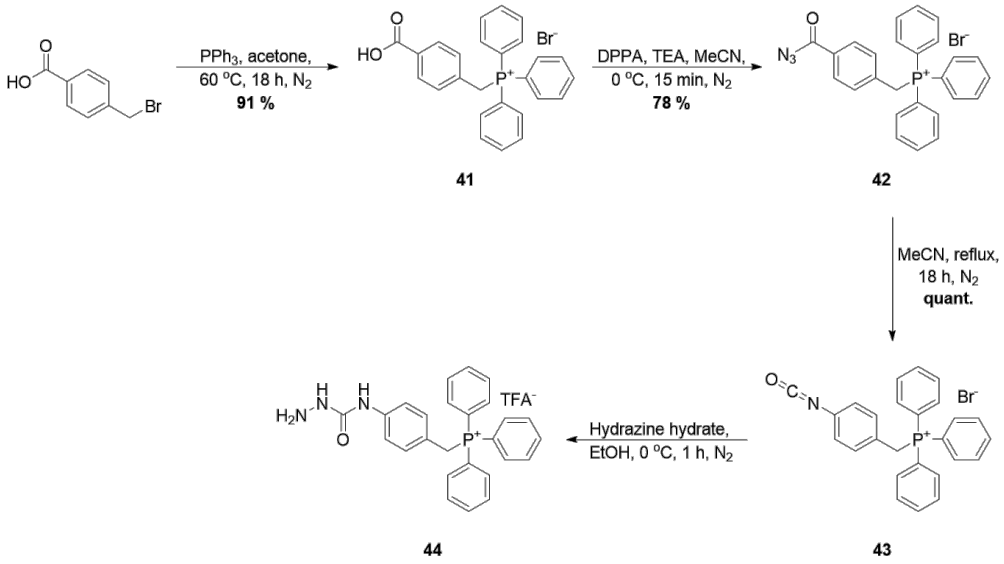

Scheme 5.16 Schematic outline of the synthesis of SC_BnTPP **44**. A TPP-functionalised benzoic acid **41** was prepared from 4-bromomethyl-benzoic acid and triphenylphosphine. The benzoic acid **41** was converted into the benzoyl azide **42** using an adaptation of the method by Shi *et al*.[70] The benzoyl azide precursor **42** underwent a Curtius rearrangement to form the intermediate isocyanate species **43**, which was reacted with hydrazine hydrate to form the target semicarbazide SC_BnTPP **44**, by combining methodologies by Loughlin *et al*. and Abdelatef *et al*.[71,72]

Starting with 4-bromomethyl-benzoic acid, the TPP-functionalised benzoic acid **41** was prepared using triphenylphosphine in acetone with heating at 60 °C in very good yield. Conversion of the benzoic acid **41** to the respective benzoyl azide **42** proceeded rapidly with the use of diphenylphosphorylazide (DPPA) and triethylamine at 0 °C over a 15 minute period.[70] Upon heating the acyl azide **42**, typically in acetonitrile, the compound underwent thermal decomposition to form the reactive isocyanate species **43**, via a Curtius

rearrangement.[71] After one hour of refluxing a white precipitate had started to form. This precipitate became more abundant in the solution overnight and the isocyanate species **43** was characterised by $^{31}P\{^{1}H\}$ NMR spectroscopy, which showed a single peak at 21.1 ppm, shifted from 22.4 ppm which corresponded to the precursor **42**. The extremely electrophilic isocyanate group makes **43** easily susceptible to nucleophilic attack from a range of nucleophiles, such as alcohols, amines and even water. To add to this, if the isocyanate nitrogen atom is situated next to an aromatic group, which is the case for compound **43**, the negative charge becomes delocalized across the ring system, making the isocyanate even more reactive. This would lend itself to the rapid subsequent reaction with hydrazine to form the target semicarbazide SC_BnTPP **44**, as has been shown by Abdelatef *et al*. for a range of phenylisocyanate compounds who achieved an average yield of 80 % with stirring in ethanol at 0 °C for one hour.[72]

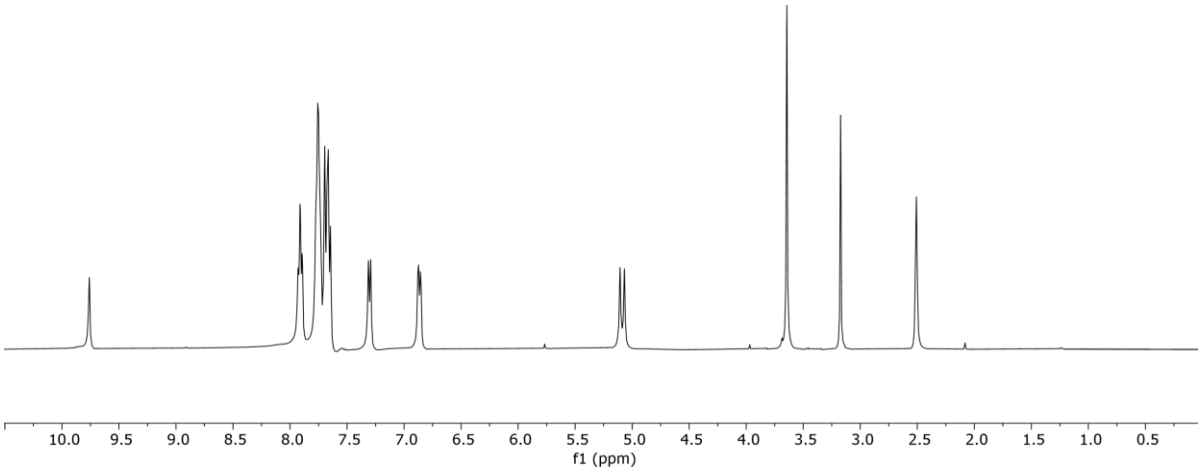

Figure 5.35 ^{1}H NMR spectrum of **44** post-purification (DMSO-d_6, 400 MHz, 298 K).

Instead of carrying this product forward without any further purification, as described in the literature procedure, the white solid obtained from the reaction was purified by reverse-phase chromatography, and the collected product fraction was analysed by NMR spectroscopy (**Figure 5.35**). All expected aromatic protons and methylene bridge protons (5.10 ppm) could be assigned, however a singlet at 3.64 ppm, with an integral referring to three protons, could not be assigned. At first, this was associated with an inert solvent impurity, therefore preliminary condensation reactions were commenced with HFMA, compound **39**, in the hope of synthesising the target ligand H_4bsc-$(TPP)_2$. However, first attempts of the condensation reaction using the first batch of SC_BnTPP did not work, resulting in both starting materials being collected from the reaction purification. A new batch of **44** was synthesised, this time characterisation using NMR spectroscopy gave two new peaks in the aliphatic region,

integrating as two and three protons respectively. Mass spectrometry was then used to elucidate the reason for these peaks observed in the NMR spectra, shown in **Figure 5.36**.

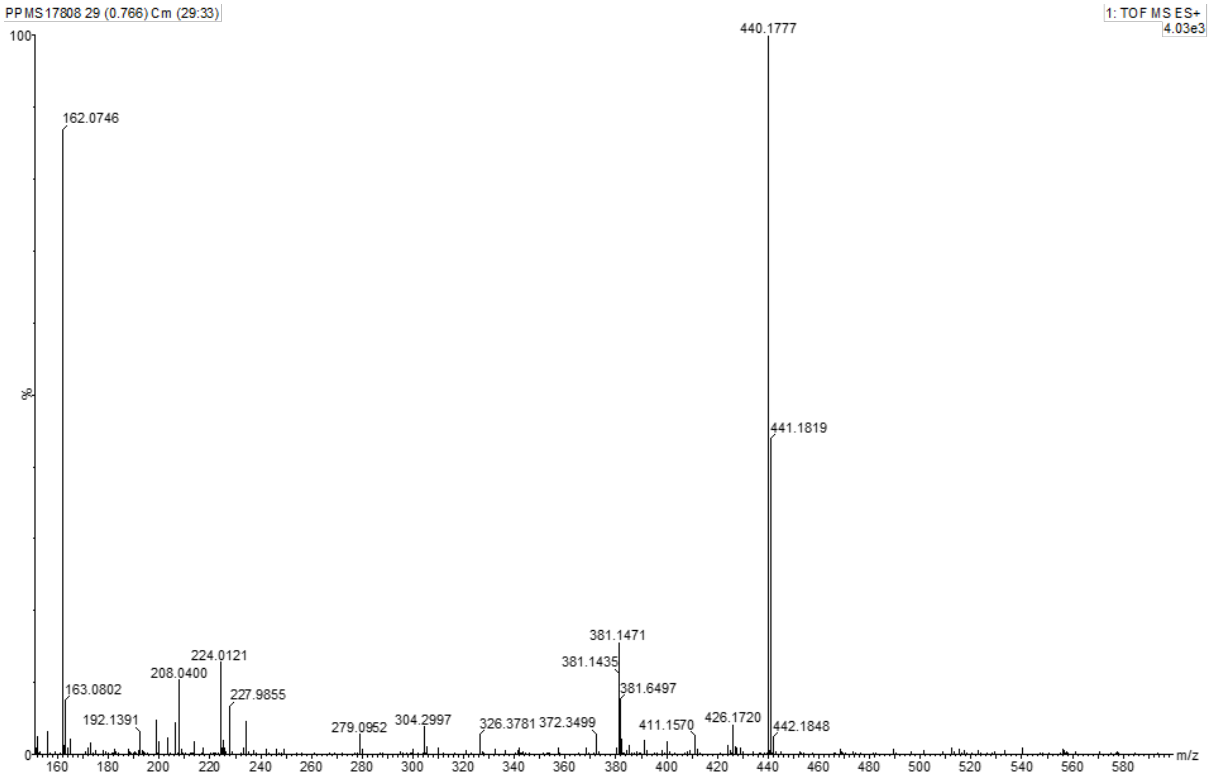

Figure 5.36 ESI-MS spectrum of the second batch of **44** synthesised.

The expected *m*/*z* value of 426 for the semicarbazide **44** was observed, albeit a very small peak, however the major peak at *m*/*z* value of 440 corresponded to an ethyl carbamate analogue of **44**, depicted in **Figure 5.37a**. This was corroborated by the two peaks observed in the NMR spectrum integrated to two and three protons referring to the ethyl group protons. As explained previously, reactivity of the isocyanate group with alcohols is well known, as such, reaction of the isocyanate group of **43** with the reaction solvents, such as methanol and ethanol, was not surprising. This explanation was applied to the first synthesised batch of **44** where the singlet at 3.64 ppm, shown in the NMR spectrum of **Figure 5.35**, corresponds to the methyl protons of the methyl carbamate analogue of **44**, shown in **Figure 5.37b**. The methyl carbamate analogue also has the same *m*/*z* value, 426, as the semicarbazide **44**, which further supports the formation of this analogue.

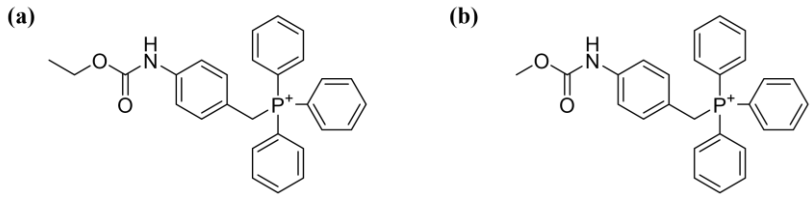

Figure 5.37 (a) Chemical structure of the ethyl carbamate derivative of **44**. **(b)** Chemical structure of the methyl carbamate derivative of **44**.

Carbamates are known to react with amine-based functional groups, such as hydrazine, to form semicarbazide products.[73] Knowing the synthesis of the target semicarbazide **44** results in the formation of carbamate analogues using the synthetic route shown in **Scheme 5.16**, this was still pursued with the aim of reacting these carbamates with hydrazine to form compound **44**. However, further manipulations of these carbamate compounds proved unsuccessful, therefore efforts were made to investigate the conversion of more reactive carbamate species with hydrazine to generate **44**, as an alternative strategy. Phenyl carbamates are known in the literature to be very reactive with amines, including hydrazine, and therefore a route to a TPP-functionalised phenyl carbamate was designed, shown in **Scheme 5.17**.[73]

This alternative synthetic route exploited the ease of nitro group reduction to the respective amine species, which can undergo amine protection with phenyl chloroformate to give the reactive phenyl carbamate compound. This route was initiated with the preparation of nitro-BnTPP **45** from the substitution of 4-nitrobenzylbromide and triphenylphosphine. The phosphonium salt product **45** was easily isolated from any unreacted starting materials via a simple filtration, which gave the product in near quantitative yields. Compound **45** then underwent nitro reduction to the amine-BnTPP salt **46** using a mixture of tin chloride and hydrochloric acid in methanol.[74] After gentle heating of the mixture overnight, the mixture was basified to pH 9 using 2 M sodium hydroxide solution, resulting in the precipitation of tin hydroxide, and as such, removing any tin from the reaction mixture. The filtrate was concentrated under reduced pressure and purified by column chromatography to yield pure **46**.

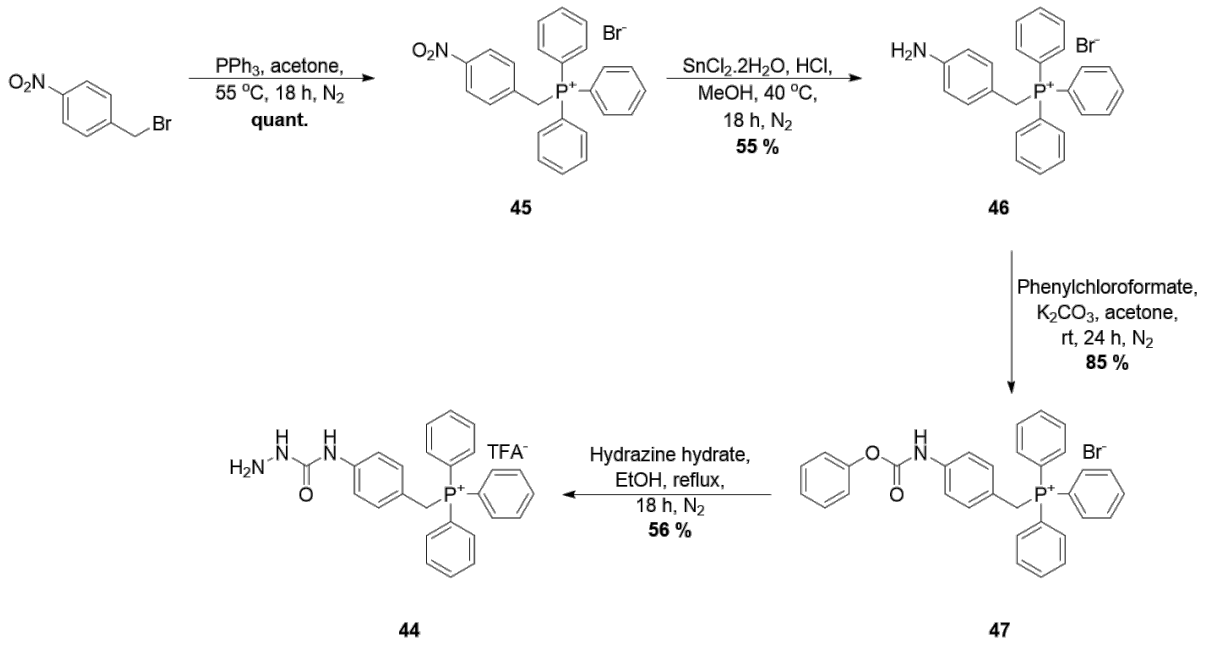

Scheme 5.17 The alternative synthetic route for the generation of SC_BnTPP **44**. The synthesis was initiated with the preparation of nitro-benzylTPP **45**. This was followed by the reduction of **45** to the respective amine species **46** using an adaptation of the method by Javadi *et al*.[74] The amine-benzylTPP **46** was then reacted with phenyl chloroformate to form the reactive phenyl carbamate-BnTPP **47** using a modified method by Noonepalle *et al*.[75] The reactive phenyl carbamate was converted into the desired semicarbazide **44** through refluxing with hydrazine hydrate.

The yellow solid, compound **46**, was reacted with phenyl chloroformate at room temperature for 24 hours to give the reactive phenyl carbamate species **47**, post-chromatographic purification, in very good yield. This carbamate was reacted immediately with hydrazine hydrate, with refluxing in ethanol overnight, to give the product, SC_BnTPP **44**, as a white solid. The pure product was obtained after the crude material was purified using reverse-phase chromatography, in water and acetonitrile doped with TFA, meaning formation of the TFA counter-ion to the phosphonium cation was highly probable, but not guaranteed. NMR and MS spectroscopic techniques facilitated comprehensive characterisation of **44**. This semicarbazide was ready for condensation with compound **39**, HFMA.

5.4.3 Condensation Reaction of Semicarbazide-benzylTPP and HFMA

The TPP-functionalised benzylsemicarbazide precursor **44** was reacted with HFMA **39** using standard imine condensation conditions, refluxing in anhydrous ethanol in the presence of molecular sieves, shown in **Scheme 5.18** below.

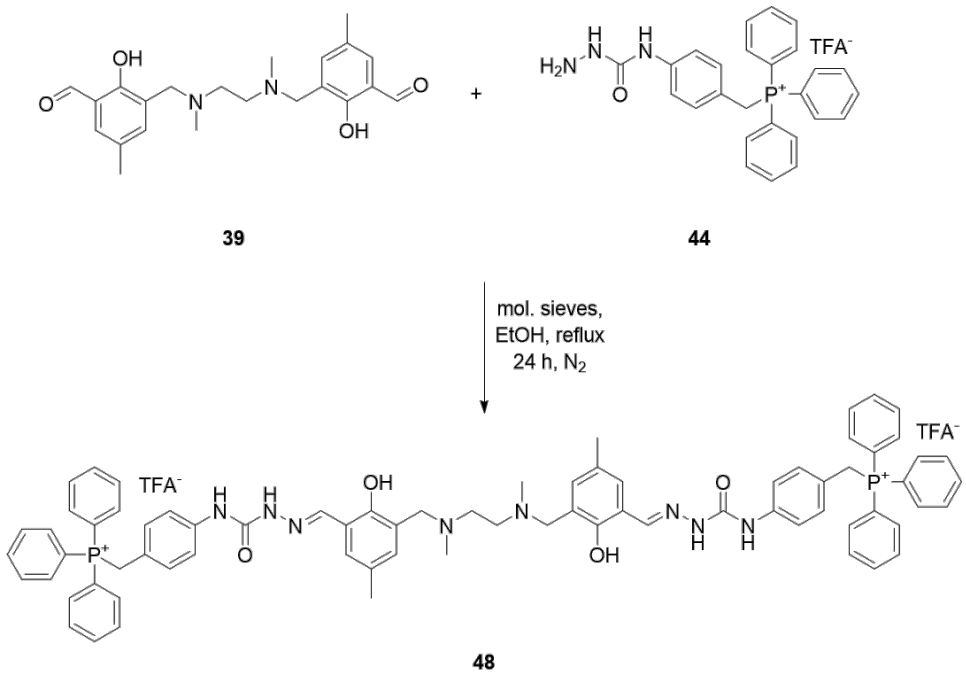

Scheme 5.18 The synthesis of H_4bsc-$(TPP)_2$ ligand **48**.

Two equivalents of the semicarbazide **44** were used to promote the formation of imines at both aldehyde group positions of HFMA **39**. The expected precipitation of the imine product **48** was not observed until the mixture had been refluxing for approximately 18 hours. After this reaction time point a grey precipitate started to form, and the mixture was stirred for an additional 6 hours before an aliquot of the grey precipitate was submitted for analysis by NMR spectroscopy and mass spectrometry. NMR spectroscopic experiments were not successful in helping identify the progress of the reaction due to the insolubility of the grey precipitate in all deuterated solvents.

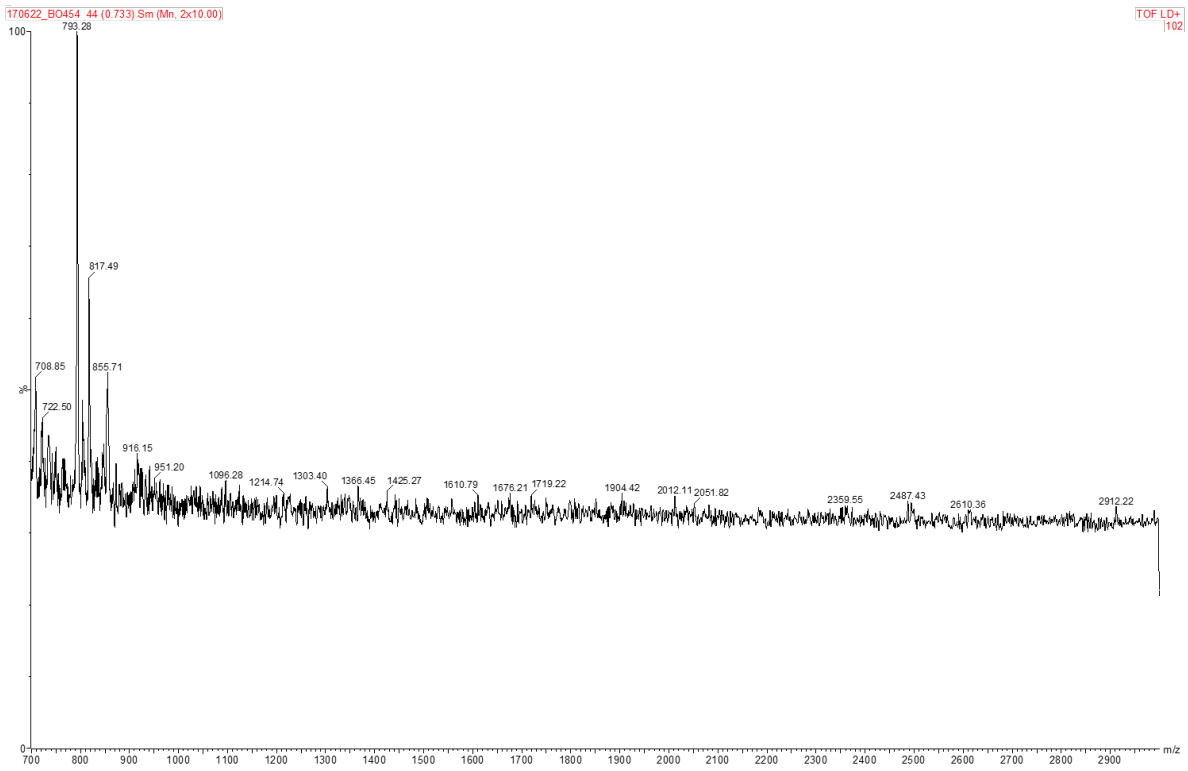

Figure 5.38 MALDI-MS spectrum of the grey precipitate formed in the synthesis of **48**.

Analysis by MALDI-MS, shown in **Figure 5.38**, showed a peak with *m*/*z* value of 793, referring to one of the aldehydes of **39** undergoing a condensation reaction with **44**. This was a promising observation as it proved that the two starting materials will react together, but the resulting mono-imine phosphonium salt is very insoluble meaning once it has formed, the second equivalent of **44** does not react with this intermediate to form the final ligand **48**. Condensation reactions performed by Prado *et al*. involved using a 1-to-1 mixture of methanol and acetonitrile, which is thought to be due to the solubility of the intermediate imine species formed, meaning it remains soluble in the solvent mixture and allows for the second imine group to form and generate the literature H_4bsc ligand.[64] Assessing the use of different solvent mixtures in aiding the formation of the desired ligand **48** would be the next step. However, due to time constraints, further investigations into the effect solvent systems will have on the formation of **48** was not carried out, but does provide a basis for future work to be performed for this family of ligands.

5.5 Concluding Remarks

This chapter outlines the synthesis of multiple series of acyclic ligands for the eventual formation of lipophilic and cationic gallium-68 complexes. First, the synthesis of new

bis(salicylaldimine) analogues based on 3,5-dialkoxy substituted salicylaldehyde precursors was investigated, with the Duff reaction proving to be the viable route in synthesising the target salicylaldehyde compounds.[28] 3,5- and 4,6-disubstituted salicylaldehydes were then reacted with two different tetraamine backbones to generate bis(salicylaldimine) ligands, however due to time constraints this ligand series could not be investigated further.[7] Secondly, the preparation of phosphinic acid analogues, bisAAPA ligands, of known bis(salicylaldimine) compounds was explored to assess the changes in gallium(III) labelling efficiency between phosphinate and phenolate coordinating groups, including the effect on the lipophilicity of the final complex. Purification of the methoxy analogue of the bisAAPA ligand series proved unsuccessful, unfortunately time constraints meant a viable purification method could not be found, however this work will instead provide a platform for any future endeavours involving this class of ligand.

Thirdly, the use of tridentate aroylhydrazone-based ligands, which selectively form lipophilic and monocationic 2:1 complexes with Fe(III), were explored as Ga(III) ligands, due to the similar charge, ionic radii, preferred coordination number and chemical behaviour of both metal ions.[37,38,46] These ligands would therefore lend themselves to be used as ^{68}Ga-based radiotracers for mitochondrial dysfunction. A new synthetic route was designed for the synthesis of the literature ligand HAPI, using a combination of literature procedures.[44,47,48] A non-radioactive reference compound, $[Ga(HAPI)_2][NO_3]$, was prepared using gallium nitrate as the Ga(III) source. Characterisation by NMR spectroscopy was inconclusive, whereas mass spectrometry did confirm formation of the complex, however the abundance of the complex compared to the ligand could not be determined. Along with this, the complex was obtained as an insoluble orange solid meaning it would be difficult to translate to radiosynthetic and biological settings. Analogues of the HAPI ligand were synthesised with a range of different functional groups to improve the solubility of the final complexes, however the solubility issue persisted even with these analogues.

Following on from the synthesis of the third aroylhydrazone ligand set, a second family of tridentate ligands were investigated, also selectively forming 2:1 Ga(III) complexes.[52] This fourth family of [NN′O] compounds incorporated further methoxy functionalisation of the aromatic rings to assess the effect on lipophilicity. Compared to the aroylhydrazone family of compounds, this family contains an amine bridge, thought to improve solubility, instead of the insoluble hydrazone bridge, which was also assessed. The ligand was synthesised using

2-picolylamine and 2-hydroxy-3,5-dimethoxysalicylaldehyde, prepared for the bis(salicylaldimine) compounds, using an adapted method described by Shakya *et al*.[52] The preparation of a non-radioactive reference compound was attempted, NMR spectroscopic data was inconclusive and mass spectrometry showed only the ligand was present, with no clear evidence of the Ga(III) complex having formed.

The final acyclic ligand family discussed in the chapter were the bis(semicarbazone-phosphonium) compounds which looked at combining the promise of bis(semicarbazone) chelates synthesised by Prado *et al*. for gallium-68 labelling, and the expertise in the Long group involving the functionalisation of triarylphosphonium cations for mitochondrial targeting.[64] Two structural sites, the phenyl unit of the semicarbazide precursor and the aromatic ring of the salan backbone, were functionalised with TPP groups. The attempted TPP-functionalisation of the salan backbone via the preparation of salan-(2-formyl-4-methylTPP)$_2$ was not successful.[65–67] Instead TPP-functionalisation of the semicarbazide precursor proved more successful. Initial condensation reactions of the TPP-functionalised semicarbazide and the literature HFMA compound was attempted. This resulted in the formation of an insoluble grey precipitate, confirmed by mass spectrometry only one of the HFMA aldehyde groups had reacted with the semicarbazide precursor, and the intermediate was very insoluble. Due to time constraints, a solvent system designed to keep this mono-imine intermediate species could not be achieved, however this provides a good starting point for any future work concerning this family of compounds.

5.6 References for Chapter 5

1 E. W. Price and C. Orvig, *Chem. Soc. Rev.*, 2014, **43**, 260–290.

2 B. W. Tsang, C. J. Mathias and M. A. Green, *J. Nucl. Med.*, 1993, **34**, 1127–31.

3 M. A. Green, C. J. Mathias, W. L. Neumann, P. E. Fanwick, M. Janik and E. A. Deutsch, *J. Nucl. Med.*, 1993, **34**, 228–233.

4 B. W. Tsang, C. J. Mathias, P. E. Fanwick and M. A. Green, *J. Med. Chem.*, 1994, **37**, 4400–4406.

5 Y.-M. Hsiao, C. J. Mathias, S.-P. Wey, P. E. Fanwick and M. A. Green, *Nucl. Med. Biol.*, 2009, **36**, 39–45.

6 M. Tarkia, A. Saraste, T. Saanijoki, V. Oikonen, T. Vähäsilta, M. Strandberg, C. Stark, T. Tolvanen, M. Teräs, T. Savunen, M. A. Green, J. Knuuti and A. Roivainen, *Nucl. Med. Biol.*, 2012, **39**, 715–723.

7 V. Sharma, J. Sivapackiam, S. E. Harpstrite, J. L. Prior, H. Gu, N. P. Rath and D. Piwnica-Worms, *PLoS One*, 2014, **9**, e109361.

8 D.-Y. Kim, S.-G. Cho and H.-S. Bom, *Nucl. Med. Mol. Imaging (2010).*, 2018, **52**, 266–278.

9 B. Das Sarma and J. C. Bailar, *J. Am. Chem. Soc.*, 1955, **77**, 5476–5480.

10 B. D. Sarma, K. R. Ray, R. E. Sievers and J. C. Bailar, *J. Am. Chem. Soc.*, 1964, **86**, 14–16.

11 E. Sinn, G. Sim, E. V Dose, M. F. Tweedle and L. J. Wilson, *J. Am. Chem. Soc.*, 1978, **100**, 3375–3390.

12 J. Sivapackiam, S. Kabra, S. Speidel, M. Sharma, R. Laforest, A. Salter, M. P. Rettig and V. Sharma, *PLoS One*, 2019, **14**, e0215579.

13 E. T. H. Yeh, A. T. Tong, D. J. Lenihan, S. W. Yusuf, J. Swafford, C. Champion, J.-B. Durand, H. Gibbs, A. A. Zafarmand and M. S. Ewer, *Circulation*, 2004, **109**, 3122–3131.

14 Z. M. Safee, F. Baark, E. C. T. Waters, M. Veronese, V. R. Pell, J. E. Clark, F. Mota, L. Livieratos, T. R. Eykyn, P. J. Blower and R. Southworth, *Sci. Rep.*, 2019, **9**, 216.

15 F. Mota, V. R. Pell, N. Singh, F. Baark, E. Waters, P. Sadasivam, R. Southworth and R. Yan, *Mol. Pharm.*, 2022, **19**, 18–25.

16 S. P. McCluskey, A. Haslop, C. Coello, R. N. Gunn, E. W. Tate, R. Southworth, C. Plisson, N. J. Long and L. A. Wells, *J. Nucl. Med.*, 2019, **60**, 1750–1756.

17 G. Máté, J. Šimeček, M. Pniok, I. Kertész, J. Notni, H.-J. Wester, L. Galuska and P. Hermann, *Molecules*, 2015, **20**, 13112–13126.

18 J. Notni, J. Šimeček, P. Hermann and H.-J. Wester, *Chem. - A Eur. J.*, 2011, **17**, 14718–14722.

19 M. I. Tsionou, C. E. Knapp, C. A. Foley, C. R. Munteanu, A. Cakebread, C. Imberti, T. R. Eykyn, J. D. Young, B. M. Paterson, P. J. Blower and M. T. Ma, *RSC Adv.*, 2017, **7**, 49586–49599.

20 T. M. Jones-Wilson, R. J. Motekaitis, Y. Sun, C. J. Anderson, A. E. Martell and M. J. Welch, *Nucl. Med. Biol.*, 1995, **22**, 859–868.

21 G. Gudipudi, S. R. Sagurthi, S. Perugu, G. Achaiah and G. L. David Krupadanam, *RSC Adv.*, 2014, **4**, 56489–56501.

22 C. M. G. Azevedo, C. M. M. Afonso, J. X. Soares, S. Reis, D. Sousa, R. T. Lima, M. H. Vasconcelos, M. Pedro, J. Barbosa, L. Gales and M. M. M. Pinto, *Eur. J. Med. Chem.*, 2013, **69**, 798–816.

23 M. Matsumoto, K. Kobayashi and Y. Hotta, *J. Org. Chem.*, 1984, **49**, 4740–4741.

24 T. V. Hansen and L. Skattebøl, *Org. Synth.*, 2005, 64–68.

25 World Intellectual Property Organization, WO 2008/107363 A1, 2008, 1–53.

26 Y.-R. Liao, P.-C. Kuo, S.-C. Huang, J.-W. Liang and T.-S. Wu, *Tetrahedron Lett.*, 2012, **53**, 6202–6204.

27 J. E. Ellis and S. R. Lenger, *Synth. Commun.*, 1998, **28**, 1517–1524.

28 J. Zhang, K. Mu, P. Yang, X. Feng, D. Zhang, X. Fan, Q. Wang and S. Mao, *Bioorg. Chem.*, 2021, **115**, 105179.

29 C. B. Lindler, *The Duff Reaction: Researching A Modification*, 2014, https://thescholarship.ecu.edu/handle/10342/4463.

30 S. E. Harpstrite, J. L. Prior, J. Sivapackiam, S. D. Collins, N. P. Rath and V. Sharma, *Med. Chem.*, 2010, 6, 191–199.

31 S. E. Harpstrite, J. L. Prior, J. Sivapackiam, S. D. Collins, N. P. Rath and V. Sharma, *Med. Chem.*, 2017, **6**, 191–199.

32 H. D. Janse van Rensburg, L. J. Legoabe, G. Terre'Blanche and J. Aucamp, *Bioorg. Chem.*, 2020, **94**, 103459.

33 H. D. Janse van Rensburg, L. J. Legoabe, G. Terre'Blanche and J. Aucamp, *Bioorg. Chem.*, 2020, **94**, 103459.

34 E. R. H. Walter, M. A. Fox, D. Parker and J. A. G. Williams, *Dalton Trans.*, 2018, **47**, 1879–1887.

35 L. Gavara, C. Petit and J.-L. Montchamp, *Tetrahedron Lett.*, 2012, **53**, 5000–5003.

36 E. L. Deal, C. Petit and J.-L. Montchamp, *Org. Lett.*, 2011, **13**, 3270–3273.

37 J. T. Edward, M. Gauthier, F. L. Chubb and P. Ponka, *J. Chem. Eng. Data*, 1988, **33**, 538–540.

38 J. L. Buss, M. Hermes-Lima and P. Ponka, ed. C. Hershko, Springer US, Boston, MA, 2002, pp. 205–229.

39 M. Horackova, P. Ponka and Z. Byczko, *Cardiovasc. Res.*, 2000, **47**, 529–536.

40 T. Kurz, B. Gustafsson and U. T. Brunk, *FEBS J.*, 2006, **273**, 3106–3117.

41 T. Simůnek, C. Boer, R. A. Bouwman, R. Vlasblom, A. M. G. Versteilen, M. Sterba, V. Gersl, R. Hrdina, P. Ponka, J. J. de Lange, W. J. Paulus and R. J. P. Musters, *J. Mol. Cell. Cardiol.*, 2005, **39**, 345–354.

42 T. Simůnek, M. Sterba, O. Popelová, H. Kaiserová, M. Adamcová, M. Hroch, P. Hasková, P. Ponka and V. Gersl, *Br. J. Pharmacol.*, 2008, **155**, 138–148.

43 M. Štěrba, O. Popelová, T. Šimůnek, Y. Mazurová, A. Potáčová, M. Adamcová, I. Gunčová, H. Kaiserová, V. Palička, P. Poňka and V. Geršl, *Toxicology*, 2007, **235**, 150–166.

44 K. Hruskova, P. Kovarikova, P. Bendova, P. Haskova, E. Mackova, J. Stariat, A. Vavrova, K. Vavrova and T. Simunek, *Chem. Res. Toxicol.*, 2011, **24**, 290–302.

45 P. Hašková, H. Jansová, J. Bureš, M. Macháček, A. Jirkovská, K. J. Franz, P. Kovaříková and T. Šimůnek, *Toxicology*, 2016, **371**, 17–28.

46 K. D. Mjos, J. F. Cawthray, E. Polishchuk, M. J. Abrams and C. Orvig, *Dalton Trans.*, 2016, **45**, 13146–13160.

47 Patent Application Publications, US2013/0102600 A1, 2013.

48 L. N. F. Cardoso, T. C. M. Nogueira, F. A. R. Rodrigues, A. C. A. Oliveira, M. C. dos S. Luciano, C. Pessoa and M. V. N. de Souza, *Med. Chem. Res.*, 2017, **26**, 1605–1608.

49 M. Pocrnić, D. Kontrec, S. Miljanić, Ž. Soldin, A. Budimir and N. Galić, *J. Mol. Struct.*, 2021, **1227**, 129564.

50 R. Shakya, M. M. Allard, M. Johann, M. J. Heeg, E. Rentschler, J. M. Shearer, B. McGarvey and C. N. Verani, *Inorg. Chem.*, 2011, **50**, 8356–8366.

51 R. Shakya, C. Imbert, H. P. Hratchian, M. Lanznaster, M. J. Heeg, B. R. McGarvey, M. Allard, H. B. Schlegel and C. N. Verani, *Dalton Trans.*, 2006, 2517–2525.

52 R. Shakya, F. Peng, J. Liu, M. J. Heeg and C. N. Verani, *Inorg. Chem.*, 2006, **45**, 6263–6268.

53 R. Shakya, M. M. Allard, M. Johann, M. J. Heeg, E. Rentschler, J. M. Shearer, B. McGarvey and C. N. Verani, *Inorg. Chem.*, 2011, **50**, 8356–8366.

54 R. Shakya, C. Imbert, H. P. Hratchian, M. Lanznaster, M. J. Heeg, B. R. McGarvey, M. Allard, H. B. Schlegel and C. N. Verani, *Dalton Trans.*, 2006, 2517–2525.

55 J. S. Casas, M. S. García-Tasende and J. Sordo, *Coord. Chem. Rev.*, 2000, **209**, 197–261.

56 F. R. Pavan, P. I. d. S. Maia, S. R. A. Leite, V. M. Deflon, A. A. Batista, D. N. Sato, S. G. Franzblau and C. Q. F. Leite, *Eur. J. Med. Chem.*, 2010, **45**, 1898–1905.

57 J. L. J. Dearling and P. J. Blower, *Chem. Commun.*, 1998, 2531–2532.

58 J. P. Holland, F. I. Aigbirhio, H. M. Betts, P. D. Bonnitcha, P. Burke, M. Christlieb, G. C. Churchill, A. R. Cowley, J. R. Dilworth, P. S. Donnelly, J. C. Green, J. M. Peach, S. R. Vasudevan and J. E. Warren, *Inorg. Chem.*, 2007, **46**, 465–485.

59 P. D. Bonnitcha, A. L. Vāvere, J. S. Lewis and J. R. Dilworth, *J. Med. Chem.*, 2008, **51**, 2985–2991.

60 R. L. Arrowsmith, P. A. Waghorn, M. W. Jones, A. Bauman, S. K. Brayshaw, Z. Hu, G. Kociok-Köhn, T. L. Mindt, R. M. Tyrrell, S. W. Botchway, J. R. Dilworth and S. I. Pascu, *Dalton Trans.*, 2011, **40**, 6238–6252.

61 J. R. Dilworth and R. Hueting, *Inorganica Chim. Acta*, 2012, **389**, 3–15.

62 N. S. Al-Hokbany, B. Alotaibi, S. Bin Amer, S. M. Okarvi and I. Al-Jammaz, *J. Chem.*, 2014, **2014**, 616459.

63 I. S. Alam, R. L. Arrowsmith, F. Cortezon-Tamarit, F. Twyman, G. Kociok-Köhn, S. W. Botchway, J. R. Dilworth, L. Carroll, E. O. Aboagye and S. I. Pascu, *Dalton Trans.*, 2016, **45**, 144–155.

64 V. S. Prado, R. C. F. Leitao, F. Silva, L. Gano, I. C. Santos, F. L. N. Marques, A. Paulo and V. M. Deflon, *Dalton Trans.*, 2021, **50**, 1631–1640.

65 R.-Y. Zhang, Y. Zhang, J. Tong, L. Liu and Z.-B. Han, *Catal. Letters*, 2021, **151**, 2833–2841.

66 A. J. Smith, P. J. Gawne, M. T. Ma, P. J. Blower, R. Southworth and N. J. Long, *Dalton Trans.*, 2018, **47**, 15448–15457.

67 P. Thilagar, P. Sudhakar, P. Chinna Ayya Swamy and S. Mukherjee, *Inorganica Chim. Acta*, 2012, **390**, 163–166.

68 K. Akutsu-Suyama, S. Mori and T. Hanashima, *Photochem. Photobiol. Sci.*, 2019, **18**, 2531–2538.

69 L. Lecarme, E. Prado, A. De Rache, M.-L. Nicolau-Travers, G. Gellon, J. Dejeu, T. Lavergne, H. Jamet, D. Gomez, J.-L. Mergny, E. Defrancq, O. Jarjayes and F. Thomas, *ChemMedChem*, 2016, **11**, 1133–1136.

70 S. Shi, C. Yao, J. Cen, L. Li, G. Liu, J. Hu and S. Liu, *Angew. Chem. Int. Ed.*, 2020, **59**, 18172–18178.

71 W. A. Loughlin, I. D. Jenkins, N. D. Karis, S. S. Schweiker and P. C. Healy, *Eur. J. Med. Chem.*, 2016, **111**, 1–14.

72 S. A. Abdelatef, M. T. El-Saadi, N. H. Amin, A. H. Abdelazeem, H. A. Omar and K. R. A. Abdellatif, *Eur. J. Med. Chem.*, 2018, **150**, 567–578.

73 A. K. Ghosh and M. Brindisi, *J. Med. Chem.*, 2015, **58**, 2895–2940.

74 M. S. Javadi and J. Mokhtari, *J. Chinese Chem. Soc.*, 2012, **59**, 793–801.

75 S. Noonepalle, S. Shen, J. Ptáček, M. T. Tavares, G. Zhang, J. Stránský, J. Pavlíček, G. M. Ferreira, M. Hadley, G. Pelaez, C. Bařinka, A. P. Kozikowski and A. Villagra, *J.*

Med. Chem., 2020, **63**, 10246–10262.

CHAPTER 6 – CONCLUSIONS AND FUTURE WORK

6. Conclusions and Future Work

The focus of the work presented in this thesis was to synthesise a series of ligands for the formation of lipophilic and cationic gallium-68 complexes to report on mitochondrial dysfunction. This thesis was divided into four results chapters, first was the synthesis of macrocyclic-based ligands, with the subsequent assessment of their radiochemistry with gallium-68 and characterisation in the Langendorff isolated perfused heart model. The final results chapter describes the synthesis of acyclic-based ligands for the formation of lipophilic and cationic complexes with gallium-68.

6.1 The Synthesis of Lipophilic and Cationic Macrocyclic Ligands for Gallium-68

Chapter 2 begins with a summary of work performed by Dr Adam Smith in the Long group involving the preparation of DO2A-(xy-TAP)$_2$ and DO2A-Ar$_2$ compounds, and my subsequent synthetic contribution towards this work. This involved the synthesis of non-radioactive reference Ga(III) analogues of DO2A-(xy-TPP)$_2$ and DO2A-Bn$_2$ to aid in the investigation of the speciation observed for the radiolabelled counterparts.

Chapter 2 continues with the synthesis of a series of NODAGA-xy-TAP ligands. Initially, TAP-functionalised aminoxylene compounds were prepared from the respective TAP-functionalised bromoxylenes. Functionalisation of NODAGA(^{t}Bu)$_3$ with aminoxylenes afforded the protected NODAGA-xy-TAP compounds, which were subsequently deprotected using TFA to give a novel analogous series of ligands ready for labelling with gallium-68. Non-radioactive complexes were synthesised and found to exhibit one peak by HPLC analysis.

The final compounds mentioned in this chapter were the NODAGA-xy-TAEP series, which explored the effect ether-functionalisation has on the lipophilicity of the final complexes, compared to alkyl-functionalisation present in the NODAGA-xy-TAP compounds. This series of ligands and the respective reference Ga-NODAGA-xy-TAEP compounds were synthesised in an analogous fashion to the NODAGA-xy-TAP compounds.

Importantly, both NODAGA-based series of compounds illustrate the efficacy of TAP motifs to modulate radiotracer lipophilicity, and illustrate the compatibility of a range of aryl functionalisation with the acquisition of pure final compounds.

6.2 Gallium-68 Radiolabelling of Lipophilic and Cationic Macrocyclic Ligands

Chapter 3 describes the synthesis of [^{68}Ga]Ga-DO2A-(xy-TAP)$_2$ and [^{68}Ga]Ga-DO2A-Ar$_2$ compounds, with initial radiolabelling work on this series performed by Dr Adam Smith. RadioHPLC analysis showed the formation of kinetic and thermodynamic products in the reaction mixture, which was further confirmed through a series of experiments involving the alteration of reaction conditions.

The chapter continues with a discussion of the radiolabelling of macrocyclic NODAGA-based compounds with generator-produced gallium-68, together with an assessment of their potential as lipophilic and cationic radiotracers. Initially, [^{68}Ga]Ga-NODAGA-xy-TAP compounds were prepared in quantitative RCYs using high temperature conditions, with RCY values calculated using two fast iTLC QC methods. Through a series of reaction optimisation experiments, near quantitative radiolabelling was achieved at room temperature using a clinical grade buffer within 15 min. Each radiolabelled compound demonstrated a single peak by radioHPLC, which co-eluted with the non-radioactive reference compound, showing no presence of speciation and isomerism. These radiotracers exhibit superior lipophilicities compared to their DO3A-based counterparts, with [^{68}Ga]Ga-NODAGA-xy-TXP showing a log *D* value of -0.37 ± 0.21, a result of the removal of the unbound carboxylate arm in the DO3A counterparts discussed previously.

The radiolabelling of NODAGA-xy-TAEP ligands is then described, with the aim of assessing the effect of replacing alkyl groups with ether groups on the lipophilicity of the final compounds. The three radiolabelled [^{68}Ga]Ga-NODAGA-xy-TAEP compounds were prepared, using the radiolabelling conditions developed for the analogous NODAGA-xy-TAP series, in high to near-quantitative RCYs. Upon radioHPLC analysis, all three radiolabelled compounds demonstrated a single peak in the reaction mixture, which co-eluted with the non-radioactive reference compounds, showing a lack of speciation and isomerism. The incorporation of ether group on the TAP motif did not improve the lipophilicity of the radiotracer significantly compared to alkyl-functionalisation of the TAP motif. However, increasing the alkyl chain length of the methyl groups to ethyl groups considerably increased the log *D* value from -1.47 ± 0.26 for[^{68}Ga]Ga-NODAGA-xy-TMeOPP, to 0.01 ± 0.04 for [^{68}Ga]Ga-NODAGA-xy-TEtOPP, therefore showing an increase in the overall lipophilicity of the final radiotracer.

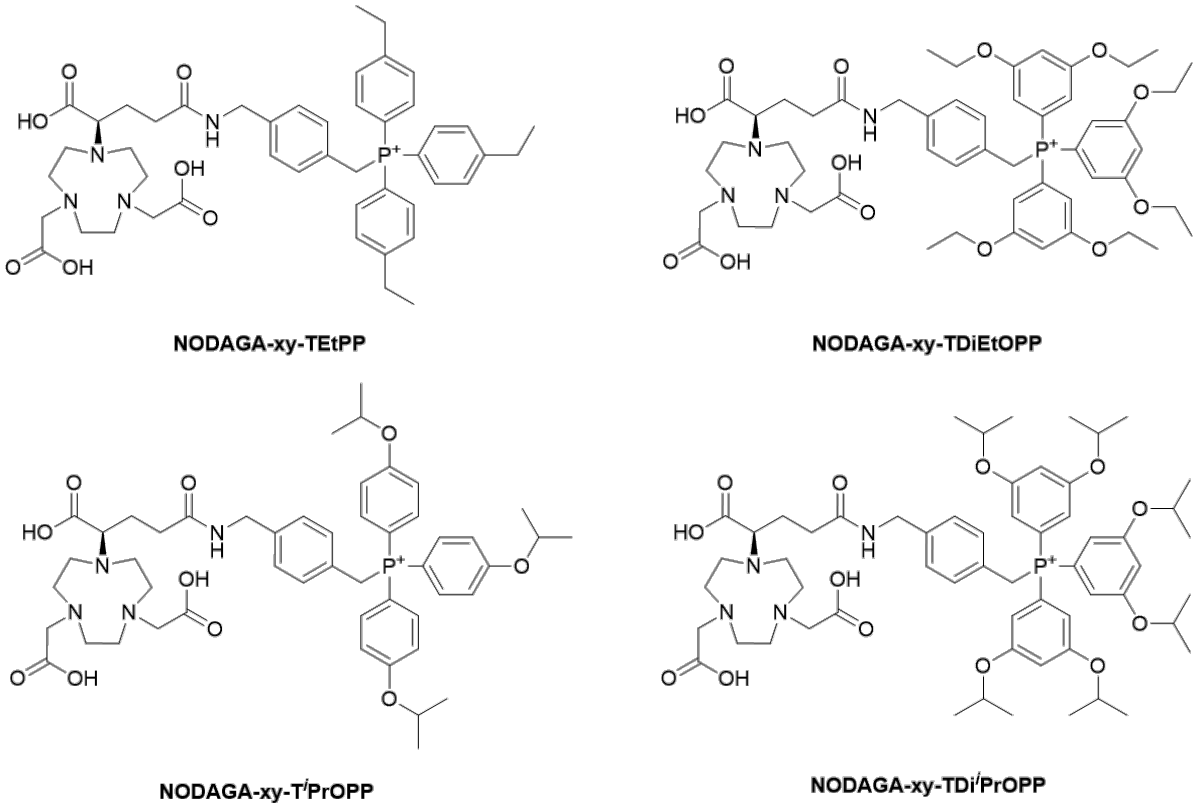

Figure 6.1 NODAGA-xy-TEtPP, NODAGA-xy-TDiEtOPP, NODAGA-xy-T^{i}PrOPP and NODAGA-xy-TDi^{i}PrOPP; potential future variants of the NODAGA-based series of compounds.

Due to the findings of the effect of alkyl and ether group functionalisation of the TAP motif on radiotracer lipophilicity, future work could explore the synthesis of a *para*-ethyl analogue to determine if this variant is more lipophilic than the NODAGA-xy-TEtOPP compound. The synthesis of *m*,*m'*-diethoxy, *p*-isopropoxy and *m*,*m'*-diisopropoxy analogues, shown in **Figure 6.1**, could also be explored to assess the effect of branched and linear alkyl groups on the lipophilicity of the final compound. If these new variants exhibit superior lipophilicity and log *D* values within a similar range to MIBI, the *ex vivo* model discussed in chapter 4 will be used to assess the pharmacokinetic behaviour of these radiotracers to report on mitochondrial function.

6.3 Biological Evaluation of Lipophilic and Cationic Gallium-68 Complexes

Chapter 4 describes the investigation of the behaviour of the radiotracers in a preclinical *ex vivo* biological model. This model was the Langendorff isolated perfused heart model, consisting of a unique triple-gamma detector system. Using the clinical 'gold' standard

SPECT-based lipophilic and cationic myocardial perfusion imaging agent MIBI, a foundation for radiotracer cardiac uptake and retention was established using a two-injection protocol for the screening of candidate radiotracers. The most lipophilic example of the NODAGA-xy-TAP series was screened using this model, [^{68}Ga]Ga-NODAGA-xy-TXP. Unfortunately, [^{68}Ga]Ga-NODAGA-xy-TXP did not show appreciable uptake and retention in healthy mitochondria, and this was not significantly diminished in depolarised mitochondria, highlighting a lack of $\Delta\Psi_m$-dependent uptake and retention in cardiac tissue. This work established a non-linear relationship between log *D* and the capacity of a radiotracer to report on mitochondrial function. It was found that a number of factors play a role in determining a radiotracers uptake and retention in cardiac tissue, namely the positive charge distribution across the surface area of the entire molecule. Ideally, the chemical structures of future mitochondrially-targeted radiotracers should mimic that of MIBI, with the ligand structure acting as a hydrophobic barrier, protecting the metal centre from any hydrophilic interactions and improving the lipophilicity of the final radiotracer. Nevertheless, this work will help to inform on the design and development of future ^{68}Ga-based lipophilic and cationic radiotracers for reporting on mitochondrial function.

6.4 The Synthesis of Acyclic Ligands for the Generation of Lipophilic and Cationic Gallium-68 Complexes

The final results chapter of this thesis explored the synthesis of multiple families of acyclic ligands towards the eventual formation of gallium-68 lipophilic cations. This chapter begins with the synthesis of new bis(salicylaldimine) analogues based on 3,5-dialkoxy substituted salicylaldehyde precursors. 3,5- and 4,6 -disubsitituted salicylaldehydes were reacted with two different tetraamine backbones to attempt the synthesis of this first bis(salicylaldimine) compounds. The second part of this section discussed the preparation of phosphinic acid analogues, bisAAPA compounds (**Figure 6.2**), of known bis(salicylaldimine) compounds containing phenolate groups, to assess the effect phosphinate coordinating groups have on Ga(III) chelation compared to phenolate groups. The lipophilicity of the final compounds was also assessed as an effect of changing coordinating groups.

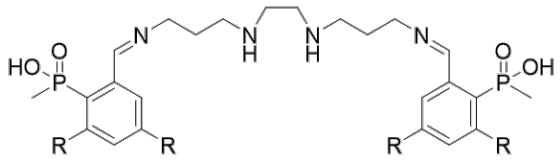

Figure 6.2 The general structure of bis(AAPA)BAPEN compounds. R = OMe, OEt, ^{i}OPr.

Unfortunately, due to time constraints the synthesis of this family could not be completed. Future work would involve the investigation of a viable purification method for the target ligand compounds ready for labelling with gallium-68. One method could be reverse-phase chromatography, which was initially ruled out due to the ease of imine hydrolysis in aqueous media. However, radioHPLC analysis of a similar bis(salicylaldimine) radiocomplex, ^{68}Ga-Galmydar mentioned in section 5.1, used a saline/ethanol solvent system meaning the imine groups may be stable enough to purify bis(AAPA)BAPEN compounds using this method. Once the methoxy analogue has been synthesised, the ethoxy and *iso*-propoxy variants will be synthesised analogously. Following the preparation of these three ligands, they will be radiolabelled with gallium-68, their log *D* values measured, and if suitable, their ability to report on mitochondrial function will be assessed using the Langendorff isolated perfused heart model.

The chapter continues with the synthesis of tridentate aroylhydrazone compounds, which selectively form 2:1 complexes with Fe(III), and in this work they were investigated as Ga(III) ligands. In this work a new synthetic route was designed and developed for the synthesis of the literature ligand HAPI. Complexation of Ga(III) using HAPI was inconclusive by NMR spectroscopic analysis, however mass spectrometry confirmed the formation of the desired complex. The solid obtained from the complexation reaction proved insoluble in all solvents, making it difficult to translate to the radiosynthetic and biological settings, and HAPI analogues aimed at improving the solubility of the final complex did not prove fruitful. A second series of tridentate [NN′O] ligands, which have been shown to selectively form 2:1 Ga(III) complexes, were investigated next, however Ga(III) coordination reactions were not successful.

The final acyclic ligand family discussed in this chapter were the bis(semicarbazone-phosphonium) compounds which looked at building on literature bis(semicarbazone) chelates, which exhibited desirable ^{68}Ga-labelling properties, by incorporating TAP moieties to generate a series of mitochondrially-targeted radiotracers. Formation of the desired ligand H_4bsc-$(TPP)_2$ through a final imine condensation afforded an

insoluble grey precipitate which was confirmed to be the mono-imine intermediate by mass spectrometry, shown in **Figure 6.3**.

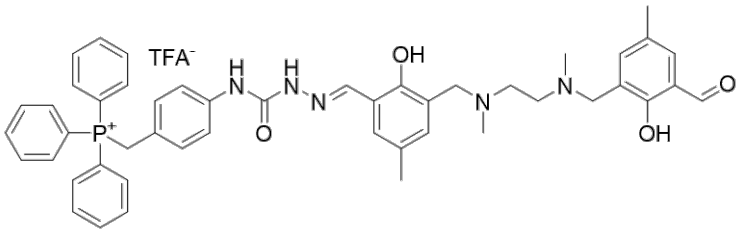

Figure 6.3 The intermediate of the imine condensation reaction to synthesise H_4bsc-$(TPP)_2$, H_4bsc-TPP.

The synthesis of the literature H_4bsc ligand was formed by an imine condensation reaction using a solvent mixture of methanol and acetonitrile. It seems the synthesis of the ligand depends on ensuring the mono-imine intermediate remains soluble in the solvent system to promote the formation of the second imine group, which was not the case in ethanol. Future work will involve the investigation of a solvent system that can be used to successfully synthesise the target ligand ready for gallium-68 radiolabelling.

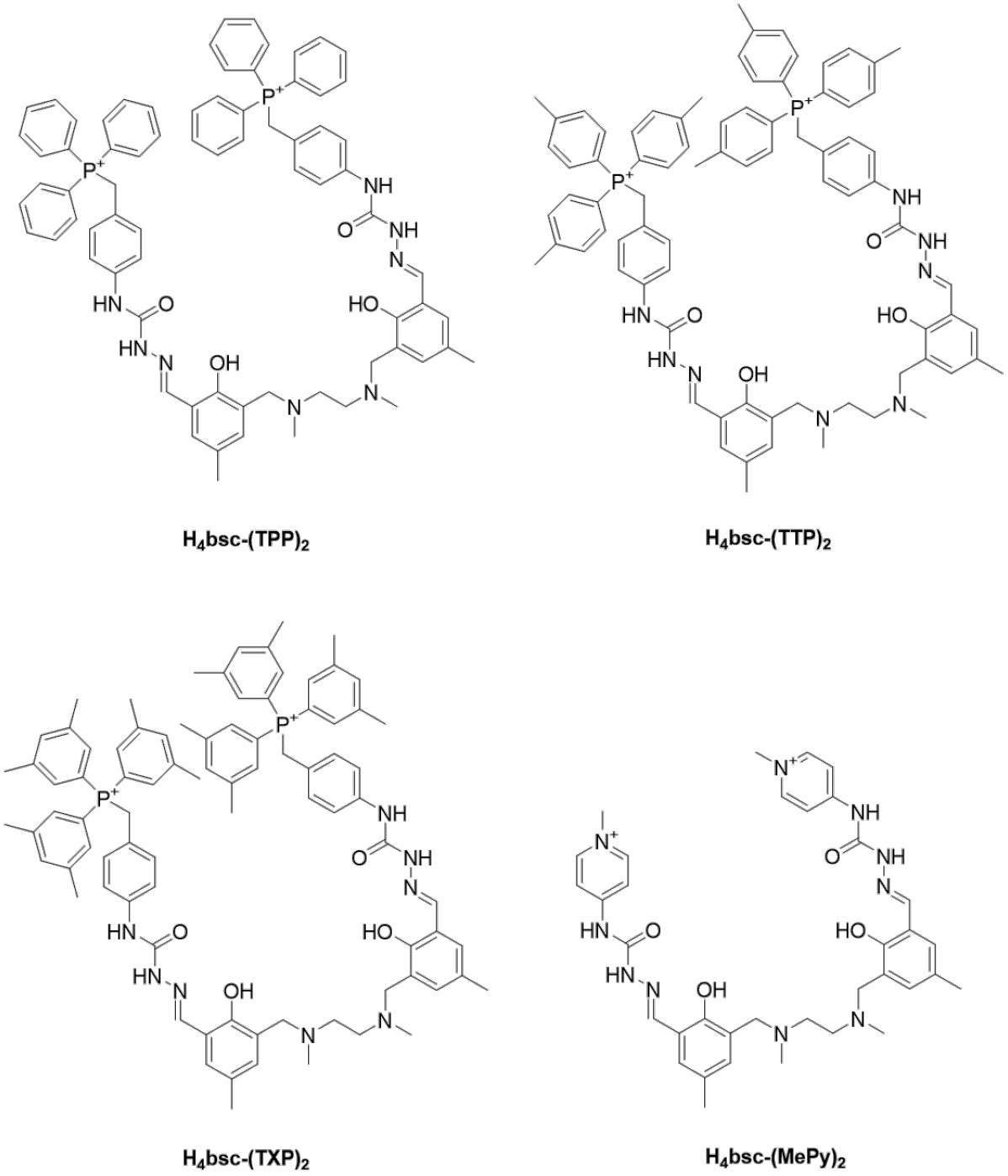

Figure 6.4 The chemical structures of future H_4bsc compounds, including TPP, TTP, TXP and methyl-pyridinium (MePy) functionalisation.

Once a successful solvent system for the formation of the target ligand has been found for the TPP analogue H_4bsc-$(TPP)_2$, the TTP and TXP variants will be synthesised in an analogous manner, shown in **Figure 6.4**. This will be followed by the labelling of these compounds with gallium-68, their log *D* values measured and, if suitable candidates are identified, their ability to report on mitochondrial function will be assessed using the *ex vivo* Langendorff model.

Additionally, the preparation of a methyl-pyridinium (MePy) analogue, shown in **Figure 6.4**, would be interesting to assess the effect the pyridinium cation has on the uptake and retention of the final compound in mitochondria, compared to the triarylphosphonium analogues.

CHAPTER 7 – EXPERIMENTAL

7.1 Synthetic Chemistry

7.1.1 General

7.1.1.1 Conditions and Materials

All reactions were carried out at atmospheric pressure with stirring unless otherwise stated. No special precautions were taken to exclude air or moisture during reactions, work-ups or purification unless otherwise stated. All solvents and reagents were obtained from commercial sources and used without further purification. Compounds **3b**, **3c**[1], **7**[2], **8a**[3], **11**[4], **16a**[5], **17**[6], **20**[7], **22**[8], **27**[9], **31**[10], **35**[11], and **38**[12] were prepared by literature procedures from commercially available starting materials. Synthetic chemistry was conducted as part of Chapter 2 and Chapter 5 of this thesis.

7.1.1.2 Physical Measurements

^{1}H, $^{1}H\{^{31}P\}$, $^{31}P\{^{1}H\}$, $^{13}C\{^{1}H\}$ and $^{19}F\{^{1}H\}$ NMR spectra were recorded on Bruker AV-400, AV-500, or DRX-400 spectrometers. Chemical shifts are reported in ppm. ^{1}H, $^{13}C\{^{1}H\}$ spectra were internally referenced to the residual solvent peaks of $CDCl_3$ at δ = 7.26 (^{1}H) and 77.2 ($^{13}C\{^{1}H\}$); CD_3OD at δ = 3.31 (^{1}H) and 49.2 ppm ($^{13}C\{^{1}H\}$); D_2O at δ = 4.79 ppm (^{1}H); DMSO-d_6 at δ = 2.50 (^{1}H) and 39.5 ppm ($^{13}C\{^{1}H\}$);[13] and external $CFCl_3$ and H_3PO_4 standards for $^{19}F\{^{1}H\}$ and $^{31}P\{^{1}H\}$ spectra respectively. $^{13}C\{^{1}H\}$ were assigned where possible using 2D correlation spectroscopy, such as HMQC and HMBC. Spectra were processed and analysed using Mestrenova software. Signal multiplicities are indicated as: s (singlet), d (doublet), t (triplet), q (quartet), dd (doublet of doublets), dt (doublet of triplets), ddd (doublet of doublets of doublets), ddt (doublet of doublets of triplets), ddq (doublet of doublets of quartets), m (multiplet); defined as all multi-peak signals where overlap or complex coupling of signals makes definitive descriptions of peaks difficult. Coupling constants are defined as *J* given in Hz quoted to one decimal place. Numbering of magnetically inequivalent environments is recorded where full assignment was achieved.

High resolution ES+ mass spectrometry analyses were conducted by Dr. Lisa Haigh at the Mass Spectrometry Service, Imperial College London on a Waters LCT Premier (ES-ToF)/Acquity i-Class spectrometer.

TLC was performed on Kieselgel 60 F_{254} plates (Merck) and visualisation achieved under UV fluorescence (254 and 366 nm) or I_2 vapour. Flash silica column chromatography was performed on a Biotage Isolera Prime advanced automated flash purification unit using 10 g, 25 g, or 50 g, SNAP KP-Sil or Sfar Duo cartridges, unless otherwise stated. Reverse-phase flash chromatography was performed using the same Biotage Isolera instrument with SNAP-KP-C18-HS or Sfar C18 cartridges. For reverse-phase chromatography, mobile phase A contained water with 0.1 % TFA, and mobile phase B contained MeCN with 0.1 % TFA.

pH measurements were performed using a Jenway model 3510 pH/mV/temperature meter, calibrated against 'NIST' pH 10.00, pH 7.00 and pH 4.00 buffers. Room temperature (rt) is defined as between 18-22 ºC. 'Reduced pressure' is used to describe solvent removal by Büchi rotary evaporation between 20-50 ºC at approximately 0.75 mmHg. 'Degassed' refers to the process of removing O_2 from a solution by bubbling N_2 through the solution in the reaction vessel prior to use.

7.1.2 DO2A-(xy-TAP)$_2$ and DO2A-Ar$_2$ (Section 2.1)

7.1.2.1 General Procedure 1 – Ga(III) Complexation of DO2A-(xy-TAP)$_2$ and DO2A-Ar$_2$ Compounds

DO2A-based compounds (1 eq.) and $Ga(NO_3)_3.xH_2O$ (1 eq.) were added to 0.5 M NH_4OAc and stirred at 100 ºC overnight. The mixture was concentrated under reduced pressure, and the resulting crude residue was purified by reverse-phase flash chromatography (C-18 SiO_2, 0-100 % B in A) to yield the desired product.

Ga-DO2A(-xy-TPP)$_2$.3NO$_3$ (Ga1a)

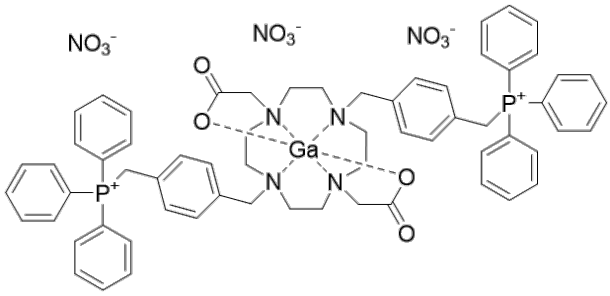

Following **general procedure 1**, the title compound was prepared from **1a** (0.08 g, 0.07 mmol), $Ga(NO_3)_3.xH_2O$ (0.02 g, 0.07 mmol) and 0.5 M NH_4OAc (0.15 mL) as a white solid (0.05 g, 0.04 mmol, 58 %). **^{1}H NMR (400 MHz, CD$_3$OD) δ$_H$ (ppm):** 7.90 (6H, td, $^3J_{HH}$ = 7.3,

$^{4}J_{HH}$ = 1.9 Hz, *p*-Ph), 7.77 – 7.63 (24H, m, *o*/*m*-Ph), 7.41 (4H, d, $^{3}J_{HH}$ = 8.1 Hz, $C_6\underline{H}_4$), 7.08 (4H, dd, $^{3}J_{HH}$ = 8.3, $^{4}J_{HP}$ = 2.6 Hz, $C_6\underline{H}_4$), 4.99 (4H, d, $^{2}J_{HP}$ = 15.3, $C\underline{H}_2$), 4.01 (4H, s, $C\underline{H}_2$), 3.94 (4H, s, $C\underline{H}_2$), 3.58 – 3.34 (12H, m, macrocycle $\underline{H}$), 3.02 – 2.90 (4H, m, macrocycle $\underline{H}$). **$^{13}C\{^{1}H\}$ NMR (100 MHz, CD_3OD) δ_C (ppm):** 173.7 ($\underline{C}$=O), 136.5 (*p*-Ph), 135.4 (d, $^{3}J_{CP}$ = 9.5 Hz, *m*-Ph), 133.3 ($\underline{C}_6H_4$), 132.7 (d, $^{3}J_{CP}$ = 5.3 Hz, $\underline{C}_6H_4$), 132.4 ($\underline{C}_6H_4$), 131.4 (d, $^{2}J_{CP}$ = 12.7 Hz, *o*-Ph), 130.7 ($\underline{C}_6H_4$), 119.0 (d, $^{1}J_{CP}$ = 85.7 Hz, *i*-Ph), 65.6 ($\underline{C}H_2$), 61.1 ($\underline{C}H_2$), 58.4 (macrocycle $\underline{C}$), 55.6 (macrocycle $\underline{C}$), 51.9 (macrocycle $\underline{C}$), 30.4 (d, $^{1}J_{CP}$ = 48.5 Hz, $\underline{C}H_2P$). **$^{31}P\{^{1}H\}$ NMR (162 MHz, CD_3OD) δ_P (ppm):** 22.9. **HRMS (ES-TOF+):** *m/z* calcd for $C_{64}H_{66}N_4O_4P_2Ga$ ($[M-(NO_3)_3]^{3+}$) 361.7938. found: 361.7928.

Ga-DO2A-Bn$_2$.NO$_3$ (Ga1b)

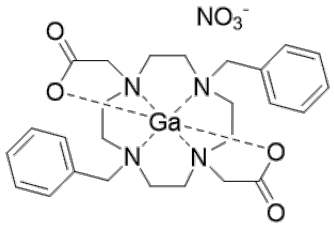

Following **general procedure 1**, the title compound was prepared from **1b** (0.10 g, 0.21 mmol), $Ga(NO_3)_3.xH_2O$ (0.06 g, 0.21 mmol) and 0.5 M NH_4OAc (1.00 mL) as a white solid (0.01 g, 0.02 mmol, 11 %). **^{1}H NMR (400 MHz, CD_3OD) δ_H (ppm):** 7.55 (4H, m, *m*-Ph), 7.45 (6H, m, *o*/*p*-Ph), 4.12 (4H, s, $C\underline{H}_2$), 4.00 (4H, s, $C\underline{H}_2$), 3.60 (4H, td, $^{3}J_{HH}$ = 13.8, $^{4}J_{HH}$ = 4.9 Hz, macrocycle $\underline{H}$), 3.41 (8H, m, macrocycle $\underline{H}$), 2.98 (4H, m, macrocycle $\underline{H}$). **$^{13}C\{^{1}H\}$ NMR (101 MHz, CD_3OD) δ_C (ppm):** 173.8 (C=O), 132.7 (*m*-Ph), 132.2 (*o*-Ph), 130.6 (*p*-Ph), 130.0 (*i*-Ph), 66.6, 61.1 ($\underline{C}H_2$), 58.3, 55.7 (macrocycle, $\underline{C}$). **HRMS (ES-TOF+):** *m/z* calcd. for $C_{26}H_{34}N_4O_4Ga$ ($[M-NO_3]^{+}$) 535.1830. found: 535.1836.

7.1.3 (R)-NODAGA-xy-TAP and (R)-NODAGA-xy-TAEP (Section 2.2 and Section 2.3)

7.1.3.1 General Procedure 2 – Synthesis of Aryl-Functionalised Triphenylphosphines

The procedure was adapted from the method described by Smith *et al.*[1] A solution of the aryl bromide (3 eq.) in anhydrous THF was added dropwise to magnesium turnings (3 eq.) under an N_2 atmosphere whilst maintaining reflux. The resulting grey suspension was stirred for 2 h

before a solution of PCl_3 (1 eq.) in anhydrous THF was added. The resulting mixture was stirred for a further 2 h, before being quenched with water (10 mL), and the aqueous phase was removed using a separating funnel. The organic phase was concentrated under reduced pressure and the desired product was recrystallised from ethanol.

Tris(4-methoxyphenyl)phosphine (3d)[14]

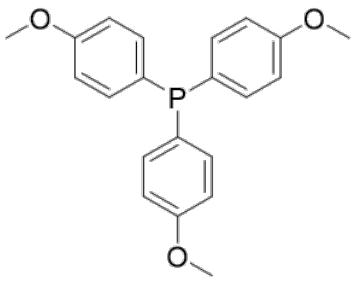

Following **general procedure 2**, the title compound was prepared from 4-bromoanisole (3.00 g, 16.0 mmol) in anhydrous THF (6 mL), magnesium turnings (0.39 g, 16.0 mmol) and PCl_3 (0.73 g, 5.33 mmol) in anhydrous THF (9 mL) as a yellow solid (0.87 g, 2.51 mmol, 46 %). **^{1}H NMR (400 MHz, $CDCl_3$) δ_H (ppm):** 7.22 (6H m, *o*-Ar), 6.87 (6H, m, *m*-Ar), 3.80 (9H, s, $OC\underline{H}_3$). **^{13}C{^{1}H} NMR (101 MHz, $CDCl_3$) δ_C (ppm):** 160.2 (*p*-Ar), 135.1 (d, $^2J_{CP}$ = 20.8 Hz, *o*-Ar), 129.1 (d, $^1J_{CP}$ = 8.4 Hz, *i*-Ar), 114.2 (d, $^3J_{CP}$ = 8.5 Hz, *m*-Ar), 55.3 ($O\underline{C}H_3$). **^{31}P{^{1}H} NMR (162 MHz, $CDCl_3$) δ_P (ppm):** -10.2. **HRMS (ES-TOF+):** *m/z* calcd. for $C_{21}H_{22}O_3P$ ($[M+H]^+$) 353.1307. found: 353.1313.

Tris(4-ethoxyphenyl)phosphine (3e)[15]

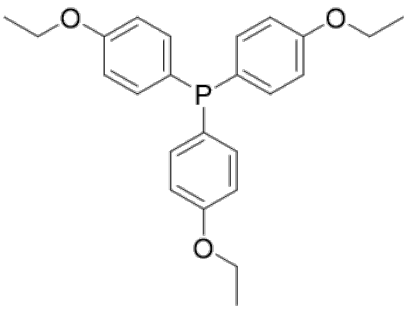

Following **general procedure 2**, the title compound was prepared from 4-bromoethoxybenzene (3.00 g, 14.9 mmol) in anhydrous THF (6 mL), magnesium turnings (0.36 g, 14.9 mmol) and PCl_3 (0.68 g, 4.97 mmol) in anhydrous THF (9 mL) as a yellow oil (1.27 g, 3.22 mmol, 65 %). **^{1}H NMR (400 MHz, $CDCl_3$) δ_H (ppm):** 7.22 (6H, dd, $^3J_{HH}$ = 8.7, $^3J_{HP}$ = 7.3 Hz, *o*-Ar), 6.87 (6H, m, *m*-Ar), 4.00 (6H, q, $^3J_{HH}$ = 7.0 Hz, $OC\underline{H}_2CH_3$), 1.41 (9H, t,

$^{3}J_{HH}$ = 7.0 Hz, $OCH_2C\underline{H}_3$). **$^{13}C\{^{1}H\}$ NMR (101 MHz, $CDCl_3$) δ_C (ppm):** 159.6 (*p*-Ar), 135.0 (d, $^{2}J_{CP}$ = 20.8 Hz, *o*-Ar), 128.7 (d, $^{1}J_{CP}$ = 7.3 Hz, *i*-Ar), 114.7 (d, $^{3}J_{CP}$ = 8.0 Hz, *m*-Ar), 63.4 ($O\underline{C}H_2CH_3$), 14.9 ($OCH_2\underline{C}H_3$). **$^{31}P\{^{1}H\}$ NMR (162 MHz, $CDCl_3$) δ_P (ppm):** -10.2. **HRMS (ES-TOF+):** *m/z* calcd. for $C_{24}H_{28}O_3P$ ($[M+H]^+$) 395.1771. found: 395.1765.

Tris(3,5-dimethoxyphenyl)phosphine (3f)[16]

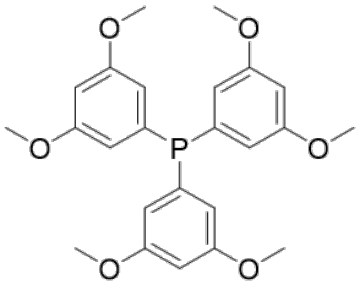

Following **general procedure 2**, the title compound was prepared from 1-bromo-3,5-dimethoxybenzene (3.00 g, 13.8 mmol) in anhydrous THF (8 mL), magnesium turnings (0.34 g, 13.8 mmol) and PCl_3 (0.63 g, 4.61 mmol) in anhydrous THF (12 mL) as an orange solid (2.00 g, 4.52 mmol, 98 %). **^{1}H NMR (400 MHz, $CDCl_3$) δ_H (ppm):** 6.48 (6H, dd, $^{3}J_{HP}$ = 8.4, $^{4}J_{HH}$ = 2.3 Hz, *o*-Ar), 6.42 (3H, t, $^{4}J_{HH}$ = 2.2 Hz, *p*-Ar), 3.71 (18 H, s, Ar-$OC\underline{H}_3$). **$^{13}C\{^{1}H\}$ NMR (101 MHz, $CDCl_3$) δ_C (ppm):** 160.8 (*m*-Ar), 130.0 (*i*-Ar), 111.6 (d, $^{2}J_{CP}$ = 20.8 Hz, *o*-Ar), 101.3 (*p*-Ar), 55.4 (Ar-$O\underline{C}H_3$). **$^{31}P\{^{1}H\}$ NMR (162 MHz, $CDCl_3$) δ_P (ppm):** 0.72. **HRMS (ES-TOF+):** *m/z* calcd. for $C_{24}H_{28}O_6P$ ($[M+H]^+$) 443.1618. found: 443.1613.

7.1.3.2 General Procedure 3 – Monosubstitution of α,α′-Dibromo-*p*-xylene with Aryl Functionalised Triarylphosphines

The procedure was adapted from the method described by Smith *et al*.[1] α,α′-Dibromo-*p*-xylene (1 eq.) was added to anhydrous toluene, and heated to 60 ºC until all the solid was dissolved. To this, a solution of triarylphosphine (1 eq.) in anhydrous toluene was added dropwise, before the mixture was stirred at 60 ºC under an N_2 atmosphere overnight. The precipitate was isolated by filtration, before being washed with toluene (20 mL) and Et_2O (2 × 40 mL), then dried under vacuum to yield the desired product.

(4-(Bromomethyl)benzyl)triphenylphosphonium bromide (4a)[1]

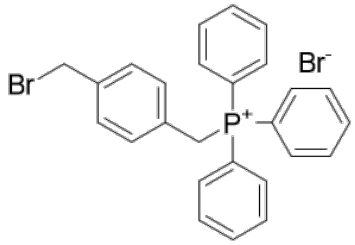

Following **general procedure 3**, the title compound was prepared from α,α′-dibromo-*p*-xylene (2.11 g, 8.00 mmol) in anhydrous toluene (20 mL), and triphenylphosphine (2.10 g, 8.00 mmol) in anhydrous toluene (24 mL) as a white solid (3.55 g, 7.95 mmol, 99 %). **^{1}H NMR (400 MHz, $CDCl_3$) δ_H (ppm):** 7.73 (9H, m, *m/p*-Ar), 7.61 (6H, td, $^{3}J_{HH}$ = 7.7, $^{4}J_{HH}$ = 3.5 Hz, *o*-Ar), 7.11 (4H, m, $C_6\underline{H}_4$), 5.49 (2H, d, $^{2}J_{HP}$ = 14.3 Hz, $C\underline{H}_2P$), 4.37 (2H, d, $^{4}J_{HH}$ = 1.3 Hz, $C\underline{H}_2Br$). **^{13}C{^{1}H} NMR (101 MHz, $CDCl_3$) δ_C (ppm):** 138.3 (*p*-Ar), 135.1 ($\underline{C}_6H_4$), 134.6 (d, $^{2}J_{CP}$ = 10.3 Hz, *o*-Ar), 132.1 (d, $^{3}J_{CP}$ = 6.3 Hz, $\underline{C}_6H_4$), 130.3 (d, $^{3}J_{CP}$ = 13.3 Hz, *m*-Ar), 129.5 ($\underline{C}_6H_4$), 127.8 (d, $^{2}J_{CP}$ = 8.7 Hz, $\underline{C}_6H_4$), 117.9 (d, $^{1}J_{CP}$ = 85.2 Hz, *i*-Ar), 33.0 ($\underline{C}H_2Br$), 30.6 (d, $^{1}J_{CP}$ = 46.7 Hz, $\underline{C}H_2P$). **^{31}P{^{1}H} NMR (162 MHz, $CDCl_3$) δ_P (ppm):** 23.4. **HRMS (ES-TOF+):** *m/z* calcd. for $C_{26}H_{23}PBr$ ($[M\text{-}Br]^+$) 445.0721. found: 445.0715.

(4-(Bromomethyl)benzyl)tri-*p*-tolylphosphonium bromide (4b)[1]

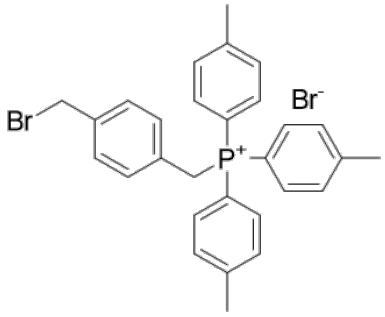

Following **general procedure 3**, the title compound was prepared from α,α′-dibromo-*p*-xylene (0.53 g, 2.00 mmol) in anhydrous toluene (5 mL), and tri-*p*-tolylphosphine (0.72 g, 2.00 mmol) in anhydrous toluene (6 mL) as a pale-yellow solid (1.04 g, 2.12 mmol, 92 %). **^{1}H NMR (400 MHz, $CDCl_3$) δ_H (ppm):** 7.54 (6H, dd, $^{3}J_{HH}$ = 12.3, $^{4}J_{HP}$ = 8.2 Hz, *m*-Ar), 7.39 (6H, dd, $^{3}J_{HP}$ = 8.2, $^{3}J_{HH}$ = 3.3 Hz, *o*-Ar), 7.14 (2H, d, $^{3}J_{HH}$ = 8.1 Hz, $C_6\underline{H}_4$), 7.08 (2H, dd, $^{3}J_{HH}$ = 8.4, $^{4}J_{HP}$ = 2.4 Hz, $C_6\underline{H}_4$), 5.26 (2H, d, $^{2}J_{HP}$ = 14.4 Hz, $C\underline{H}_2P$), 4.39 (2H, s, $C\underline{H}_2Br$), 2.45 (9H, s, Ar-$C\underline{H}_3$). **^{13}C{^{1}H} NMR (101 MHz, $CDCl_3$) δ_C (ppm):** 146.3 ($\underline{C}_6H_4$), 138.1 (*o*-Ar), 134.4 (d, $^{2}J_{CP}$ = 10.3 Hz, *p*-Ar), 132.1 (d, $^{3}J_{CP}$ = 5.2 Hz, $\underline{C}_6H_4$), 131.0 (d, $^{3}J_{CP}$ = 13.7 Hz, *m*-Ar), 129.5

($\underline{C}_6H_4$), 128.2 (d, $^2J_{CP}$ = 8.7 Hz, $\underline{C}_6H_4$), 114.7 (d, $^1J_{CP}$ = 88.4 Hz, *i*-Ar), 33.1 ($\underline{C}H_2Br$), 31.0 (d, $^1J_{CP}$ = 48.6 Hz, $\underline{C}H_2P$), 22.0 (Ar-$\underline{C}H_3$). **$^{31}P\{^1H\}$ NMR (162 MHz, $CDCl_3$) δ_P (ppm):** 22.4. **HRMS (ES-TOF+):** *m/z* calcd. for $C_{29}H_{29}PBr$ ($[M\text{-}Br]^+$) 487.1190. found: 487.1203.

(4-(Bromomethyl)benzyl)tris(3,5-dimethylphenyl)phosphonium bromide (4c)[1]

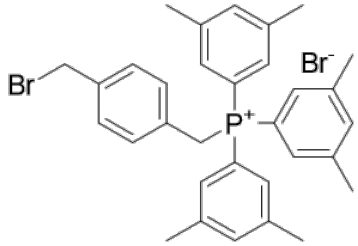

Following **general procedure 3**, the title compound was prepared from α,α′-dibromo-*p*-xylene (2.00 g, 7.59 mmol) in anhydrous toluene (20 mL), and tris(3,5-dimethylphenyl)phosphine (2.63 g, 7.59 mmol) in anhydrous toluene (24 mL) as a pale-yellow solid (3.75 g, 7.07 mmol, 93 %). **^1H NMR (400 MHz, $CDCl_3$) δ_H (ppm):** 7.34 (3H, s, *p*-Ar), 7.22 (6H, m, *o*-Ar), 7.15 (2H, d, $^3J_{HH}$ = 7.8 Hz, $C_6\underline{H}_4$), 7.03 (2H, dd, $^3J_{HH}$ = 8.3, $^4J_{HP}$ = 2.5 Hz, $C_6\underline{H}_4$), 5.22 (2H, d, $^2J_{HP}$ = 14.2 Hz, $C\underline{H}_2P$), 4.40 (2H, s, $C\underline{H}_2Br$), 2.36 (9H, s, Ar-$C\underline{H}_3$). **$^{13}C\{^1H\}$ NMR (101 MHz, $CDCl_3$) δ_C (ppm):** 140.3 ($\underline{C}_6H_4$), 138.0 ($\underline{C}_6H_4$), 136.8 ($\underline{C}_6H_4$), 132.1 (d, $^3J_{CP}$ = 6.2 Hz, $\underline{C}_6H_4$), 131.7 (d, $^2J_{CP}$ = 9.0 Hz, *o*-Ar), 129.3 (*p*-Ar), 128.5 (d, $^3J_{CP}$ = 7.5 Hz, *m*-Ar), 117.2 (d, $^1J_{CP}$ = 84.7 Hz, *i*-Ar), 33.1 ($\underline{C}H_2Br$), 30.9 (d, $^1J_{CP}$ = 47.2 Hz, $\underline{C}H_2P$), 21.6 (Ar-$\underline{C}H_3$). **$^{31}P\{^1H\}$ NMR (162 MHz, $CDCl_3$) δ_P (ppm):** 22.8. **HRMS (ES-TOF+):** *m/z* calcd. for $C_{32}H_{35}PBr$ ($[M\text{-}Br]^+$) 529.1660. found: 529.1655.

(4-(Bromomethyl)benzyl)tris(4-methoxyphenyl)phosphonium bromide (4d)

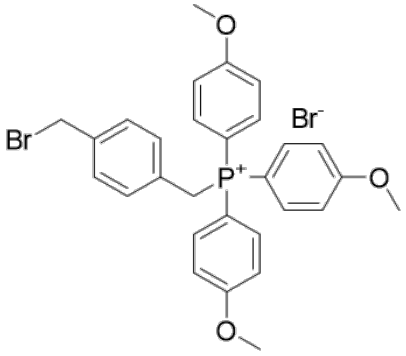

Following **general procedure 3**, the title compound was prepared from α,α′-dibromo-*p*-xylene (0.66 g, 2.51 mmol) in anhydrous toluene (6 mL), and tris(4-methoxyphenyl)phosphine (0.89 g, 2.51 mmol) in anhydrous toluene (8 mL) as a pale-yellow solid.

(4-(Bromomethyl)benzyl)tris(4-ethoxyphenyl)phosphonium bromide (4e)

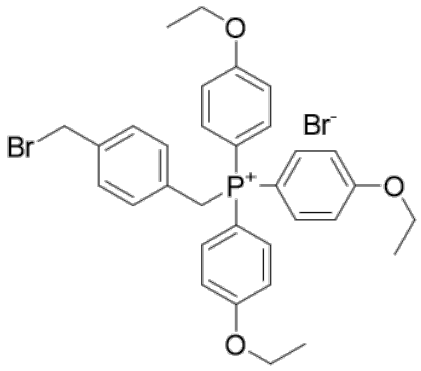

Following **general procedure 3**, the title compound was prepared from α,α′-dibromo-*p*-xylene (0.85 g, 3.22 mmol) in anhydrous toluene (8 mL), and tris(4-ethoxyphenyl)phosphine (1.27 g, 3.22 mmol) in anhydrous toluene (12 mL) as an off-white solid.

(4-(Bromomethyl)benzyl)tris(3,5-dimethoxyphenyl)phosphonium bromide (4f)

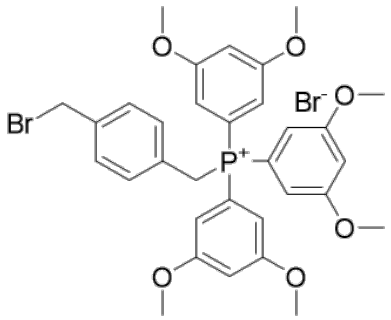

Following an adaptation of **general procedure 3**, the title compound was prepared from α,α′-dibromo-*p*-xylene (1.19 g, 4.52 mmol) in anhydrous acetonitrile (10 mL), and tris(3,5-dimethoxyphenyl)phosphine (2.00 g, 4.52 mmol) in anhydrous acetonitrile (20 mL). The mixture was concentrated under reduced pressure and purified by silica flash chromatography (SiO_2, DCM:MeOH, 70:30) to give a yellow solid. **^{1}H NMR (400 MHz, $CDCl_3$) δ_H (ppm):** 7.36 (2H, m, $C_6\underline{H}_4$), 7.09 (2H, dd, $^4J_{HP}$ = 8.3, $^4J_{HH}$ = 2.4 Hz, $C_6\underline{H}_4$), 6.97 (3H, m, *p*-Ar), 6.68 (6H, dt, $^3J_{HP}$ = 14.1, $^4J_{HH}$ = 2.2 Hz, *o*-Ar), 4.91 (2H, m, $C_6\underline{H}_4$), 4.54 (2H, s, $C_6\underline{H}_4$), 3.78 (18H, s, Ar-OC$\underline{H}_3$). **^{31}P{^{1}H} NMR (162 MHz, $CDCl_3$) δ_P (ppm):** 25.4.

7.1.3.3 General Procedure 4 – Preparation of Phthalimidoxylene-TAP Intermediates

The procedure was adapted from the method reported by Kim *et al*.[17] To a solution of bromoxylene-TAP (1 eq.) in acetonitrile (30 mL), potassium phthalimide (1.05 eq.) was added and the mixture was refluxed for 22 h. The resulting precipitate was removed by filtration and the filtrate was concentrated under reduced pressure. The residue was redissolved in DCM, washed with water and the organic layer was dried over $MgSO_4$, filtered and concentrated under reduced pressure. The crude material was recrystallised from a methanol/ether mixture, and the precipitate was isolated by filtration and dried under reduced pressure to give a white solid.

(4-((1,3-Dioxoisoindolin-2-yl)methyl)benzyl)triphenylphosphonium bromide (5a)[17]

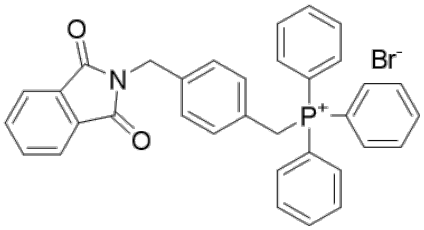

Following **general procedure 4**, the title compound was synthesised from (4-(bromomethyl)benzyl)triphenylphosphonium bromide (0.87 g, 1.94 mmol) and potassium phthalimide (0.38 g, 2.04 mmol) as a white solid (0.06 g, 0.12 mmol, 6 %). **^{1}H-NMR (400 MHz, $CDCl_3$) δ_H (ppm):** 7.85 (4H, dd, $^3J_{HH}$ = 5.4, $^4J_{HH}$ = 3.3 Hz, $N(CO)_2Ar$), 7.73 (9H, m, *m/p*-Ar), 7.62 (6H, m, *o*-Ar), 7.16 (2H, d, $^3J_{HH}$ = 8.1 Hz, $C_6\underline{H}_4$), 7.06 (2H, dd, $^3J_{HH}$ = 8.4, $^4J_{HH}$ = 2.5 Hz, $C_6\underline{H}_4$) 5.44 (2H, d, $^2J_{HP}$ = 14.3 Hz, $C\underline{H}_2P$), 4.76 (2H, d, $^4J_{HH}$ = 1.8 Hz, $NC\underline{H}_2$). **^{31}P{^{1}H}-NMR (162 MHz, $CDCl_3$) δ_P (ppm):** 23.1.

(4-((1,3-Dioxoisoindolin-2-yl)methyl)benzyl)tri-*p*-tolylphosphonium bromide (5b)

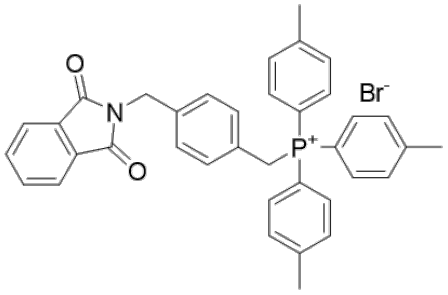

Following **general procedure 4**, the title compound was synthesised from (4-(bromomethyl)benzyl)tri-*p*-tolylphosphonium bromide (0.52 g, 1.06 mmol) and potassium phthalimide (0.21 g, 1.11 mmol) as a white solid (0.13 g, 0.24 mmol, 22 %). **^{1}H NMR (400 MHz, $CDCl_3$) δ_H (ppm):** 7.85 (2H, dd, $^{3}J_{HH}$ = 5.5, $^{4}J_{HH}$ = 3.1 Hz, $N(CO)_2Ar$), 7.73 (2H, dd, $^{3}J_{HH}$ = 5.5, $^{4}J_{HH}$ = 3.1 Hz, $N(CO)_2Ar$), 7.51 (6H, m, *m*-Ar), 7.38 (6H, m, *o*-Ar), 7.15 (2H, d, $^{3}J_{HH}$ = 8.0 Hz, $C_6\underline{H}_4$), 7.03 (2H, dd, $^{3}J_{HH}$ = 8.3, $^{4}J_{HH}$ = 2.5 Hz, $C_6\underline{H}_4$), 5.18 (2H, d, $^{2}J_{HP}$ = 14.3 Hz, $C\underline{H}_2P$), 4.76 (2H, d, $^{4}J_{HH}$ = 1.9 Hz, $NC\underline{H}_2$), 2.44 (9H, s, Ar-$C\underline{H}_3$). **^{31}P{^{1}H} NMR (162 MHz, $CDCl_3$) δ_P (ppm):** 22.2. **HRMS (ES-TOF+):** *m/z* calcd. for $C_{37}H_{33}NO_2P$ ($[M\text{-}Br]^+$) 554.2249. found: 554.2261.

7.1.3.4 General Procedure 5 – Synthesis of TAP-Functionalised Aminoxylenes

To a solution of bromoxylene-TAP (1 eq.) in ethanol, aqueous ammonia (28 % wt.) was added, and the mixture was then stirred at room temperature for 48 h. The solvent was removed under reduced pressure, before the crude residue was purified using reverse-phase flash chromatography (C-18 SiO_2, 0-100 % B in A) to give a white solid.

(4-(Aminomethyl)benzyl)triphenylphosphonium bromide (6a)

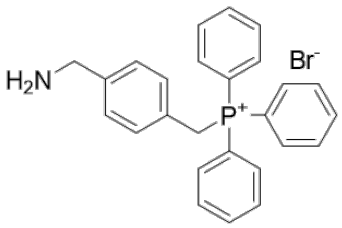

Following **general procedure 5**, the title compound was synthesised from (4-(bromomethyl)benzyl)triphenylphosphonium bromide (1.50 g, 2.85 mmol), EtOH (150 mL) and NH_3/H_2O (28 % wt., 40 mL) as a white solid (0.68 g, 1.47 mmol, 52 %). **^{1}H NMR (400 MHz, CD_3OD) δ_H (ppm):** 7.90 (3H, m, *p*-Ph), 7.73 (6H, m, *m*-Ph), 7.66 (6H, dd, $^{3}J_{HP}$ = 12.6, $^{3}J_{HH}$ = 7.7 Hz, *o*-Ph), 7.35 (2H, d, $^{3}J_{HH}$ = 8.0 Hz, $C_6\underline{H}_4$), 7.09 (2H, dd, $^{3}J_{HH}$ = 8.3, $^{4}J_{HH}$ = 2.5 Hz, $C_6\underline{H}_4$), 4.97 (2H, d, $^{2}J_{HP}$ = 15.3 Hz, $C\underline{H}_2P$), 4.10 (2H, s, $C\underline{H}_2NH_2$). **^{13}C{^{1}H} NMR (101 MHz, CD_3OD) δ_C (ppm):** 136.5 (*p*-Ph), 135.4 (d, $^{2}J_{CP}$ = 9.6 Hz, *o*-Ph), 132.9 (d, $^{2}J_{CP}$ = 5.6 Hz, $\underline{C}_6H_4$), 131.4 (d, $^{3}J_{CP}$ = 12.9 Hz, *m*-Ph), 130.7 ($\underline{C}_6H_4$), 129.9 (d, $^{2}J_{CP}$ = 9.3 Hz, $\underline{C}_6H_4$), 118.9 (d, $^{1}J_{CP}$ = 85.9 Hz, *i*-Ph), 43.6 ($\underline{C}H_2NH_2$), 30.3 (d, $^{1}J_{CP}$ = 48.4 Hz, $\underline{C}H_2P$). **^{31}P{^{1}H} NMR (162 MHz, CD_3OD) δ_P (ppm):** 22.9. **HRMS (ES-TOF+):** *m/z* calcd. for $C_{26}H_{25}NP$ ($[M\text{-}Br]^+$) 382.1725. found: 382.1723.

(4-(Aminomethyl)benzyl)tri(4-methylphenyl)phosphonium bromide (6b)

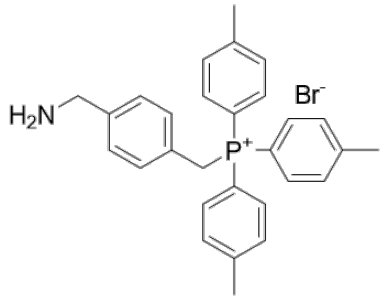

Following **general procedure 5**, the title compound was synthesised from (4-(bromomethyl)benzyl)tri(4-methylphenyl)phosphonium bromide (1.50 g, 2.64 mmol), EtOH (150 mL) and NH_3/H_2O (28 % wt., 40 mL) as a white solid (0.63 g, 1.25 mmol, 47 %). **^{1}H NMR (400 MHz, CD_3OD) δ_H (ppm):** 7.56 (6H, dd, $^3J_{HH}$ = 8.5, $^4J_{HH}$ = 4.1 Hz, *m*-Ar), 7.51 (6H, d, $^3J_{HH}$ = 8.0 Hz, *o*-Ar), 7.40 (2H, d, $^3J_{HH}$ = 7.7 Hz, $C_6\underline{H}_4$), 7.12 (2H, dd, $^3J_{HH}$ = 8.1, $^4J_{HH}$ = 2.6 Hz, $C_6\underline{H}_4$), 4.92 (2H, d, $^2J_{HP}$ = 15.1 Hz, $C\underline{H}_2P$), 4.13 (2H, s, $C\underline{H}_2NH_2$), 2.51 (9H, s, Ar-$C\underline{H}_3$). **^{13}C{^{1}H} NMR (101 MHz, CD_3OD) δ_C (ppm):** 148.0 (*p*-Ar), 135.3 (d, $^2J_{CP}$ = 9.8 Hz, *o*-Ar), 135.1 ($\underline{C}_6H_4$), 132.9 (d, $^3J_{CP}$ = 5.6 Hz, $\underline{C}_6H_4$), 132.0 (d, $^3J_{CP}$ = 12.9 Hz, *m*-Ar), 130.7 ($\underline{C}_6H_4$), 130.3 (d, $^2J_{CP}$ = 8.1 Hz $\underline{C}_6H_4$), 115.8 (d, $^1J_{CP}$ = 85.3 Hz, *i*-Ar), 43.7 ($\underline{C}H_2NH_2$), 30.7 (d, $^1J_{CP}$ = 49.6 Hz, $\underline{C}H_2P$), 21.8 (Ar-$\underline{C}H_3$). **^{31}P{^{1}H} NMR (162 MHz, CD_3OD) δ_P (ppm):** 22.1. **HRMS (ES-TOF+):** *m/z* calcd. for $C_{29}H_{31}NP$ ($[M\text{-}Br]^+$) 424.2194. found: 424.2193.

(4-(Aminomethyl)benzyl)tri(3,5-dimethylphenyl)phosphonium bromide (6c)

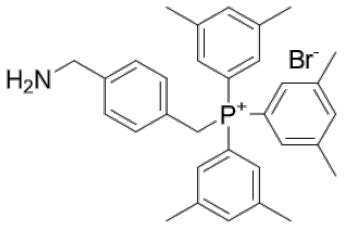

Following **general procedure 5**, the title compound was synthesised from (4-(bromomethyl)benzyl)tri(3,5-dimethylphenyl)phosphonium bromide (1.99 g, 3.26 mmol), EtOH (150 mL) and NH_3/H_2O (28 % wt., 40 mL) as a white solid (0.55 g, 1.01 mmol, 31 %). **^{1}H NMR (400 MHz, CD_3OD) δ_H (ppm):** 7.54 (3H, s, *p*-Ar), 7.41 (2H, d, $^3J_{HH}$ = 7.8 Hz, $C_6\underline{H}_4$), 7.23 (6H, d, $^3J_{HH}$ = 13.0 Hz, *o*-Ar), 7.09 (2H, dd, $^3J_{HH}$ = 8.1, $^4J_{HH}$ = 2.7 Hz, $C_6\underline{H}_4$), 4.90 (2H, dd, $^2J_{HP}$ = 15.1, $^3J_{HH}$ = 5.9 Hz, $C\underline{H}_2P$), 4.13 (2H, s, $C\underline{H}_2NH_2$), 2.38 (18H, s, Ar-$C\underline{H}_3$). **^{13}C{^{1}H} NMR (101 MHz, CD_3OD) δ_C (ppm):** 141.7 (d, $^3J_{CP}$ = 13.9 Hz, *m*-Ar), 137.9 (*p*-Ar), 135.1 ($\underline{C}_6H_4$), 133.1 (d, $^3J_{CP}$ = 5.7 Hz, $\underline{C}_6H_4$), 132.6 (d, $^2J_{CP}$ = 10.0 Hz, *o*-Ar), 130.5 ($\underline{C}_6H_4$), 118.9 (d,

$^{1}J_{CP}$ = 85.1 Hz, *i*-Ar), 43.7 (CH_2NH_2), 30.5 (d, $^{1}J_{CP}$ = 49.3 Hz, CH_2P), 21.3 (Ar-CH_3). **^{31}P{^{1}H} NMR (162 MHz, CD_3OD) δ_P (ppm):** 22.2. **HRMS (ES-TOF+):** *m/z* calcd. for $C_{32}H_{37}NP$ ($[M\text{-}Br]^+$) 466.2664. found: 466.2646.

(4-(Aminomethyl)benzyl)tris(4-methoxyphenyl)phosphonium bromide (6d)

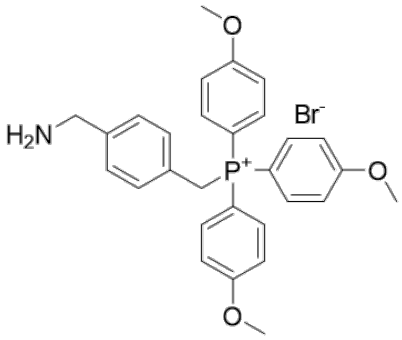

Following **general procedure 5**, the title compound was synthesised from (4-(bromomethyl)benzyl)tris(4-methoxyphenyl)phosphonium bromide (3.40 g, 5.52 mmol), EtOH (350 mL) and NH_3/H_2O (28 % wt., 80 mL) as a white solid (0.43 g, 0.78 mmol, 14 %). **^{1}H NMR (400 MHz, CD_3OD) δ_H (ppm):** 7.51 (6H, m, *o*-Ar), 7.37 (2H, d, $^{3}J_{HH}$ = 7.8 Hz, C_6H_4), 7.23 (6H, m, *m*-Ar), 7.09 (2H, dd, $^{3}J_{HH}$ = 8.4, $^{4}J_{HH}$ = 2.5 Hz, C_6H_4), 4.74 (2H, d, $^{2}J_{HP}$ = 15.0 Hz, CH_2P), 4.12 (2H, s, CH_2NH_2), 3.93 (9H, s, Ar-OCH_3). **^{13}C{^{1}H} NMR (101 MHz, CD_3OD) δ_C (ppm):** 165.1 (*p*-Ar), 135.9 (d, $^{2}J_{CP}$ = 10.9 Hz, *o*-Ar), 133.7 (C_6H_4), 131.5 (d, $^{3}J_{CP}$ = 5.3 Hz, C_6H_4), 129.2 (C_6H_4), 115.6 (d, $^{3}J_{CP}$ = 13.8 Hz, *m*-Ar), 108.2 (d, $^{1}J_{CP}$ = 95.2 Hz, *i*-Ar), 55.1 (Ar-OCH_3) 42.4 (CH_2NH_2), 30.3 (d, $^{1}J_{CP}$ = 51.1 Hz, CH_2P). **^{31}P{^{1}H} NMR (162 MHz, CD_3OD) δ_P (ppm):** 20.8. **HRMS (ES-TOF+):** *m/z* calcd. for $C_{29}H_{31}NO_3P$ ($[M\text{-}Br]^+$) 472.2042. found: 472.2047.

(4-(Aminomethyl)benzyl)tris(4-ethoxyphenyl)phosphonium bromide (6e)

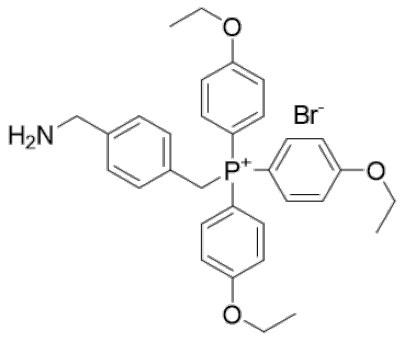

Following **general procedure 5**, the title compound was synthesised from (4-(bromomethyl)benzyl)tris(4-ethoxyphenyl)phosphonium bromide (1.86 g, 2.82 mmol), EtOH (180 mL) and NH_3/H_2O (28 % wt., 40 mL) as a white solid (0.26 g, 0.44 mmol, 15 %). **^{1}H NMR (400 MHz, CD_3OD) δ_H (ppm):** 7.49 (6H, m, *o*-Ar), 7.37 (2H, d, $^3J_{HH}$ = 7.9 Hz, $C_6\underline{H}_4$), 7.21 (6H, m, *m*-Ar), 7.09 (2H, dd, $^3J_{HH}$ = 8.3, $^4J_{HH}$ = 2.5 Hz, $C_6\underline{H}_4$), 4.73 (2H, d, $^2J_{HP}$ = 15.1 Hz, $C\underline{H}_2P$), 4.18 (6H, q, $^3J_{HH}$ = 7.0 Hz, Ar-$OC\underline{H}_2CH_3$), 4.12 (2H, s, $C\underline{H}_2NH_2$), 1.44 (9H, t, $^3J_{HH}$ = 7.0 Hz, Ar-$OCH_2C\underline{H}_3$). **^{13}C{^{1}H} NMR (101 MHz, CD_3OD) δ_C (ppm):** 165.7 (*p*-Ar), 137.2 (d, $^2J_{CP}$ = 11.9 Hz, *o*-Ar), 135.0 ($\underline{C}_6H_4$), 132.8 (d, $^3J_{CP}$ = 5.2 Hz, $\underline{C}_6H_4$), 130.7 (d, $^2J_{CP}$ = 8.6 Hz, $\underline{C}_6H_4$), 130.5 ($\underline{C}_6H_4$), 117.3 (d, $^3J_{CP}$ = 13.8 Hz, *m*-Ar), 109.3 (d, $^1J_{CP}$ = 95.2 Hz, *i*-Ar), 65.4 ($O\underline{C}H_2CH_3$) 43.7 ($\underline{C}H_2NH_2$), 31.6 (d, $^1J_{CP}$ = 51.3 Hz, $\underline{C}H_2P$), 14.8 ($OCH_2\underline{C}H_3$). **^{31}P{^{1}H} NMR (162 MHz, CD_3OD) δ_P (ppm):** 20.7. **HRMS (ES-TOF+):** *m/z* calcd. for $C_{32}H_{37}NO_3P$ ($[M\text{-}Br]^+$) 514.2511. found: 514.2522.

(4-(Aminomethyl)benzyl)tris(3,5-dimethoxyphenyl)phosphonium bromide (6f)

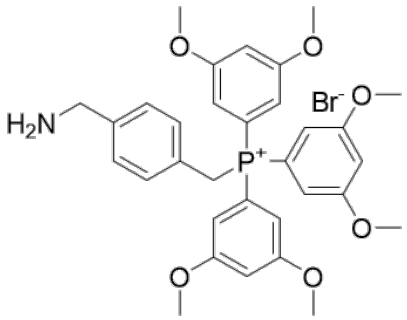

Following **general procedure 5**, the title compound was synthesised from (4-(bromomethyl)benzyl)tris(3,5-dimethoxyphenyl)phosphonium bromide (1.01 g, 1.43 mmol), EtOH (80 mL) and NH_3/H_2O (28 % wt., 25 mL) as a white solid (0.13 g, 0.20 mmol, 14 %). **^{1}H NMR (400 MHz, CD_3OD) δ_H (ppm):** 7.41 (2H, d, $^3J_{HH}$ = 7.7 Hz, $C_6\underline{H}_4$), 7.21 (2H, dd, $^3J_{HH}$ = 8.3, $^4J_{HH}$ = 2.4 Hz, $C_6\underline{H}_4$), 6.97 (3H, m, *p*-Ar), 6.70 (6H, dd, $^3J_{HP}$ = 14.1, $^4J_{HH}$ = 2.2 Hz, *o*-Ar), 5.00 (2H, m, $C\underline{H}_2P$), 4.11 (2H, s, $C\underline{H}_2NH_2$), 3.80 (18H, s, *m*-Ar($C\underline{H}_3$)). **^{13}C{^{1}H} NMR (101 MHz, CD_3OD) δ_C (ppm):** 163.4 (d, $^3J_{CP}$ = 19.0 Hz, *m*-Ar), 135.2 ($\underline{C}_6H_4$), 132.9 (d, $^3J_{CP}$ = 5.5 Hz, $\underline{C}_6H_4$), 130.6 ($\underline{C}_6H_4$), 130.2 ($\underline{C}_6H_4$), 120.3 (d, $^1J_{CP}$ = 87.0 Hz, *i*-Ar), 113.0 (d, $^2J_{CP}$ = 11.2 Hz, *o*-Ar), 107.2 (*p*-Ar), 56.60 (*m*-Ar($\underline{C}H_3$)), 43.61 ($\underline{C}H_2NH_2$), 30.09 (d, $^1J_{CP}$ = 48.1 Hz, $\underline{C}H_2P$). **^{31}P{^{1}H}-NMR (162 MHz, CD_3OD) δ_P (ppm):** 25.1. **HRMS (ES-TOF+):** *m/z* calcd. for $C_{32}H_{37}NO_6P$ ($[M\text{-}Br]^+$) 562.2359. found: 562.2349.

7.1.3.5 General Procedure 6 – Synthesis of TAP-Functionalised Cyanoxylenes

The procedure was carried out as a modification of the methodology by Nomura *et al*.[3] To a heated solution of (4-cyanobenzyl)bromide (1 eq.) in anhydrous MeCN (45 mL), triarylphosphine (1.50 eq.) was added. The mixture was stirred at reflux for 4.5 h under a N_2 atmosphere before being concentrated under reduced pressure. Addition of toluene to the crude material resulted in a white precipitate which was isolated by filtration. The precipitate was washed with hexane and dried under reduced pressure to give a white solid.

(4-Cyanobenzyl)tri-*p*-tolylphosphonium bromide (8b)

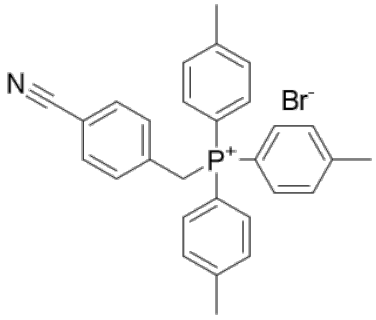

Following **general procedure 6**, the title compound was prepared from (4-cyanobenzyl)bromide (1.00 g, 5.10 mmol) and tri-*p*-tolylphosphine (2.33 g, 7.65 mmol) as a white solid (1.80 g, 3.60 mmol, 71 %). **^{1}H NMR (400 MHz, $CDCl_3$) δ_H (ppm):** 7.59 (6H, dd, $^3J_{HP}$ = 12.5, $^3J_{HH}$ = 8.1 Hz, *o*-Ar), 7.38 (6H, m, *m*-Ar), 7.36 (4H, m, $C_6\underline{H}_4$), 5.60 (2H, d, $^2J_{HP}$ = 15.4 Hz, $C\underline{H}_2P$), 2.44 (9H, s, Ar-$C\underline{H}_3$). **^{13}C{^{1}H} NMR (101 MHz, $CDCl_3$) δ_C (ppm):** 146.5 (*p*-Ar), 134.4 (d, $^2J_{CP}$ = 9.9 Hz, *o*-Ar), 134.1 (d, $^2J_{CP}$ = 8.4 Hz, $\underline{C}_6H_4$), 132.7 (d, $^3J_{CP}$ = 5.8 Hz, $\underline{C}_6H_4$), 132.2 ($\underline{C}_6H_4$), 131.0 (d, $^3J_{CP}$ = 13.0 Hz, *m*-Ar), 118.5 ($\underline{C}N$), 114.2 (d, $^1J_{CP}$ = 88.8 Hz, *i*-Ar), 30.7 (d, $^1J_{CP}$ = 48.5 Hz, $\underline{C}H_2P$), 22.0 (Ar-$\underline{C}H_3$). **^{31}P{^{1}H} NMR (162 MHz, $CDCl_3$) δ_P (ppm):** 23.1. **HRMS (ES-TOF+):** *m/z* calcd. for $C_{29}H_{27}NP$ ($[M\text{-}Br]^+$) 420.1876. found: 420.1874.

7.1.3.6 General Procedure 7 – Amide Coupling of TAP-Functionalised Aminoxylene to NODAGAtri-*tert*-butylester

The methodology was a modification of the procedure described by Schirrmacher *et al*.[18] (R)-NODAGA(^{t}Bu)$_3$ (1 eq.) and TAP-functionalised aminoxylene (1.20 eq.) were dissolved in a mixture of water and MeCN (1:1). DCC (1.10 eq.) was dissolved in pyridine, before it was added in a dropwise manner to the mixture and stirred at rt for 48 h. Solvent was removed

under reduced pressure, before the crude residue was dissolved in acetonitrile (8.00 mL) and the urea by-product was removed by filtration. The mixture was then concentrated under reduced pressure and the resulting crude material was purified by reverse-phase flash chromatography (C-18 SiO_2, 0-100 % B in A) to give the desired product.

(R)-(4-((4-(4,7-Bis(2-*tert*-butoxy)-2-oxoethyl)-1,4,7-triazonan-1-yl)-5-(*tert*-butoxy)-5-oxopentanamido)methyl)benzyl)triphenylphosphonium bromide (9a)

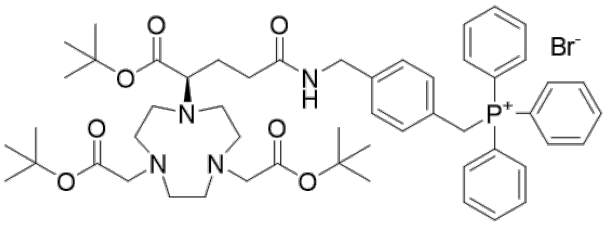

Following **general procedure 7**, the title compound was prepared from (R)-NODAGA(^{t}Bu)$_3$ (0.10 g, 0.19 mmol), (4-(aminomethyl)benzyl)triphenylphosphonium bromide (0.10 g, 0.21 mmol), H_2O:MeCN (1:1, 9.00 mL), DCC (0.04 g, 0.20 mmol) and pyridine (1.15 mL) as a pale-yellow solid (0.07 g, 0.07 mmol, 39 %). **^{1}H NMR (400 MHz, CD_3OD) δ_H (ppm):** 7.88 (3H, t, $^3J_{HH}$ = 7.6 Hz, *p*-Ph), 7.70 (6H, m, *m*-Ph), 7.62 (6H, dd, $^3J_{HP}$ = 12.7, $^3J_{HH}$ = 8.0 Hz, *o*-Ph), 7.14 (2H, d, $^3J_{HH}$ = 7.7 Hz, $C_6\underline{H}_4$), 6.95 (2H, dd, $^3J_{HH}$ = 7.9, $^4J_{HH}$ = 2.6 Hz, $C_6\underline{H}_4$), 4.88 (2H, d, $^2J_{HP}$ = 15.1 Hz, $C\underline{H}_2P$), 4.31 (2H, s, $C\underline{H}_2NH$), 3.51 (5H, m, $C\underline{H}N$/$C\underline{H}_2COO^tBu$), 3.09 (12H, m, macrocycle $\underline{H}$), 2.41 (2H, t, $^3J_{HH}$ = 7.8 Hz, $C\underline{H}_2CONH$), 2.02 (2H, m, $NCHC\underline{H}_2$), 1.48 (27H, m, $COOC(C\underline{H}_3)_3$). **^{13}C{^{1}H} NMR (101 MHz, CD_3OD) δ_C (ppm):** 175.0 ($\underline{C}ONH$), 173.1 ($\underline{C}OO^tBu$), 141.2 ($\underline{C}_6H_4$), 136.5 (*p*-Ph), 135.3 (d, $^2J_{CP}$ = 9.7 Hz, *o*-Ph), 132.3 (d, $^2J_{CP}$ = 5.7 Hz, $\underline{C}_6H_4$), 131.4 (d, $^3J_{CP}$ = 12.4 Hz, *m*-Ph), 129.1 ($\underline{C}_6H_4$), 127.4 ($\underline{C}_6H_4$), 119.1 (d, $^1J_{CP}$ = 86.5 Hz, *i*-Ph), 84.4, 83.5, 83.3 ($\underline{C}(CH_3)_3$), 64.9 ($\underline{C}HNH$), 56.4 ($\underline{C}H_2COO^tBu$), 52.8, 51.5, 46.9, 45.9 (macrocycle $\underline{C}$), 43.5 ($\underline{C}H_2NH$), 33.8 ($\underline{C}H_2CONH$), 30.4 (d, $^1J_{CP}$ = 46.9 Hz, $\underline{C}H_2P$), 28.4 ($C(\underline{C}H_3)_3$), 27.1 ($NCH\underline{C}H_2$). **^{31}P{^{1}H} NMR (162 MHz, CD_3OD) δ_P (ppm):** 22.4. **HRMS (ES-TOF+):** *m/z* calcd. for $C_{53}H_{72}N_4O_7P$ ($[M\text{-}Br]^+$) 907.5139. found: 907.5150.

(R)-(4-((4-(4,7-Bis(2-(*tert*-butoxy)-2-oxoethyl)-1,4,7-triazonan-1-yl)-5-(*tert*-butoxy)-5-oxopentanamido)methyl)benzyl)tri(4-methylphenyl)phosphonium bromide (9b)

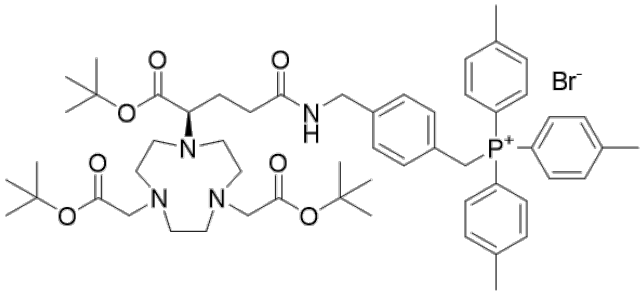

Following **general procedure 7**, the title compound was prepared from (R)-NODAGA(^{t}Bu)$_3$ (0.10 g, 0.19 mmol), (4-(aminomethyl)benzyl)tri(4-methylphenyl)phosphonium bromide (0.11 g, 0.22 mmol), H_2O:MeCN (1:1, 9.00 mL), DCC (0.04 g, 0.20 mmol) and pyridine (1.25 mL) as a pale-yellow solid (0.09 g, 0.09 mmol, 46 %). **^{1}H NMR (400 MHz, CD_3OD) δ_H (ppm):** 7.52 (6H, dd, $^3J_{HH}$ = 8.1, $^4J_{HH}$ = 3.4 Hz, *m*-Ar), 7.45 (6H, dd, $^3J_{HP}$ = 12.3, $^3J_{HH}$ = 8.1 Hz, *o*-Ar), 7.15 (2H, d, $^3J_{HH}$ = 7.0 Hz, $C_6\underline{H}_4$), 6.95 (2H, dd, $^3J_{HH}$ = 7.8, $^4J_{HH}$ = 2.7 Hz, $C_6\underline{H}_4$), 4.77 (2H, d, $^2J_{HP}$ = 14.9 Hz, $C\underline{H}_2P$), 4.33 (2H, s, $C\underline{H}_2NH$), 3.58 (5H, m, $C\underline{H}_2COO^tBu/C\underline{H}N$), 3.04 (12H, m, macrocycle $\underline{H}$), 2.50 (9H, s, Ar-$C\underline{H}_3$), 2.40 (2H, m, $C\underline{H}_2CONH$), 2.03 (2H, m, $NCHC\underline{H}_2$), 1.49 (27H, m, $COOC(C\underline{H}_3)_3$). **^{13}C{^{1}H} NMR (101 MHz, CD_3OD) δ_C (ppm):** 175.0 ($\underline{C}ONH$), 173.1 ($\underline{C}OO^tBu$), 171.2 ($\underline{C}OO^tBu$), 168.5 ($\underline{C}OO^tBu$), 148.0 (*p*-Ar), 141.0 ($\underline{C}_6H_4$), 135.2 (d, $^2J_{CP}$ = 9.7 Hz, *o*-Ar), 132.3 (d, $^2J_{CP}$ = 6.1 Hz, $\underline{C}_6H_4$), 131.9 (d, $^3J_{CP}$ = 12.9 Hz, *m*-Ar), 129.0 ($\underline{C}_6H_4$), 127.8 ($\underline{C}_6H_4$), 115.9 (d, $^1J_{CP}$ = 89.5 Hz, *i*-Ar), 84.4, 83.4, 83.2 ($COO\underline{C}(CH_3)_3$), 64.9 ($\underline{C}HN$), 56.4 ($\underline{C}H_2COO^tBu$), 52.9, 51.3, 46.9, 46.0 (macrocycle $\underline{C}$), 43.5 ($\underline{C}H_2NH$), 33.8 ($\underline{C}H_2CONH$), 30.7 (d, $^1J_{CP}$ = 48.1 Hz, $\underline{C}H_2P$), 28.5, 28.4, 28.2 ($COOC(\underline{C}H_3)_3$), 27.2 ($NCH\underline{C}H_2$), 21.8 (Ar-$\underline{C}H_3$). **^{31}P{^{1}H} NMR (162 MHz, CD_3OD) δ_P (ppm):** 21.8. **HRMS (ES-TOF+):** *m/z* calcd. for $C_{56}H_{78}N_4O_7P$ ($[M\text{-}Br]^+$) 949.5603. found: 949.5592.

(R)-(4-((4-(4,7-Bis(2-(*tert*-butoxy)-2-oxoethyl)-1,4,7-triazonan-1-yl)-5-(*tert*-butoxy)-5-oxopentanamido)methyl)benzyl)tri(3,5-methylphenyl)phosphonium bromide (9c)

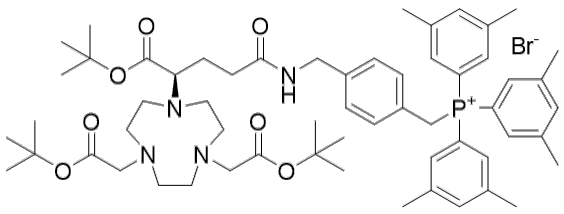

Following **general procedure 7**, the title compound was prepared from (R)-NODAGA(^{t}Bu)$_3$ (0.10 g, 0.19 mmol), (4-(aminomethyl)benzyl)tri(3,5-dimethylphenyl)phosphonium bromide (0.12 g, 0.22 mmol), H_2O:MeCN (1:1, 9.00 mL), DCC (0.04 g, 0.20 mmol) and pyridine (1.25 mL) as a pale-yellow solid (0.09 g, 0.09 mmol, 46 %). **^{1}H NMR (400 MHz, CD_3OD) δ_H (ppm):** 7.51 (3H, m, *p*-Ar), 7.15 (8H, m, *o*-Ar/$C_6\underline{H}_4$), 6.91 (2H, dd, $^3J_{HH}$ = 8.2, $^4J_{HH}$ = 2.5 Hz, $C_6\underline{H}_4$), 4.75 (2H, d, $^2J_{HP}$ = 14.8 Hz, $C\underline{H}_2P$), 4.34 (2H, s, $C\underline{H}_2NH$), 3.79 (4H, m, $C\underline{H}_2COO^tBu$), 3.54 (1H, t, $^3J_{HH}$ = 7.3 Hz, C<u>H</u>N), 3.11 (12H, m, macrocycle <u>H</u>), 2.48 (2H, m, $C\underline{H}_2CONH$), 2.35 (18H, s, Ar-$C\underline{H}_3$), 2.02 (2H, m, NCHC<u>H</u>$_2$), 1.49 (27H, s, COOC($C\underline{H}_3$)$_3$). **^{13}C{^{1}H} NMR (101 MHz, CD_3OD) δ_C (ppm):** 175.0 (<u>C</u>ONH) 173.0 (<u>C</u>OO^{t}Bu), 141.7 (d, $^3J_{CP}$ = 13.1 Hz, *m*-Ar), 141.1 (d, $^5J_{CP}$ = 3.9 Hz, $\underline{C}_6H_4$), 137.8 (d, $^4J_{CP}$ = 3.3 Hz, *p*-Ar), 132.6 (d, $^2J_{CP}$ = 9.7 Hz, *o*-Ar), 132.4 (d, $^3J_{CP}$ = 5.6 Hz, $\underline{C}_6H_4$), 128.9 (d, $^4J_{CP}$ = 3.4 Hz, $\underline{C}_6H_4$), 128.0 (d, $^2J_{CP}$ = 8.6 Hz, $\underline{C}_6H_4$), 119.1 (d, $^1J_{CP}$ = 71.5 Hz, *i*-Ar), 83.2 (COO<u>C</u>(CH$_3$)$_3$), 65.0 (<u>C</u>HN), 56.4 ($\underline{C}H_2COO^tBu$), 52.8, 51.4, 46.9, 46.0 (macrocycle <u>C</u>), 43.5 ($\underline{C}H_2NH$), 33.8 ($\underline{C}H_2CONH$), 30.5 (d, $^1J_{CP}$ = 48.3 Hz, $\underline{C}H_2P$), 28.5, 28.4, 28.3 (COOC(<u>C</u>H$_3$)$_3$), 27.1 (NCH<u>C</u>H$_2$), 21.3 (Ar-<u>C</u>H$_3$). **^{31}P{^{1}H} NMR (162 MHz, CD_3OD) δ_P (ppm):** 22.2. **HRMS (ES-TOF+):** *m/z* calcd. for $C_{59}H_{84}N_4O_7P$ ($[M\text{-}Br]^+$) 991.6078. found: 991.6077.

(R)-(4-((4-(4,7-Bis(2-(*tert*-butoxy)-2-oxoethyl)-1,4,7-triazonan-1-yl)-5-(*tert*-butoxy)-5-oxopentanamido)methyl)benzyl)tris(4-methoxyphenyl)phosphonium bromide (9d)

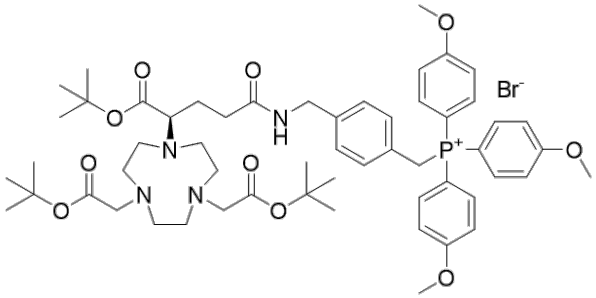

Following **general procedure 7**, the title compound was prepared from (R)-NODAGA(^{t}Bu)$_3$ (0.09 g, 0.16 mmol), (4-(aminomethyl)benzyl)tris(4-methoxyphenyl)phosphonium bromide (0.11 g, 0.19 mmol), H_2O:MeCN (1:1, 9.00 mL), DCC (0.04 g, 0.20 mmol) and pyridine (1.15 mL) as a pale-yellow solid (0.15 g, 0.14 mmol, 86 %). **^{1}H NMR (400 MHz, CD_3OD) δ_H (ppm):** 7.49 (6H, dd, $^3J_{HP}$ = 11.8, $^3J_{HH}$ = 8.6 Hz, *o*-Ar), 7.23 (6H, dd, $^3J_{HH}$ = 8.8, $^4J_{HH}$ = 2.7 Hz, *m*-Ar), 7.18 (2H, d, $^3J_{HH}$ = 7.8 Hz, $C_6\underline{H}_4$), 6.97 (2H, m, $C_6\underline{H}_4$), 4.68 (2H, d, $^2J_{HP}$ = 14.8 Hz, $C\underline{H}_2P$), 4.35 (2H, s, $C\underline{H}_2NH$), 3.94 (9H, s, $OC\underline{H}_3$), 3.62 (5H, m, $C\underline{H}_2COO^tBu$/C<u>H</u>N), 3.06 (12H, m, macrocycle <u>H</u>), 2.44 (2H, t, $^3J_{HH}$ = 7.8 Hz, $C\underline{H}_2CONH$), 2.03 (2H, m, NCHC<u>H</u>$_2$), 1.50 (27H,

m, COOC($C\underline{H}_3$)$_3$). **^{13}C{^{1}H} NMR (101 MHz, CD_3OD) δ_C (ppm):** 176.6 ($\underline{C}OO^tBu$), 175.0 ($\underline{C}ONH$), 173.1 ($\underline{C}OO^tBu$), 171.2 ($\underline{C}OO^tBu$), 166.4 (*p*-Ar), 140.9 ($\underline{C}_6H_4$), 137.2 (d, $^2J_{CP}$ = 11.9 Hz, *o*-Ar), 132.3 (d, $^3J_{CP}$ = 5.4 Hz, $\underline{C}_6H_4$), 129.0 ($\underline{C}_6H_4$), 128.2 ($\underline{C}_6H_4$), 116.9 (d, $^3J_{CP}$ = 13.8 Hz, *m*-Ar), 109.7 (d, $^1J_{CP}$ = 93.8 Hz, *i*-Ar), 84.4, 83.4, 83.2 (COO$\underline{C}$(CH$_3$)$_3$), 64.9 ($\underline{C}HN$), 56.4 ($\underline{C}H_2COO^tBu$/O$\underline{C}H_3$), 52.9, 51.5, 46.9, 46.0 (macrocycle $\underline{C}$), 43.5 ($\underline{C}H_2NH$), 33.8 ($\underline{C}H_2CONH$), 31.6 (d, $^1J_{CP}$ = 51.7 Hz, $\underline{C}H_2P$), 28.4 (COOC($\underline{C}H_3$)$_3$), 27.1 (NCH$\underline{C}H_2$). **^{31}P{^{1}H} NMR (162 MHz, CD_3OD) δ_P (ppm):** 20.6. **HRMS (ES-TOF+):** *m/z* calcd. for $C_{56}H_{78}N_4O_{10}P$ ([M-Br]$^+$) 997.5415. found: 997.5456.

(R)-(4-((4-(4,7-Bis(2-(*tert*-butoxy)-2-oxoethyl)-1,4,7-triazonan-1-yl)-5-(*tert*-butoxy)-5-oxopentanamido)methyl)benzyl)tris(4-ethoxyphenyl)phosphonium bromide (9e)

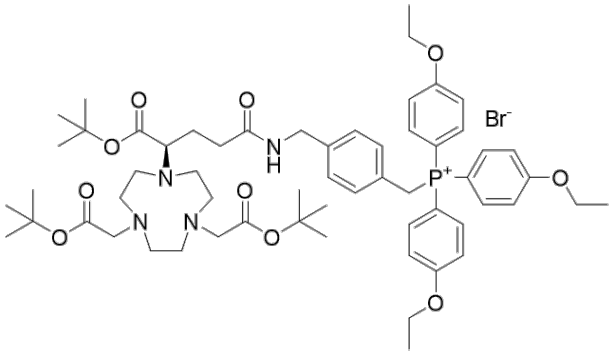

Following **general procedure 7**, the title compound was prepared from (R)-NODAGA(^{t}Bu)$_3$ (0.09 g, 0.16 mmol), (4-(aminomethyl)benzyl)tris(4-ethoxyphenyl)phosphonium bromide (0.11 g, 0.19 mmol), H_2O:MeCN (1:1, 9.00 mL), DCC (0.04 g, 0.20 mmol) and pyridine (1.15 mL) as a pale-yellow solid (0.06 g, 0.06 mmol, 35 %). **^{1}H NMR (400 MHz, CD_3OD) δ_H (ppm):** 7.47 (6H, m, *o*-Ar), 7.20 (6H, dd, $^3J_{HH}$ = 9.0, $^4J_{HH}$ = 2.5 Hz, *m*-Ar), 7.17 (2H, m, $C_6\underline{H}_4$), 6.97 (2H, dd, $^3J_{HH}$ = 8.3, $^4J_{HH}$ = 2.5 Hz, $C_6\underline{H}_4$), 4.65 (2H, d, $^2J_{HP}$ = 14.8 Hz, $C\underline{H}_2P$), 4.35 (2H, s, $C\underline{H}_2NH$), 4.19 (6H, q, $^3J_{HH}$ = 7.0 Hz, $OC\underline{H}_2CH_3$), 3.90 (4H, m, $C\underline{H}_2COO^tBu$), 3.56 (1H, m, $C\underline{H}N$), 3.11 (12H, m, macrocycle $\underline{H}$), 2.44 (2H, t, $^3J_{HH}$ = 7.7 Hz, $C\underline{H}_2CONH$), 2.05 (2H, m, NCHC$\underline{H}_2$), 1.50 (27H, m, COOC($C\underline{H}_3$)$_3$), 1.45 (9H, t, $^3J_{HH}$ = 7.0 Hz, $OCH_2C\underline{H}_3$). **^{13}C{^{1}H} NMR (101 MHz, CD_3OD) δ_C (ppm):** 176.7 ($\underline{C}OO^tBu$), 175.0 ($\underline{C}ONH$), 173.1 ($\underline{C}OO^tBu$), 165.6 (*p*-Ar), 140.9 ($\underline{C}_6H_4$), 137.2 (d, $^2J_{CP}$ = 10.6 Hz, *o*-Ar), 132.2 (d, $^3J_{CP}$ = 6.2 Hz, $\underline{C}_6H_4$), 128.9 ($\underline{C}_6H_4$), 128.2 ($\underline{C}_6H_4$), 117.2 (d, $^3J_{CP}$ = 13.8 Hz, *m*-Ar), 109.5 (d, $^1J_{CP}$ = 95.2 Hz, *i*-Ar), 84.3, 83.4, 83.2 (COO$\underline{C}$(CH$_3$)$_3$), 65.4 (O$\underline{C}H_2CH_3$), 64.9 ($\underline{C}HN$), 56.4 ($\underline{C}H_2COO^tBu$), 52.8, 51.4, 46.8, 46.0 (macrocycle $\underline{C}$), 43.5 ($\underline{C}H_2NH$), 33.7 ($\underline{C}H_2CONH$), 31.6 (d, $^1J_{CP}$ = 51.1 Hz, $\underline{C}H_2P$), 28.4 (COOC($\underline{C}H_3$)$_3$), 27.1 (NCH$\underline{C}H_2$), 14.8 ($OCH_2\underline{C}H_3$). **^{31}P{^{1}H} NMR**

(162 MHz, CD_3OD) δ_P (ppm): 20.4. **HRMS (ES-TOF+):** *m/z* calcd. for $C_{59}H_{84}N_4O_{10}P$ ($[M-Br]^+$) 1039.5925. found: 1039.5945.

(R)-(4-((4-(4,7-Bis(2-(*tert*-butoxy)-2-oxoethyl)-1,4,7-triazonan-1-yl)-5-(*tert*-butoxy)-5-oxopentanamido)methyl)benzyl)tris(3,5-dimethoxyphenyl)phosphonium bromide (9f)

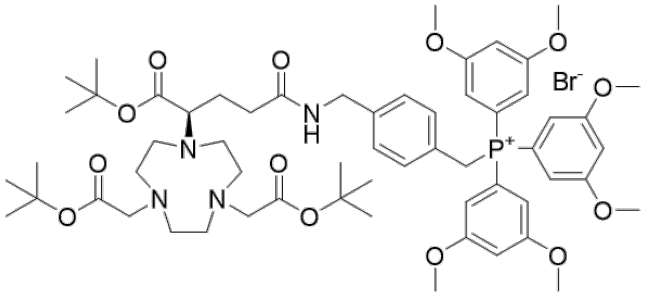

Following **general procedure 7**, the title compound was prepared from (R)-NODAGA(^{t}Bu)$_3$ (0.10 g, 0.18 mmol), (4-(aminomethyl)benzyl)tris(3,5-dimethoxyphenyl)phosphonium bromide (0.13 g, 0.21 mmol), H_2O:MeCN (1:1, 9.00 mL), DCC (0.04 g, 0.20 mmol) and pyridine (1.25 mL) as a pale-yellow oil (0.21 g, 0.18 mmol, 100 %). **^{1}H NMR (400 MHz, CD_3OD) δ_H (ppm):** 7.16 (2H, d, $^3J_{HH}$ = 7.9 Hz, $C_6\underline{H}_4$), 6.91 (2H, dd, $^3J_{HH}$ = 8.2, $^4J_{HH}$ = 2.4 Hz, $C_6\underline{H}_4$), 6.78 (3H, t, $^4J_{HH}$ = 2.2 Hz, *p*-Ar), 6.48 (6H, dd, $^3J_{HP}$ = 14.1, $^4J_{HH}$ = 2.2 Hz, *o*-Ar), 4.42 (2H, d, $^2J_{HP}$ = 14.1 Hz, $C\underline{H}_2P$), 4.34 (2H, m, $C\underline{H}_2NH$), 3.72 (18H, s, *m*-Ar($C\underline{H}_3$)$_3$), 3.50 (5H, m, $C\underline{H}_2COO^tBu$/$C\underline{H}N$), 3.10 (12H, m, macrocycle $\underline{H}$), 2.51 (2H, m, $C\underline{H}_2CONH$), 2.09 (2H, m, $NCHC\underline{H}_2$), 1.43 (27H, s, $COOC(C\underline{H}_3)_3$). **^{13}C{^{1}H} NMR (101 MHz, CD_3OD) δ_C (ppm):** 176.9 ($\underline{C}OO^tBu$), 174.8 ($\underline{C}ONH$), 171.1 ($\underline{C}OO^tBu$), 171.0 ($\underline{C}OO^tBu$), 162.1 (d, $^3J_{CP}$ = 19.0 Hz, *m*-Ar), 139.0 ($\underline{C}_6H_4$), 131.1 ($\underline{C}_6H_4$), 128.7 ($\underline{C}_6H_4$), 125.8 (d, $^2J_{CP}$ = 8.1 Hz, $\underline{C}_6H_4$), 119.4 (d, $^1J_{CP}$ = 91.1 Hz, *i*-Ar), 111.8 (d, $^2J_{CP}$ = 11.0 Hz, *o*-Ar), 106.4 (*p*-Ar), 83.3 ($COO\underline{C}(CH_3)_3$), 83.1 ($COO\underline{C}(CH_3)_3$), 63.6 ($\underline{C}H_2COO^tBu$/$\underline{C}HN$), 55.8 ($O\underline{C}H_3$), 53.5, 50.5, 46.3, 45.8 (macrocycle $\underline{C}$), 43.2 ($\underline{C}H_2NH$), 33.0 ($\underline{C}H_2CONH$), 31.7 ($COOC(\underline{C}H_3)_3$), 30.9 ($\underline{C}H_2P$), 24.7 ($NCH\underline{C}H_2$). **^{31}P{^{1}H} NMR (162 MHz, CD_3OD) δ_P (ppm):** 24.0. **HRMS (ES-TOF+):** *m/z* calcd. for $C_{59}H_{84}N_4O_{13}P$ ($[M-Br]^+$). 1087.5773. found: 1087.5793.

7.1.3.7 General Procedure 8 – Deprotection of *Tert*-Butyl Protected (R)-NODAGA-xy-TAP Compounds using Trifluoroacetic Acid

Tert-butyl protected (R)-NODAGA-xy-TAP compounds **9a-f** were dissolved in trifluoroacetic acid (reaction mixture concentration 0.1 g mL^{-1}) and stirred at room temperature under an N_2 atmosphere for 48 h. The acid was removed under reduced pressure, before the crude residue

was purified by reverse-phase chromatography (C-18 SiO_2, 0-100 % B in A) to give the product as a white solid.

(R)-NODAGA-xy-TPP trifluoroacetate (10a)

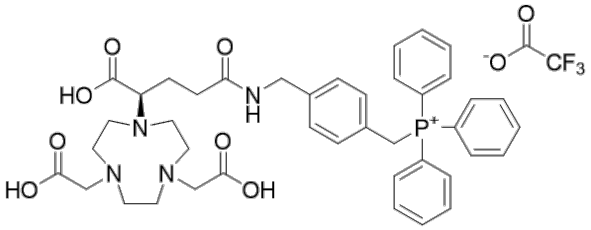

Following **general procedure 8**, the title compound was prepared from **9a** (0.18 g, 0.18 mmol) and trifluoroacetic acid (1.80 mL) as a white solid (0.10 g, 0.12 mmol, 67 %). **^{1}H NMR (400 MHz, CD_3OD) δ_H (ppm):** 7.89 (3H, t, $^3J_{HH}$ = 7.5 Hz, *p*-Ph), 7.72 (6H, dt, $^3J_{HH}$ = 7.7, $^4J_{HH}$ = 3.5 Hz, *m*-Ph), 7.63 (6H, dd, $^3J_{HP}$ = 12.6, $^3J_{HH}$ = 7.7 Hz, *o*-Ph), 7.16 (2H, d, $^3J_{HH}$ = 7.7 Hz, $C_6\underline{H}_4$), 6.95 (2H, dd, $^3J_{HH}$ = 7.9, $^4J_{HH}$ = 2.7 Hz, $C_6\underline{H}_4$), 4.88 (2H, d, $^2J_{HP}$ = 14.9 Hz, $C\underline{H}_2P$), 4.33 (2H, s, $C\underline{H}_2NH$), 3.97 (4H, m, $C\underline{H}_2COOH$), 3.61 (1H, t, $^3J_{HH}$ = 7.1 Hz, $\underline{C}HN$), 3.11 (12H, m, macrocycle $\underline{H}$), 2.47 (2H, m, $C\underline{H}_2CONH$), 2.09 (2H, m, $NCHC\underline{H}_2$). **$^{13}C\{^1H\}$ NMR (101 MHz, CD_3OD) δ_C (ppm):** 175.1 ($\underline{C}ONH$), 175.0 ($\underline{C}OOH$), 141.2 (d, $^5J_{CP}$ = 4.2 Hz, $\underline{C}_6H_4$), 136.5 (d, $^4J_{CP}$ = 3.2 Hz, *p*-Ph), 135.3 (d, $^2J_{CP}$ = 9.7 Hz, *o*-Ph), 132.3 (d, $^2J_{CP}$ = 5.5 Hz, $\underline{C}_6H_4$), 131.3 (d, $^3J_{CP}$ = 12.8 Hz, *m*-Ph), 129.1 (d, $^4J_{CP}$ = 3.5 Hz, $\underline{C}_6H_4$), 127.4 (d, $^3J_{CP}$ = 8.8 Hz, $\underline{C}_6H_4$), 119.1 (d, $^1J_{CP}$ = 86.5 Hz, *i*-Ph), 64.3 ($\underline{C}HN$), 55.8 ($\underline{C}H_2COOH$), 52.1, 47.2 (macrocycle $\underline{C}$), 43.5 ($\underline{C}H_2NH$), 33.6 ($\underline{C}H_2CONH$), 30.4 (d, $^1J_{CP}$ = 48.4 Hz, $\underline{C}H_2P$), 26.6 ($NCH\underline{C}H_2$). **$^{31}P\{^1H\}$ NMR (162 MHz, CD_3OD) δ_P (ppm):** 22.6. **$^{19}F\{^1H\}$ NMR (377 MHz, CD_3OD) δ_F (ppm):** -77.1. **HRMS (ES-TOF+):** *m/z* calcd. for $C_{41}H_{48}N_4O_7P$ ($[M\text{-}CF_3CO_2]^+$) 739.3261. found: 739.3265.

(R)-NODAGA-xy-TTP trifluoroacetate (10b)

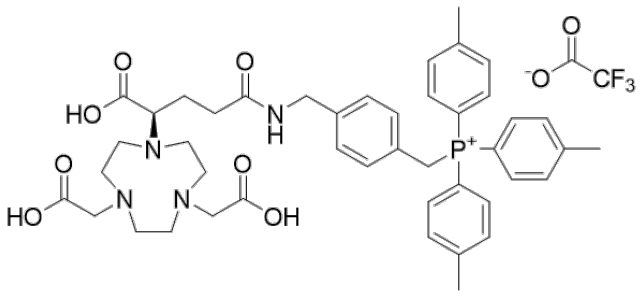

Following **general procedure 8**, the title compound was prepared from **9b** (0.09 g, 0.09 mmol) and trifluoroacetic acid (0.90 mL) as a white solid (0.05 g, 0.06 mmol, 61 %). **^{1}H NMR (400**

MHz, CD_3OD) δ_H (ppm): 7.52 (6H, dd, $^3J_{HH}$ = 8.3, $^4J_{HH}$ = 3.4 Hz, *m*-Ar), 7.45 (6H, dd, $^3J_{HP}$ = 12.2, $^3J_{HH}$ = 8.1 Hz, *o*-Ar), 7.16 (2H, d, $^3J_{HH}$ = 7.9 Hz, $C_6\underline{H}_4$), 6.94 (2H, dd, $^3J_{HH}$ = 8.1, $^4J_{HH}$ = 2.7 Hz, $C_6\underline{H}_4$), 4.75 (2H, d, $^2J_{HP}$ = 14.9 Hz, $C\underline{H}_2P$), 4.33 (2H, s, $C\underline{H}_2NH$), 3.88 (5H, m, $C\underline{H}_2COOH/C\underline{H}N$), 3.10 (12H, m, macrocycle $\underline{H}$), 2.50 (9H, s, Ar-$C\underline{H}_3$), 2.46 (2H, m, $C\underline{H}_2CONH$), 2.08 (2H, m, $NCHC\underline{H}_2$). **$^{13}C\{^1H\}$ NMR (101 MHz, CD_3OD) δ_C (ppm):** 175.1 ($\underline{C}ONH/\underline{C}OOH$), 148.1 (*p*-Ar), 141.1 ($\underline{C}_6H_4$), 135.2 (d, $^2J_{CP}$ = 9.9 Hz, *o*-Ar), 132.2 (d, $^3J_{CP}$ = 5.2 Hz, $\underline{C}_6H_4$), 131.9 (d, $^3J_{CP}$ = 12.4 Hz, *m*-Ar), 129.0 ($\underline{C}_6H_4$), 127.8 (d, $^2J_{CP}$ = 8.7 Hz, $\underline{C}_6H_4$), 115.9 (d, $^1J_{CP}$ = 88.5 Hz, *i*-Ar), 64.3 ($\underline{C}HN$), 55.8 ($\underline{C}H_2COOH$), 52.0, 47.0 (macrocycle $\underline{C}$), 43.6 ($\underline{C}H_2NH$), 33.6 ($\underline{C}H_2CONH$), 30.8 (d, $^1J_{CP}$ = 48.8 Hz, $\underline{C}H_2P$), 26.6 ($NCH\underline{C}H_2$), 21.8 (Ar-$\underline{C}H_3$). **$^{31}P\{^1H\}$ NMR (162 MHz, CD_3OD) δ_P (ppm):** 21.8. **HRMS (ES-TOF+):** *m/z* calcd. for $C_{44}H_{54}N_4O_7P$ ($[M\text{-}CF_3CO_2]^+$) 781.3730. found: 781.3740.

(R)-NODAGA-xy-TXP trifluoroacetate (10c)

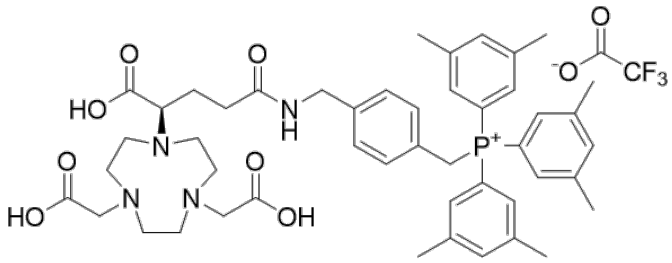

Following **general procedure 8**, the title compound was prepared from **9c** (0.10 g, 0.09 mmol) and trifluoroacetic acid (1.00 mL) as a white solid (0.06 g, 0.07 mmol, 76 %). **^1H NMR (400 MHz, CD_3OD) δ_H (ppm):** 7.52 (3H, m, *p*-Ar), 7.15 (8H, m, *o*-Ar/$C_6\underline{H}_4$), 6.91 (2H, dd, $^3J_{HH}$ = 8.2, $^4J_{HH}$ = 2.5 Hz, $C_6\underline{H}_4$), 4.74 (2H, d, $^2J_{HP}$ = 14.8 Hz, $C\underline{H}_2P$), 4.33 (2H, s, $C\underline{H}_2NH$), 3.84 (4H, m, $C\underline{H}_2COO^tBu$), 3.60 (1H, t, $^3J_{HH}$ = 7.2 Hz, $C\underline{H}N$), 3.15 (12H, m, macrocycle $\underline{H}$), 2.46 (2H, m, $C\underline{H}_2CONH$), 2.35 (18H, s, Ar-$C\underline{H}_3$), 2.06 (2H, m, $NCHC\underline{H}_2$). **$^{13}C\{^1H\}$ NMR (101 MHz, CD_3OD) δ_C (ppm):** 175.1 ($\underline{C}ONH/\underline{C}OOH$), 141.7 (d, $^3J_{CP}$ = 13.0 Hz, *m*-Ar), 141.2 ($\underline{C}_6H_4$), 137.9 (*p*-Ar), 132.6 (d, $^2J_{CP}$ = 9.7 Hz, *o*-Ar), 132.4 ($\underline{C}_6H_4$), 128.9 ($\underline{C}_6H_4$), 128.0 ($\underline{C}_6H_4$), 119.0 (d, $^1J_{CP}$ = 85.0 Hz, *i*-Ar), 64.2 ($\underline{C}HN$), 55.8 ($\underline{C}H_2COOH$), 52.2, 51.6, 47.3, 46.5 (macrocycle $\underline{C}$), 43.5 ($\underline{C}H_2NH$), 33.6 ($\underline{C}H_2CONH$), 30.6 (d, $^1J_{CP}$ = 48.0 Hz, $\underline{C}H_2P$), 26.6 ($NCH\underline{C}H_2$), 21.3 (Ar-$\underline{C}H_3$). **$^{31}P\{^1H\}$ NMR (162 MHz, CD_3OD) δ_P (ppm):** 22.2. **$^{19}F\{^1H\}$ NMR (377 MHz, CD_3OD) δ_F (ppm):** -77.4. **HRMS (ES-TOF+):** *m/z* calcd. for $C_{47}H_{60}N_4O_7P$ ($[M\text{-}CF_3CO_2]^+$) 823.4200. found: 823.4175.

(R)-NODAGA-xy-TMeOPP trifluoroacetate (10d)

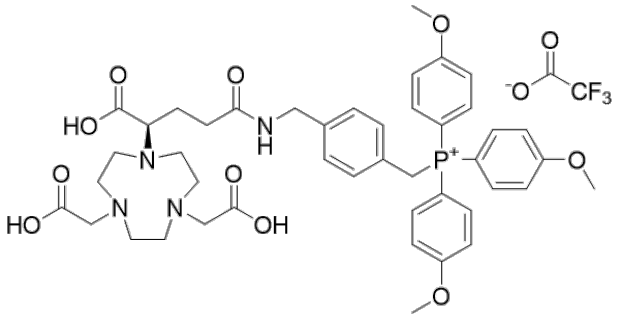

Following **general procedure 8**, the title compound was prepared from **9d** (0.15 g, 0.14 mmol) and trifluoroacetic acid (1.50 mL) as a white solid (0.05 g, 0.05 mmol, 38 %). **^{1}H NMR (400 MHz, CD_3OD) δ_H (ppm):** 7.49 (6H, dd, $^{3}J_{HP}$ = 11.9, $^{3}J_{HH}$ = 8.5 Hz, *o*-Ar), 7.21 (6H, dd, $^{3}J_{HH}$ = 8.7, $^{4}J_{HH}$ = 2.6 Hz, *m*-Ar), 7.17 (2H, d, $^{3}J_{HH}$ = 7.7 Hz, $C_6\underline{H}_4$), 6.95 (2H, dd, $^{3}J_{HH}$ = 8.0, $^{4}J_{HH}$ = 2.6 Hz, $C_6\underline{H}_4$), 4.64 (2H, d, $^{2}J_{HP}$ = 14.7 Hz, $C\underline{H}_2P$), 4.34 (2H, s, $C\underline{H}_2NH$), 3.92 (9H, s, $OC\underline{H}_3$), 3.72 (4H, m, $C\underline{H}_2COOH$) 3.59 (1H, t, $^{3}J_{HH}$ = 7.1 Hz, C<u>H</u>N), 3.11 (12H, m, macrocycle <u>H</u>), 2.46 (2H, m, $C\underline{H}_2CONH$), 2.09 (2H, m, $NCHC\underline{H}_2$). **^{13}C{^{1}H} NMR (101 MHz, CD_3OD) δ_C (ppm):** 175.1 (<u>C</u>ONH/<u>C</u>OOH), 166.4 (*p*-Ar), 140.9 ($\underline{C}_6H_4$), 137.2 (d, $^{2}J_{CP}$ = 10.8 Hz, *o*-Ar), 132.3 (d, $^{3}J_{CP}$ = 5.1 Hz, $\underline{C}_6H_4$), 129.0 ($\underline{C}_6H_4$), 128.1 (d, $^{2}J_{CP}$ = 8.8 Hz, $\underline{C}_6H_4$), 116.9 (d, $^{3}J_{CP}$ = 13.8 Hz, *m*-Ar), 109.7 (d, $^{1}J_{CP}$ = 93.8 Hz, *i*-Ar), 64.3 (<u>C</u>HN), 56.4 ($O\underline{C}H_3$), 55.8 ($\underline{C}H_2COOH$), 52.0, 51.3, 47.3, 46.7 (macrocycle <u>C</u>), 43.6 ($\underline{C}H_2NH$), 33.6 ($\underline{C}H_2CONH$), 31.7 (d, $^{1}J_{CP}$ = 50.6 Hz, $\underline{C}H_2P$), 26.6 ($NCH\underline{C}H_2$). **^{31}P{^{1}H} NMR (162 MHz, CD_3OD) δ_P (ppm):** 20.6. **HRMS (ES-TOF+):** *m/z* calcd. for $C_{44}H_{54}N_4O_{10}P$ ($[M\text{-}Br]^+$) 829.3578. found: 829.3597.

(R)-NODAGA-xy-TEtOPP trifluoroacetate (10e)

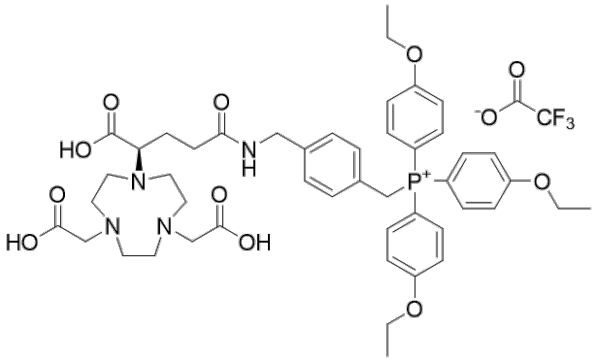

Following **general procedure 8**, the title compound was prepared from **9e** (0.06 g, 0.06 mmol) and trifluoroacetic acid (0.60 mL) as a white solid (0.06 g, 0.06 mmol, 95 %). **^{1}H NMR (400 MHz, CD_3OD) δ_H (ppm):** 7.45 (6H, dd, $^{4}J_{HP}$ = 12.0, $^{3}J_{HH}$ = 8.7 Hz, *o*-Ar), 7.18 (8H, m,

m-Ar/$C_6\underline{H}_4$), 6.95 (2H, dd, $^3J_{HH}$ = 8.1, $^4J_{HH}$ = 2.6 Hz, $C_6\underline{H}_4$), 4.63 (2H, d, $^2J_{HP}$ = 14.7 Hz, $C\underline{H}_2P$), 4.34 (2H, t, $^4J_{HH}$ = 2.5 Hz, $C\underline{H}_2NH$), 4.17 (6H, q, $^3J_{HH}$ = 6.9 Hz, $OC\underline{H}_2CH_3$), 3.79 (4H, m, $C\underline{H}_2COOH$), 3.59 (1H, t, $^3J_{HH}$ = 7.1 Hz, $C\underline{H}N$), 3.14 (12H, m, macrocycle $\underline{H}$), 2.47 (2H, t, $^3J_{HH}$ = 7.0 Hz, $C\underline{H}_2CONH$), 2.02 (2H, m, $NCHC\underline{H}_2$), 1.44 (9H, t, $^3J_{HH}$ = 6.9 Hz, $OCH_2C\underline{H}_3$). **$^{13}C\{^1H\}$ NMR (101 MHz, CD_3OD) δ_C (ppm):** 175.1 ($\underline{C}OOH/\underline{C}ONH$), 165.7 (*p*-Ar), 140.9 ($\underline{C}_6H_4$), 137.2 (d, $^2J_{CP}$ = 10.4 Hz, *o*-Ar), 132.3 (d, $^3J_{CP}$ = 5.9 Hz, $\underline{C}_6H_4$), 129.0 ($\underline{C}_6H_4$), 128.2 (d, $^2J_{CP}$ = 8.6 Hz, $\underline{C}_6H_4$), 117.2 (d, $^3J_{CP}$ = 12.9 Hz, *m*-Ar), 109.5 (d, $^1J_{CP}$ = 94.9 Hz, *i*-Ar), 65.5 ($O\underline{C}H_2CH_3$), 64.3 ($\underline{C}HN$), 55.8 ($\underline{C}H_2COOH$), 52.8, 47.3 (macrocycle $\underline{C}$), 43.6 ($\underline{C}H_2NH$), 33.6 ($\underline{C}H_2CONH$), 31.7 (d, $^1J_{CP}$ = 51.1 Hz, $\underline{C}H_2P$), 26.6 ($NCH\underline{C}H_2$), 14.8 ($OCH_2\underline{C}H_3$). **$^{31}P\{^1H\}$ NMR (162 MHz, CD_3OD) δ_P (ppm):** 20.4. **HRMS (ES-TOF+):** *m/z* calcd. for $C_{47}H_{60}N_4O_{10}P$ ($[M\text{-}Br]^+$) 871.4047. found: 871.4052.

(R)-NODAGA-xy-TDiMeOPP trifluoroacetate (10f)

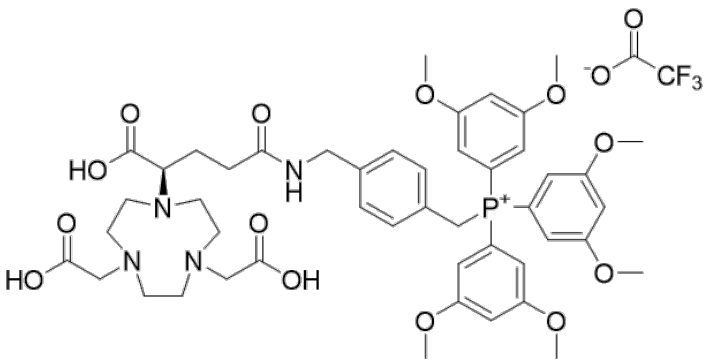

Following **general procedure 8**, the title compound was prepared from **9f** (0.21 g, 0.18 mmol) and trifluoroacetic acid (2.10 mL) as a white solid (0.09 g, 0.09 mmol, 48 %). **^1H NMR (400 MHz, CD_3OD) δ_H (ppm):** 7.22 (2H, d, $^3J_{HH}$ = 7.8 Hz, $C_6\underline{H}_4$), 7.07 (2H, dd, $^3J_{HH}$ = 8.1, $^4J_{HH}$ = 2.5 Hz, $C_6\underline{H}_4$), 6.95 (3H, t, $^4J_{HH}$ = 2.3 Hz, *p*-Ar), 6.66 (6H, dd, $^3J_{HP}$ = 14.0, $^4J_{HH}$ = 2.2 Hz, *o*-Ar), 4.88 (2H, d, $^2J_{HP}$ = 15.2 Hz, $C\underline{H}_2P$), 4.33 (2H, m, $C\underline{H}_2NH$), 3.87 (4H, m, $C\underline{H}_2COOH$), 3.77 (18H, s, *m*-Ar($C\underline{H}_3$)$_3$), 3.60 (1H, m, $C\underline{H}N$), 3.11 (12H, m, macrocycle $\underline{H}$), 2.47 (2H, m, $C\underline{H}_2CONH$), 2.02 (2H, m, $NCHC\underline{H}_2$). **$^{13}C\{^1H\}$ NMR (101 MHz, CD_3OD) δ_C (ppm):** 175.1 ($\underline{C}OOH/\underline{C}ONH$), 163.4 (d, $^3J_{CP}$ = 19.1 Hz, *m*-Ar), 141.3 ($\underline{C}_6H_4$), 132.6 ($\underline{C}_6H_4$), 129.1 ($\underline{C}_6H_4$), 127.9 (d, $^2J_{CP}$ = 8.7 Hz, $\underline{C}_6H_4$), 120.6 (d, $^1J_{CP}$ = 86.8 Hz, *i*-Ar), 113.0 (d, $^2J_{CP}$ = 11.1 Hz, *o*-Ar), 107.4 (*p*-Ar), 64.2 ($\underline{C}HN$), 56.5 ($O\underline{C}H_3$), 55.8 ($\underline{C}H_2COOH$), 52.0, 47.0 (macrocycle $\underline{C}$), 43.4 ($\underline{C}H_2NH$), 33.6 ($\underline{C}H_2CONH$), 30.2 (d, $^1J_{CP}$ = 48.3 Hz, $\underline{C}H_2P$), 26.6 ($NCH\underline{C}H_2$). **$^{31}P\{^1H\}$ NMR (162 MHz, CD_3OD) δ_P (ppm):** 25.1. **HRMS (ES-TOF+):** *m/z* calcd. for $C_{47}H_{60}N_4O_{13}P$ ($[M\text{-}CF_3CO_2]^+$) 919.3895. found: 919.3904.

7.1.3.8 General Procedure 9 – Complexation of (R)-NODAGA-xy-TAP Ligands with $^{nat}Ga^{3+}$

To a solution of (R)-NODAGA-xy-TAP **10a-c** (1 eq.) in NaOAc buffer (3.60 M, 5.00 mL, pH 5), $Ga(NO_3)_3.xH_2O$ (1.5 eq.) was added, and the resulting suspension was stirred at room temperature for 15 min. The mixture was concentrated under reduced pressure, before the crude residue was purified by reverse-phase flash chromatography (C-18 SiO_2, 0-100 % B in A) to yield a white solid.

Ga-(R)-NODAGA-xy-TPP trifluoroacetate (Ga10a)

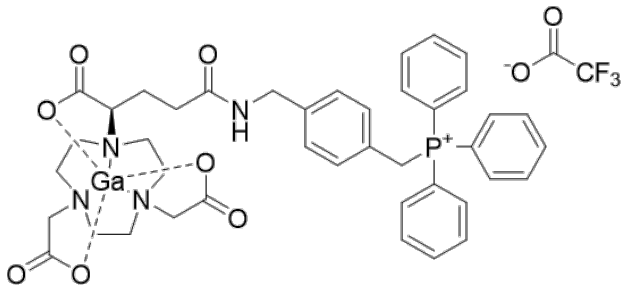

Following **general procedure 9**, the title compound was synthesised from (R)-NODAGA-xy-TPP **10a** (0.03 g, 0.04 mmol) and $Ga(NO_3)_3.xH_2O$ (0.01 g, 0.05 mmol) as a white solid (0.03 g, 0.03 mmol, 83 %). **^{1}H NMR (400 MHz, CD_3OD) δ_H (ppm):** 7.88 (3H, m, *p*-Ph), 7.71 (6H, td, $^3J_{HH}$ = 7.7, $^4J_{HH}$ = 3.5 Hz, *m*-Ph), 7.63 (6H, dd, $^3J_{HP}$ = 12.5, $^3J_{HH}$ = 7.7 Hz, *o*-Ph), 7.14 (2H, d, $^3J_{HH}$ = 7.5 Hz, $C_6\underline{H}_4$), 6.99 (2H, m, $C_6\underline{H}_4$), 4.88 (2H, m, $C\underline{H}_2P$), 4.29 (2H, m, $C\underline{H}_2NH$), 3.67 (5H, m, $C\underline{H}_2COOGa/C\underline{H}N$), 3.49 (4H, m, macrocycle $\underline{H}$), 3.13 (8H, m, macrocycle $\underline{H}$), 2.63 (2H, m, $C\underline{H}_2CONH$), 2.20 (2H, m, $NCHC\underline{H}_2$). **$^{13}C\{^1H\}$ NMR (101 MHz, CD_3OD) δ_C (ppm):** 175.7 ($\underline{C}ONH$), 174.6 ($\underline{C}OOGa$), 174.5 ($\underline{C}OOGa$), 174.4 ($\underline{C}OOGa$), 141.1 ($\underline{C}_6H_4$), 136.5 (*p*-Ph), 135.4 (d, $^2J_{CP}$ = 9.7 Hz, *o*-Ph), 132.5 (d, $^2J_{CP}$ = 5.5 Hz, $\underline{C}_6H_4$), 131.4 (d, $^3J_{CP}$ = 12.6 Hz, *m*-Ph), 129.2 (d, $^4J_{CP}$ = 3.3 Hz, $\underline{C}_6H_4$), 127.4 ($\underline{C}_6H_4$), 119.1 (d, $^1J_{CP}$ = 86.1 Hz, *i*-Ph), 68.5 ($\underline{C}HN$), 63.43 ($\underline{C}H_2COOGa$), 54.8, 54.5, 54.1, 53.8 (macrocycle $\underline{C}$), 43.5 ($\underline{C}H_2NH$), 34.04 ($\underline{C}H_2CONH$), 30.4 (d, $^1J_{CP}$ = 48.4 Hz, $\underline{C}H_2P$), 23.7 ($NCH\underline{C}H_2$). **$^{31}P\{^1H\}$ NMR (162 MHz, CD_3OD) δ_P (ppm):** 22.6. **HRMS (ES-TOF+):** *m/z* calcd. for $C_{41}H_{45}N_4O_7PGa$ ($[M\text{-}NO_3]^+$) 806.2360. found: 806.2341.

Ga-(R)-NODAGA-xy-TTP trifluoroacetate (Ga10b)

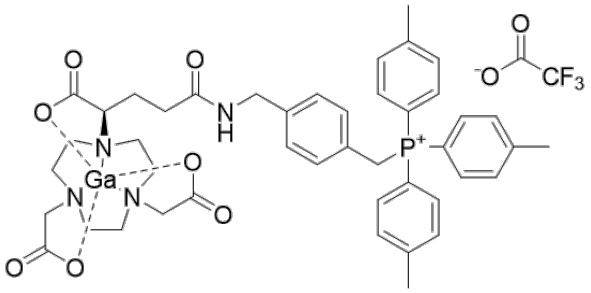

Following **general procedure 9**, the title compound was synthesised from (R)-NODAGA-xy-TTP **10b** (0.03 g, 0.03 mmol) and $Ga(NO_3)_3.xH_2O$ (0.01 g, 0.04 mmol) as a white solid (0.03 g, 0.03 mmol, 97 %). **^{1}H NMR (400 MHz, CD_3OD) δ_H (ppm):** 7.52 (6H, dd, $^3J_{HH}$ = 8.2, $^4J_{HH}$ = 3.4 Hz, *m*-Ar), 7.45 (6H, dd, $^3J_{HP}$ = 12.2, $^3J_{HH}$ = 8.1 Hz, *o*-Ar), 7.14 (2H, d, $^3J_{HH}$ = 7.7 Hz, $C_6\underline{H}_4$), 6.98 (2H, m, $C_6\underline{H}_4$), 4.76 (2H, d, $^2J_{HP}$ = 14.9 Hz, $C\underline{H}_2P$), 4.32 (2H, m, $C\underline{H}_2NH$), 3.67 (5H, m, $C\underline{H}_2COOGa/C\underline{H}N$), 3.47 (4H, m, macrocycle $\underline{H}$), 3.22 (8H, m, macrocycle $\underline{H}$), 2.62 (2H, m, $C\underline{H}_2CONH$), 2.49 (9H, s, Ar-$C\underline{H}_3$), 2.23 (2H, m, $NCHC\underline{H}_2$). **^{13}C{^{1}H} NMR (101 MHz, CD_3OD) δ_C (ppm):** 175.7 ($\underline{C}ONH$), 174.6 ($\underline{C}OOGa$), 174.5 ($\underline{C}OOGa$), 174.4 ($\underline{C}OOGa$), 148.0 (d, $^4J_{CP}$ = 3.2 Hz, *p*-Ar), 141.0 (d, $^4J_{CP}$ = 4.2 Hz, $\underline{C}_6H_4$), 135.2 (d, $^2J_{CP}$ = 9.8 Hz, *o*-Ar), 132.5 (d, $^3J_{CP}$ = 5.3 Hz, $\underline{C}_6H_4$), 131.9 (d, $^3J_{CP}$ = 12.9 Hz, *m*-Ar), 129.1 (d, $^5J_{CP}$ = 3.3 Hz, $\underline{C}_6H_4$), 127.8 (d, $^2J_{CP}$ = 8.7 Hz, $\underline{C}_6H_4$), 115.9 (d, $^1J_{CP}$ = 89.1 Hz, *i*-Ar), 68.5 ($\underline{C}HN$), 63.4 ($\underline{C}H_2COOGa$), 54.8, 54.5, 54.1, 53.8 (macrocycle $\underline{C}$), 43.6 ($\underline{C}H_2NH$), 34.03 ($\underline{C}H_2CONH$), 30.8 (d, $^1J_{CP}$ = 48.8 Hz, $\underline{C}H_2P$), 22.9 ($NCH\underline{C}H_2$), 21.8 (Ar-$\underline{C}H_3$). **^{31}P{^{1}H} NMR (162 MHz, CD_3OD) δ_P (ppm):** 21.8. **HRMS (ES-TOF+):** *m/z* calcd. for $C_{44}H_{51}N_4O_7PGa$ ($[M\text{-}NO_3]^+$) 848.2829. found: 848.2817.

Ga-(R)-NODAGA-xy-TXP trifluoroacetate (Ga10c)

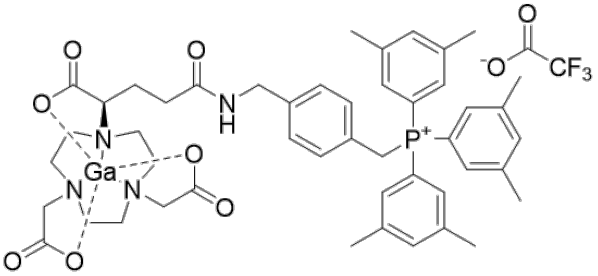

Following **general procedure 9**, the title compound was synthesised from (R)-NODAGA-xy-TXP **10c** (0.03 g, 0.03 mmol) and $Ga(NO_3)_3.xH_2O$ (0.01 g, 0.05 mmol) as a white solid (0.03 g, 0.03 mmol, 99 %). **^{1}H NMR (400 MHz, CD_3OD) δ_H (ppm):** 7.51 (3H,

m, *p*-Ar), 7.14 (8H, m, *o*-Ar/C$_6$H$_4$), 6.94 (2H, dd, $^3J_{HH}$ = 8.2, $^4J_{HH}$ = 2.5 Hz, C$_6$H$_4$), 4.75 (2H, d, $^2J_{HP}$ = 14.7 Hz, CH$_2$P), 4.33 (2H, m, CH$_2$NH), 3.67 (5H, m, CH$_2$COOGa/CHN), 3.45 (4H, m, macrocycle H), 3.10 (8H, m, macrocycle H), 2.58 (2H, m, CH$_2$CONH), 2.35 (18H, s, Ar-CH$_3$), 2.01 (2H, m, NCHCH$_2$). **^{13}C{^{1}H} NMR (101 MHz, CD$_3$OD) δ$_C$ (ppm):** 175.4 (CONH), 174.6 (COOGa), 174.5 (COOGa), 174.4 (COOGa), 141.7 (*m*-Ar), 141.6 (C$_6$H$_4$), 137.9 (*p*-Ar), 132.6 (d, $^2J_{CP}$ = 8.7 Hz, *o*-Ar), 128.9 (C$_6$H$_4$), 128.0 (C$_6$H$_4$), 119.0 (d, $^1J_{CP}$ = 84.8 Hz, *i*-Ar), 63.4 (CHN), 54.8 (CH$_2$COOGa), 54.1, 53.8 (macrocycle C), 43.5 (CH$_2$NH), 34.0 (CH$_2$CONH), 30.3 (d, $^1J_{CP}$ = 48.0 Hz, CH$_2$P), 22.8 (NCHCH$_2$), 21.3 (Ar-CH$_3$). **^{31}P{^{1}H} NMR (162 MHz, CD$_3$OD) δ$_P$ (ppm):** 22.2. **HRMS (ES-TOF+):** *m/z* calcd. for $C_{47}H_{57}N_4O_7PGa$ ([M-NO$_3$]$^+$) 890.3299. found: 890.3305.

Ga-(R)-NODAGA-xy-TMeOPP trifluoroacetate (Ga10d)

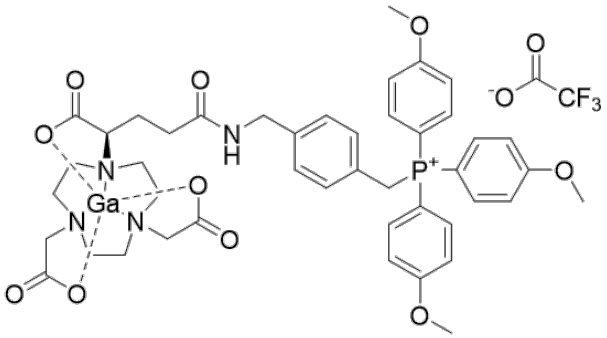

Following **general procedure 9**, the title compound was synthesised from (R)-NODAGA-xy-TMeOPP **10d** (0.03 g, 0.03 mmol) and Ga(NO$_3$)$_3$.xH$_2$O (0.01 g, 0.05 mmol) as a white solid (0.02 g, 0.02 mmol, 67 %). **^{1}H NMR (400 MHz, CD$_3$OD) δ$_H$ (ppm):** 7.48 (6H, dd, $^3J_{HP}$ = 11.9, $^3J_{HH}$ = 8.5 Hz, *o*-Ar), 7.21 (6H, dd, $^3J_{HH}$ = 8.6, $^4J_{HH}$ = 2.7 Hz, *m*-Ar), 7.15 (2H, d, $^3J_{HH}$ = 7.6 Hz, C$_6$H$_4$), 6.99 (2H, m, C$_6$H$_4$), 4.67 (2H, d, $^2J_{HP}$ = 14.9 Hz, CH$_2$P), 4.33 (2H, m, CH$_2$NH), 3.92 (9H, s, OCH$_3$), 3.70 (4H, m, CH$_2$COOGa/CHN), 3.19 (12H, m, macrocycle H), 2.62 (2H, m, CH$_2$CONH), 2.21 (2H, m, NCHCH$_2$). **^{13}C{^{1}H} NMR (101 MHz, CD$_3$OD) δ$_C$ (ppm):** 174.5 (CONH/COOGa), 166.4 (*p*-Ar), 140.8 (C$_6$H$_4$), 137.2 (d, $^2J_{CP}$ = 11.2 Hz, *o*-Ar), 132.4 (d, $^3J_{CP}$ = 5.3 Hz, C$_6$H$_4$), 129.0 (C$_6$H$_4$), 128.2 (C$_6$H$_4$), 116.9 (d, $^3J_{CP}$ = 13.7 Hz, *m*-Ar), 109.8 (d, $^1J_{CP}$ = 94.4 Hz, *i*-Ar), 63.4 (CHN), 56.5 (OCH$_3$), 54.7 (CH$_2$COOGa), 54.5, 54.1, 53.8, 45.1 (macrocycle C), 43.6 (CH$_2$NH), 34.0 (CH$_2$CONH), 31.3 (CH$_2$P), 22.8 (NCHCH$_2$). **^{31}P{^{1}H} NMR (162 MHz, CD$_3$OD) δ$_P$ (ppm):** 20.5. **HRMS (ES-TOF+):** *m/z* calcd. for $C_{44}H_{51}N_4O_{10}PGa$ ([M-TFA]$^+$) 895.2599. found: 895.2621.

Ga-(R)-NODAGA-xy-TEtOPP trifluoroacetate (Ga10e)

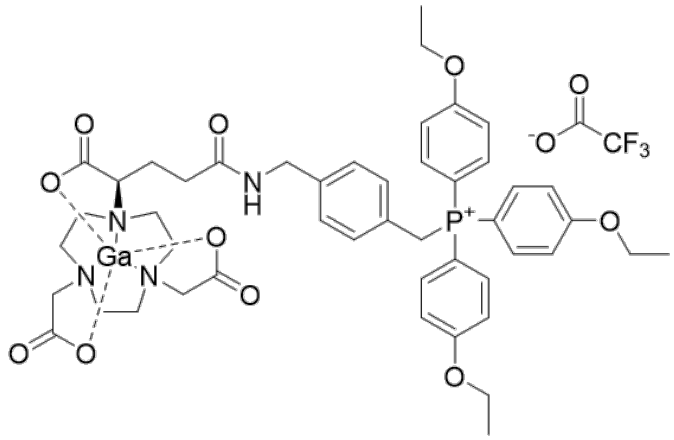

Following **general procedure 9**, the title compound was synthesised from (R)-NODAGA-xy-TEtOPP **10e** (0.03 g, 0.03 mmol) and $Ga(NO_3)_3.xH_2O$ (0.01 g, 0.05 mmol) as a white solid (0.03 g, 0.03 mmol, 88 %). **^{1}H NMR (400 MHz, CD_3OD) δ_H (ppm):** 7.46 (6H, dd, $^3J_{HP}$ = 11.9, $^3J_{HH}$ = 8.6 Hz, *o*-Ar), 7.17 (8H, m, *m*-Ar/$C_6\underline{H}_4$), 6.99 (2H, dd, $^3J_{HH}$ = 8.1, $^4J_{HH}$ = 2.5 Hz, $C_6\underline{H}_4$), 4.64 (2H, dd, $^2J_{HP}$ = 14.8, $^4J_{HH}$ = 3.9 Hz, $C\underline{H}_2P$), 4.34 (2H, m, $C\underline{H}_2NH$), 4.17 (6H, q, $^3J_{HH}$ = 7.0 Hz, $OC\underline{H}_2CH_3$), 3.68 (4H, m, $C\underline{H}_2COOGa/C\underline{H}N$), 3.47 (12H, m, macrocycle $\underline{H}$), 2.62 (2H, m, $C\underline{H}_2CONH$), 2.20 (2H, m, $NCHC\underline{H}_2$), 1.43 (9H, t, $^3J_{HH}$ = 7.0 Hz, $OCH_2C\underline{H}_3$). **^{13}C{^{1}H} NMR (101 MHz, CD_3OD) δ_C (ppm):** 174.5 ($\underline{C}OOGa/\underline{C}ONH$), 165.7 (*p*-Ar), 140.8 ($\underline{C}_6H_4$), 137.2 (d, $^2J_{CP}$ = 11.2 Hz, *o*-Ar), 132.4 (d, $^3J_{CP}$ = 5.5 Hz, $\underline{C}_6H_4$), 129.0 ($\underline{C}_6H_4$), 128.3 ($\underline{C}_6H_4$), 117.3 (d, $^3J_{CP}$ = 13.7 Hz, *m*-Ar), 109.6 (d, $^1J_{CP}$ = 94.5 Hz, *i*-Ar), 65.5 ($O\underline{C}H_2CH_3$), 63.4 ($\underline{C}HN$), 54.8 ($\underline{C}H_2COOH$), 54.5, 54.1, 53.8, 45.0 (macrocycle $\underline{C}$), 43.6 ($\underline{C}H_2NH$), 34.0 ($\underline{C}H_2CONH$), 31.6 ($\underline{C}H_2P$), 22.8 ($NCH\underline{C}H_2$), 14.9 ($OCH_2\underline{C}H_3$). **^{31}P{^{1}H} NMR (162 MHz, CD_3OD) δ_P (ppm):** 20.4. **HRMS (ES-TOF+):** *m/z* calcd. for $C_{47}H_{57}N_4O_{10}PGa$ ($[M\text{-}TFA]^+$) 937.3068. found: 937.3100.

Ga-(R)-NODAGA-xy-TDiMeOPP trifluoroacetate (Ga10f)

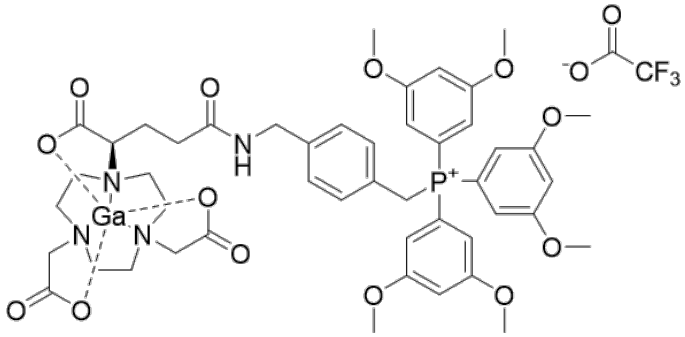

HRMS (ES-TOF+): *m/z* calcd. for $C_{47}H_{57}N_4O_{13}PGa$ ($[M\text{-}TFA]^+$) 985.2916. found: 985.2917.

7.1.4 BisAAPA Ligands (Section 5.1)

7.1.4.1 General Procedure 10 – *O*-Alkylation of 2,4-Dihydroxybenzaldehyde using Alkyl Iodides – Attempted Synthesis

This procedure was adapted from the methodology by Gudipudi *et al*.[4] To a cooled solution of 2,4-dihydroxybenzaldehyde (1 eq.) in acetone, K_2CO_3 (2.2 eq.) and ethyl iodide (2.2 eq.) were added in a dropwise manner over 10 min, maintaining the temperature at 0-5 °C. Once the addition was complete, the mixture was stirred at room temperature for 18 h, before the mixture was concentrated under reduced pressure. The crude residue was dissolved in H_2O and the product was extracted with EtOAc, the organic phases were combined, dried over Na_2SO_4, filtered and the solvent was removed under reduced pressure. The crude product was purified by silica flash chromatography (SiO_2, hexane:EtOAc, 7:3) to give the pure product.

2,4-Diethoxybenzaldehyde (12b) – Attempted Synthesis

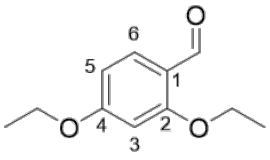

This compound was originally synthesised by Bowie *et al*.[19] Following **general procedure 10**, the preparation of the title compound was attempted from 2,4-dihydroxybenzaldehyde (1.00g, 7.24 mmol), acetone (15 mL), K_2CO_3 (2.20 g, 15.9 mmol) and ethyl iodide (1.27 mL, 15.9 mmol).

7.1.4.2 General Procedure 11 – Acid-Catalysed Dakin Oxidation of 2,4-Dialkoxybenzaldehydes

This procedure was adapted from the methodology reported by Azevedo *et al*.[20] 2,4-Dialkoxybenzaldehyde (1 eq.) and $H_2O_{2(aq)}$ (30 % wt.) were suspended in MeOH (50 mL). H_2SO_4 was added to the suspension in a dropwise manner and the resulting mixture was stirred at room temperature for 22 h. The solvent was removed under reduced pressure and the crude residue was purified by silica flash chromatography (SiO_2, hexane:EtOAc, 8:2) to give the pure product.

2,4-Dimethoxyphenol (13a)[20]

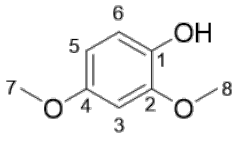

Following **general procedure 11**, the title compound was prepared from 2,4-dimethoxybenzaldehyde (5.00 g, 30.1 mmol), $H_2O_{2(aq)}$ (30 % wt., 5.00 mL) and H_2SO_4 (0.50 mL) as a yellow oil (3.24 g, 21.0 mmol, 70 %). **^{1}H NMR (400 MHz, $CDCl_3$) δ_H (ppm):** 6.83 (1H, d, $^3J_{HH}$ = 8.7 Hz, H_6), 6.49 (1H, d, $^4J_{HH}$ = 2.7 Hz, H_3), 6.39 (1H, dd, $^3J_{HH}$ = 8.7, $^4J_{HH}$ = 2.8 Hz, H_5), 3.85 (3H, s, H_7), 3.76 (3H, s, H_8). **^{13}C{^{1}H} NMR (101 MHz, $CDCl_3$) δ_C (ppm):** 153.4 (C_4), 147.2 (C_2), 139.7 (C_1), 114.3 (C_6), 104.2 (C_5), 99.4 (C_3), 55.8 (C_8), 55.7 (C_7). **HRMS (ES-TOF+):** *m/z* calcd. for $C_8H_{10}O_3$ ($[M]^+$) 154.0624. found: 154.0622.

7.1.4.3 General Procedure 12 – *Ortho*-Formylation of Dialkoxyphenols using $MgCl_2$ – Attempted Synthesis

This procedure was adapted from the methodology described by Sharma *et al*.[21] To a solution of 2,4-dialkoxyphenol (1 eq.) in anhydrous MeCN, anhydrous $MgCl_2$ (5 eq.) and anhydrous Et_3N (10 eq.) were added slowly and the resulting mixture was stirred at room temperature for 1 h under a N_2 atmosphere. Paraformaldehyde (5 eq.) was then added to the mixture, which was stirred at reflux for 4 h. The mixture was cooled, H_2O was added, and the mixture was acidified to pH 3 with HCl (3 M). The product was extracted with Et_2O (3 × 100 mL), the organic phases were combined, dried over Na_2SO_4, filtered, and concentrated under reduced pressure. The crude residue was purified by silica flash chromatography (SiO_2, hexane:EtOAc, 7:3).

2-Hydroxy-3,5-dimethoxybenzaldehyde (14a) – Attempted Synthesis

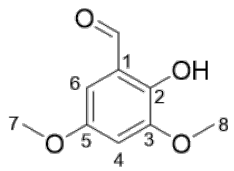

Following **general procedure 12**, the synthesis of the title compound was attempted from 2,4-dimethoxyphenol (0.60 g, 3.89 mmol), $MgCl_2$ (1.85 g, 19.5 mmol), Et_3N (5.41 mL, 38.9 mmol), MeCN (100 mL) and paraformaldehyde (0.58 g, 19.5 mmol).

7.1.4.4 General Procedure 13 – *O*-Alkylation of 3,5-Dihydroxybenzaldehyde using Alkyl Iodides

This procedure was performed as a modification of the methodology reported by Döerwald *et al*.[22] To a solution of 3,5-dihydroxybenzaldehyde (1 eq.) in DMSO, alkyl iodide (3.3 eq.) and K_2CO_3 (2.7 eq.) were added and the resulting mixture was stirred at 60 °C for 24 h under a N_2 atmosphere. After 24 h, the mixture was cooled to room temperature and stirred for an additional 48 h. Excess alkyl iodide was removed under vacuum using an in-line trap over 2 h period. The crude residue was dissolved in H_2O (100 mL) and acidified using conc. HCl. The product was extracted with EtOAc (2 × 100 mL) and washed with brine (100 mL). The organic layer was then dried over $MgSO_4$, filtered and concentrated under reduced pressure to give the desired product.

3,5-Diethoxybenzaldehyde (15b)

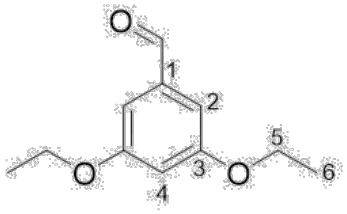

Following **general procedure 13**, the title compound was prepared from 3,5-dihydroxybenzaldehyde (0.64 g, 4.63 mmol), DMSO (5.00 mL), ethyl iodide (1.25 mL, 15.5 mmol) and K_2CO_3 (1.73 g, 12.5 mmol) to give an orange oil (0.61 g, 3.14 mmol, 68 %). **^{1}H NMR (400 MHz, $CDCl_3$) δ_H (ppm):** 9.82 (1H, s, C<u>H</u>O), 6.92 (2H, d, $^4J_{HH}$ = 2.4 Hz, H_2), 6.63 (1H, t, $^4J_{HH}$ = 2.3 Hz, H_4), 4.00 (4H, q, $^3J_{HH}$ = 6.9 Hz, H_5), 4.00 (6H, t, $^3J_{HH}$ = 7.0 Hz, H_6). **^{13}C{^{1}H} NMR (101 MHz, $CDCl_3$) δ_C (ppm):** 192.0 (C_1), 160.5 (C_3), 138.3 (<u>C</u>HO), 107.9 (C_4), 107.5 (C_2), 63.8 (C_5), 14.7 (C_6). **HRMS (ES-TOF+):** *m*/*z* calcd. for $C_{11}H_{15}O_3$ ($[M+H]^+$) 195.1021. found: 195.1022.

7.1.4.5 General Procedure 14 – NBS-Assisted Bromination of 3,5-Dialkoxybenzaldehydes

This procedure was performed as an adaptation of the method described by Liao *et al*.[5] To a cooled solution of 3,5-dialkoxybenzaldehyde (1 eq.) in MeCN, NBS (1 eq.) was added portionwise and the temperature was maintained between 0 and 5 °C. Upon completion of the addition, the mixture was stirred at room temperature for 24 h, before the reaction was diluted

with H_2O and extracted with EtOAc (3 ×). The organic layers were combined and washed with brine (3 ×), dried over $MgSO_4$, filtered and concentrated under reduced pressure to give the product.

2-Bromo-3,5-diethoxybenzaldehyde (16b)

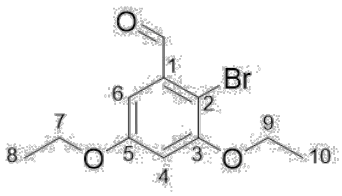

Following **general procedure 14**, the title compound was prepared from 3,5-diethoxybenzaldehyde (2.07 g, 10.7 mmol), MeCN (20 mL), NBS (1.90 g, 10.7 mmol), H_2O (200 mL), EtOAc (3 × 100 mL) and brine (3 × 100 mL) to give an off-white solid (1.92 g, 7.03 mmol, 66 %). **^{1}H NMR (400 MHz, $CDCl_3$) δ_H (ppm):** 10.40 (1H, s, C<u>H</u>O), 7.01 (1H, d, $^4J_{HH}$ = 2.9 Hz, H_6), 6.69 (1H, d, $^4J_{HH}$ = 2.9 Hz, H_4), 4.08 (4H, m, H_7/H_9), 1.49 (3H, t, $^3J_{HH}$ = 7.0 Hz, H_8), 1.42 (3H, t, $^3J_{HH}$ = 7.1 Hz, H_{10}). **^{13}C{^{1}H} NMR (101 MHz, $CDCl_3$) δ_C (ppm):** 192.4 (C_1), 159.3 (C_5), 156.6 (C_3), 134.8 (<u>C</u>HO), 109.5 (C_2), 107.3 (C_4), 104.1 (C_6), 65.4 (C_7), 64.2 (C_9), 14.8 (C_{10}), 14.7 (C_8). **HRMS (ES-TOF+):** *m*/*z* calcd. for $C_{11}H_{14}O_3Br$ ($[M+H]^+$) 273.0121. found: 273.0120.

7.1.4.6 General Procedure 15 – Synthesis of 2-Hydroxy-3,5-dialkoxybenzaldehydes – Attempted Synthesis

This procedure was carried out as an adaptation of the method developed by Liao *et al*.[5] A solution of $NaOH_{(aq)}$ (8 % w/w) and 2-bromo-3,5-dialkoxybenzaldehyde (1 eq.) was prepared and Cu powder (0.1 eq.) was added to the solution. The mixture was heated at reflux for 24 h, followed by the addition of Na_2CO_3 to quench the reaction. The mixture was allowed to cool to room temperature, filtered and the filtrate was acidified using conc. HCl and extracted with EtOAc (3 × 70 mL). The organic layers were combined, washed with brine, dried over $MgSO_4$, filtered and concentrated under reduced pressure. The crude residue was recrystallized in toluene to give the product.

2-Hydroxy-3,5-dimethoxybenzaldehyde (14a) – Attempted Synthesis

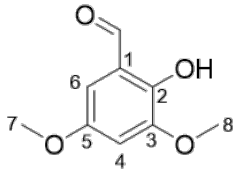

Following **general procedure 15**, the synthesis of the title compound was attempted from 2-bromo-3,5-dimethoxybenzaldehyde (3.00 g, 12.3 mmol) and Cu powder (0.09 g, 1.40 mmol).

7.1.4.7 General Procedure 16 – Hexamine Aromatic Formylation of 2,4-Dialkoxyphenols towards the synthesis of 2-Hydroxy-3,5-Dialkoxybenzaldehydes

This procedure was performed as an adaptation of the method reported by Zhang *et al*.[23] 2,4-Dialkoxyphenol (1 eq.) and hexamethylenetetramine (2 eq.) were dissolved in neat TFA, and the mixture was stirred at reflux overnight under a flow of N_2. The mixture was cooled to room temperature and 0.1 M HCl was added. The mixture was stirred at room temperature for 6 h before extraction with EtOAc (4 ×). The organic layers were combined, dried over $MgSO_4$, filtered and concentrated under vacuum. The crude material was purified by flash silica chromatography (SiO_2, hexane:EtOAc, 6:4) to give the pure product.

2-Hydroxy-3,5-dimethoxybenzaldehyde (14a)[24]

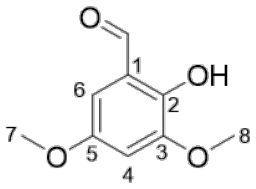

Following **general procedure 16**, the title compound was prepared with 2,4-dimethoxyphenol (1.00 g, 6.49 mmol), hexamethylenetetramine (1.82 g, 13.0 mmol), TFA (30 mL), 0.1 M HCl (100 mL) and EtOAc (4 × 150 mL) to give an off-white solid (0.42 g, 2.31 mmol, 36 %). **^{1}H NMR (400 MHz, $CDCl_3$) δ_H (ppm):** 10.27 (1H, s, C<u>H</u>O), 7.36 (1H, s, H_6), 6.46 (1H, s, H_4), 3.97 (3H, s, H_8), 3.89 (3H, s, H_7). **^{13}C{^{1}H} NMR (101 MHz, $CDCl_3$) δ_C (ppm):** 188.6 (<u>C</u>HO), 158.1 (C_5), 153.3 (C_3), 140.0 (C_2), 118.3 (C_1), 112.9 (C_6), 95.5 (C_4), 56.5 (C_7), 56.3 (C_8). **HRMS (ES-TOF+):** *m*/*z* calcd. for $C_9H_{11}O_4$ ($[M+H]^+$) 183.0652. found: 183.0653.

7.1.4.8 General Procedure 17 – Imine Condensation of 2-Hydroxy-3,5-dialkoxybenzaldehydes and BDMAPEN – Attempted Synthesis

This procedure was a modification of method reported by Tsang *et al.*[25] 2-Hydroxy-3,5-dialkoxybenzaldehyde (3 eq.) was added to a solution of bis(amino-2,2-dimethylpropane)ethylenediamine (1 eq.) in anhydrous MeOH, and the mixture was heated at reflux for 20 min under a N_2 atmosphere. The mixture was then cooled to room temperature and concentrated under reduced pressure. Diethyl ether was added to the crude residue, and the resulting precipitate was removed by filtration. The filtrate was left to stand at 4 °C overnight. The newly formed precipitate was isolated by filtration and dried under reduced pressure to give the product.

Bis(3,5-dimethoxysalicylaldehyde)BDMAPEN (18a) – Attempted Synthesis

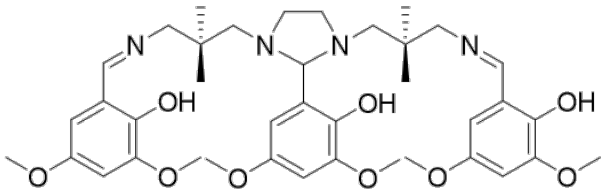

Following **general procedure 17**, the synthesis of the title compound was attempted from 2-hydroxy-3,5-dimethoxybenzaldehyde (0.10 g, 0.55 mmol), bis(amino-2,2-dimethylpropane)ethylenediamine (0.04 g, 0.18 mmol), anhydrous MeOH (3.00 mL) and Et_2O (10 mL).

7.1.4.9 General Procedure 18 – Imine Condensation of 2-Hydroxy-3,5-dialkoxybenzaldehydes and BAPEN – Attempted Synthesis

This procedure was a modification of method reported by Tsang *et al.*[26] 2-hydroxy-3,5-dialkoxybenzaldehyde (3 eq.) was added to a solution of bis(3-aminopropyl)ethylenediamine (1 eq.) in anhydrous MeOH, and the mixture was heated at reflux for 20 min under a N_2 atmosphere. The mixture was then cooled to room temperature and concentrated under reduced pressure. Diethyl ether was added to the crude residue, and the resulting precipitate was removed by filtration. The filtrate was left to stand at 4 °C overnight. The newly formed precipitate was isolated by filtration and dried under reduced pressure to give the product.

Bis(3,5-dimethoxysalicylaldehyde)BAPEN (19a) – Attempted Synthesis

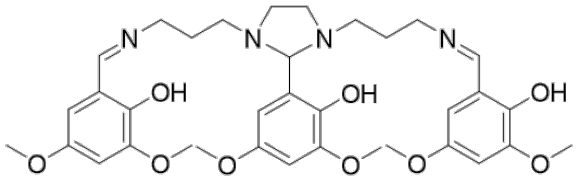

Following **general procedure 18**, the synthesis of the title compound was attempted from 2-hydroxy-3,5-dimethoxybenzaldehyde (0.10 g, 0.55 mmol), bis(3-aminopropyl)ethylenediamine (0.03 mL, 0.18 mmol), anhydrous MeOH (3.00 mL) and Et_2O (10 mL).

7.1.4.10 Synthesis of (4,6-(MeO)$_2$sal)$_2$BAPEN (21)[26]

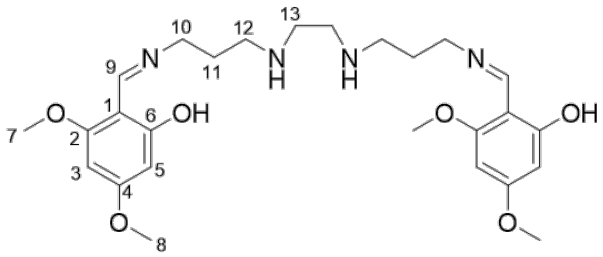

This compound was synthesised according to the methodology reported by Tsang *et al*.[26] To a solution of 2-hydroxy-4,6-dimethoxybenzaldehyde (0.50 g, 2.74 mmol) in anhydrous MeOH (15 mL), bis(3-aminopropyl)ethylenediamine (0.17 mL, 0.91 mmol) and molecular sieves were added. The mixture was stirred at reflux for 1 h before being cooled to room temperature and concentrated under reduced pressure. Et_2O (15 mL) was added to the crude material and the resulting precipitate was removed by filtration. The filtrate was left to stand at 4 °C overnight, and the newly formed precipitate was isolated by filtration, washed with cold Et_2O (15 mL) and dried under reduced pressure to give a yellow solid. **^{1}H NMR (400 MHz, $CDCl_3$) δ_H (ppm):** 8.28 (2H, s, H_9), 5.83 (2H, d, $^4J_{HH}$ = 2.0 Hz, H_3), 5.56 (2H, d, $^4J_{HH}$ = 2.1 Hz, H_5), 3.76 (12H, s, H_7/H_8), 3.56 (3H, t, $^3J_{HH}$ = 6.6 Hz, H_{10}), 2.76 (8H, m, H_{12}/H_{13}), 1.86 (4H, p, $^3J_{HH}$ = 6.7 Hz, H_{11}). **^{13}C{^{1}H} NMR (101 MHz, $CDCl_3$) δ_C (ppm):** 176.4 (C_1), 167.3 (C_2), 161.0 (C_4), 158.2 (C_9), 102.4 (C_6), 95.7 (C_3), 87.7 (C_5), 55.5 (C_7/C_8), 51.4 (C_{10}), 49.2 (C_{12}), 47.3 (C_{13}), 30.7 (C_{11}). **HRMS (ES-TOF+):** *m/z* calcd. for $C_{26}H_{39}N_4O_6$ ($[M+H]^+$) 503.2864. found: 503.2874.

7.1.4.11 General Procedure 19 – Palladium-catalysed Cross-coupling of Ethyl Methylphosphinate with 2-Bromo-3.5-dialkoxybenzaldehyde Compounds

This procedure was performed as an adaptation of the methodology reported by Gavara *et al*.[27] To a mixture of *i*-Pr$_2$NEt (1.3 eq.), Pd(OAc)$_2$ (2 mol %), xantphos (2.2 mol %) and 2-bromo-3,5-dialkoxybenzaldehyde (1.5 eq.) in anhydrous toluene/DME (9:1, v/v) under a N_2 atmosphere, was added ethyl methylphosphinate (1 eq.). The mixture was stirred at room temperature for 10 min before being heated at 115 °C for 48 h. The mixture was then concentrated under reduced pressure and the crude residue was purified by silica flash chromatography (SiO_2, hexane:EtOAc, 1:9) to give the desired product.

2-Ethyl(methyl)phosphinate-3,5-dimethoxybenzaldehyde (23a)

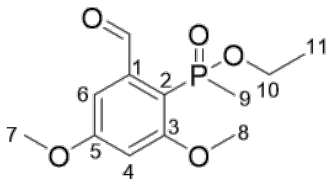

Following **general procedure 19**, the title compound was prepared from *i*-Pr$_2$NEt (0.62 g, 4.77 mmol), Pd(OAc)$_2$ (0.02 g, 0.07 mmol), xantphos (0.05 g, 0.08 mmol), 2-bromo-3,5-dimethoxybenzaldehyde (1.35 g, 5.51 mmol), toluene/DME (9:1, v/v, 18.35 mL) and ethyl methylphosphinate (0.40 g, 3.67 mmol) to give a yellow solid (0.30 g, 1.11 mmol, 30 %). **^{1}H NMR (400 MHz, CDCl$_3$) δ_H (ppm):** 11.08 (1H, s, C<u>H</u>O), 7.01 (1H, t, $^4J_{HH}$ = 2.4 Hz, H_6), 6.66 (1H, dd, $^4J_{HP}$ = 4.2, $^4J_{HH}$ = 2.3 Hz, H_4), 4.02 (2H, m, H_{10}), 3.90 (3H, s, H_7), 3.89 (3H, s, H_8), 1.82 (3H, d, $^1J_{HP}$ = 15.6 Hz, H_9), 1.24 (3H, t, $^3J_{HH}$ = 7.0 Hz, H_{11}). **^{13}C{^{1}H} NMR (101 MHz, CDCl$_3$) δ_C (ppm):** 194.4 (C_1), 164.3 (C_5), 162.8 (d, $^2J_{CP}$ = 4.0 Hz, C_3), 145.8 (d, $^3J_{CP}$ = 8.7 Hz, <u>C</u>HO), 112.0 (d, $^1J_{CP}$ = 123 Hz, C_2), 104.3 (d, $^3J_{CP}$ = 10.6 Hz, C_6), 102.8 (d, $^3J_{CP}$ = 7.6 Hz, C_4), 60.6 (d, $^2J_{CP}$ = 6.7 Hz, C_{10}), 56.2 (C_7), 55.8 (C_8), 17.3 (d, $^1J_{CP}$ = 107 Hz, C_9), 16.4 (d, $^3J_{CP}$ = 7.0 Hz, C_{11}). **^{31}P{^{1}H} NMR (162 MHz, CDCl$_3$) δ_P (ppm):** 42.3. **HRMS (ES-TOF+):** *m/z* calcd. for $C_{12}H_{18}O_5P$ ($[M+H]^+$) 273.0892. found: 273.0904.

2-Ethyl(methyl)phosphinate-3,5-diethoxybenzaldehyde (23b) – Attempted Synthesis

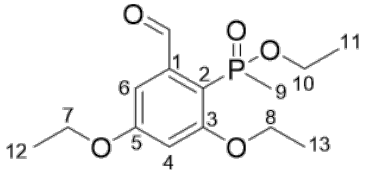

Following **general procedure 19**, the attempted synthesis of the title compound was performed from *i*-Pr_2NEt (0.62 g, 4.77 mmol), $Pd(OAc)_2$ (0.02 g, 0.07 mmol), xantphos (0.05 g, 0.08 mmol), 2-bromo-3,5-diethoxybenzaldehyde (1.50 g, 5.51 mmol), toluene/DME (9:1, v/v, 18.4 mL) and ethyl methylphosphinate (0.40 g, 3.67 mmol).

7.1.4.12 General Procedure 20 – Deprotection of Ethyl Protected Benzaldehyde-phosphinate compounds using Sodium Hydroxide

This procedure was performed as an adaptation to the method reported by Walter *et al*.[8] To a solution of 0.4 M NaOH in H_2O (1.00 mL) and MeOH (2.50 mL), 2-ethyl(methyl)phosphinate-3,5-dialkoxybenzaldehyde (1 eq.) was added, and the mixture was stirred at room temperature for 18 h under a N_2 atmosphere. The mixture was concentrated under reduced pressure and the crude residue was purified by reverse-phase column chromatography (C18-SiO_2, MeCN + 0.1 % TFA in H_2O + 0.1 % TFA) and lyophilised to give the product.

2-Methylphosphinic acid-3,5-dimethoxybenzaldehyde (24a)

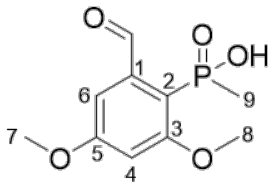

Following **general procedure 20**, the title compound was prepared from 2-ethyl(methyl)phosphinate-3,5-dimethoxybenzaldehyde (0.50 g, 1.84 mmol) to give a yellow oil (0.22 g, 0.90 mmol, 49 %). **^{1}H NMR (400 MHz, CD_3OD) δ_H (ppm):** 10.95 (1H, s, C<u>H</u>O), 6.84 (1H, t, $^4J_{HH}$ = 2.2 Hz, H_6), 6.75 (1H, dd, $^4J_{HP}$ = 3.9, $^4J_{HH}$ = 2.3 Hz, H_4), 3.88 (3H, s, H_7), 3.85 (3H, s, H_8), 1.57 (3H, d, $^1J_{HP}$ = 15.0 Hz, H_9). **^{13}C{^{1}H} NMR (101 MHz, CD_3OD) δ_C (ppm):** 164.1 (d, $^2J_{CP}$ = 5.0 Hz, C_3), 163.8 (C_5), 144.4 (d, $^2J_{CP}$ = 6.3 Hz, C_1), 122.4 (d, $^1J_{CP}$ = 120.2 Hz, C_2), 104.2 (d, $^3J_{CP}$ = 9.5 Hz, C_6), 103.3 (d, $^3J_{CP}$ = 6.4 Hz, C_4), 56.3 (C_7), 56.0 (C_8), 20.7 (d, $^1J_{CP}$ = 102.1 Hz, C_9). **^{31}P{^{1}H} NMR (162 MHz, CD_3OD) δ_P (ppm):** 29.5. **HRMS (ES-TOF+):** *m/z* calcd. for $C_{10}H_{13}O_5P$ ($[M+H]^+$) 245.0579. found: 245.0578.

7.1.4.13 General Procedure 21 – Imine Condensation of Benzaldehyde-phosphinic acid compounds and BDMAPEN – Attempted Synthesis

This procedure was an adaptation of the methodology developed by Tsang *et al*.[25,26] To a solution of BDMAPEN (1 eq.) in anhydrous MeOH, 2-methylphosphinicacid-3,5-dialkoxybenzaldehyde (3 eq.) was added and the mixture was refluxed for 3 h. The mixture was cooled to room temperature, concentrated under reduced pressure and Et_2O was added. The precipitate was removed by filtration and left to stand at 4 °C overnight, and the newly formed precipitate was isolated by filtration, washed with cold Et_2O (15 mL) and dried under reduced pressure to give the product.

(2-methylphosphinicacid-3,5-dimethoxyphenyl)$_2$BDMAPEN (25a) – Attempted Synthesis

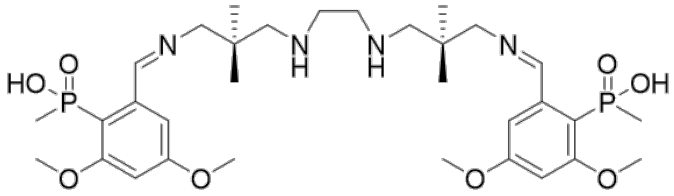

Following **general procedure 21**, the title compound was attempted to be prepared from BDMAPEN (0.01 g, 0.04 mmol), anhydrous MeOH (1.00 mL), 2-methylphosphinicacid-3,5-dimethoxybenzaldehyde (0.03 g, 0.11 mmol).

7.1.4.14 General Procedure 22 – Imine Condensation of Benzaldehyde-phosphinic acid compounds and BAPEN – Attempted Synthesis

This procedure was an adaptation of the methodology developed by Sharma *et al*.[21] To a solution of BAPEN (1 eq.) in anhydrous EtOH, 2-methylphosphinicacid-3,5-dialkoxybenzaldehyde (3 eq.) was added and the mixture was refluxed for 3 h. The mixture was cooled to rt, concentrated under reduced pressure and Et_2O (10 mL) was added. The precipitate was removed by filtration and left to stand at 4 °C overnight, and the newly formed precipitate was isolated by filtration, washed with cold Et_2O (15 mL) and dried under reduced pressure to give the product.

(2-methylphosphinicacid-3,5-dimethoxyphenyl)$_2$BAPEN (26a) – Attempted Synthesis

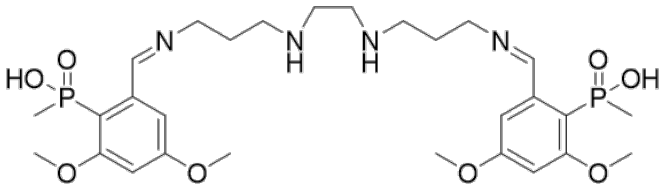

Following **general procedure 22**, the title compound was attempted to be prepared from BAPEN (0.03 mL, 0.14 mmol), anhydrous EtOH (2.00 mL), 2-methylphosphinicacid-3,5-dimethoxybenzaldehyde (0.10 g, 0.41 mmol).

7.1.5 Diaroylhydrazone Ligands (Section 5.2)

7.1.5.1 Synthesis of Isonicotinohydrazide (28)

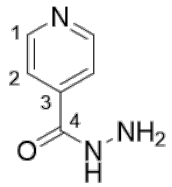

This compound was synthesised using an adaptation of the method reported by Cardoso *et al*.[28] A mixture of methyl isonicotinate (1.00 g, 7.29 mmol) and hydrazine hydrate (65% wt., 0.53 mL, 10.9 mmol) in EtOH (20 mL) was refluxed overnight under a N_2 atmosphere. The solvent was then removed under vacuum to yield the product as a white solid (0.92 g, 6.71 mmol, 92 %). **^{1}H NMR (400 MHz, CD_3OD) δ_H (ppm):** 8.69 (2H, m, H_1), 7.75 (2H, m, H_2). **$^{13}C\{^1H\}$ NMR (101 MHz, CD_3OD) δ_C (ppm):** 167.0 (C_4), 150.9 (C_1), 142.6 (C_3), 122.8 (C_2). **HRMS (ES-TOF+):** *m/z* calcd. for $C_6H_8N_3O$ ($[M+H]^+$) 138.0662. found: 138.0665.

7.1.5.2 Formation of (*E*)-*N*′-(1-(2-hydroxyphenyl)ethylidene)isonicotinohydrazide (29)

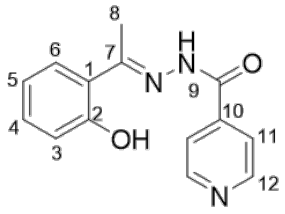

This compound was synthesised according to Hruskova *et al*.[29] Isonicotinohydrazide (0.44 g, 3.21 mmol), 2-hydroxyacetophenone (0.40 mL, 3.21 mmol) and AcOH (0.83 mL, 14.5 mmol) were dissolved in EtOH (10 mL), and the mixture was refluxed overnight under N_2. The resulting precipitate was filtered off, washed with H_2O (10 mL) and dried under vacuum to give a beige solid (0.50 g, 1.96 mmol, 61 %). **^{1}H NMR (400 MHz, DMSO-*d*$_6$) δ_H (ppm):** 13.20 (1H, s, OH), 11.60 (1H, s, NH), 8.80 (2H, d, $^3J_{HH}$ = 5.1 Hz, H_{12}), 7.85 (2H, d, $^3J_{HH}$ = 5.0 Hz, H_{11}), 7.66 (1H, d, $^3J_{HH}$ = 7.9 Hz, H_3), 7.33 (1H, t, $^3J_{HH}$ = 7.7 Hz, H_6), 6.92 (2H, t, $^3J_{HH}$ = 7.9 Hz, H_4/H_5), 2.50 (3H, s, H_8). **^{13}C{^{1}H} NMR (101 MHz, DMSO-*d*$_6$) δ_C (ppm):** 163.0 (C_7), 159.5 (C_9), 158.7 (C_2), 150.2 (C_{12}), 140.1 (C_{10}), 131.6 (C_6), 128.8 (C_3), 122.0 (C_{11}), 119.2 (C_4), 118.6 (C_5), 117.4 (C_1), 14.3 (C_8). **HRMS (ES-TOF+):** *m/z* calcd. for $C_{14}H_{14}N_3O_2$ ($[M+H]^+$) 256.1086. found: 256.1076.

7.1.5.3 Synthesis of [Ga(HAPI)$_2$][NO$_3$] (30) – Attempted Synthesis

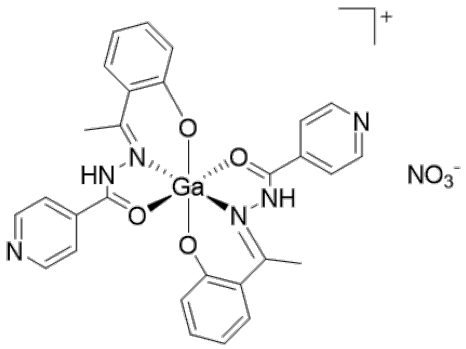

This compound was synthesised using an adaptation of the protocol described by Pocrnić *et al*.[30] (*E*)-*N*′-(1-(2-hydroxyphenyl)ethylidene)isonicotinohydrazide (0.10 g, 0.39 mmol) was dissolved in anhydrous EtOH (5.00 mL) under a N_2 atmosphere. $Ga(NO_3)_3.xH_2O$ (0.05 g, 0.20 mmol) was added to the solution and the mixture was refluxed overnight. The mixture was cooled to room temperature and the formed orange precipitate was isolated by filtration, washed with EtOH (5.00 mL) and dried under reduced pressure. **HRMS (ES-TOF+):** *m/z* calcd. for $C_{28}H_{24}N_6O_4Ga$ ($[M-NO_3]^+$) 577.1115. found: 577.1139.

7.1.5.4 Synthesis of (*E*)-*N*′-(1-(2-hydroxyphenyl)ethylidene)benzohydrazide (32)

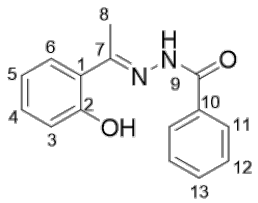

The title compound was synthesised using an adaptation of the procedure by Hruskova *et al*.[29] Benzohydrazide (0.99 g, 7.27 mmol), 2-hydroxyacetophenone (0.88 mL, 7.27 mmol) and acetic acid (0.50 mL) in EtOH (15 mL) were refluxed overnight under a N_2 atmosphere. The mixture was cooled to room temperature, followed by the addition of H_2O (10 mL). The mixture was left to stand at 0 °C overnight before the resulting white precipitate was isolated by filtration, washed with EtOH (40 mL) and dried under reduced pressure to give a yellow solid (1.13 g, 4.44 mmol, 61 %). **^{1}H NMR (400 MHz, CD_3OD) δ_H (ppm):** 7.95 (2H, m, H_{11}), 7.64 (2H, ddt, $^3J_{HH}$ = 8.8, $^3J_{HH}$ = 6.6, $^4J_{HH}$ = 1.5 Hz, H_4/H_5), 7.55 (2H, ddd, $^3J_{HH}$ = 8.3, $^3J_{HH}$ = 6.7, $^4J_{HH}$ = 1.4 Hz, H_{12}), 7.32 (1H, ddd, $^3J_{HH}$ = 8.7, $^3J_{HH}$ = 7.2, $^4J_{HH}$ = 1.6 Hz, H_{13}), 6.96 (2H, m, H_3/H_6), 2.51 (3H, s, H_8). **HRMS (ES-TOF+):** *m/z* calcd. for $C_{15}H_{15}N_2O_2$ ($[M+H]^+$) 255.1134. found: 255.1132.

7.1.5.5 Synthesis of (*E*)-*N*′-((2-hydroxyphenyl)(phenyl)methylene)isonicotino hydrazide (33)[29]

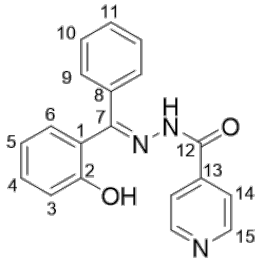

This compound was originally synthesised by Tsutsumi *et al*.[31] Isonicotinohydrazide (0.50 g, 3.65 mmol), 2-hydroxybenzophenone (0.72 g, 3.65 mmol) and acetic acid (0.20 mL) in EtOH (15 mL) were refluxed overnight under a N_2 atmosphere. The mixture was cooled to room temperature, followed by the addition of H_2O (10 mL). The mixture was left to stand at 0 °C overnight before the resulting white precipitate was isolated by filtration, washed with EtOH (40 mL) and dried under reduced pressure to give a yellow solid (0.60 g, 1.90 mmol, 52 %). **^{1}H NMR (400 MHz, DMSO-d_6) δ_H (ppm):** 8.69 (2H, m, H_{15}), 7.70 (4H, m, H_9/H_{10}), 7.62 (1H, t, $^3J_{HH}$ = 7.5 Hz, H_6), 7.51 (2H, t, $^3J_{HH}$ = 7.6 Hz, H_{14}), 7.44 (1H, t, $^3J_{HH}$ = 7.8 Hz, H_{11}), 7.34 (1H, $^3J_{HH}$ = 7.7 Hz, H_4), 6.96 (2H, m, H_3/H_5). **HRMS (ES-TOF+):** *m/z* calcd. for $C_{19}H_{16}N_3O_2$ ($[M+H]^+$) 318.1243. found: 318.1244.

7.1.6 Asymmetric [NN′O] Ligands (Section 5.3)

7.1.6.1 Synthesis of 2,4-dimethoxy-6-(((pyridin-2-ylmethyl)amino)methyl)phenol (34)

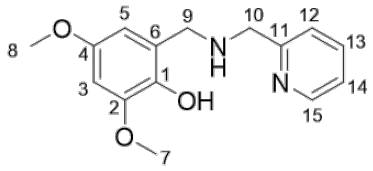

This compound was prepared using a modification of the literature procedure by Shakya *et al*.[32] A mixture of 2-hydroxy-3,5-dimethoxybenzaldehyde (0.10 g, 0.55 mmol), 2-picolylamine (0.06 mL, 0.55 mmol) and molecular sieves in anhydrous EtOH (4 mL) was heated at 70 °C for 6 h under a N_2 atmosphere. The mixture was cooled to 0 °C and $NaBH_4$ (0.03 g, 0.83 mmol) was added to the mixture in a portionwise manner. Once the addition was complete, the mixture was warmed to room temperature and stirred overnight. The molecular sieves were removed by filtration and the filtrate was concentrated under reduced pressure. The crude residue was purified by silica flash chromatography (SiO_2, DCM:MeOH, 9:1) to yield a brown oil (0.12 g, 0.44 mmol, 79 %). **^{1}H NMR (400 MHz, CD_3OD) δ_H (ppm):** 8.53 (1H, m, H_{15}), 7.81 (1H, td, $^3J_{HH}$ = 7.7, $^4J_{HH}$ = 1.8 Hz, H_{13}), 7.43 (1H, d, $^3J_{HH}$ = 7.8 Hz, H_{12}), 7.33 (1H, m, H_{14}), 6.76 (1H, s, H_5), 6.64 (1H, s, H_3), 3.98 (2H, s, H_{10}), 3.87 (3H, s, H_7), 3.84 (2H, s, H_9), 3.82 (3H, s, H_8). **^{13}C{^{1}H} NMR (101 MHz, CD_3OD) δ_C (ppm):** 157.5 (C_{11}), 152.8 (C_6), 150.0 (C_{15}), 149.6 (C_2), 141.0 (C_4), 138.7 (C_{13}), 124.2 (C_{14}), 124.1 (C_{12}), 118.6 (C_5), 117.0 (C_1), 98.3 (C_3), 56.7 (C_8), 56.6 (C_7), 54.8 (C_{10}), 53.2 (C_9). **HRMS (ES-TOF+):** *m/z* calcd. for $C_{15}H_{19}N_2O_3$ ($[M+H]^+$) 275.1396. found: 275.1403.

7.1.6.2 Synthesis of the Non-Radioactive Reference Compound $[Ga(L^{DiOMe})_2]^+$ - Attempted Synthesis

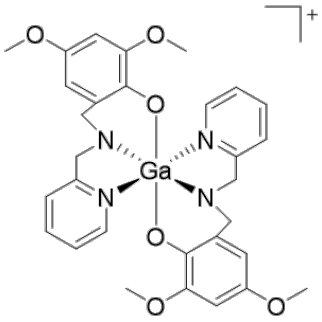

This complex was prepared using an adaptation of the literature protocol by Shakya *et al*.[33] 2,4-dimethoxy-6-(((pyridin-2-ylmethyl)amino)methyl)phenol (0.02 g, 0.07 mmol) and $Ga(NO_3)_3.xH_2O$ (0.01 g, 0.04 mmol) were added to anhydrous MeOH (10 mL). Triethylamine (0.10 mL, 0.07 mmol) was added to the mixture, which was then stirred at room temperature for 1 h under a N_2 atmosphere. $NaClO_4$ (0.01 g, 0.04 mmol) was then added, and the mixture was left to stir at room temperature overnight.

7.1.7 Bis(semicarbazone-phosphonium) Chelates (Section 5.4)

7.1.7.1 (3-Formyl-4-hydroxybenzyl)triphenylphosphonium bromide (36)

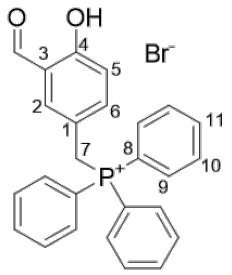

This compound was synthesised using a modified procedure by Smith *et al*.[1] 5-(bromomethyl)-2-hydroxybenzaldehyde (2.00 g, 9.30 mmol) was dissolved in anhydrous toluene (24 mL) at 60 °C under N_2. PPh_3 (2.44 g, 9.30 mmol) was dissolved in anhydrous toluene (25 mL) which was added to the reaction mixture and stirred at 60 °C overnight. The resulting precipitate was isolated by filtration, washed with toluene (50 mL) and Et_2O (50 mL) and dried under reduced pressure to give a white solid (3.53 g, 7.40 mmol, 80 %). **^{1}H NMR (400 MHz, $CDCl_3$) δ_H (ppm):** 10.89 (1H, s, Ar-O<u>H</u>), 9.59 (1H, s, C<u>H</u>O), 7.77 (9H, m, H_{10}/H_{11}), 7.61 (7H, m, H_2/H_9), 7.25 (1H, m, H_6), 6.67 (1H, d, $^3J_{HH}$ = 8.6 Hz, H_5), 5.66 (2H, d, $^2J_{HP}$ = 14.0

Hz, H_7). **$^{13}C\{^1H\}$ NMR (101 MHz, $CDCl_3$) δ_C (ppm):** 196.5 (CHO), 161.3 (C_1), 139.8 (C_6), 137.3 (C_2), 135.1 (C_{11}), 134.7 (C_{10}), 130.3 (d, $^3J_{CP}$ = 12.4 Hz, C_9), 120.6 (C_3), 118.8 (C_4),118.0 (C_5), 117.7 (d, $^1J_{CP}$ = 85.7 Hz, C_8), 29.2 (d, $^2J_{CP}$ = 46.6 Hz, C_7). **$^{31}P\{^1H\}$ NMR (162 MHz, $CDCl_3$) δ_P (ppm):** 23.3. **HRMS (ES-TOF+):** *m/z* calcd. for $C_{26}H_{22}O_2P$ ($[M\text{-}Br]^+$) 397.1357. found: 397.1355.

7.1.7.2 Salan-(2-formyl-4-methylTPP)$_2$ Dibromide (37) – Attempted Synthesis

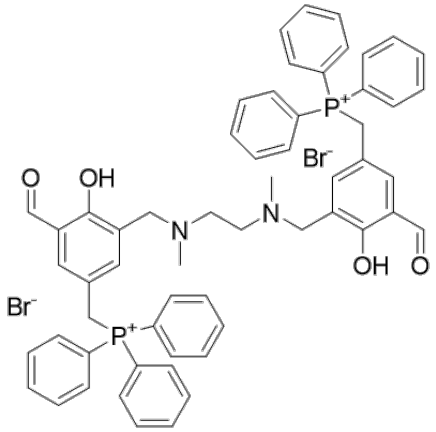

Preparation of this compound was attempted using a modification of the method by Thilagar *et al*.[34] A mixture of (3-formyl-4-hydroxybenzyl)TPP bromide (0.30 g, 0.63 mmol), *N*,*N*′-dimethylethylene-1,2-diamine (0.03 mL, 0.31 mmol) and paraformaldehyde (0.05 g, 1.57 mmol) in EtOH/AcOH (7:3, 10 mL) was stirred at reflux for 48 h under a N_2 atmosphere. The mixture was concentrated under vacuum and the crude residue was purified by silica flash chromatography (SiO_2, DCM:MeOH, 1:1).

7.1.7.3 Synthesis of HFMA (39)[35]

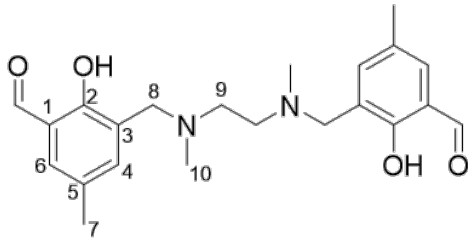

To a solution of 3-(chloromethyl)-2-hydroxy-5-methylbenzaldehyde (0.50 g, 2.71 mmol) and *N*,*N*′-dimethylethylene-1,2-diamine (0.15 mL, 1.35 mmol) in MeCN (10 mL), DIPEA (0.83 mL, 4.74 mmol) was added and the mixture was heated at reflux for 18 h under a N_2 atmosphere. The mixture was concentrated under reduced pressure and the crude residue was

purified by silica flash chromatography (SiO_2, hexane:EtOAc, 2:8) to yield an off-white solid (0.13 g ,0.34 mmol, 25 %). **^{1}H NMR (400 MHz, $CDCl_3$) δ_H (ppm):** 10.19 (2H, s, C<u>H</u>O), 7.38 (2H, m, H_6), 7.21 (2H, d, $^3J_{HH}$ = 2.2 Hz, H_4), 3.64 (4H, s, H_8), 2.67 (4H, s, H_9), 2.28 (6H, s, H_7), 2.25 (6H, s, H_{10}). **^{13}C{^{1}H} NMR (101 MHz, $CDCl_3$) δ_C (ppm):** 193.1 (<u>C</u>HO), 159.1 (C_2), 137.3 (C_4), 129.5 (C_5), 128.5 (C_1), 124.8 (C_6), 122.0 (C_3), 58.0 (C_8), 54.5 (C_9), 42.1 (C_{10}), 20.4 (C_7). **HRMS (ES-TOF+):** *m/z* calcd. for $C_{22}H_{29}N_2O_4$ ($[M+H]^+$) 385.2127. found: 385.2110.

7.1.7.4 (3-(Hydroxymethyl)-5-formyl-4-hydroxybenzyl)TPP Bromide (40)

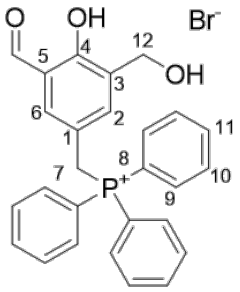

(3-Formyl-4-hydroxybenzyl)triphenylphosphonium bromide (1.30 g, 2.72 mmol) and paraformaldehyde (0.25 g, 8.17 mmol) were added to HBr (48 % wt., 30 mL). H_2SO_4 (1.50 mL) was added to the mixture before heating at 70 ºC for 24 h. The solution was cooled to room temperature and the product was extracted using DCM (3 x 150 mL). The organic phases were combined, dried over Na_2SO_4, filtered and concentrated under vacuum yielding a beige solid (1.50 g, 2.63 mmol, 97 %). **^{1}H NMR (400 MHz, $CDCl_3$) δ_H (ppm):** 11.35 (1H, s, O<u>H</u>), 9.58 (1H, s, C<u>H</u>O), 7.75 (9H, m, H_9/H_{11}), 7.60 (7H, td, $^3J_{HH}$ = 7.7, $^4J_{HH}$ = 3.5 Hz, H_6/H_{10}), 7.23 (1H, d, $^4J_{HH}$ = 2.6 Hz, H_2), 5.68 (2H, d, $^1J_{HP}$ = 14.3 Hz, H_7), 4.23 (2H, s, H_{12}). **^{13}C{^{1}H} NMR (101 MHz, $CDCl_3$) δ_C (ppm):** 196.6 (<u>C</u>HO), 159.0 (C_5), 140.7 (d, $^3J_{CP}$ = 4.5 Hz, C_2), 137.9 (d, $^2J_{CP}$ = 5.7 Hz, C_1), 135.0 (d, $^3J_{CP}$ = 3.0 Hz, C_6), 134.6 (d, $^2J_{CP}$ = 9.8 Hz, C_9), 130.3 (d, $^3J_{CP}$ = 12.4 Hz, C_{10}), 126.4 (d, $^4J_{CP}$ = 3.1 Hz, C_3), 120.5 (C_4), 119.0 (d, $^4J_{CP}$ = 8.4 Hz, C_{11}), 117.5 (d, $^1J_{CP}$ = 85.7 Hz, C_8), 29.0 (d, $^1J_{CP}$ = 46.8 Hz, C_7), 26.2 (C_{12}). **^{31}P{^{1}H} NMR (162 MHz, $CDCl_3$) δ_P (ppm):** 23.2.

7.1.7.5 (4-Carboxybenzyl)TPP Bromide (41)

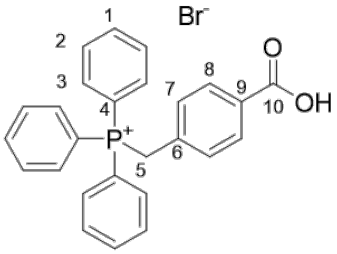

The title compound was synthesised using a modification of the literature procedure by Smith *et al*.[1] To a solution of 4-bromomethylbenzoic acid (5.00 g, 23.3 mmol) in acetone (100 mL), PPh_3 (6.10 g, 23.3 mmol) was added in a portion wise manner. Once the addition was complete, the mixture was stirred with heating at 60 °C overnight. The white precipitate was isolated by filtration, washed with acetone (20 mL) and dried under vacuum to give a white solid (10.1 g, 21.2 mmol, 91 %). **^{1}H NMR (400 MHz, $CDCl_3$) δ_H (ppm):** 7.75 (5H, m, H_1/H_8), 7.57 (12H, m, H_2/H_3), 7.01 (2H, t, $^3J_{HH}$ = 6.2 Hz, H_7), 5.06 (dd, $^2J_{HP}$ = 15.0, $^4J_{HH}$ = 5.8 Hz, H_5). **^{13}C{^{1}H} NMR (101 MHz, $CDCl_3$) δ_C (ppm):** 167.8 (C_{10}), 135.4 (C_8), 134.1 (d, $^2J_{CP}$ = 10.1 Hz, C_3), 132.0 (C_9), 131.1 (d, $^3J_{CP}$ = 5.4 Hz, C_7), 130.9 (C_6), 130.4 (C_2), 130.2 (C_1), 117.2 (d, $^1J_{CP}$ = 86.2 Hz, C_4), 30.7 (d, $^1J_{CP}$ = 47.6 Hz, C_5). **^{31}P{^{1}H} NMR (162 MHz, $CDCl_3$) δ_P (ppm):** 23.0. **HRMS (ES-TOF+):** *m/z* calcd. for $C_{26}H_{22}O_2P$ ($[M\text{-}Br]^+$) 397.1357. found: 397.1360.

7.1.7.6 (4-Azidocarboxybenzyl)TPP Bromide (42)

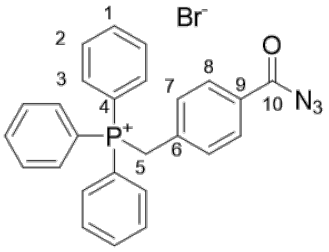

The title compound was prepared using a modification of the procedure by Shi *et al*.[36] (4-Carboxybenzyl)TPP bromide (1.00 g, 2.10 mmol) was added to anhydrous MeCN (15 mL), and the mixture was cooled to 0 °C under a N_2 atmosphere. DPPA (0.50 mL, 2.30 mmol) was added to the mixture, followed by the addition of TEA (0.32 mL, 2.30 mmol) in a dropwise manner. The mixture was stirred at 0 °C for 1 h, before the mixture was concentrated under reduced pressure and the crude material was purified by silica flash chromatography (SiO_2, DCM:MeOH, 95:5) to give an off-white solid (0.82 g, 1.63 mmol, 78 %). **^{1}H NMR (400 MHz,**

$CDCl_3$) δ_H (ppm): 7.78 (9H, m, H_1/H_3), 7.68 (2H, d, $^3J_{HH}$ = 7.9 Hz, H_8), 7.62 (6H, m, H_2), 7.27 (2H, m, H_7), 5.77 (d, $^2J_{HP}$ = 15.4 Hz, H_5). **$^{31}P\{^1H\}$ NMR (162 MHz, $CDCl_3$) δ_P (ppm):** 23.8. **HRMS (ES-TOF+):** *m/z* calcd. for $C_{26}H_{21}N_3OP$ ($[M\text{-}Br]^+$) 422.1422. found: 422.1436.

7.1.7.7 (4-(Hydrazinecarboxamido)benzyl)TPP Trifluoroacetate (44)

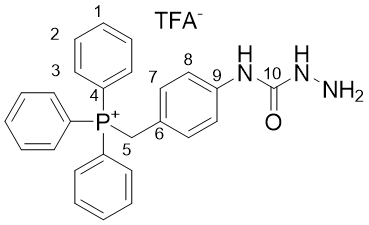

To a solution of (4-((Phenoxycarbonyl)amino)benzyl)TPP bromide (0.10 g, 0.18 mmol) and EtOH (10 mL), hydrazine hydrate (65 % wt., 0.07 mL, 0.88 mmol) was added and the subsequent mixture was heated at 75 °C overnight under a N_2 atmosphere. The mixture was concentrated under reduced pressure, and the crude material was purified by reverse-phase chromatography (C-18 SiO_2, 0–100 % MeCN + 0.1 % TFA in H_2O + 0.1 % TFA) to give the title compound as a white solid (0.05 g, 0.10 mmol, 56 %). **^1H NMR (400 MHz, CD_3OD) δ_H (ppm):** 7.90 (3H, td, $^3J_{HH}$ = 7.3, $^4J_{HH}$ = 1.8 Hz, H_1), 7.72 (6H, dt, $^3J_{HH}$ = 7.6, $^4J_{HH}$ = 4.0 Hz, H_2), 7.65 (6H, dd, $^3J_{HP}$ = 12.4, $^3J_{HH}$ = 7.4 Hz, H_3), 7.35 (2H, d, $^3J_{HH}$ = 8.3 Hz, H_8), 6.92 (2H, dd, $^3J_{HH}$ = 8.7, $^4J_{HH}$ = 2.7 Hz, H_7), 4.85 (2H, dd, $^2J_{HP}$ = 14.6, $^4J_{HH}$ = 5.9 Hz, H_5). **$^{13}C\{^1H\}$ NMR (101 MHz, CD_3OD) δ_C (ppm):** 156.4 (C_{10}), 140.5 (C_6), 136.4 (d, $^4J_{CP}$ = 3.2 Hz, C_1), 135.4 (d, $^2J_{CP}$ = 9.7 Hz, C_3), 132.7 (d, $^3J_{CP}$ = 5.6 Hz, C_7), 131.3 (d, $^3J_{CP}$ = 12.4 Hz, C_2), 122.8 (C_9), 120.5 (d, $^4J_{CP}$ = 3.3 Hz, C_8), 119.1 (d, $^1J_{CP}$ = 86.0 Hz, C_4), 30.2 (d, $^1J_{CP}$ = 48.1 Hz, C_5). **$^{31}P\{^1H\}$ NMR (162 MHz, CD_3OD) δ_P (ppm):** 22.2. **HRMS (ES-TOF+):** *m/z* calcd. for $C_{26}H_{25}N_3OP$ ($[M\text{-}TFA]^+$) 426.1735. found: 426.1752.

7.1.7.8 (4-Nitrobenzyl)TPP Bromide (45)

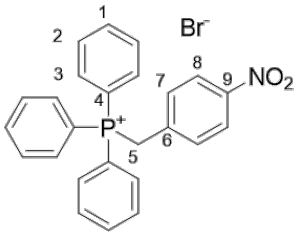

To a solution of 4-nitrobenzylbromide (3.00 g, 13.89 mmol) in anhydrous acetone (50 mL), PPh_3 (3.64 g, 13.89 mmol) was added in a portion wise manner. Once the addition was

complete, the mixture was stirred at 55 °C under a N_2 atmosphere overnight. The white precipitate was isolated by filtration, wash with acetone (20 mL) and dried under reduced pressure to give the title compound as an off-white solid (6.64 g, 13.89 mmol, quant.). **^{1}H NMR (400 MHz, CD_3OD) δ_H (ppm):** 8.10 (2H, m, H_8), 7.94 (3H, m, H_1), 7.75 (12H, m, H_2/H_3), 7.29 (2H, dd, $^3J_{HH}$ = 8.9, $^4J_{HH}$ = 2.5 Hz, H_7), 5.19 (2H, d, $^2J_{CP}$ = 15.8 Hz, H_5). **^{13}C{^{1}H} NMR (101 MHz, CD_3OD) δ_C (ppm):** 210.1 (C_9), 149.4 (C_6), 136.7 (d, $^4J_{CP}$ = 3.2 Hz, C_1), 135.4 (d, $^2J_{CP}$ = 9.7 Hz, C_2), 133.3 (d, $^3J_{CP}$ = 5.3 Hz, C_7), 131.6 (d, $^2J_{CP}$ = 12.9 Hz, C_3), 124.9 (d, $^4J_{CP}$ = 3.4 Hz, C_8), 118.5 (d, $^1J_{CP}$ = 86.7 Hz, C_4), 30.7 (C_5). **^{31}P{^{1}H} NMR (162 MHz, CD_3OD) δ_P (ppm):** 27.1. **HRMS (ES-TOF+):** *m/z* calcd. for $C_{25}H_{21}NO_2P$ ($[M\text{-}Br]^+$) 398.1310. found: 398.1325.

7.1.7.9 (4-Aminobenzyl)TPP Bromide (46)

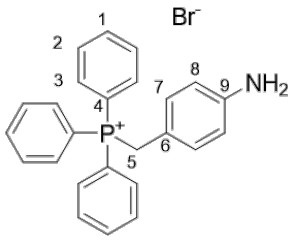

The title compound was synthesised using an adaptation of the method described by Javadi *et al*.[37] (4-Nitrobenzyl)TPP bromide (1.50 g, 3.14 mmol) was dissolved in MeOH (20 mL) before a mixture of $SnCl_2.2H_2O$ (2.47 g, 10.98 mmol) and 12 M HCl (4 mL) was added to the solution in a dropwise manner at room temperature. The mixture was then stirred at 40 °C under a N_2 atmosphere overnight, before being cooled to room temperature and the mixture pH was adjusted to pH 9 using a 2 M NaOH solution. The solvent was removed under reduced pressure and the crude residue was purified using silica flash chromatography (SiO_2, DCM:MeOH, 85:15) to give a yellow solid (0.77 g, 1.72 mmol, 55 %). **^{1}H NMR (400 MHz, DMSO-*d*$_6$) δ_H (ppm):** 7.89 (3H, dt, $^3J_{HH}$ = 7.7, $^4J_{HH}$ = 4.4 Hz, H_1), 7.73 (6H, td, $^3J_{HH}$ = 7.8, $^4J_{HH}$ = 3.5 Hz, H_2), 7.63 (6H, dd, $^3J_{HP}$ = 12.9, $^3J_{HH}$ = 7.7 Hz, H_3), 6.58 (2H, dd, $^3J_{HH}$ = 8.6, $^4J_{HH}$ = 2.6 Hz, H_7), 6.36 (2H, d, $^3J_{HH}$ = 8.1 Hz, H_8), 4.90 (2H, d, $^2J_{HP}$ = 14.3 Hz, H_5). **^{31}P{^{1}H} NMR (162 MHz, DMSO-*d*$_6$) δ_P (ppm):** 21.2. **HRMS (ES-TOF+):** *m/z* calcd. for $C_{25}H_{23}NP$ ($[M\text{-}Br]^+$) 368.1568. found: 368.1574.

7.1.7.10 (4-((Phenoxycarbonyl)amino)benzyl)TPP Bromide (47)

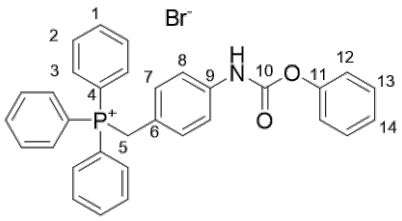

The title compound was prepared using a modification of the method described by Noonepalle *et al*.[38] A mixture of (4-aminobenzyl)TPP bromide (0.20 g, 0.45 mmol) and K_2CO_3 (0.07 g, 0.54 mmol) in anhydrous acetone (5 mL) was prepared under a N_2 atmosphere. The mixture was cooled to 0 ^oC and phenylchloroformate (0.06 mL, 0.45 mmol) was added in a portion wise manner. Once the addition was complete, the mixture was warmed to room temperature and stirred for 24 h. The mixture was concentrated under reduced pressure and the crude material was purified using flash silica chromatography (SiO_2, DCM:MeOH, 92:8) to yield a white solid (0.22 g, 0.38 mmol, 85 %). **^{1}H NMR (400 MHz, CD_3OD) δ_H (ppm):** 7.90 (3H, m, H_1), 7.73 (6H, td, $^3J_{HH}$ = 7.9, $^4J_{HH}$ = 3.7 Hz, H_2), 7.66 (6H, ddd, $^3J_{HP}$ = 12.4, $^3J_{HH}$ = 8.5, $^4J_{HH}$ = 1.4 Hz, H_3), 7.39 (4H, m, H_{12}/H_{13}), 7.24 (1H, m, H_{14}), 7.16 (2H, m, H_8), 6.93 (2H, m, H_7), 4.86 (2H, m, H_5). **^{31}P{^{1}H}-NMR (162 MHz, CD_3OD) δ_P (ppm):** 22.3. **HRMS (ES-TOF+):** *m/z* calcd. for $C_{32}H_{27}NO_2P$ ($[M\text{-}Br]^+$) 488.1779. found: 488.1779.

7.1.7.11 H_4bsc-$(TPP)_2$ Bistrifluoroacetate (48)

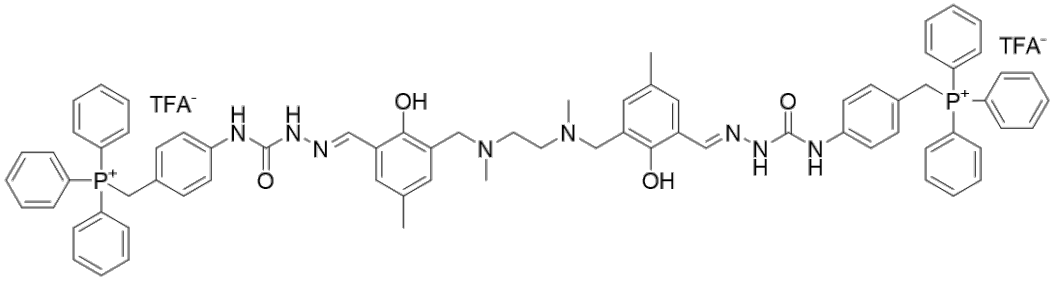

The synthesis of the title compound was attempted using an adaptation of the literature procedure developed by Prado *et al*.[35] (4-(Hydrazinecarboxamido)benzyl)TPP trifluoroacetate (0.05 g, 0.10 mmol) was dissolved in anhydrous EtOH (3 mL), and HFMA (0.02 g, 0.05 mmol) was dissolved in anhydrous EtOH (2 mL) and this solution was added to the mixture. The mixture was heated at reflux in the presence of mol. sieves for 24 h. The resulting grey precipitate was isolated by filtration.

7.2 Radiochemistry

7.2.1 General

All general experimental methodologies listed in section 7.1.1 apply. Radiolabelling was conducted as part of the studies discussed in Chapter 3.

7.2.1.1 [^{68}Ga]$GaCl_3$ Preparation

Elution of gallium-68 in the form of [^{68}Ga]$GaCl_3$ was performed from an Eckert & Ziegler gallium-68 generator using 5 mL of clinical-grade 0.1 M HCl solution.

7.2.1.2 iTLC QC Method

iTLC was performed using Agilent iTLC-SG Chromatography Paper. Aliquots of radiolabelled compound (5 μL) were spotted 10 mm from the baseline of the iTLC plate, and the iTLC was run in either 0.1 M disodium EDTA or 2.0 M NH_4OAc/MeOH to a solvent front height of 90 mm. iTLC plates were measured using a LabLogic Flow-Count detector with a Na/I probe (B-FC-3200).

7.2.1.3 RadioHPLC

Analytical reverse-phase radioHPLC was performed on an Agilent 1200 Series Liquid Chromatograph (with UV and gamma detectors) using an Agilent Eclipse XDB-C18 column (4.6 × 150 mm, 5 μm) with a 1 mL min^{-1} flow rate and UV spectroscopic detection at 250 nm. Eluent gradient: 95 % A for 5 min, 5−95 % B in A for 20 min, 95 % B in A for 5 min.

7.2.1.4 Log $D_{7.4}$ Value Measurements

Aliquots of radiolabelled compounds (5 μL, approx. 200 kBq) were added to vials containing a layered mixture of *n*-octanol (500 μL) and PBS (pH 7.4, 500 μL). After vortex mixing for 1 min, the mixture was centrifuged to separate octanol/PBS phases (10^4 rpm, 2 min) before aliquots of the two phases (100 μL) were taken and transferred into vials for counting. Relative amounts of the test compound in each phase were measured by an automatic gamma detector . The log $D_{7.4}$ values were reported as the mean ± SD of data obtained in 6 independent experiments.

7.2.2 General Radiolabelling Procedure

To a solution of ligand in radiolabelling buffer, an aliquot of [^{68}Ga]$GaCl_3$ in 0.1 M HCl (approx. 50−100 MBq, 500 μL) was added, and the resulting mixture was stirred to yield the desired radiolabelled product. QC was performed using the iTLC method described previously.

7.2.3 [^{68}Ga]Ga-DO2A-(xy-TAP)$_2$ and [^{68}Ga]Ga-DO2A-Ar$_2$ (Section 3.1)

[^{68}Ga]Ga-DO2A-(xy-TAP)$_2$/-Ar$_2$ compounds were prepared according to the general radiolabelling procedure, using DO2A-(xy-TAP)$_2$/-Ar$_2$ (500 μM) in 0.2 M NaOAc (500 μL) and heating at either 25 or 50 °C for between 30−100 min. Products were analysed by analytical reverse-phase HPLC.

7.2.4 [^{68}Ga]Ga-NODAGA-xy-TAP (Section 3.2)

7.2.4.1 Initial Radiolabelling

[^{68}Ga]Ga-NODAGA-xy-TAP compounds were initially prepared according to the general radiolabelling procedure, using NODAGA-xy-TAP (approx. 200 μM) in 0.1 M NH_4OAc (500 μL) and heating at 100 °C for 30 min.

7.2.4.2 Temperature Alteration Experiments

[^{68}Ga]Ga-NODAGA-xy-TAP was prepared by following the general radiolabelling procedure, using NODAGA-xy-TAP (approx. 200 μM) in 0.1 M NH_4OAc (500 μL) and heating at 50 °C for between 10−30 min before being analysed by the iTLC QC method.

7.2.4.3 Buffer Alteration Experiments with Varying Reaction Temperatures

[^{68}Ga]Ga-NODAGA-xy-TAP was prepared by following the general radiolabelling procedure, using NODAGA-xy-TAP (approx. 200 μM) in 0.2 M NaOAc (500 μL) or 3.6 M NaOAc (42 μL) and heating at either 25 or 50 °C for 15 min before being analysed by the iTLC QC method. The pH values measured upon addition of 0.1 M HCl (500 μL) to radiolabelling buffer by pH meter.

7.2.4.4 Final Ligand Concentration Alteration Experiments

[^{68}Ga]Ga-NODAGA-xy-TAP was prepared by following the general radiolabelling procedure, using NODAGA-xy-TAP (500, 200, 100, 50, 5 μM) in 3.6 M NaOAc (42 μL) and stirring at rt for 15 min. Products were analysed by the iTLC QC method.

7.2.4.5 Optimised Radiolabelling Procedure

[^{68}Ga]Ga-NODAGA-xy-TAP compounds were prepared according to the general radiolabelling procedure, using NODAGA-xy-TAP (100 μM) in 3.6 M NaOAc (42 μL) at room temperature for 15 min. Products were analysed by analytical reverse-phase HPLC.

7.2.5 [^{68}Ga]Ga-NODAGA-xy-TAEP (Section 3.3)

[^{68}Ga]Ga-NODAGA-xy-TAEP compounds were prepared according to the general radiolabelling procedure, using NODAGA-xy-TAEP (100 μM) in 3.6 M NaOAc (42 μL) at rt for 15 min. Products were analysed by analytical reverse-phase HPLC.

7.3 References for Chapter 7

1 A. J. Smith, P. J. Gawne, M. T. Ma, P. J. Blower, R. Southworth and N. J. Long, *Dalton Trans.*, 2018, **47**, 15448–15457.

2 M. Klika Škopić, S. Willems, B. Wagner, J. Schieven, N. Krause and A. Brunschweiger, *Org. Biomol. Chem.*, 2017, **15**, 8648–8654.

3 S. Nomura, K. Endo-Umeda, A. Aoyama, M. Makishima, Y. Hashimoto and M. Ishikawa, *ACS Med. Chem. Lett.*, 2015, **6**, 902–907.

4 G. Gudipudi, S. R. Sagurthi, S. Perugu, G. Achaiah and G. L. David Krupadanam, *RSC Adv.*, 2014, **4**, 56489–56501.

5 Y.-R. Liao, P.-C. Kuo, S.-C. Huang, J.-W. Liang and T.-S. Wu, *Tetrahedron Lett.*, 2012, **53**, 6202–6204.

6 S. E. Harpstrite, J. L. Prior, J. Sivapackiam, S. D. Collins, N. P. Rath and V. Sharma, *Med. Chem.*, 2010, 6, 191–199.

7 H. D. Janse van Rensburg, L. J. Legoabe, G. Terre'Blanche and J. Aucamp, *Bioorg. Chem.*, 2020, **94**, 103459.

8 E. R. H. Walter, M. A. Fox, D. Parker and J. A. G. Williams, *Dalton Trans.*, 2018, **47**, 1879–1887.

9 Patent Application Publications, US2013/0102600 A1, 2013.

10 R. Badar, U. Ashiq, A. R. Jamal, P. Akhter, M. Mahroof-Tahir, S. Gul and T. S. Ali, *Med. Chem.*, 2022, 18, 97–114.

11 R.-Y. Zhang, Y. Zhang, J. Tong, L. Liu and Z.-B. Han, *Catal. Letters*, 2021, **151**, 2833–2841.

12 K. Akutsu-Suyama, S. Mori and T. Hanashima, *Photochem. Photobiol. Sci.*, 2019, **18**, 2531–2538.

13 H. E. Gottlieb, V. Kotlyar and A. Nudelman, *J. Org. Chem.*, 1997, **62**, 7512–7515.

14 F. G. Mann and E. J. Chaplin, *J. Chem. Soc.*, 1937, 527.

15 V. G. Rozinov, *Izv. Nauchno-Issledovatel'skogo Instituta Neft. i Uglekhimicheskogo Sint. pri Irkutsk. Univ.*, 1969, 11, 52–53.

16 L. Lamza, *J. fuer Prakt. Chem.*, 1964, 25, 294–300.

17 Y.-S. Kim, C.-T. Yang, J. Wang, L. Wang, Z.-B. Li, X. Chen and S. Liu, *J. Med. Chem.*, 2008, **51**, 2971–2984.

18 World Intellectual Property Organization, WO 2010/066051 A1, 2010, 1–35.

19 J. H. Bowie, P. Y. White and P. J. Hoffmann, *Tetrahedron*, **25**, 1629.

20 C. M. G. Azevedo, C. M. M. Afonso, J. X. Soares, S. Reis, D. Sousa, R. T. Lima, M. H.

Vasconcelos, M. Pedro, J. Barbosa, L. Gales and M. M. M. Pinto, *Eur. J. Med. Chem.*, 2013, **69**, 798–816.

21 V. Sharma, J. Sivapackiam, S. E. Harpstrite, J. L. Prior, H. Gu, N. P. Rath and D. Piwnica-Worms, *PLoS One*, 2014, **9**, e109361.

22 World Intellectual Property Organization, WO 2008/107363 A1, 2008, 1–53.

23 J. Zhang, K. Mu, P. Yang, X. Feng, D. Zhang, X. Fan, Q. Wang and S. Mao, *Bioorg. Chem.*, 2021, **115**, 105179.

24 J. Zhang, K. Mu, P. Yang, X. Feng, D. Zhang, X. Fan, Q. Wang and S. Mao, *Bioorg. Chem.*, 2021, **115**, 105179.

25 B. W. Tsang, C. J. Mathias, P. E. Fanwick and M. A. Green, *J. Med. Chem.*, 1994, **37**, 4400–4406.

26 B. W. Tsang, C. J. Mathias and M. A. Green, *J. Nucl. Med.*, 1993, **34**, 1127–31.

27 L. Gavara, C. Petit and J.-L. Montchamp, *Tetrahedron Lett.*, 2012, **53**, 5000–5003.

28 L. N. F. Cardoso, T. C. M. Nogueira, F. A. R. Rodrigues, A. C. A. Oliveira, M. C. dos S. Luciano, C. Pessoa and M. V. N. de Souza, *Med. Chem. Res.*, 2017, **26**, 1605–1608.

29 K. Hruskova, P. Kovarikova, P. Bendova, P. Haskova, E. Mackova, J. Stariat, A. Vavrova, K. Vavrova and T. Simunek, *Chem. Res. Toxicol.*, 2011, **24**, 290–302.

30 M. Pocrnić, D. Kontrec, S. Miljanić, Ž. Soldin, A. Budimir and N. Galić, *J. Mol. Struct.*, 2021, **1227**, 129564.

31 Meiji Seika Kaisha, Ltd., *World Intellect. Prop. Organ.*, 2002.

32 R. Shakya, C. Imbert, H. P. Hratchian, M. Lanznaster, M. J. Heeg, B. R. McGarvey, M. Allard, H. B. Schlegel and C. N. Verani, *Dalton Trans.*, 2006, 2517–2525.

33 R. Shakya, F. Peng, J. Liu, M. J. Heeg and C. N. Verani, *Inorg. Chem.*, 2006, **45**, 6263–6268.

34 P. Thilagar, P. Sudhakar, P. Chinna Ayya Swamy and S. Mukherjee, *Inorganica Chim. Acta*, 2012, **390**, 163–166.

35 V. S. Prado, R. C. F. Leitao, F. Silva, L. Gano, I. C. Santos, F. L. N. Marques, A. Paulo and V. M. Deflon, *Dalton Trans.*, 2021, **50**, 1631–1640.

36 S. Shi, C. Yao, J. Cen, L. Li, G. Liu, J. Hu and S. Liu, *Angew. Chem. Int. Ed.*, 2020, **59**, 18172–18178.

37 M. S. Javadi and J. Mokhtari, *J. Chinese Chem. Soc.*, 2012, **59**, 793–801.

38 S. Noonepalle, S. Shen, J. Ptáček, M. T. Tavares, G. Zhang, J. Stránský, J. Pavlíček, G. M. Ferreira, M. Hadley, G. Pelaez, C. Bařinka, A. P. Kozikowski and A. Villagra, *J. Med. Chem.*, 2020, **63**, 10246–10262.

APPENDIX

8.1 Publications Arising From This Thesis

Dalton Transactions

ROYAL SOCIETY OF CHEMISTRY

PAPER

View Article Online
View Journal | View Issue

Check for updates

Cite this: *Dalton Trans.*, 2020, **49**, 1097

DO2A-based ligands for gallium-68 chelation: synthesis, radiochemistry and *ex vivo* cardiac uptake†

Adam J. Smith, [a,b] Bradley E. Osborne, [a,b] George P. Keeling, [b] Philip J. Blower, [b] Richard Southworth [*b] and Nicholas J. Long [*a]

Received 4th June 2019,
Accepted 17th December 2019

DOI: 10.1039/c9dt02354b

rsc.li/dalton

Radiolabelled lipophilic cations could potentially be used to non-invasively image mitochondrial dysfunction in cardiovascular disease, building on their current role as perfusion imaging agents. We have synthesised and radiolabelled two series of DO2A-based radiotracers, with bistriarylphosphonium- and bisaryl-functionalisation respectively, with gallium-68 to form lipophilic cations. Both sets of tracers radiolabel with over 90% RCP, although the tracers form kinetic/thermodynamic pairs of species upon gallium chelation that can be visualised and separated by radioHPLC. Log $D_{7.4}$ values above −0.3 are observed for the most lipophilic examples of each series of radiotracers. Both tracers show significant preferential uptake in healthy cardiac tissue over cardiac tissue depolarised by CCCP.

Dalton Transactions

ROYAL SOCIETY OF CHEMISTRY

PAPER

View Article Online
View Journal | View Issue

Check for updates

Cite this: *Dalton Trans.*, 2021, **50**, 14695

Synthesis and *ex vivo* biological evaluation of gallium-68 labelled NODAGA chelates assessing cardiac uptake and retention†

Bradley E. Osborne, [a,b] Thomas T. C. Yue, [a] Edward C. T. Waters, [b] Friedrich Baark, [b] Richard Southworth [*b] and Nicholas J. Long [*a]

Received 5th July 2021,
Accepted 17th September 2021

DOI: 10.1039/d1dt02224e

rsc.li/dalton

Radiolabelled lipophilic cations can be used to non-invasively report on mitochondrial dysfunction in diseases such as cardiovascular disease, cardiotoxicity and cancer. Several such lipophilic cations are currently used clinically to map myocardial perfusion using SPECT imaging. Since PET offers significant advantages over SPECT in terms of sensitivity, resolution and the capacity for dynamic imaging to allow pharmacokinetic modelling, we have synthesised and radiolabelled a series of NODAGA-based radiotracers, with triarylphosphonium-functionalisation, with gallium-68 to develop PET-compatible cationic complexes. To evaluate their capacity to report upon mitochondrial membrane potential, we assessed their pharmacokinetic profiles in isolated perfused rat hearts before and after mitochondrial depolarisation with the ionophore CCCP. All three tracers radiolabel with over 96% RCY, with log $D_{7.4}$ values above −0.4 observed for the most lipophilic example of this family of radiotracers. The candidate tracer **[^{68}Ga]Ga4c** exhibited non-preferential uptake in healthy cardiac tissue over CCCP-infused cardiac tissue. While this approach does show promise, the lipophilicity of this family of probes needs improving in order for them to be effective cardiac imaging agents.

8.2 Experimental Data for Compound Characterisation

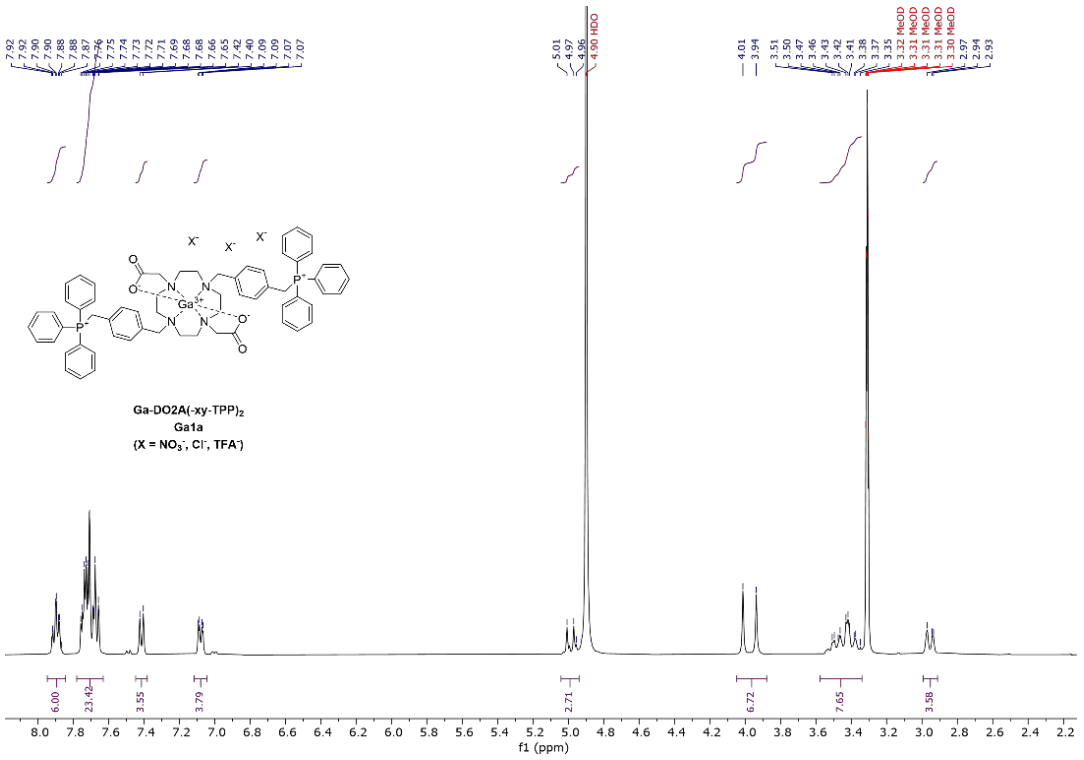

Figure 8.1 ^{1}H NMR spectrum of **Ga1a** (CD_3OD, 400 MHz, 298 K).

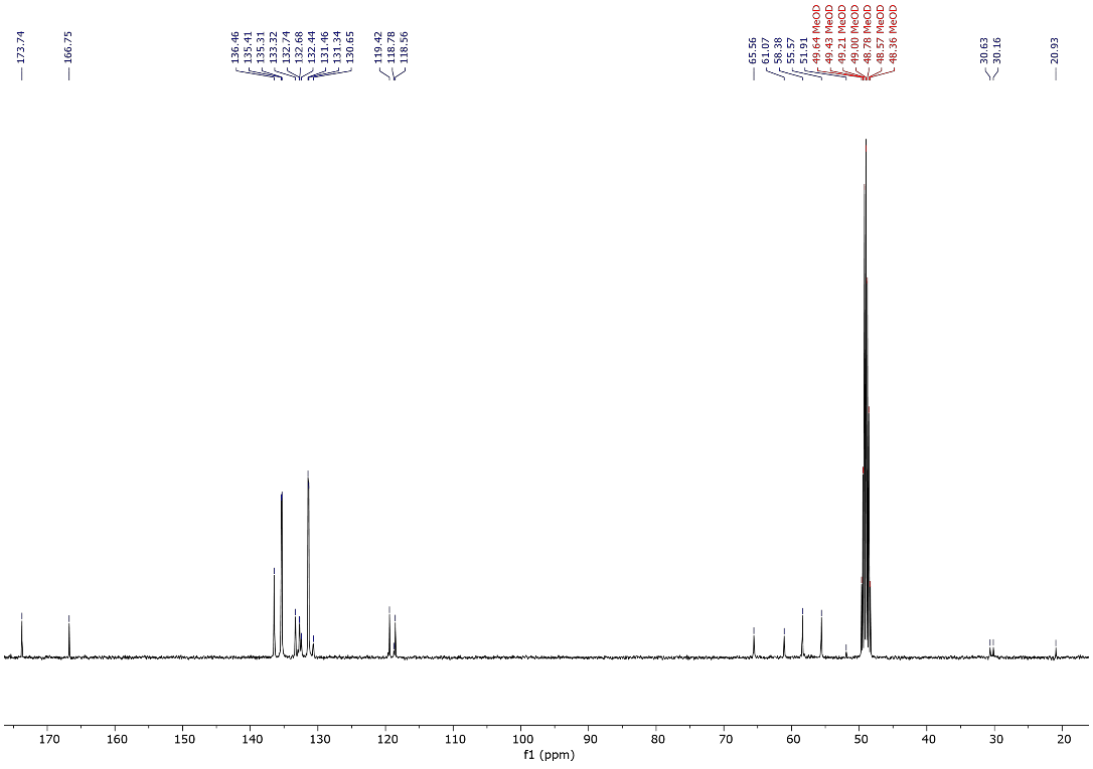

Figure 8.2 $^{13}C\{^{1}H\}$ NMR spectrum of **Ga1a** (CD_3OD, 101 MHz, 298 K).

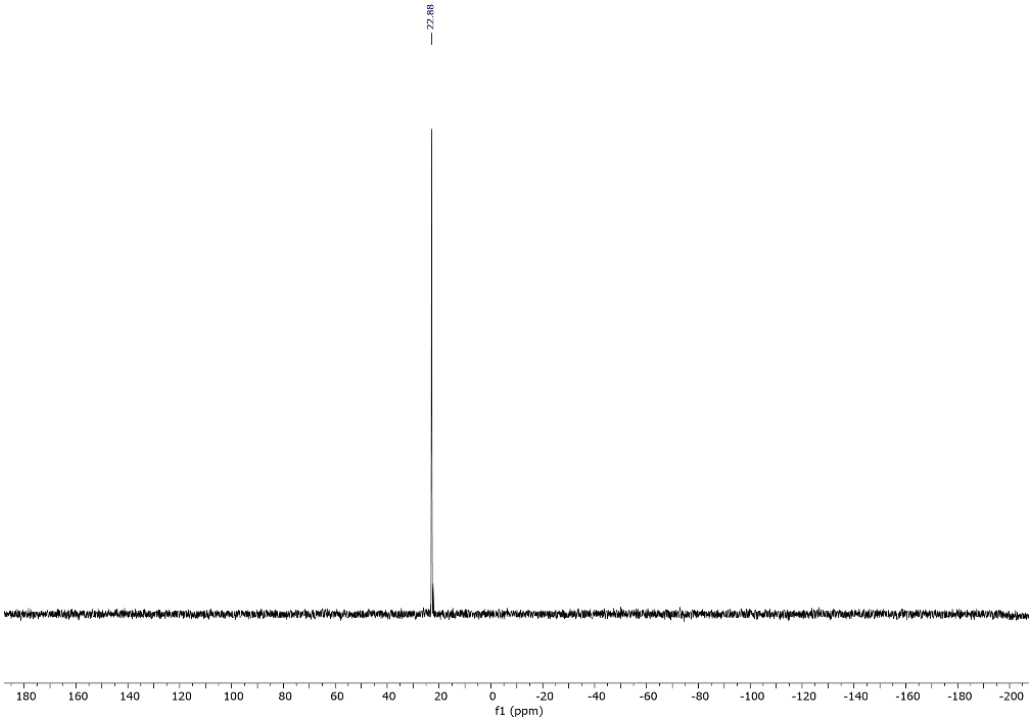

Figure 8.3 $^{31}P\{^{1}H\}$ NMR spectrum of **Ga1a** (CD_3OD, 162 MHz, 298 K).

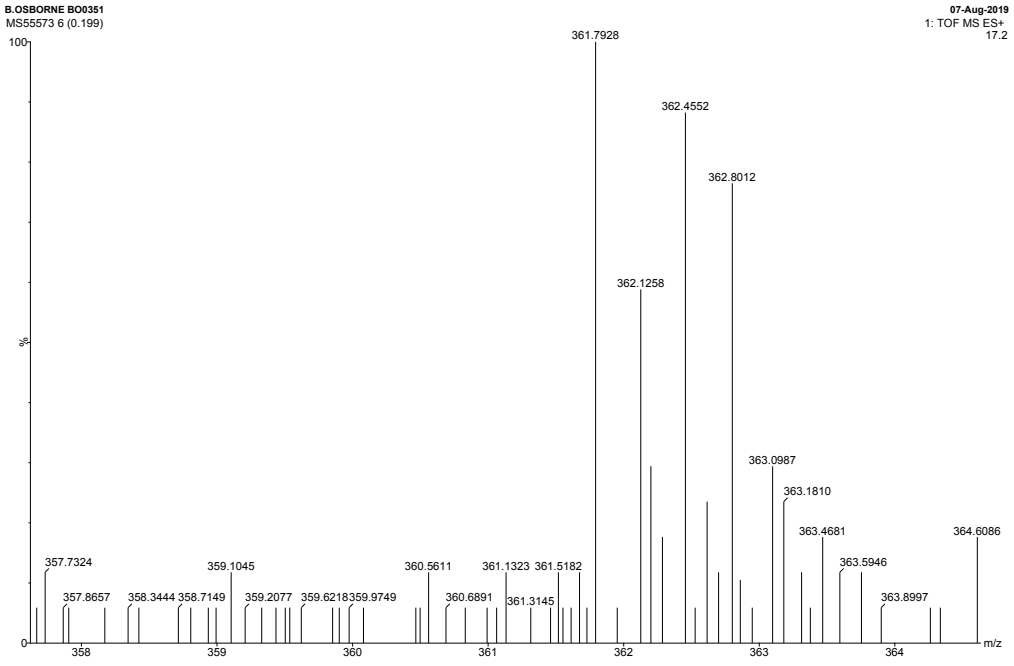

Figure 8.4 ES-TOF+ MS of **Ga1a**.

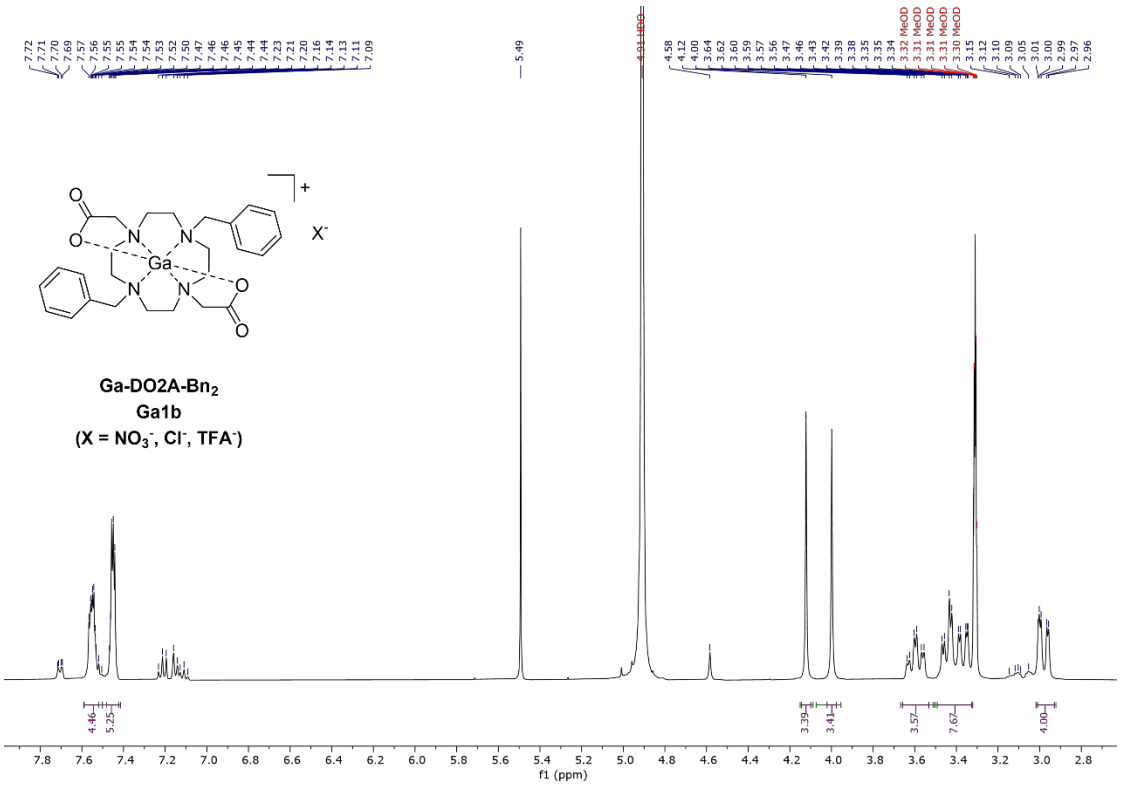

Figure 8.5 ^{1}H NMR spectrum of **Ga1b** (CD_3OD, 400 MHz, 298 K).

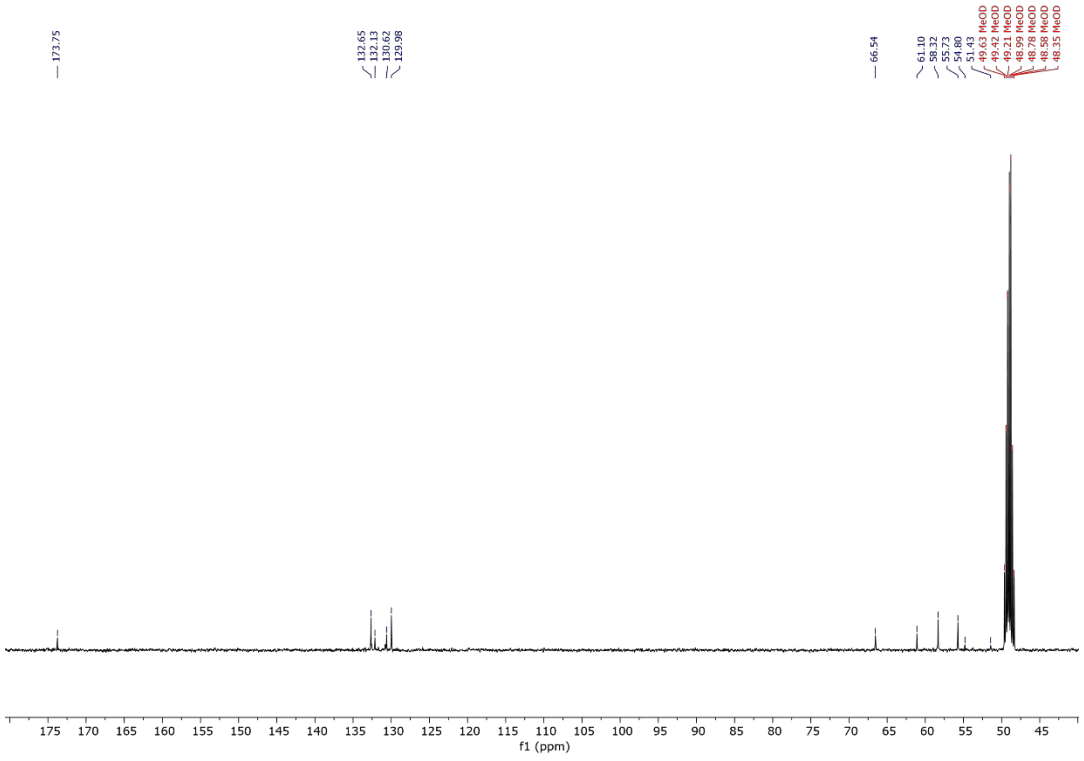

Figure 8.6 $^{13}C\{^{1}H\}$ NMR spectrum of **Ga1b** (CD_3OD, 101 MHz, 298 K).

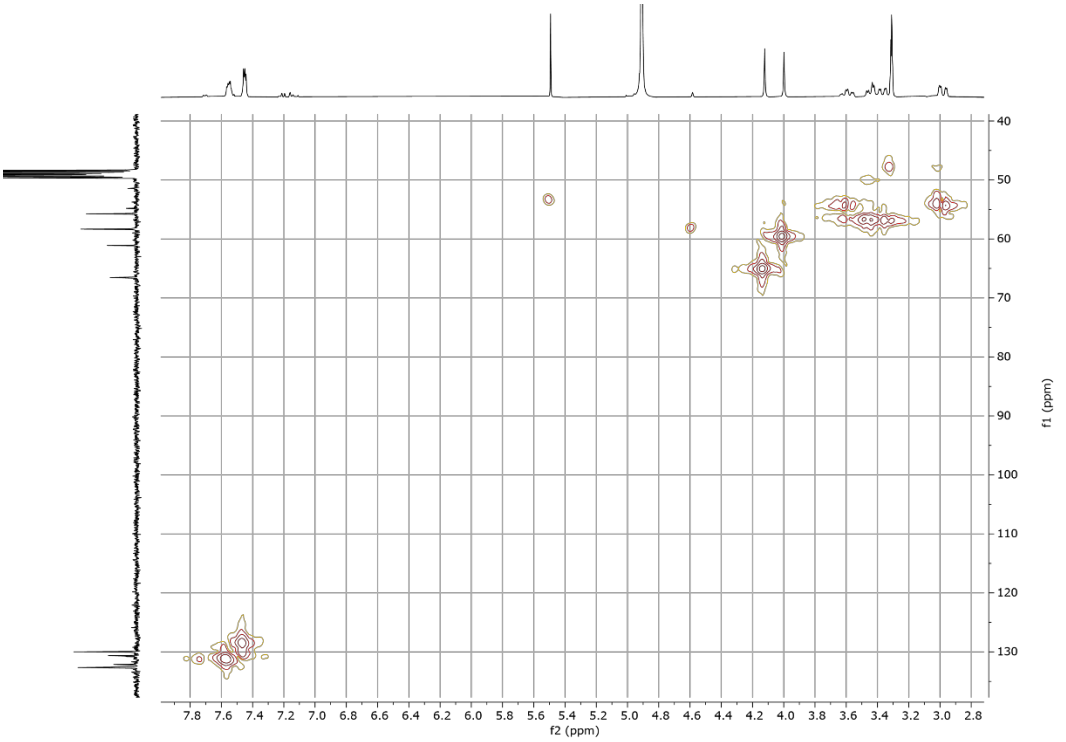

Figure 8.7 HMQC NMR spectrum of **Ga1b** (CD_3OD, 298 K).

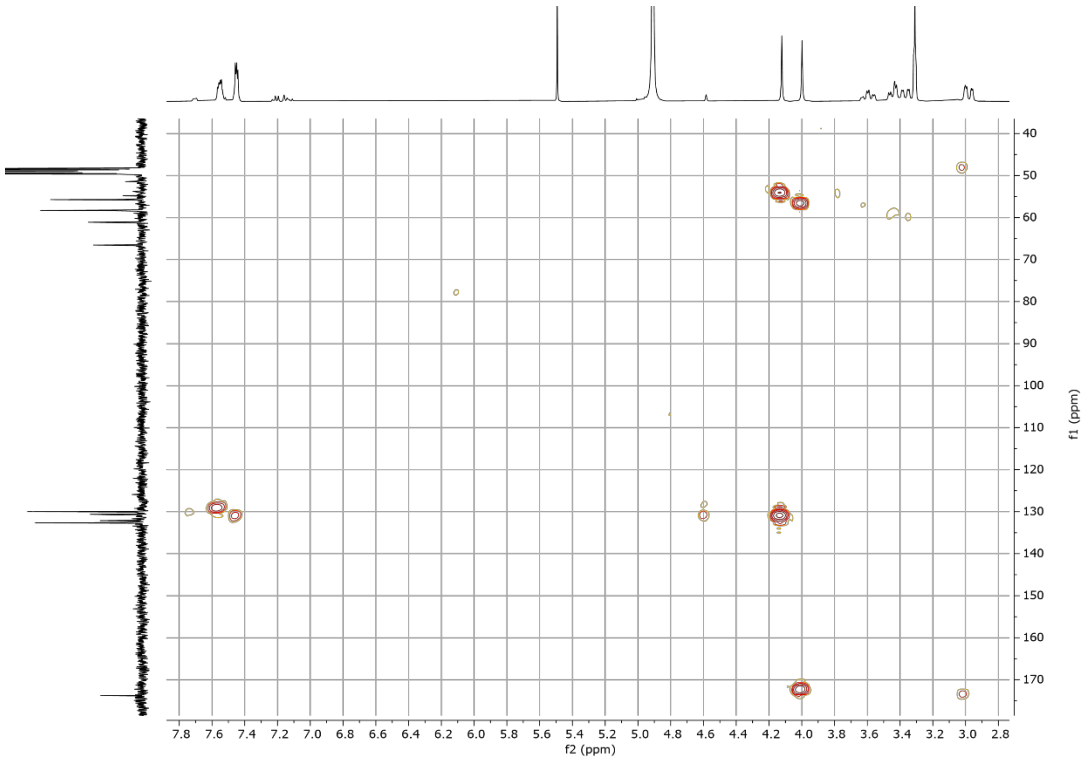

Figure 8.8 HMBC NMR spectrum of **Ga1b** (CD_3OD, 298 K).

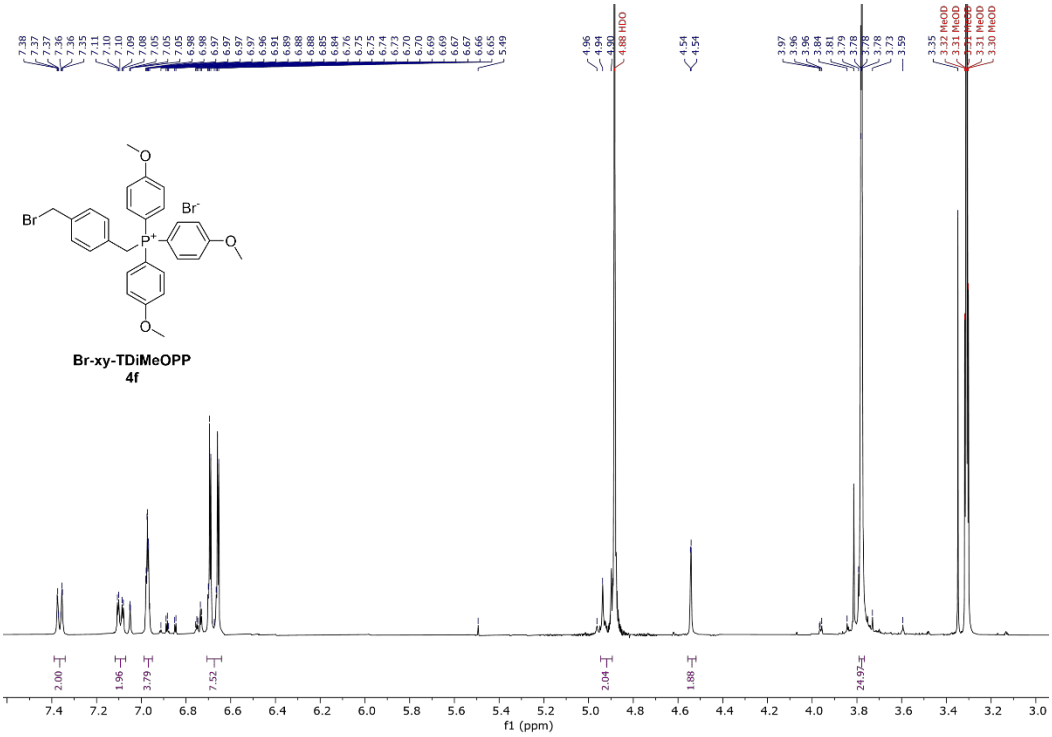

Figure 8.9 ^{1}H NMR spectrum of **4f** (CD_3OD, 400 MHz, 298 K).

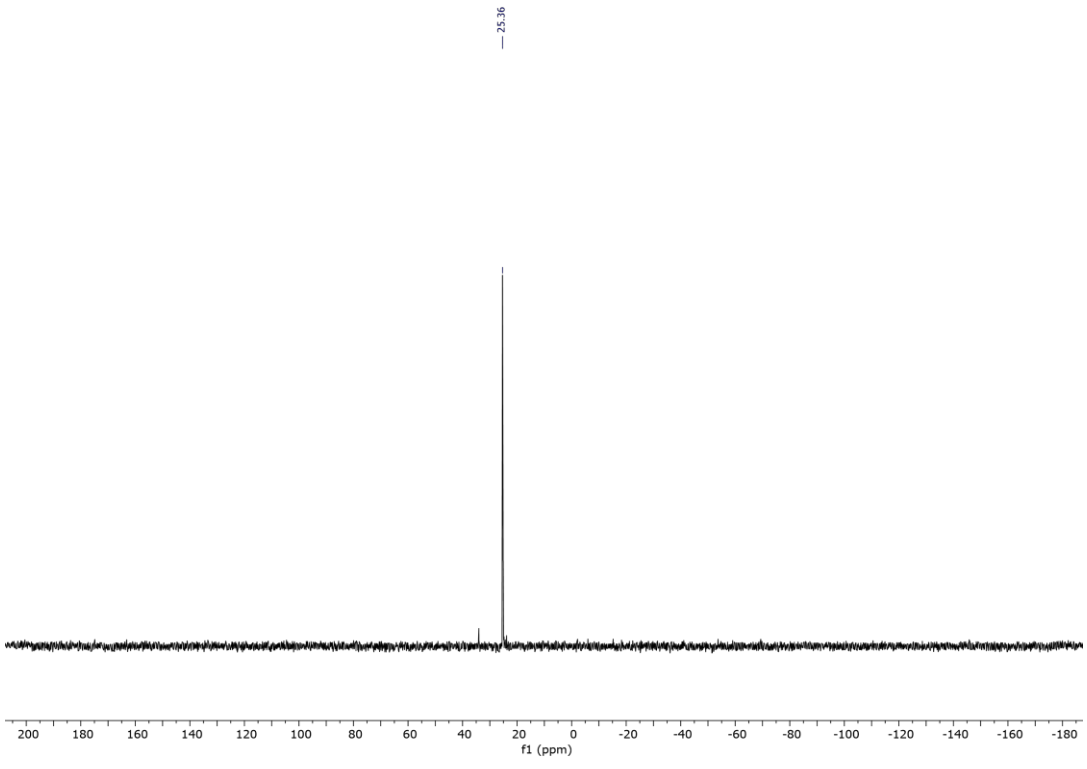

Figure 8.10 $^{31}P\{^{1}H\}$ NMR spectrum of **4f** (CD_3OD, 162 MHz, 298 K).

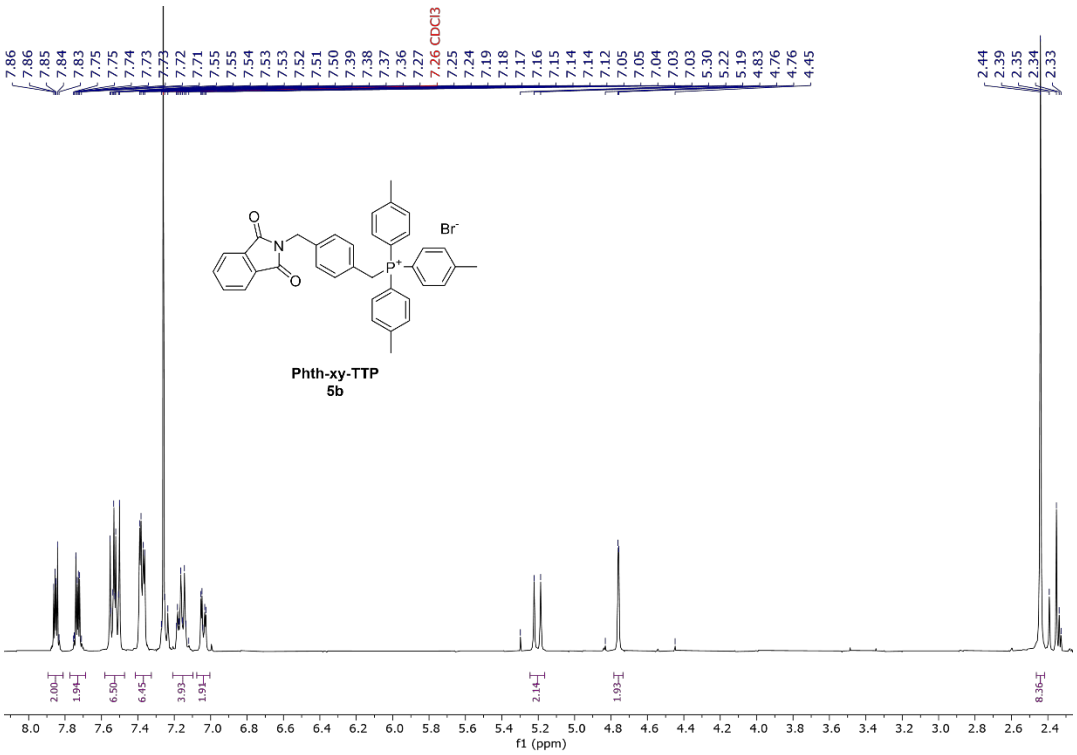

Figure 8.11 ^{1}H NMR spectrum of **5b** ($CDCl_3$, 400 MHz, 298 K).

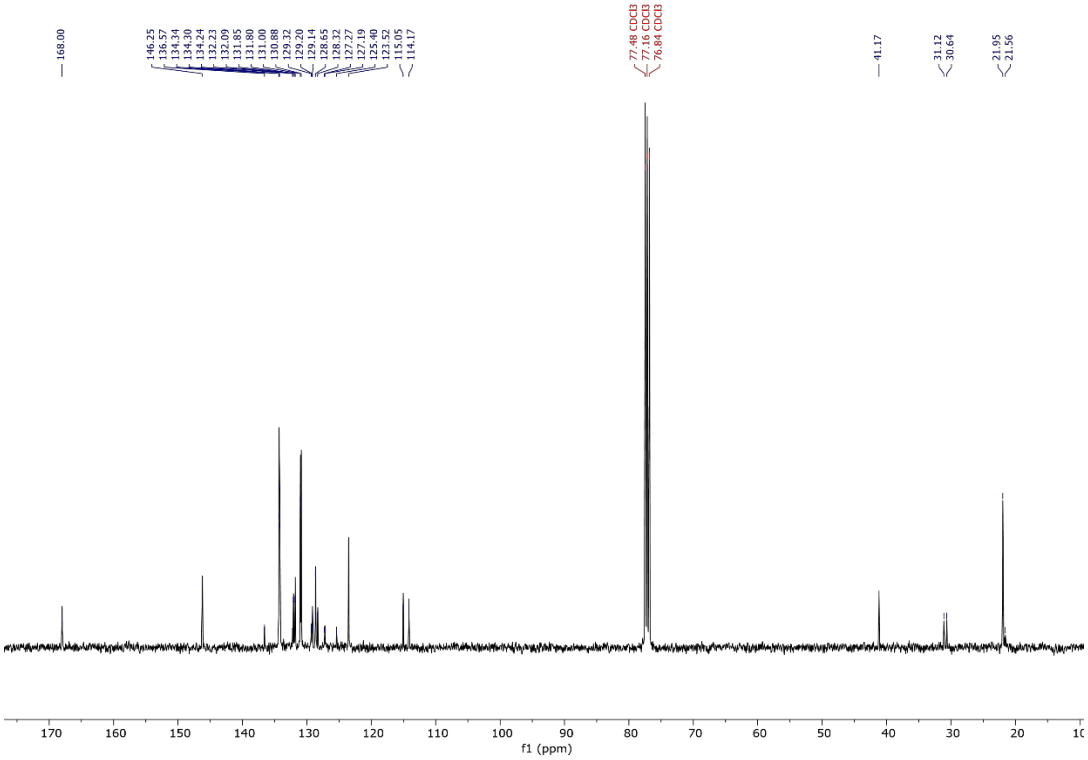

Figure 8.12 $^{13}C\{^{1}H\}$ NMR spectrum of **5b** ($CDCl_3$, 101 MHz, 298 K).

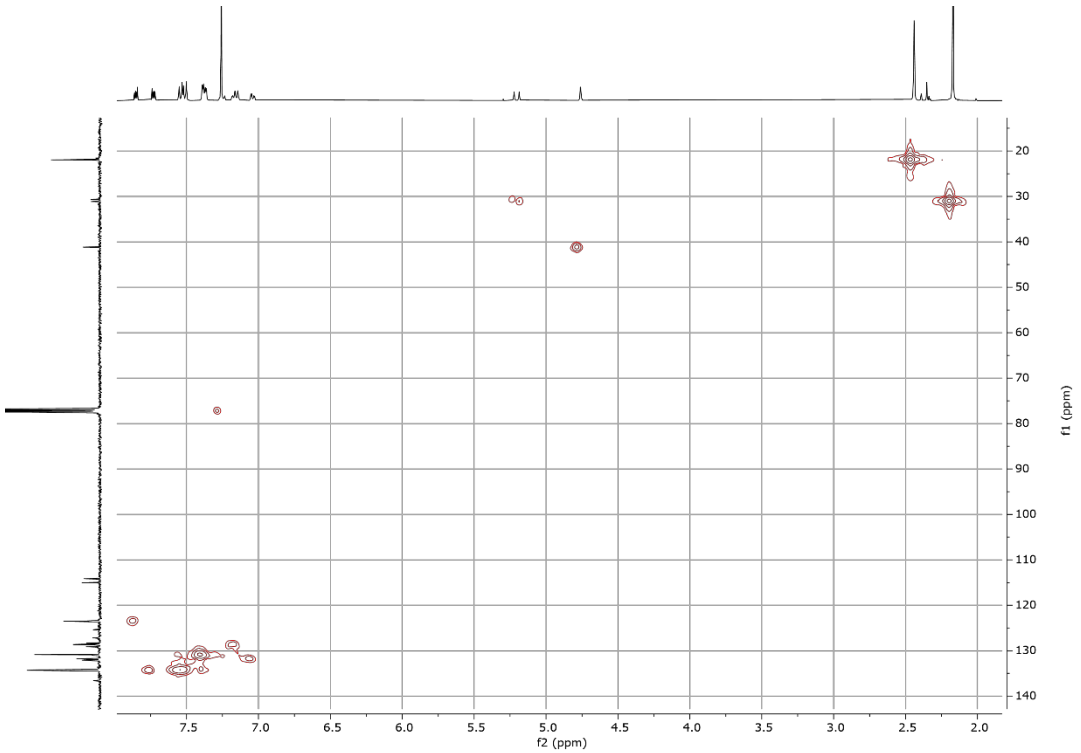

Figure 8.13 HMQC NMR spectrum of **5b** ($CDCl_3$, 298 K).

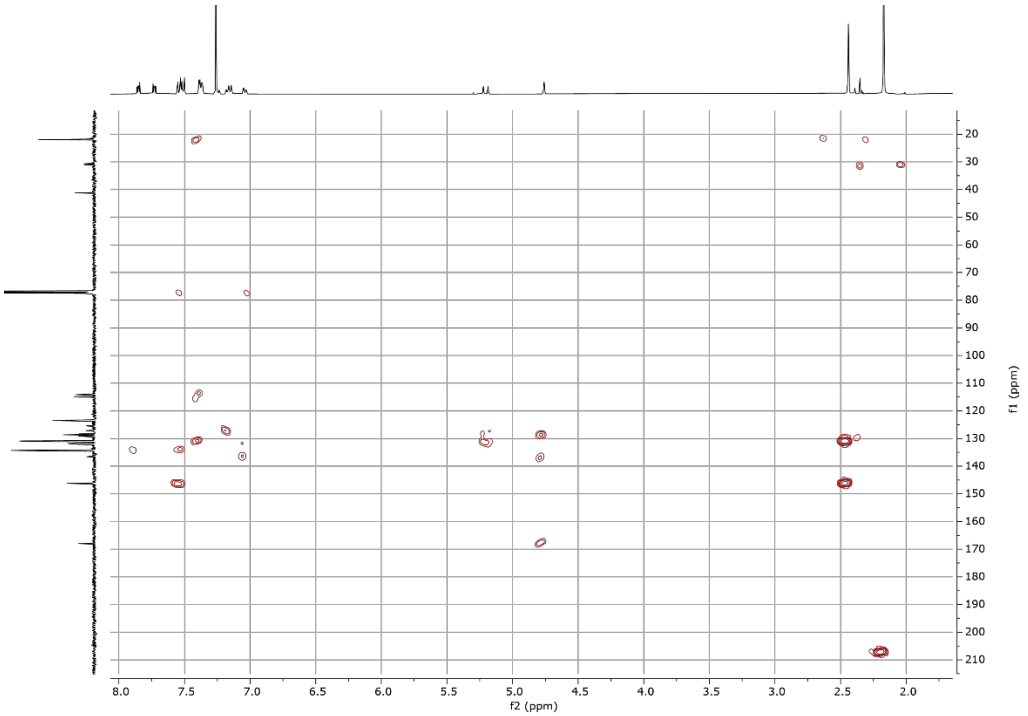

Figure 8.14 HMBC NMR spectrum of **5b** ($CDCl_3$, 298 K).

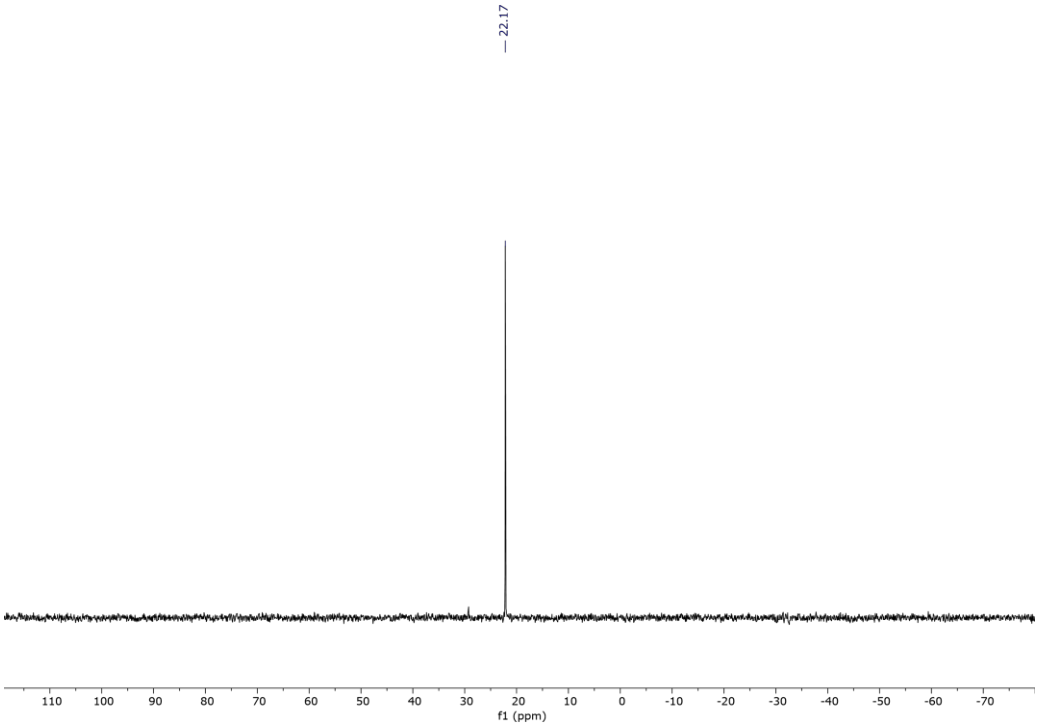

Figure 8.15 $^{31}P\{^{1}H\}$ NMR spectrum of **5b** ($CDCl_3$, 162 MHz, 298 K).

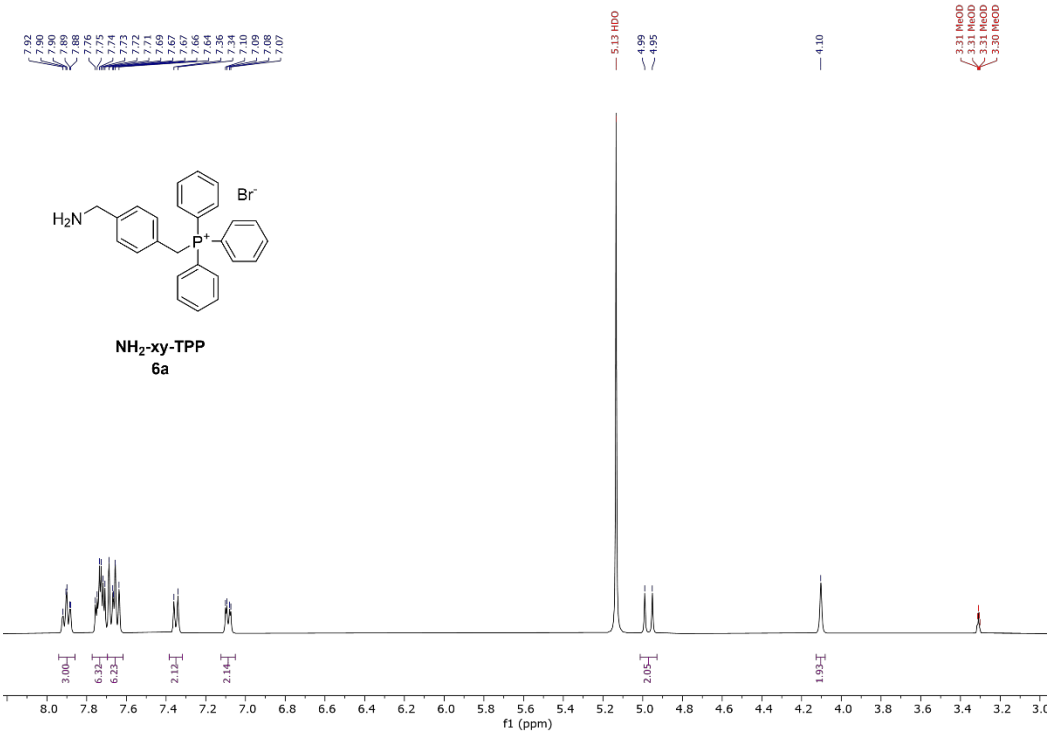

Figure 8.16 ^{1}H NMR spectrum of **6a** (CD_3OD, 400 MHz, 298 K).

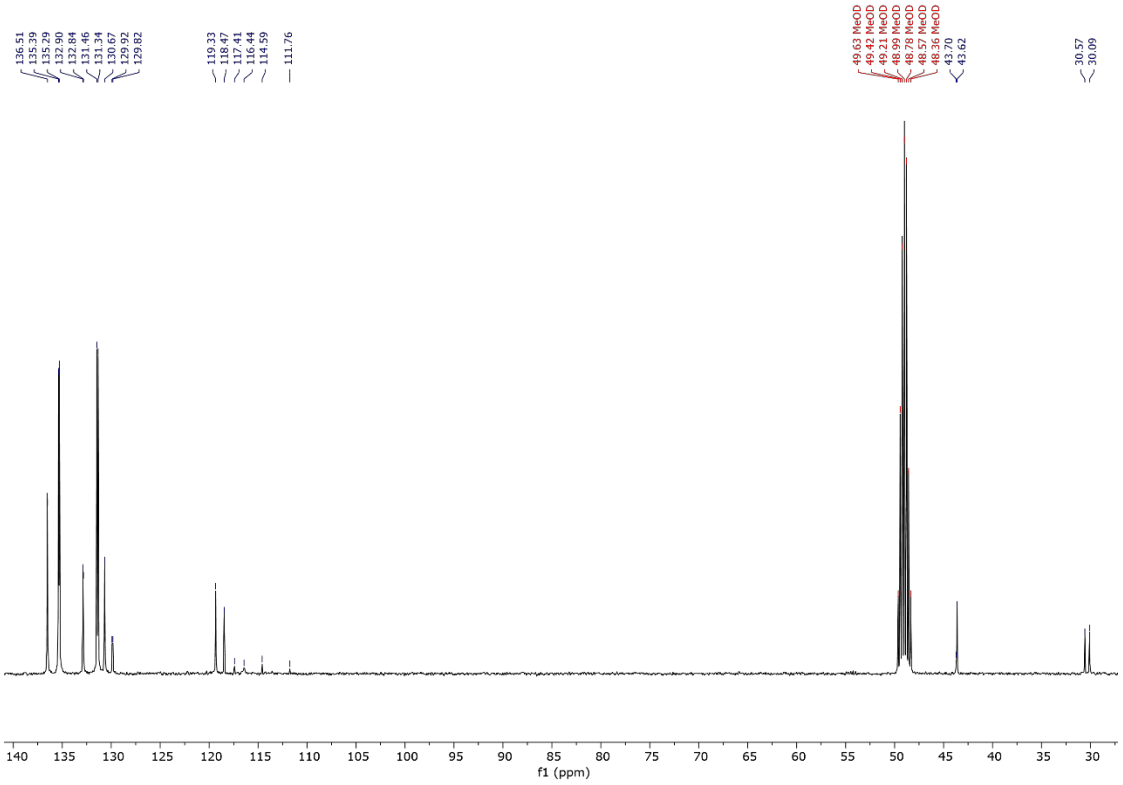

Figure 8.17 $^{13}C\{^{1}H\}$ NMR spectrum of **6a** (CD_3OD, 101 MHz, 298 K).

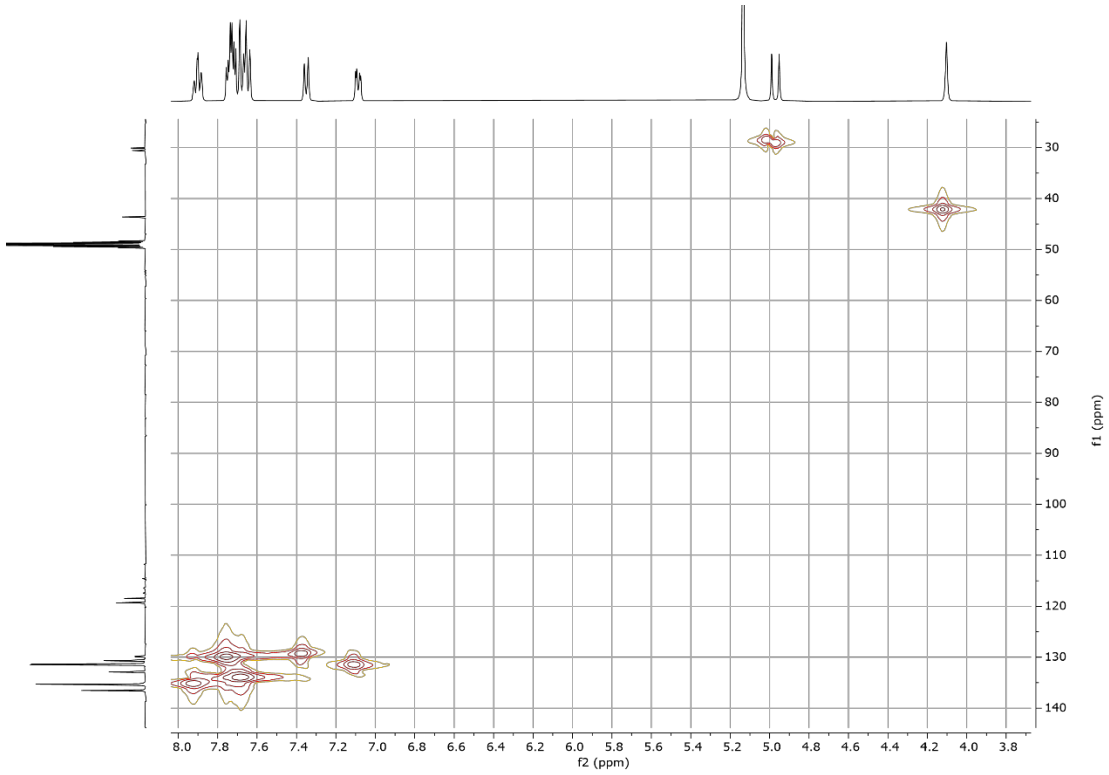

Figure 8.18 HMQC NMR spectrum of **6a** (CD_3OD, 298 K).

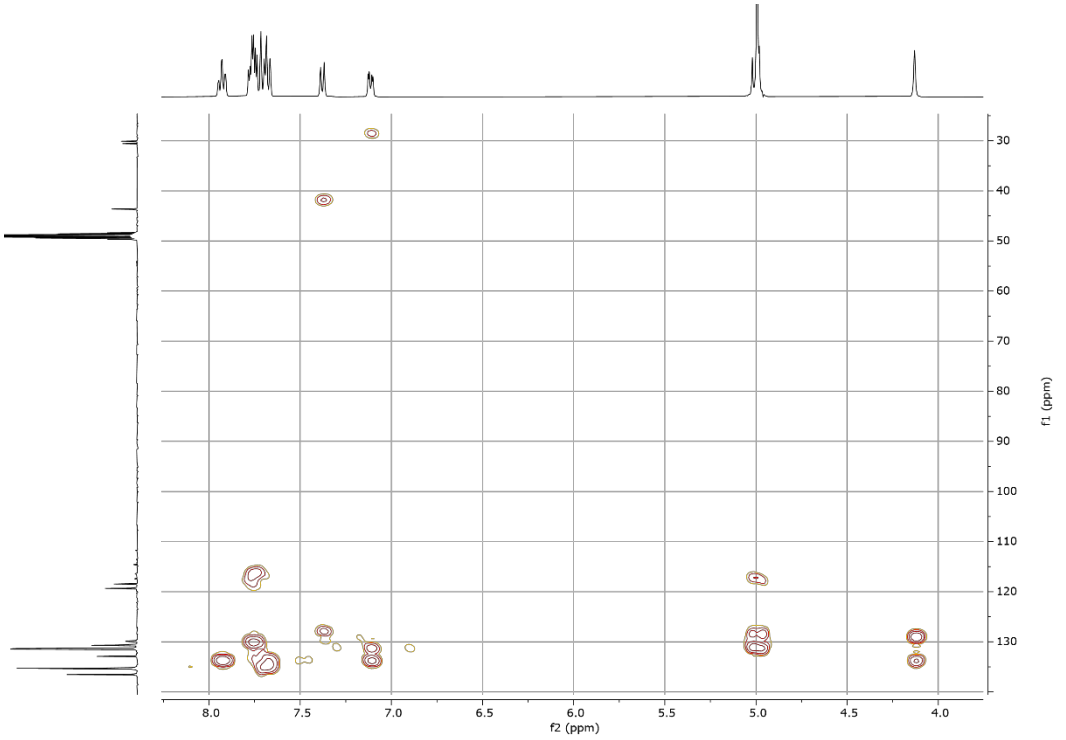

Figure 8.19 HMBC NMR spectrum of **6a** (CD_3OD, 298 K).

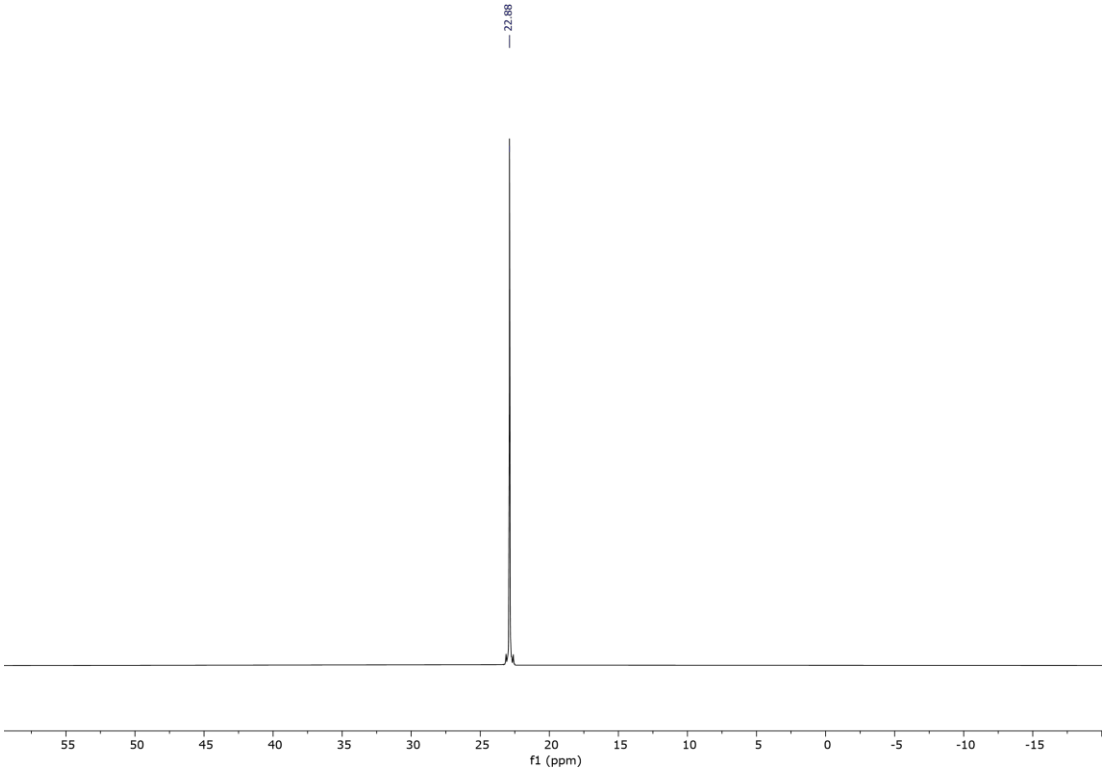

Figure 8.20 $^{31}P\{^1H\}$ NMR spectrum of **6a** (CD_3OD, 162 MHz, 298 K).

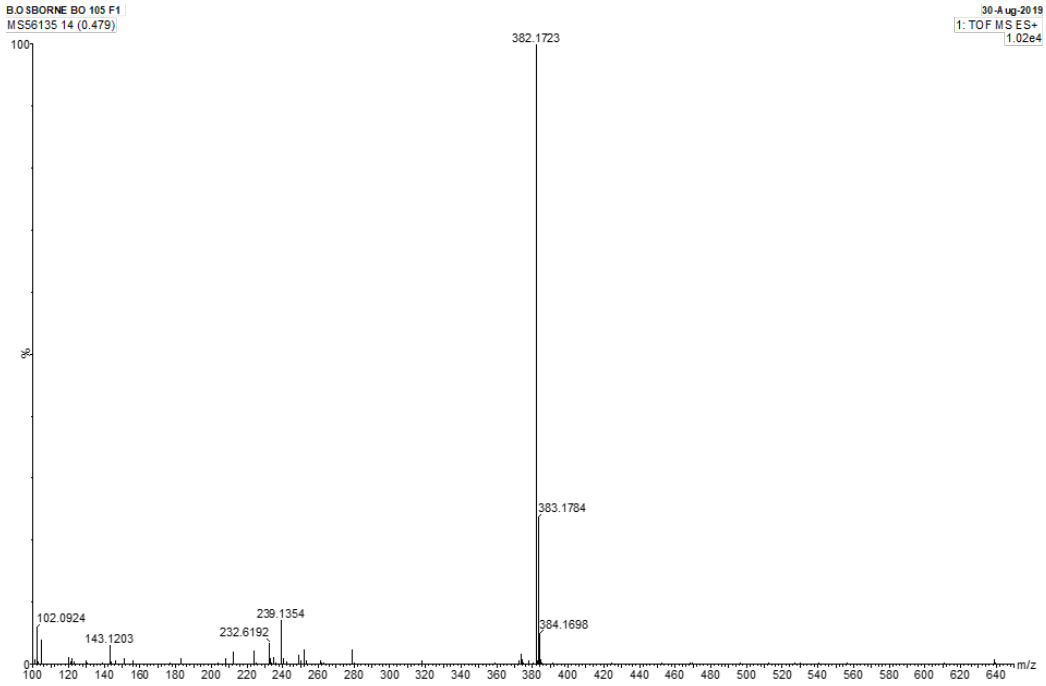

Figure 8.21 ES-TOF+ MS of **6a**.

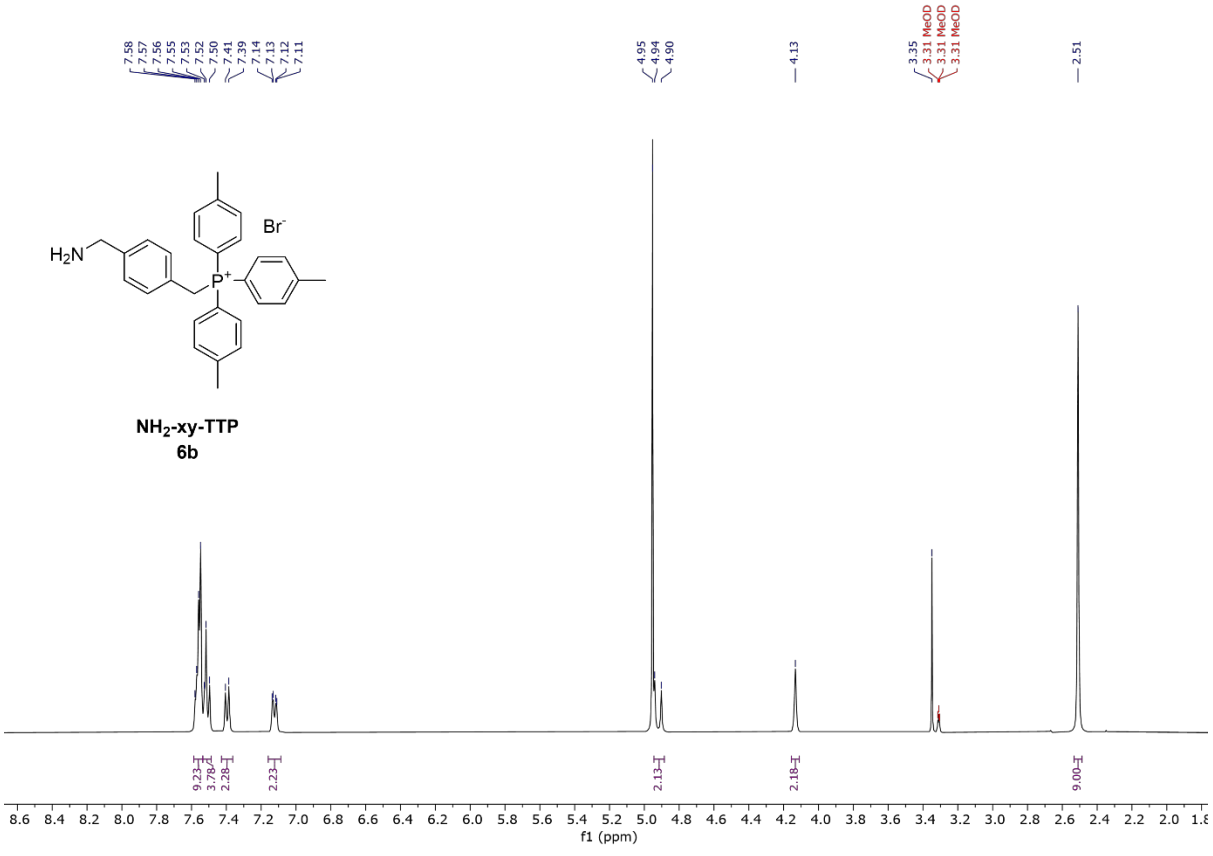

Figure 8.22 ^{1}H NMR spectrum of **6b** (CD_3OD, 400 MHz, 298 K).

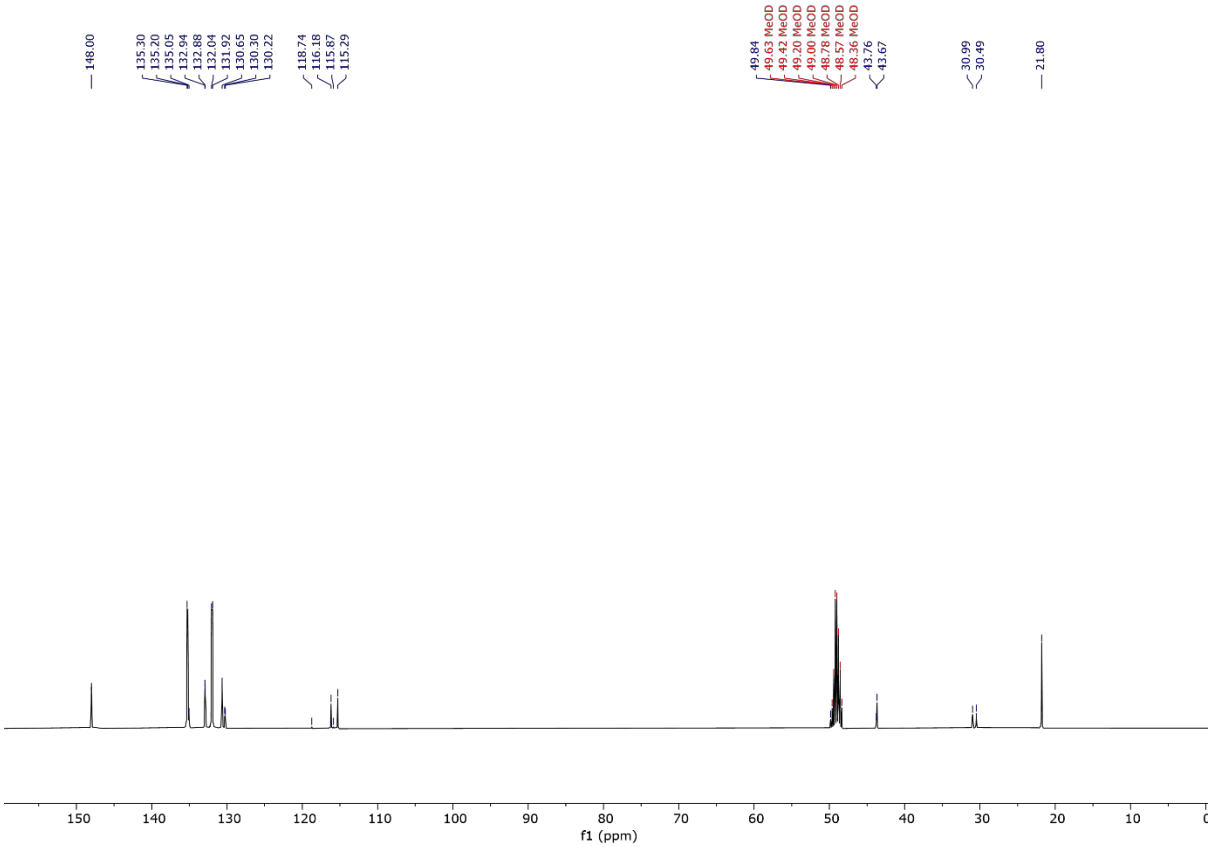

Figure 8.23 $^{13}C\{^{1}H\}$ NMR spectrum of **6b** (CD_3OD, 101 MHz, 298 K).

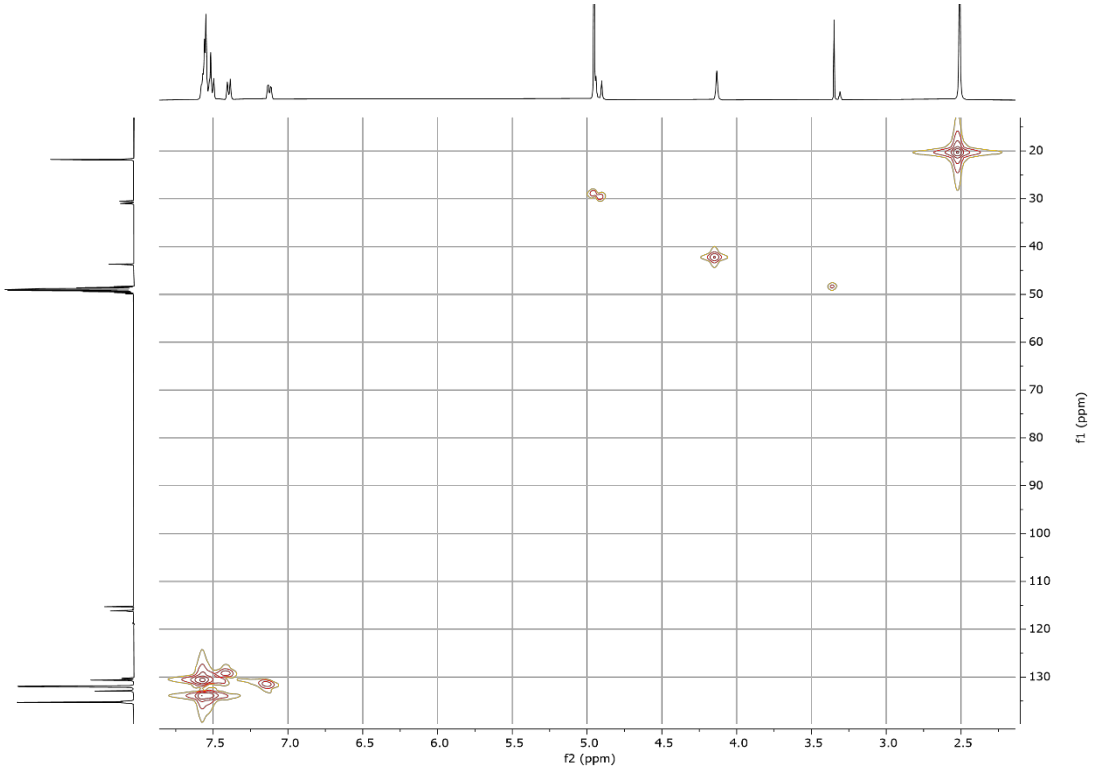

Figure 8.24 HMQC NMR spectrum of **6b** (CD_3OD, 298 K).

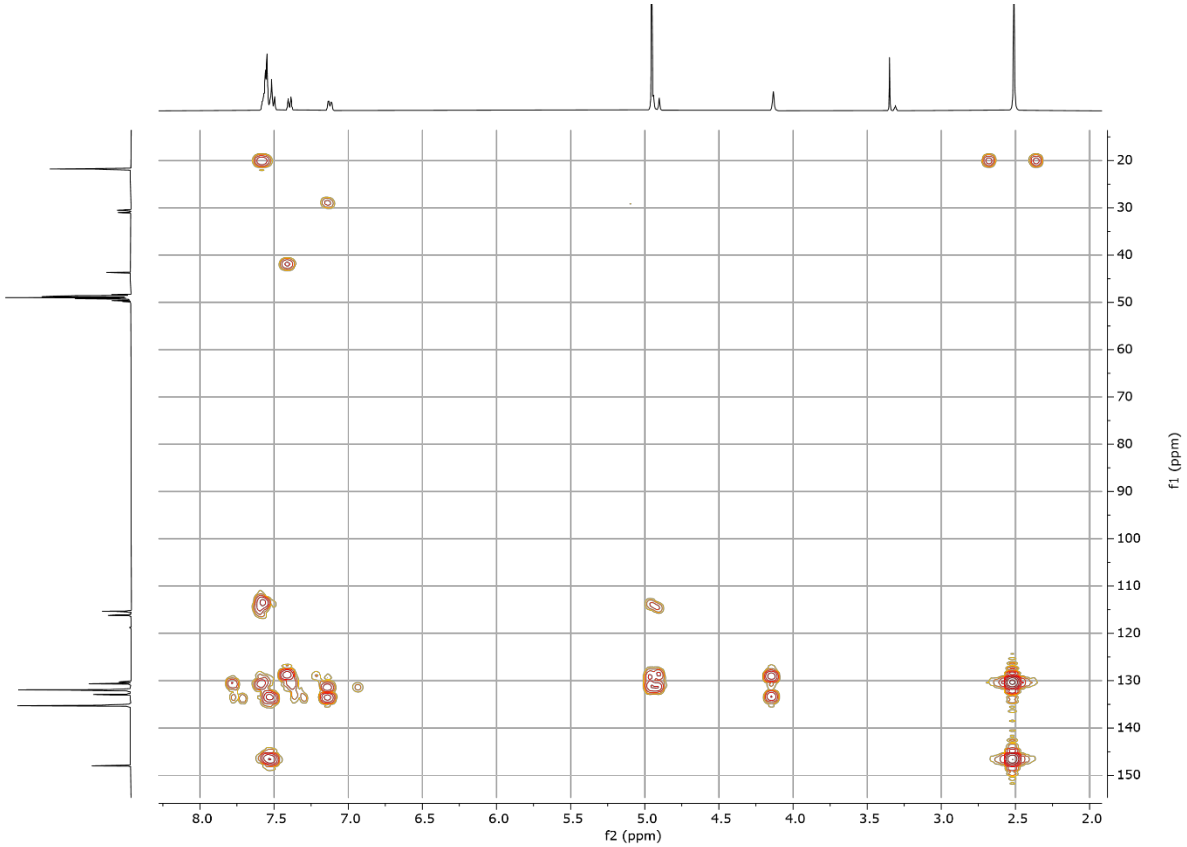

Figure 8.25 HMBC NMR spectrum of **6b** (CD_3OD, 298 K).

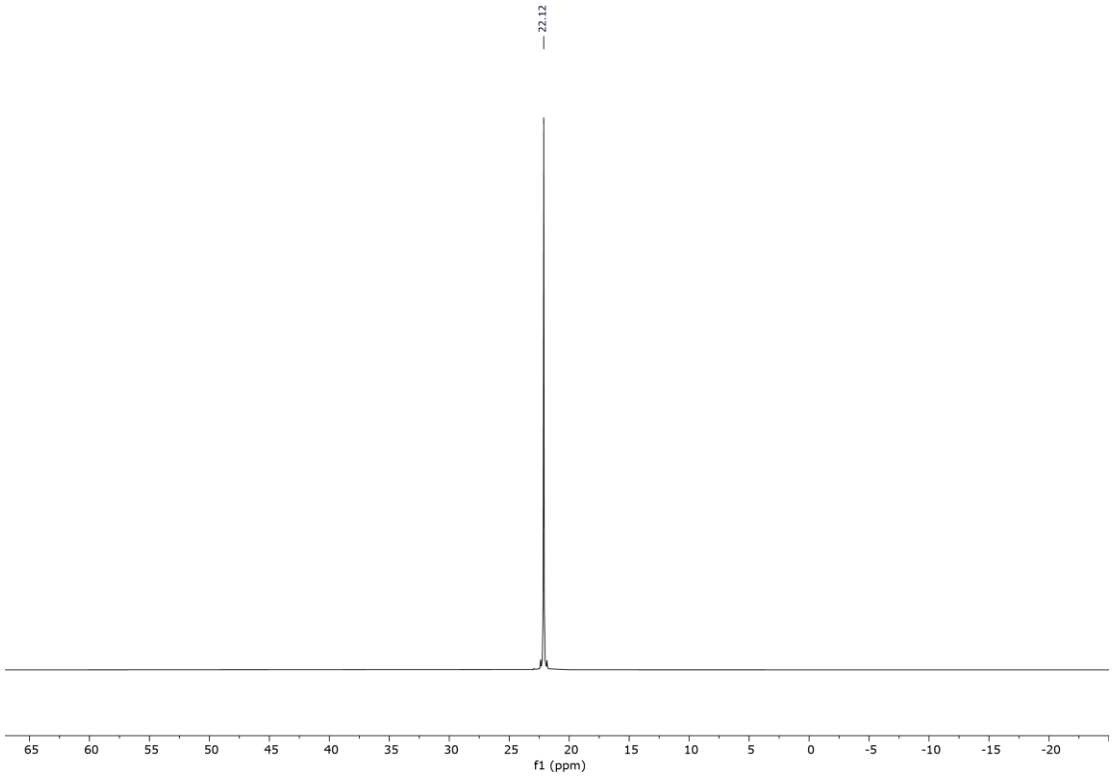

Figure 8.26 $^{31}P\{^{1}H\}$ NMR spectrum of **6b** (CD_3OD, 162 MHz, 298 K).

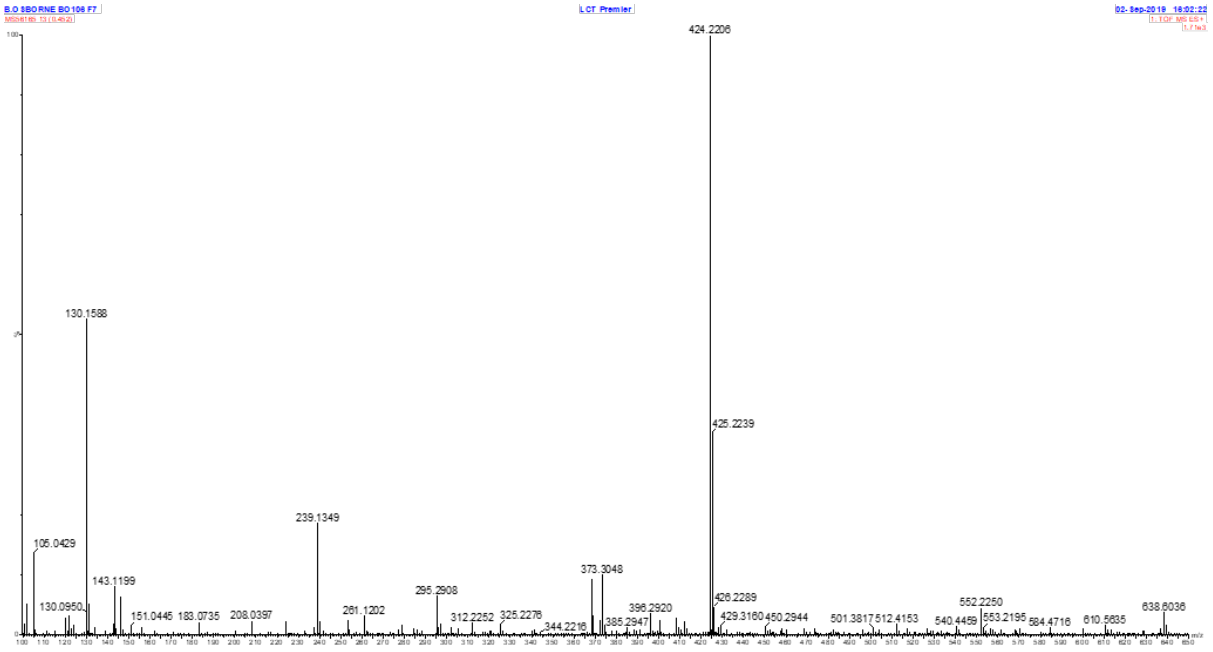

Figure 8.27 ES-TOF+ MS of **6b**.

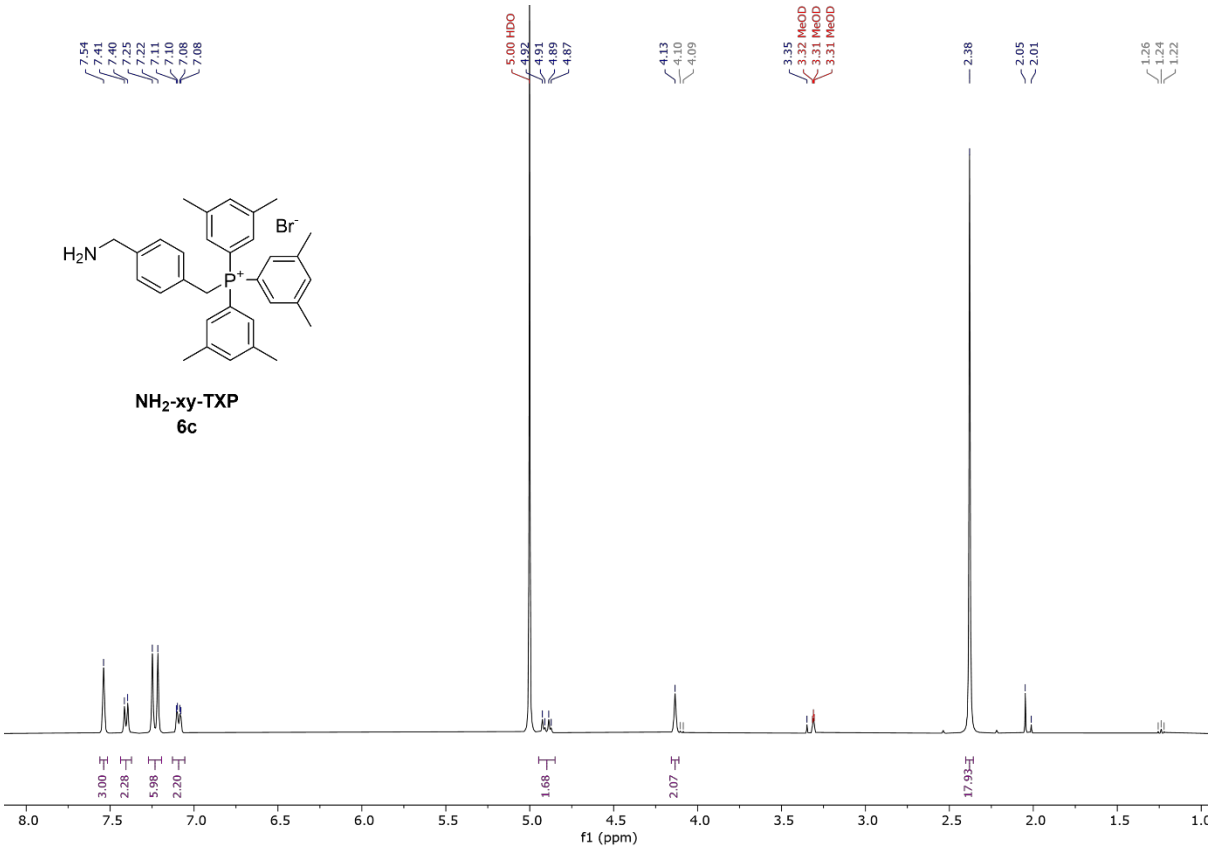

Figure 8.28 ^{1}H NMR spectrum of **6c** (CD_3OD, 400 MHz, 298 K).

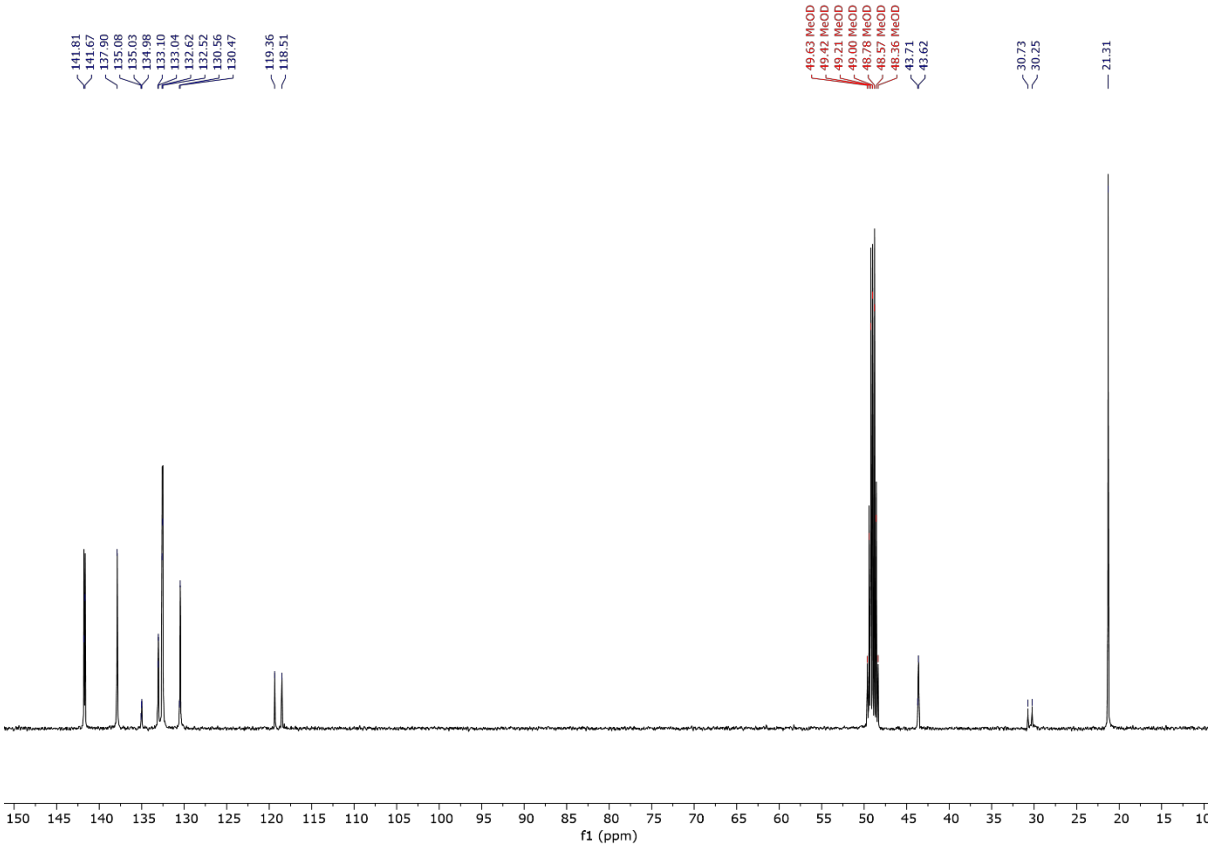

Figure 8.29 $^{13}C\{^{1}H\}$ NMR spectrum of **6c** (CD_3OD, 101 MHz, 298 K).

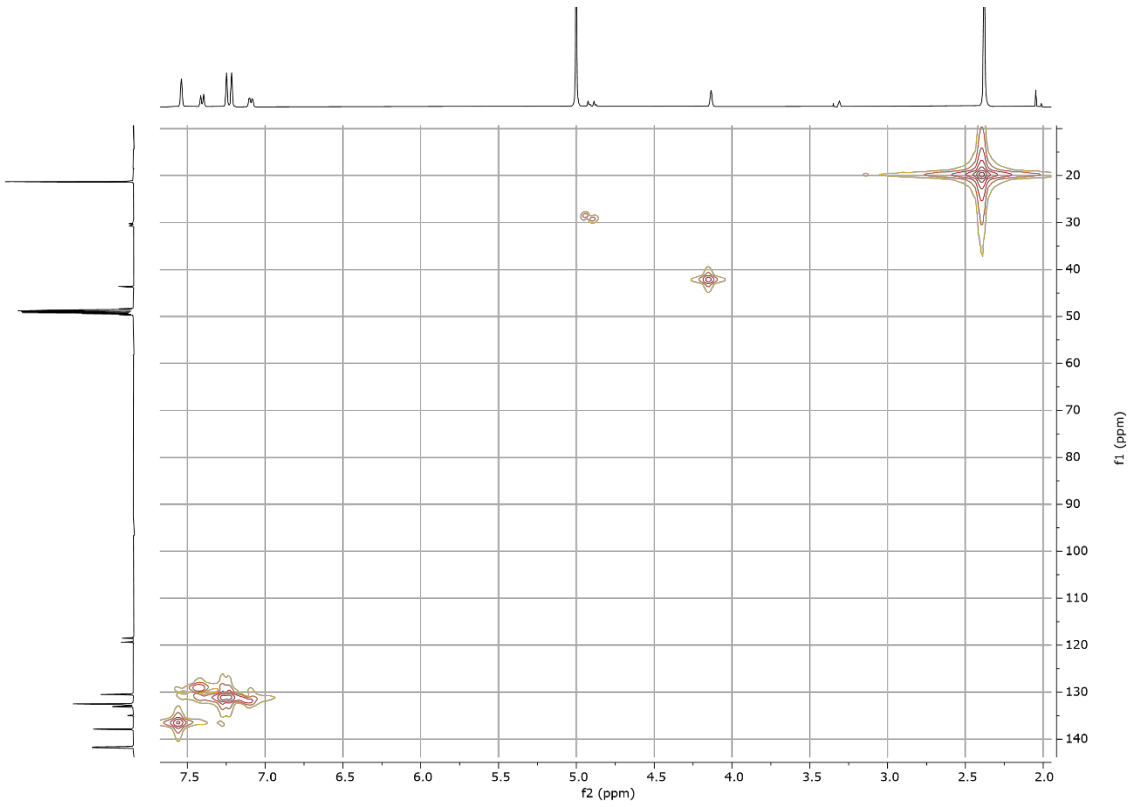

Figure 8.30 HMQC NMR spectrum of **6c** (CD_3OD, 298 K).

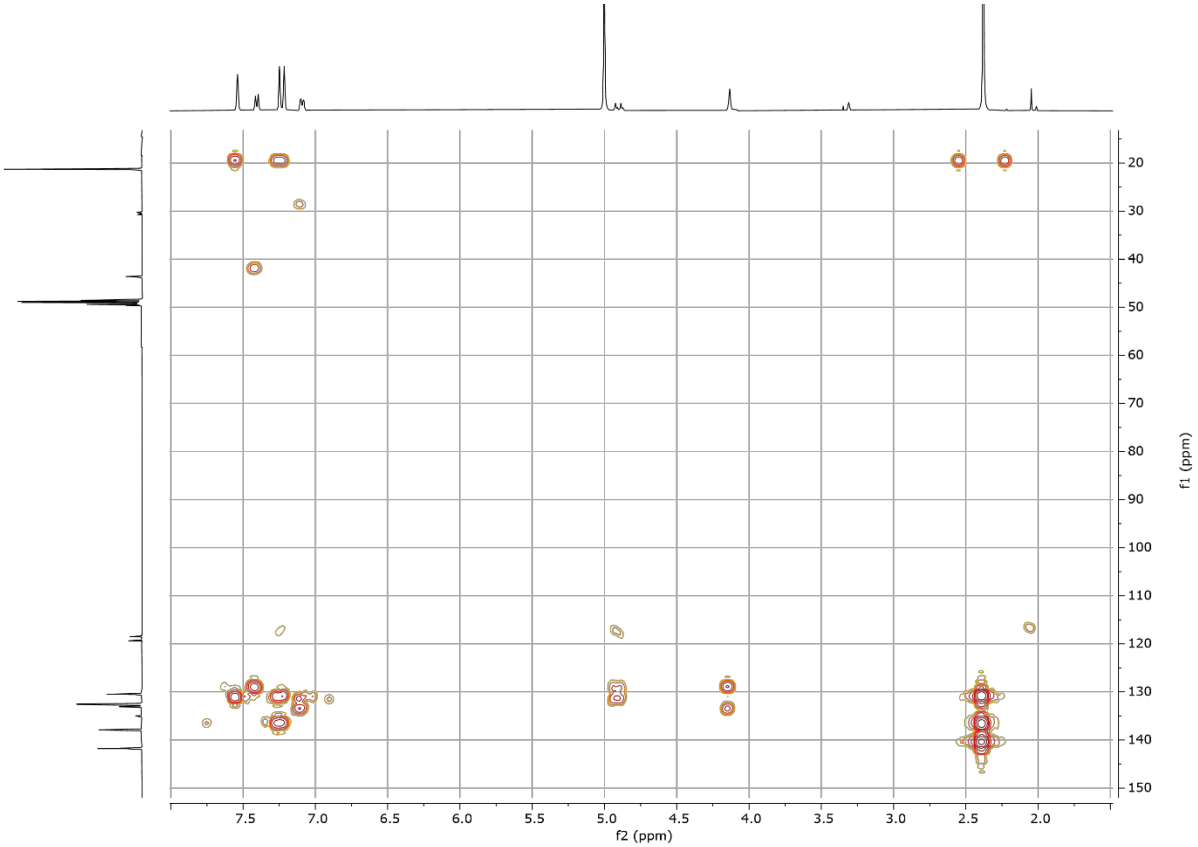

Figure 8.31 HMBC NMR spectrum of **6c** (CD_3OD, 298 K).

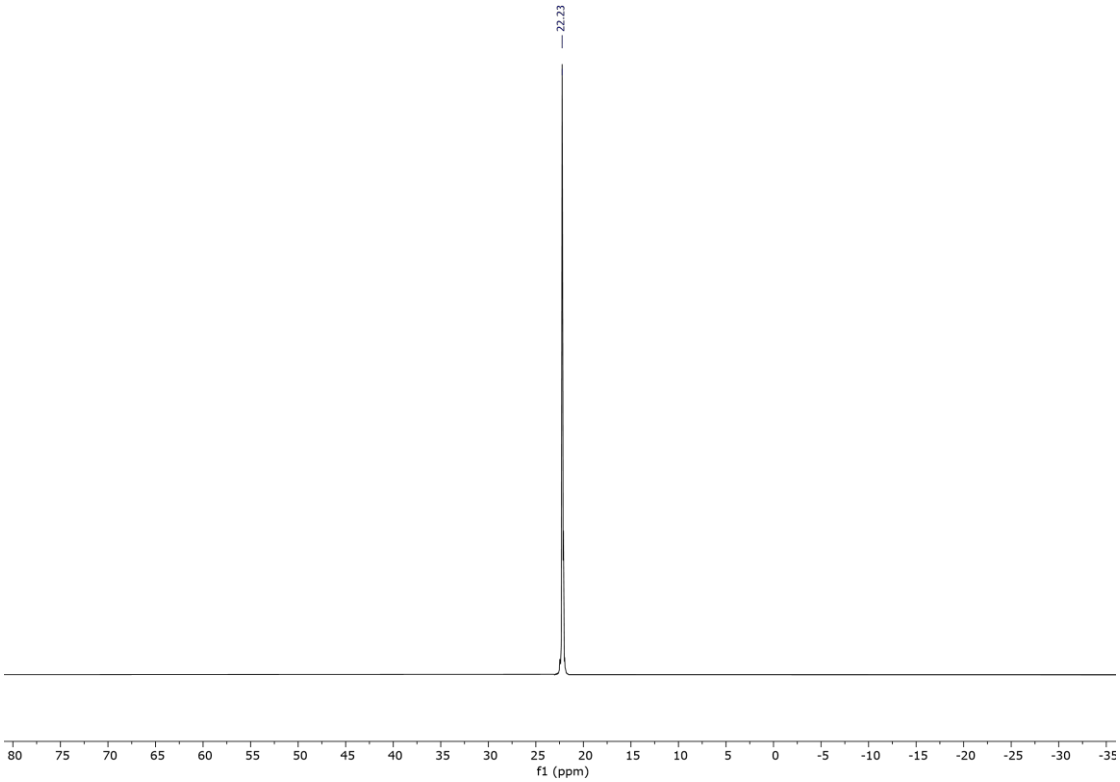

Figure 8.32 $^{31}P\{^{1}H\}$ NMR spectrum of **6c** (CD_3OD, 162 MHz, 298 K).

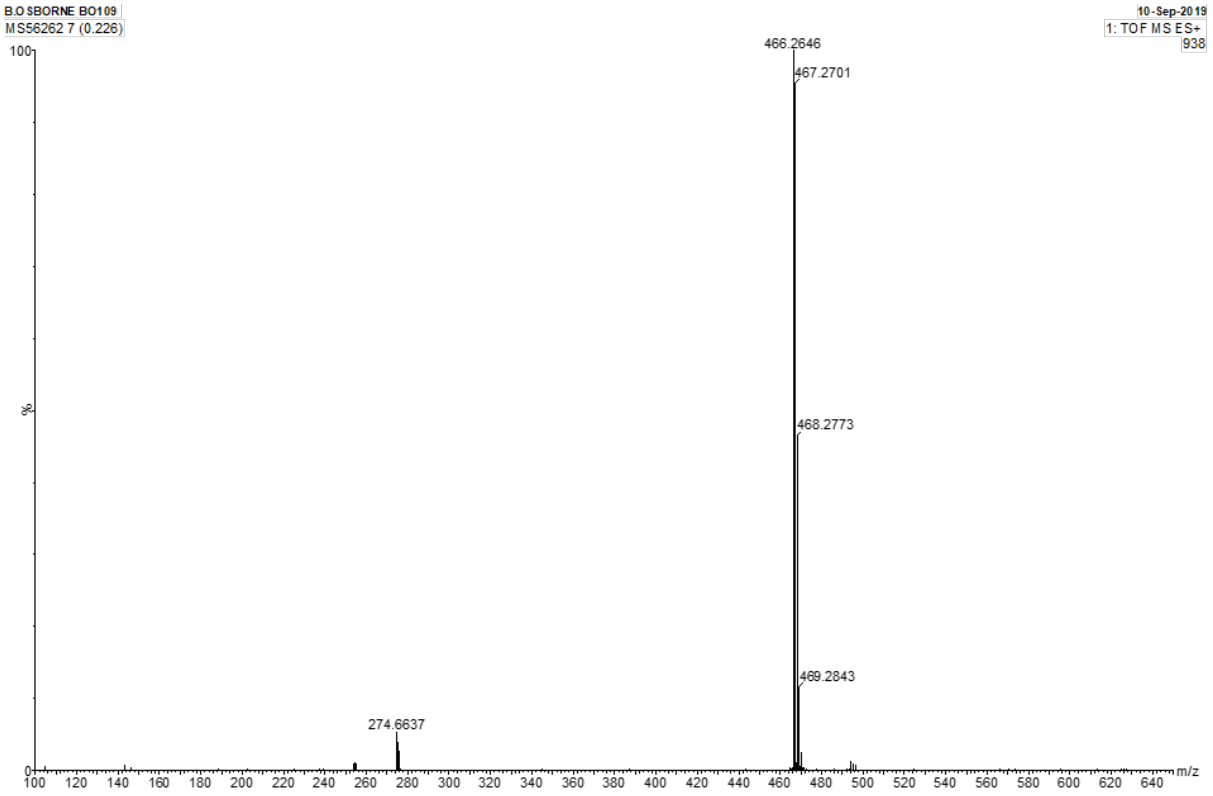

Figure 8.33 ES-TOF+ MS of **6c**.

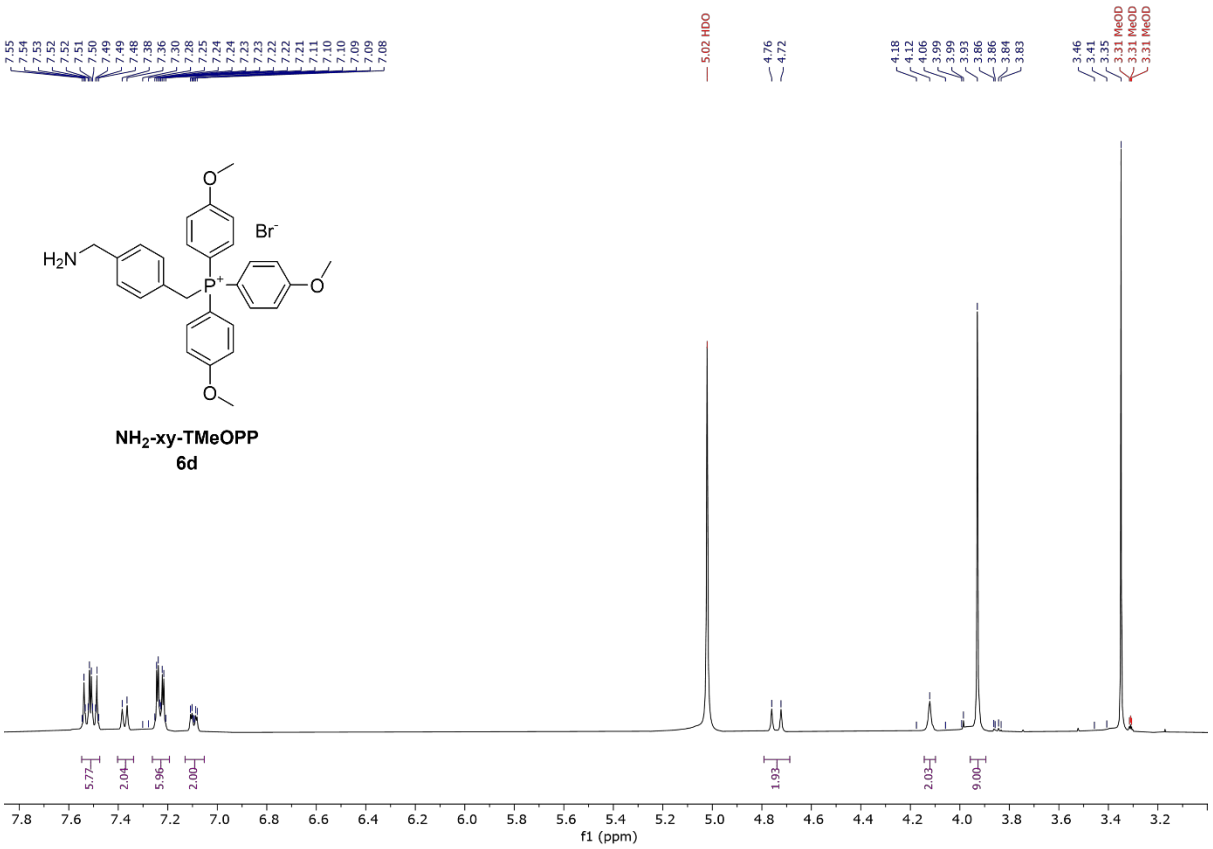

Figure 8.34 ^{1}H NMR spectrum of **6d** (CD_3OD, 400 MHz, 298 K).

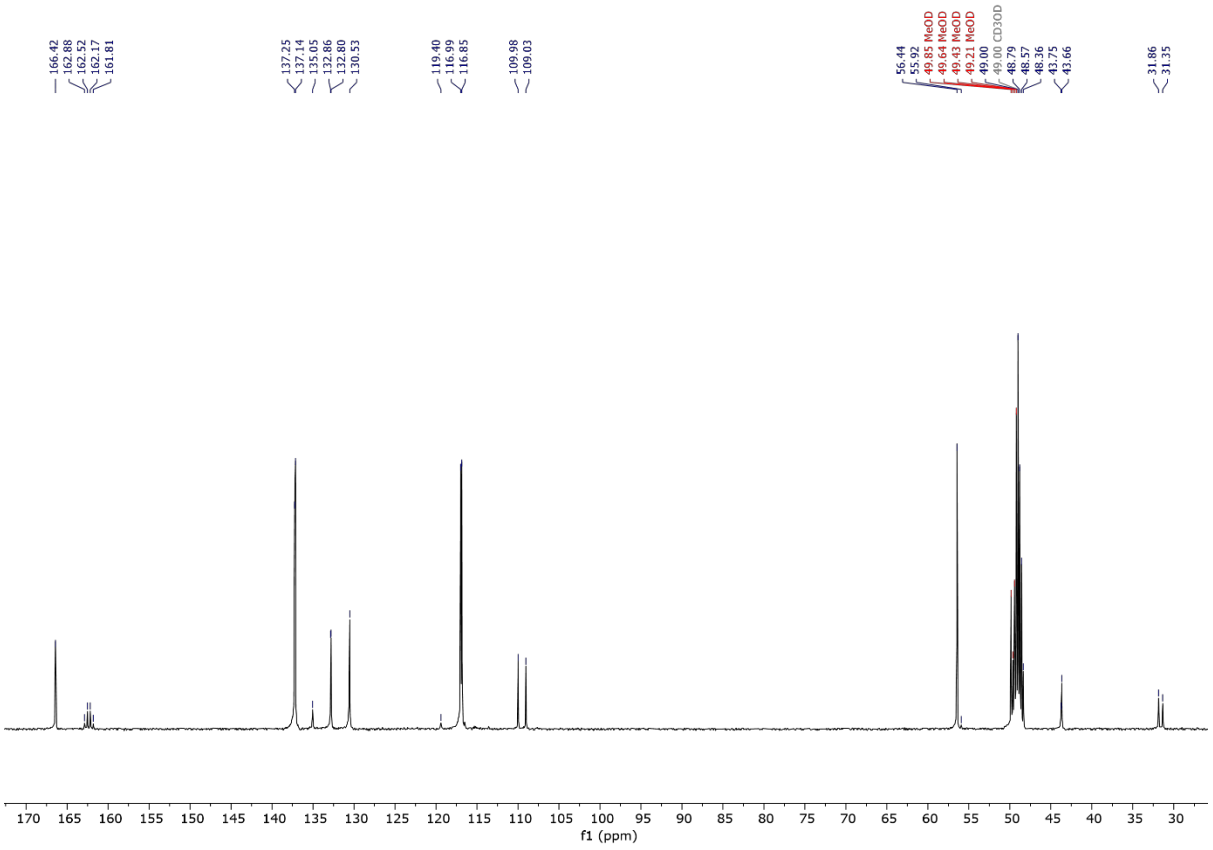

Figure 8.35 $^{13}C\{^{1}H\}$ NMR spectrum of **6d** (CD_3OD, 101 MHz, 298 K).

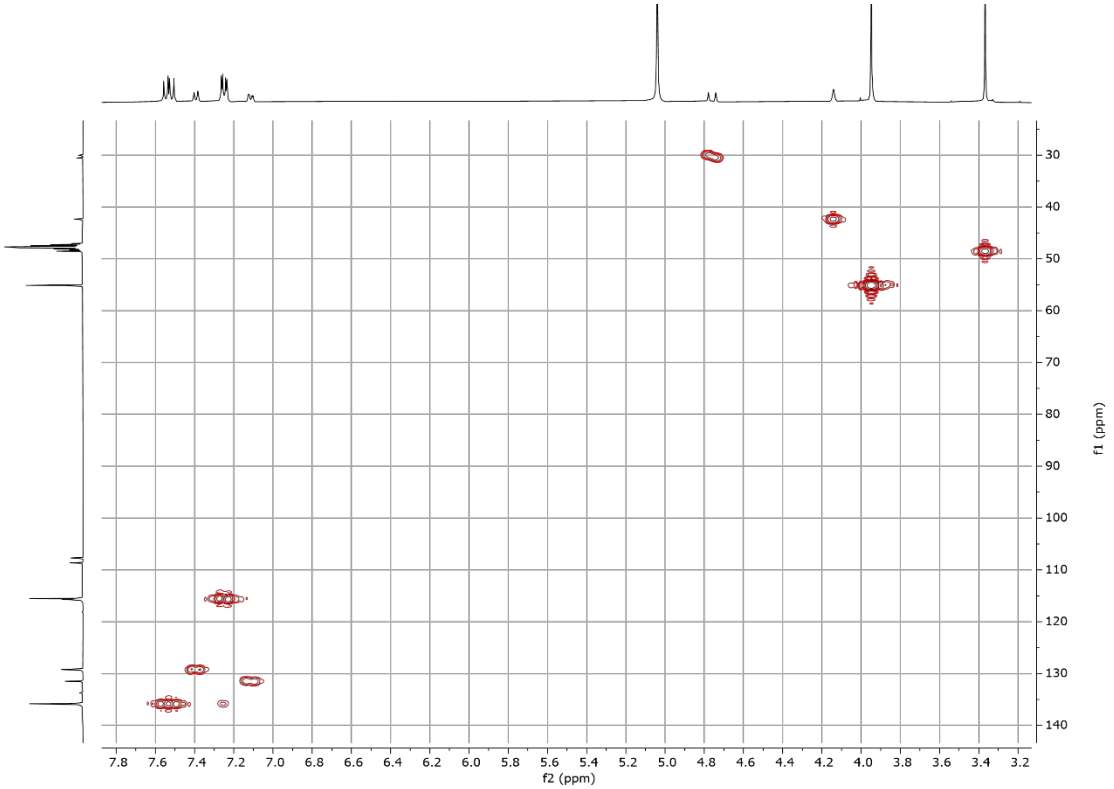

Figure 8.36 HMQC NMR spectrum of **6d** (CD_3OD, 298 K).

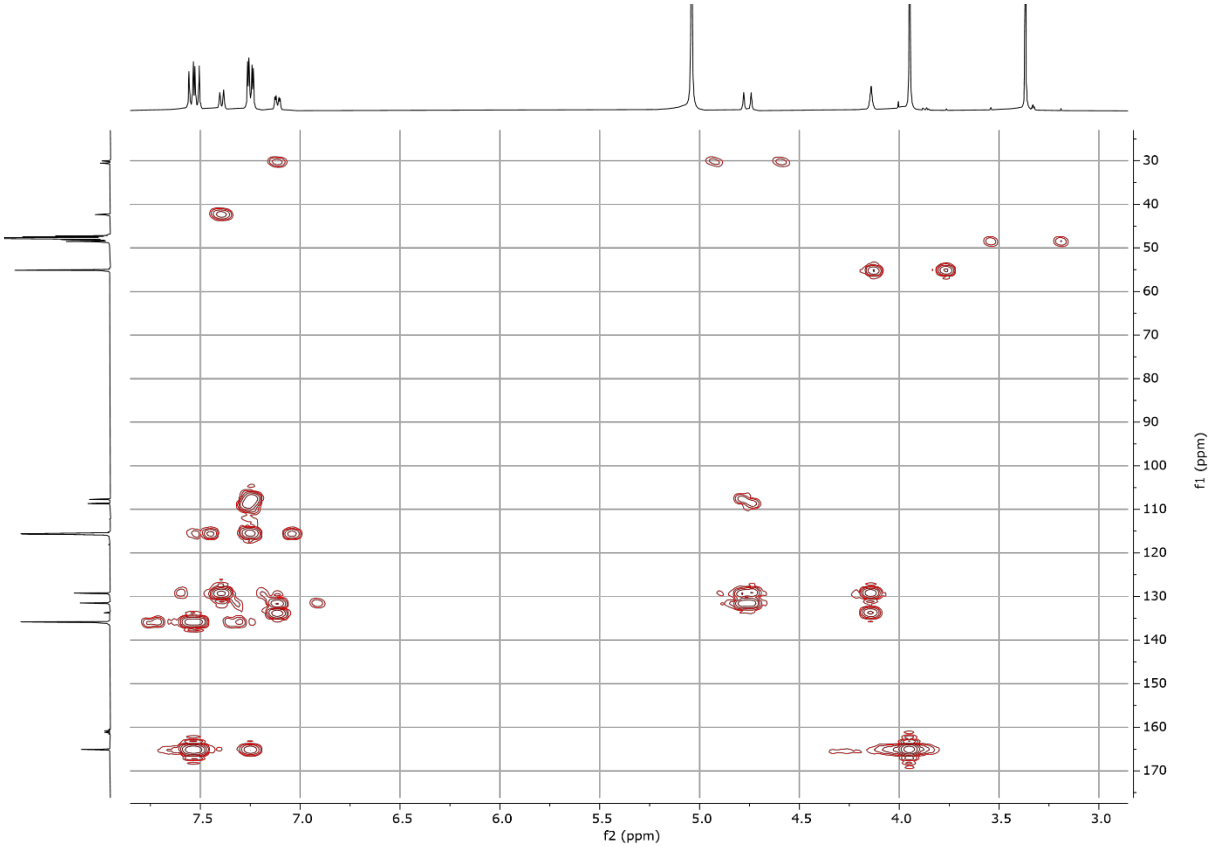

Figure 8.37 HMBC NMR spectrum of **6d** (CD_3OD, 298 K).

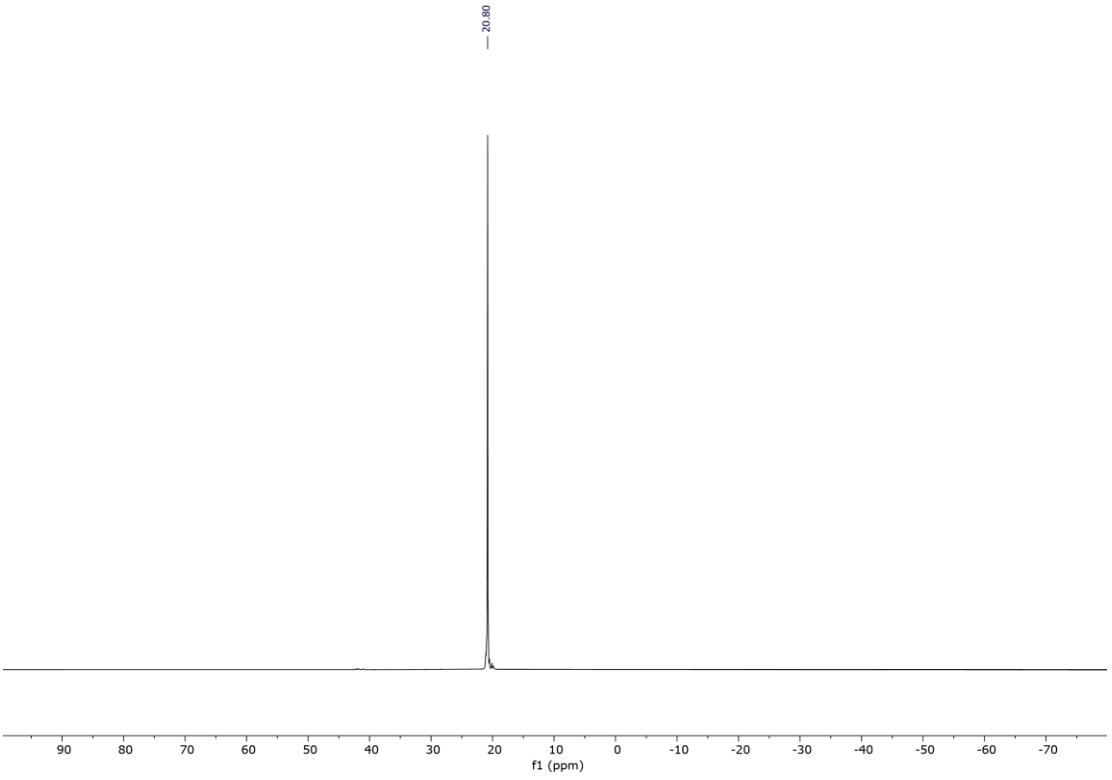

Figure 8.38 $^{31}P\{^{1}H\}$ NMR spectrum of **6d** (CD_3OD, 162 MHz, 298 K).

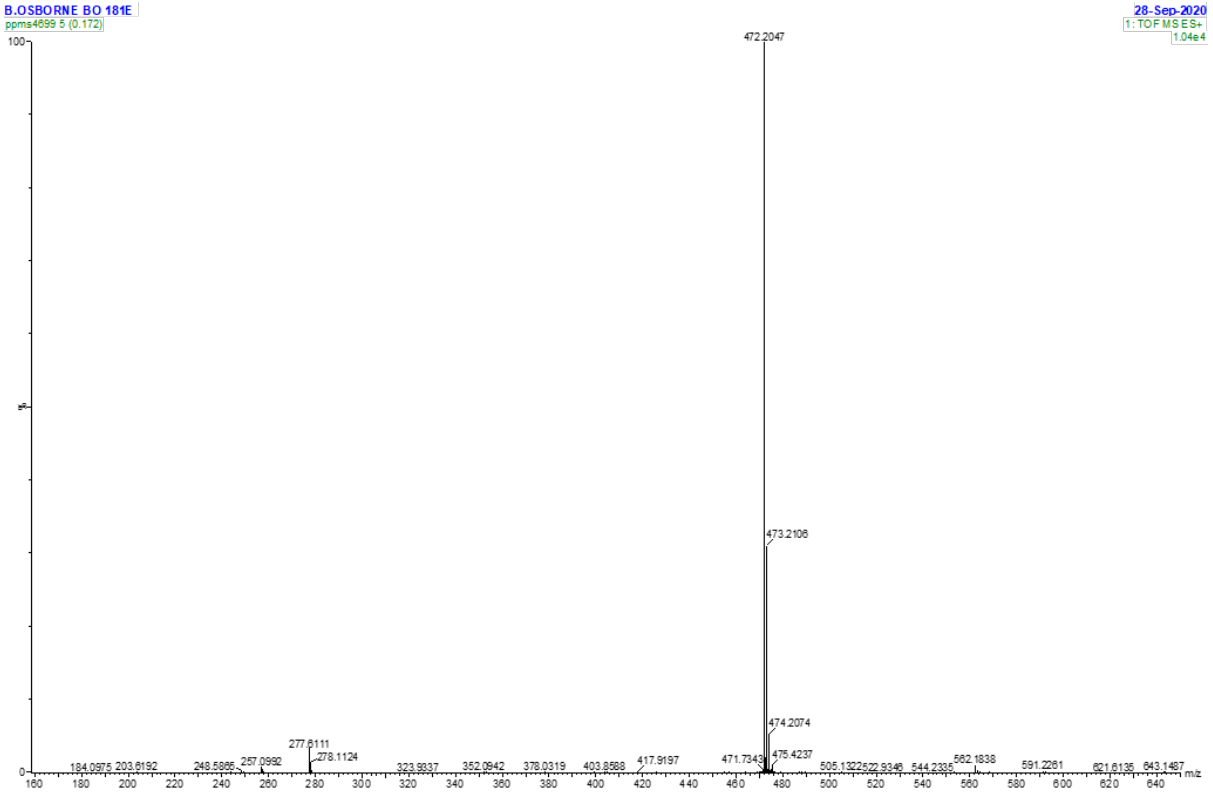

Figure 8.39 ES-TOF+ MS of **6d**.

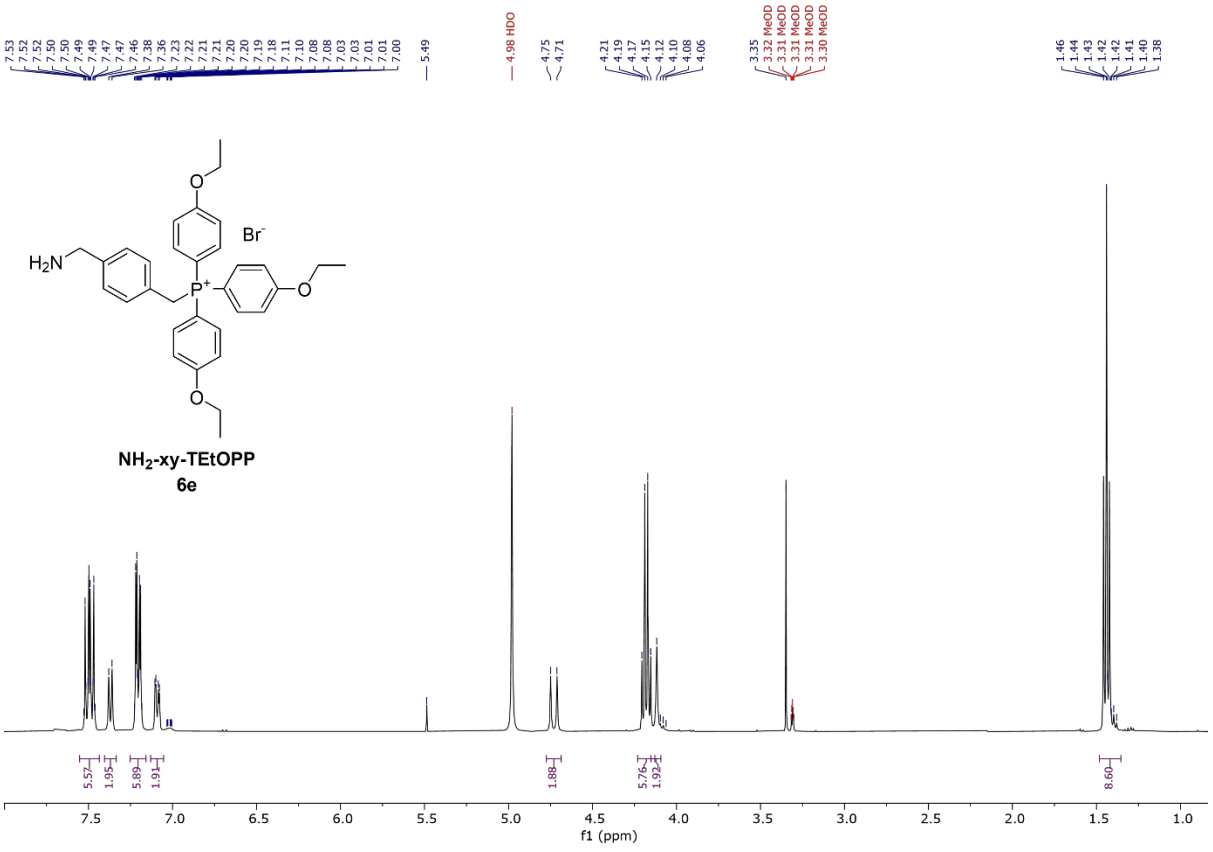

Figure 8.40 ^{1}H NMR spectrum of **6e** (CD_3OD, 400 MHz, 298 K).

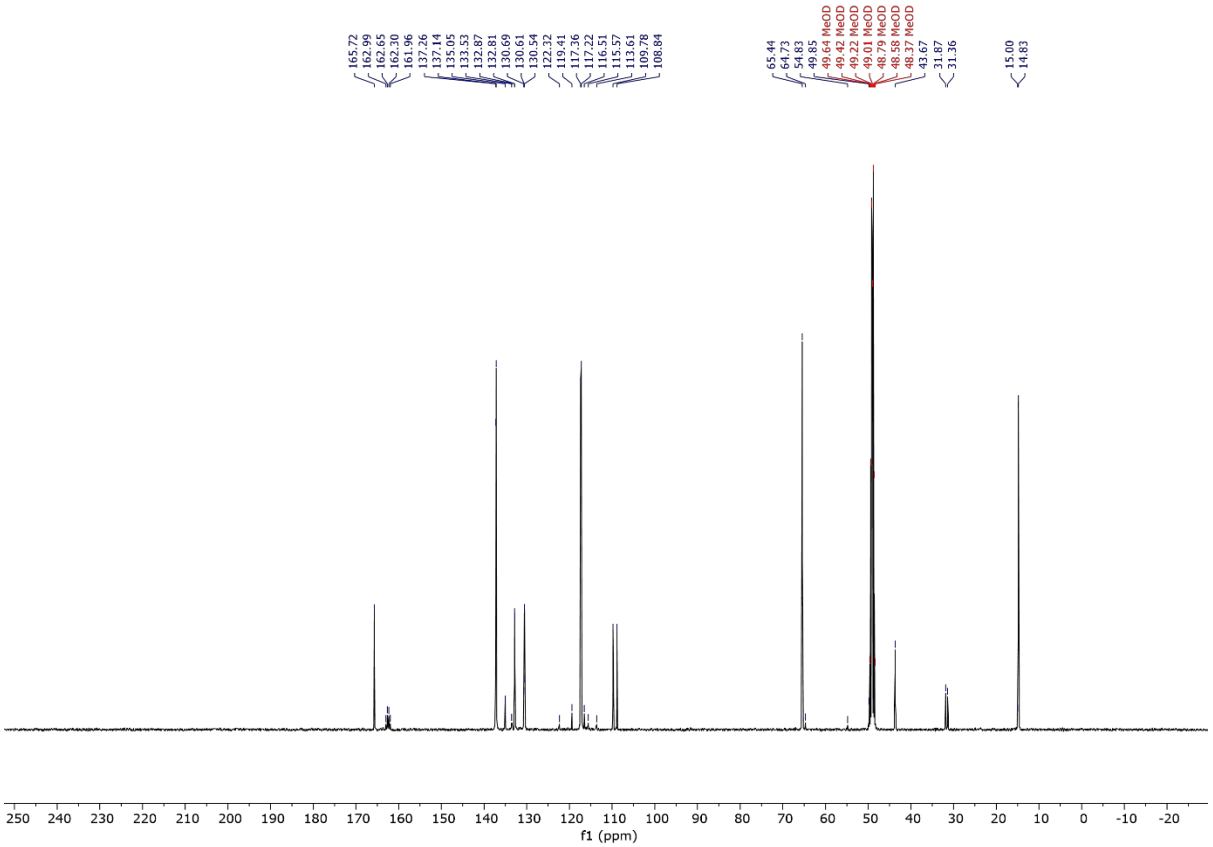

Figure 8.41 $^{13}C\{^{1}H\}$ NMR spectrum of **6e** (CD_3OD, 101 MHz, 298 K).

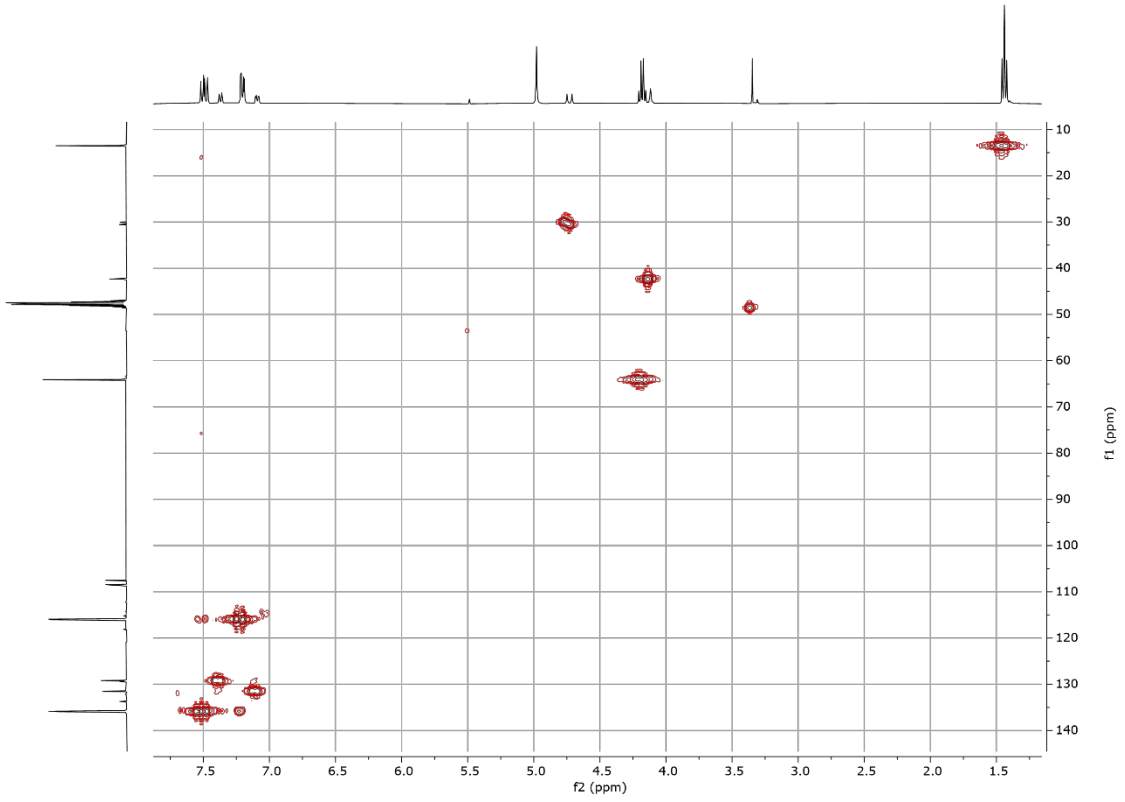

Figure 8.42 HMQC NMR spectrum of **6e** (CD_3OD, 298 K).

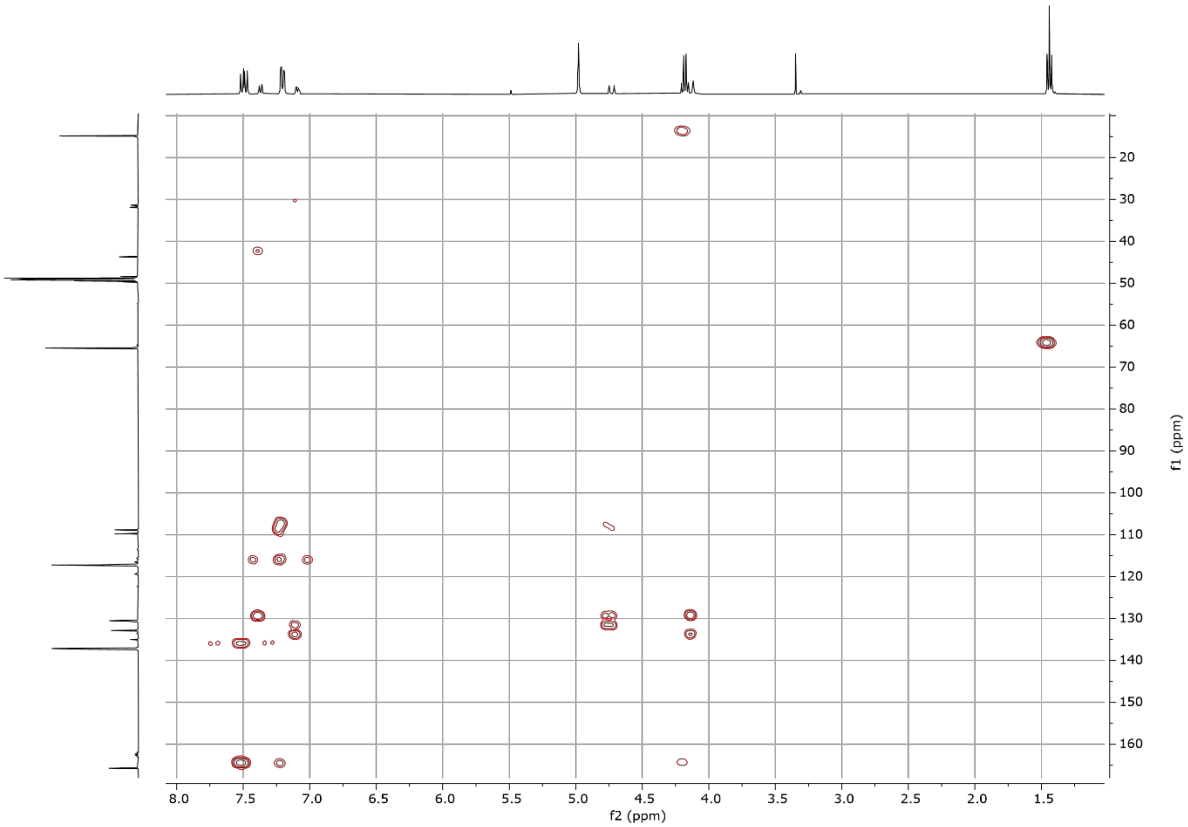

Figure 8.43 HMBC NMR spectrum of **6e** (CD_3OD, 298 K).

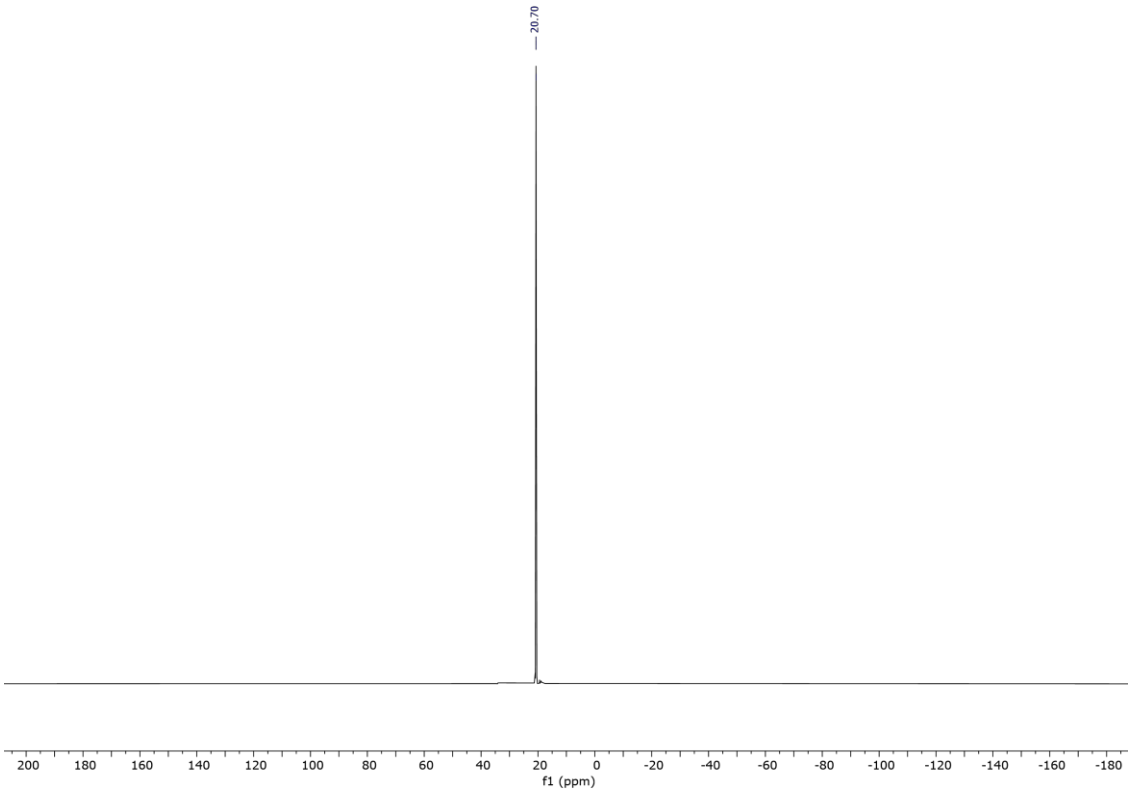

Figure 8.44 $^{31}P\{^{1}H\}$ NMR spectrum of **6e** (CD_3OD, 162 MHz, 298 K).

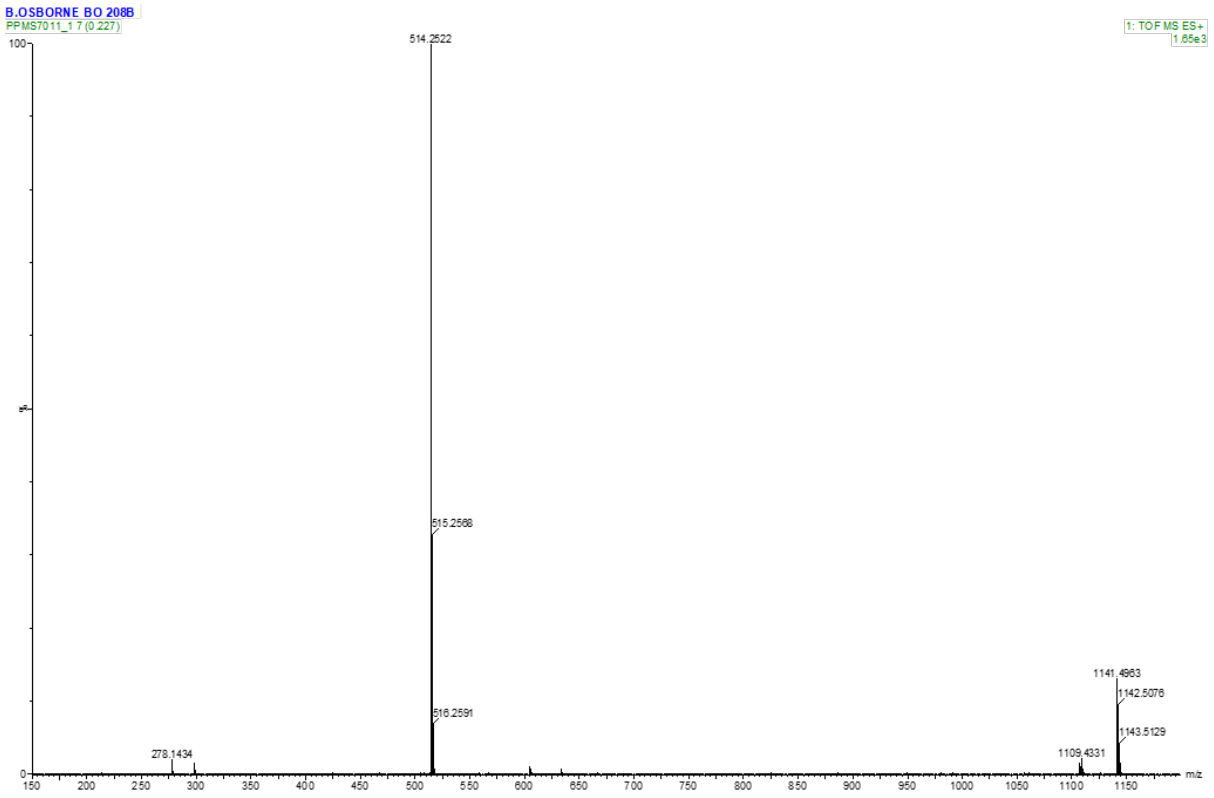

Figure 8.45 ES-TOF+ MS of **6e**.

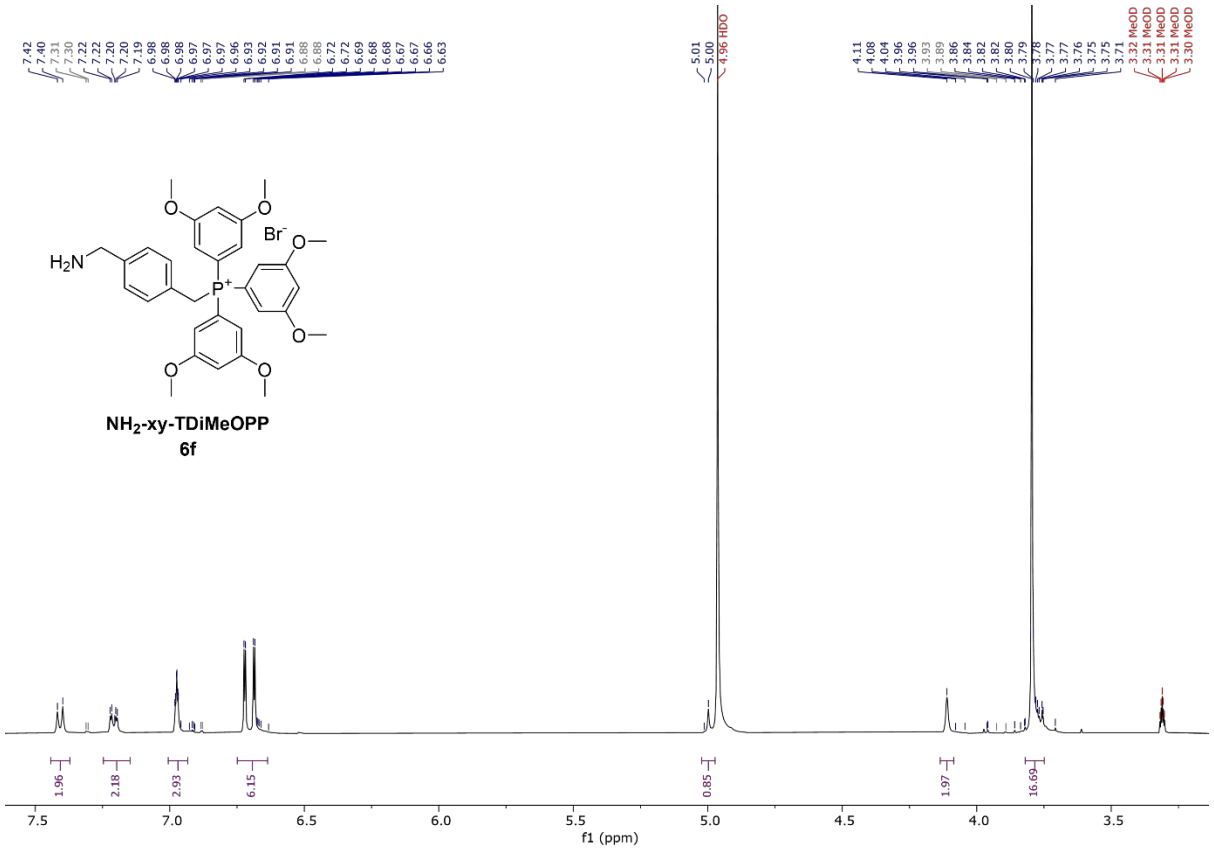

Figure 8.46 ^{1}H NMR spectrum of **6f** (CD_3OD, 400 MHz, 298 K).

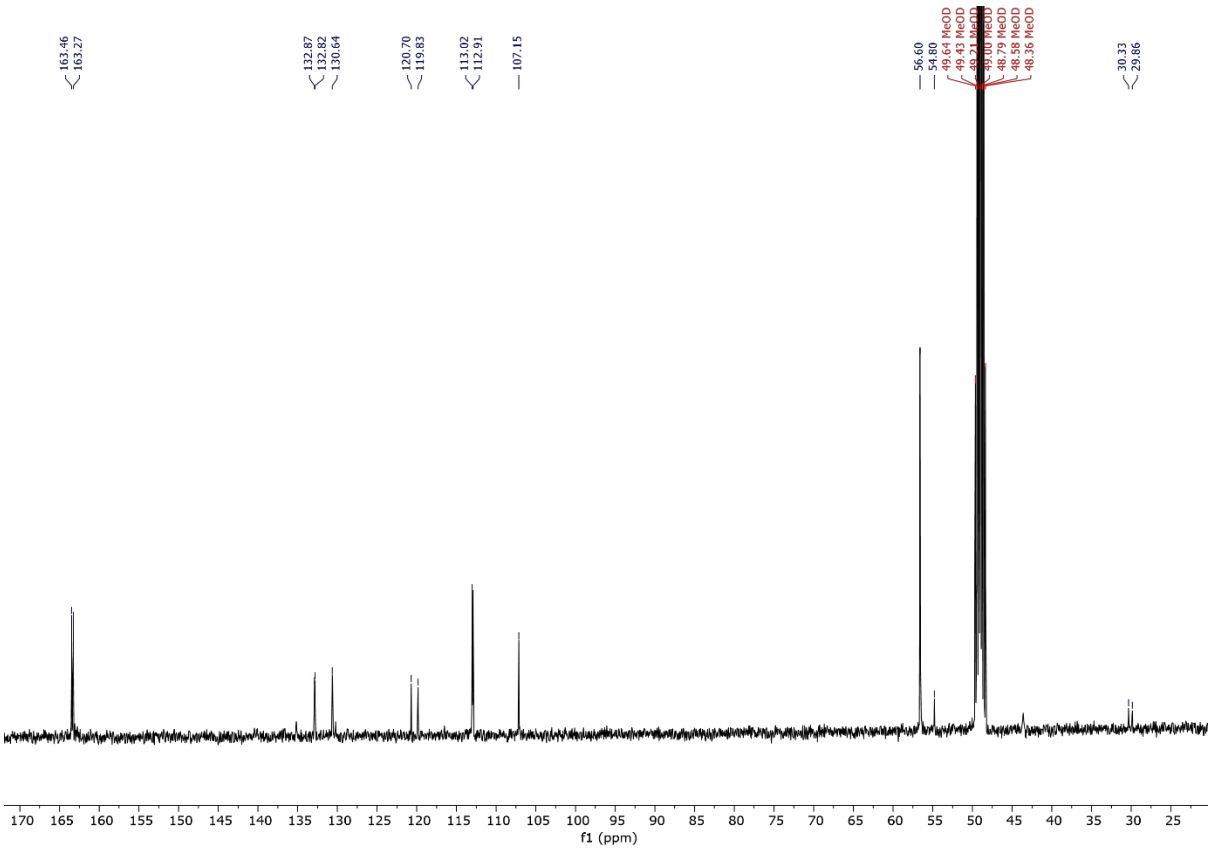

Figure 8.47 $^{13}C\{^{1}H\}$ NMR spectrum of **6f** (CD_3OD, 101 MHz, 298 K).

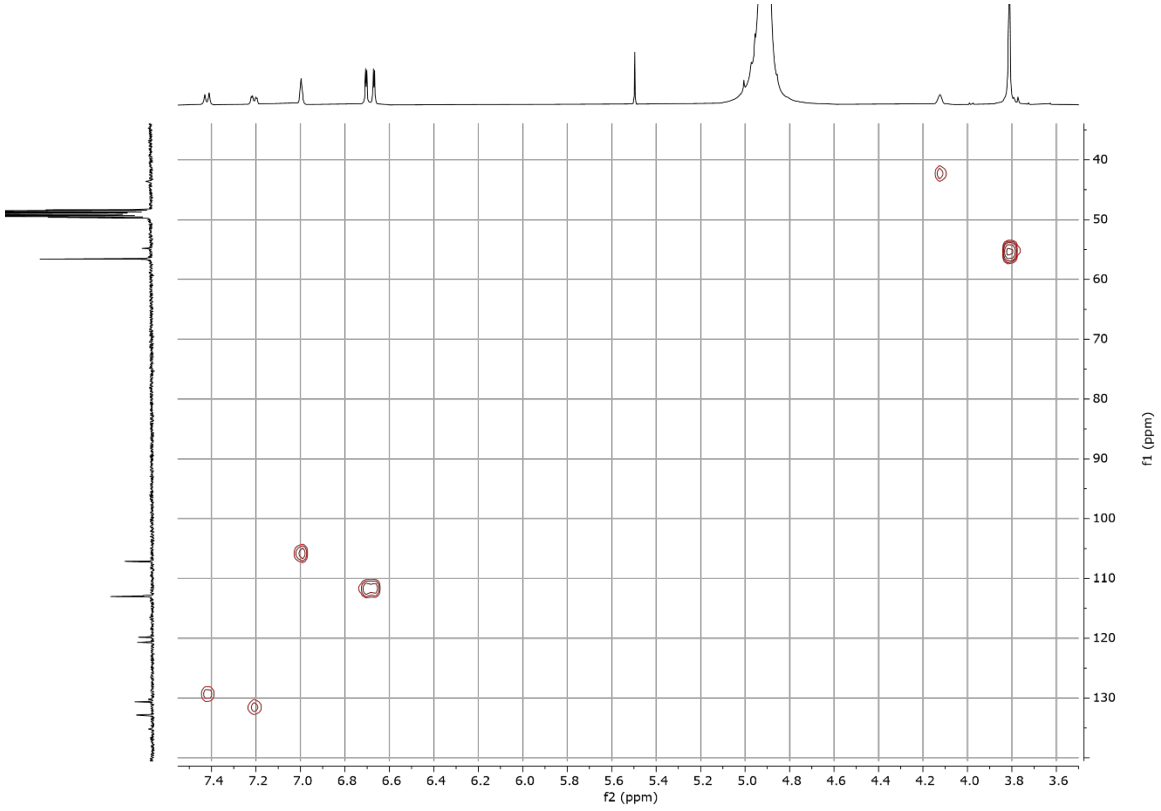

Figure 8.48 HMQC NMR spectrum of **6f** (CD_3OD, 298 K).

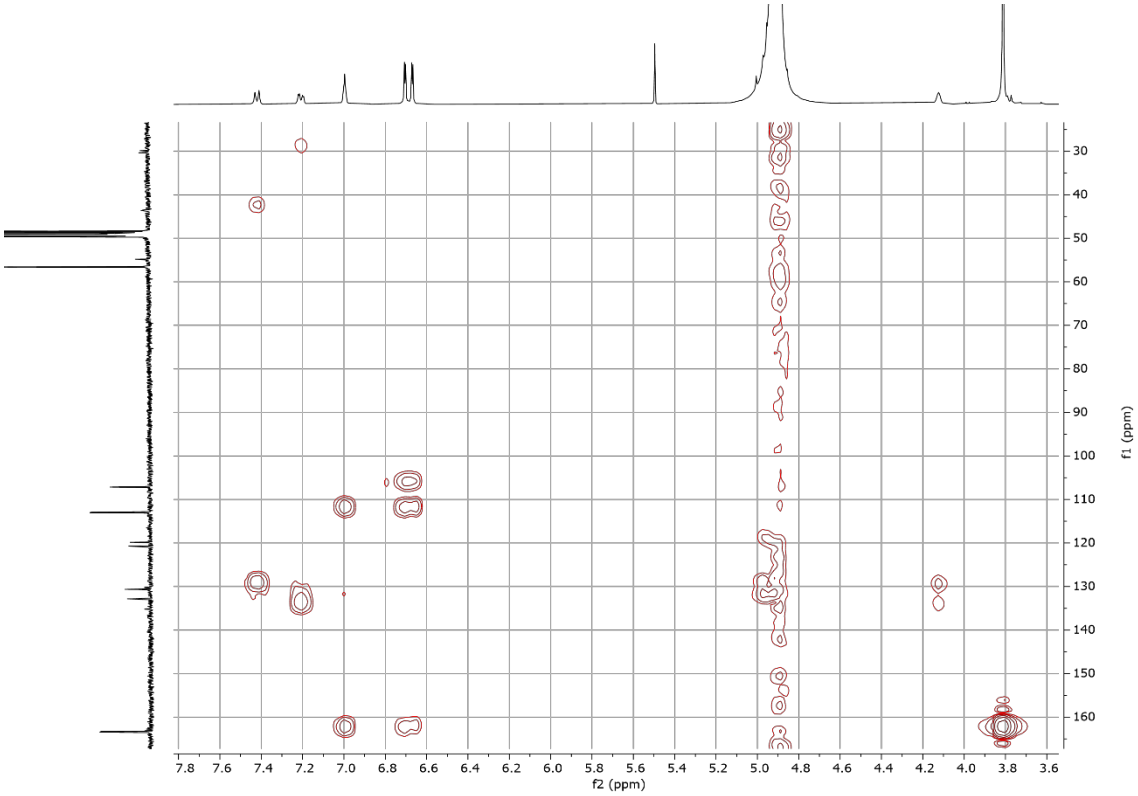

Figure 8.49 HMBC NMR spectrum of **6f** (CD_3OD, 298 K).

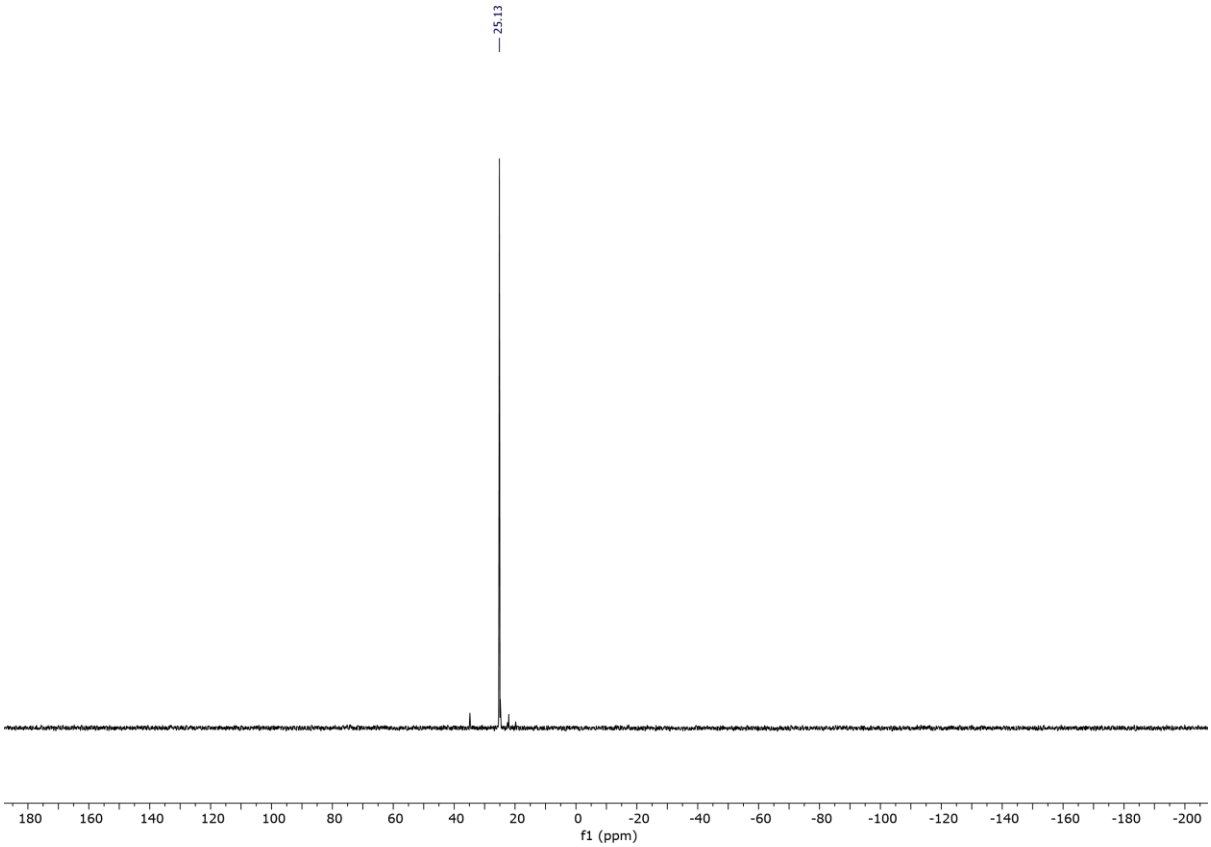

Figure 8.50 $^{31}P\{^1H\}$ NMR spectrum of **6f** (CD_3OD, 162 MHz, 298 K).

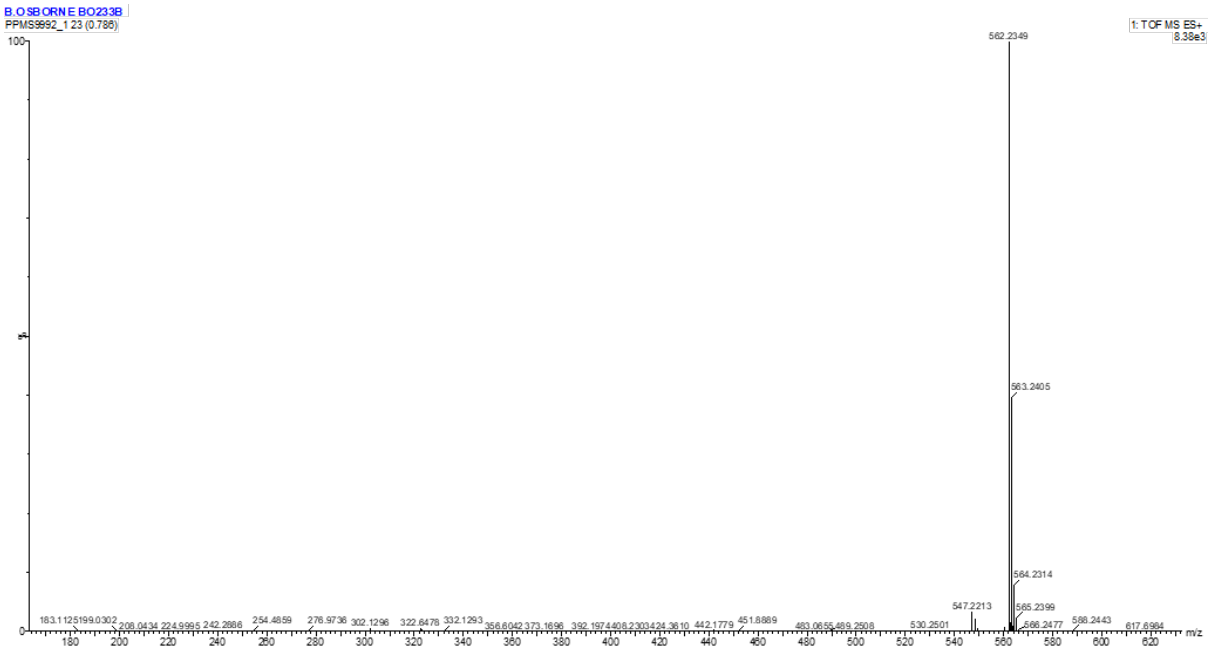

Figure 8.51 ES-TOF+ MS of **6f**.

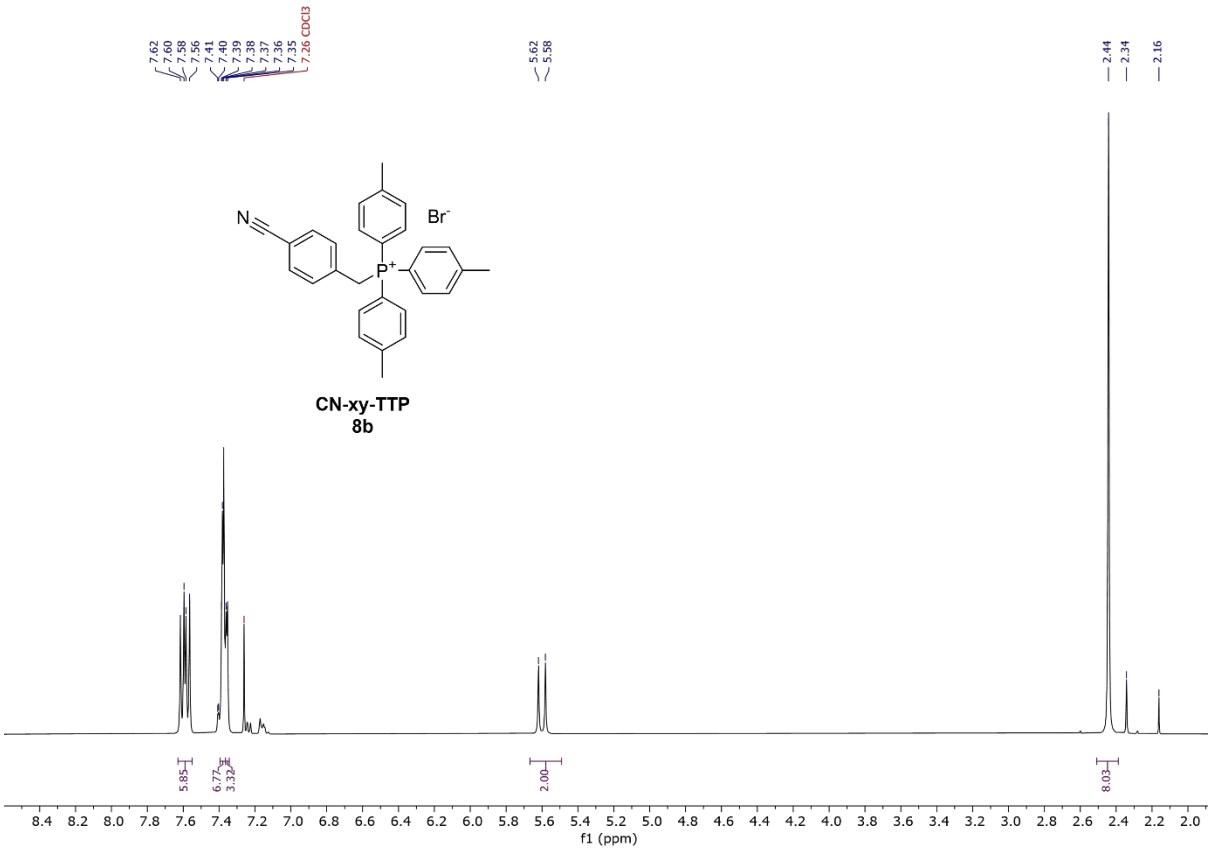

Figure 8.52 ^{1}H NMR spectrum of **8b** ($CDCl_3$, 400 MHz, 298 K).

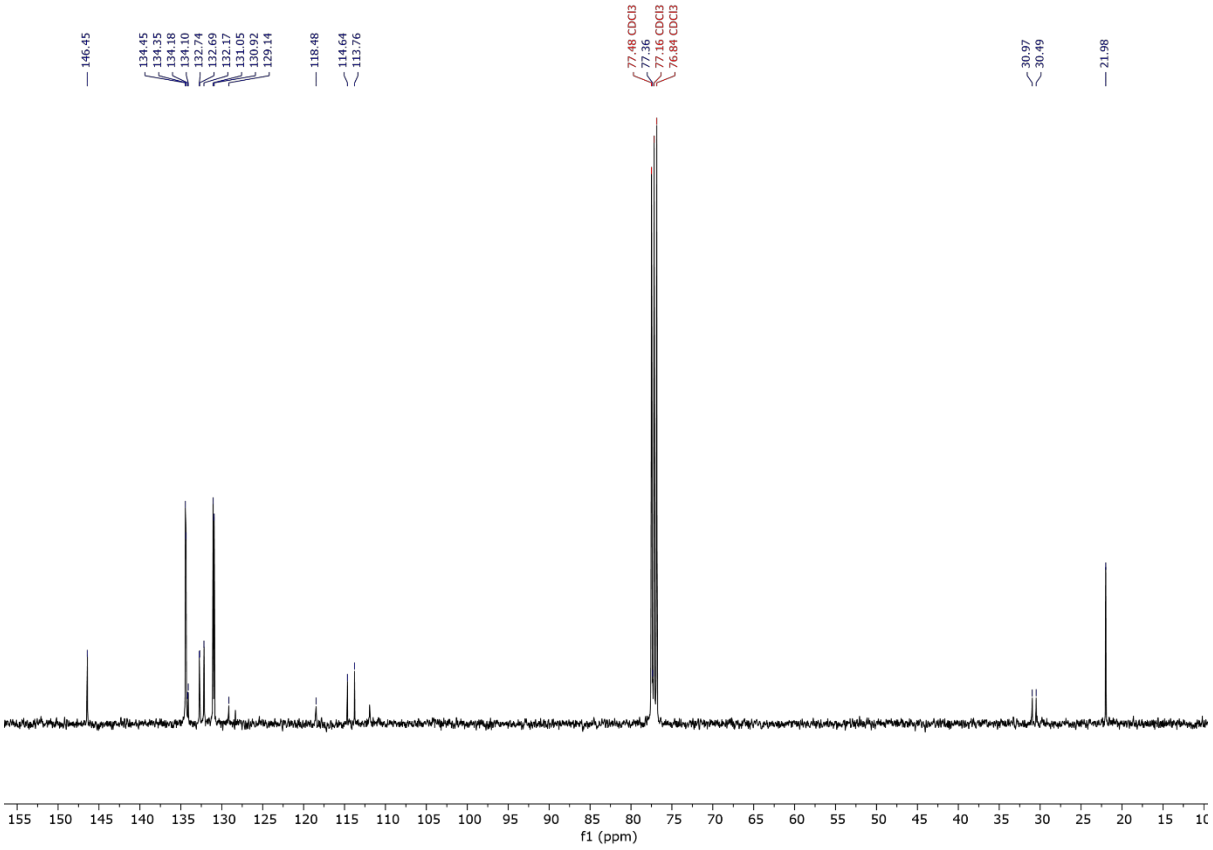

Figure 8.53 $^{13}C\{^{1}H\}$ NMR spectrum of **8b** ($CDCl_3$, 101 MHz, 298 K).

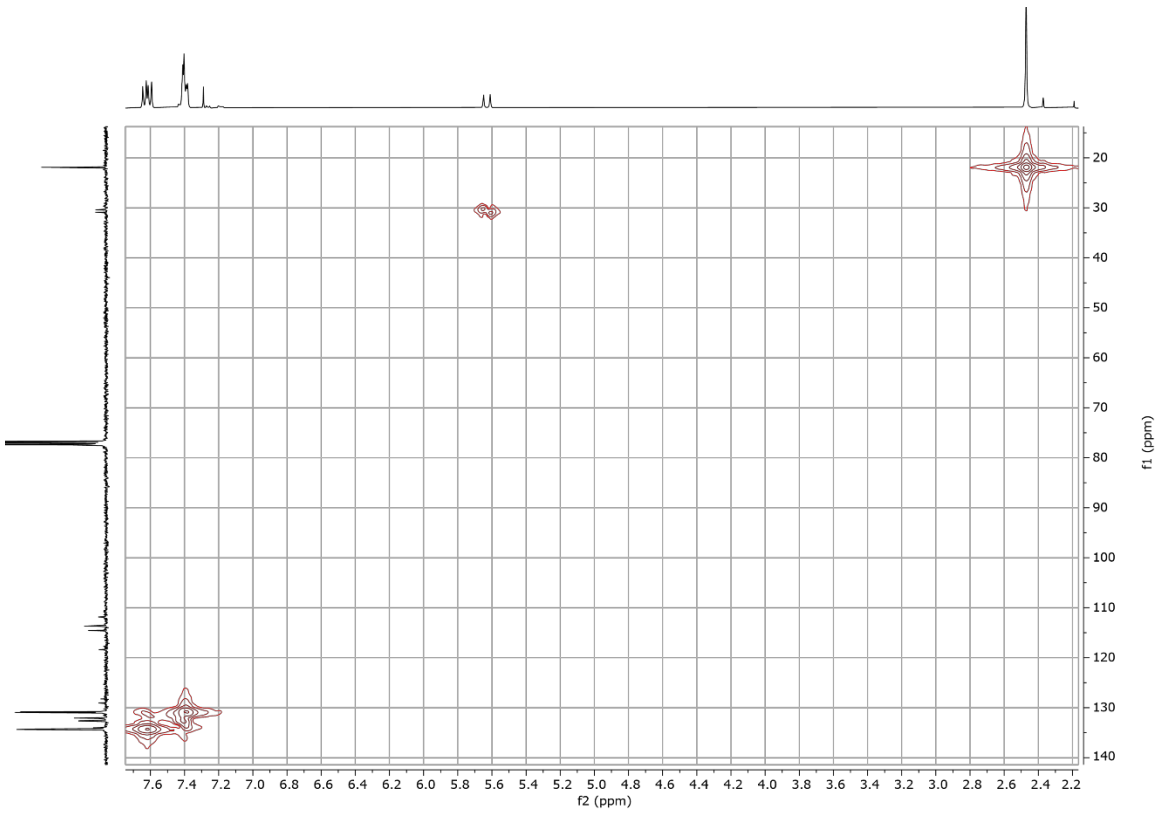

Figure 8.54 HMQC NMR spectrum of **8b** ($CDCl_3$, 298 K).

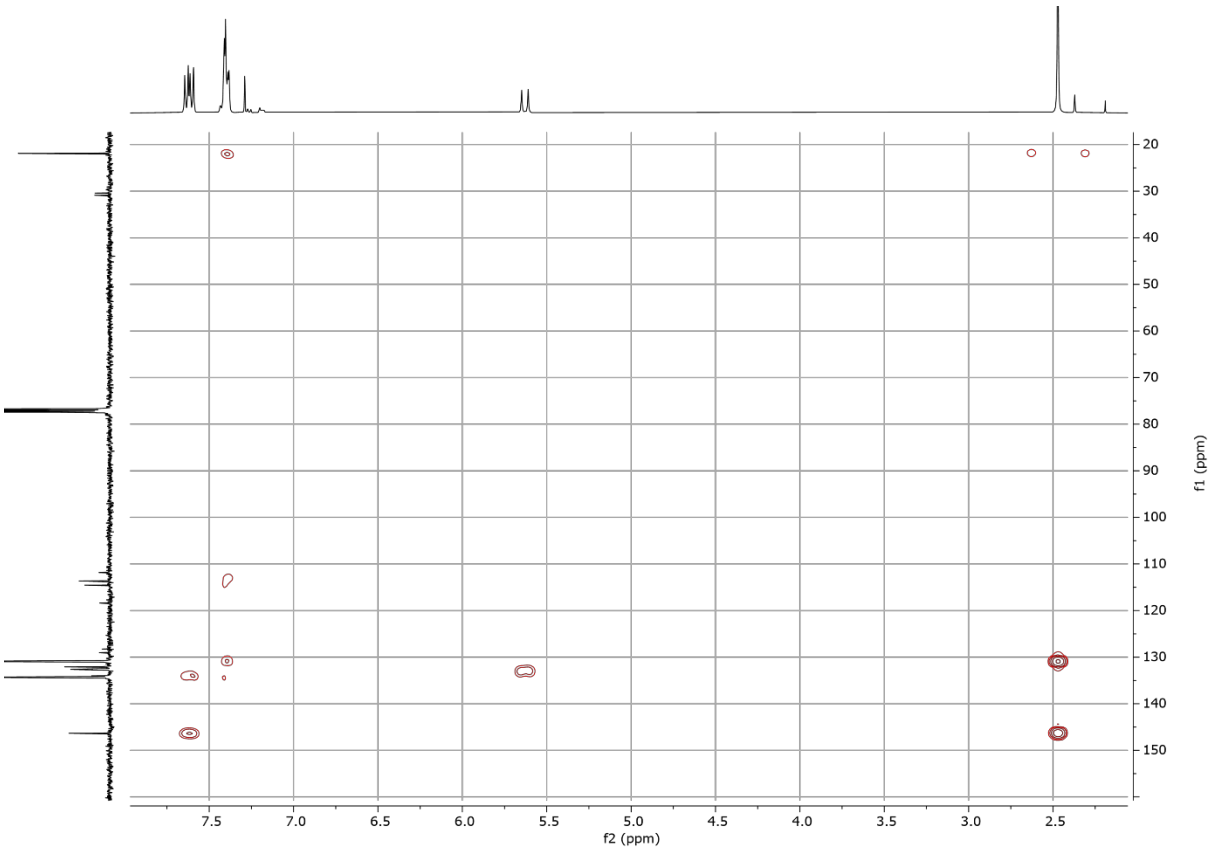

Figure 8.55 HMBC NMR spectrum of **8b** ($CDCl_3$, 298 K).

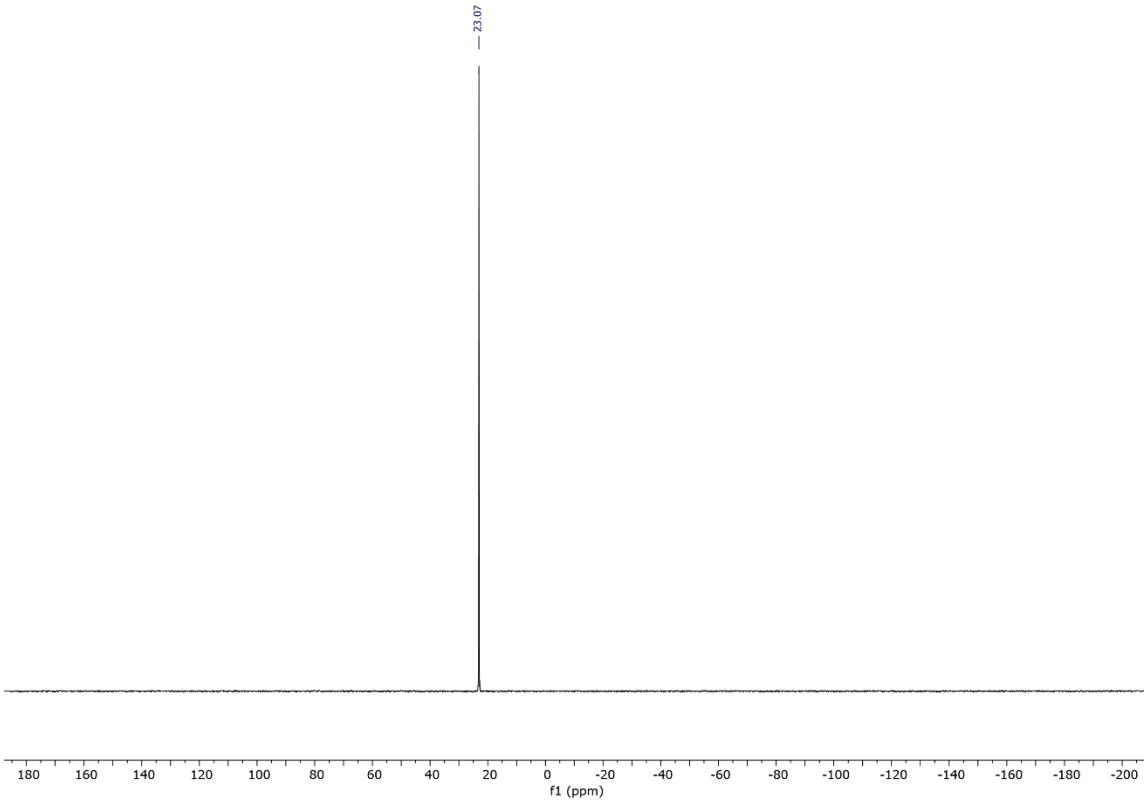

Figure 8.56 $^{31}P\{^{1}H\}$ NMR spectrum of **8b** ($CDCl_3$, 162 MHz, 298 K).

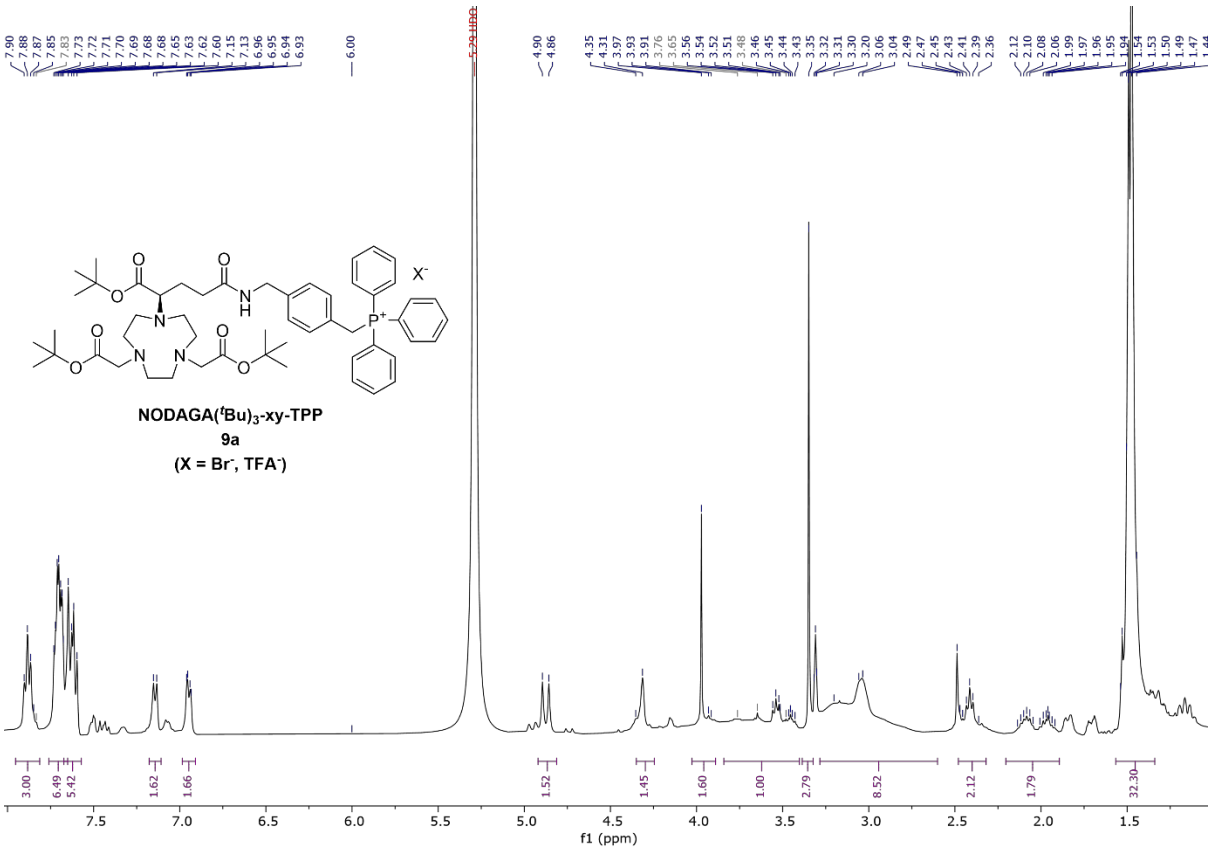

Figure 8.57 ^{1}H NMR spectrum of **9a** (CD_3OD, 400 MHz, 298 K).

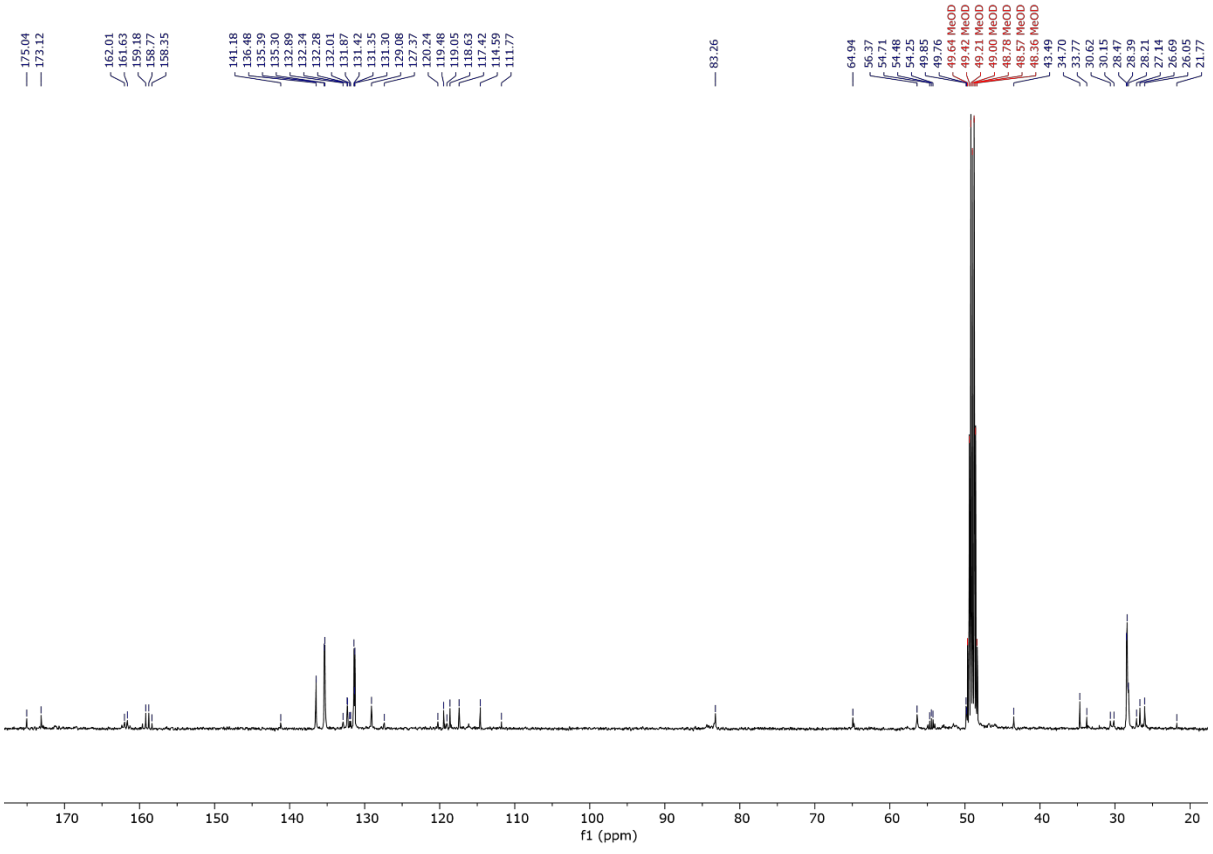

Figure 8.58 $^{13}C\{^{1}H\}$ NMR spectrum of **9a** (CD_3OD, 101 MHz, 298 K).

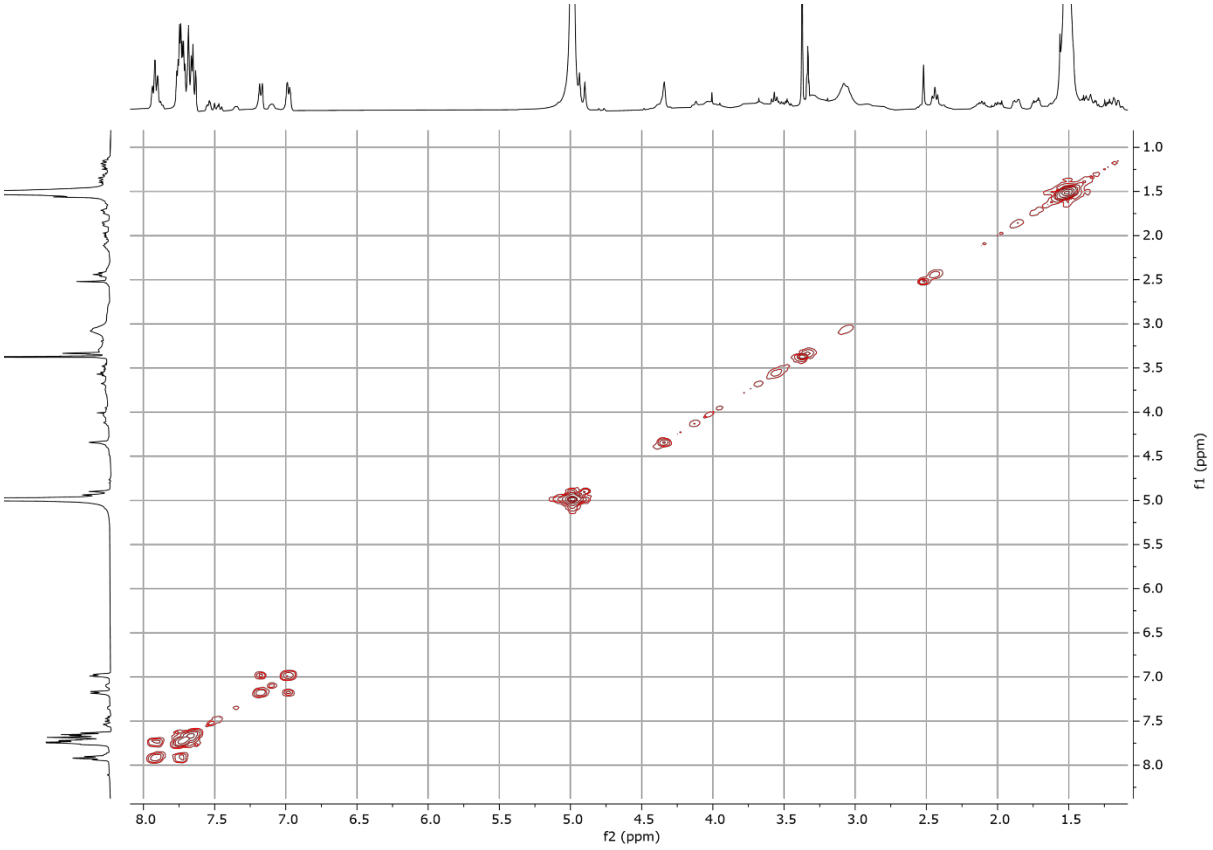

Figure 8.59 COSY NMR spectrum of **9a** (CD_3OD, 400 MHz, 298 K).

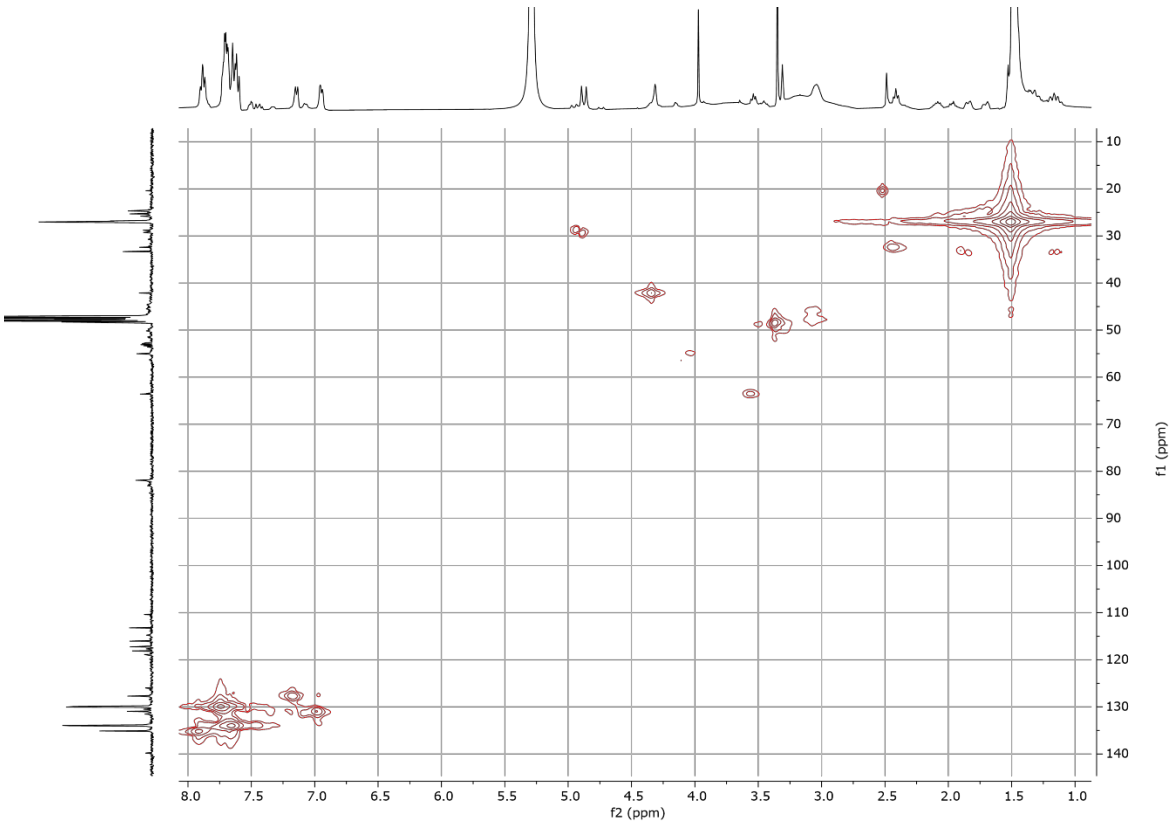

Figure 8.60 HMQC NMR spectrum of **9a** (CD_3OD, 298 K).

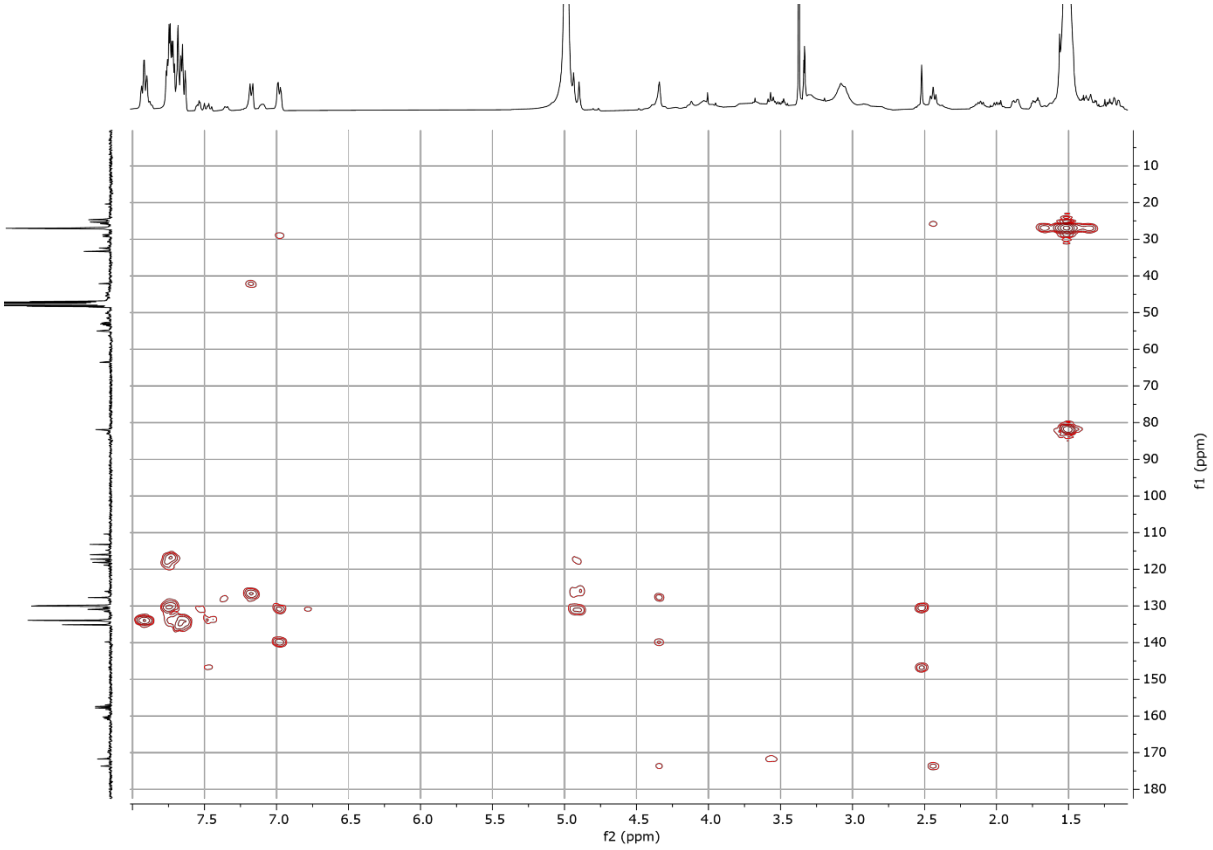

Figure 8.61 HMBC NMR spectrum of **9a** (CD_3OD, 298 K).

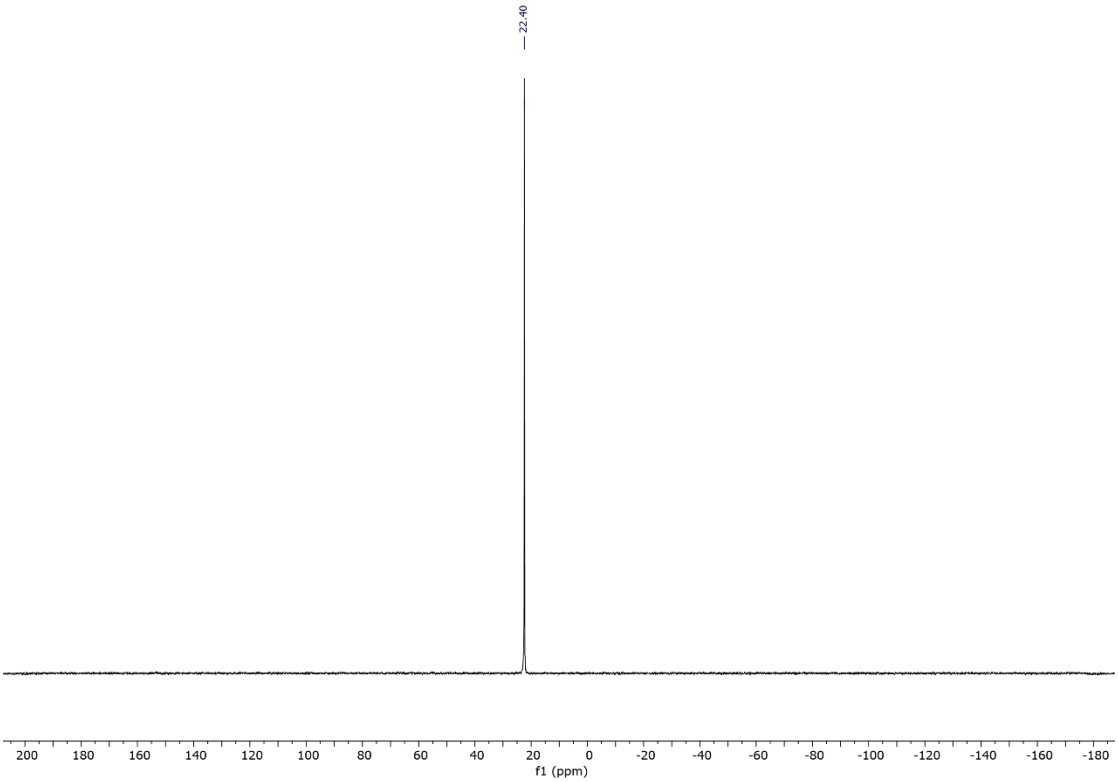

Figure 8.62 $^{31}P\{^{1}H\}$ NMR spectrum of **9a** (CD_3OD, 162 MHz, 298 K).

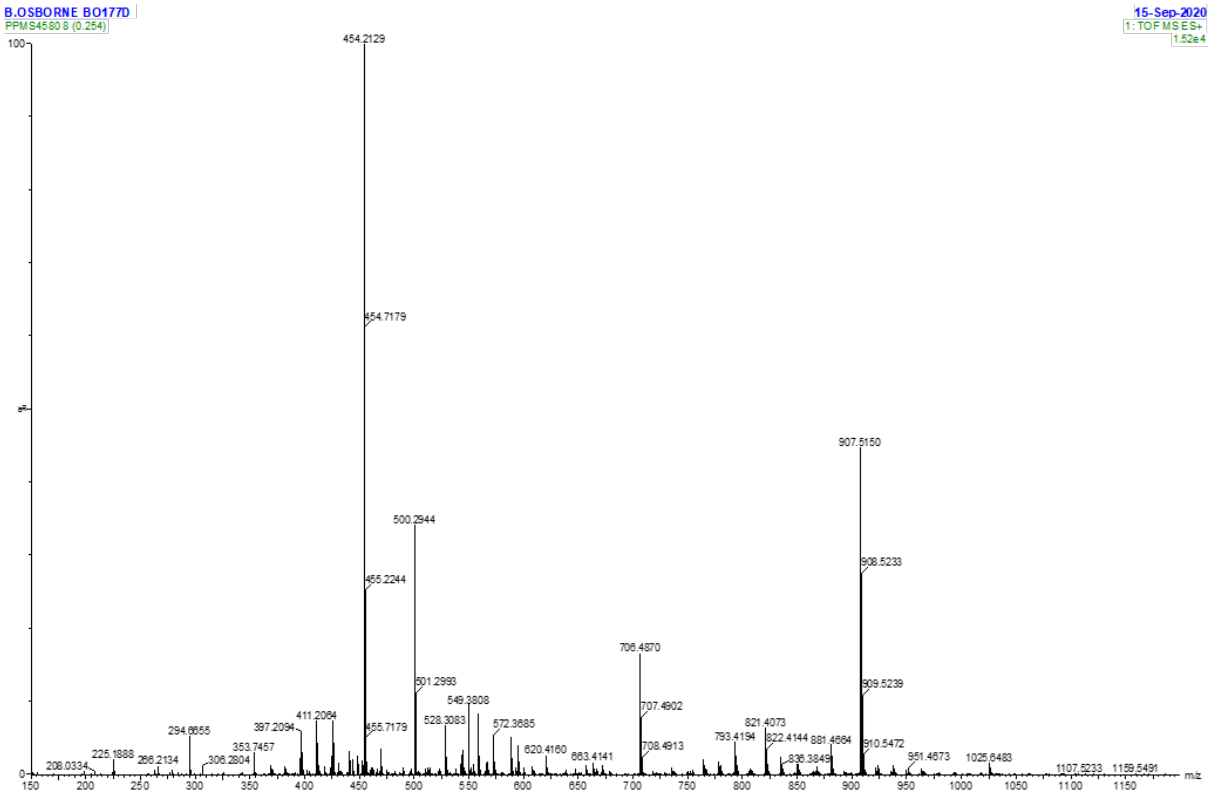

Figure 8.63 ES-TOF+ MS of **9a**.

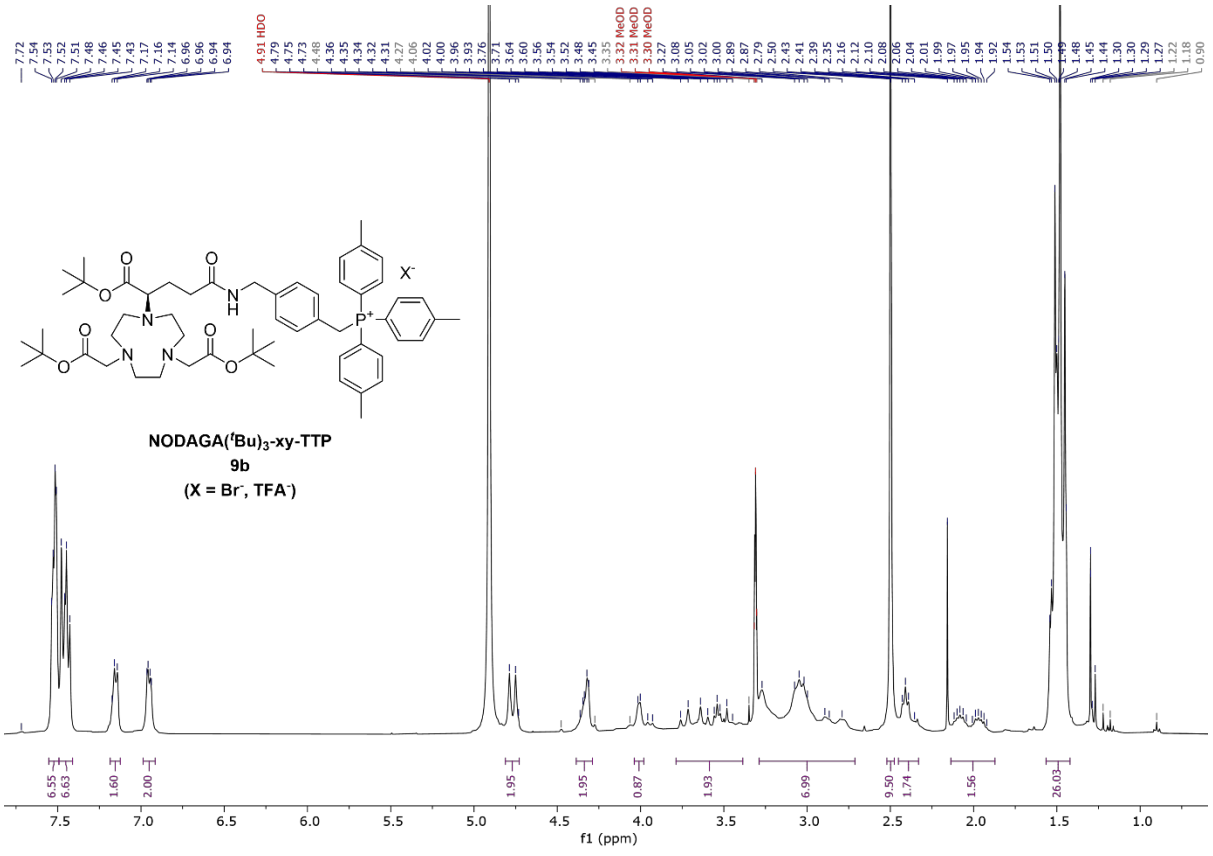

Figure 8.64 ^{1}H NMR spectrum of **9b** (CD_3OD, 400 MHz, 298 K).

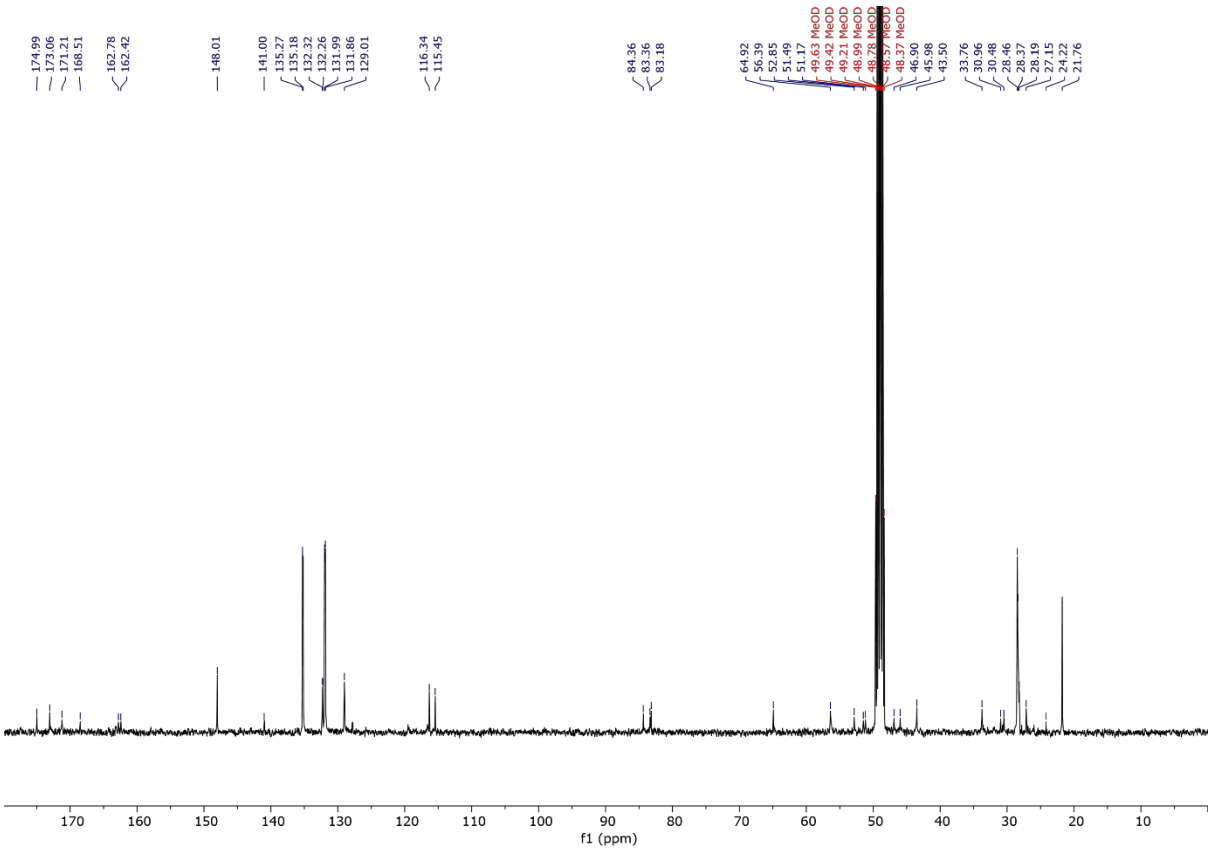

Figure 8.65 $^{13}C\{^{1}H\}$ NMR spectrum of **9b** (CD_3OD, 101 MHz, 298 K).

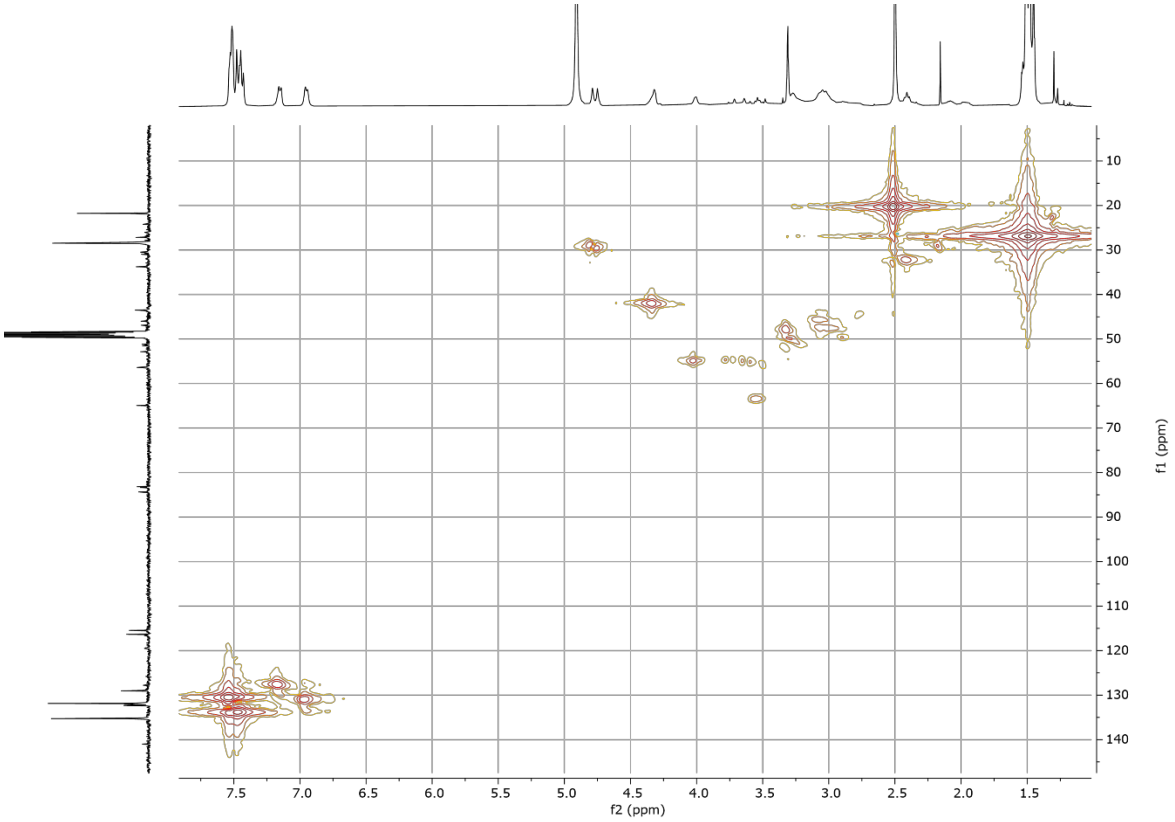

Figure 8.66 HMQC NMR spectrum of **9b** (CD_3OD, 298 K).

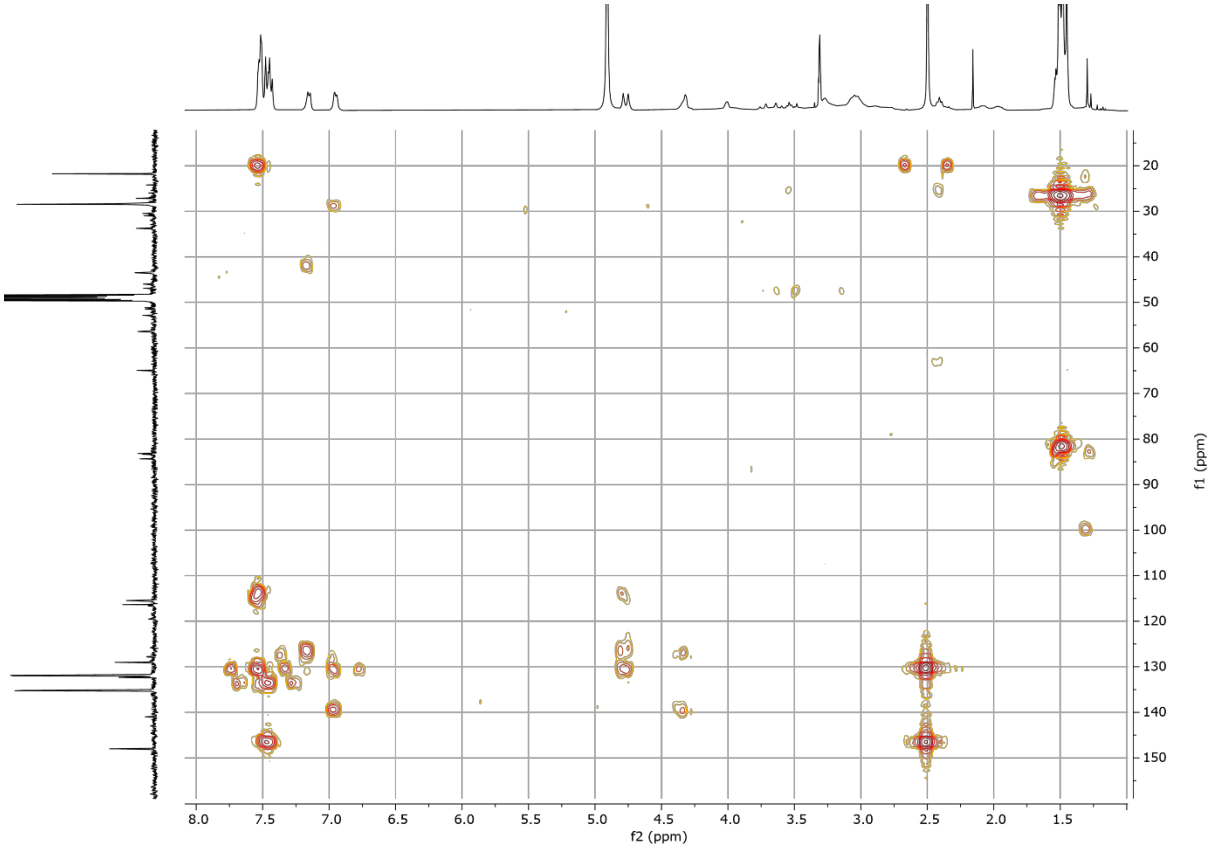

Figure 8.67 HMBC NMR spectrum of **9b** (CD_3OD, 298 K).

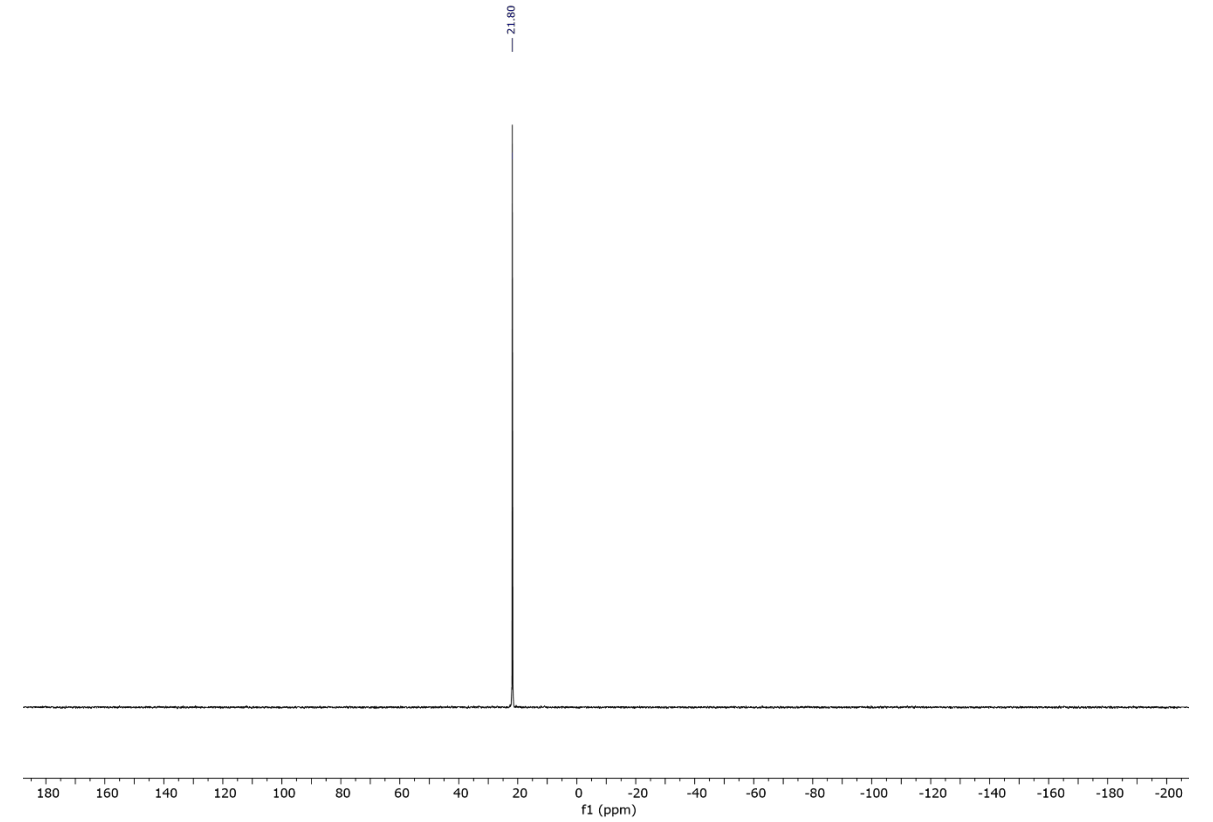

Figure 8.68 $^{31}P\{^{1}H\}$ NMR spectrum of **9b** (CD_3OD, 162 MHz, 298 K).

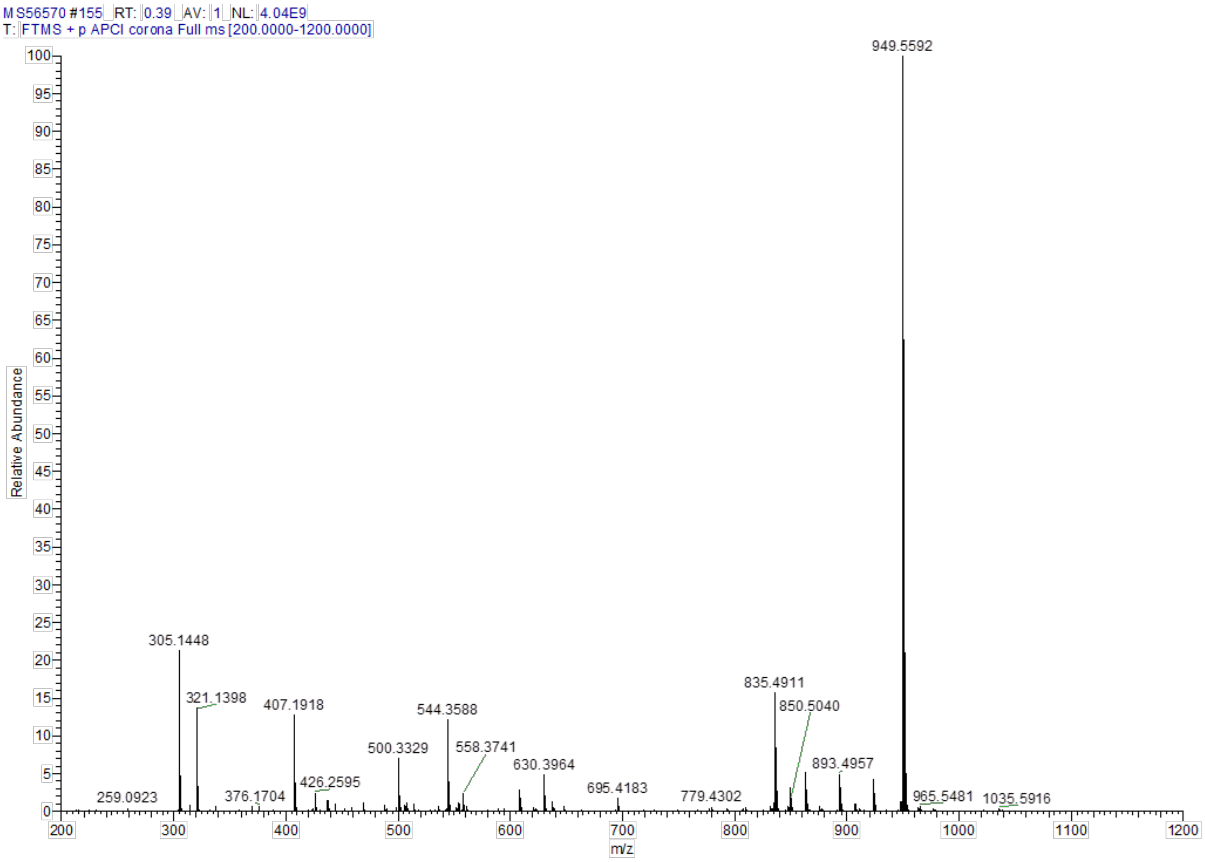

Figure 8.69 ES-TOF+ MS of **9b**.

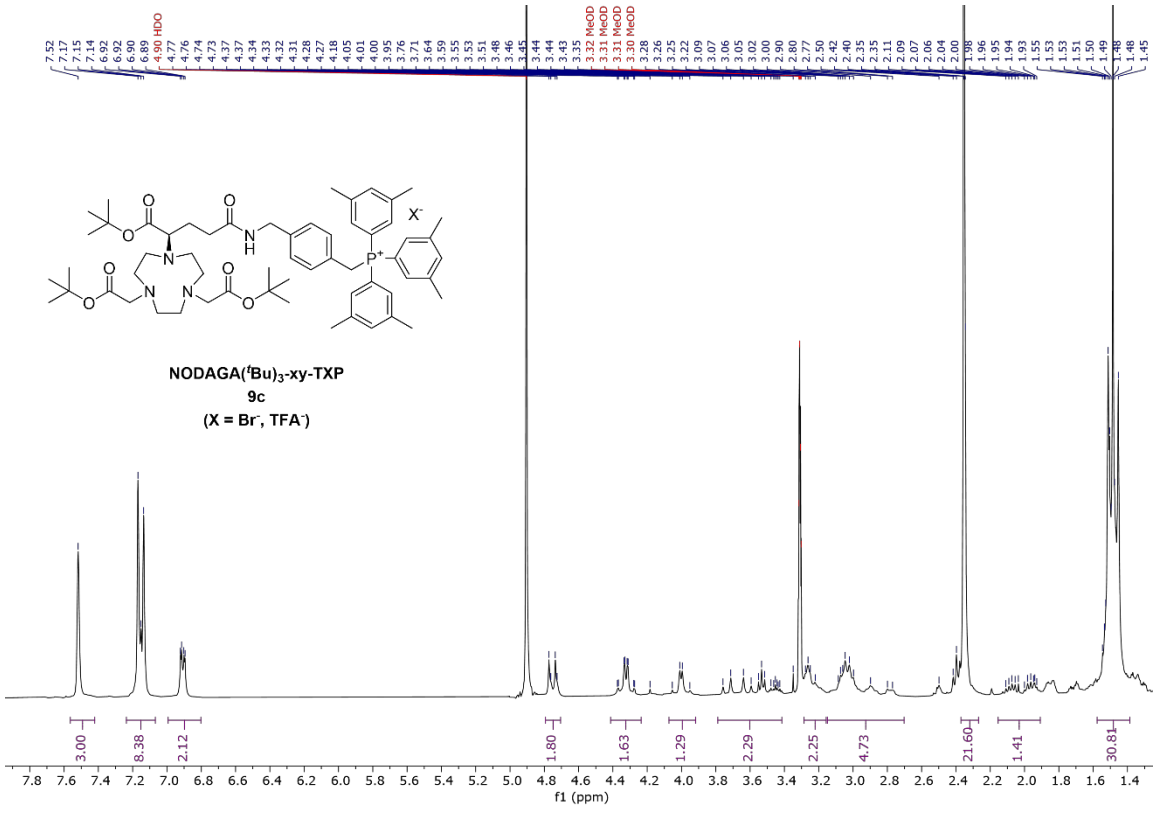

Figure 8.70 ^{1}H NMR spectrum of **9c** (CD_3OD, 400 MHz, 298 K).

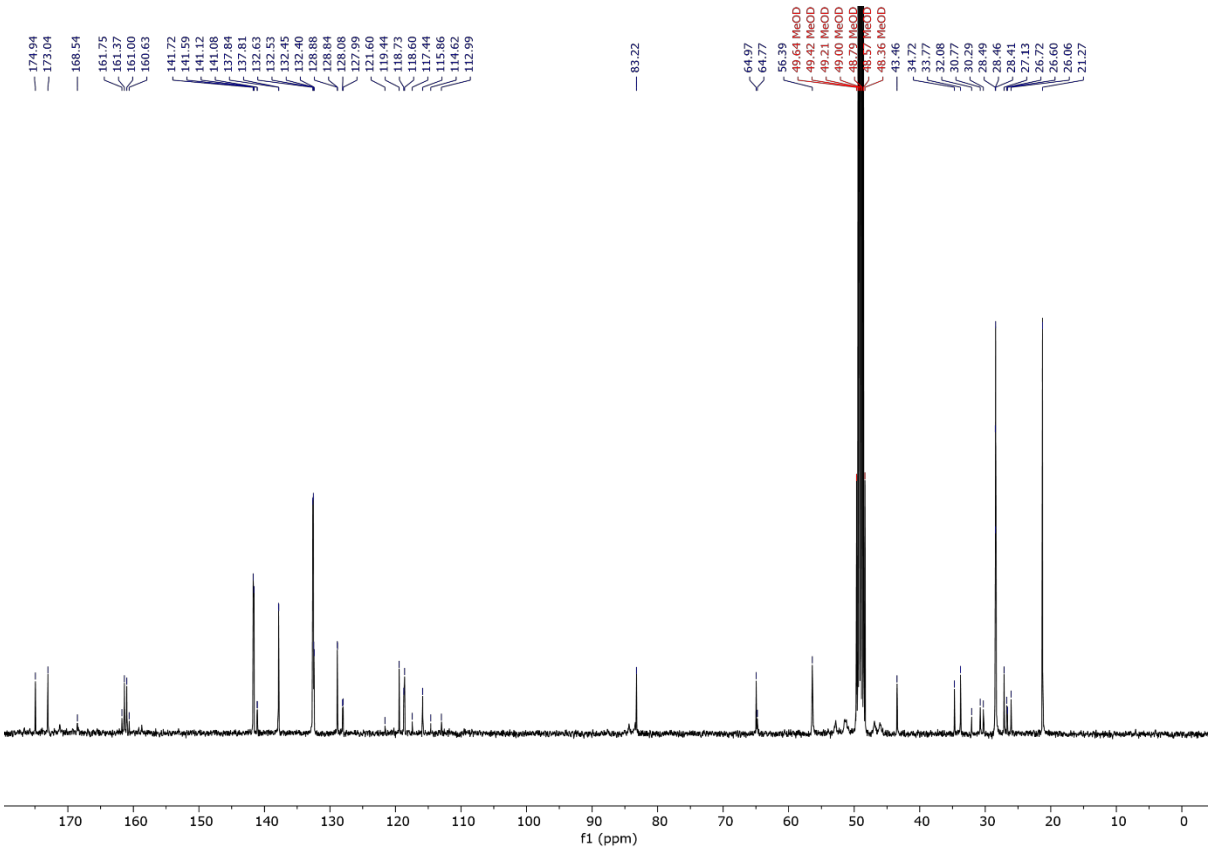

Figure 8.71 $^{13}C\{^{1}H\}$ NMR spectrum of **9c** (CD_3OD, 101 MHz, 298 K).

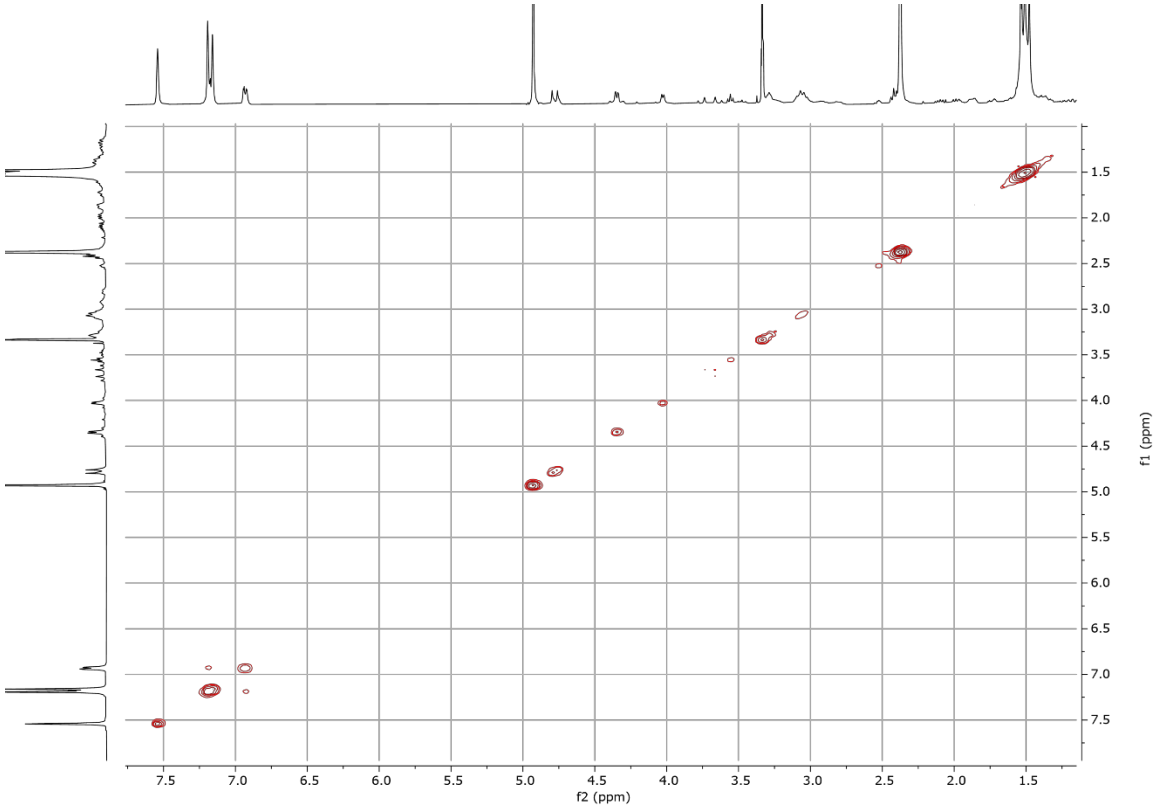

Figure 8.72 COSY NMR spectrum of **9c** (CD_3OD, 400 MHz, 298 K).

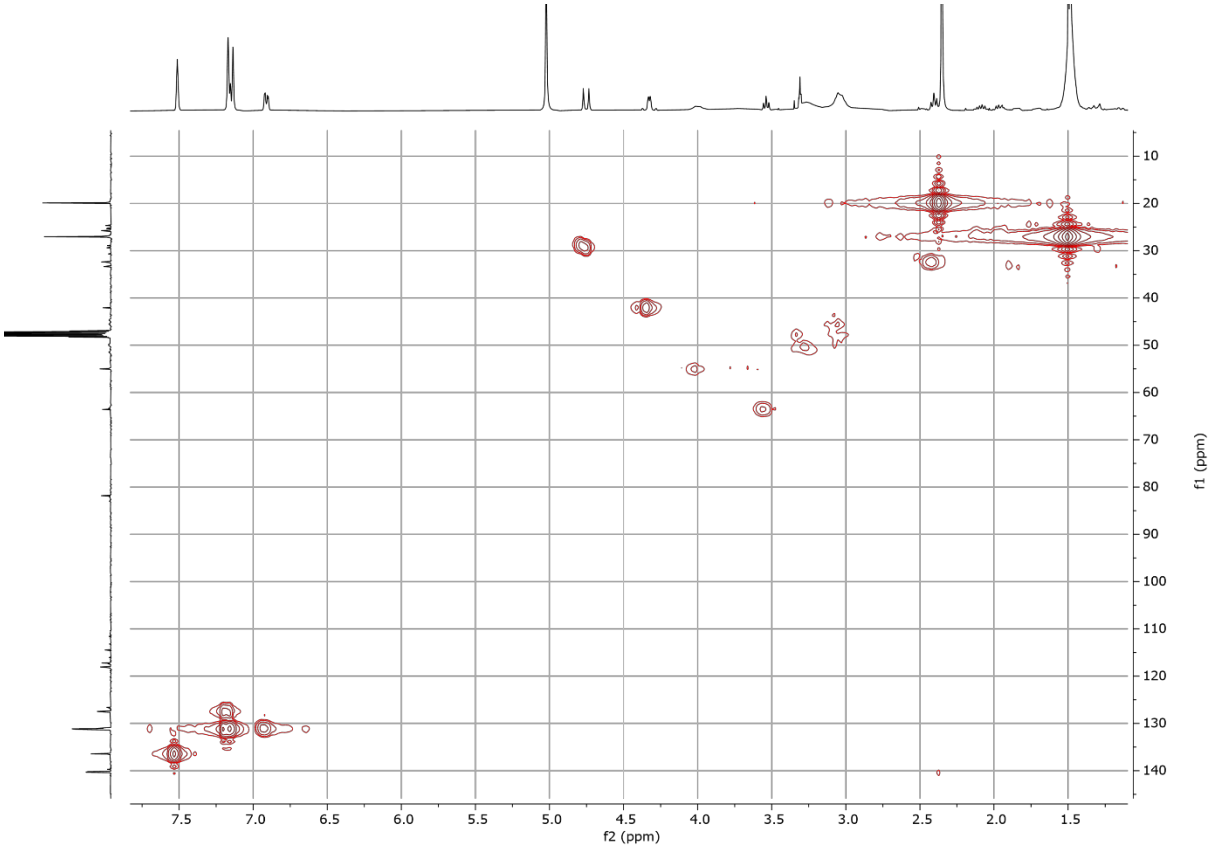

Figure 8.73 HMQC NMR spectrum of **9c** (CD_3OD, 298 K).

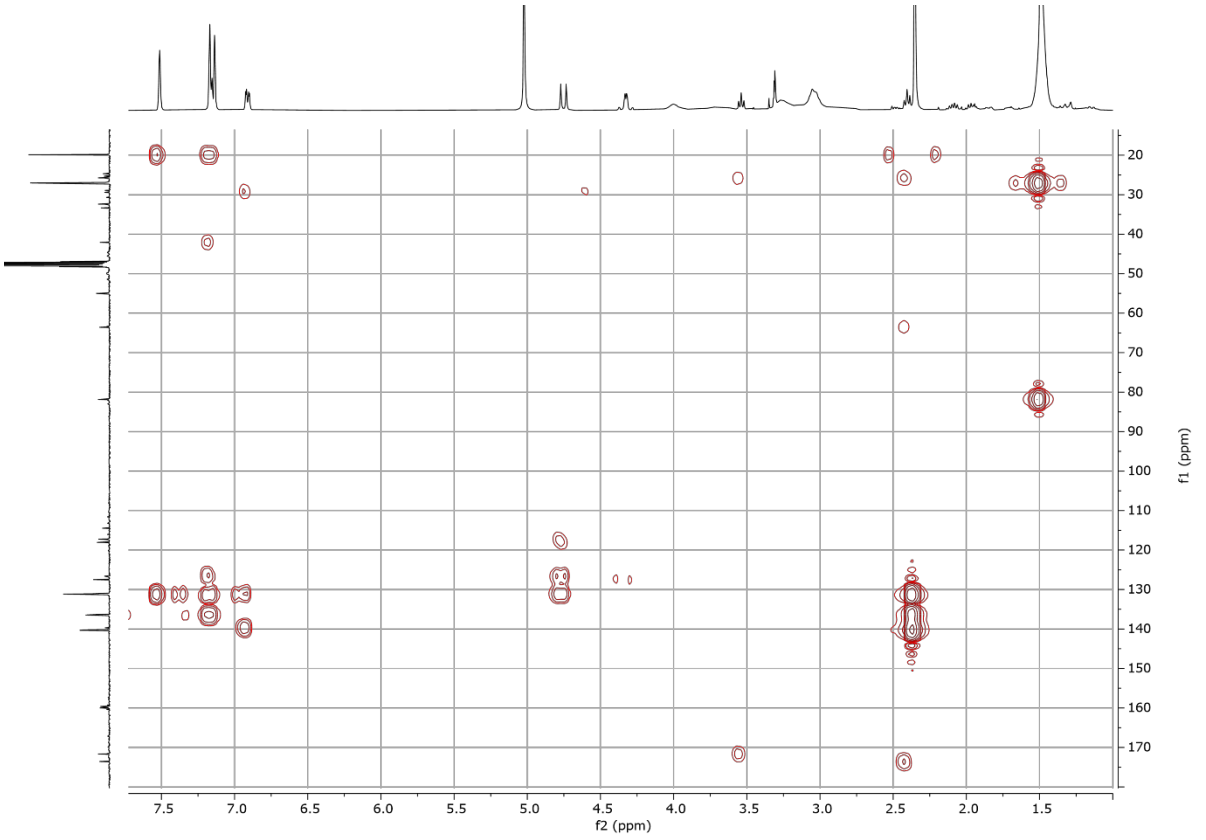

Figure 8.74 HMBC NMR spectrum of **9c** (CD_3OD, 298 K).

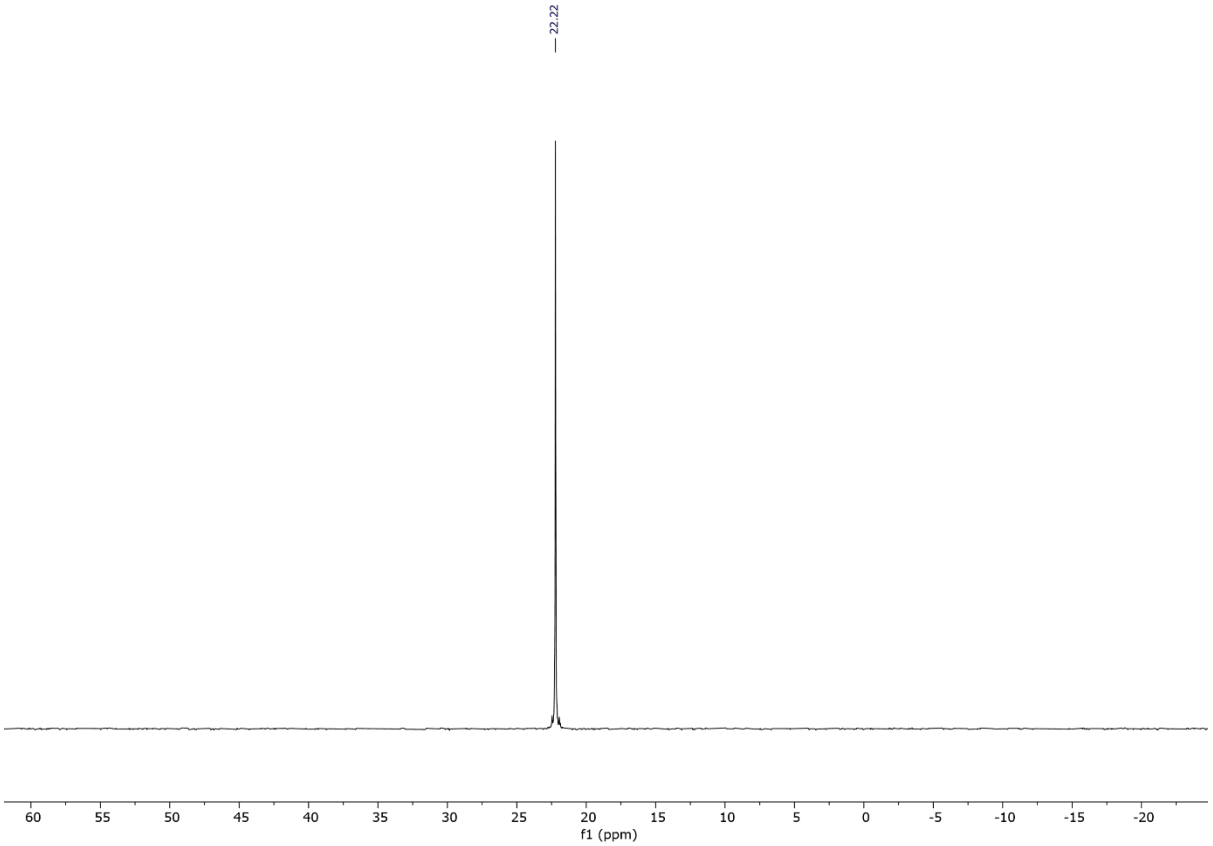

Figure 8.75 $^{31}P\{^{1}H\}$ NMR spectrum of **9c** (CD_3OD, 162 MHz, 298 K).

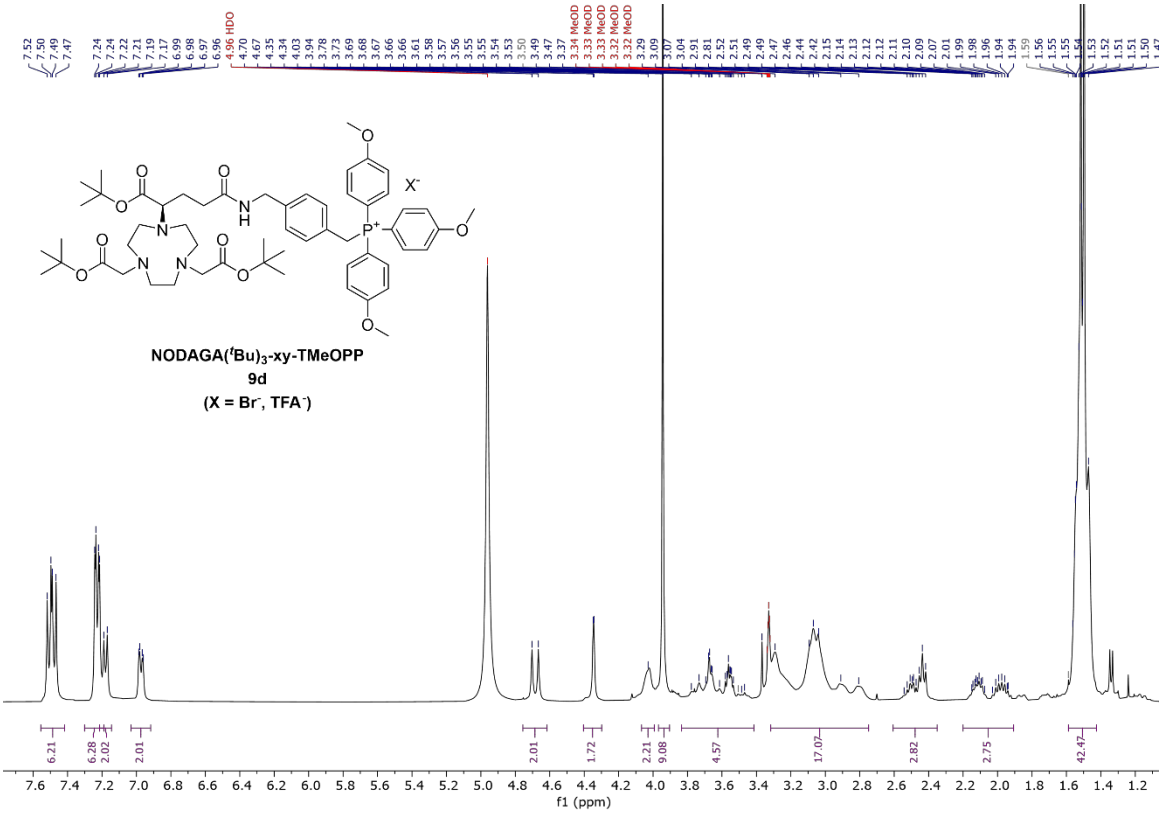

Figure 8.76 ^{1}H NMR spectrum of **9d** (CD_3OD, 400 MHz, 298 K).

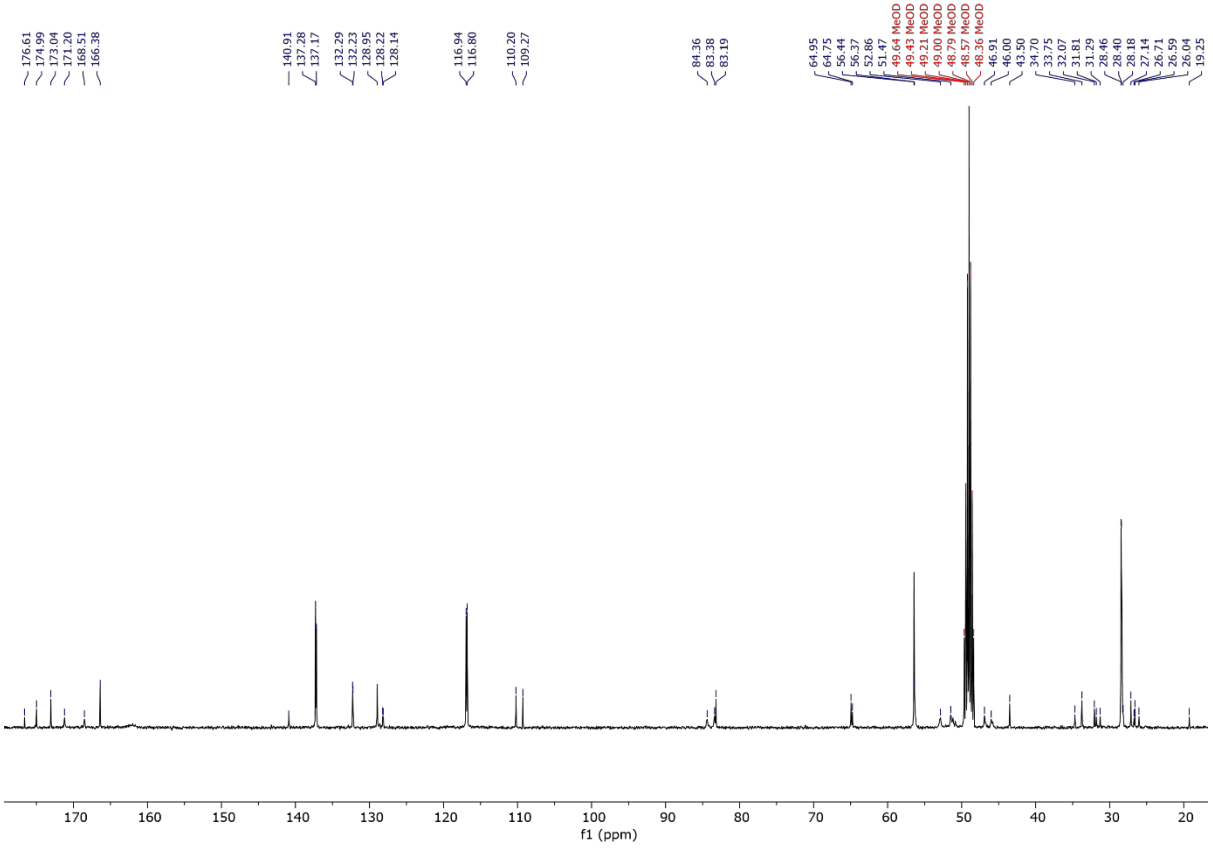

Figure 8.77 $^{13}C\{^{1}H\}$ NMR spectrum of **9d** (CD_3OD, 101 MHz, 298 K).

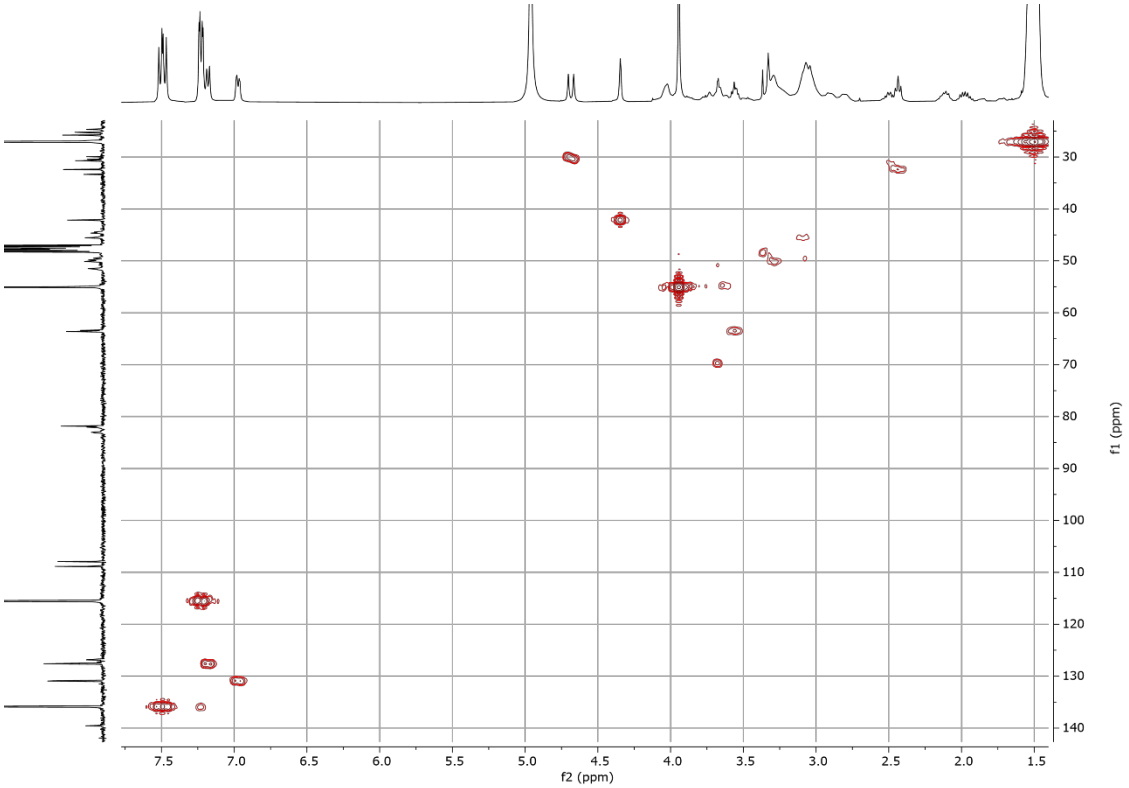

Figure 8.78 HMQC NMR spectrum of **9d** (CD_3OD, 298 K).

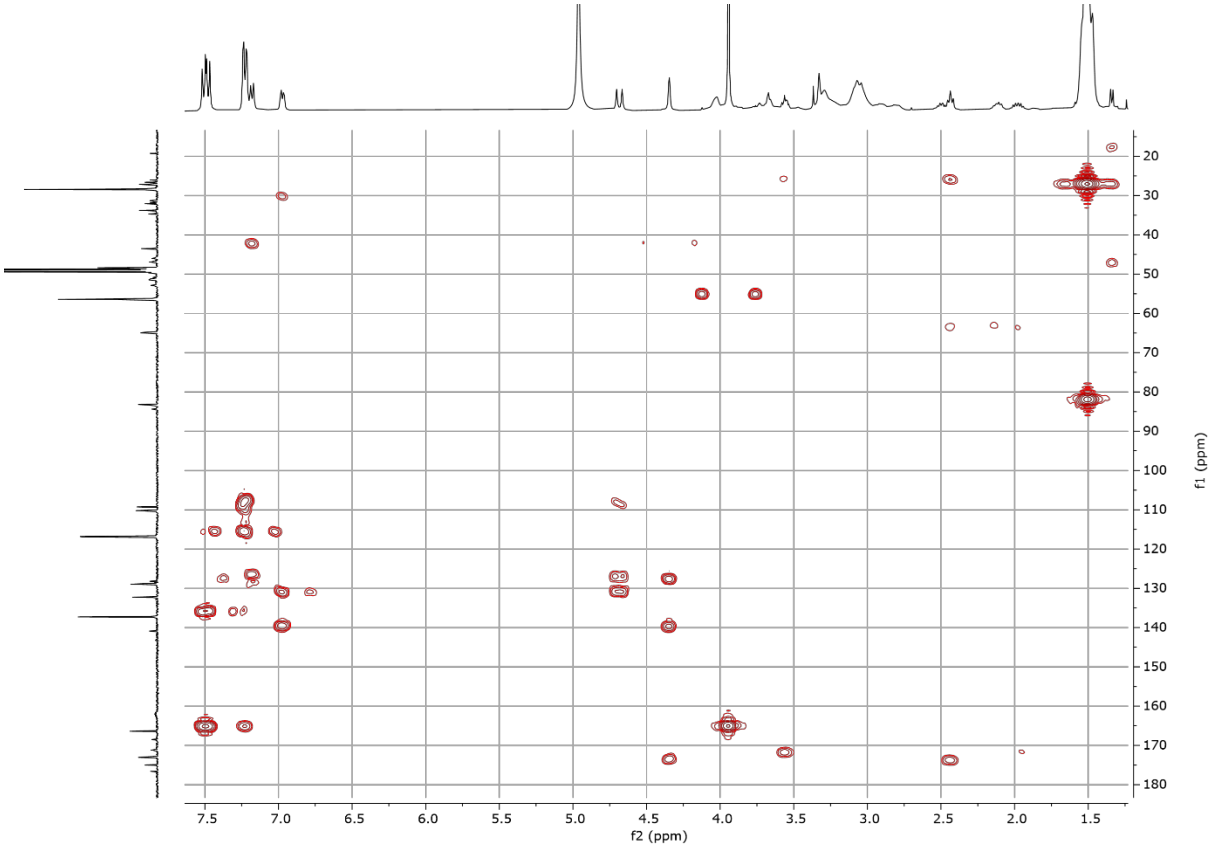

Figure 8.79 HMBC NMR spectrum of **9d** (CD_3OD, 298 K).

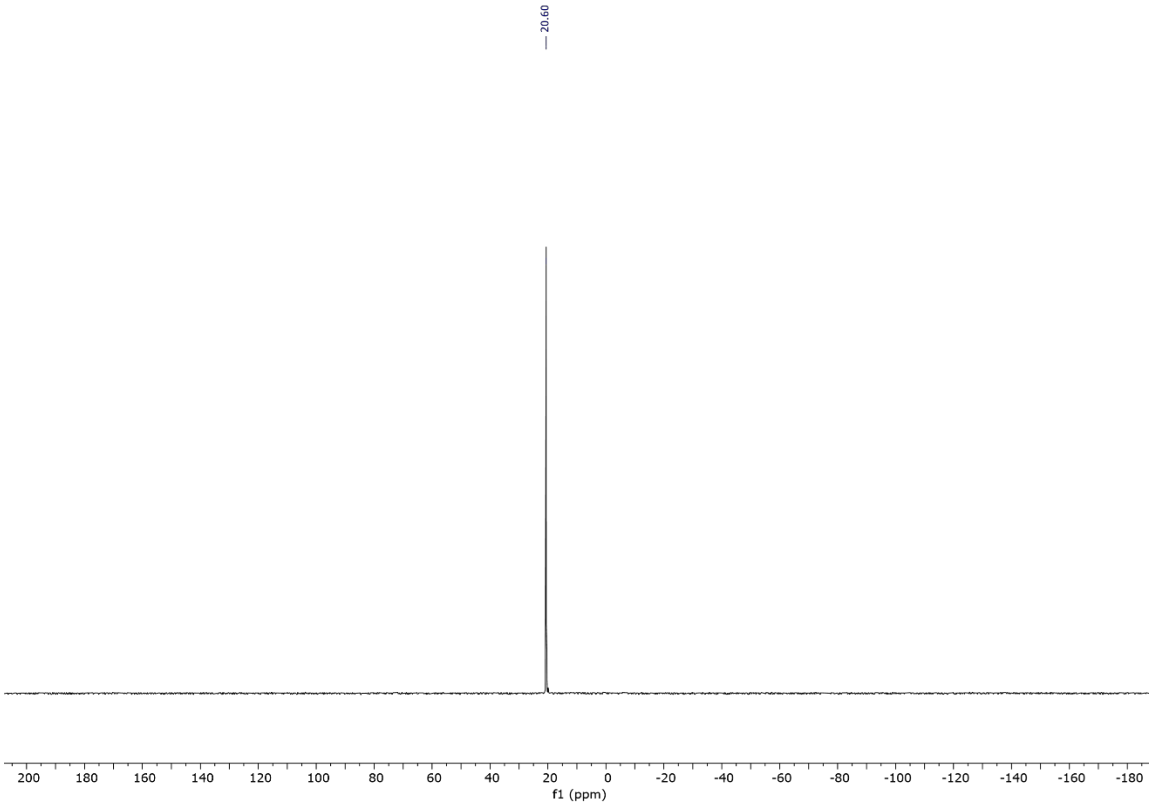

Figure 8.80 $^{31}P\{^{1}H\}$ NMR spectrum of **9d** (CD_3OD, 162 MHz, 298 K).

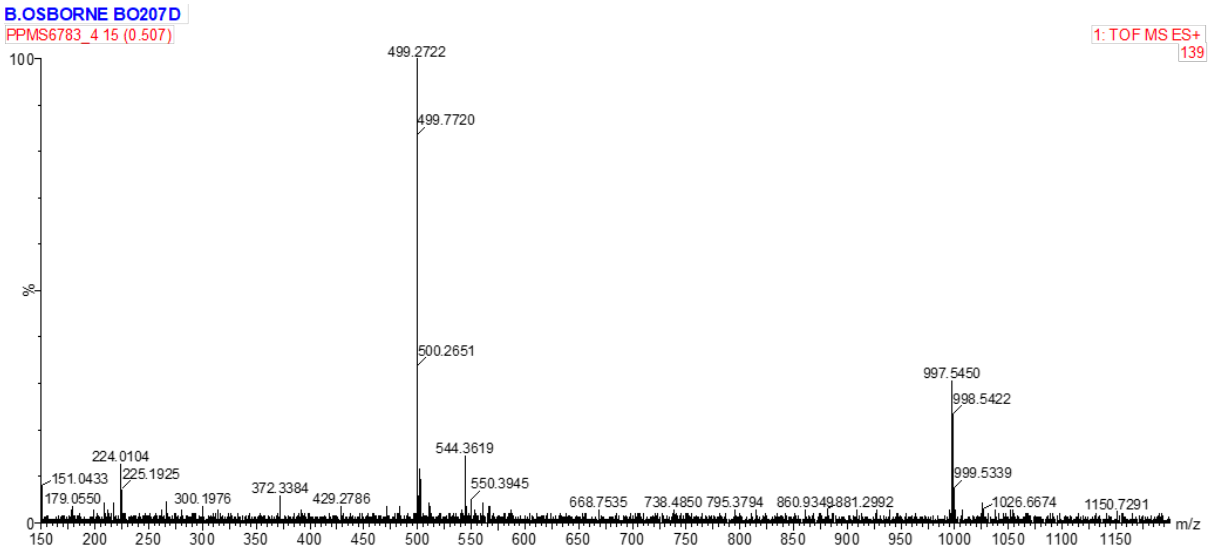

Figure 8.81 ES-TOF+ MS of **9d**.

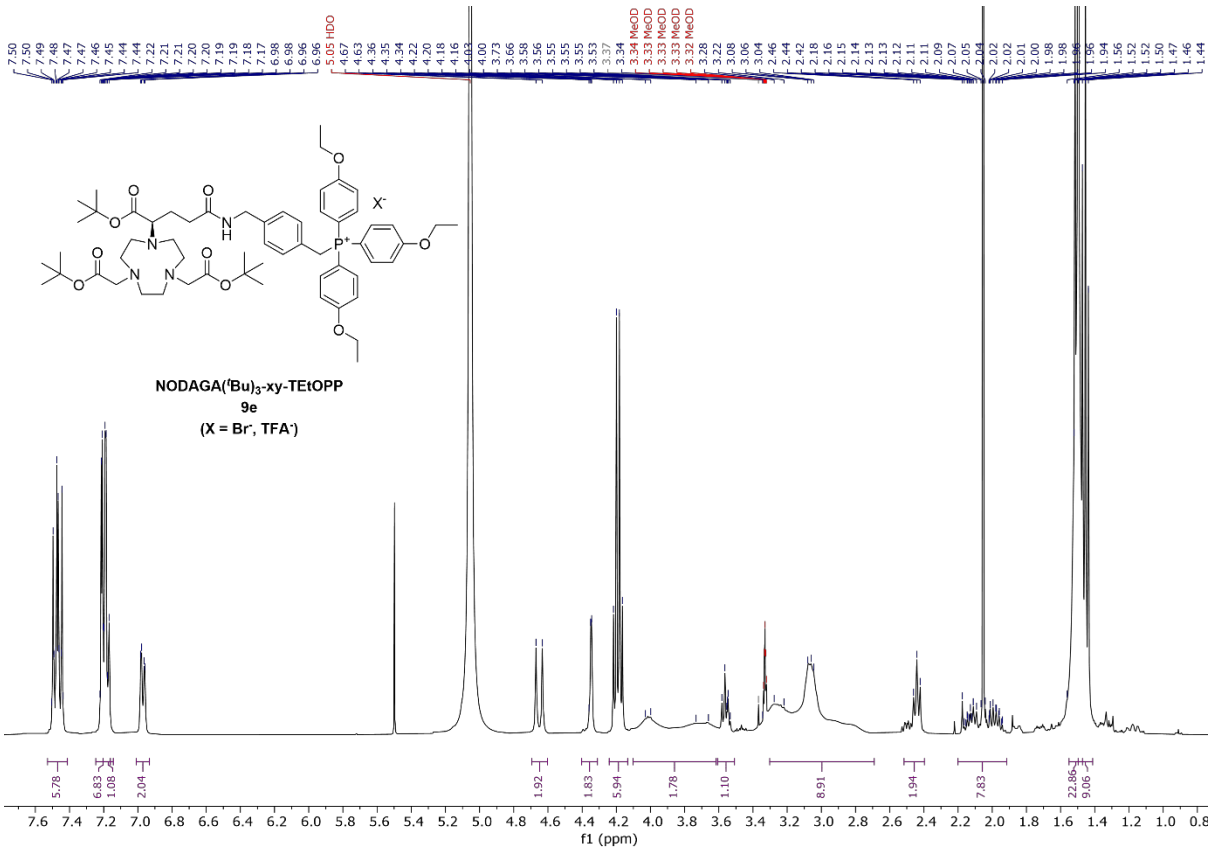

Figure 8.82 ^{1}H NMR spectrum of **9e** (CD_3OD, 400 MHz, 298 K).

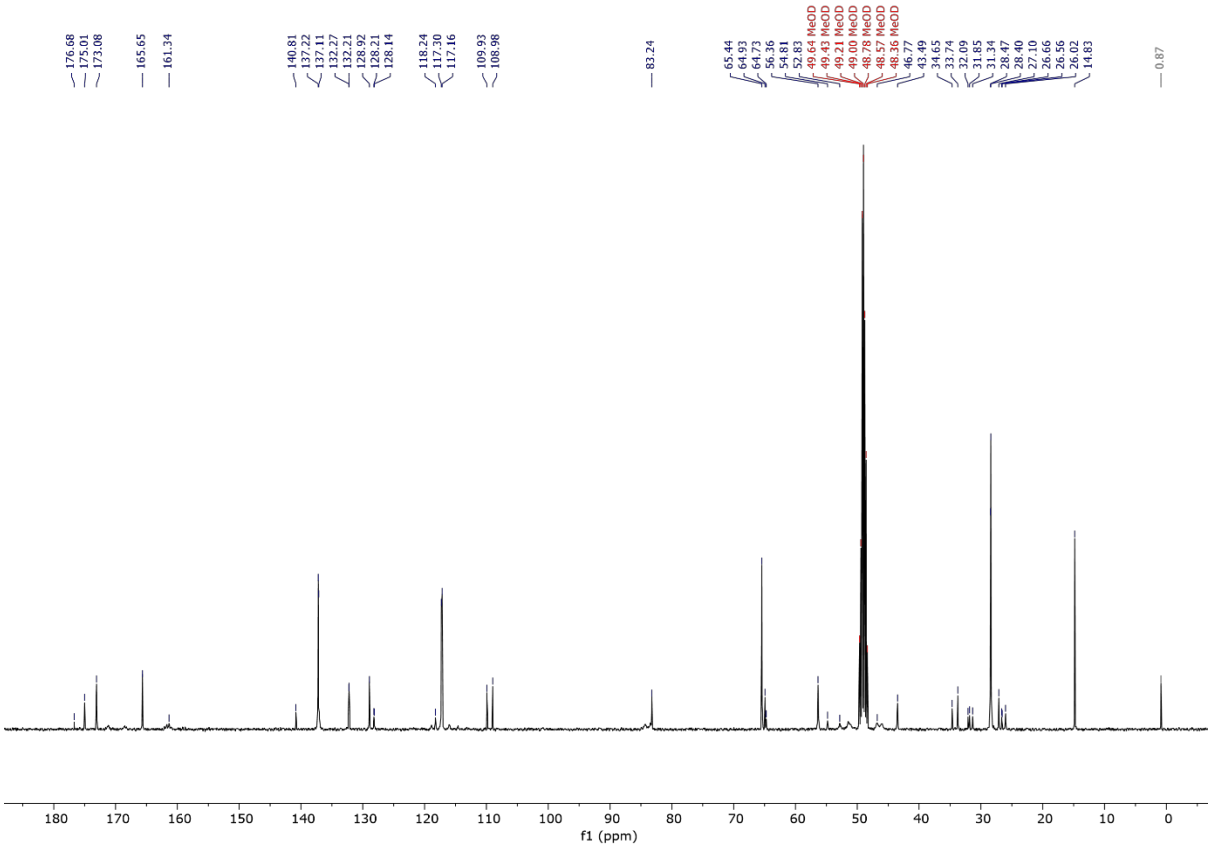

Figure 8.83 $^{13}C\{^{1}H\}$ NMR spectrum of **9e** (CD_3OD, 101 MHz, 298 K).

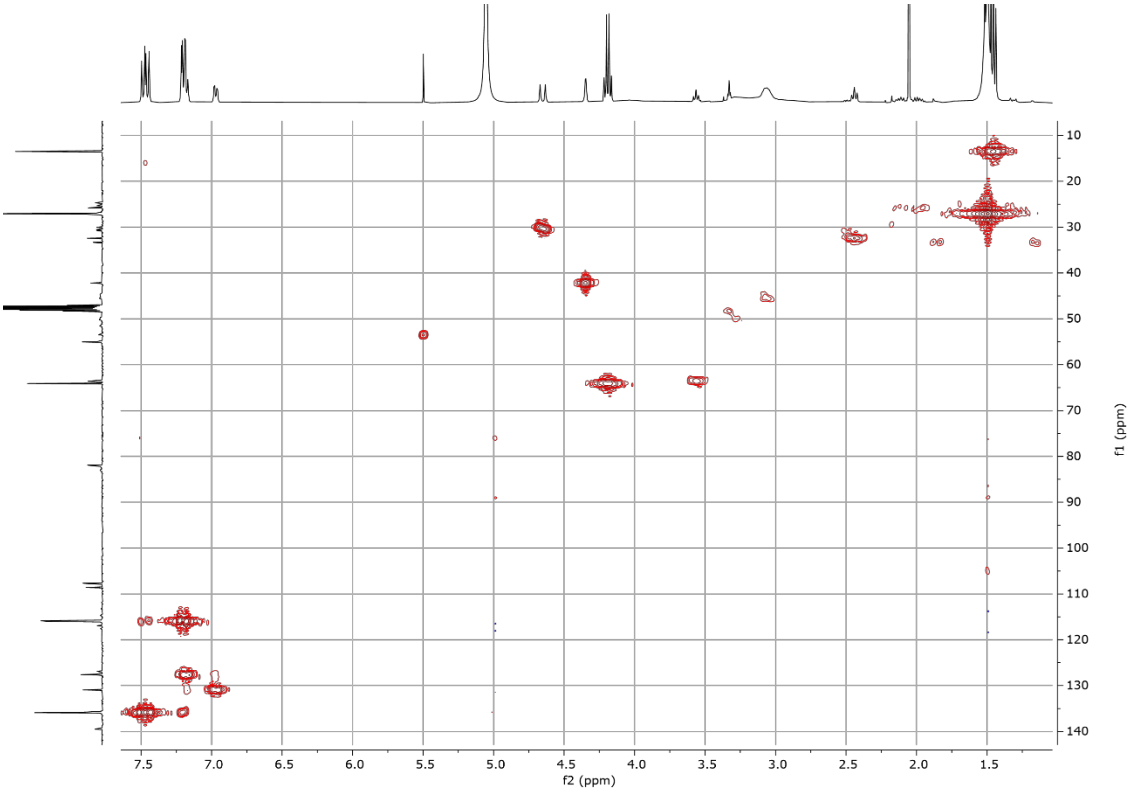

Figure 8.84 HMQC NMR spectrum of **9e** (CD_3OD, 298 K).

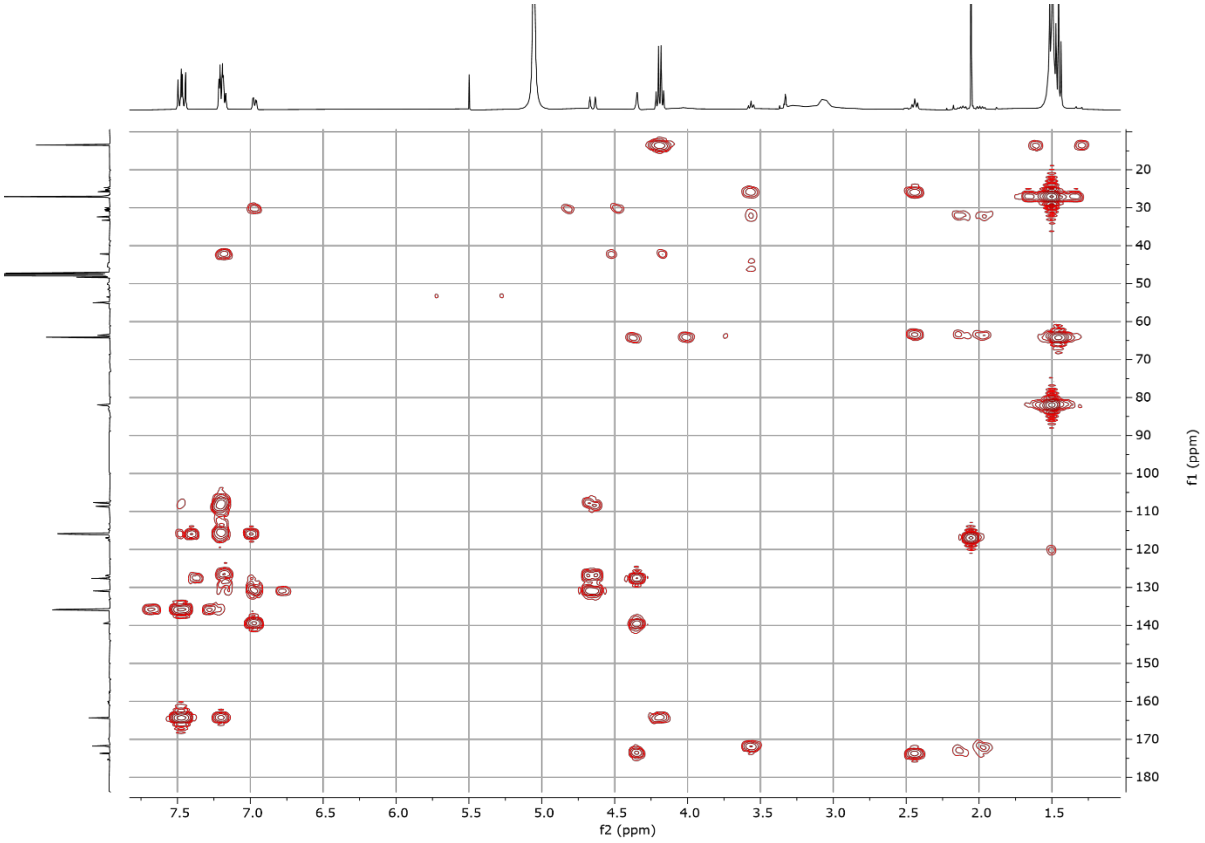

Figure 8.85 HMBC NMR spectrum of **9e** (CD_3OD, 298 K).

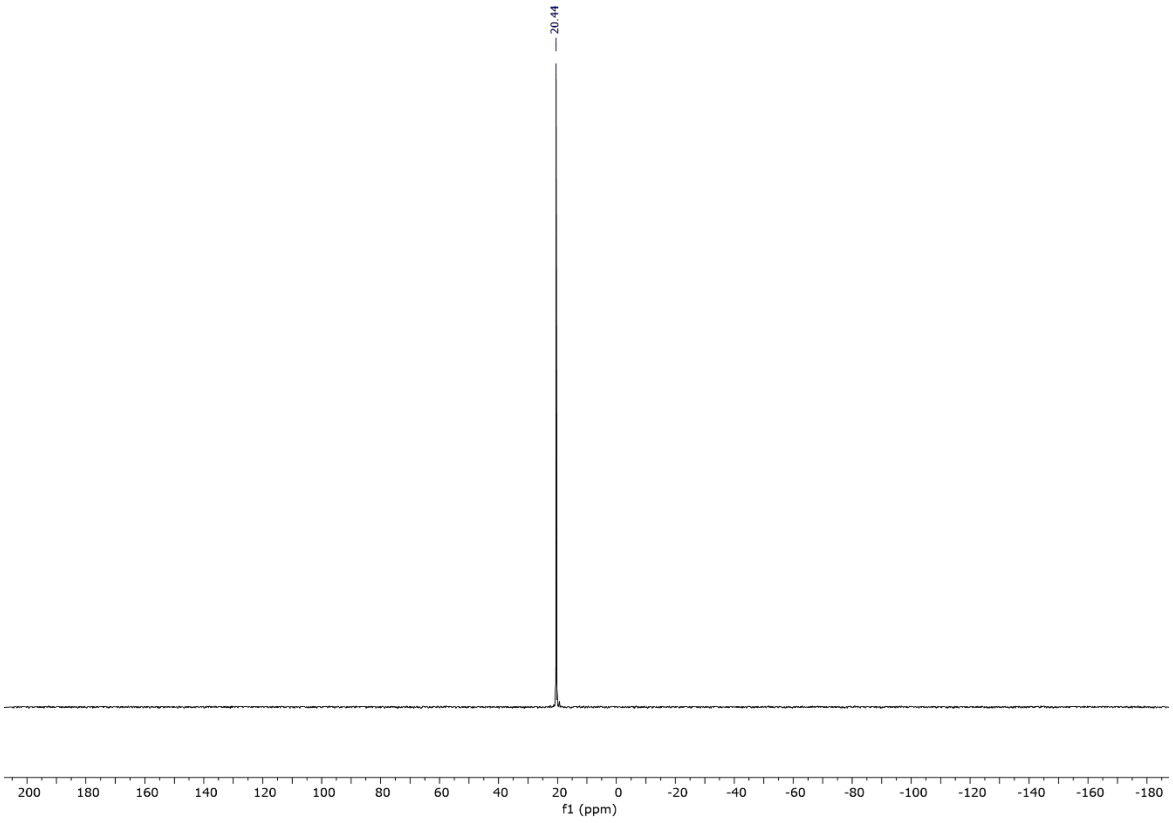

Figure 8.86 $^{31}P\{^{1}H\}$ NMR spectrum of **9e** (CD_3OD, 162 MHz, 298 K).

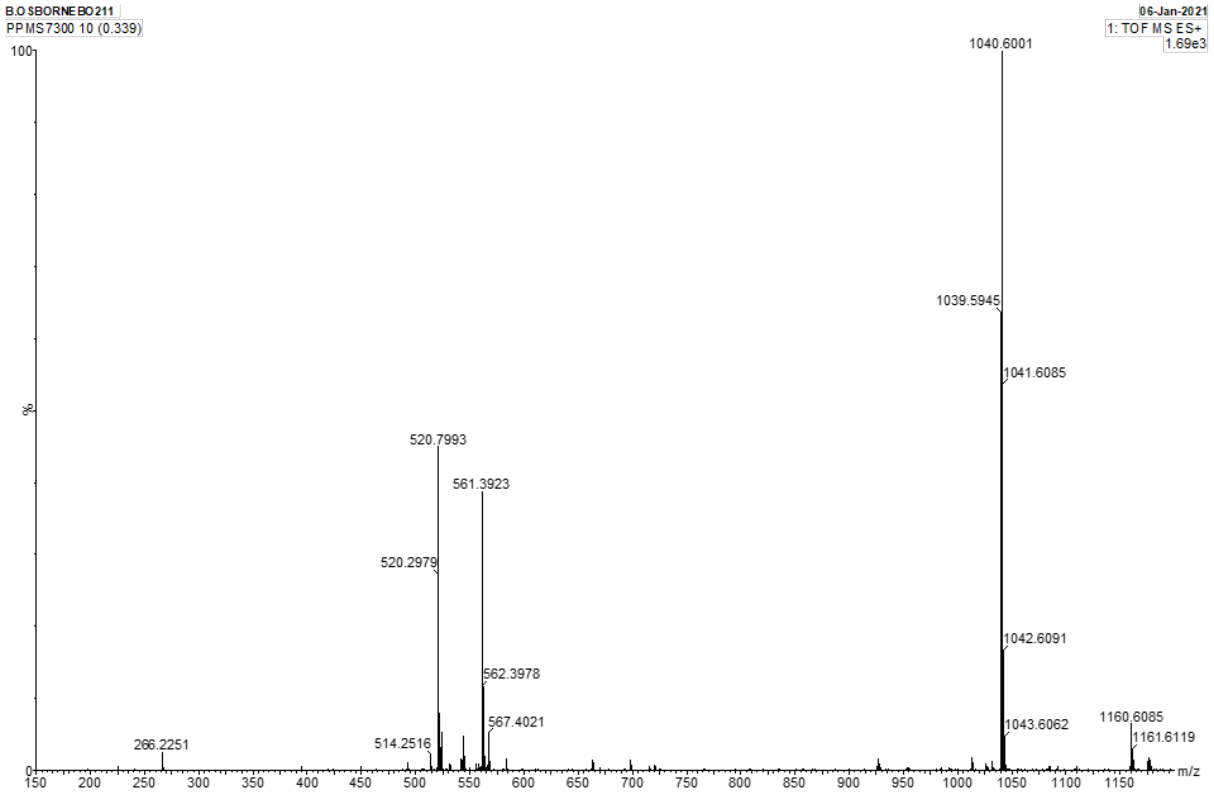

Figure 8.87 ES-TOF+ MS of **9e**.

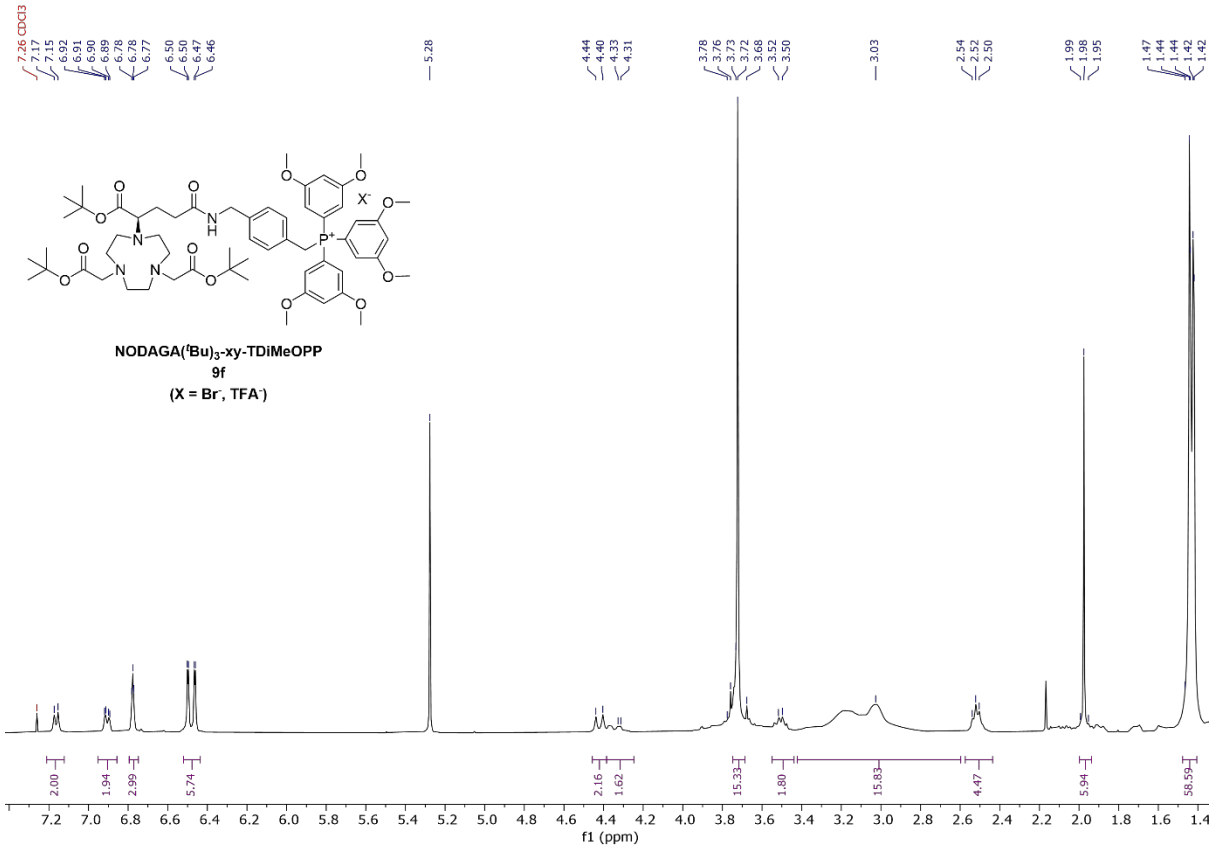

Figure 8.88 ^{1}H NMR spectrum of **9f** ($CDCl_3$, 400 MHz, 298 K).

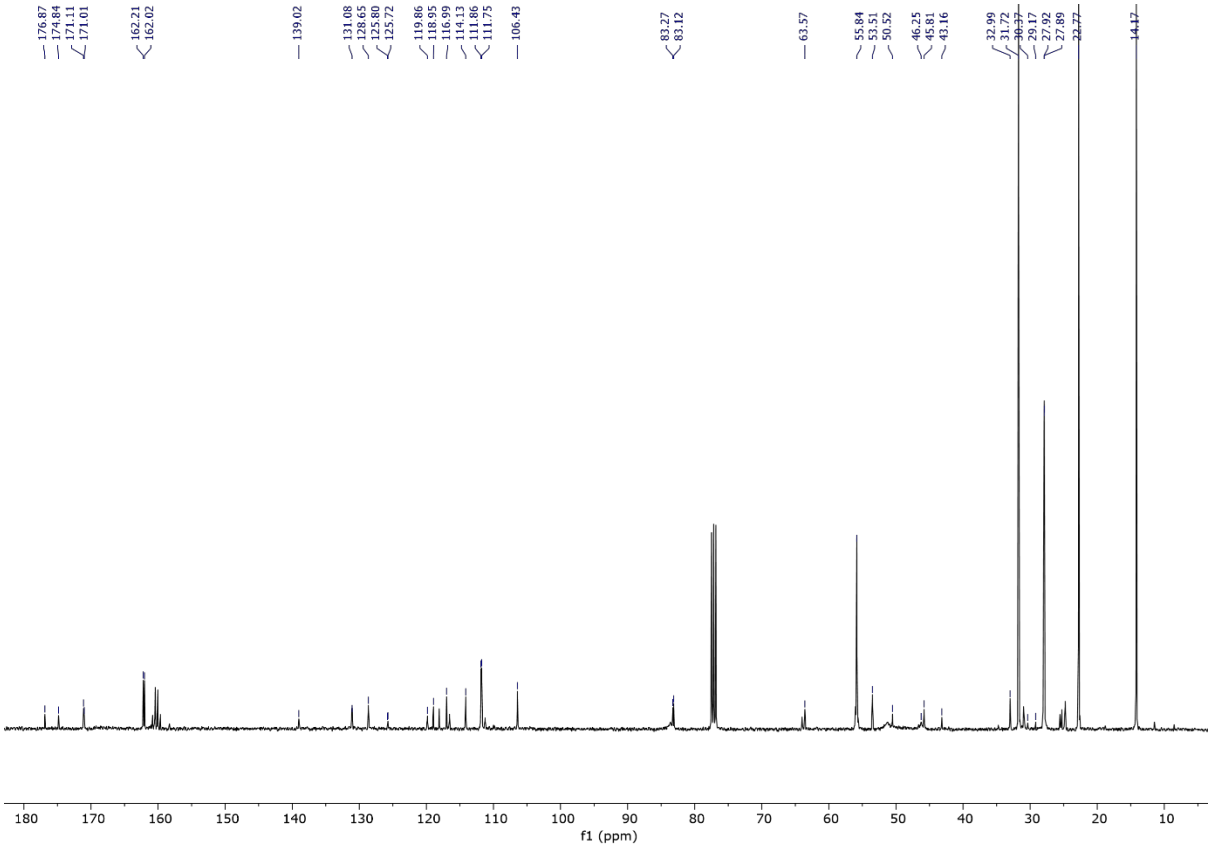

Figure 8.89 $^{13}C\{^{1}H\}$ NMR spectrum of **9f** ($CDCl_3$, 101 MHz, 298 K).

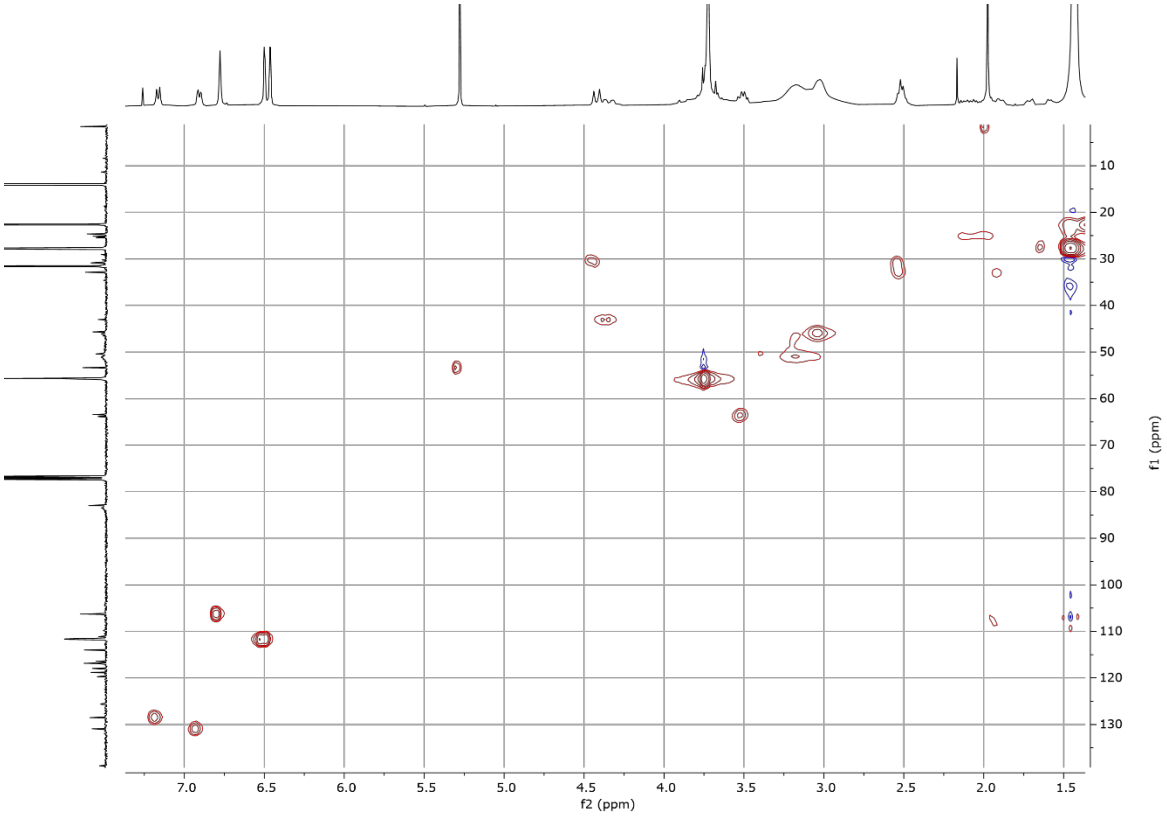

Figure 8.90 HMQC NMR spectrum of **9f** ($CDCl_3$, 298 K).

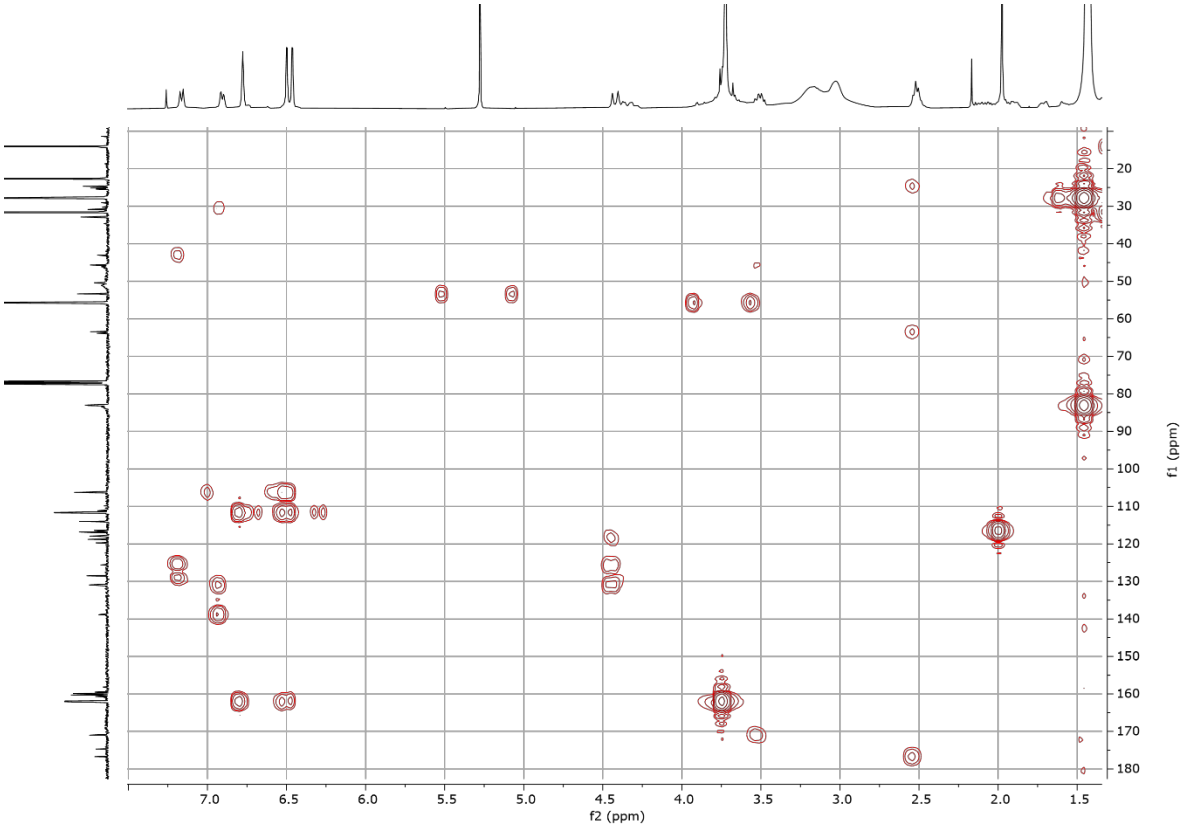

Figure 8.91 HMBC NMR spectrum of **9f** ($CDCl_3$, 298 K).

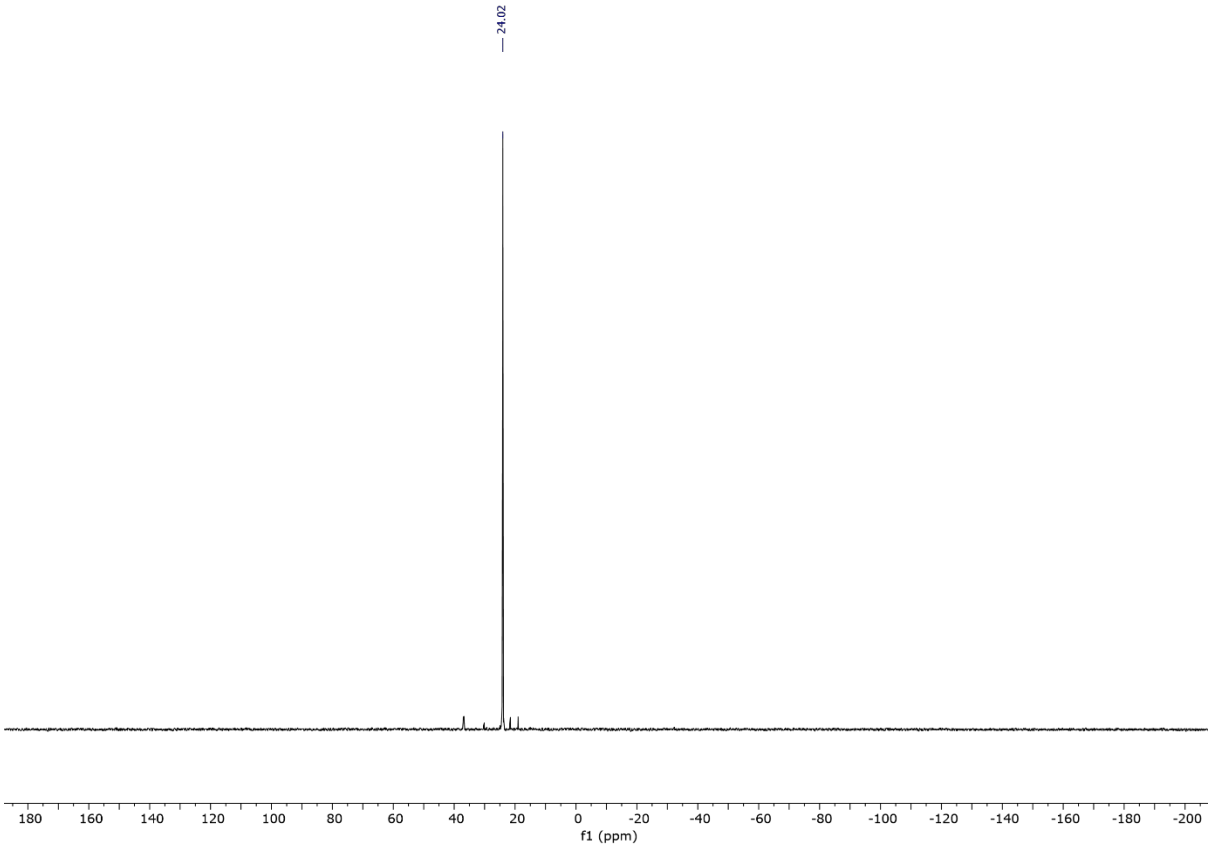

Figure 8.92 $^{31}P\{^{1}H\}$ NMR spectrum of **9f** ($CDCl_3$, 162 MHz, 298 K).

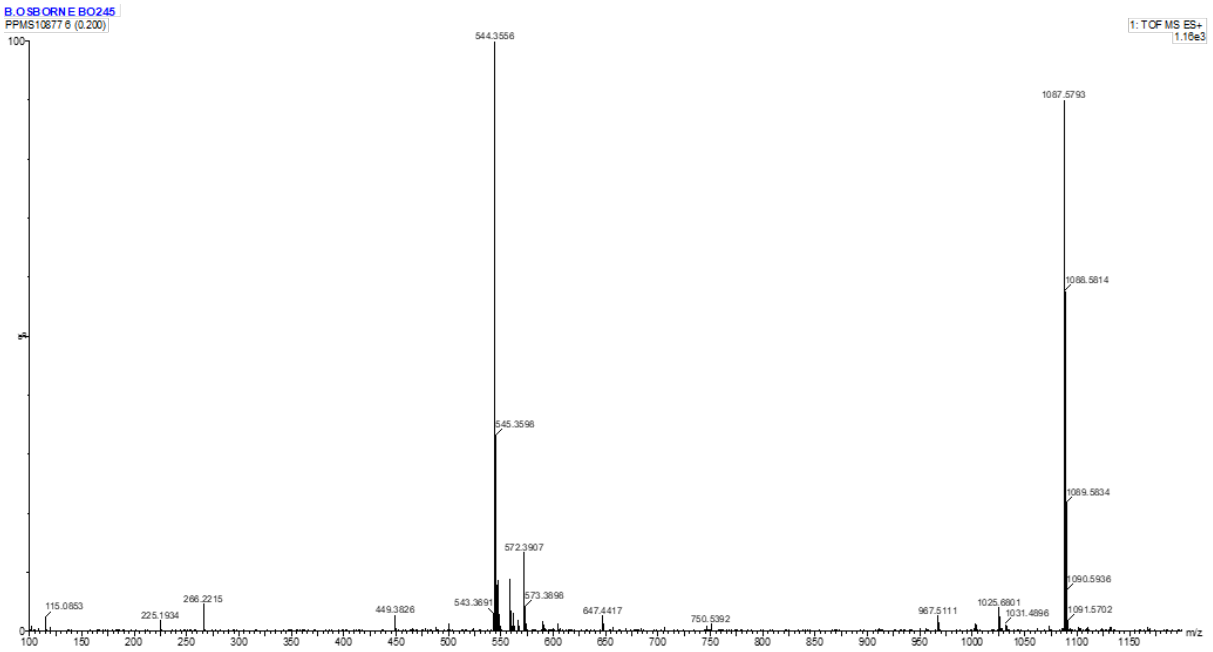

Figure 8.93 ES-TOF+ MS of **9f**.

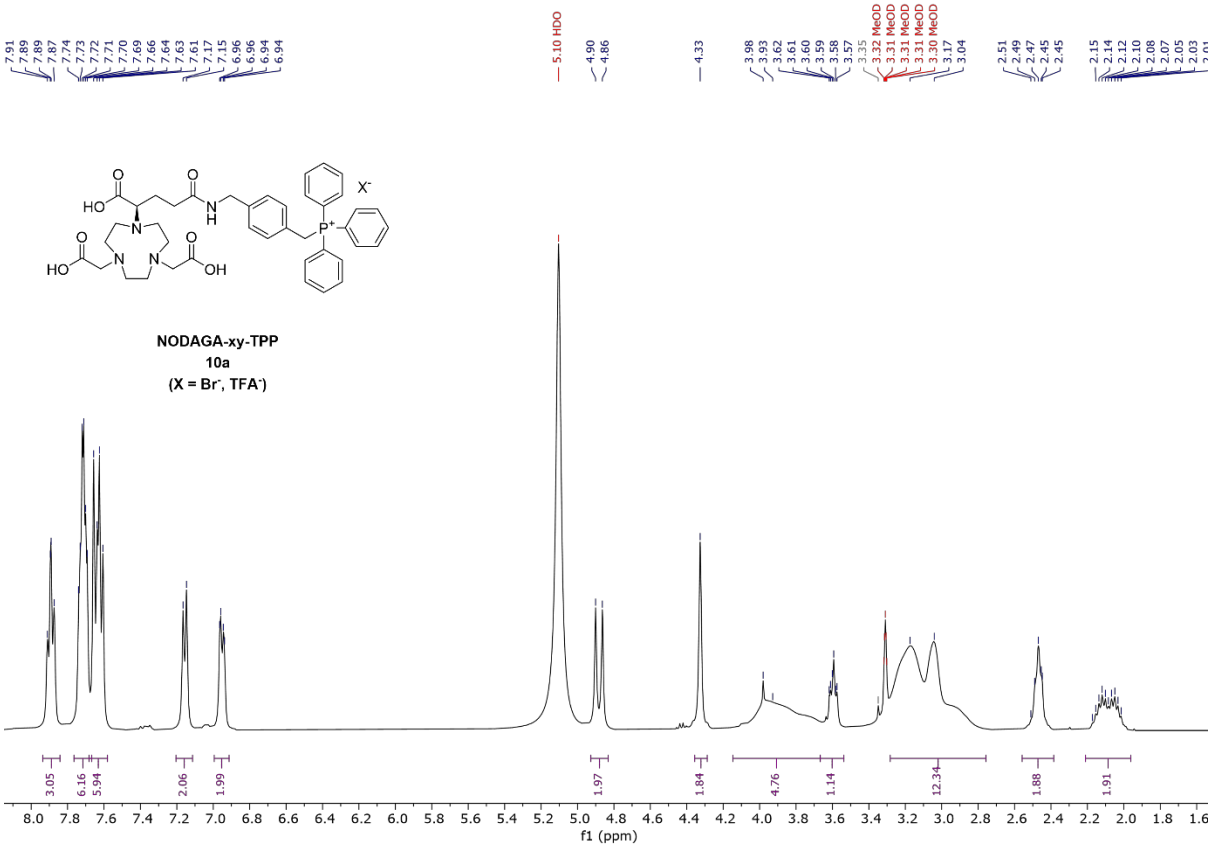

Figure 8.94 ^{1}H NMR spectrum of **10a** (CD_3OD, 400 MHz, 298 K).

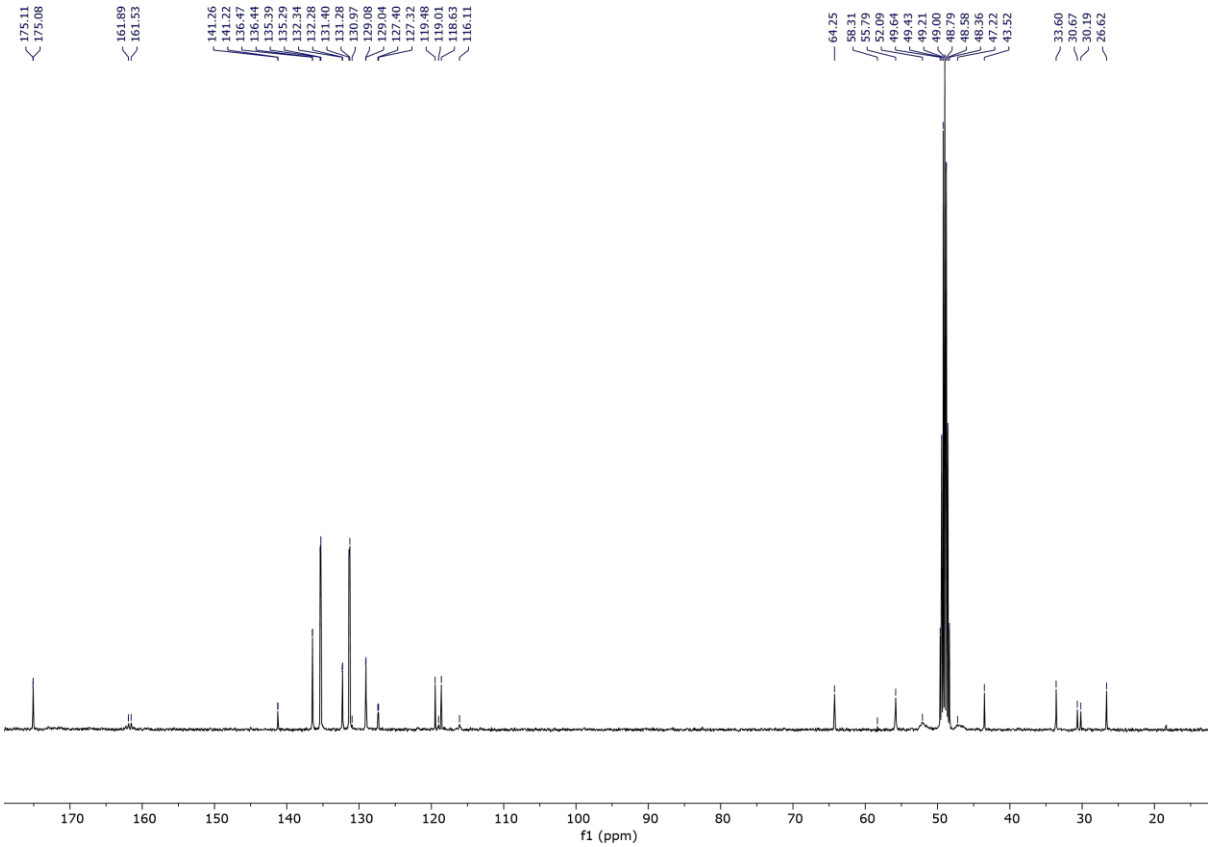

Figure 8.95 $^{13}C\{^{1}H\}$ NMR spectrum of **10a** (CD_3OD, 101 MHz, 298 K).

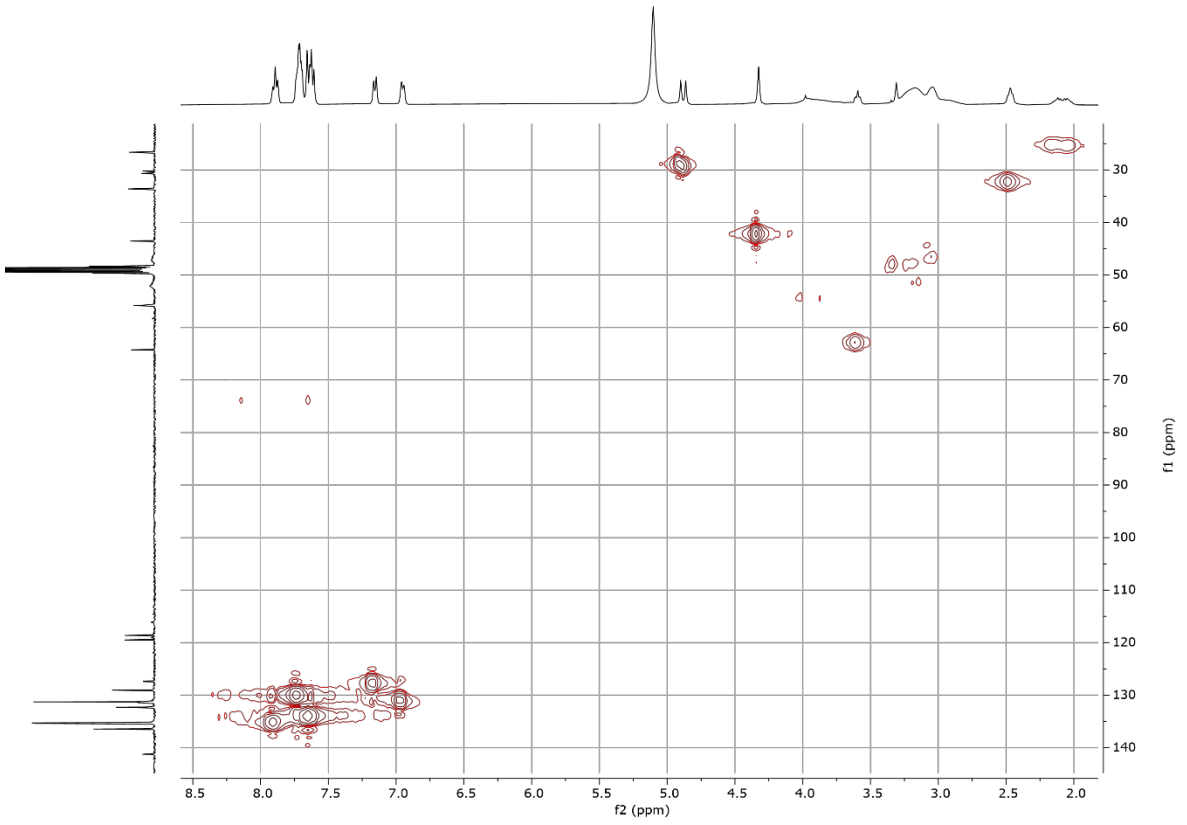

Figure 8.96 HMQC NMR spectrum of **10a** (CD_3OD, 298 K).

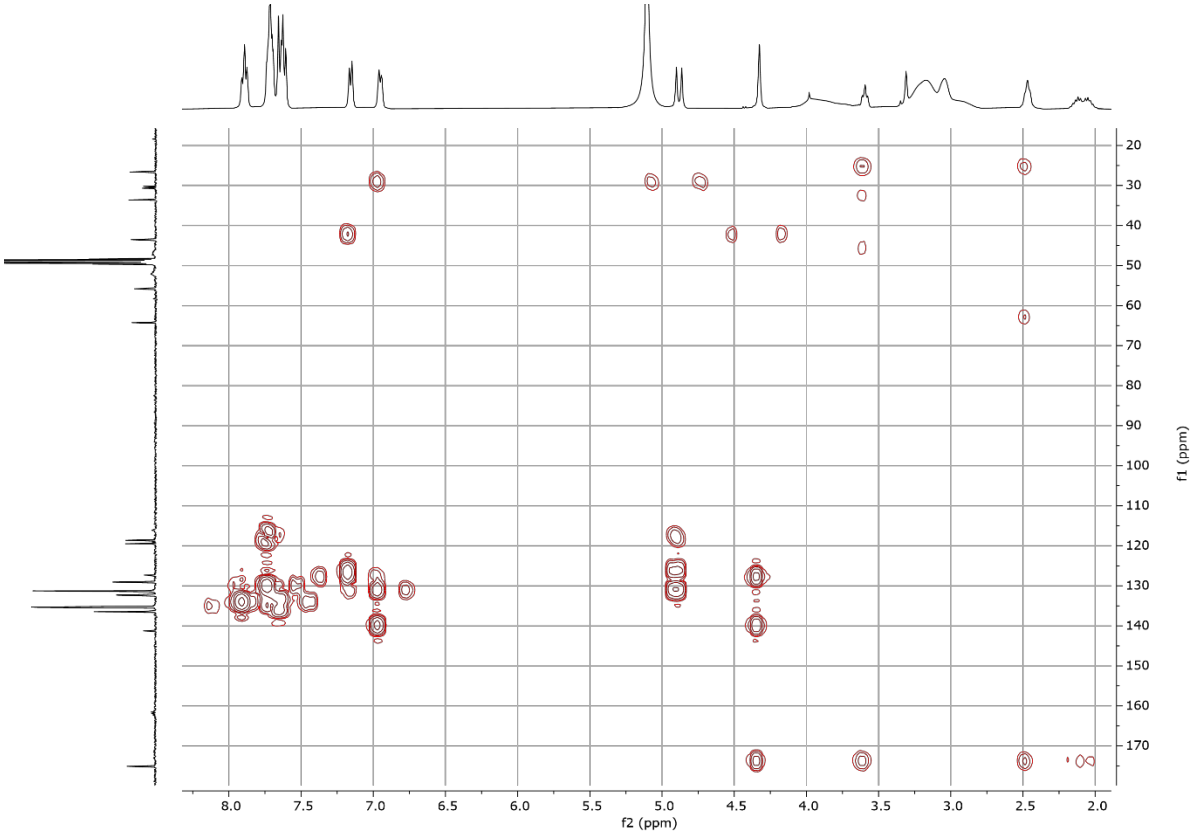

Figure 8.97 HMBC NMR spectrum of **10a** (CD_3OD, 298 K).

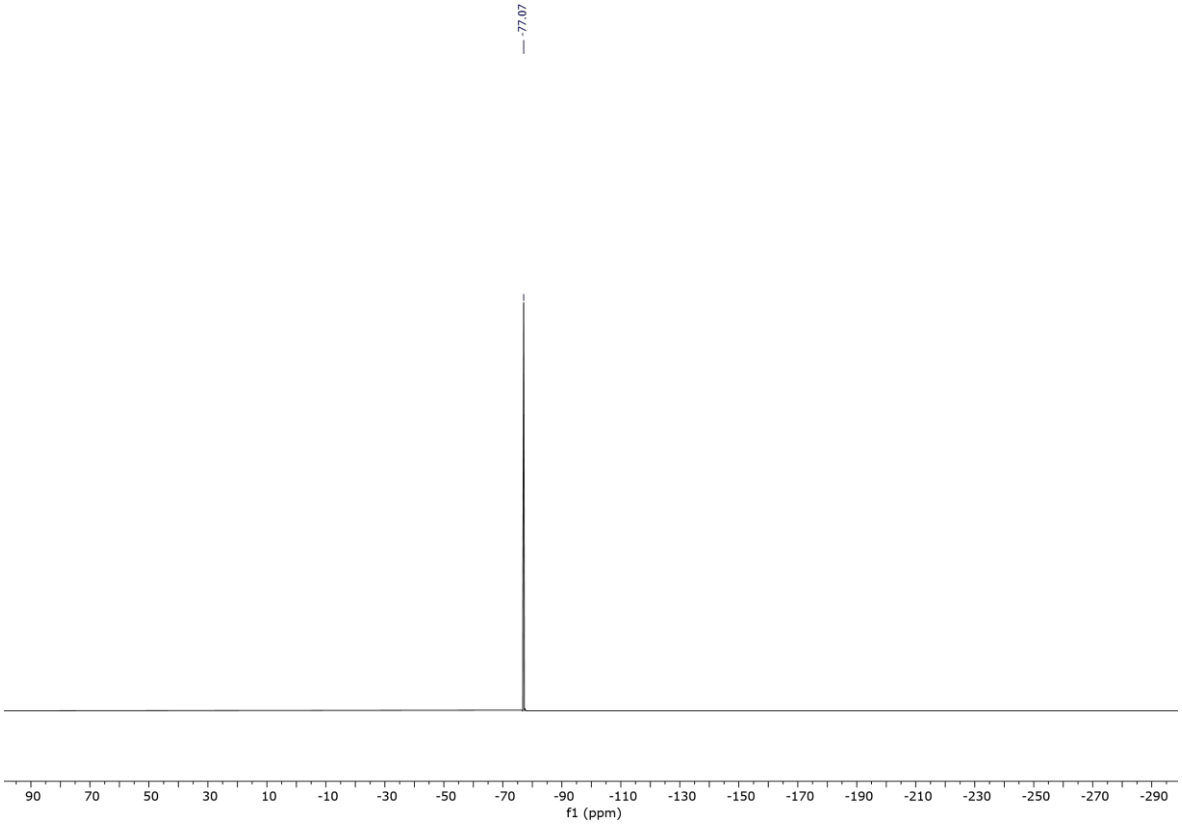

Figure 8.98 $^{19}F\{^1H\}$ NMR spectrum of **10a** (CD_3OD, 377 MHz, 298 K).

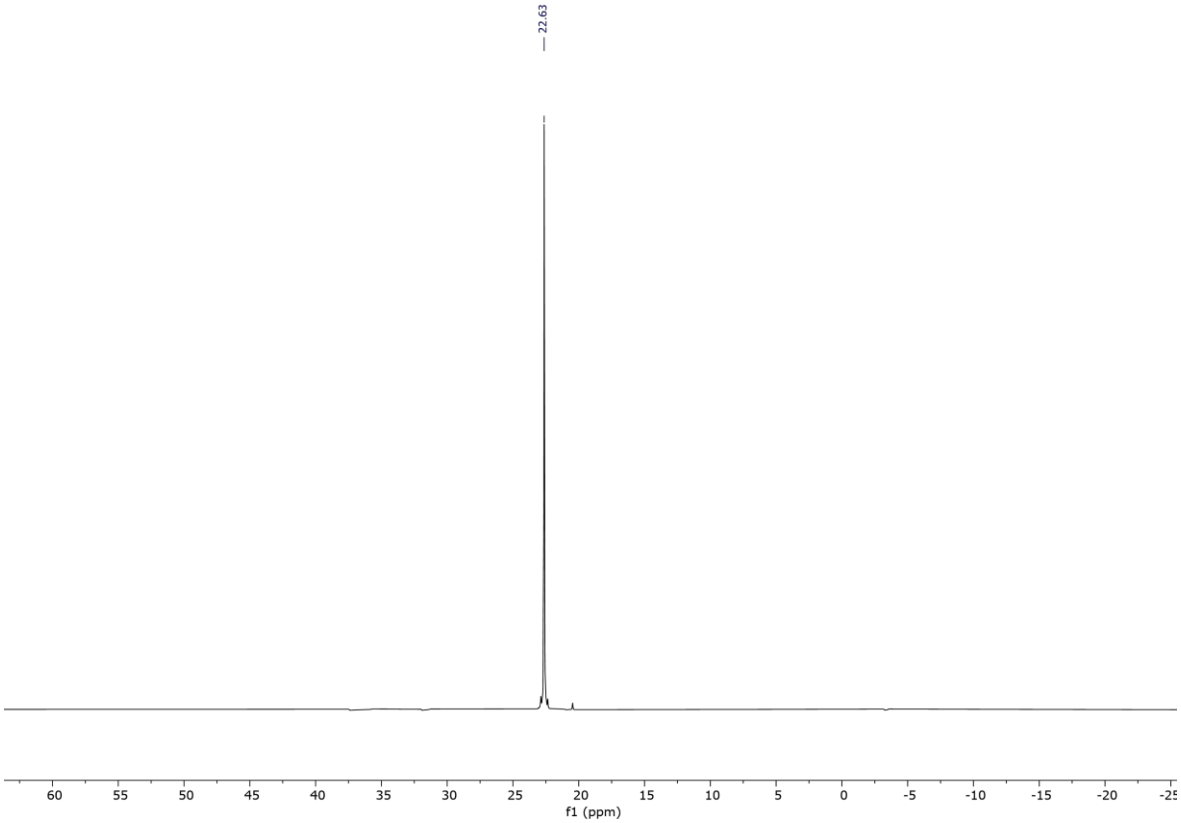

Figure 8.99 $^{31}P\{^{1}H\}$ NMR spectrum of **10a** (CD_3OD, 162 MHz, 298 K).

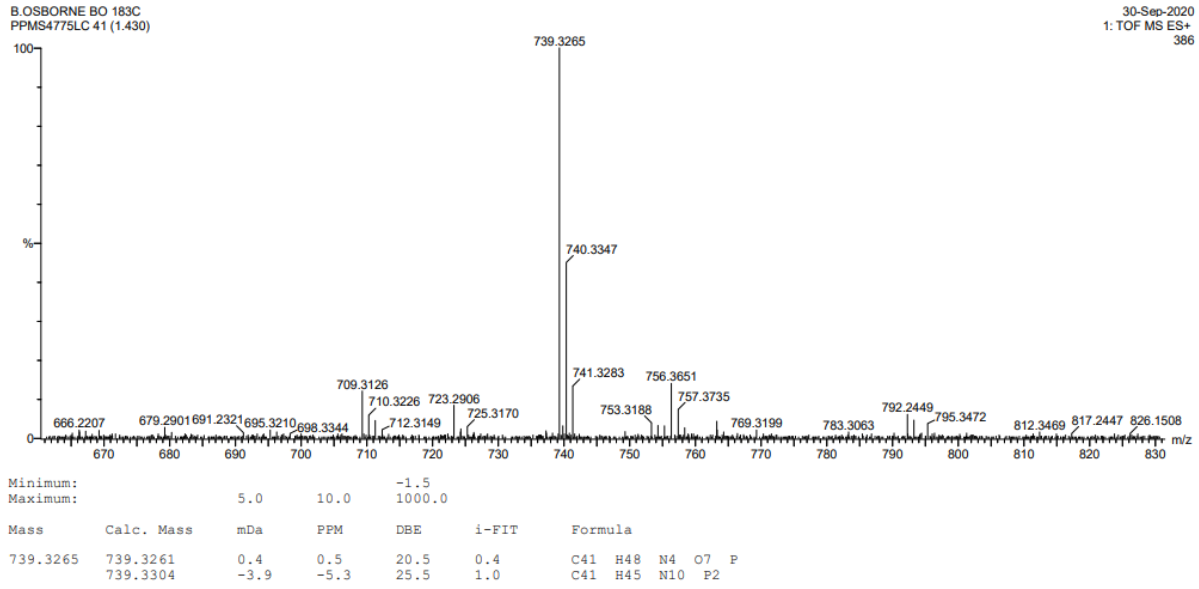

Minimum:				-1.5		
Maximum:		5.0	10.0	1000.0		
Mass	Calc. Mass	mDa	PPM	DBE	i-FIT	Formula
739.3265	739.3261	0.4	0.5	20.5	0.4	C41 H48 N4 O7 P
	739.3304	-3.9	-5.3	25.5	1.0	C41 H45 N10 P2

Figure 8.100 ES-TOF+ MS of **10a**.

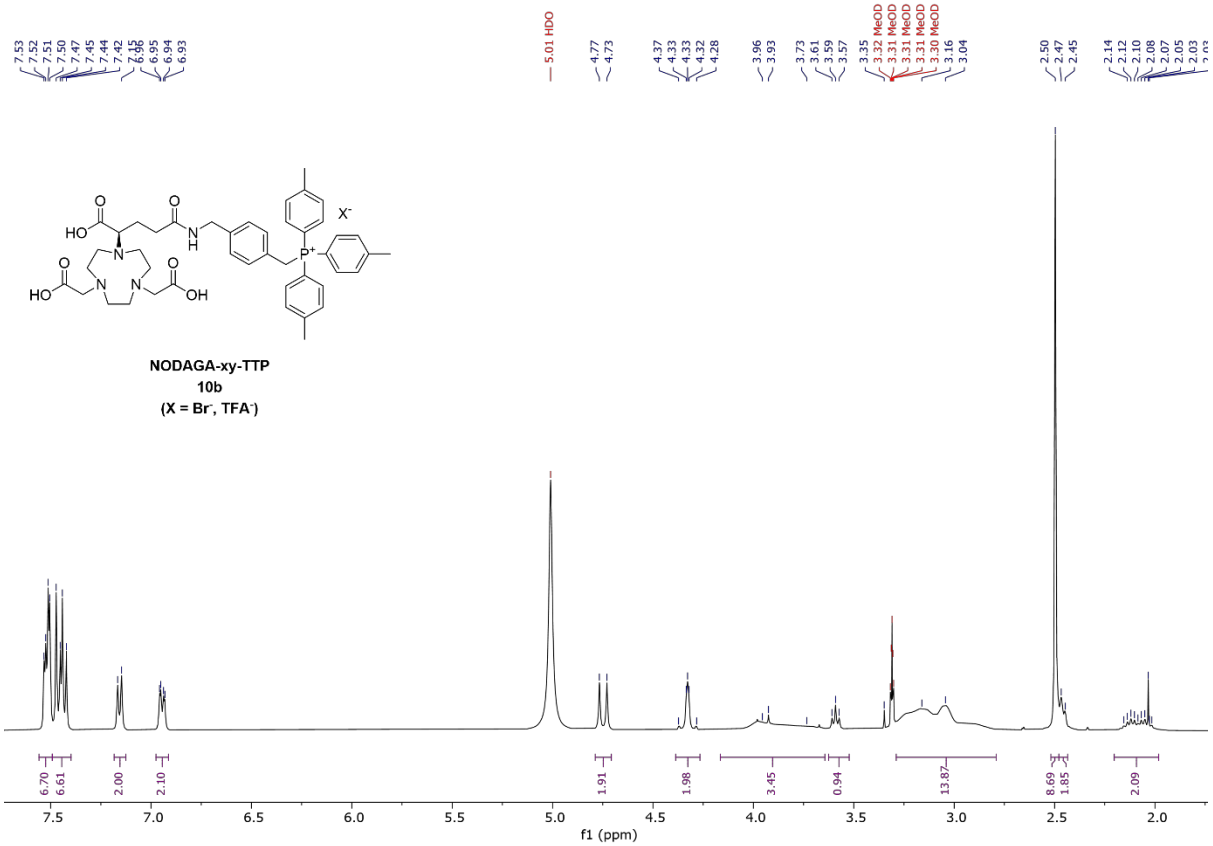

Figure 8.101 ^{1}H NMR spectrum of **10b** (CD_3OD, 400 MHz, 298 K).

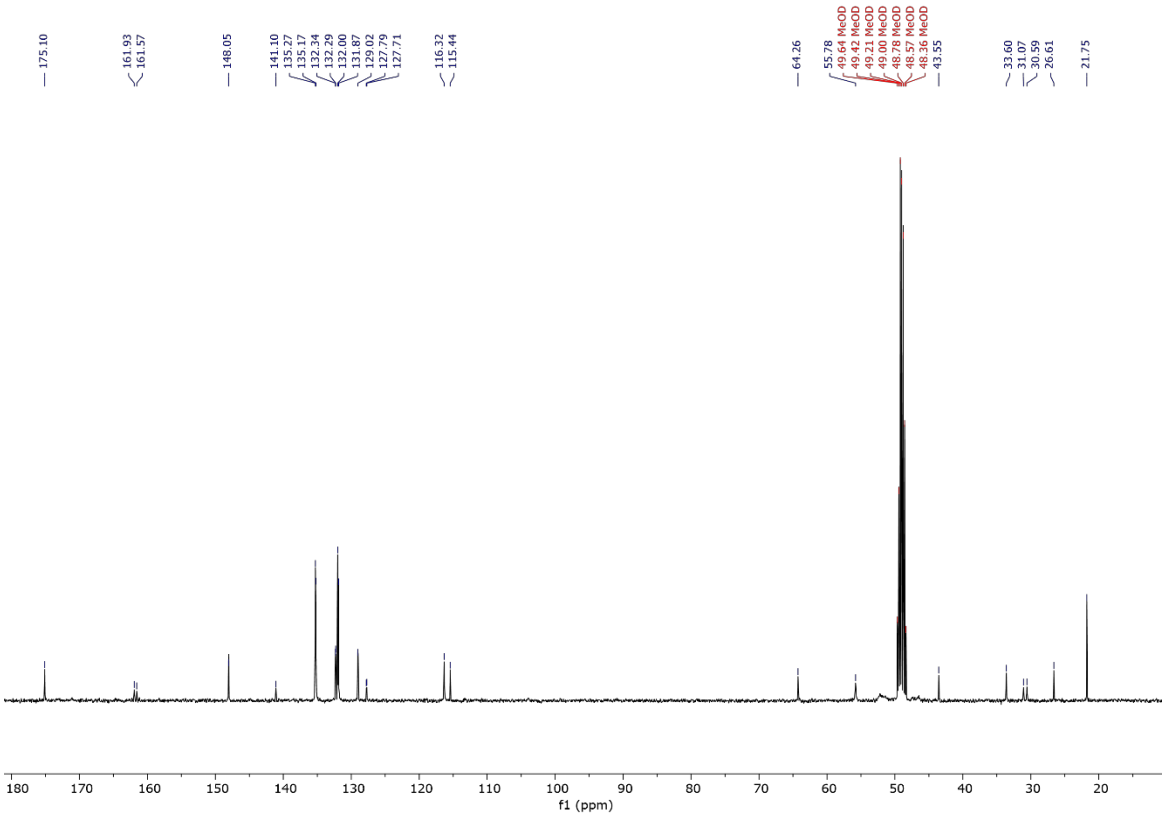

Figure 8.102 $^{13}C\{^{1}H\}$ NMR spectrum of **10b** (CD_3OD, 101 MHz, 298 K).

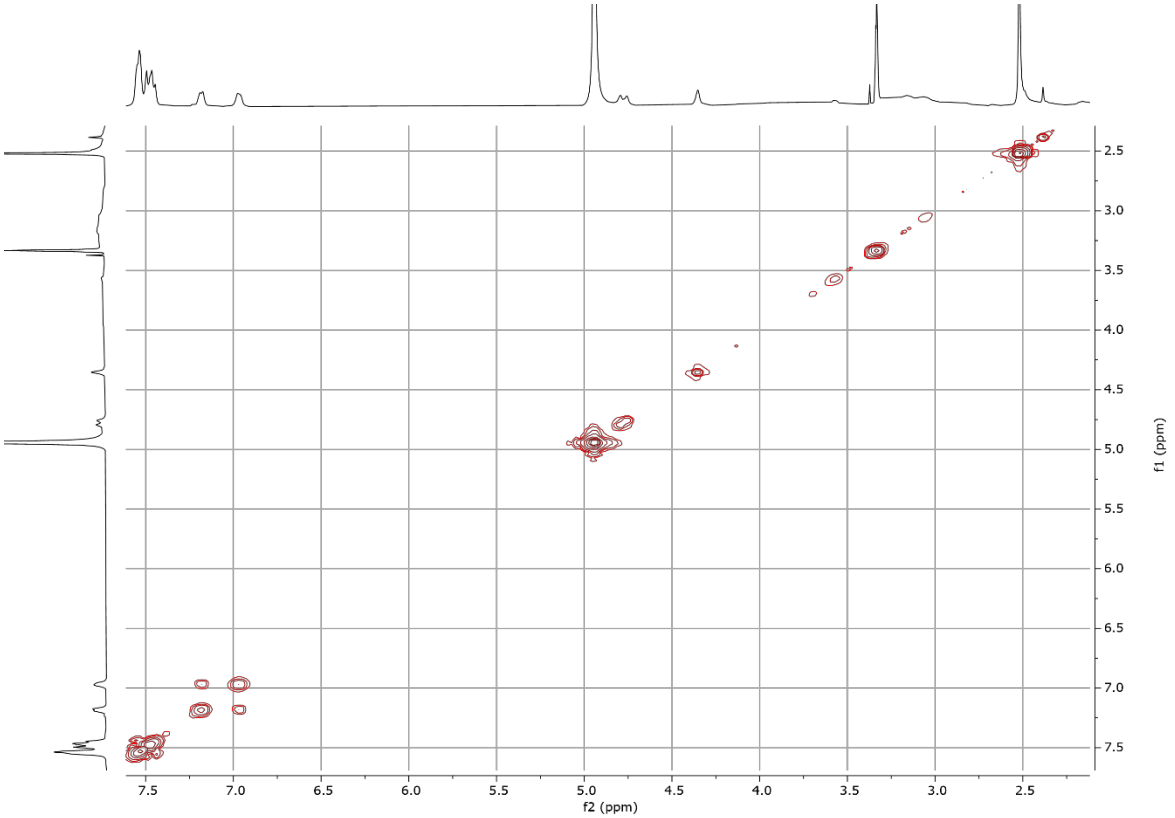

Figure 8.103 COSY NMR spectrum of **10b** (CD_3OD, 400 MHz, 298 K).

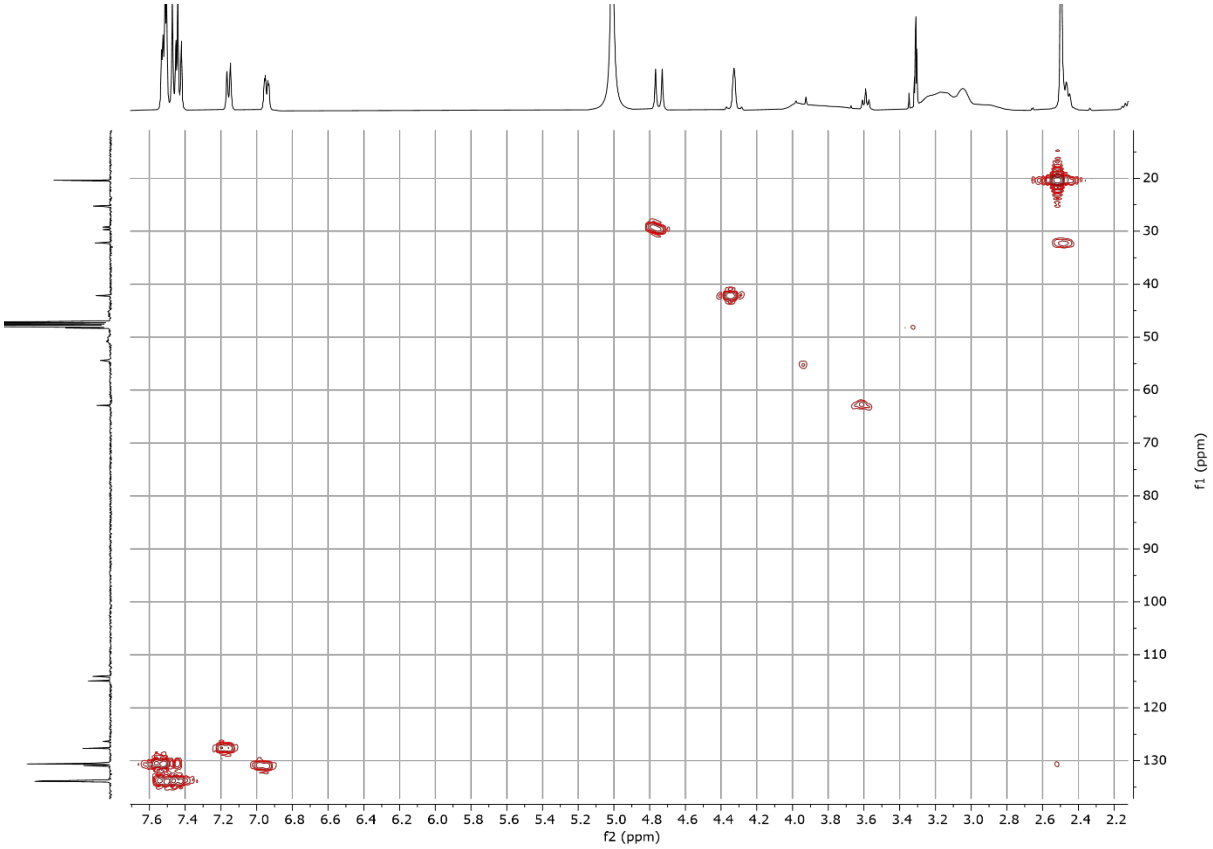

Figure 8.104 HMQC NMR spectrum of **10b** (CD_3OD, 298 K).

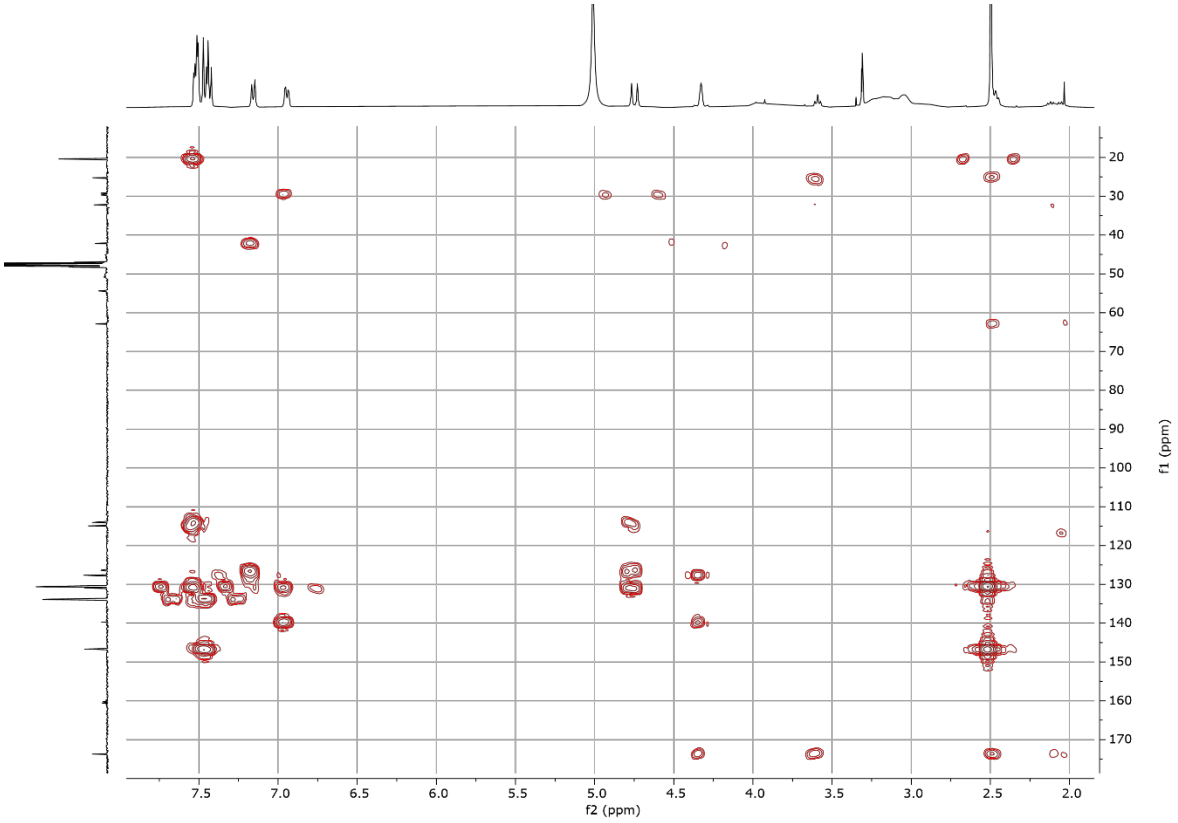

Figure 8.105 HMBC NMR spectrum of **10b** (CD_3OD, 298 K).

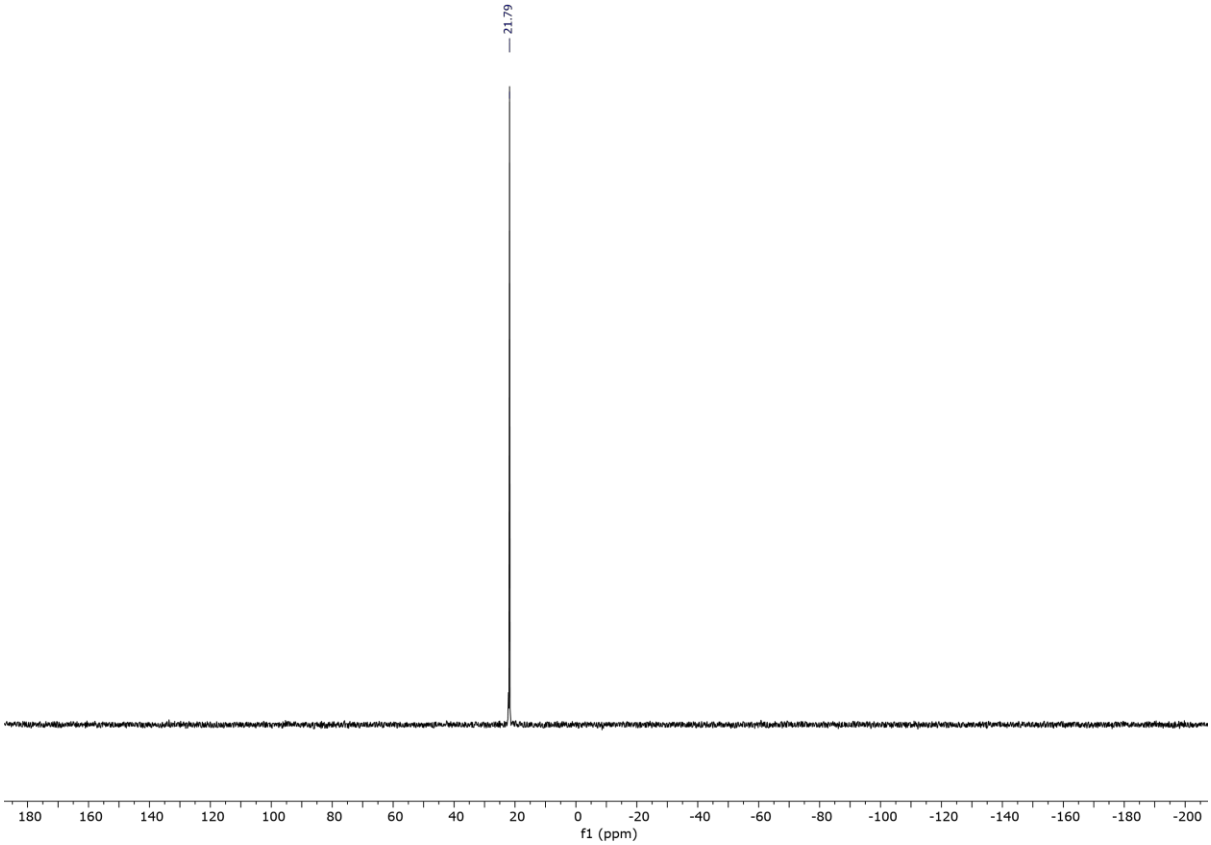

Figure 8.106 $^{31}P\{^{1}H\}$ NMR spectrum of **10b** (CD_3OD, 162 MHz, 298 K).

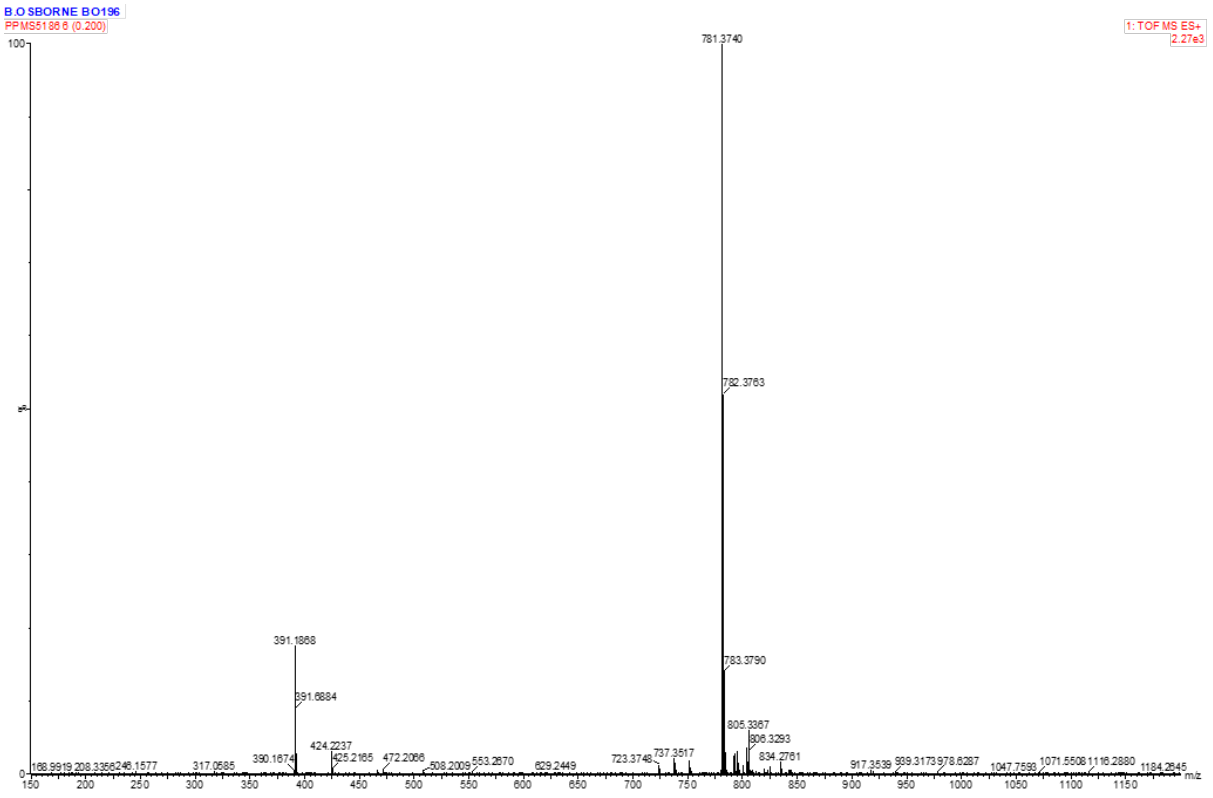

Figure 8.107 ES-TOF+ MS of **10b**.

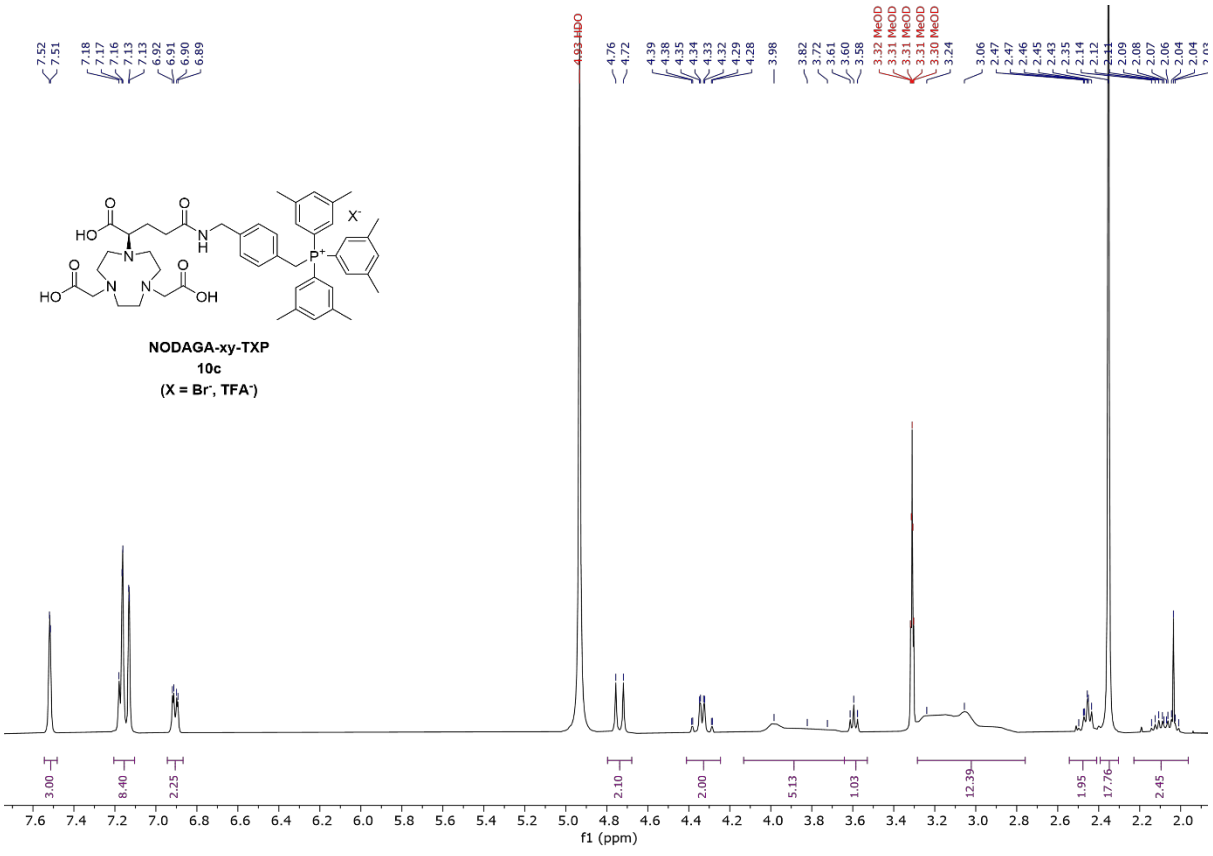

Figure 8.108 ^{1}H NMR spectrum of **10c** (CD_3OD, 400 MHz, 298 K).

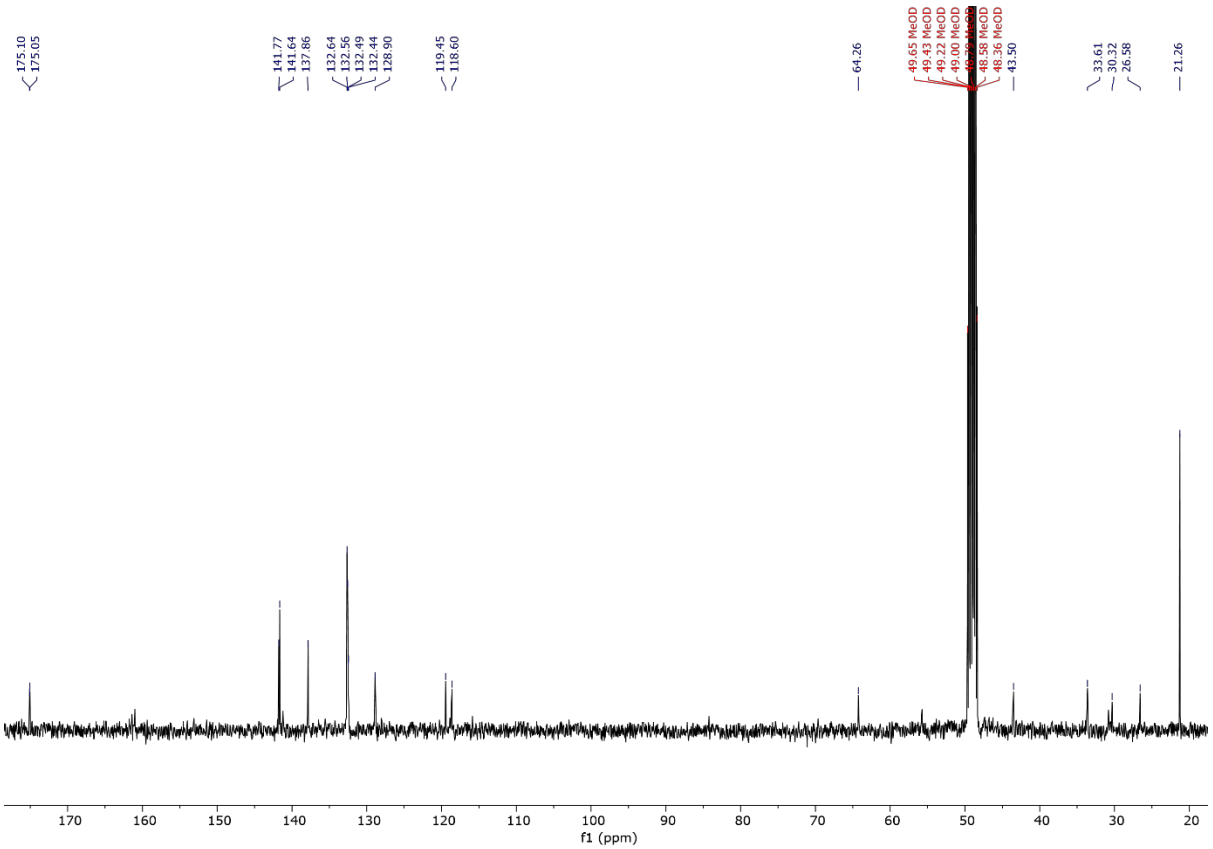

Figure 8.109 $^{13}C\{^{1}H\}$ NMR spectrum of **10c** (CD_3OD, 101 MHz, 298 K).

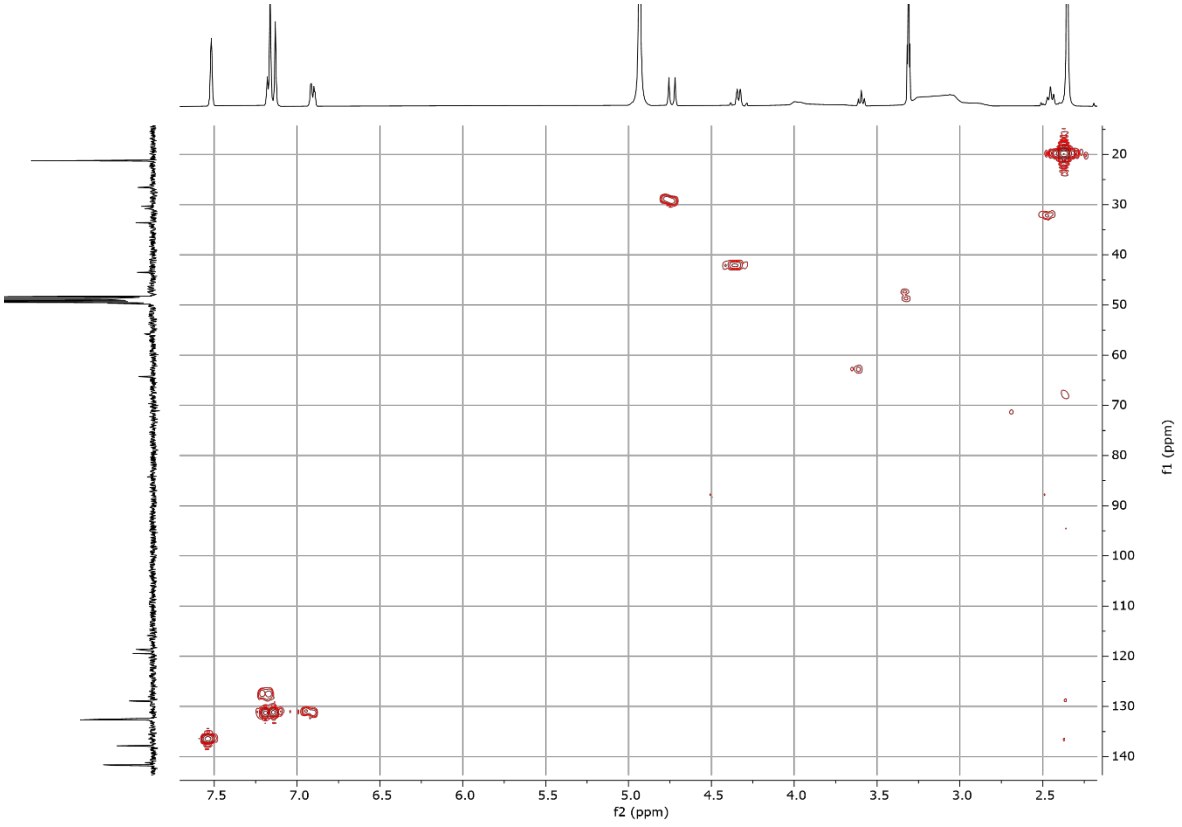

Figure 8.110 HMQC NMR spectrum of **10c** (CD_3OD, 298 K).

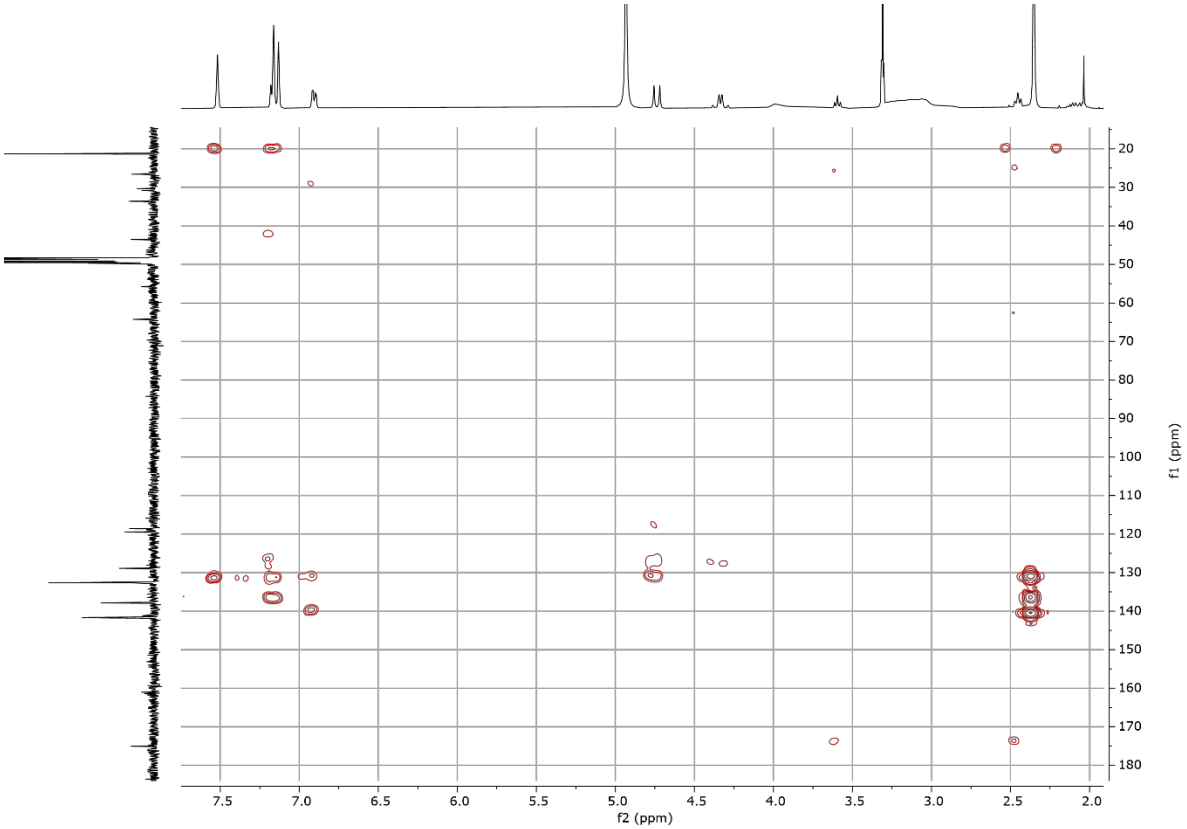

Figure 8.111 HMBC NMR spectrum of **10c** (CD_3OD, 298 K).

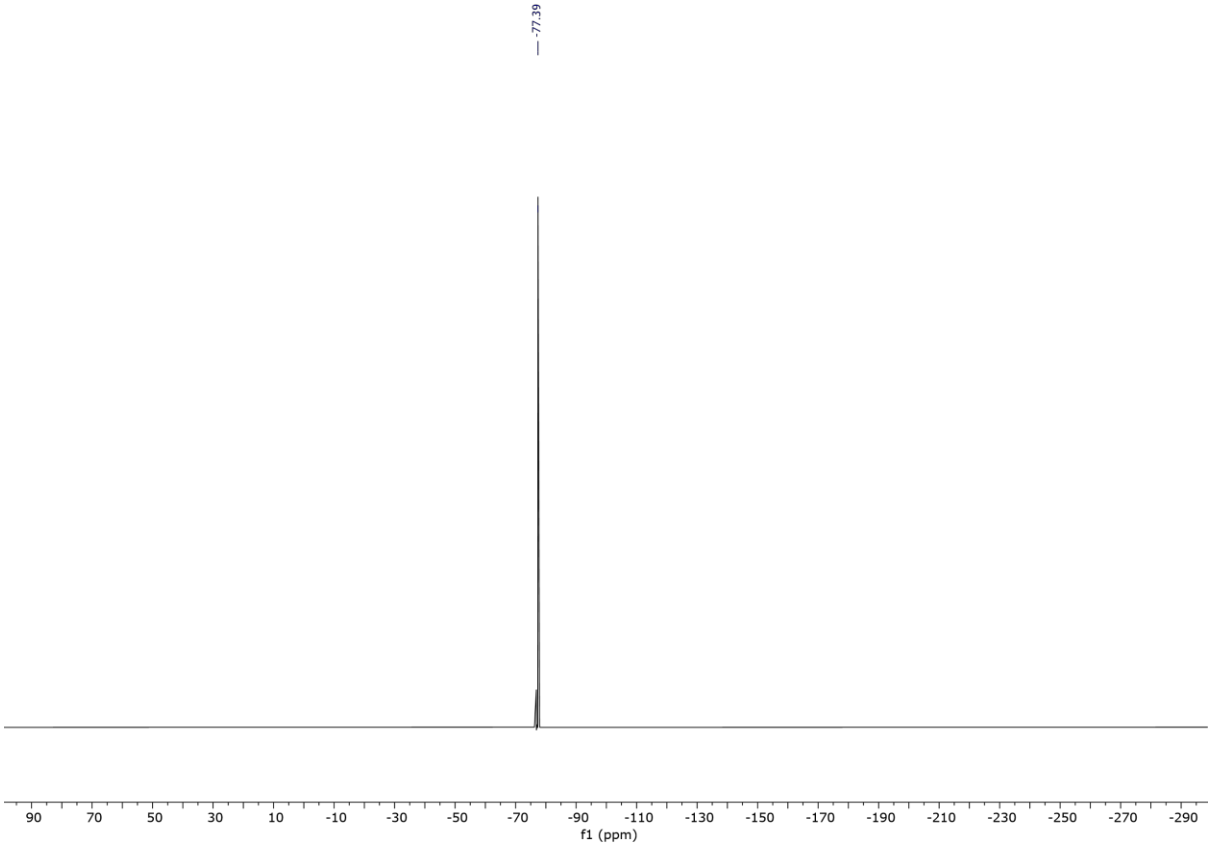

Figure 8.112 $^{19}F\{^1H\}$ NMR spectrum of **10c** (CD_3OD, 377 MHz, 298 K).

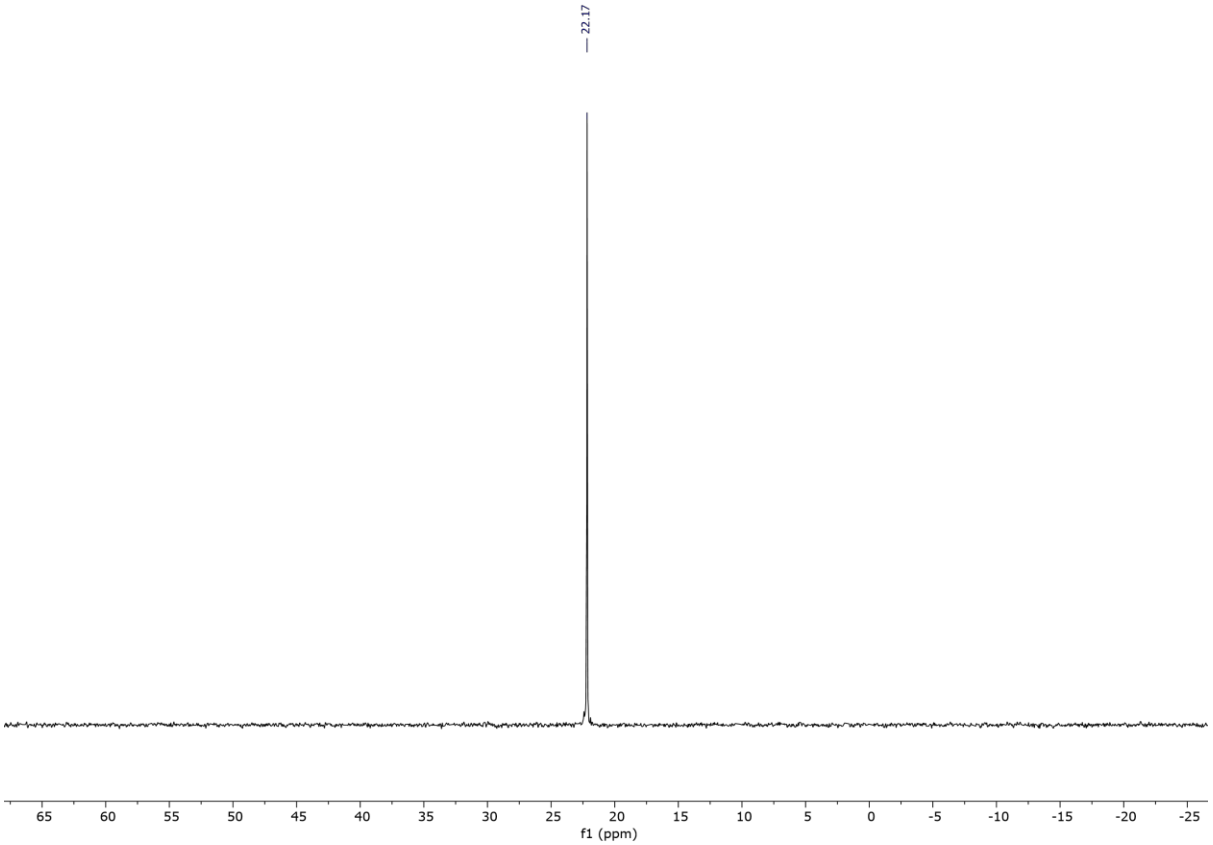

Figure 8.113 $^{31}P\{^{1}H\}$ NMR spectrum of **10c** (CD_3OD, 162 MHz, 298 K).

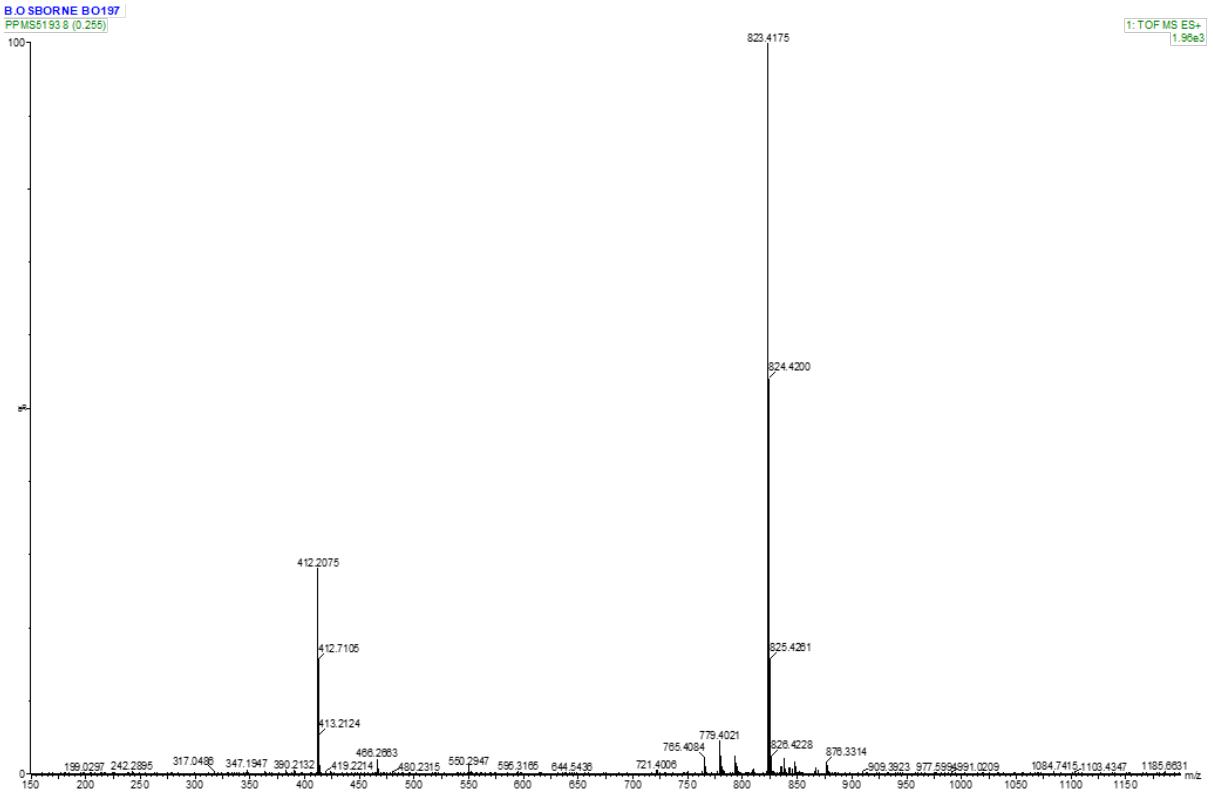

Figure 8.114 ES-TOF+ MS of **10c**.

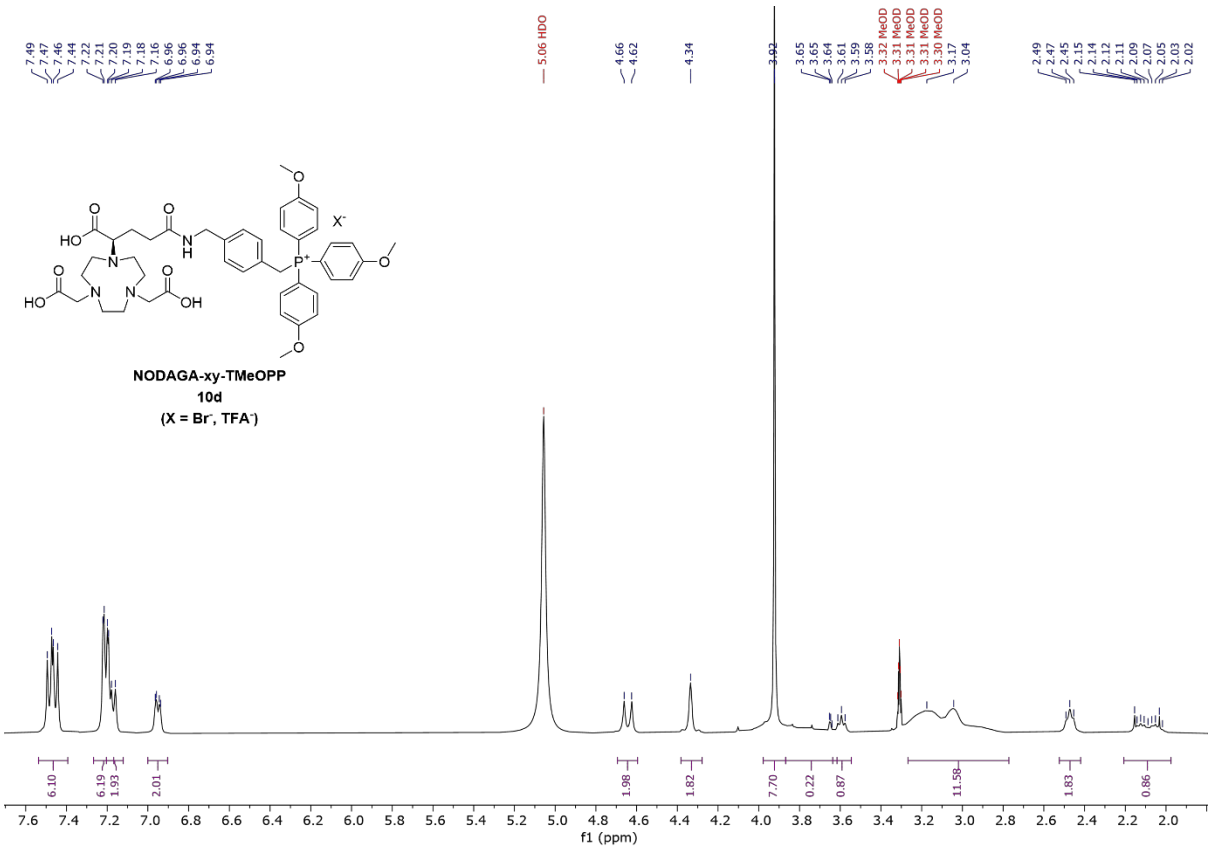

Figure 8.115 ^{1}H NMR spectrum of **10d** (CD_3OD, 400 MHz, 298 K).

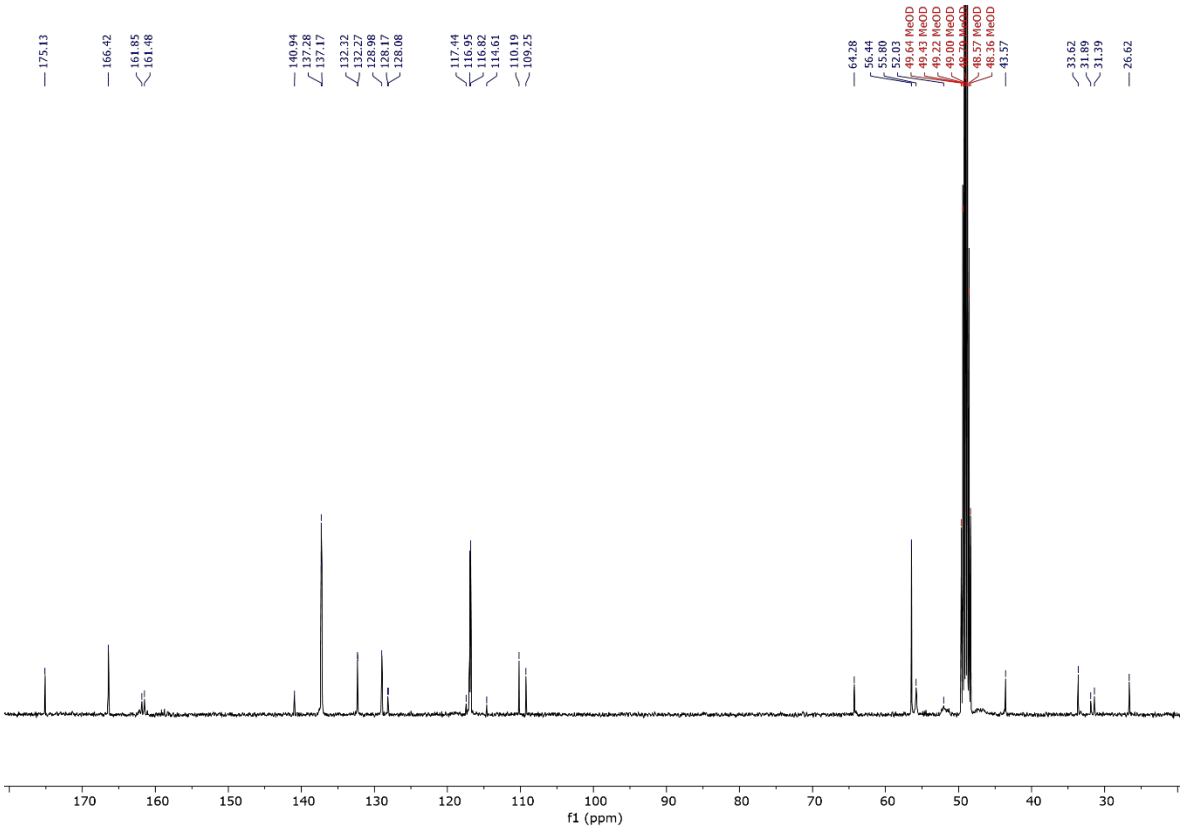

Figure 8.116 $^{13}C\{^{1}H\}$ NMR spectrum of **10d** (CD_3OD, 101 MHz, 298 K).

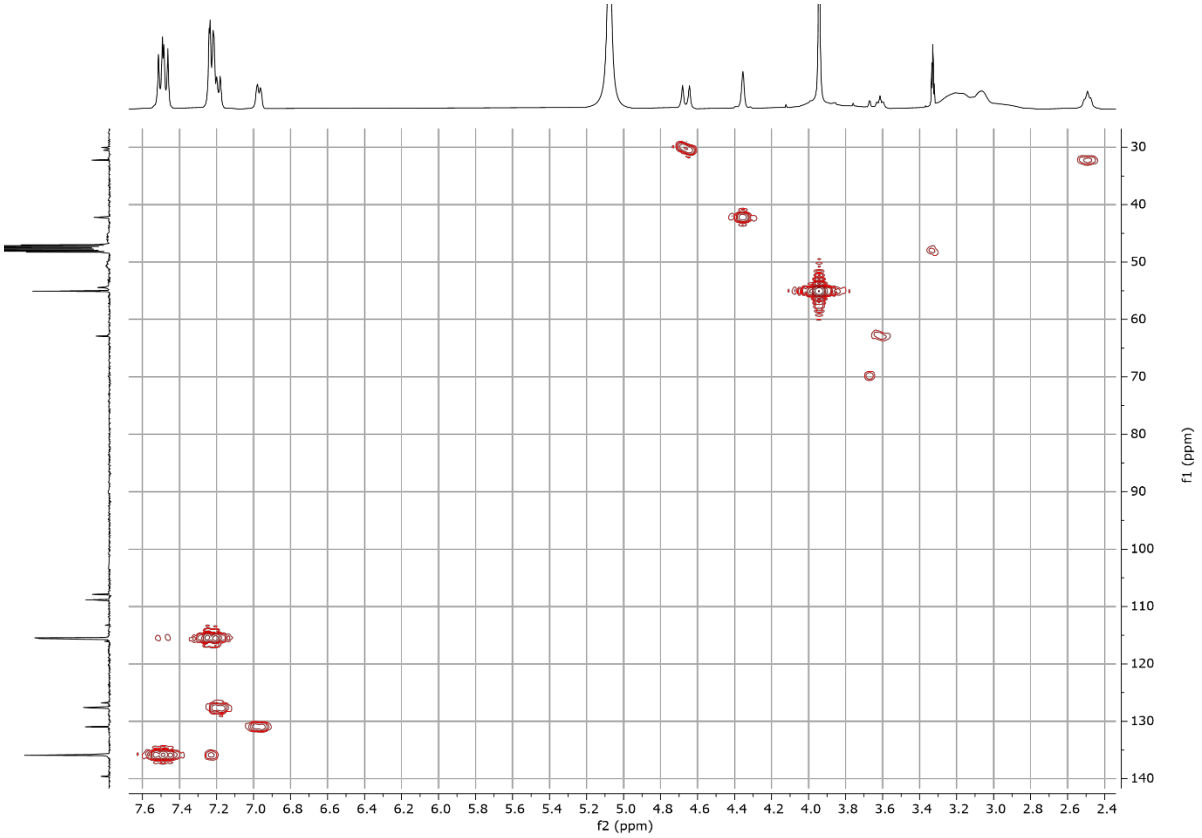

Figure 8.117 HMQC NMR spectrum of **10d** (CD_3OD, 298 K).

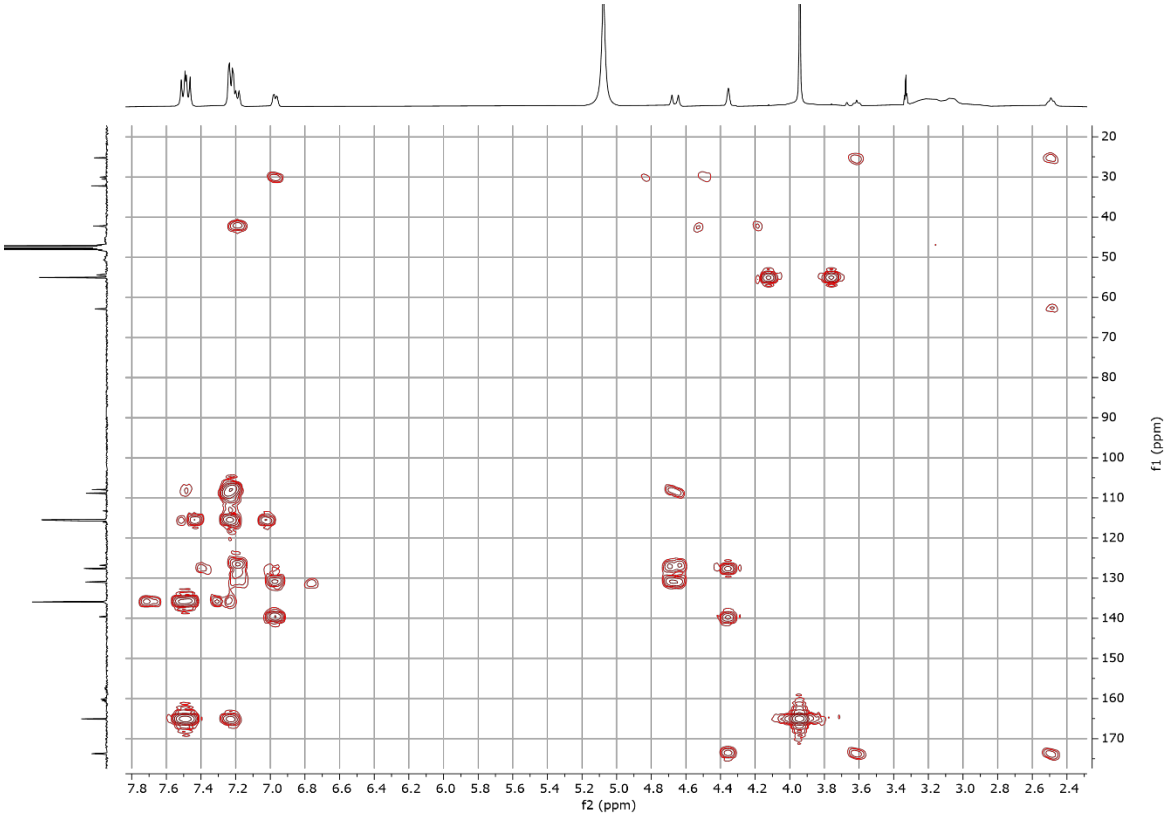

Figure 8.118 HMBC NMR spectrum of **10d** (CD_3OD, 298 K).

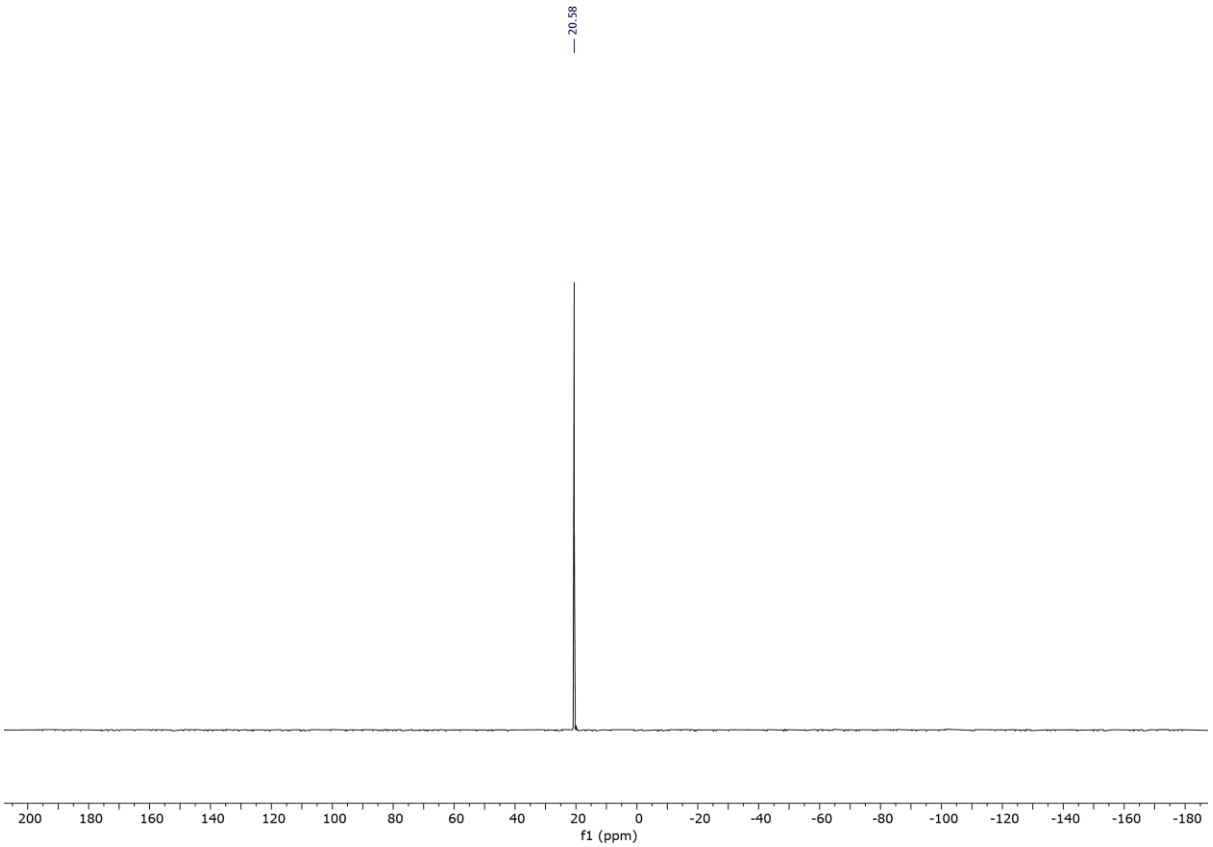

Figure 8.119 $^{31}P\{^{1}H\}$ NMR spectrum of **10d** (CD_3OD, 162 MHz, 298 K).

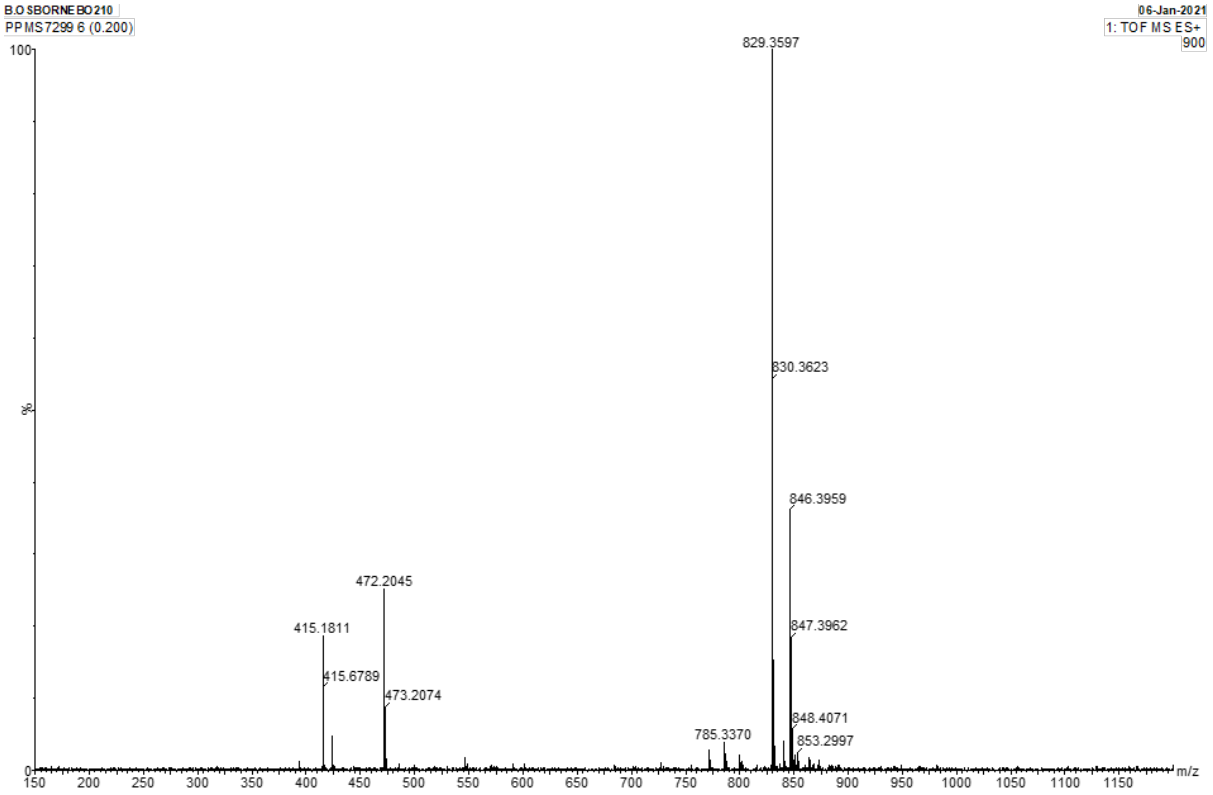

Figure 8.120 ES-TOF+ MS of **10d**.

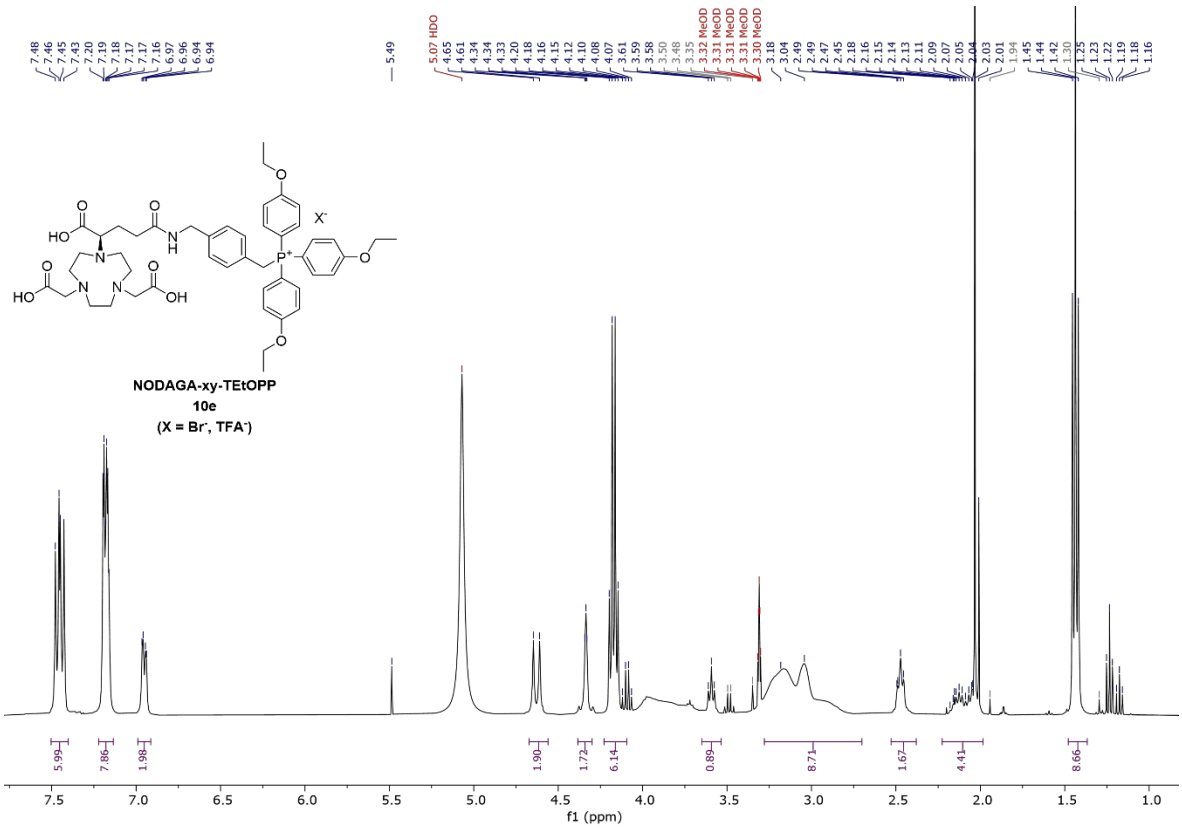

Figure 8.121 ^{1}H NMR spectrum of **10e** (CD_3OD, 400 MHz, 298 K).

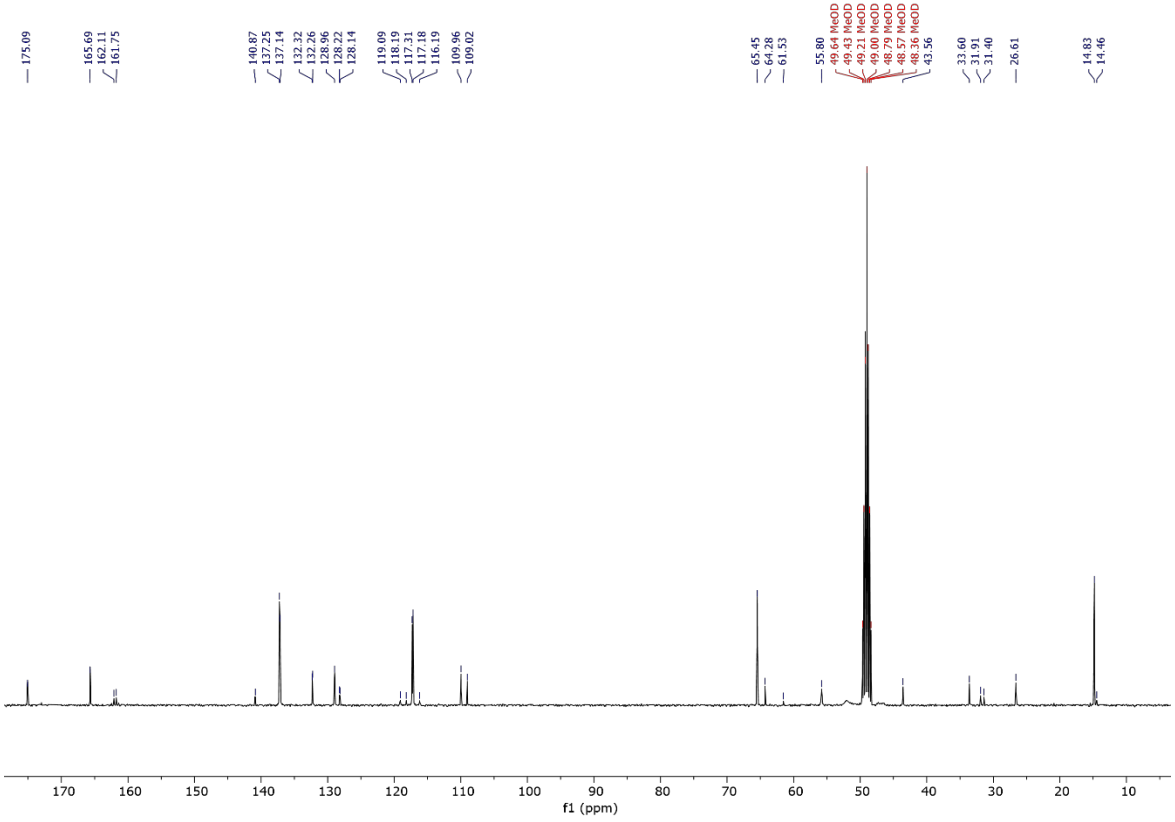

Figure 8.122 $^{13}C\{^{1}H\}$ NMR spectrum of **10e** (CD_3OD, 101 MHz, 298 K).

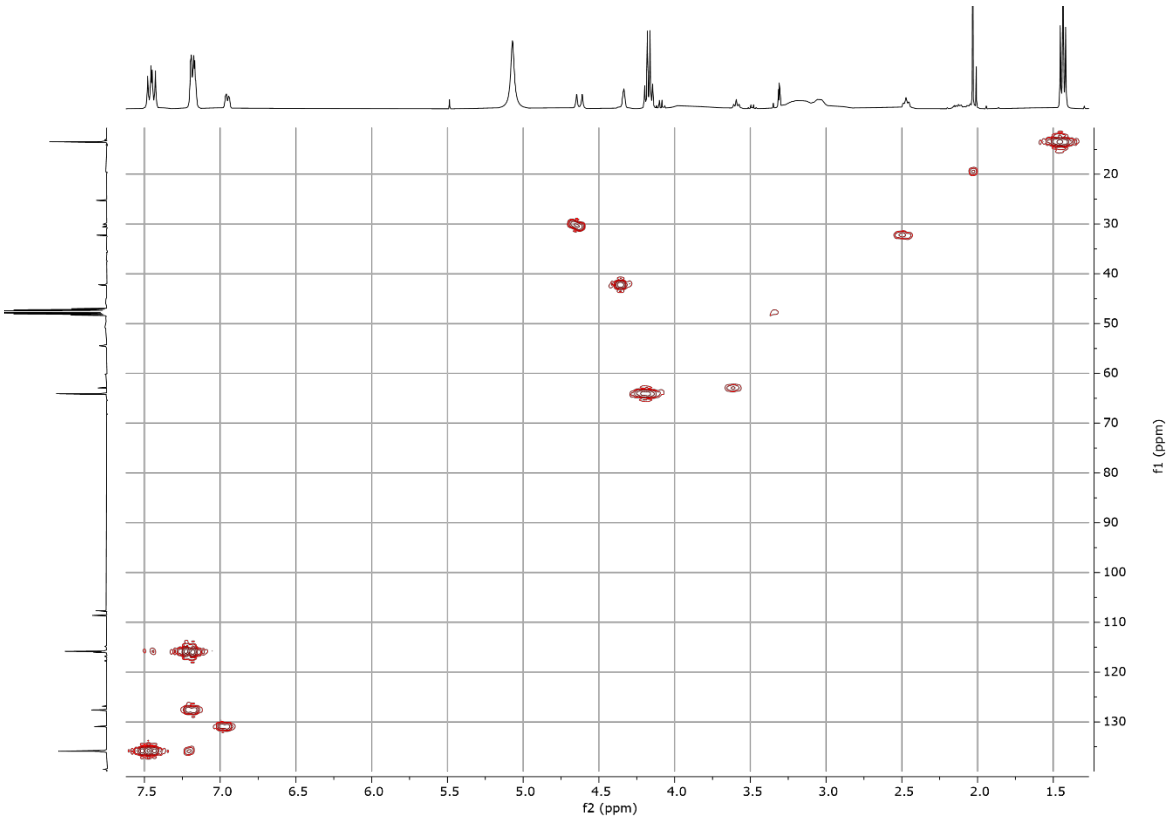

Figure 8.123 HMQC NMR spectrum of **10e** (CD_3OD, 298 K).

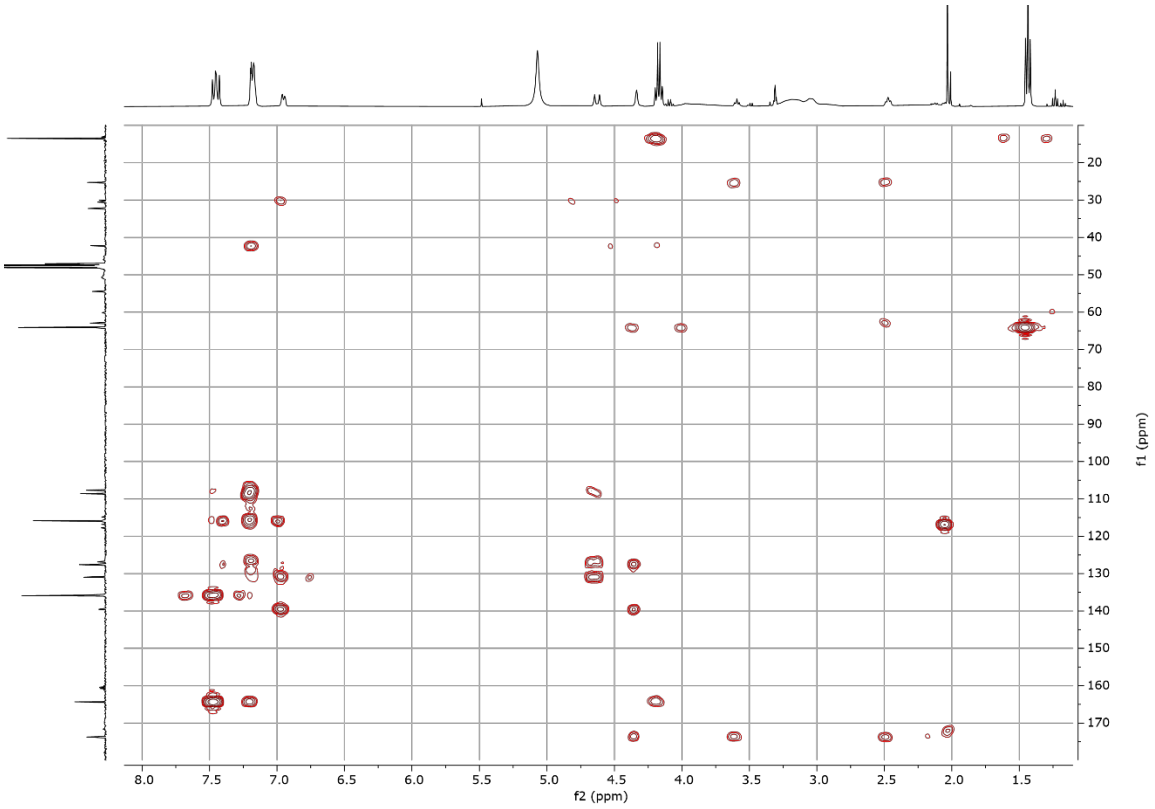

Figure 8.124 HMBC NMR spectrum of **10e** (CD_3OD, 298 K).

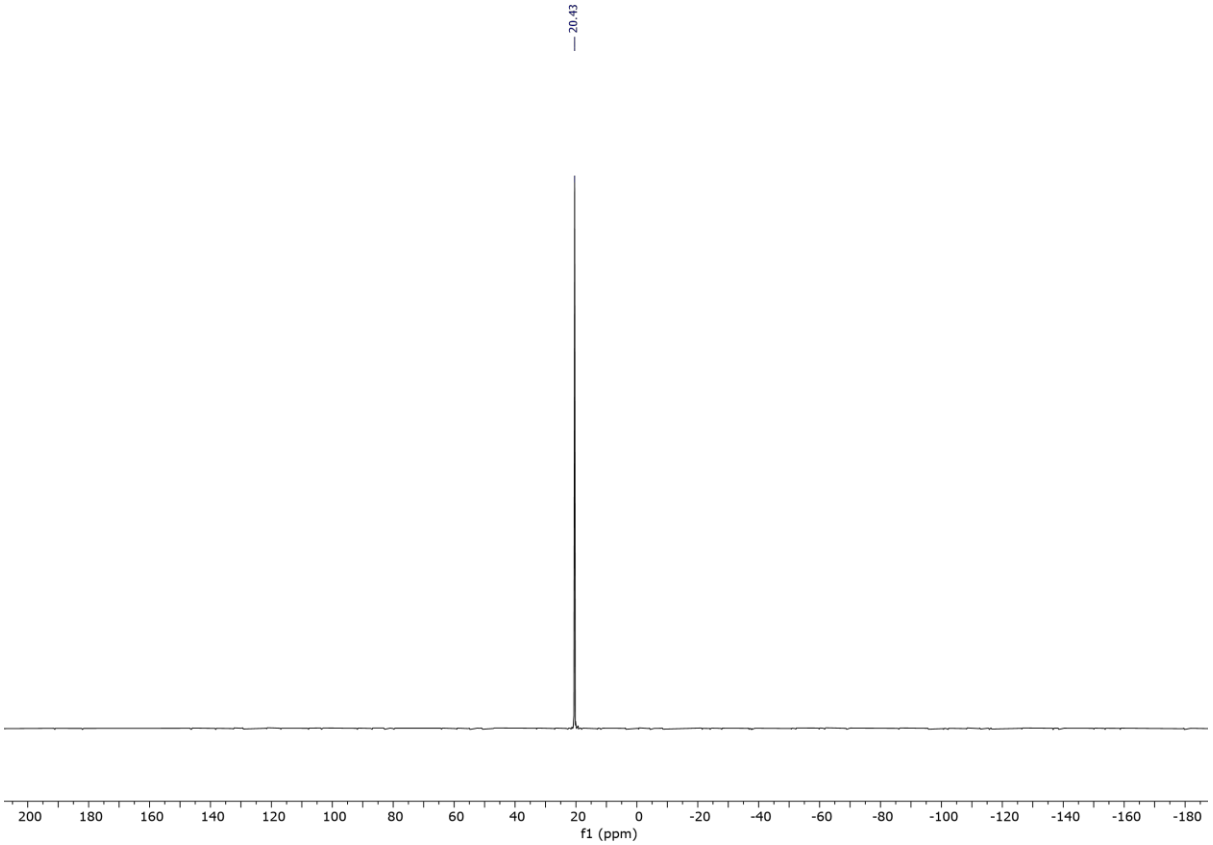

Figure 8.125 $^{31}P\{^{1}H\}$ NMR spectrum of **10e** (CD_3OD, 162 MHz, 298 K).

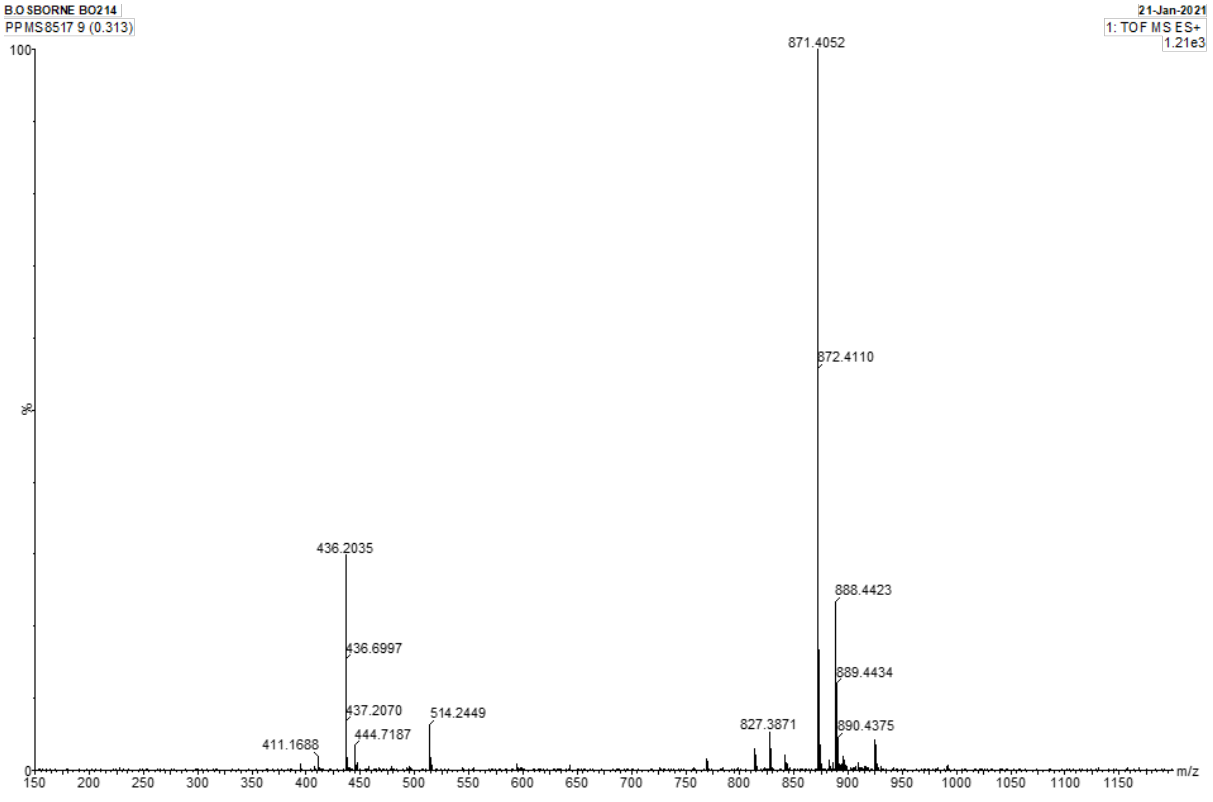

Figure 8.126 ES-TOF+ MS of **10e**.

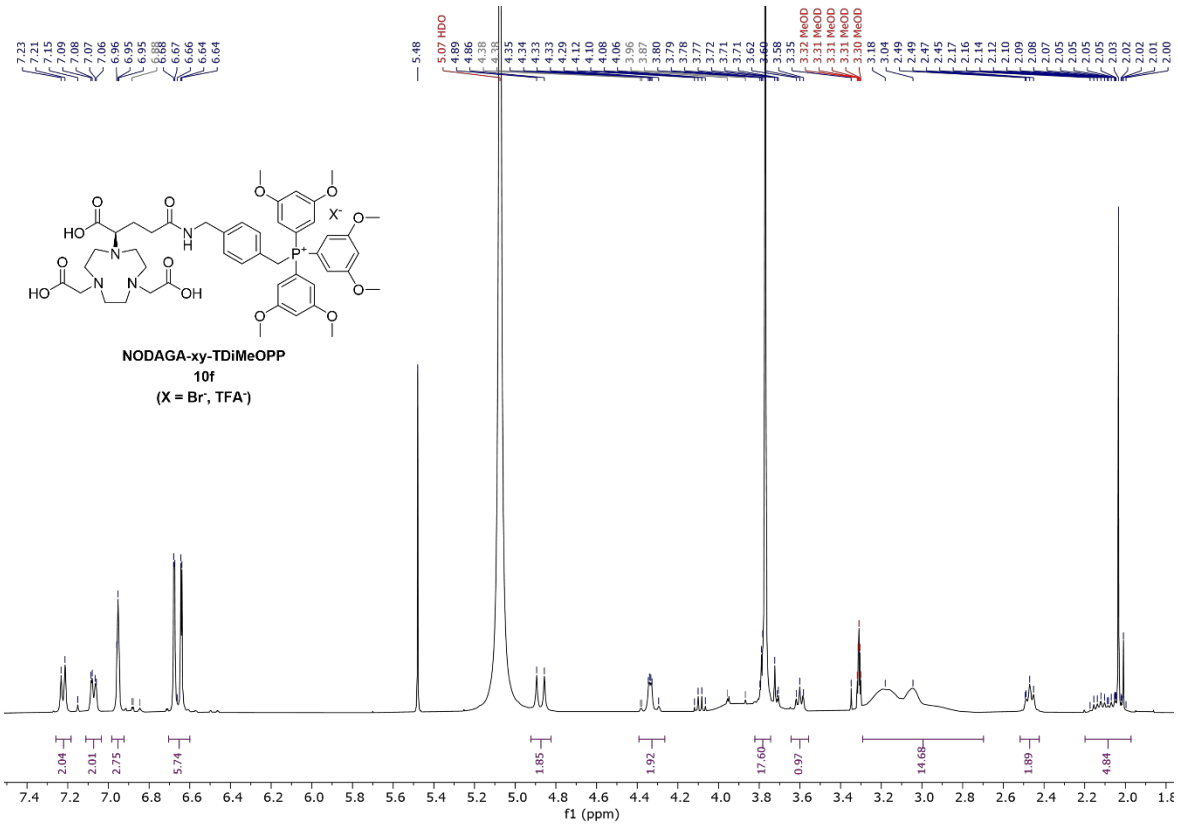

Figure 8.127 ^{1}H NMR spectrum of **10f** (CD_3OD, 400 MHz, 298 K).

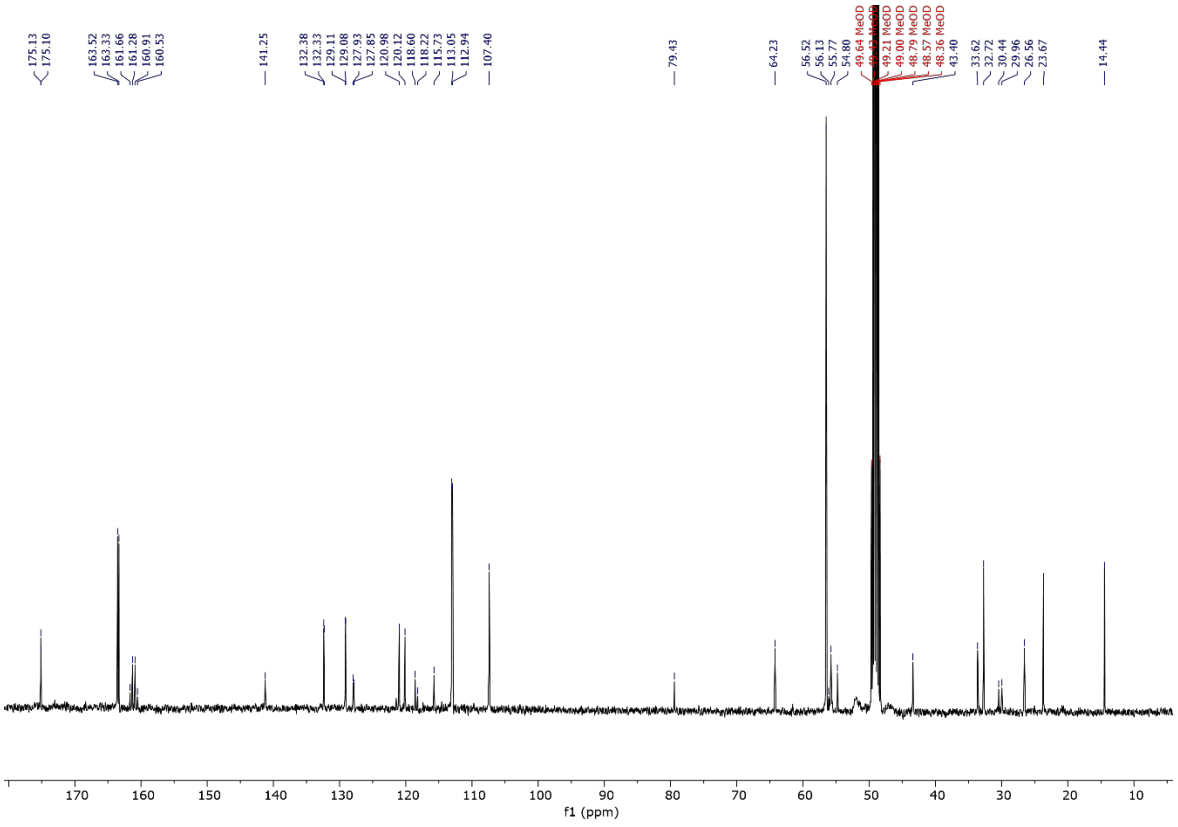

Figure 8.128 $^{13}C\{^{1}H\}$ NMR spectrum of **10f** (CD_3OD, 101 MHz, 298 K).

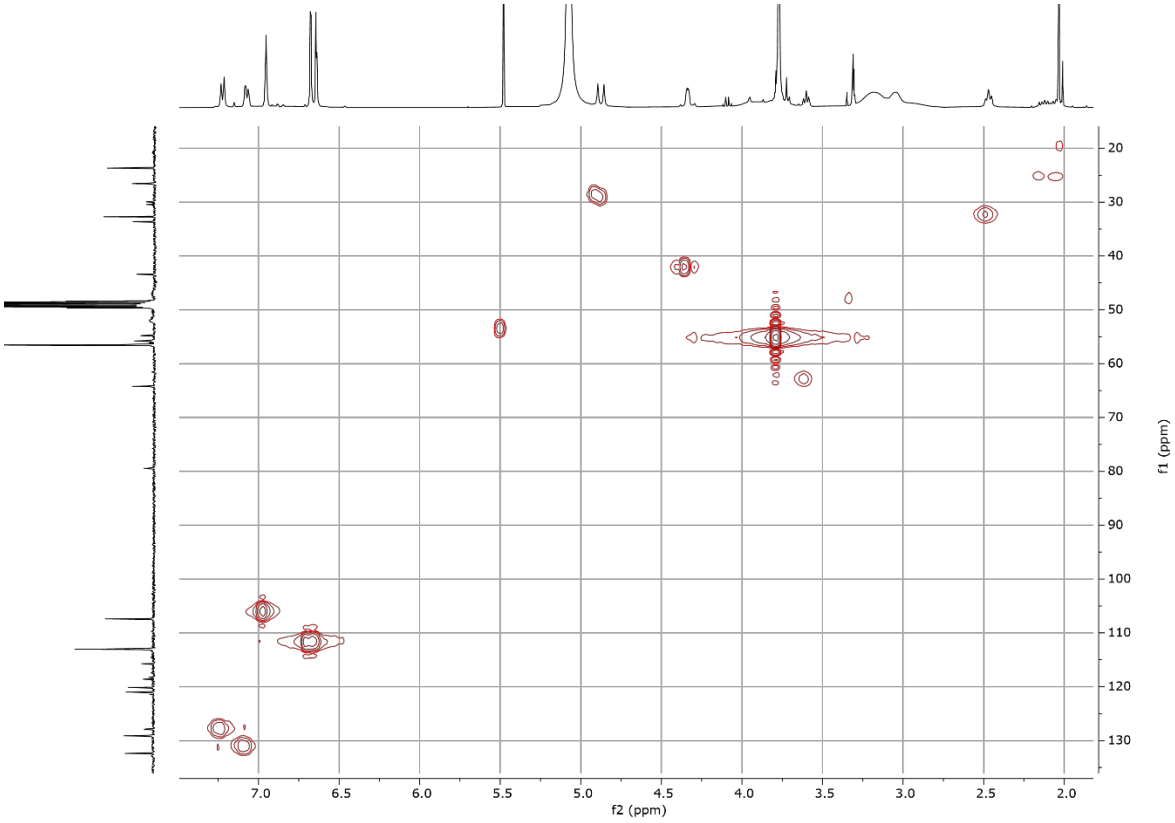

Figure 8.129 HMQC NMR spectrum of **10f** (CD_3OD, 298 K).

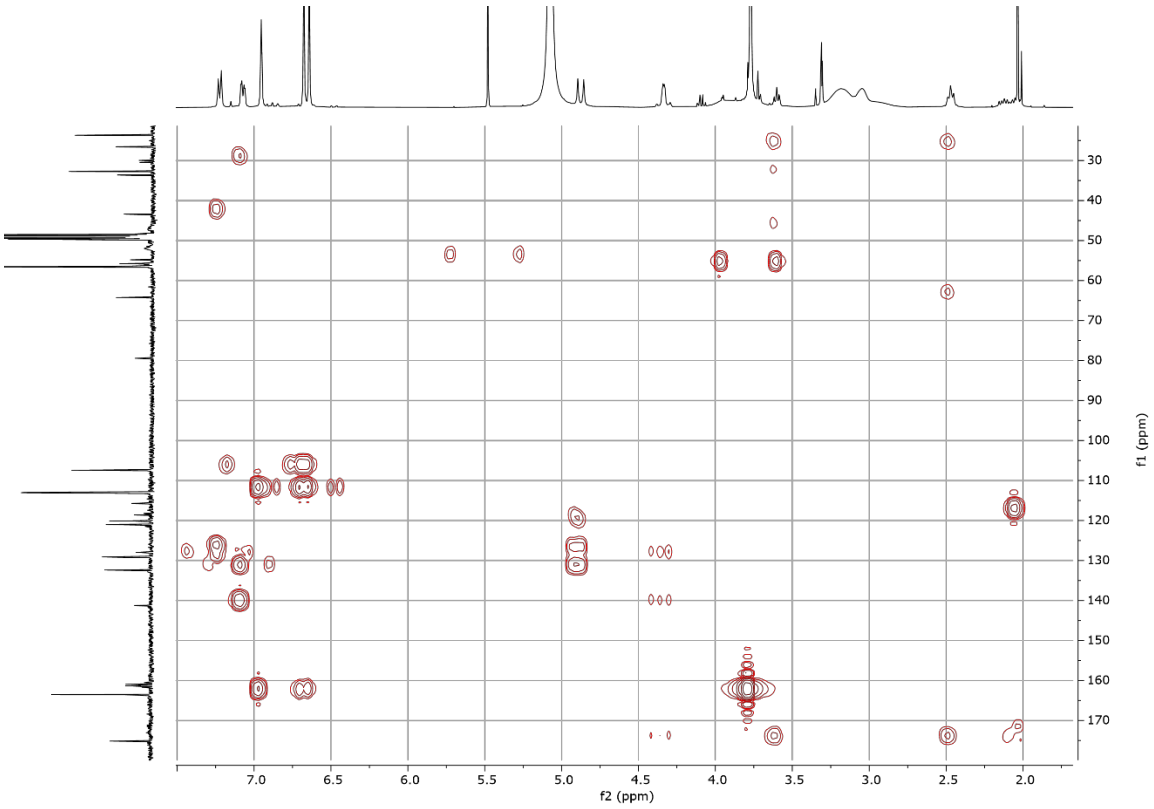

Figure 8.130 HMBC NMR spectrum of **10f** (CD_3OD, 298 K).

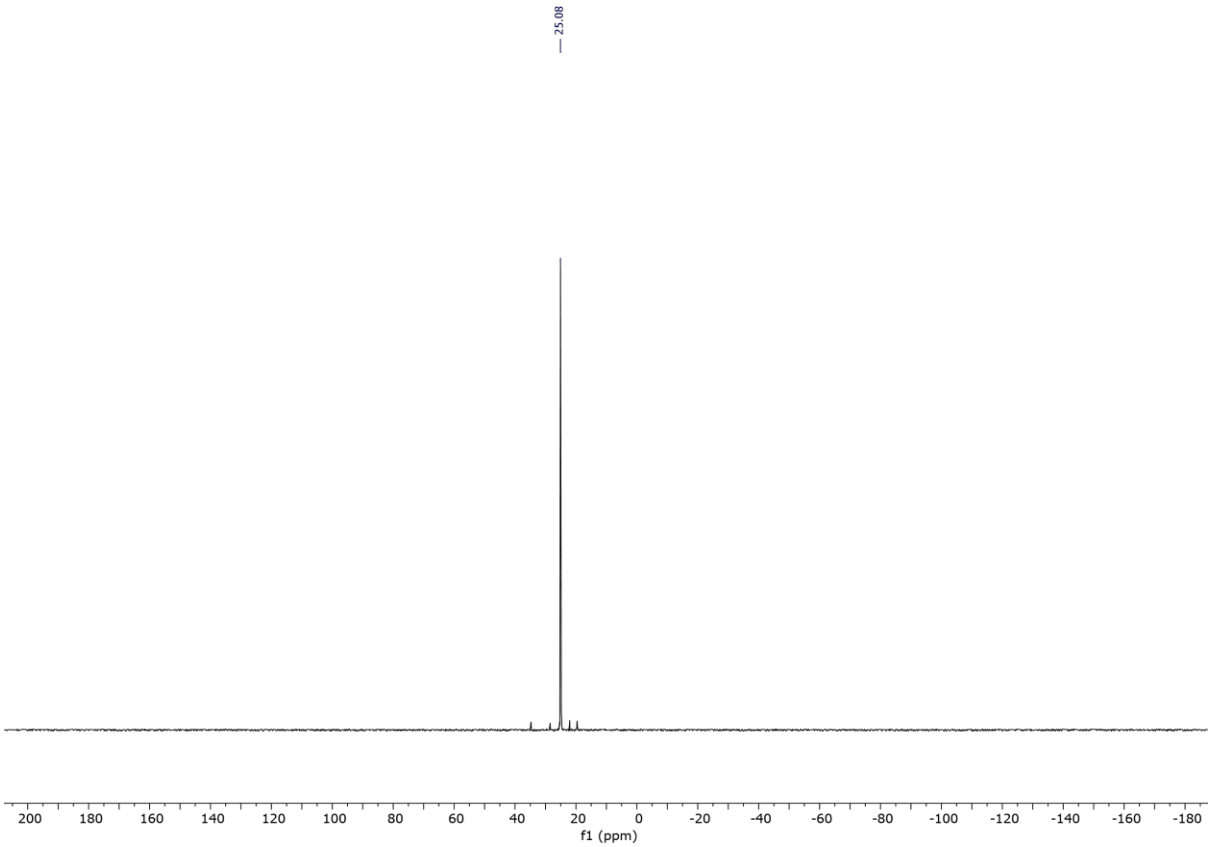

Figure 8.131 $^{31}P\{^{1}H\}$ NMR spectrum of **10f** (CD_3OD, 162 MHz, 298 K).

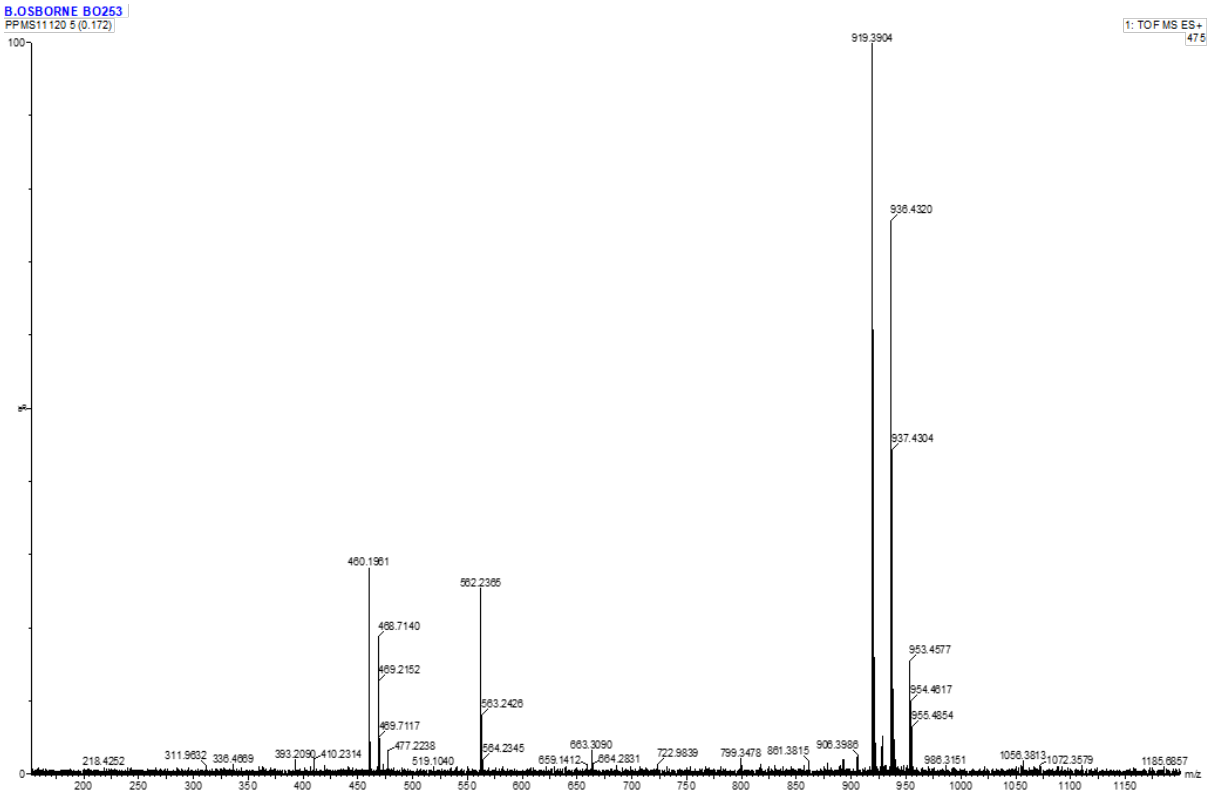

Figure 8.132 ES-TOF+ MS of **10f**.

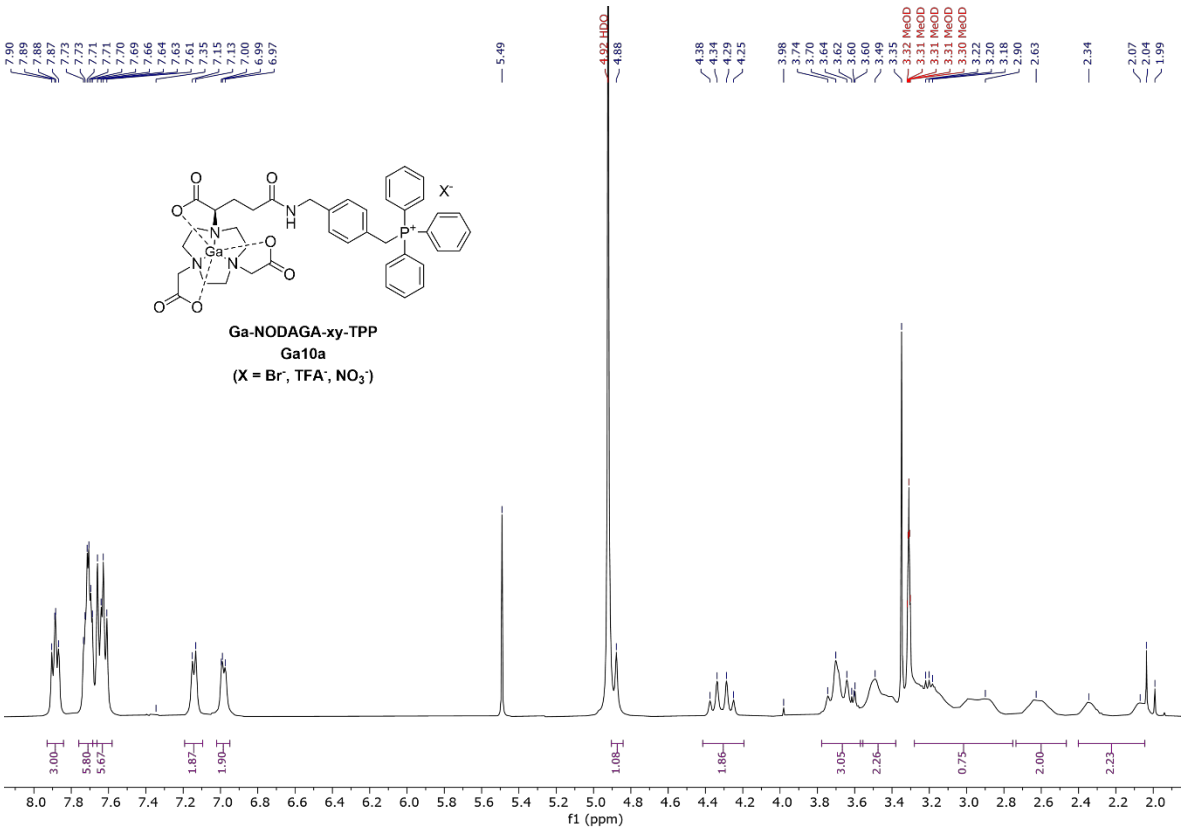

Figure 8.133 ^{1}H NMR spectrum of **Ga10a** (CD_3OD, 400 MHz, 298 K).

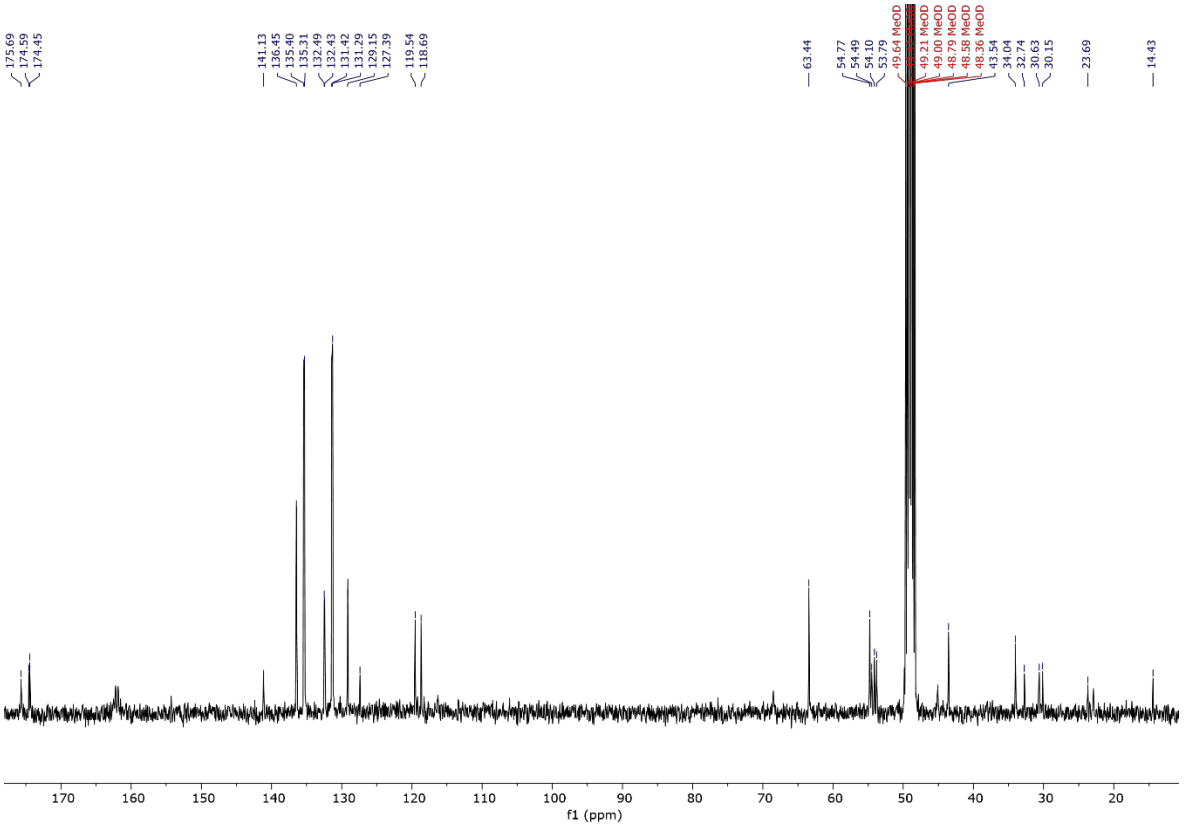

Figure 8.134 $^{13}C\{^{1}H\}$ NMR spectrum of **Ga10a** (CD_3OD, 101 MHz, 298 K).

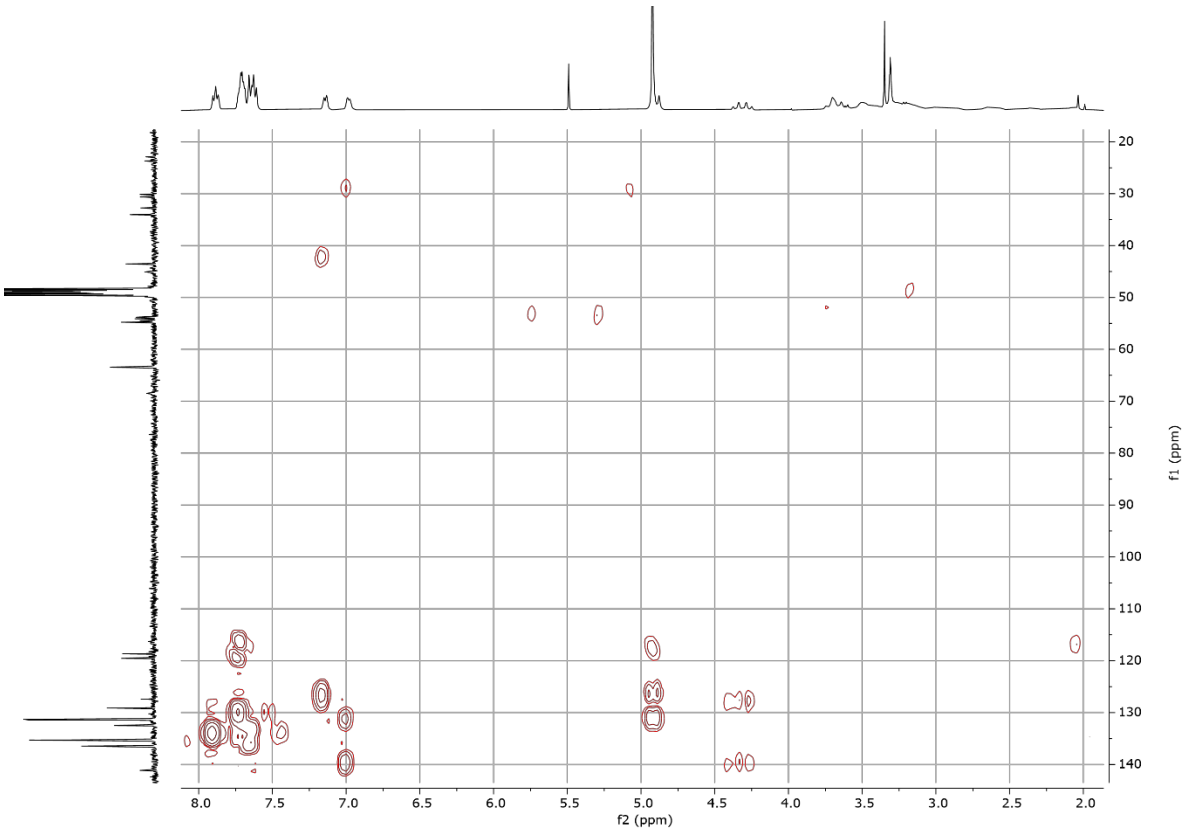

Figure 8.135 HMQC NMR spectrum of **Ga10a** (CD_3OD, 298 K).

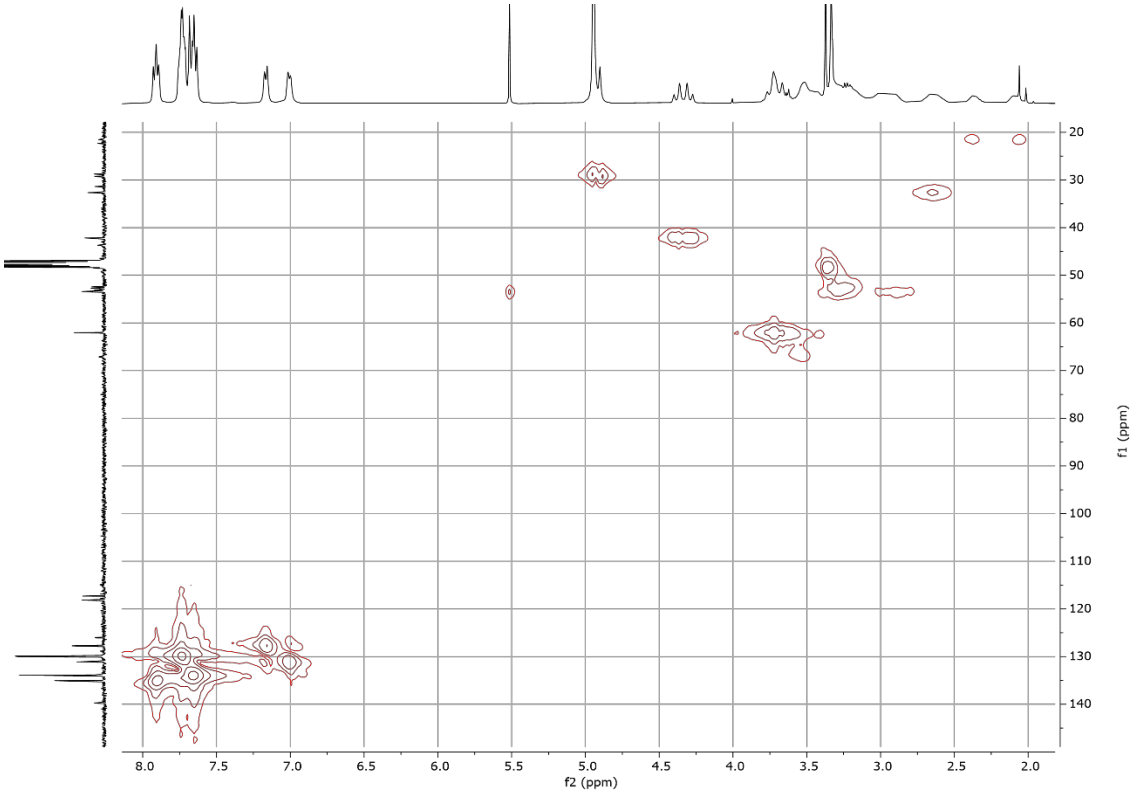

Figure 8.136 HMBC NMR spectrum of **Ga10a** (CD_3OD, 298 K).

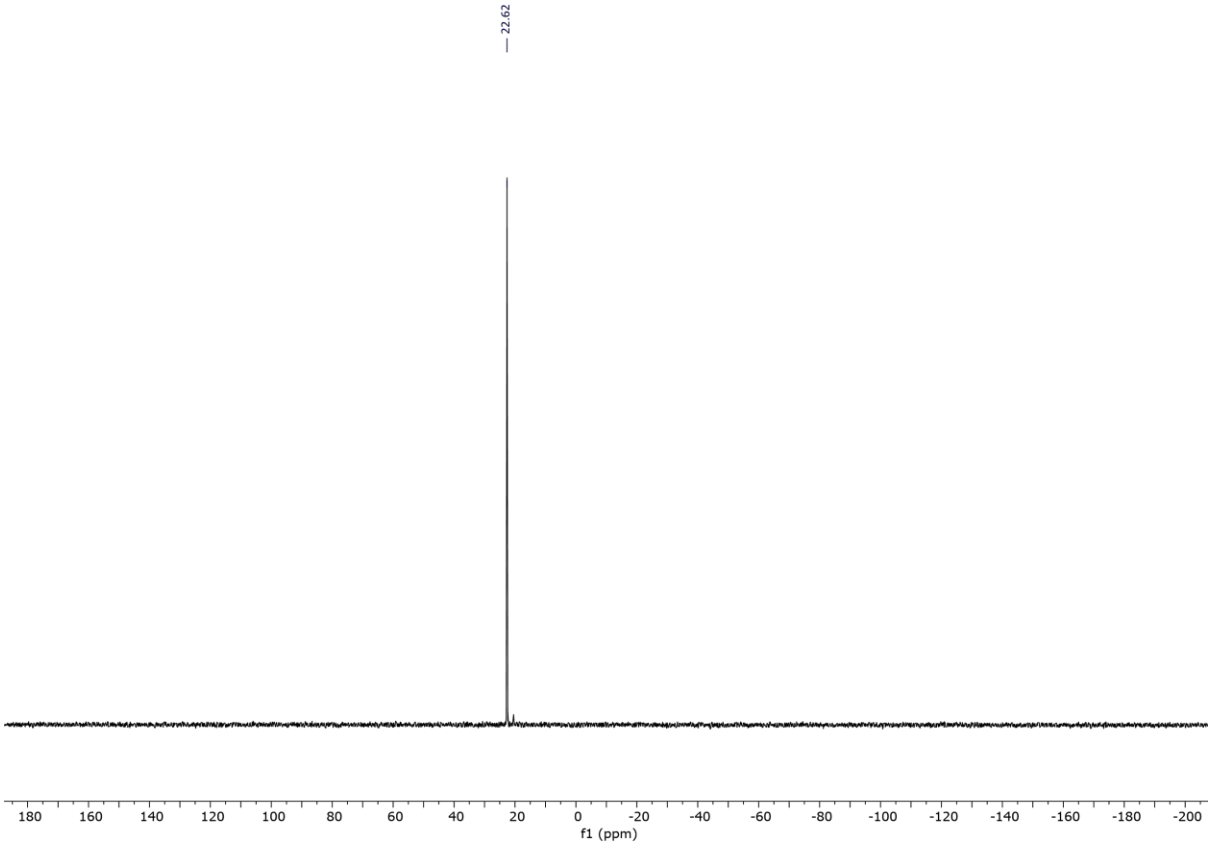

Figure 8.137 $^{31}P\{^{1}H\}$ NMR spectrum of **Ga10a** (CD_3OD, 162 MHz, 298 K).

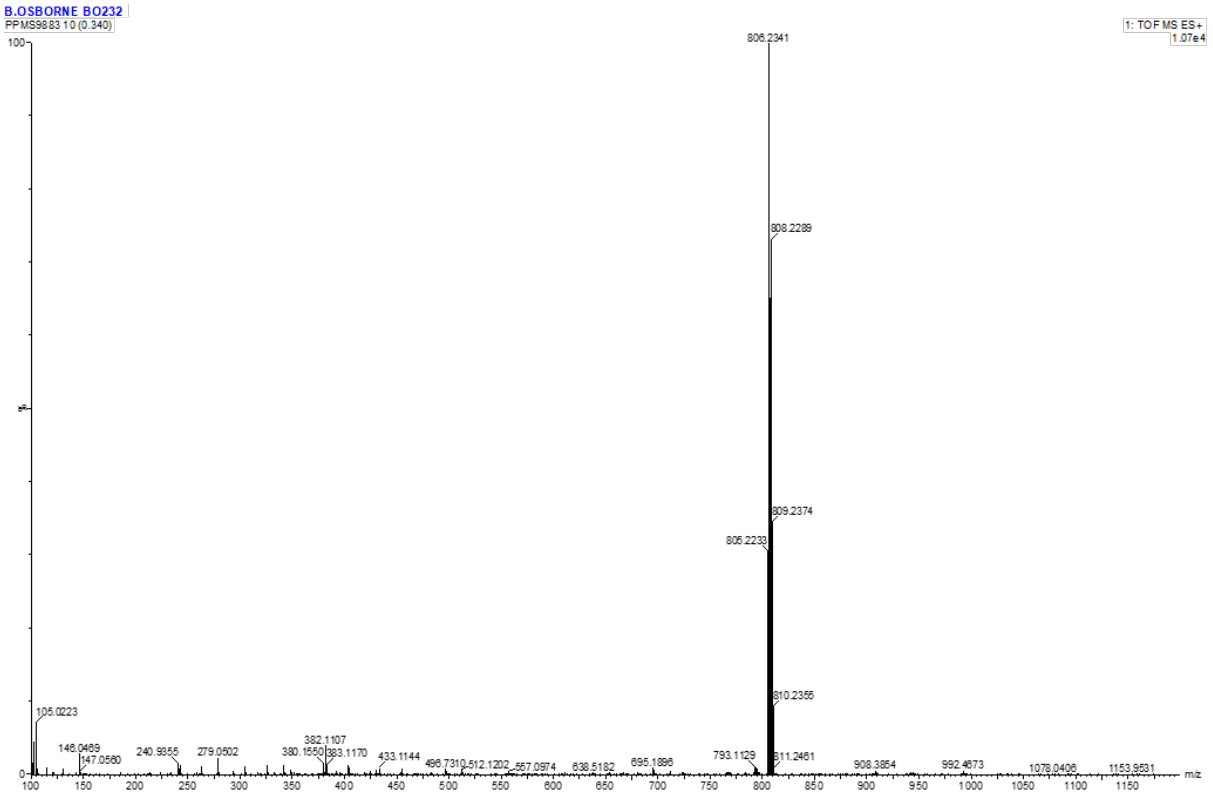

Figure 8.138 ES-TOF+ MS of **Ga10a**.

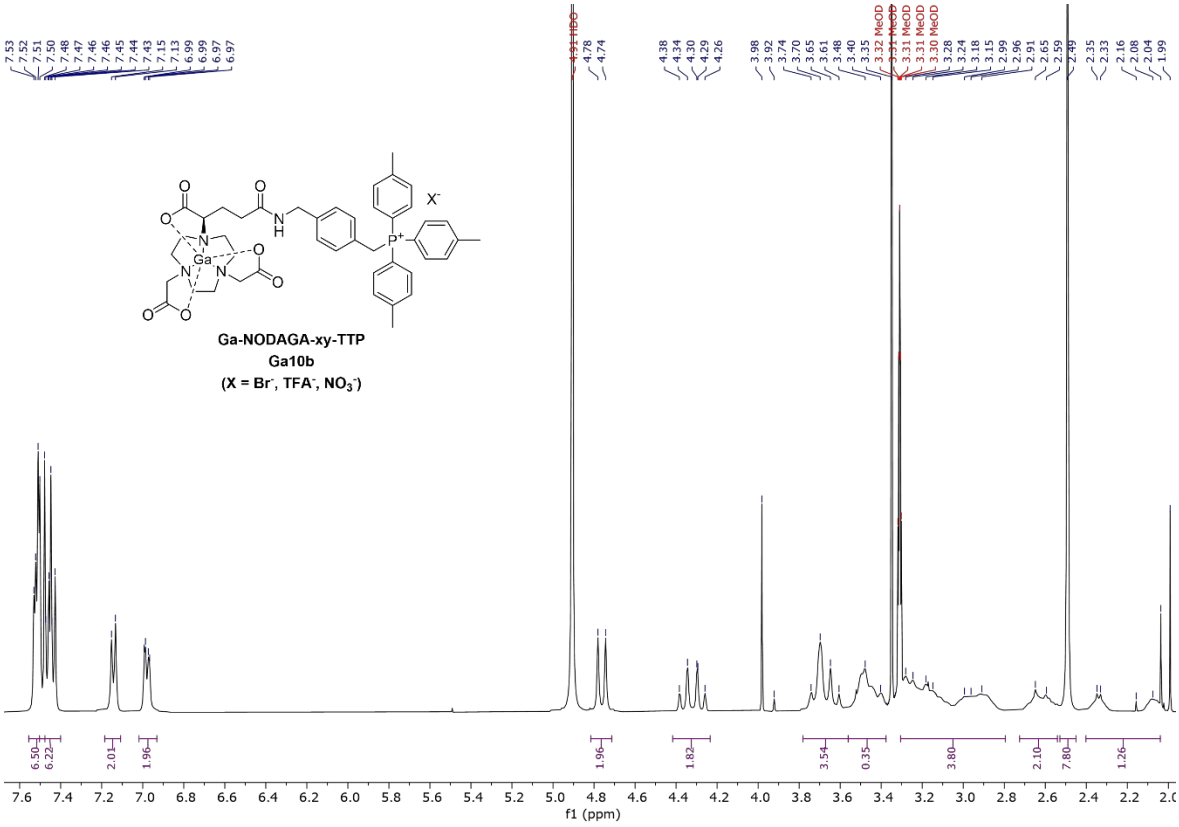

Figure 8.139 ^{1}H NMR spectrum of **Ga10b** (CD_3OD, 400 MHz, 298 K).

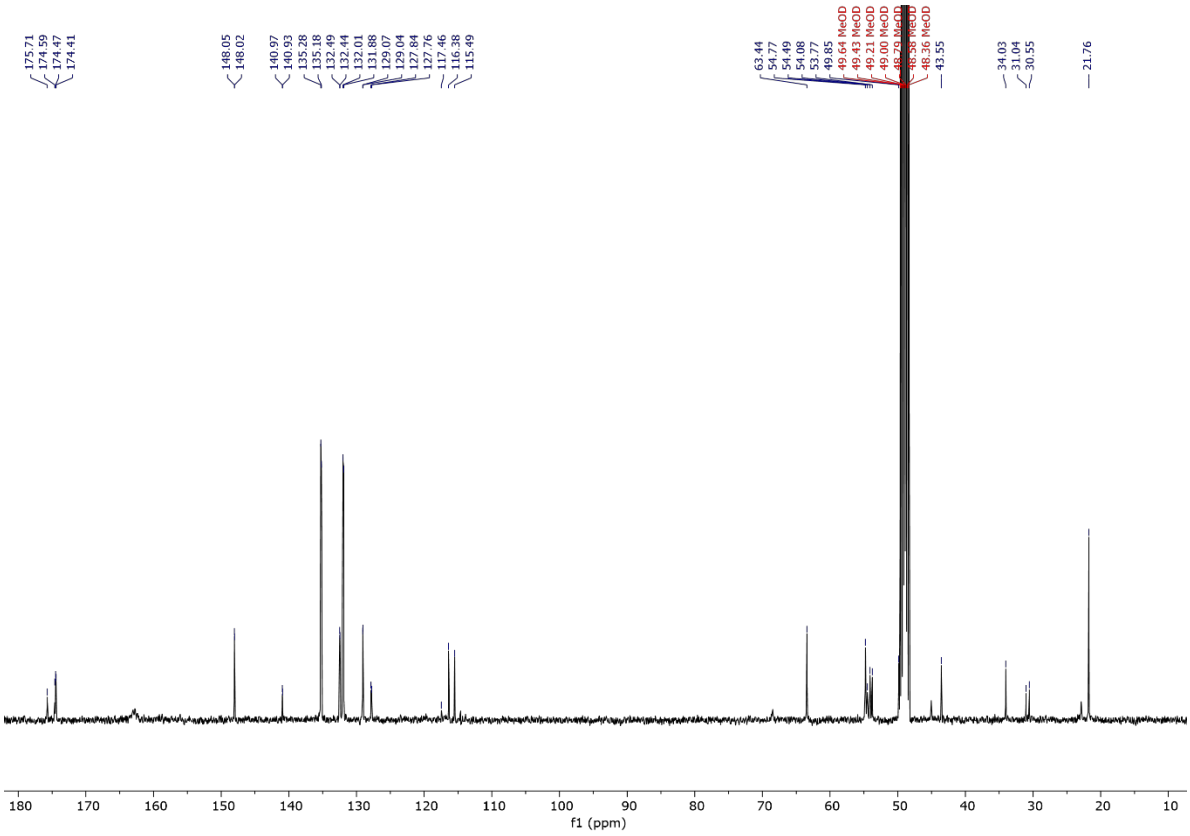

Figure 8.140 $^{13}C\{^{1}H\}$ NMR spectrum of **Ga10b** (CD_3OD, 101 MHz, 298 K).

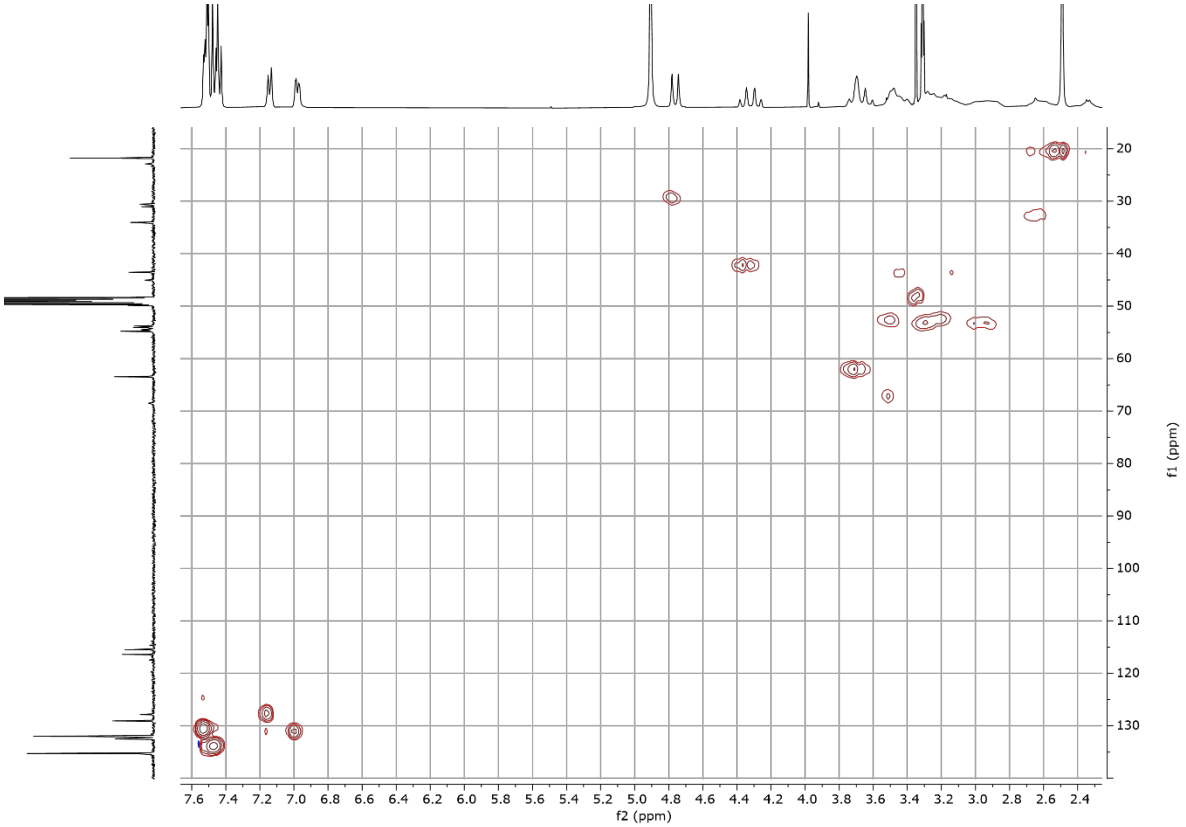

Figure 8.141 HMQC NMR spectrum of **Ga10b** (CD_3OD, 298 K).

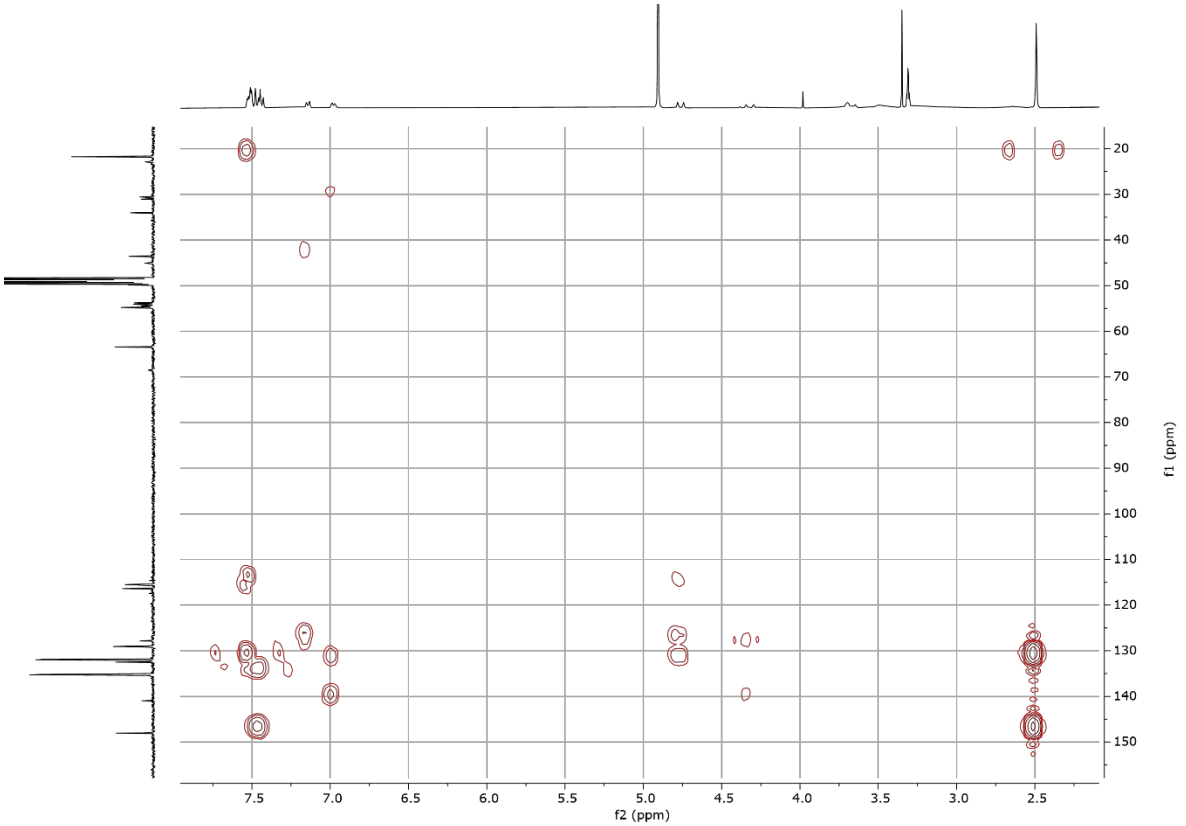

Figure 8.142 HMBC NMR spectrum of **Ga10b** (CD_3OD, 298 K).

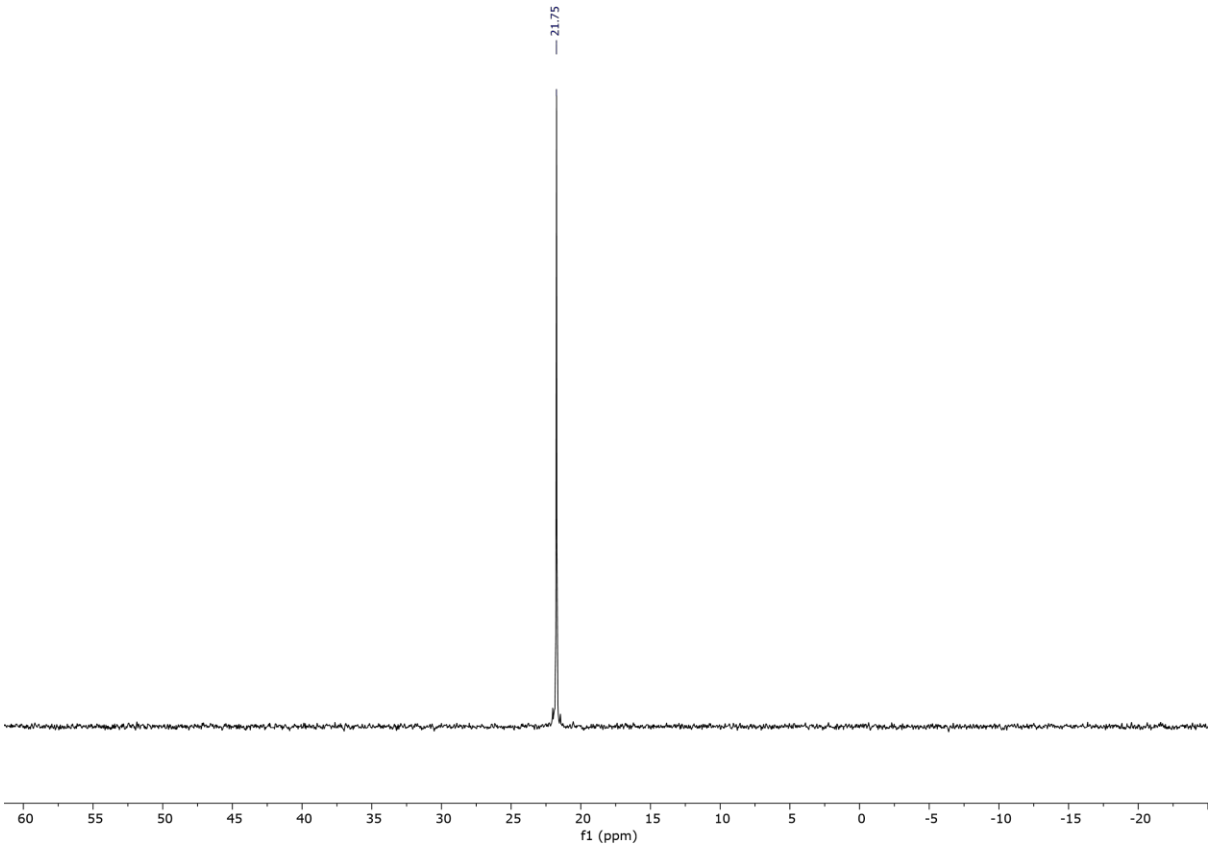

Figure 8.143 $^{31}P\{^{1}H\}$ NMR spectrum of **Ga10b** (CD_3OD, 162 MHz, 298 K).

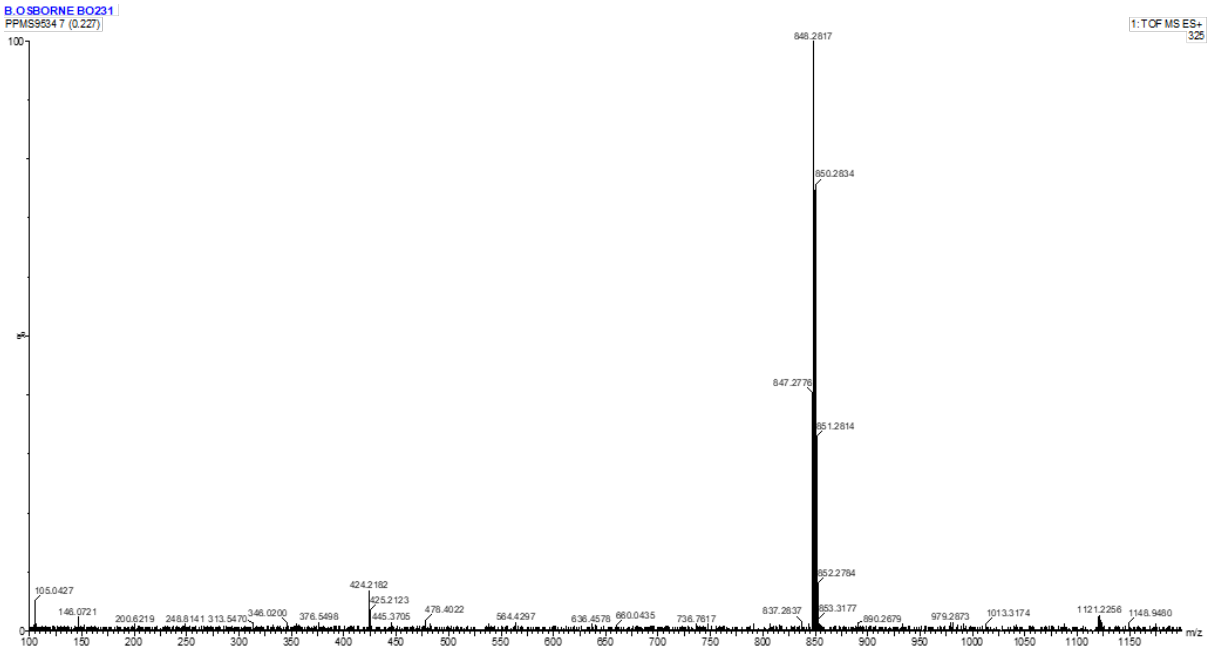

Figure 8.144 ES-TOF+ MS of **Ga10b**.

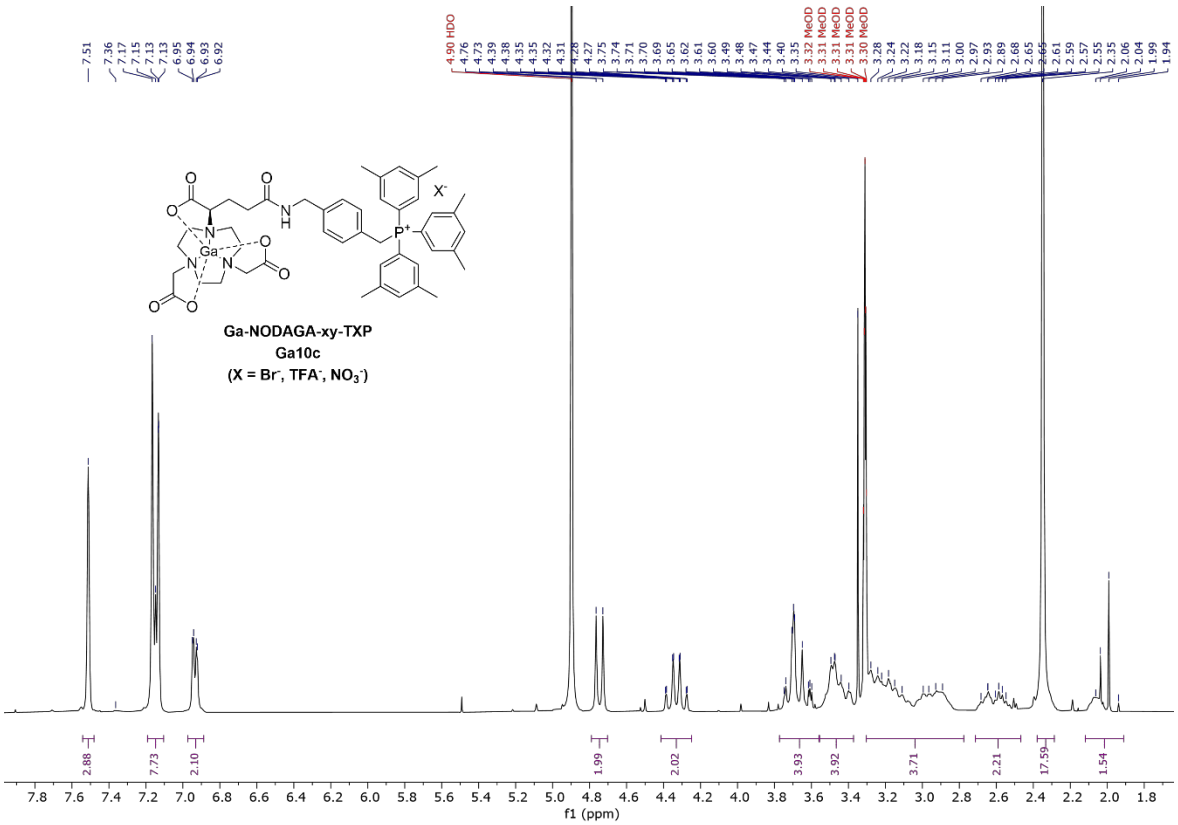

Figure 8.145 ^{1}H NMR spectrum of **Ga10c** (CD_3OD, 400 MHz, 298 K).

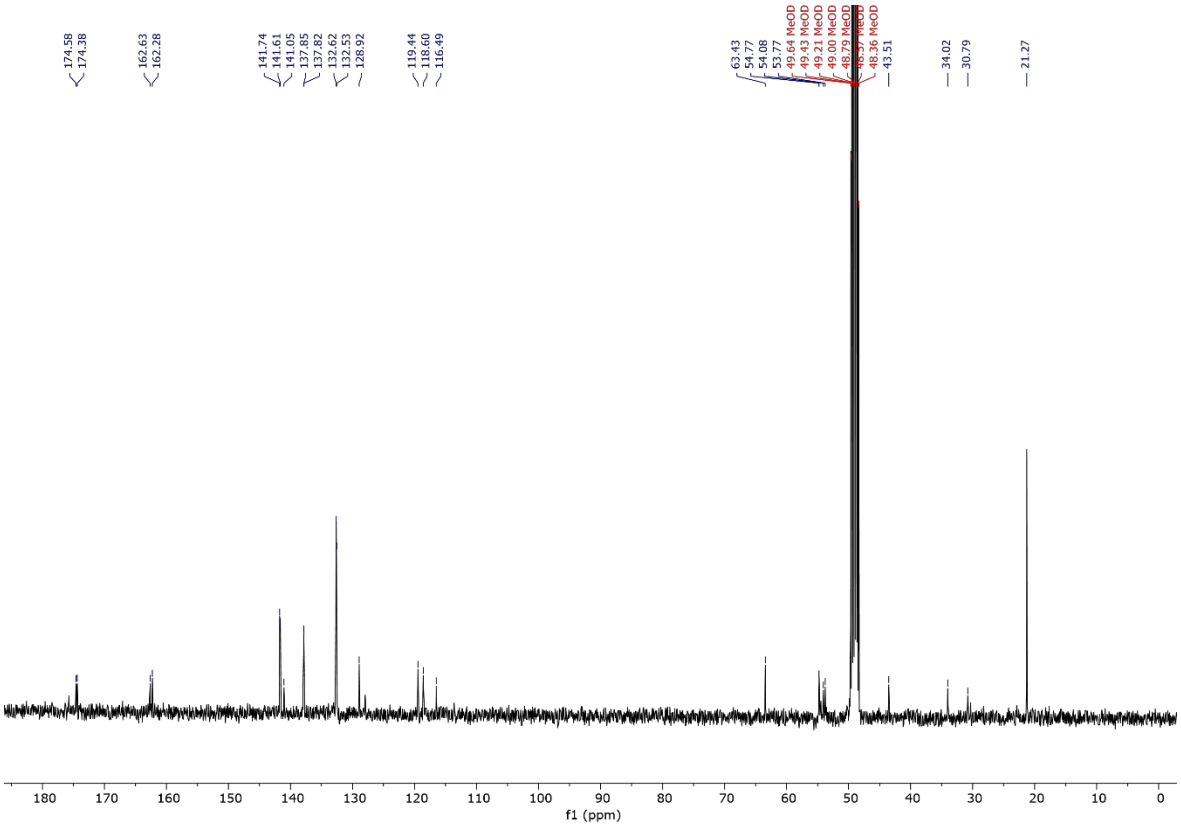

Figure 8.146 $^{13}C\{^{1}H\}$ NMR spectrum of **Ga10c** (CD_3OD, 101 MHz, 298 K).

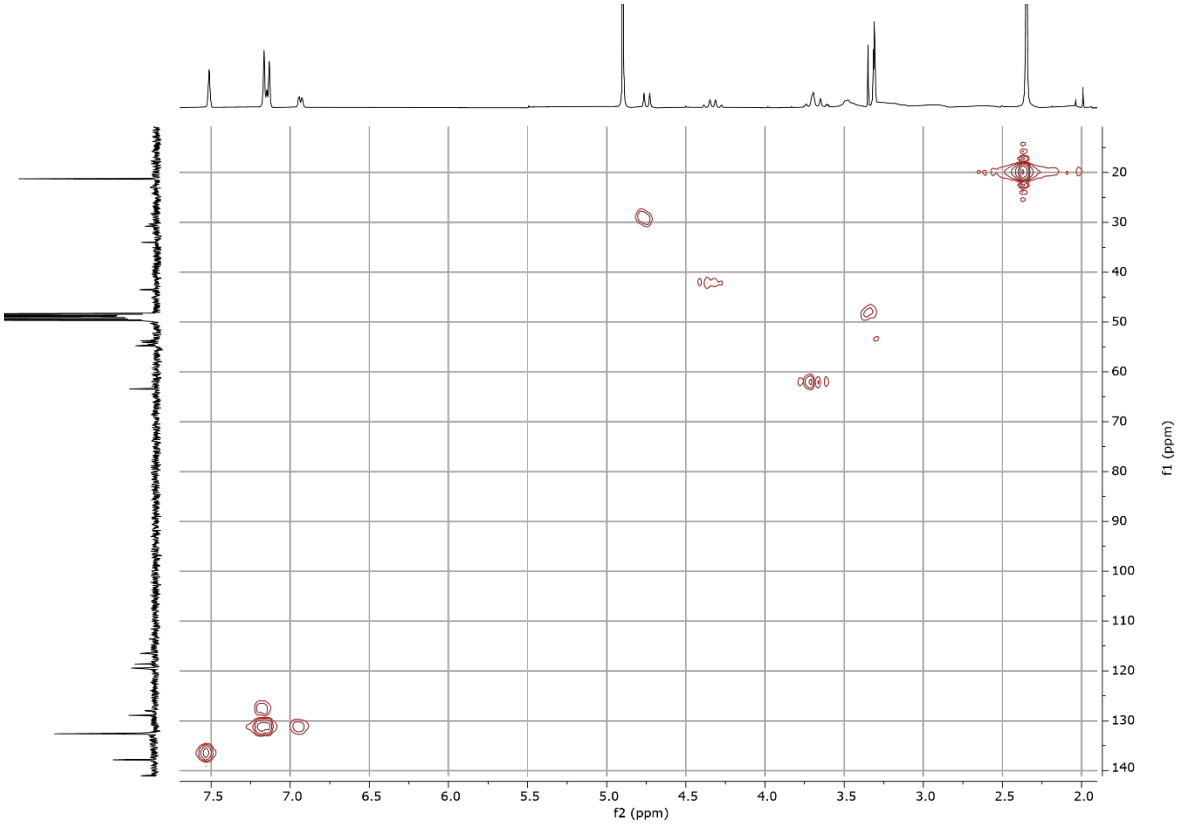

Figure 8.147 HMQC NMR spectrum of **Ga10c** (CD_3OD, 298 K).

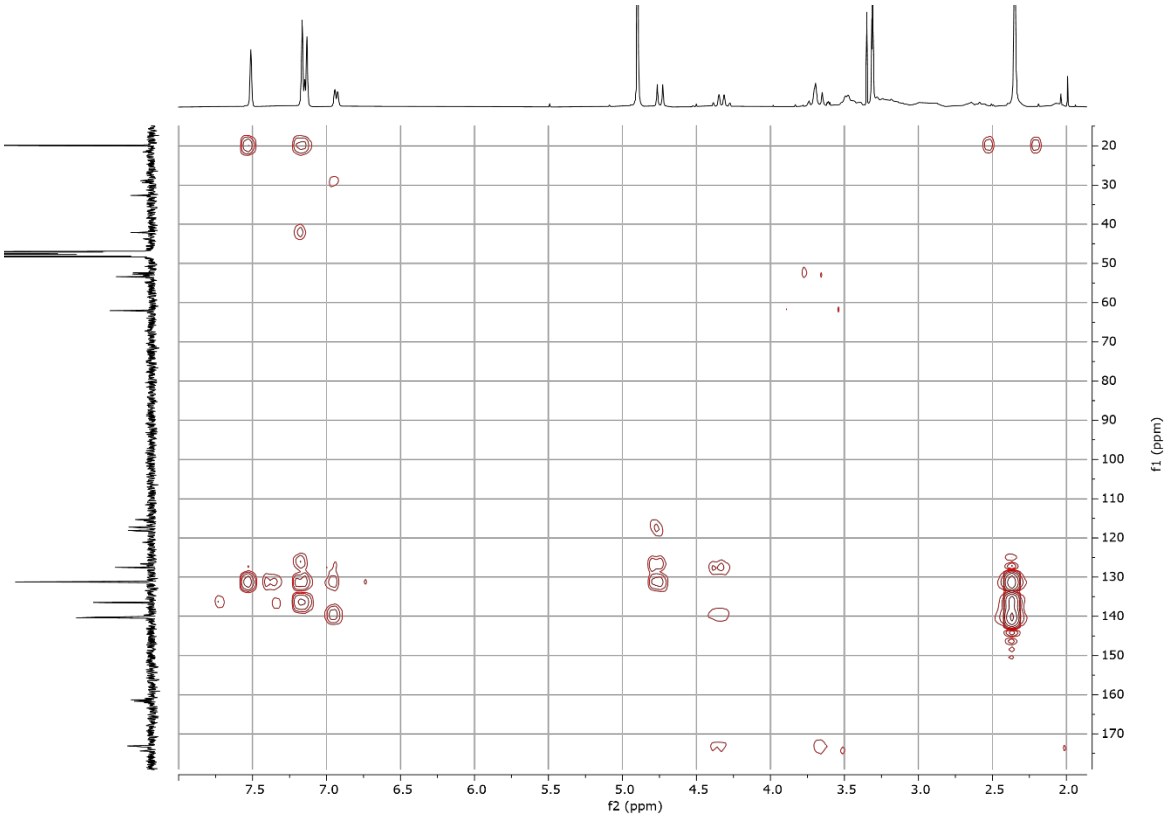

Figure 8.148 HMBC NMR spectrum of **Ga10c** (CD_3OD, 298 K).

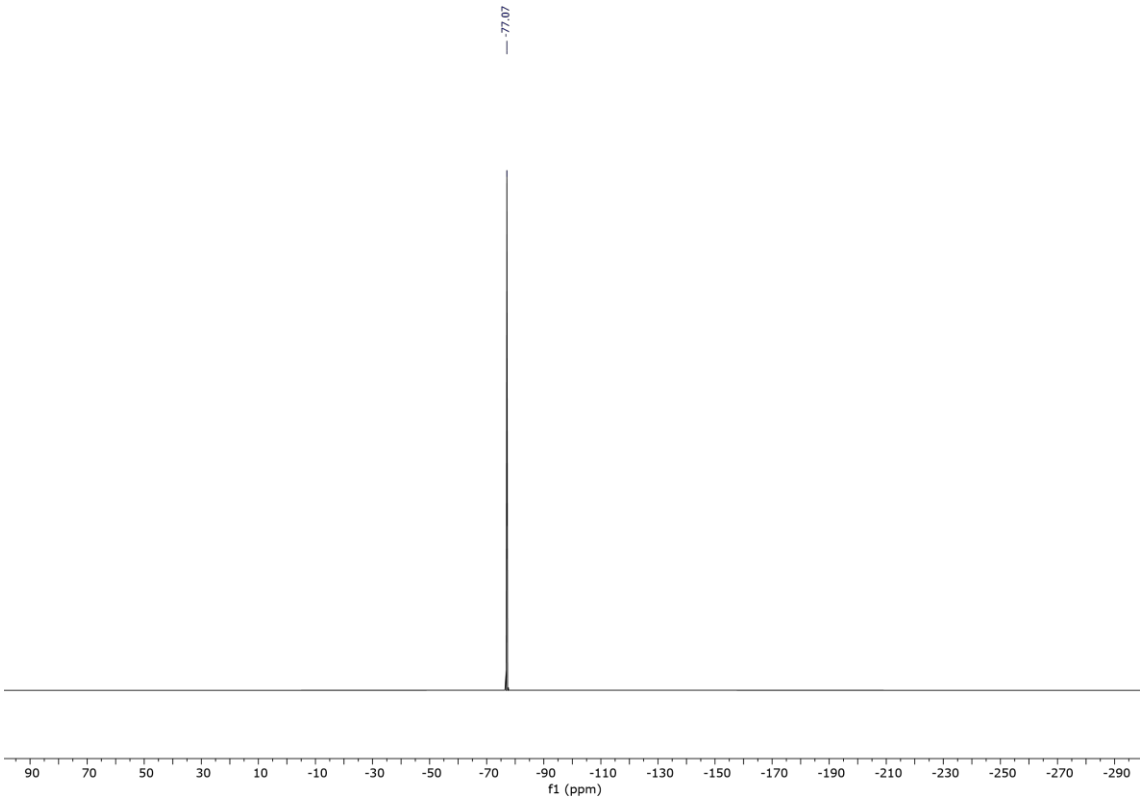

Figure 8.149 $^{19}F\{^{1}H\}$ NMR spectrum of **Ga10c** (CD_3OD, 377 MHz, 298 K).

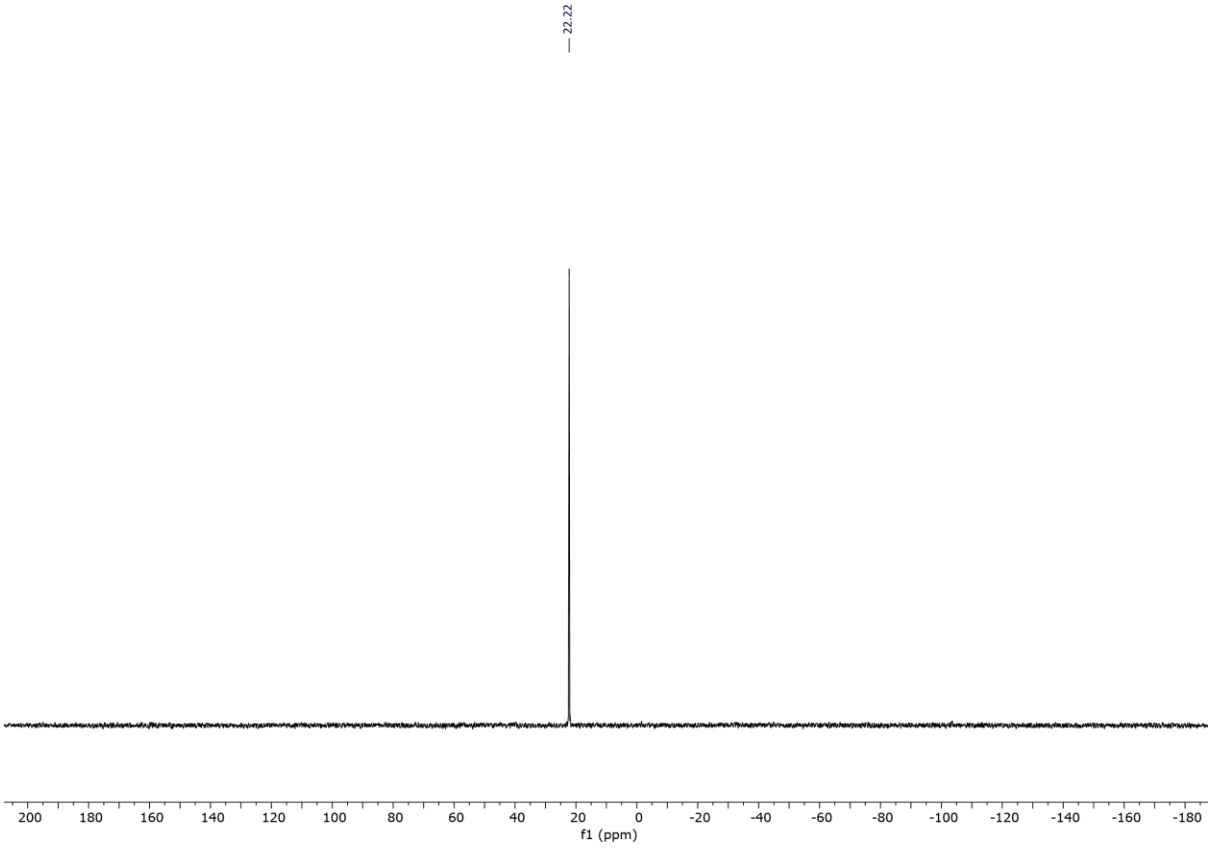

Figure 8.150 $^{31}P\{^{1}H\}$ NMR spectrum of **Ga10c** (CD_3OD, 162 MHz, 298 K).

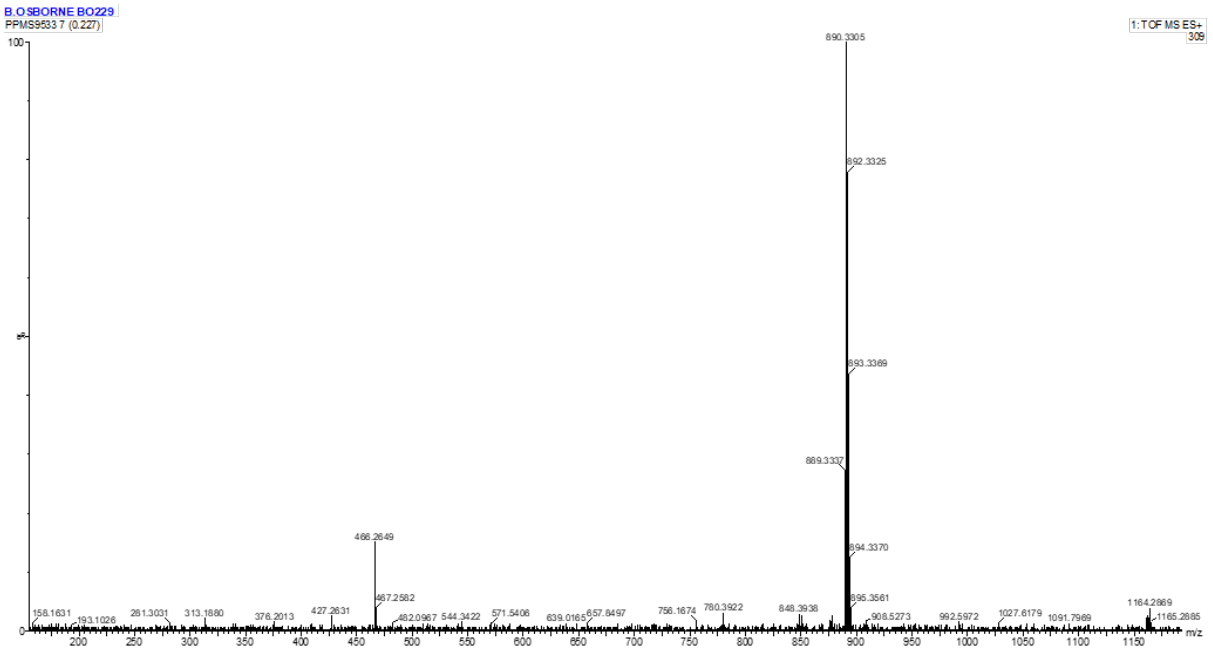

Figure 8.151 ES-TOF+ MS of **Ga10c**.

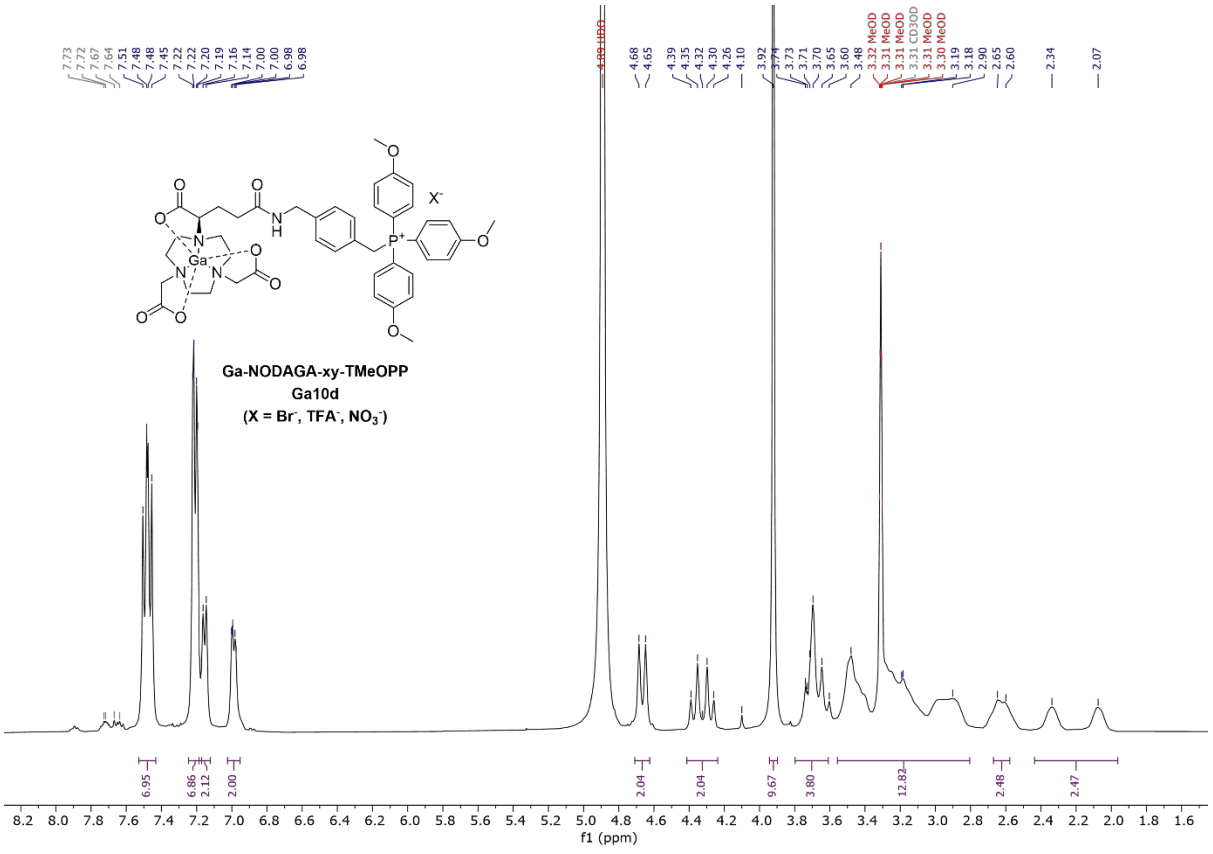

Figure 8.152 ^{1}H NMR spectrum of **Ga10d** (CD_3OD, 400 MHz, 298 K).

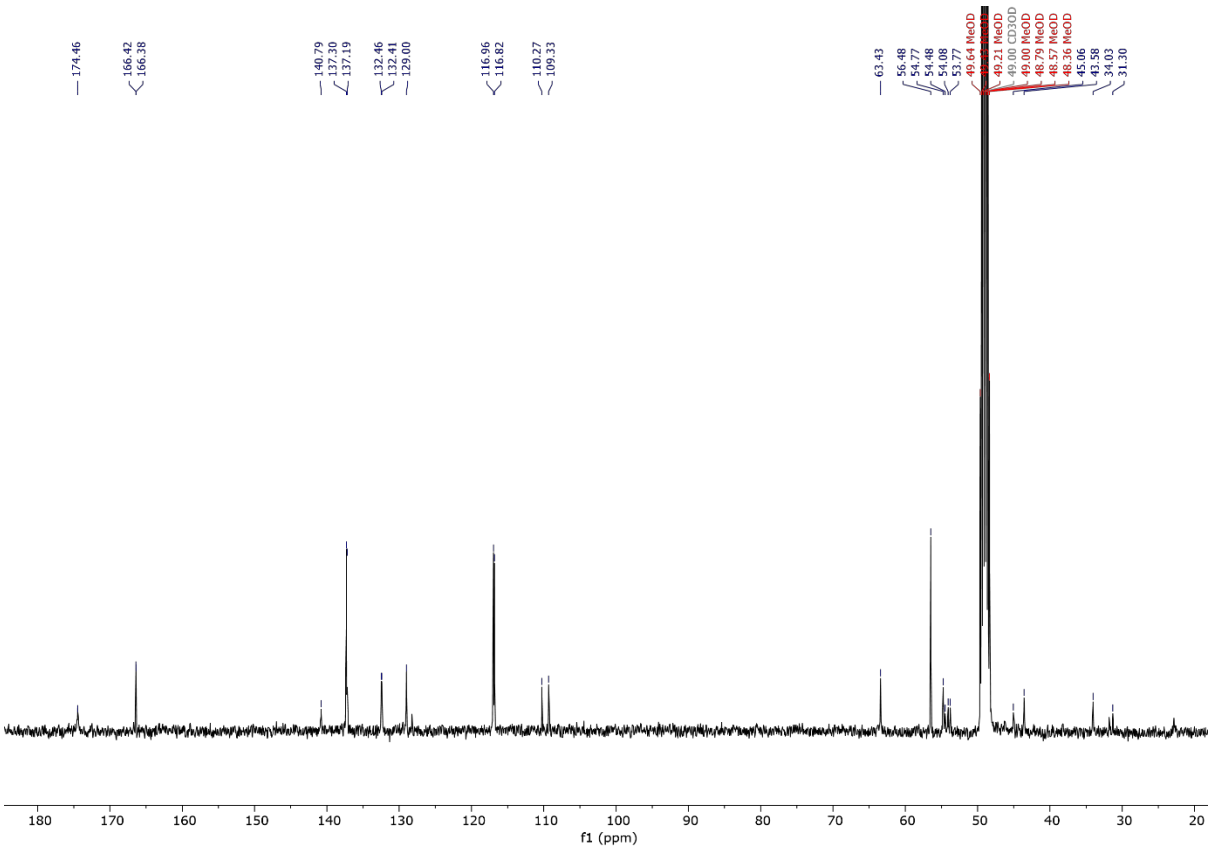

Figure 8.153 $^{13}C\{^{1}H\}$ NMR spectrum of **Ga10d** (CD_3OD, 101 MHz, 298 K).

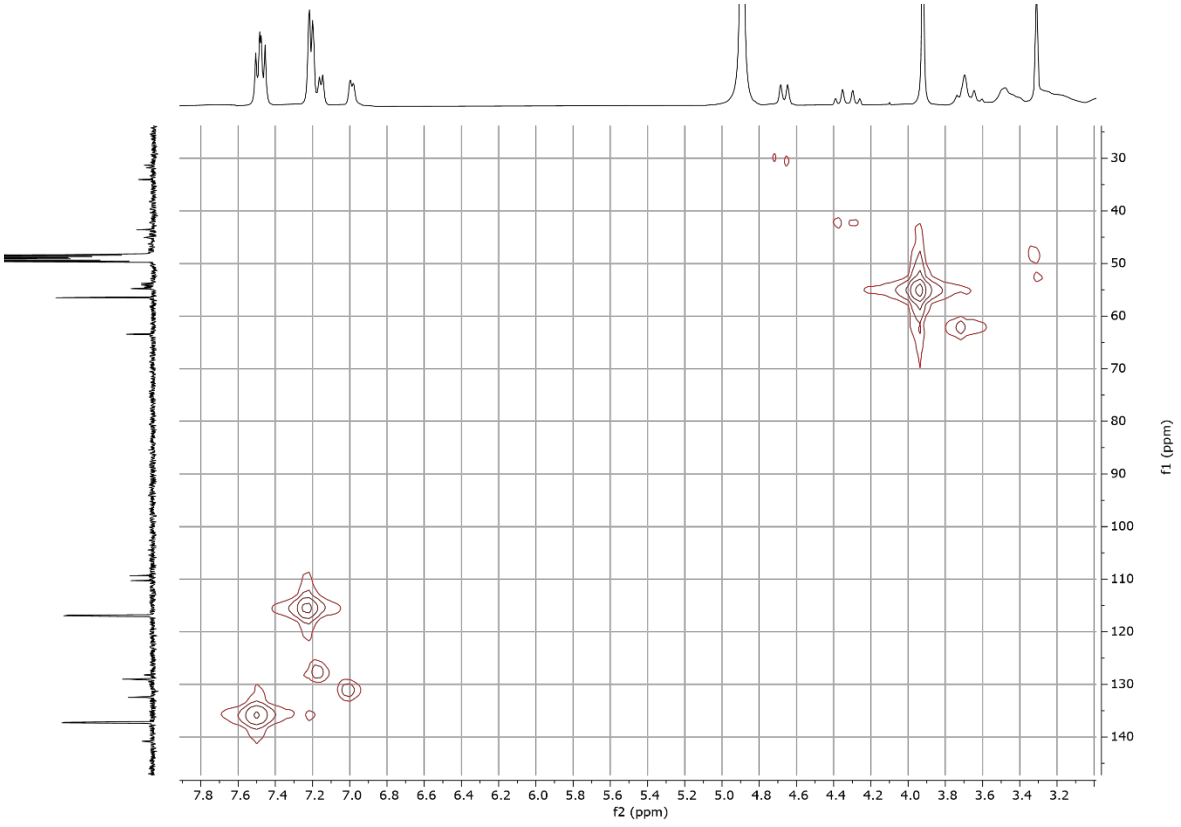

Figure 8.154 HMQC NMR spectrum of **Ga10d** (CD_3OD, 298 K).

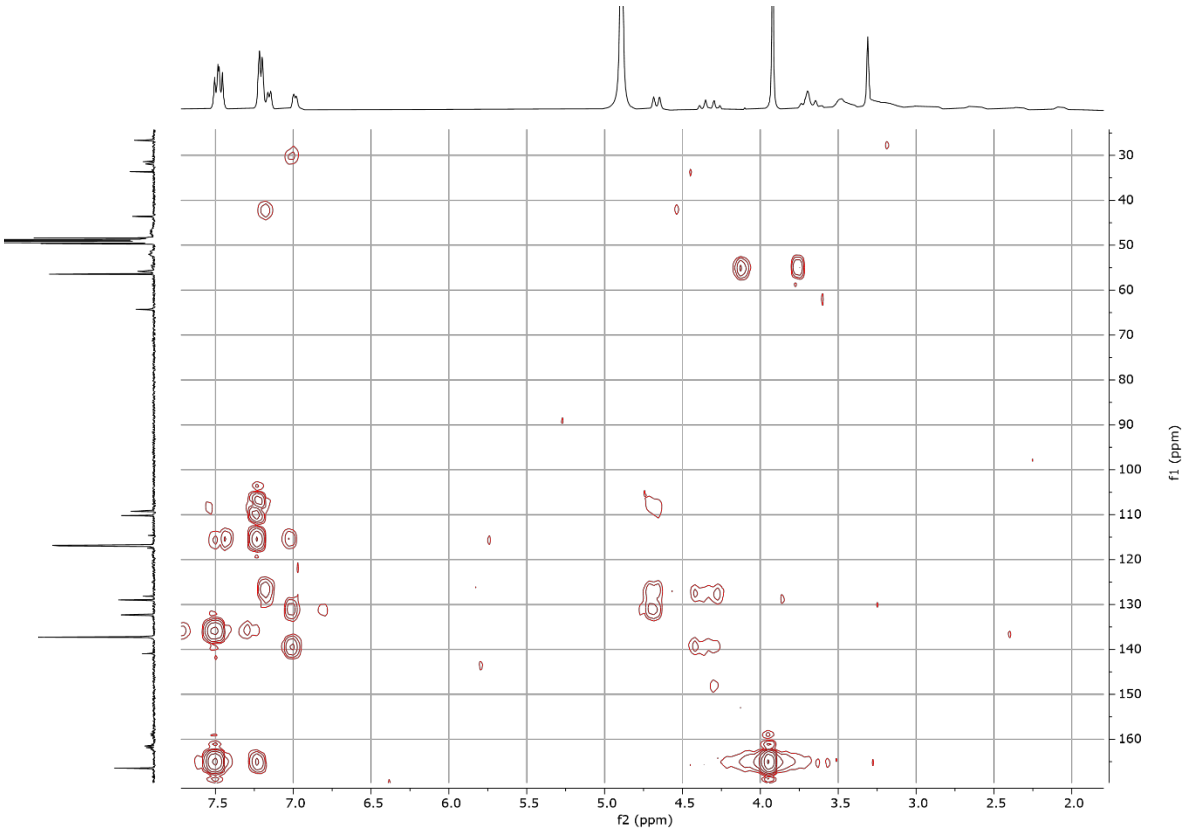

Figure 8.155 HMBC NMR spectrum of **Ga10d** (CD_3OD, 298 K).

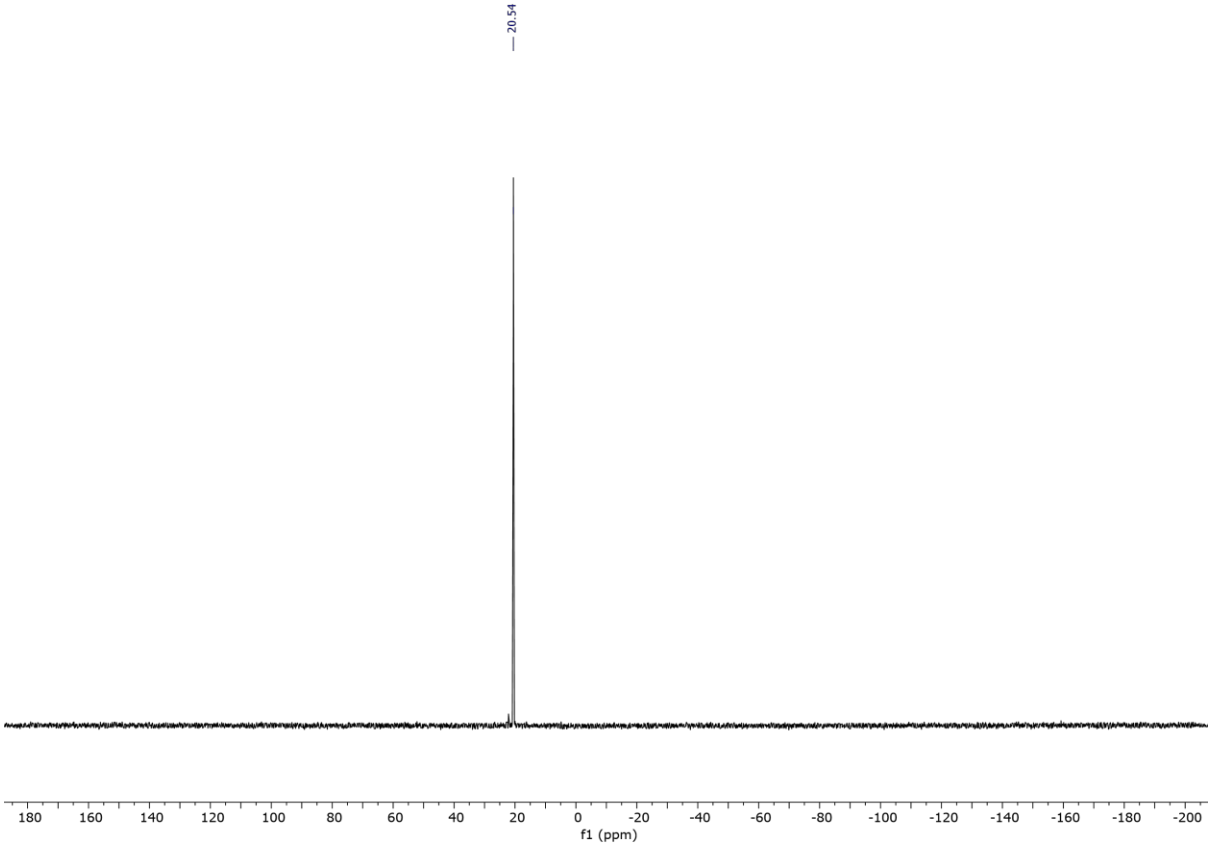

Figure 8.156 $^{31}P\{^1H\}$ NMR spectrum of **Ga10d** (CD_3OD, 162 MHz, 298 K).

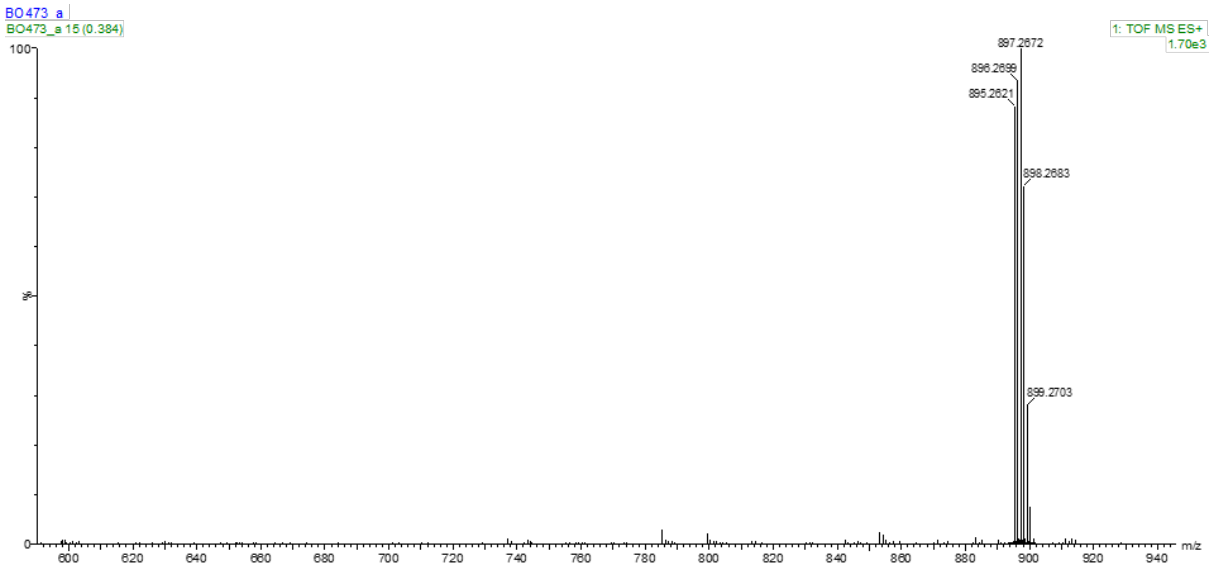

Figure 8.157 ES-TOF+ MS of **Ga10d**.

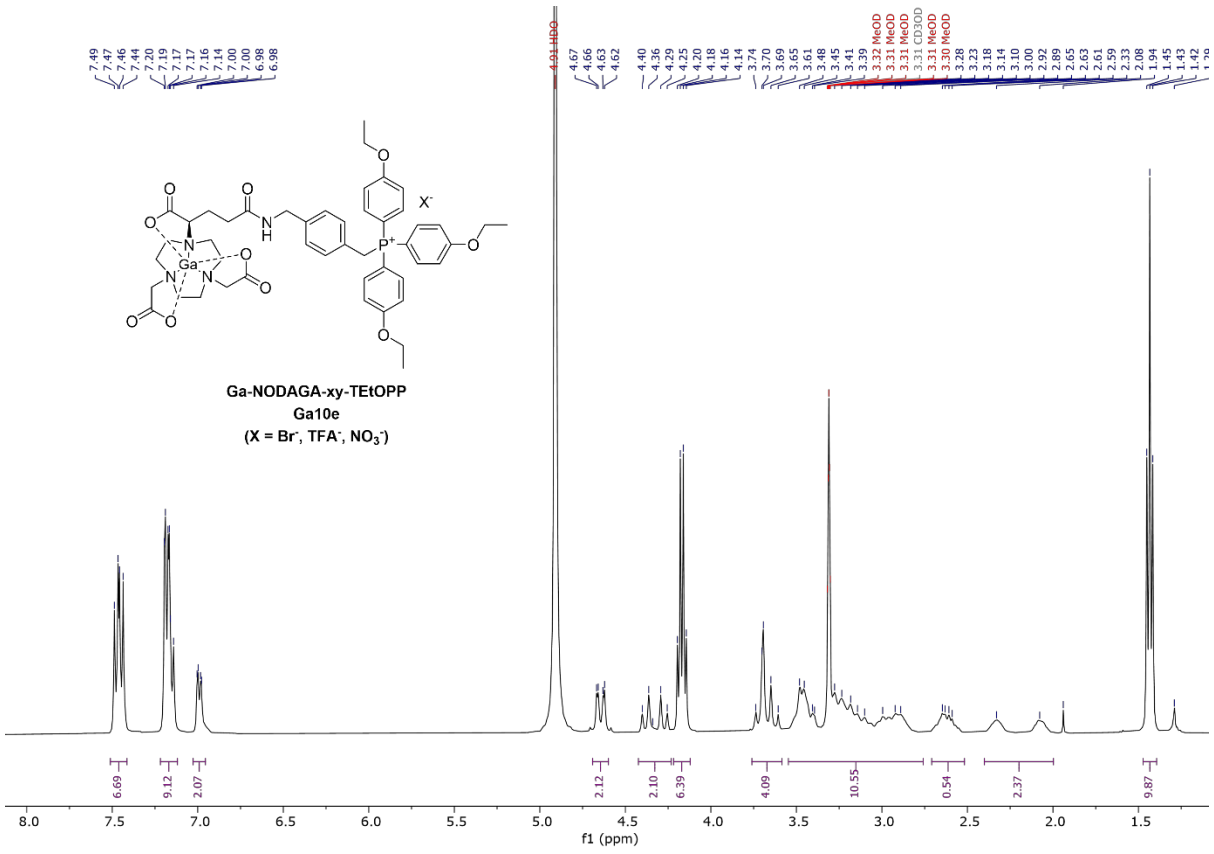

Figure 8.158 ^{1}H NMR spectrum of **Ga10e** (CD_3OD, 400 MHz, 298 K).

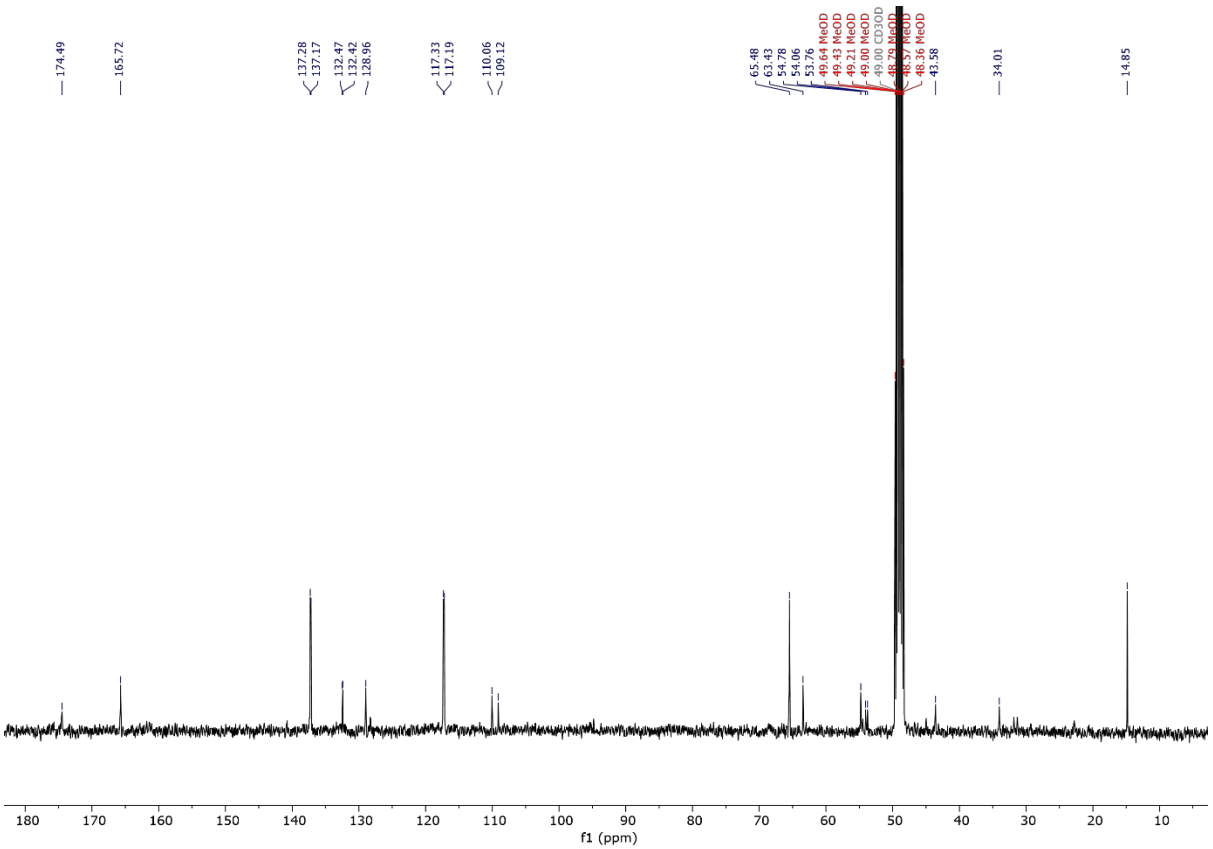

Figure 8.159 $^{13}C\{^{1}H\}$ NMR spectrum of **Ga10e** (CD_3OD, 101 MHz, 298 K).

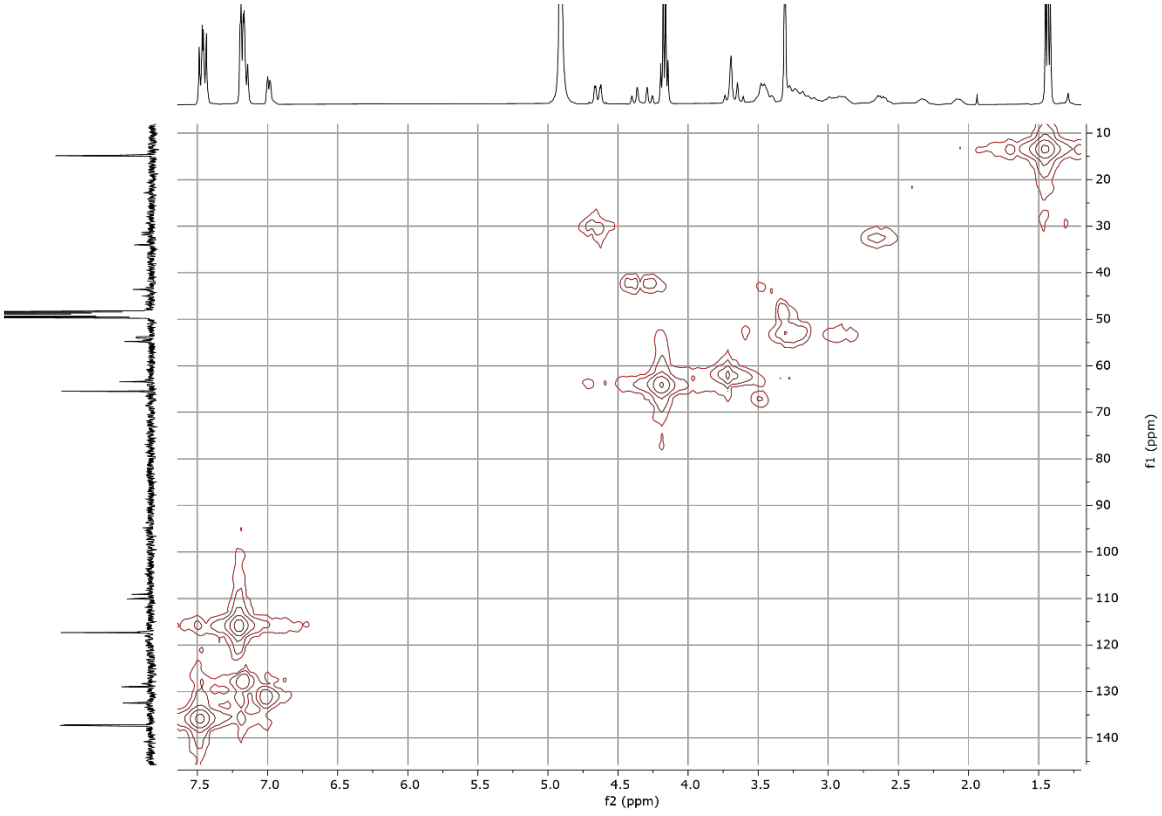

Figure 8.160 HMQC NMR spectrum of **Ga10e** (CD_3OD, 298 K).

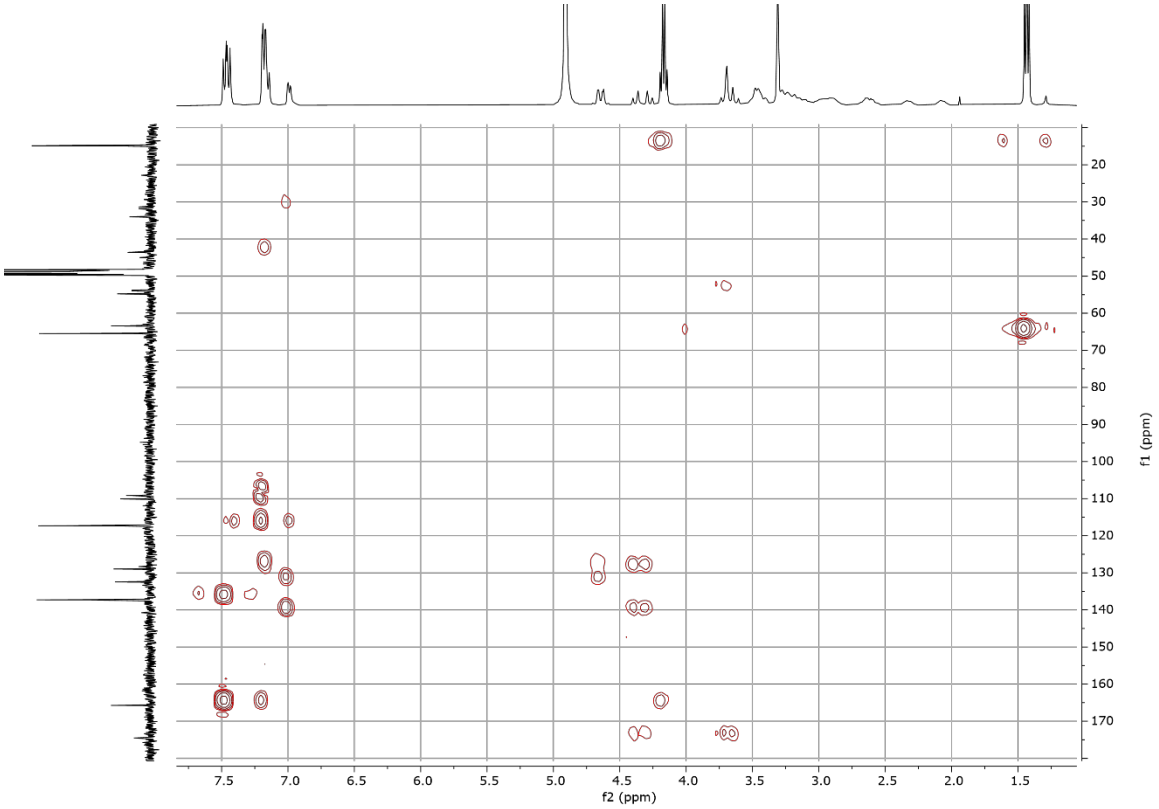

Figure 8.161 HMBC NMR spectrum of **Ga10e** (CD_3OD, 298 K).

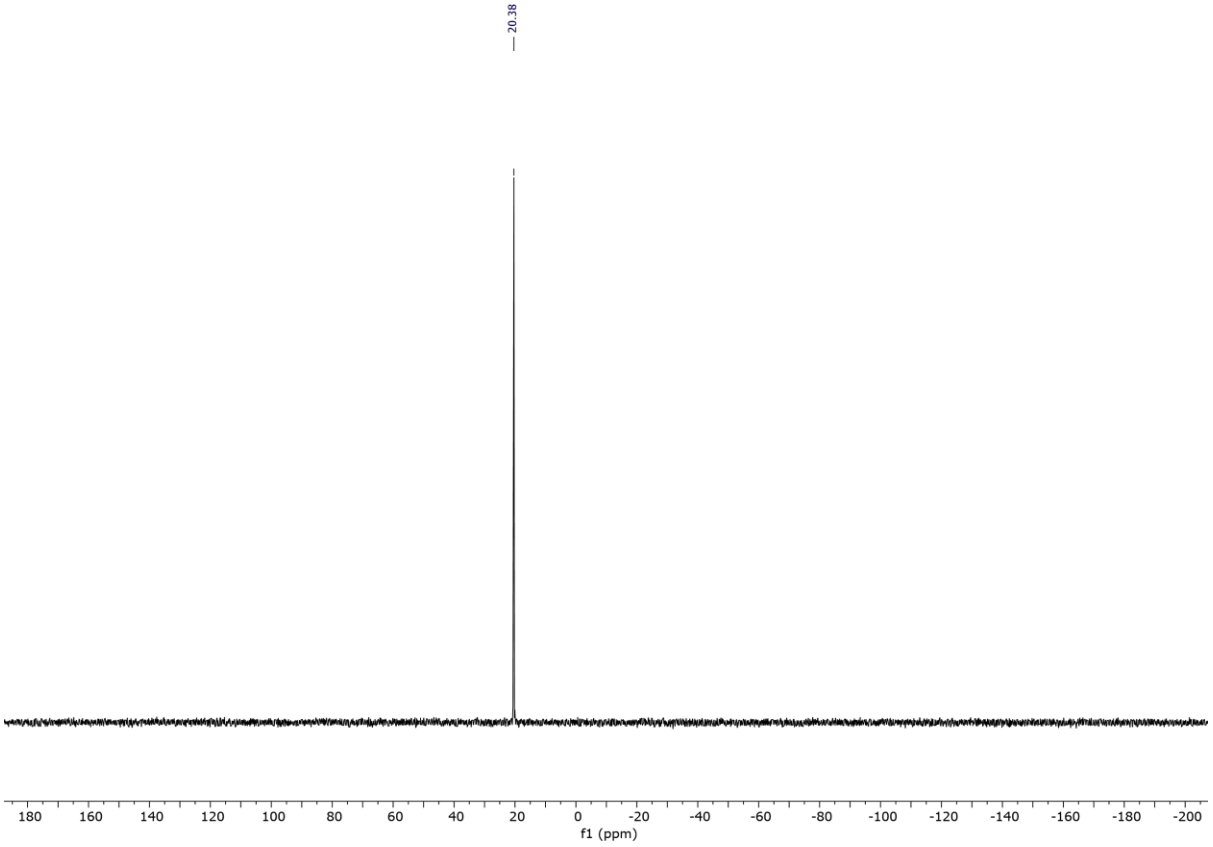

Figure 8.162 $^{31}P\{^{1}H\}$ NMR spectrum of **Ga10e** (CD_3OD, 162 MHz, 298 K).

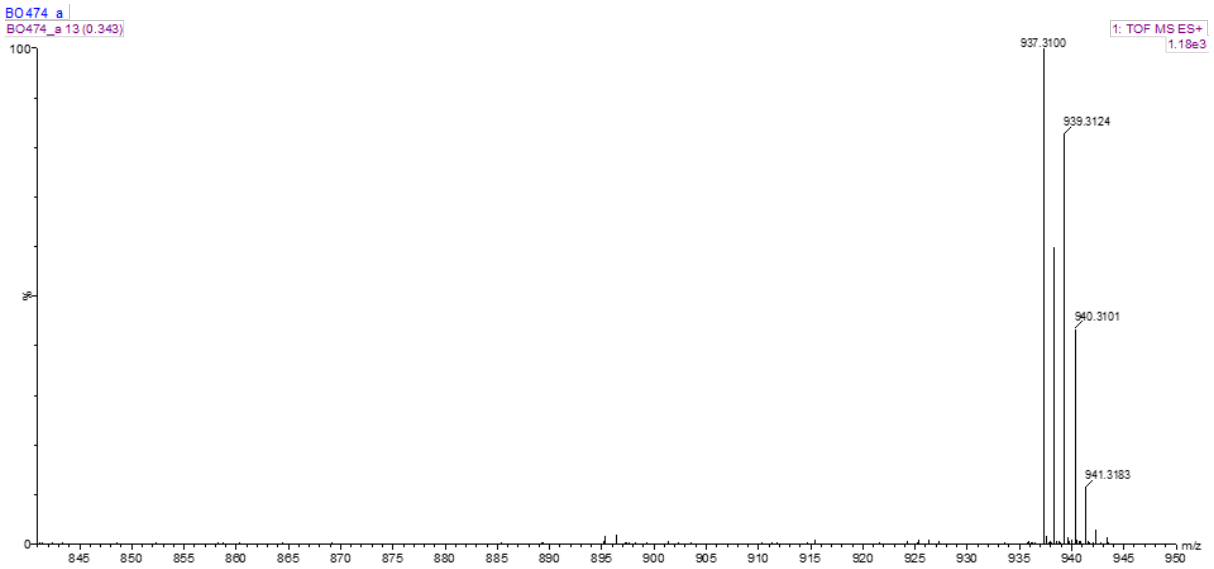

Figure 8.163 ES-TOF+ MS of **Ga10e**.

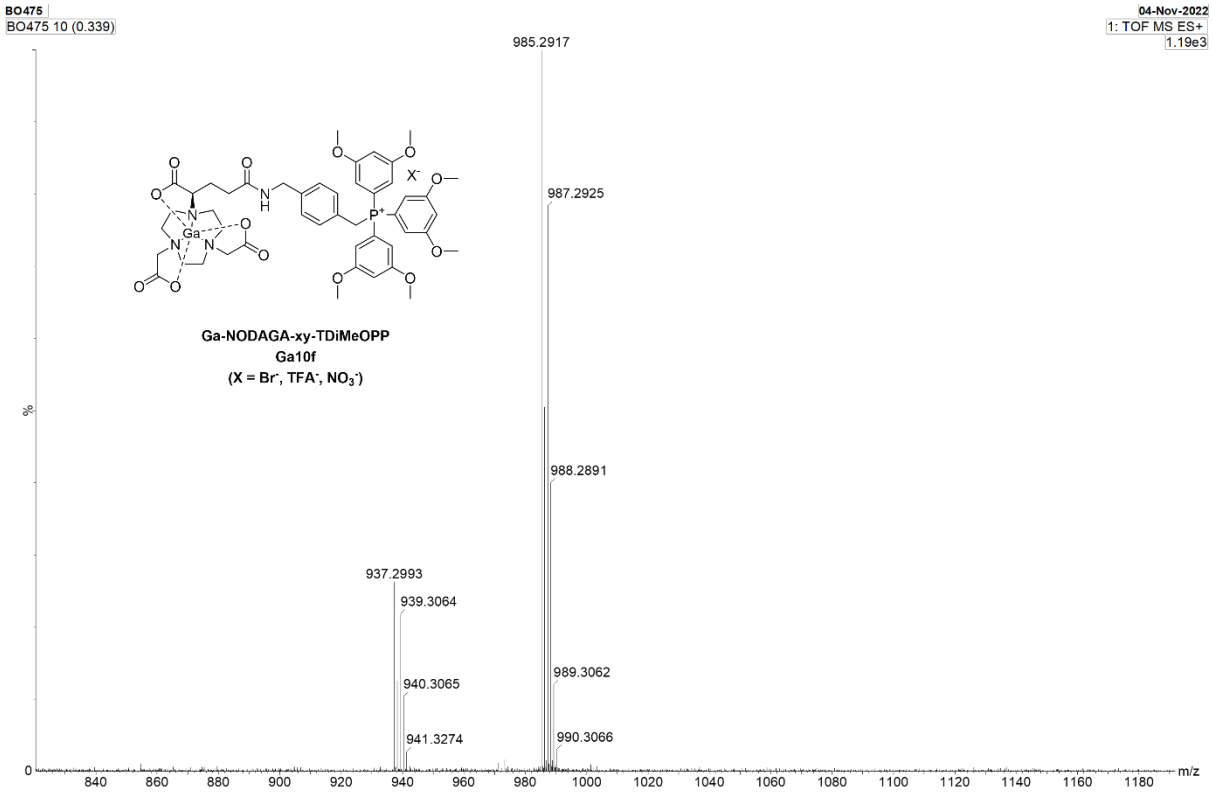

Figure 8.164 ES-TOF+ MS of **Ga10f**.

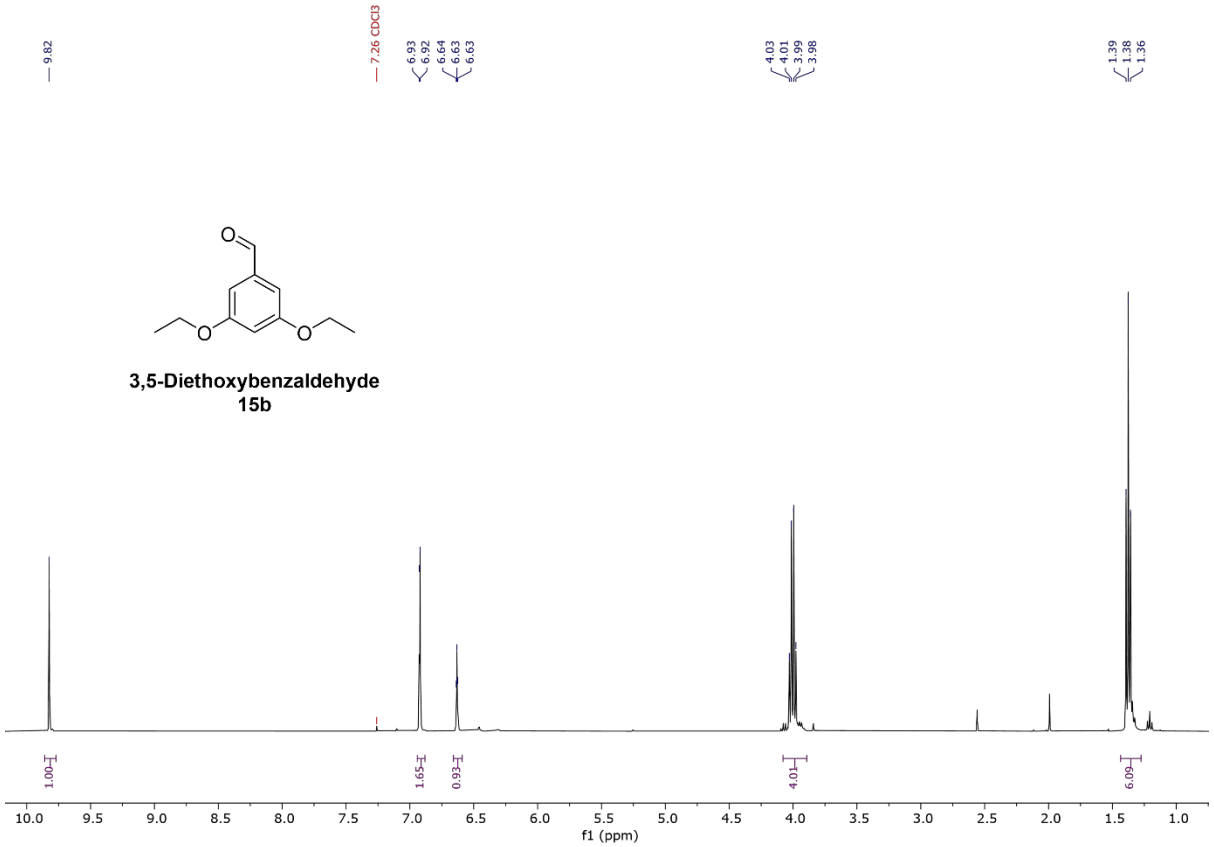

Figure 8.165 ^{1}H NMR spectrum of **15b** ($CDCl_3$, 400 MHz, 298 K).

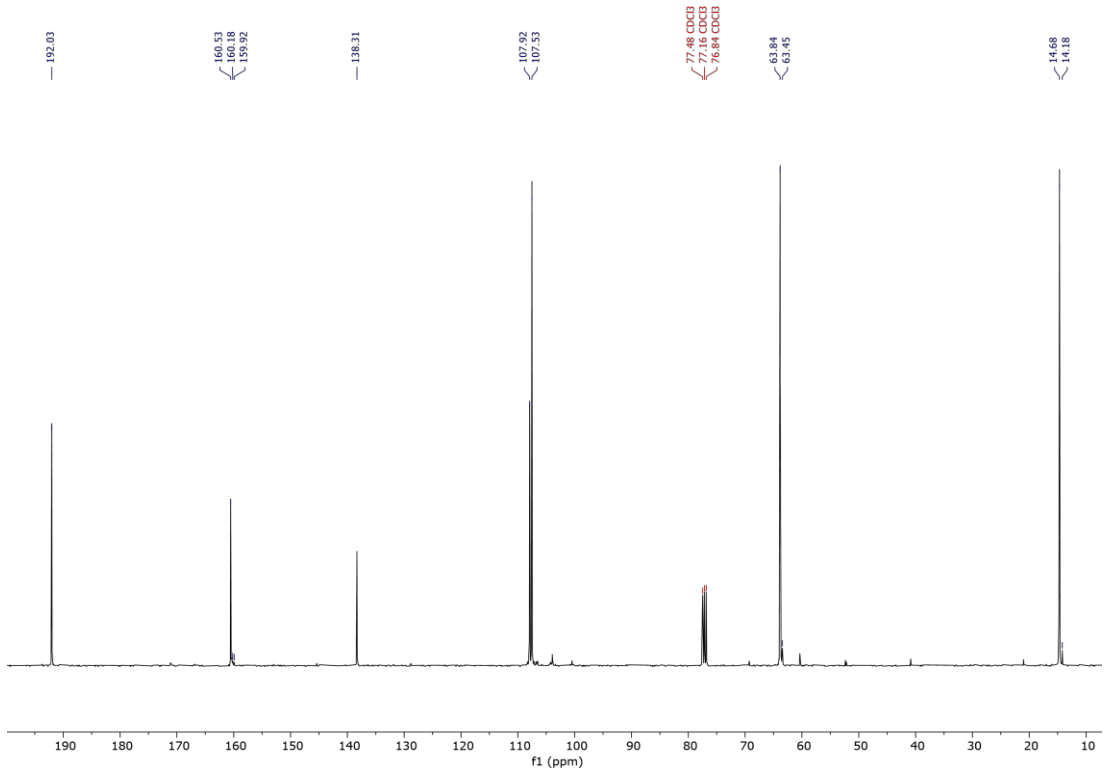

Figure 8.166 $^{13}C\{^{1}H\}$ NMR spectrum of **15b** ($CDCl_3$, 101 MHz, 298 K).

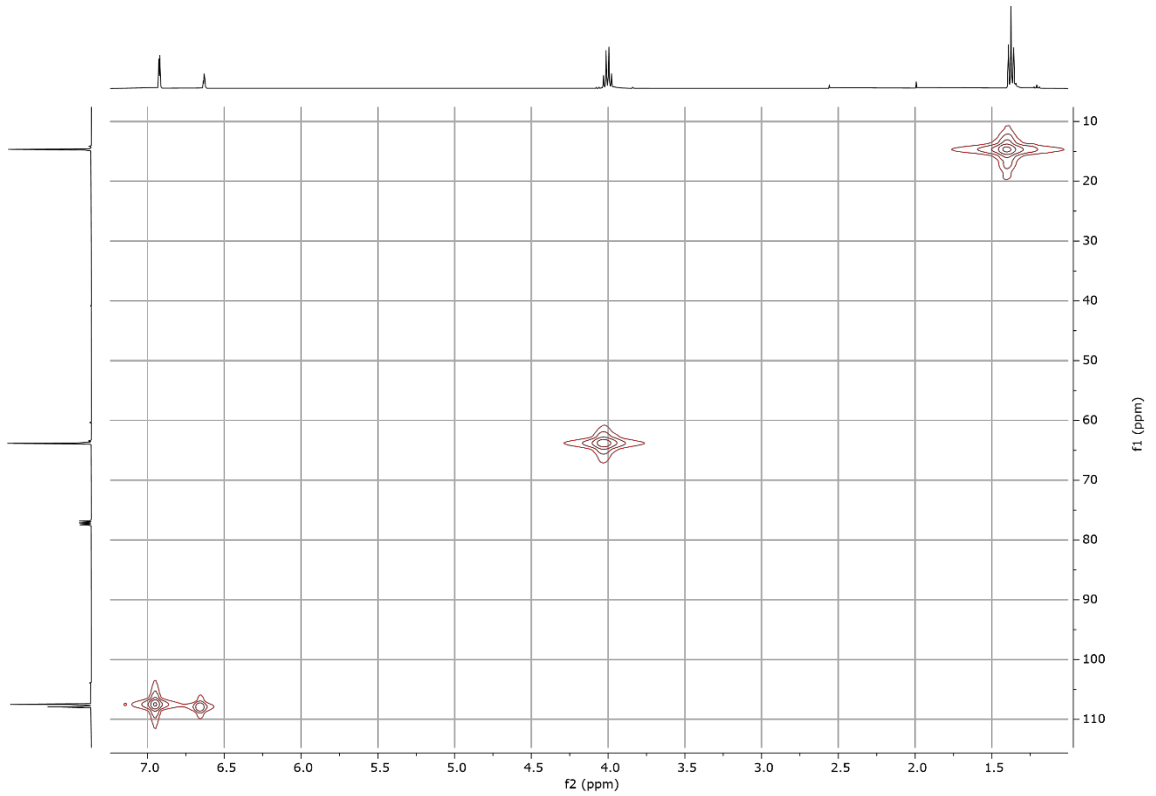

Figure 8.167 HMQC NMR spectrum of **15b** ($CDCl_3$, 298 K).

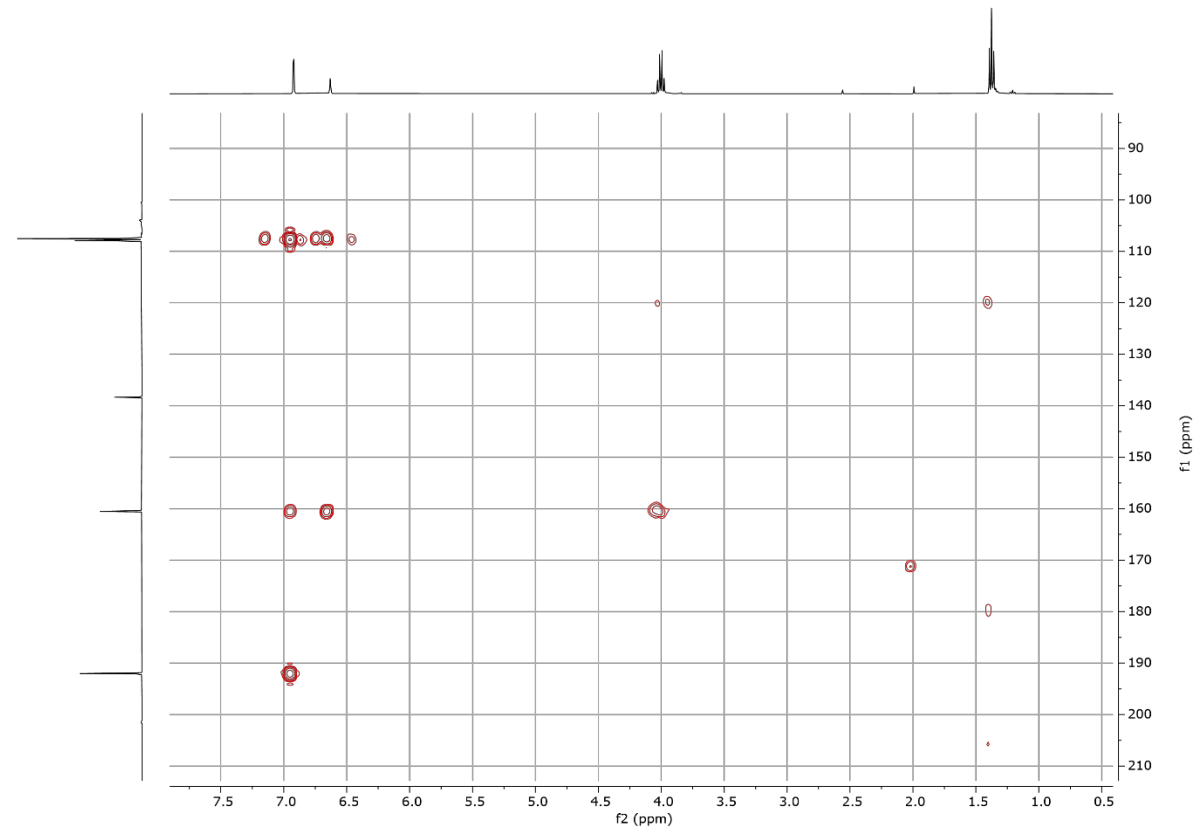

Figure 8.168 HMBC NMR spectrum of **15b** ($CDCl_3$, 298 K).

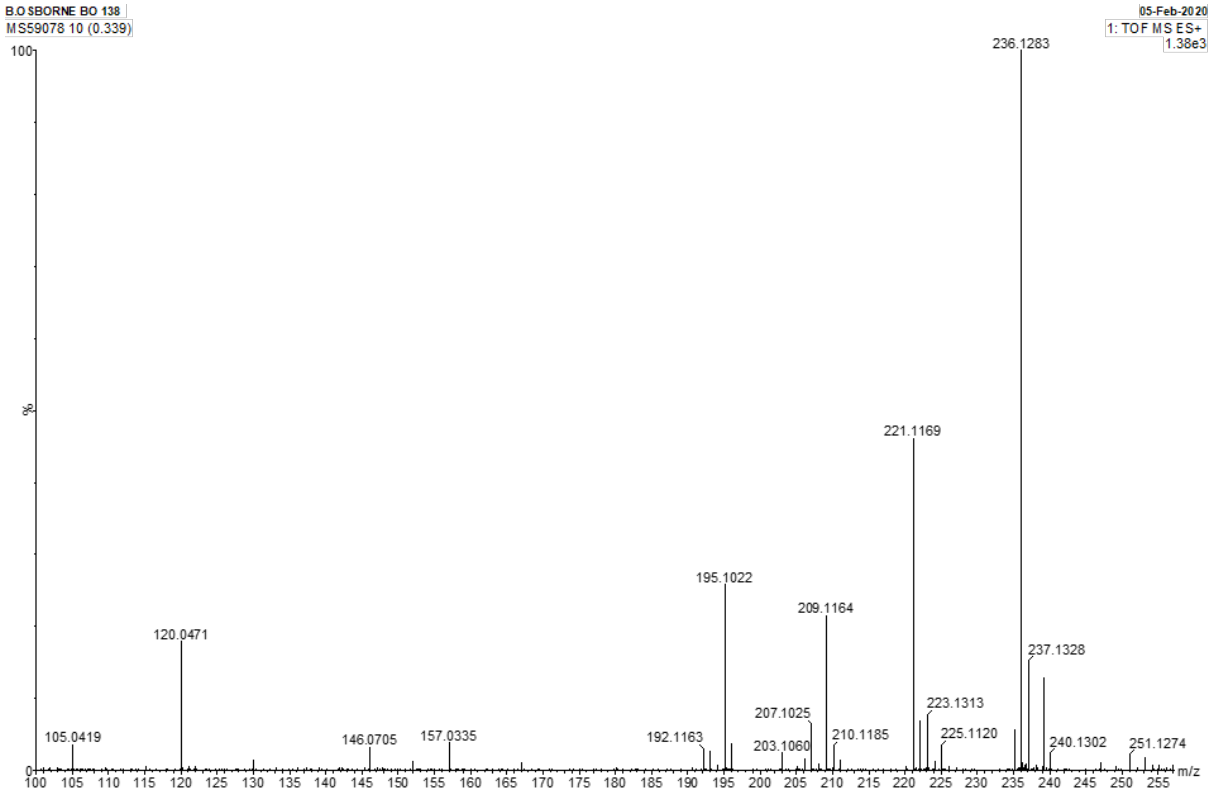

Figure 8.169 ES-TOF+ MS of **15b**.

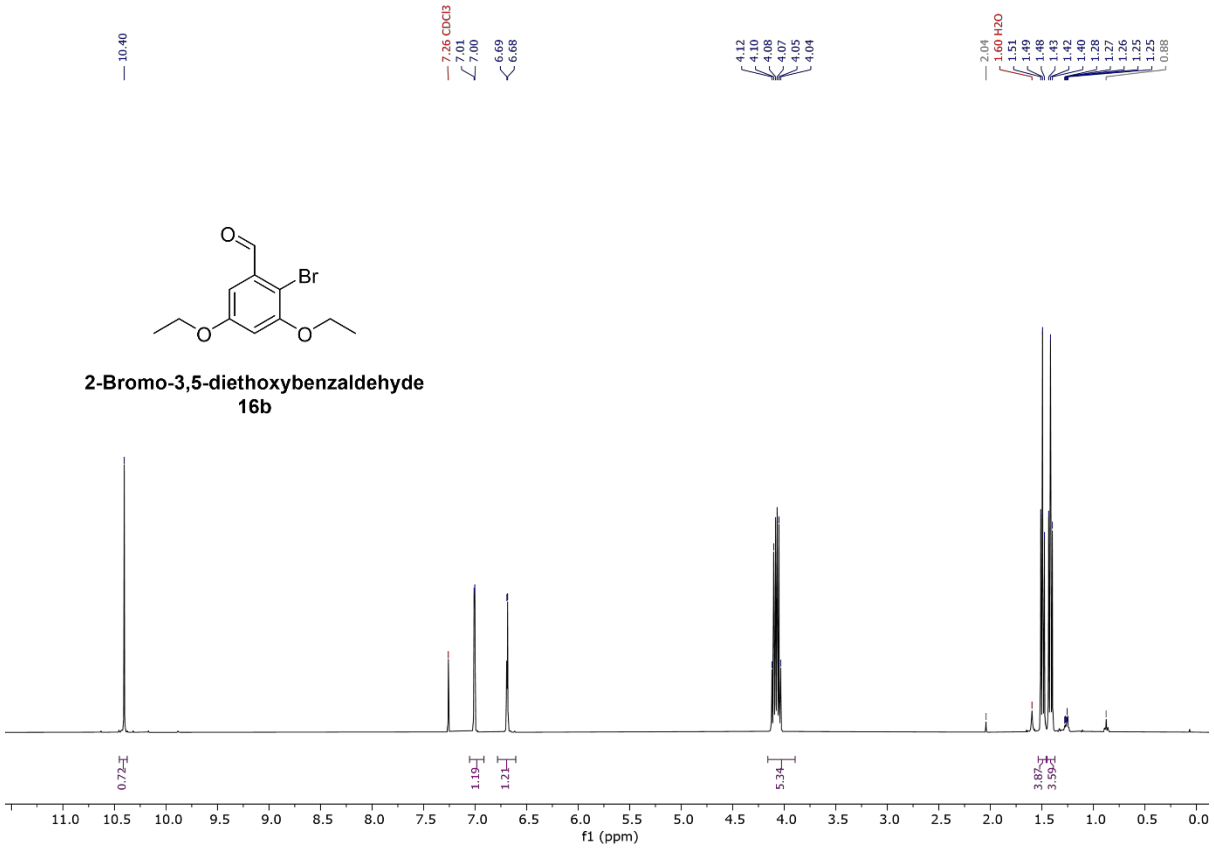

Figure 8.170 ^{1}H NMR spectrum of **16b** ($CDCl_3$, 400 MHz, 298 K).

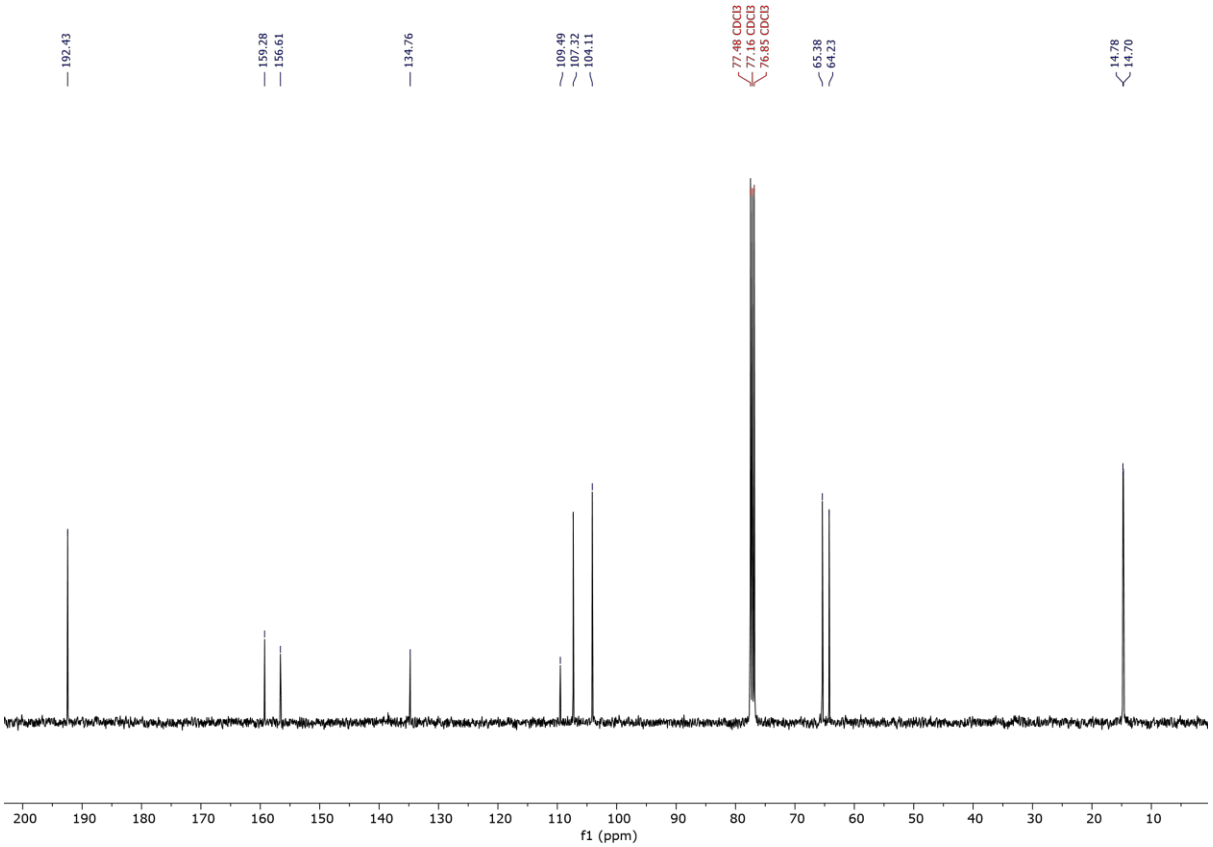

Figure 8.171 $^{13}C\{^{1}H\}$ NMR spectrum of **16b** ($CDCl_3$, 101 MHz, 298 K).

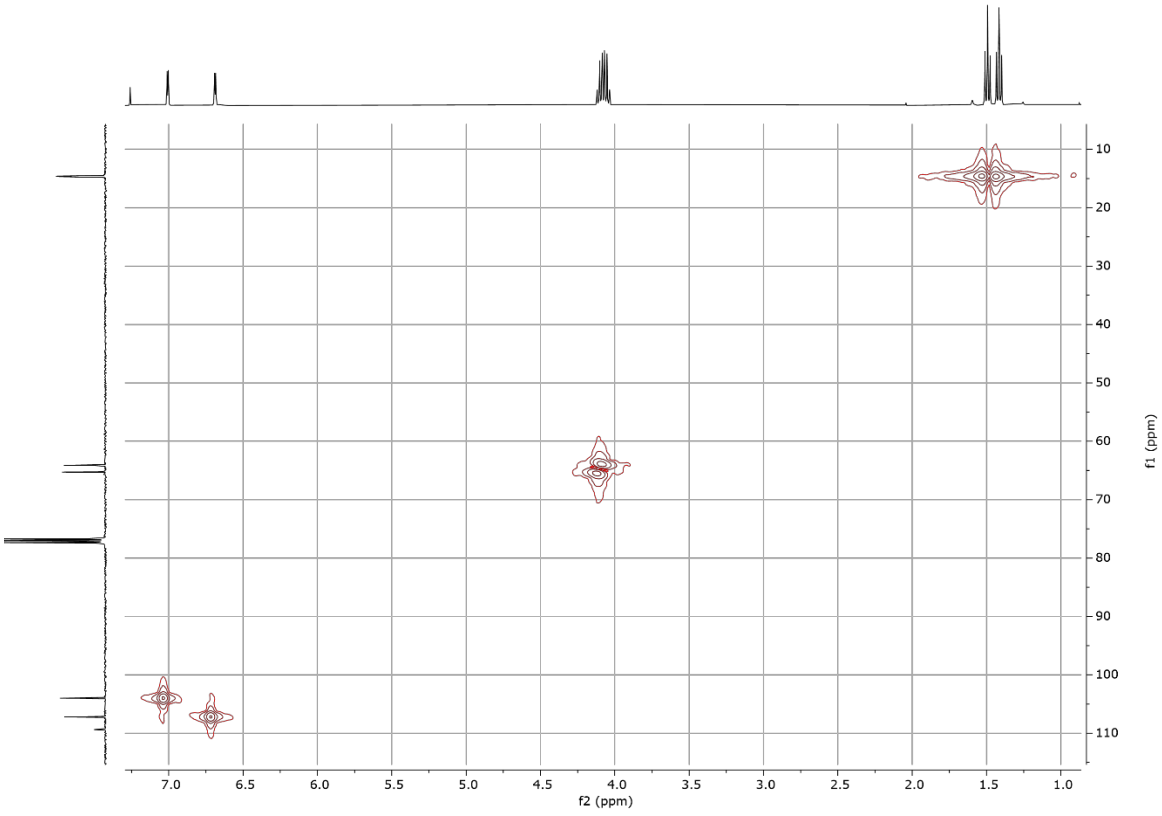

Figure 8.172 HMQC NMR spectrum of **16b** ($CDCl_3$, 298 K).

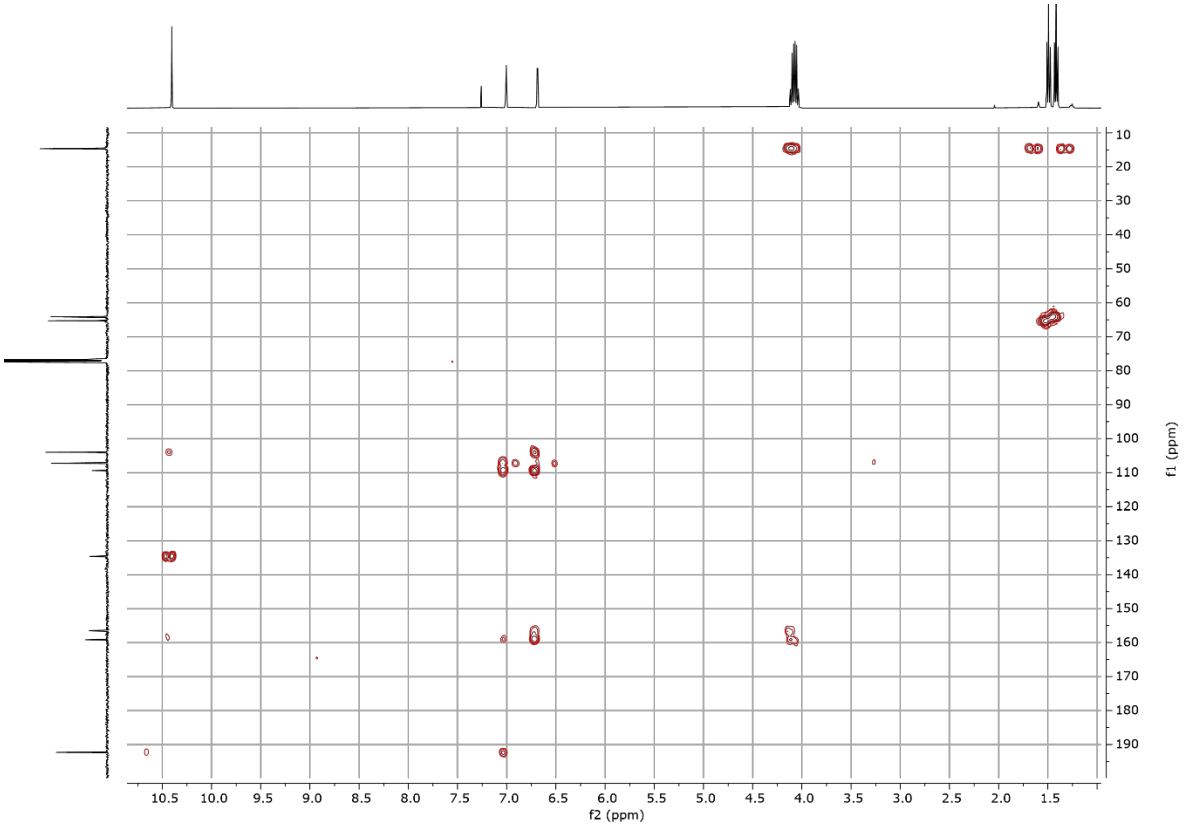

Figure 8.173 HMBC NMR spectrum of **16b** ($CDCl_3$, 298 K).

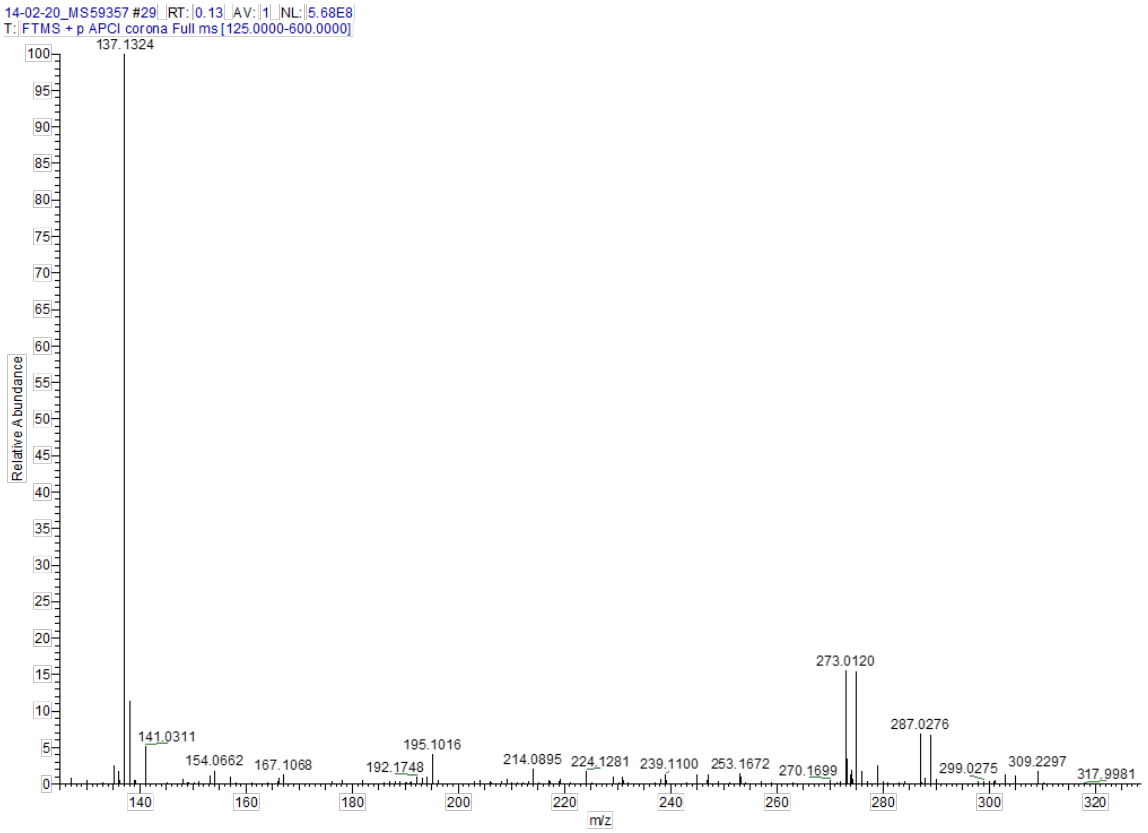

Figure 8.174 ES-TOF+ MS of **16b**.

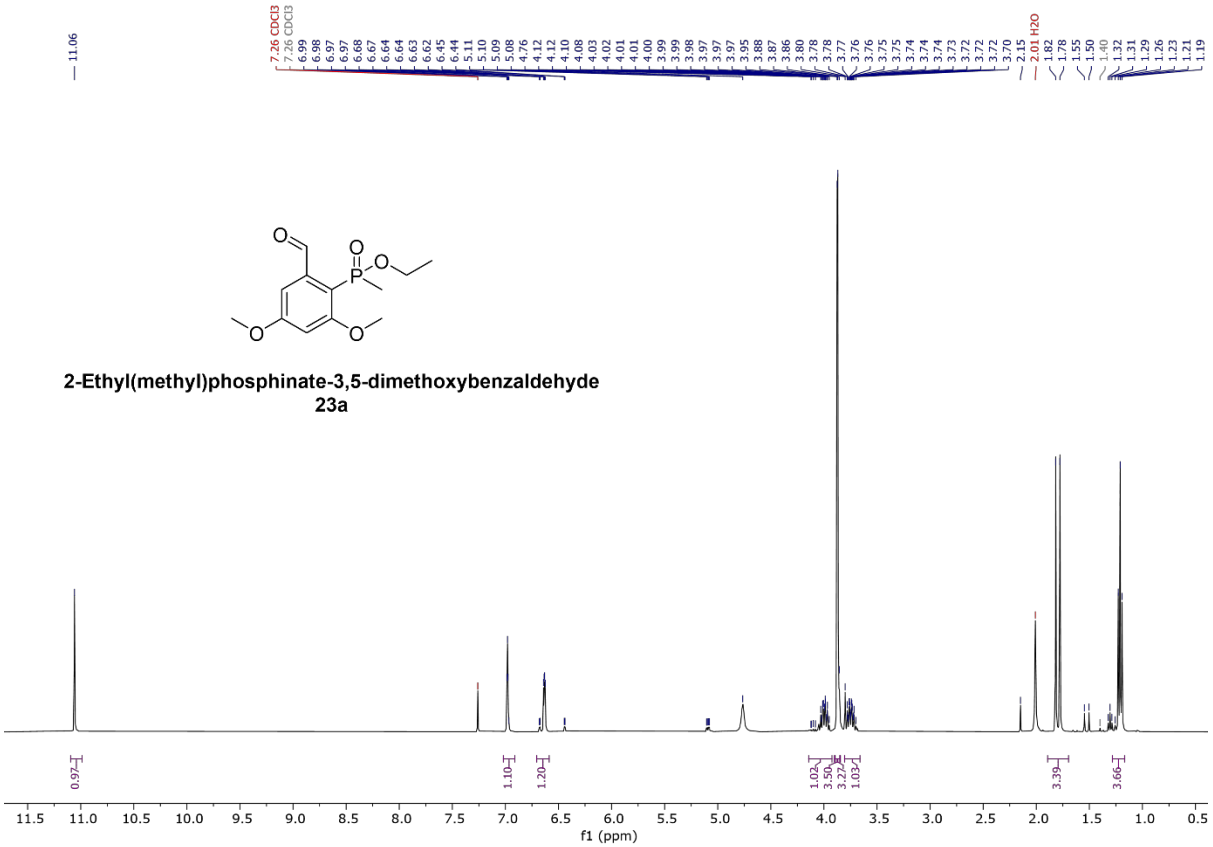

Figure 8.175 ^{1}H NMR spectrum of **23a** ($CDCl_3$, 400 MHz, 298 K).

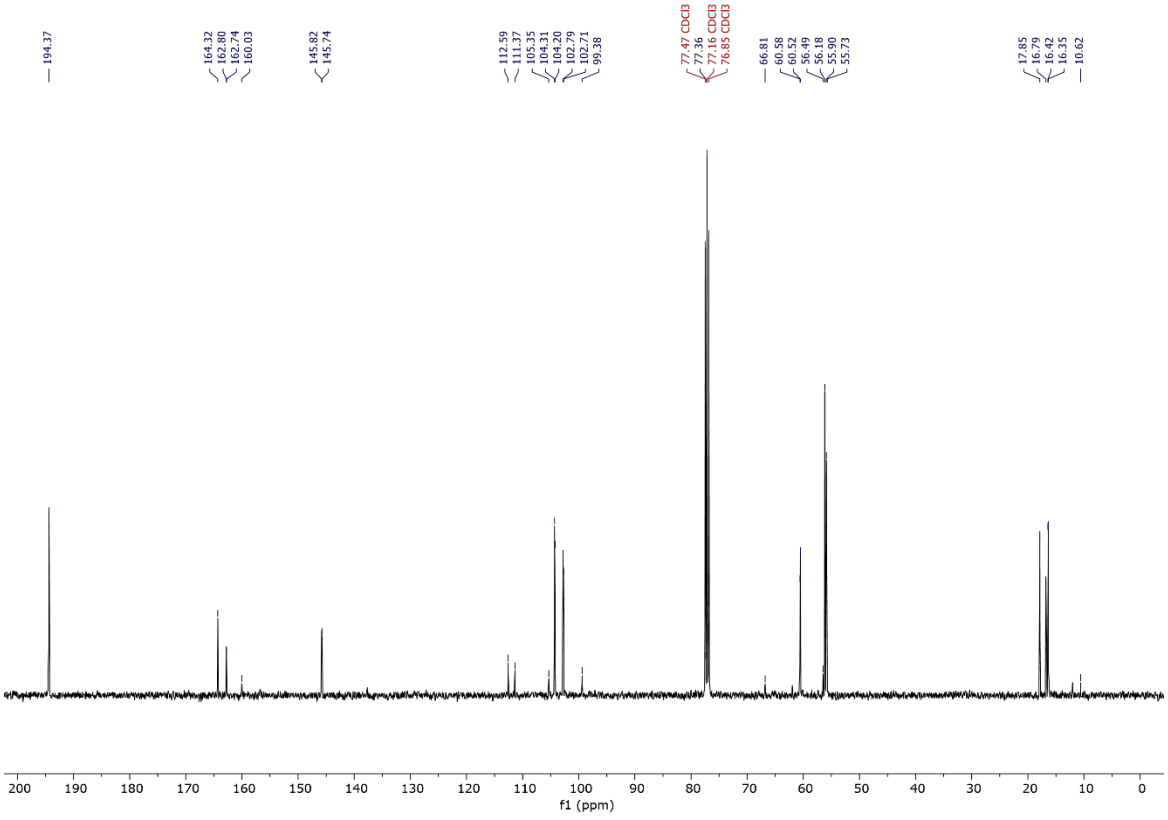

Figure 8.176 $^{13}C\{^{1}H\}$ NMR spectrum of **23a** ($CDCl_3$, 101 MHz, 298 K).

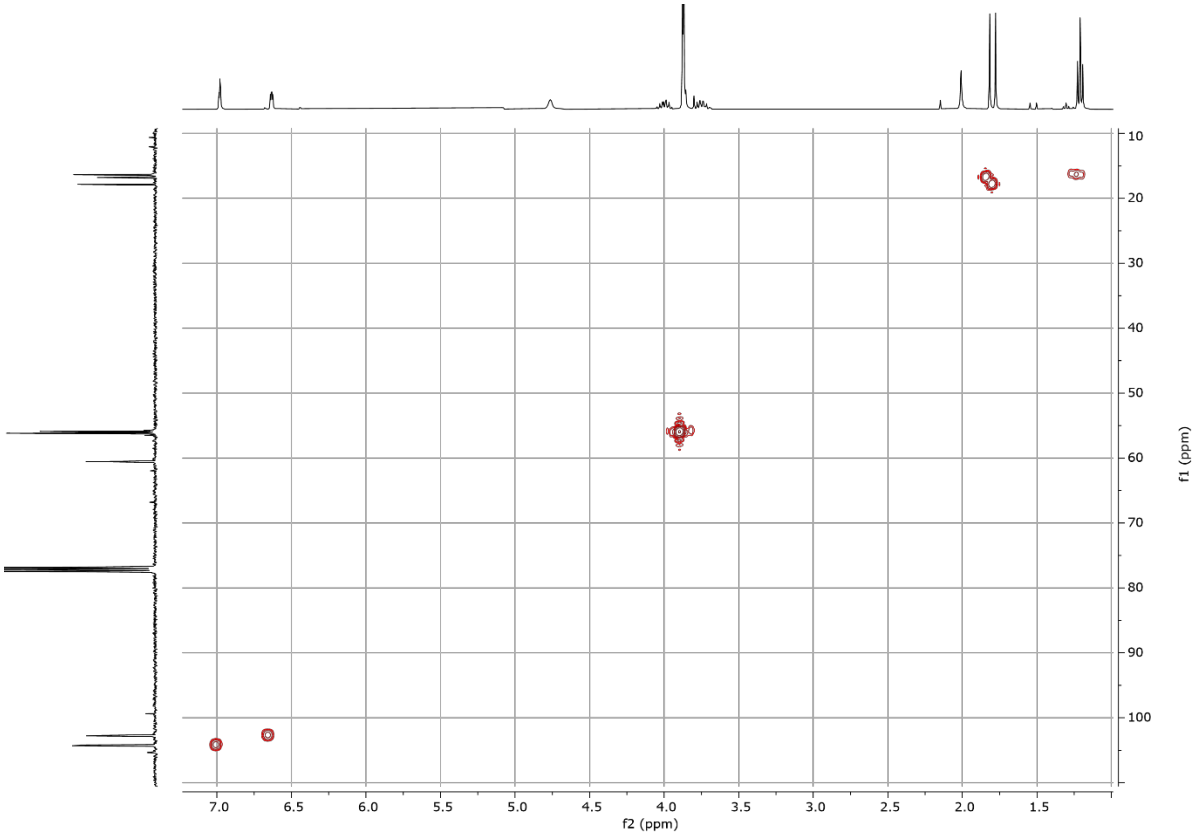

Figure 8.177 HMQC NMR spectrum of **23a** ($CDCl_3$, 298 K).

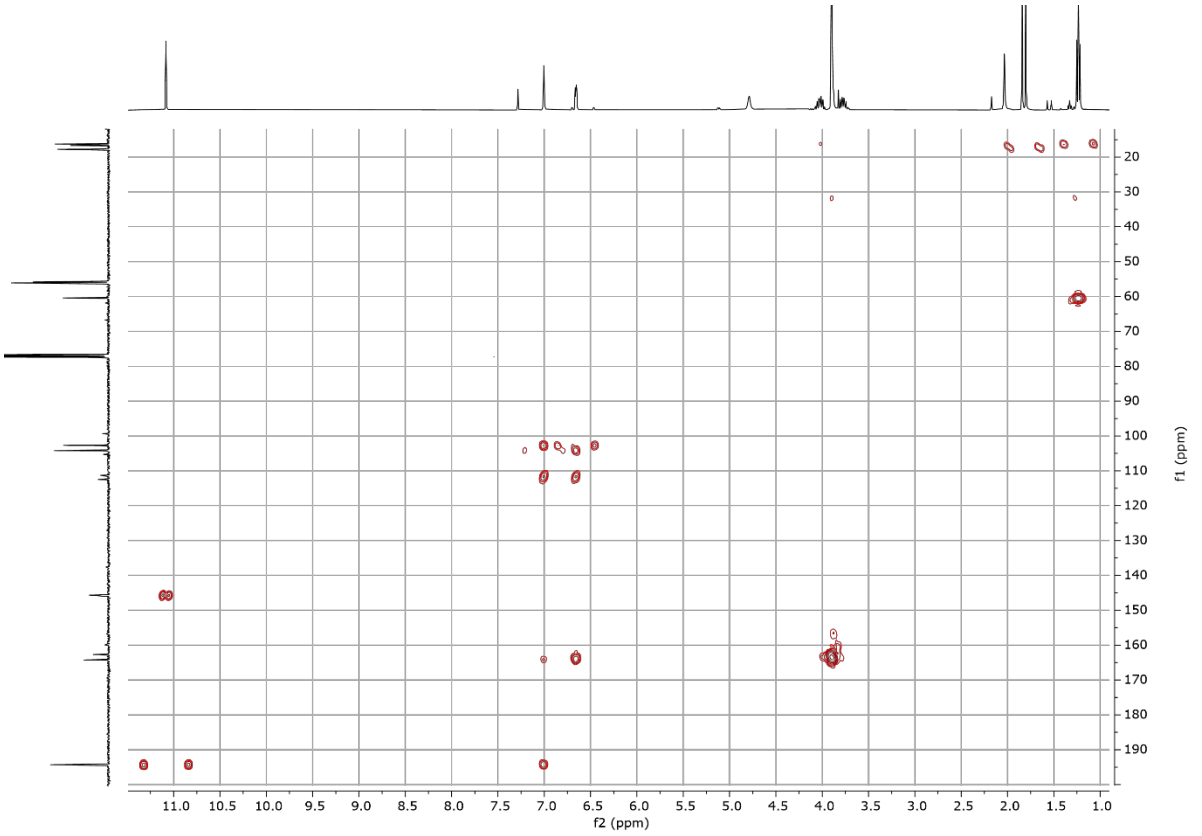

Figure 8.178 HMBC NMR spectrum of **23a** ($CDCl_3$, 298 K).

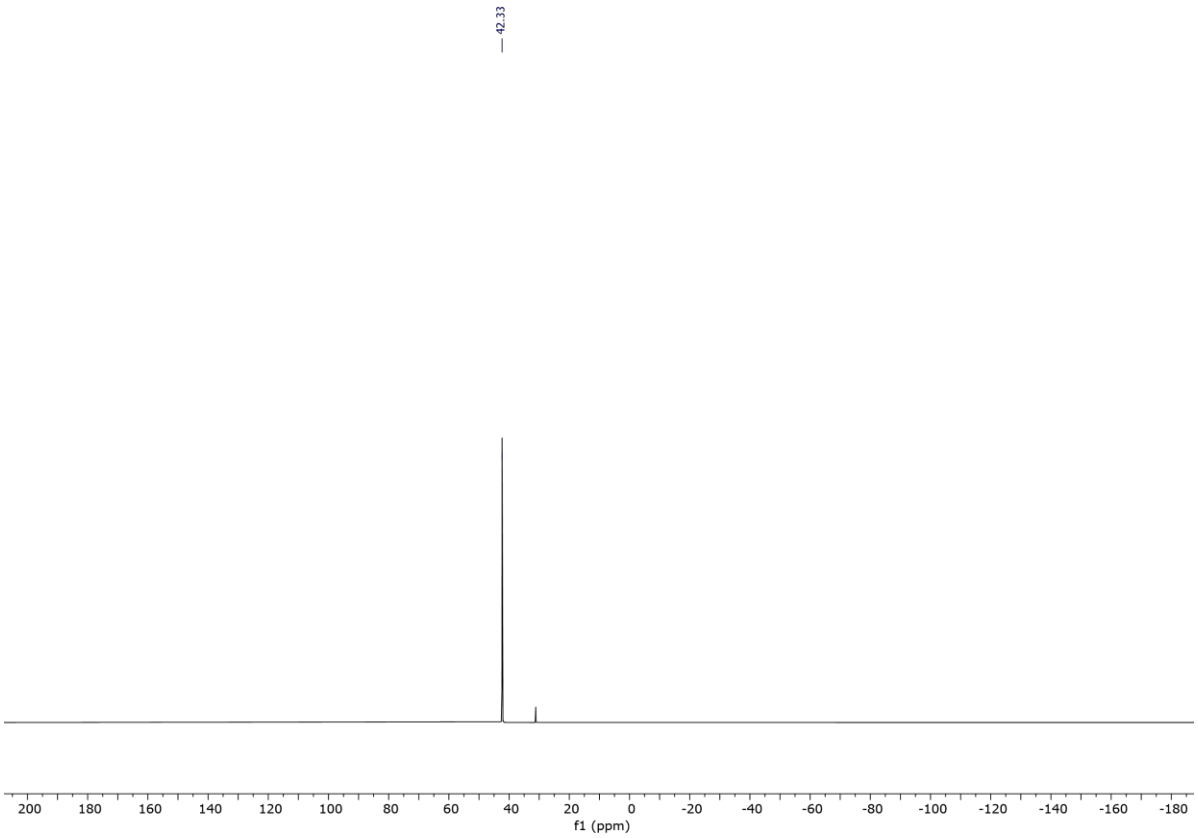

Figure 8.179 $^{31}P\{^{1}H\}$ NMR spectrum of **23a** ($CDCl_3$, 162 MHz, 298 K).

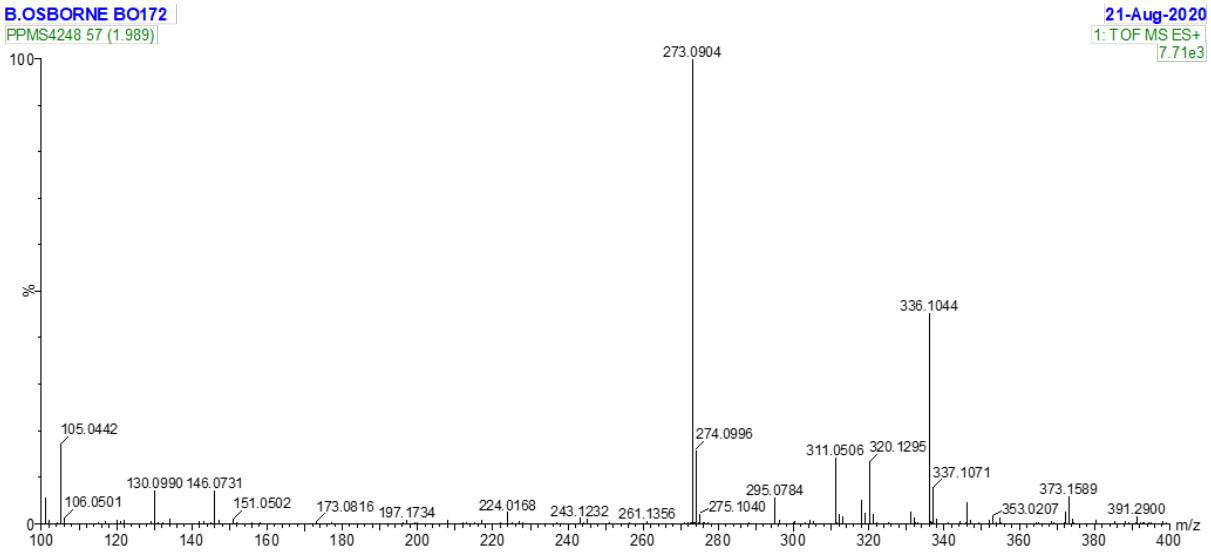

Figure 8.180 ES-TOF+ MS of **23a**.

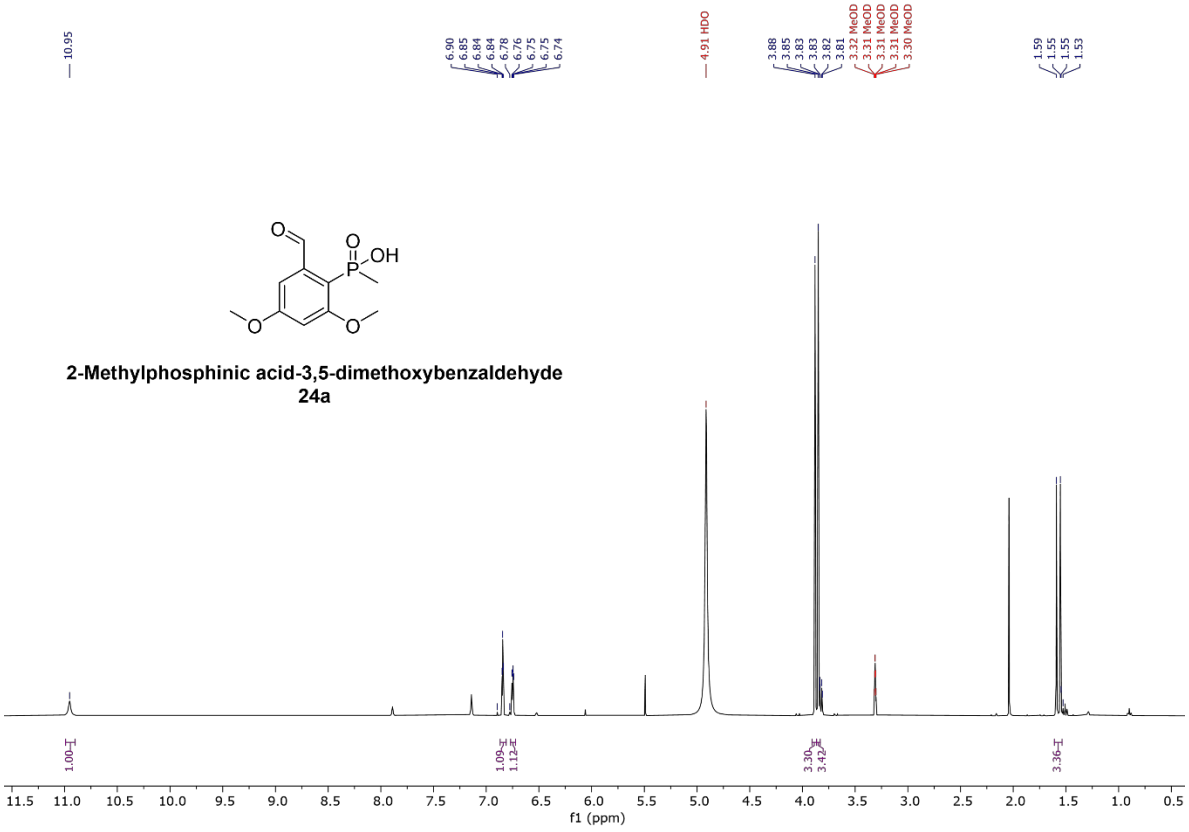

Figure 8.181 ^{1}H NMR spectrum of **24a** (CD_3OD, 400 MHz, 298 K).

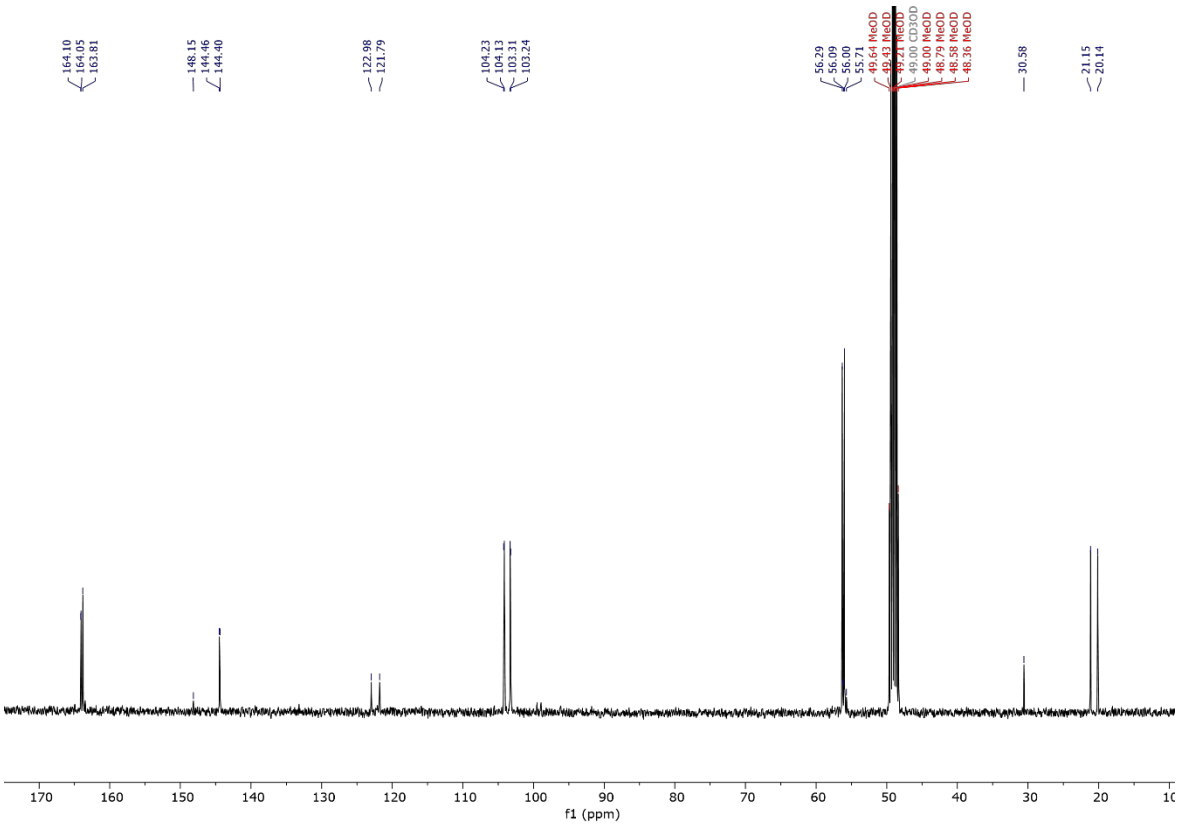

Figure 8.182 $^{13}C\{^{1}H\}$ NMR spectrum of **24a** (CD_3OD, 101 MHz, 298 K).

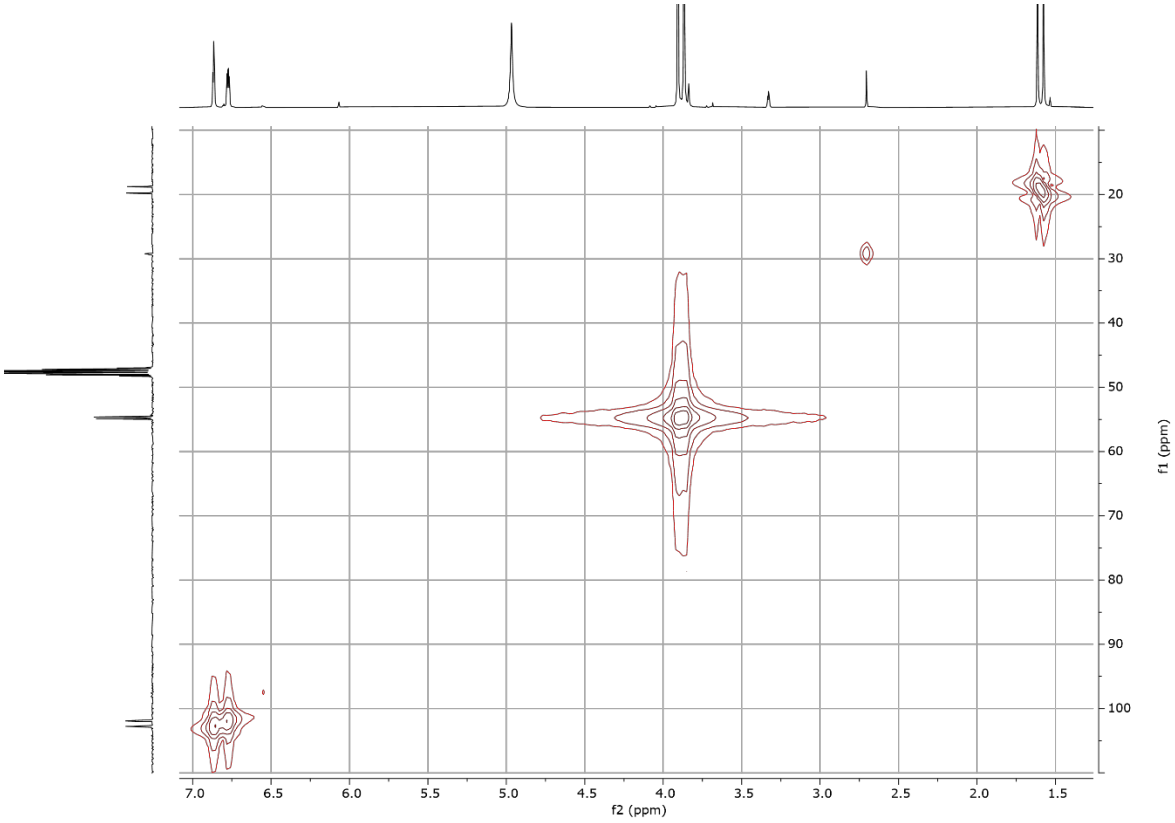

Figure 8.183 HMQC NMR spectrum of **24a** (CD_3OD, 298 K).

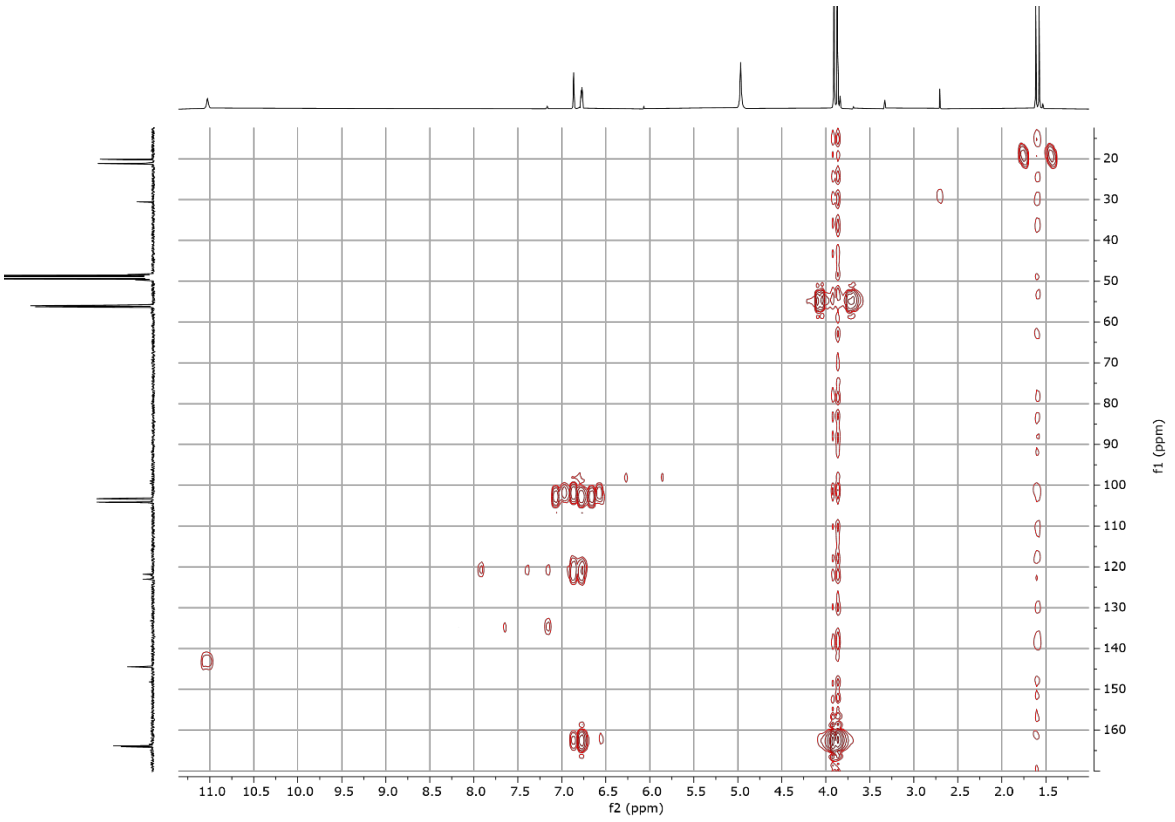

Figure 8.184 HMBC NMR spectrum of **24a** (CD_3OD, 298 K).

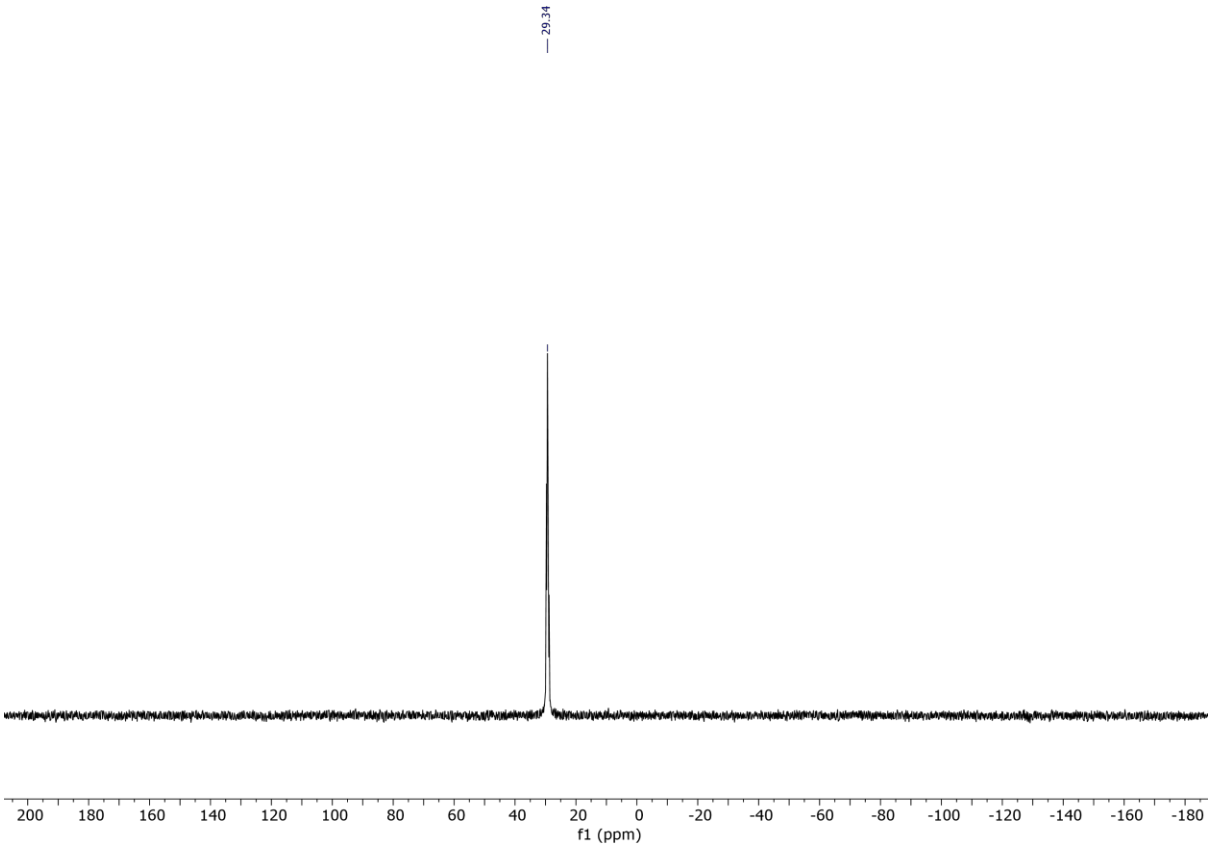

Figure 8.185 $^{31}P\{^{1}H\}$ NMR spectrum of **24a** (CD_3OD, 162 MHz, 298 K).

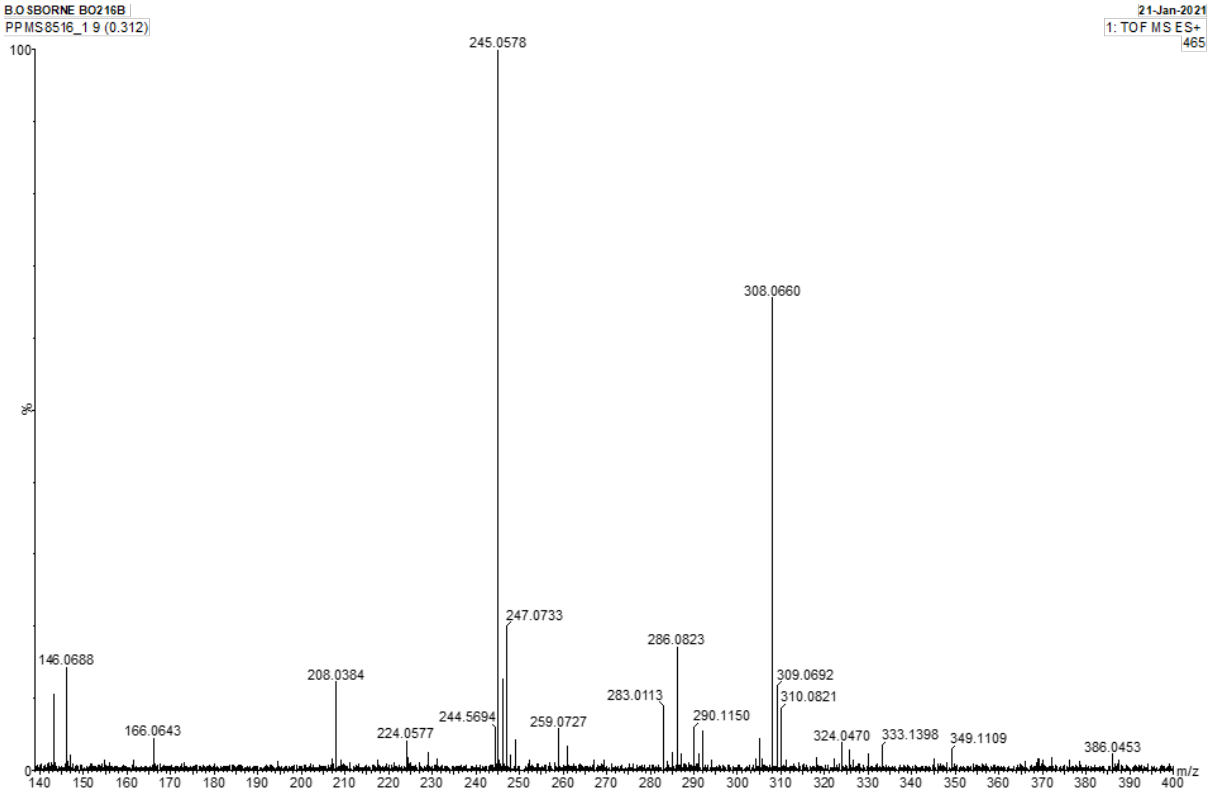

Figure 8.186 ES-TOF+ MS of **24a**.

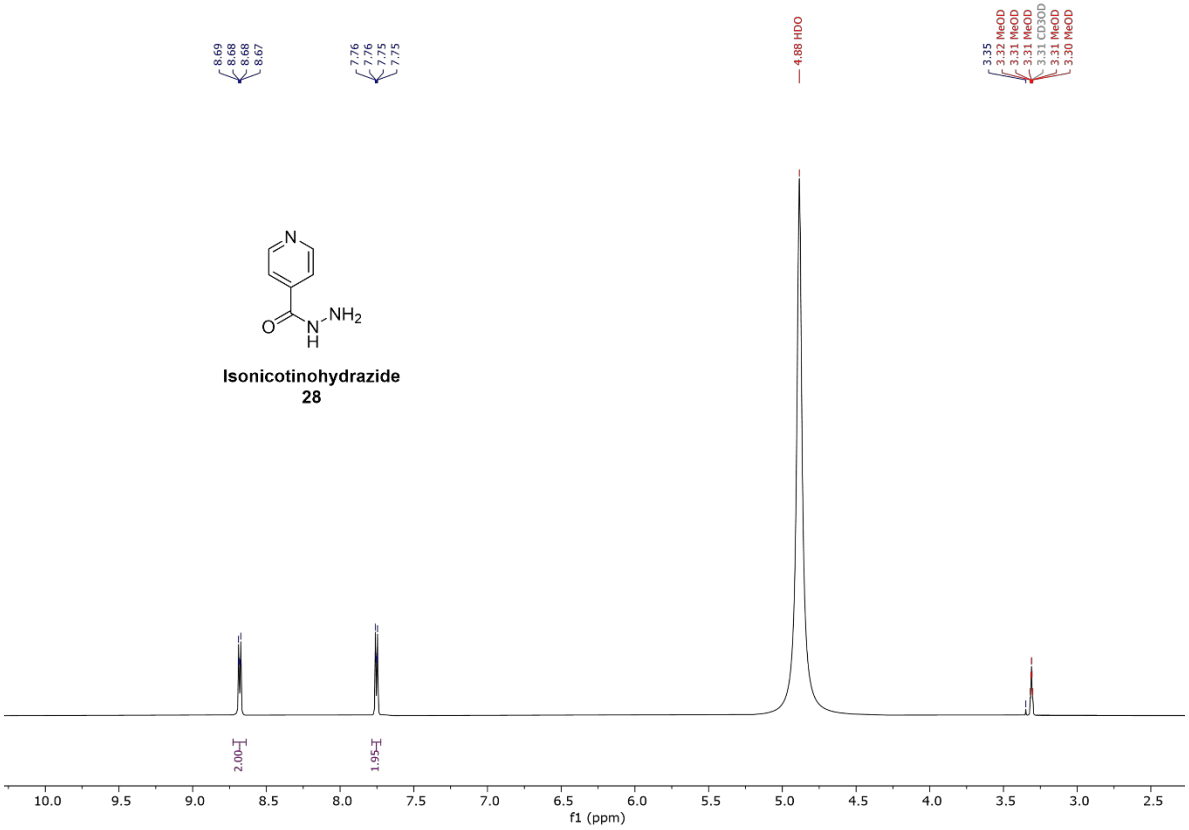

Figure 8.187 ^{1}H NMR spectrum of **28** (CD_3OD, 400 MHz, 298 K).

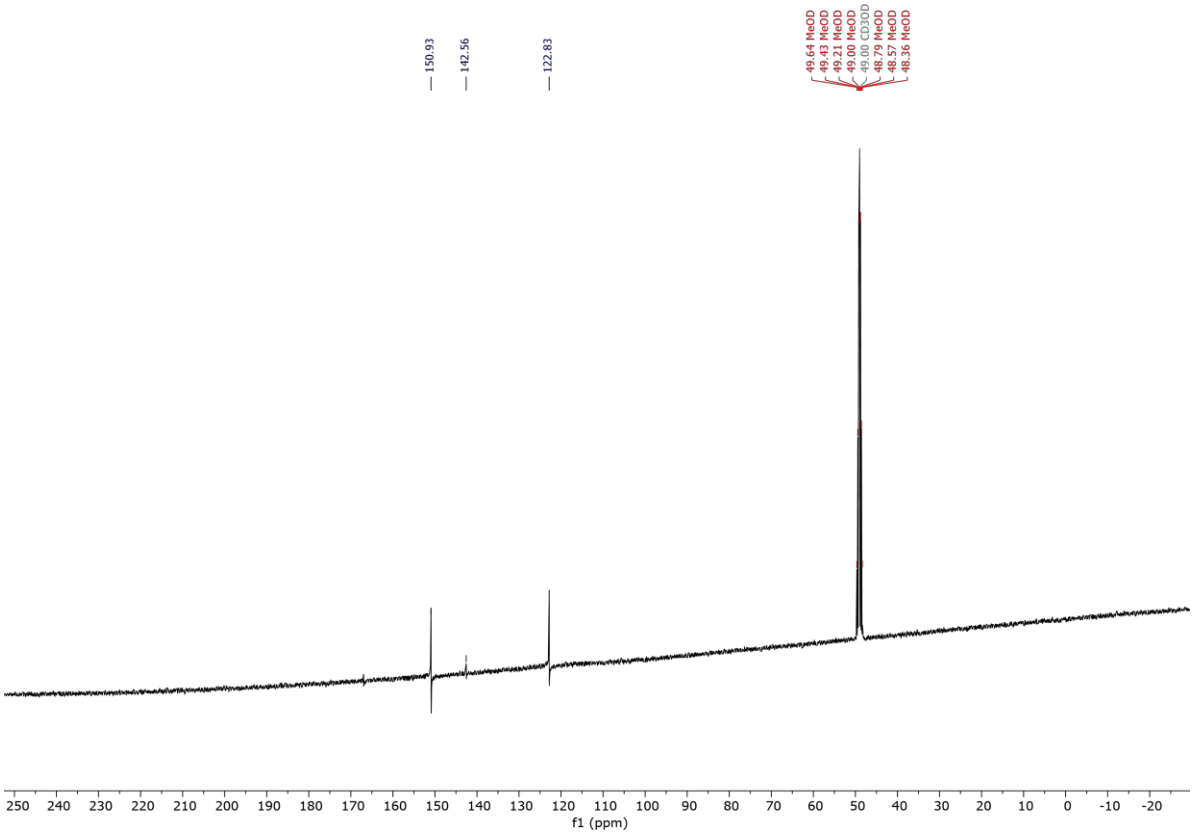

Figure 8.188 $^{13}C\{^{1}H\}$ NMR spectrum of **28** (CD_3OD, 101 MHz, 298 K).

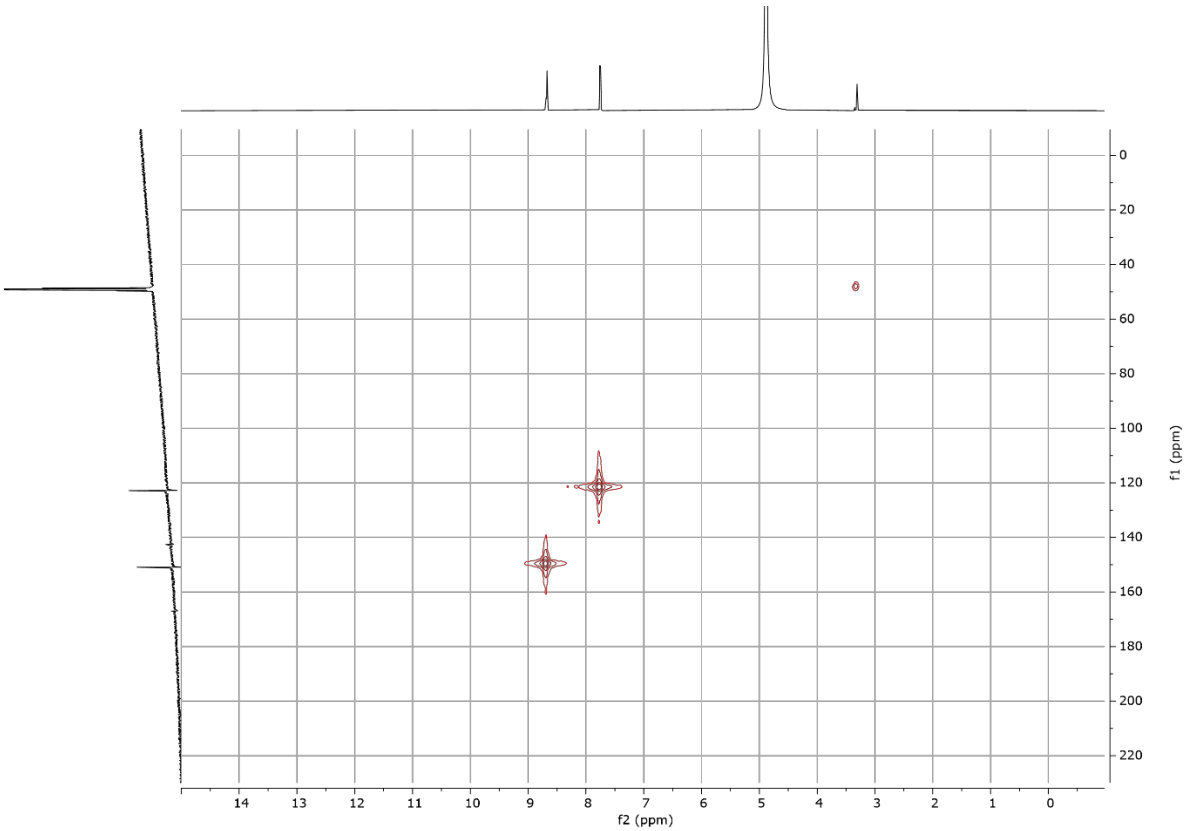

Figure 8.189 HMQC NMR spectrum of **28** (CD_3OD, 298 K).

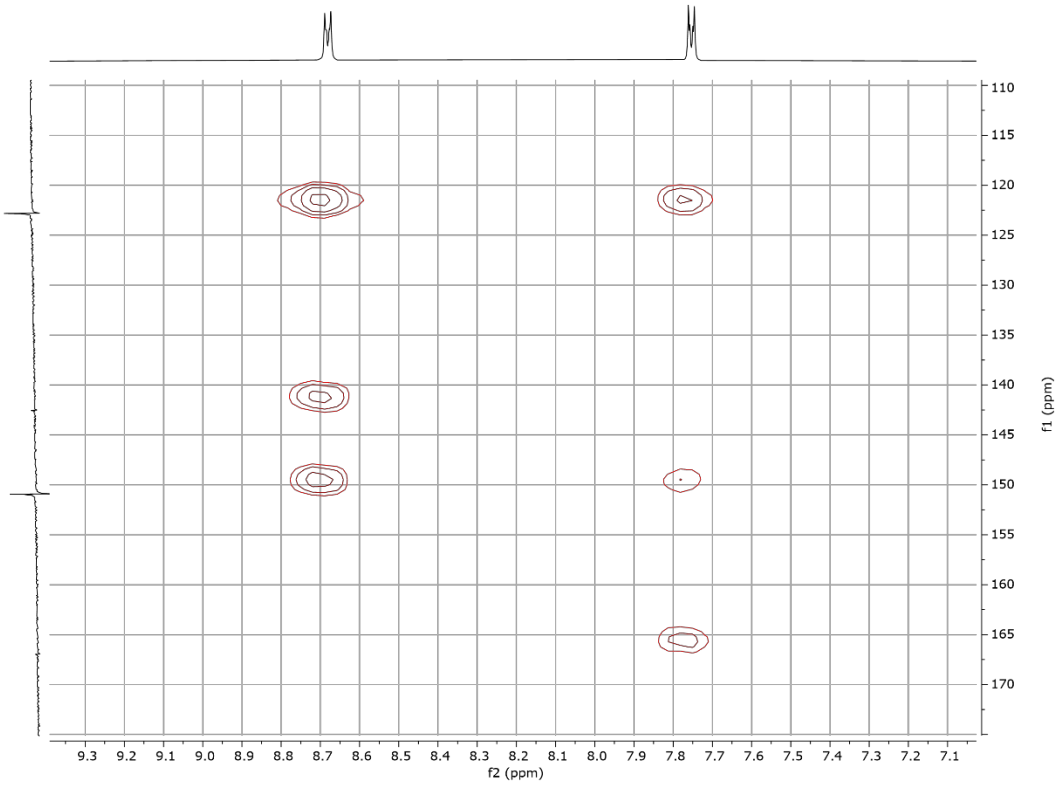

Figure 8.190 HMBC NMR spectrum of **28** (CD_3OD, 298 K).

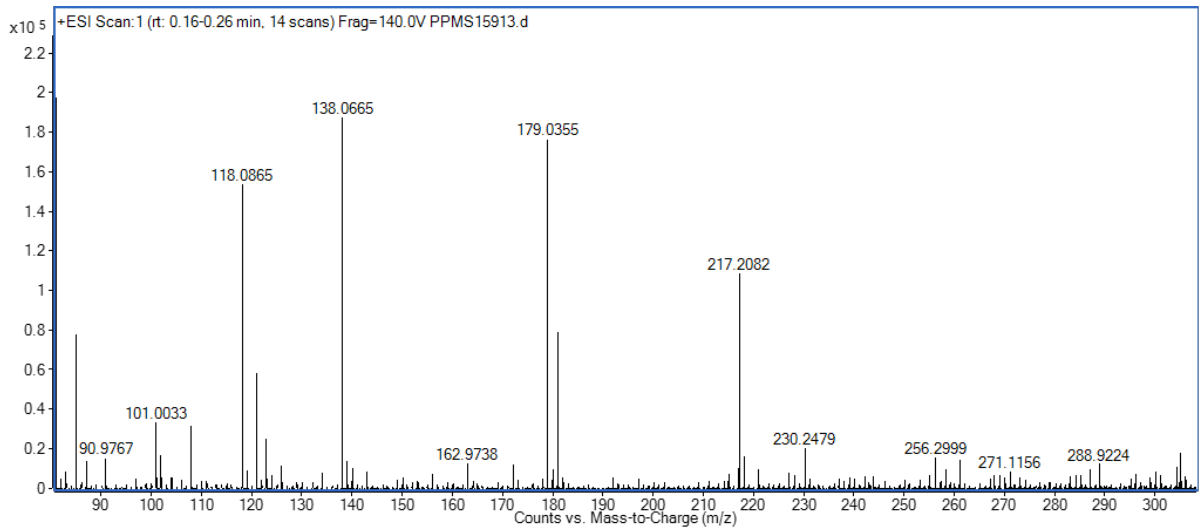

Figure 8.191 ES-TOF+ MS of **28**.

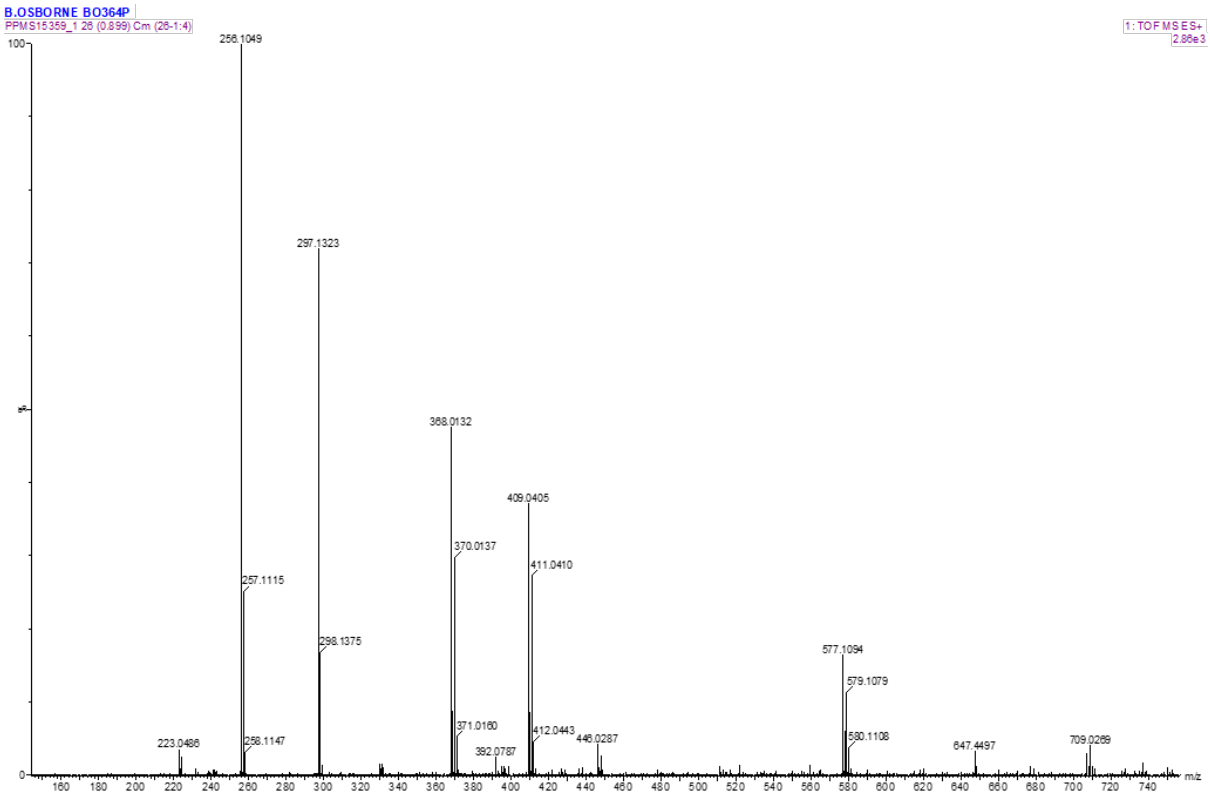

Figure 8.192 ES-TOF+ MS of **30**.

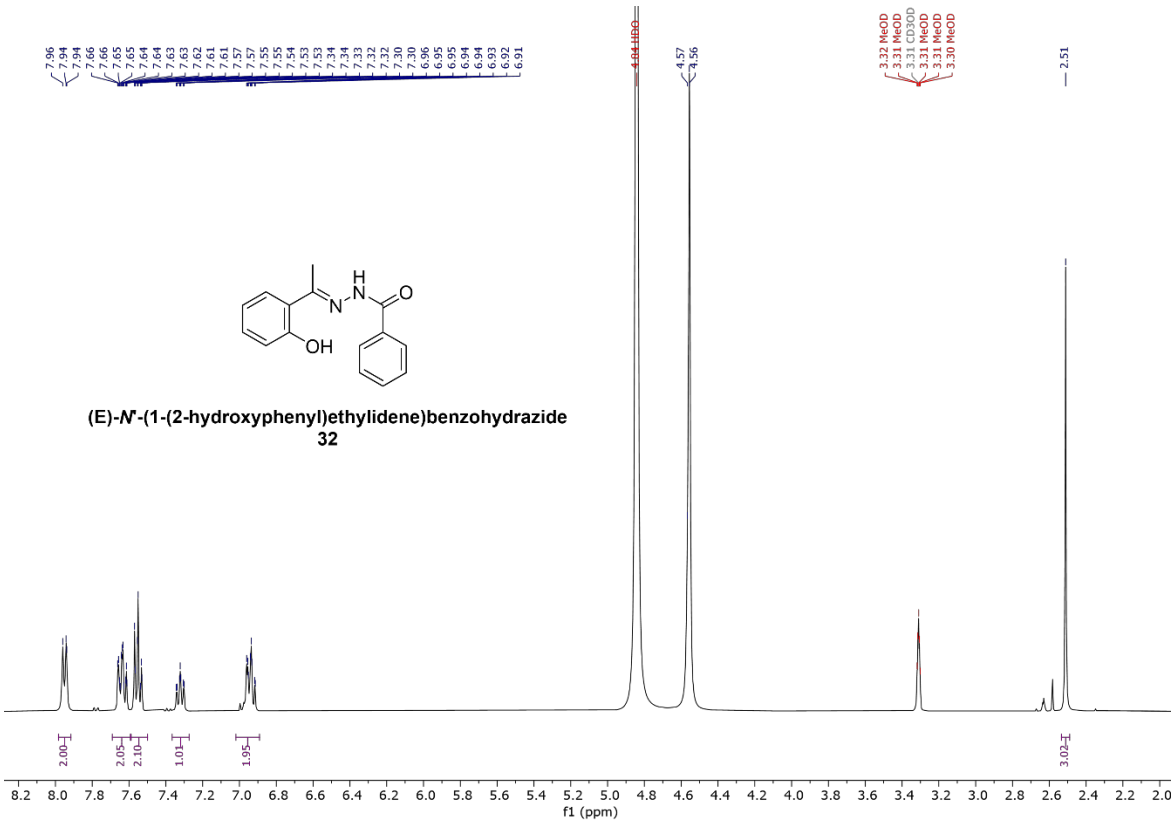

Figure 8.193 ^{1}H NMR spectrum of **32** (CD_3OD, 400 MHz, 298 K).

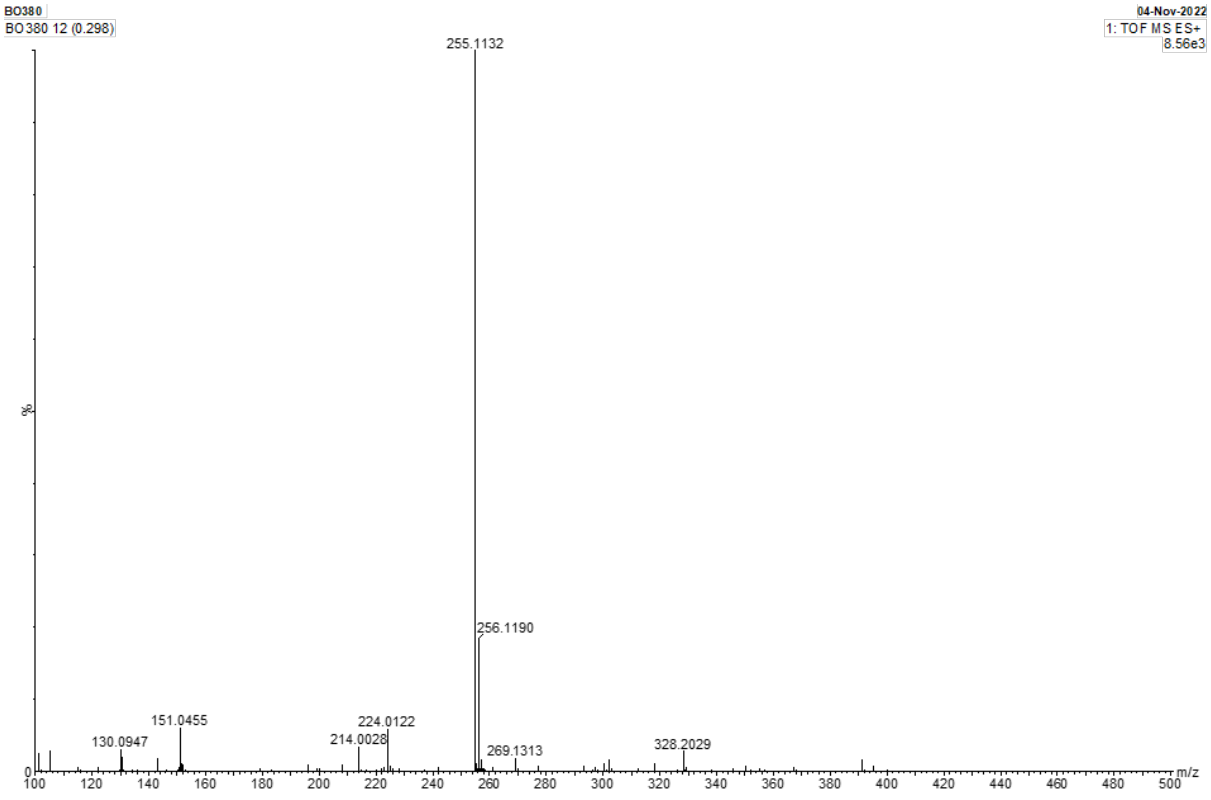

Figure 8.194 ES-TOF+ MS of **32**.

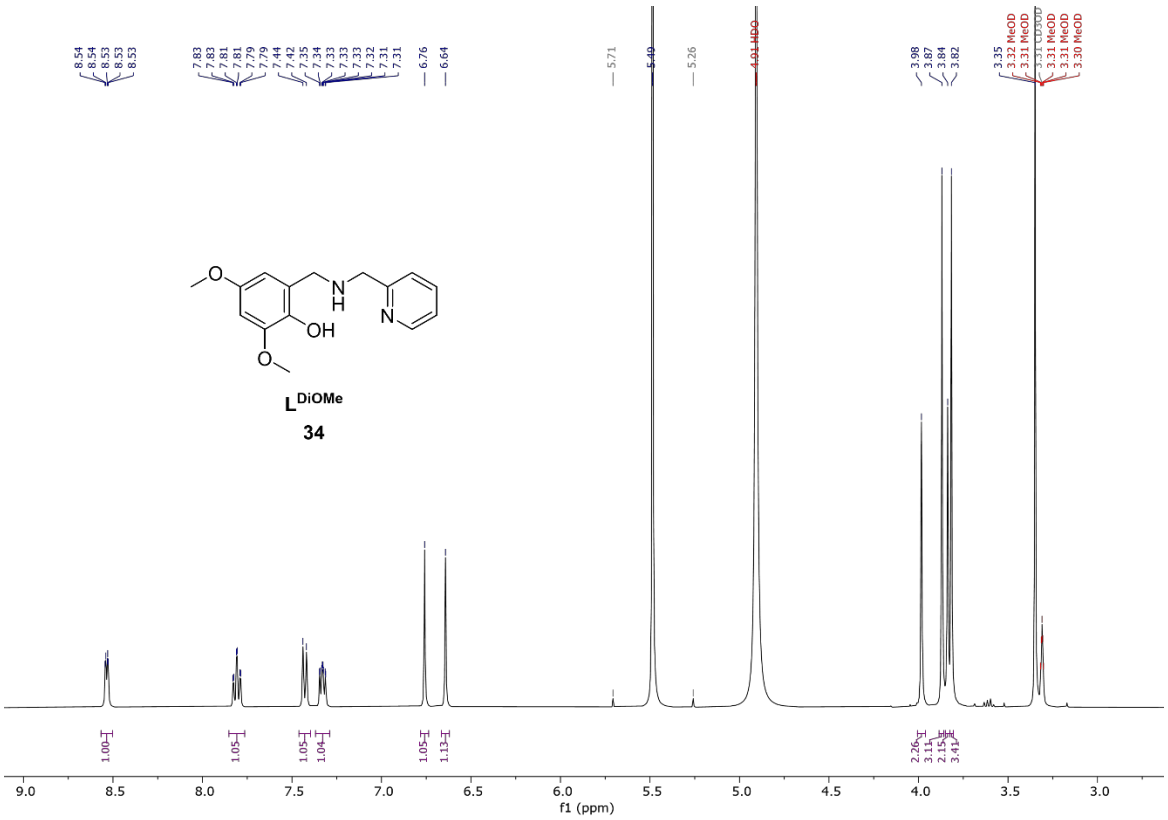

Figure 8.195 ^{1}H NMR spectrum of **34** (CD_3OD, 400 MHz, 298 K).

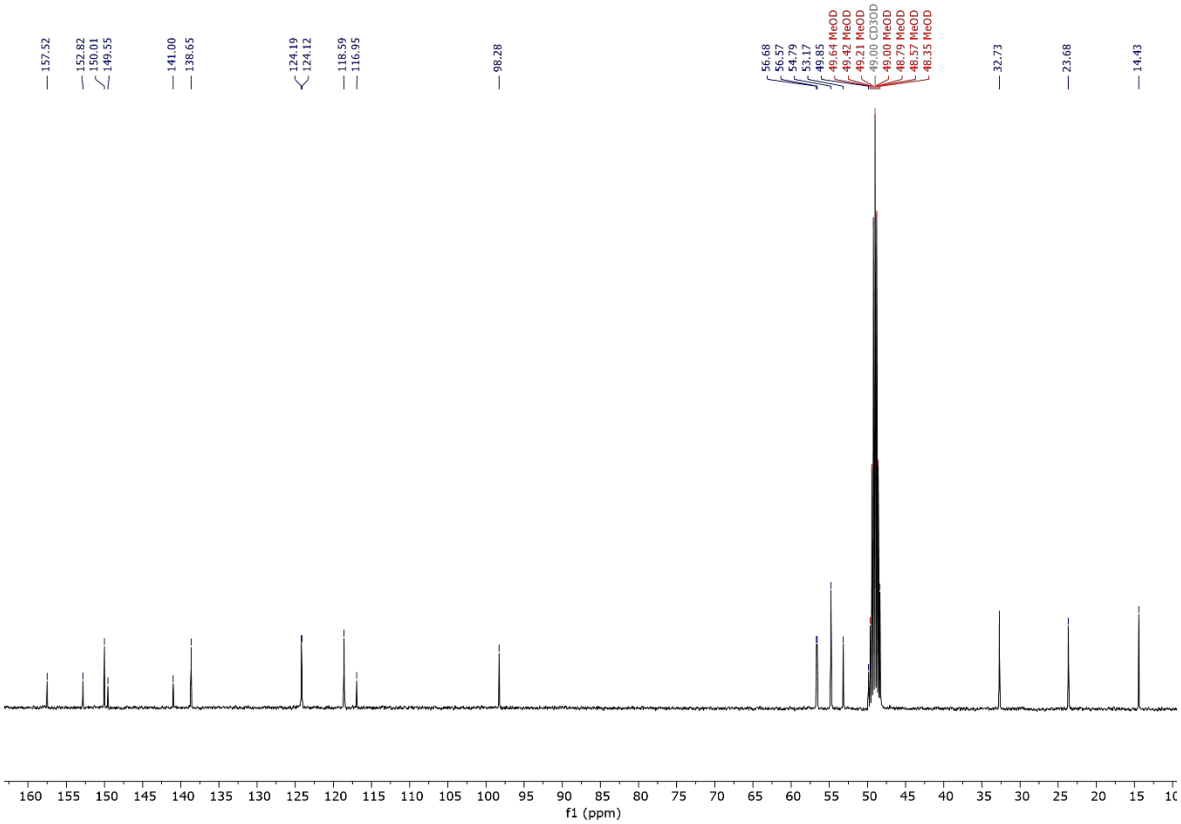

Figure 8.196 $^{13}C\{^{1}H\}$ NMR spectrum of **34** (CD_3OD, 101 MHz, 298 K).

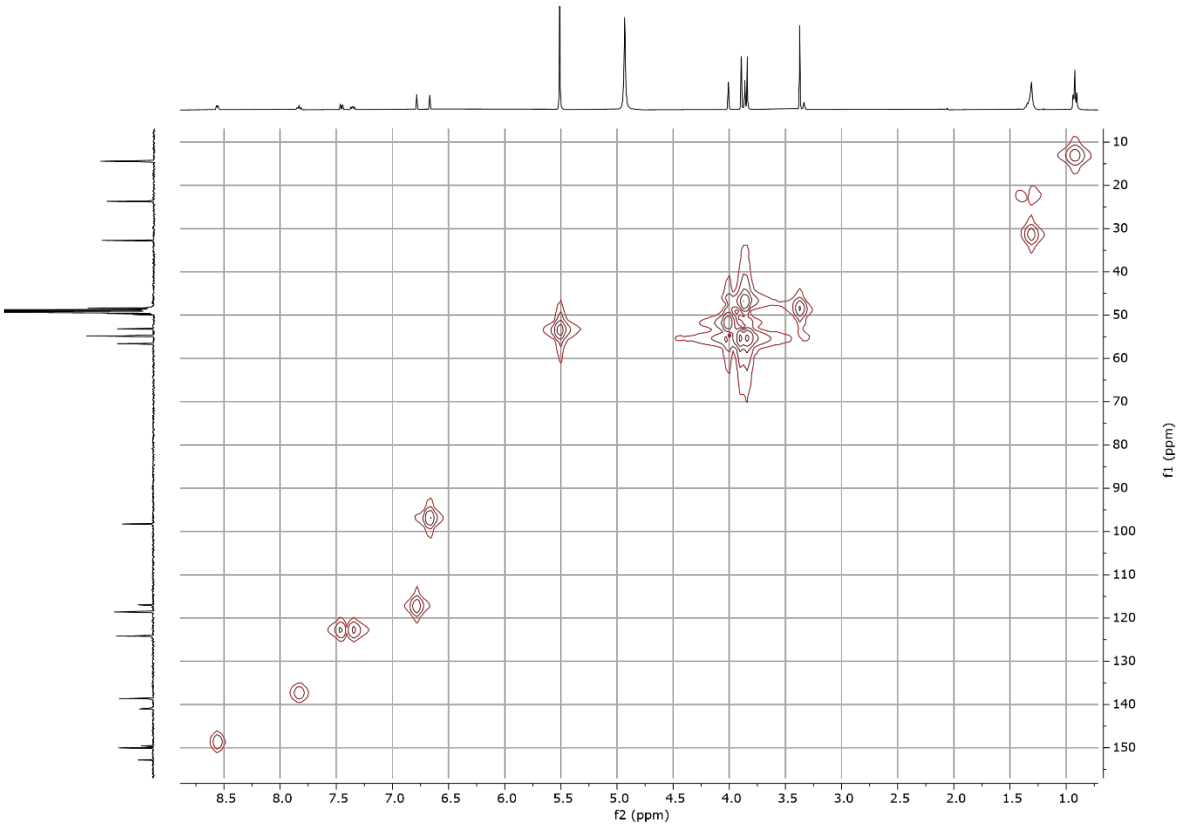

Figure 8.197 HMQC NMR spectrum of **34** (CD_3OD, 298 K).

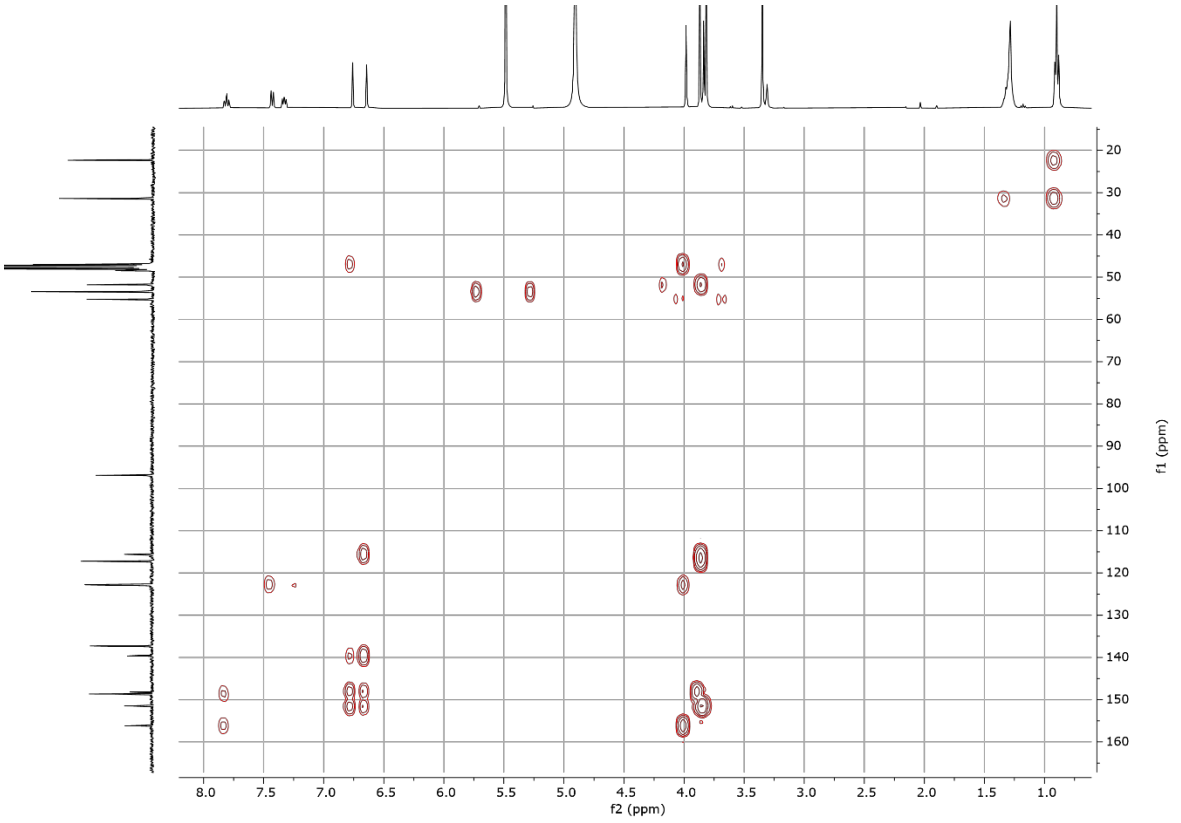

Figure 8.198 HMBC NMR spectrum of **34** (CD_3OD, 298 K).

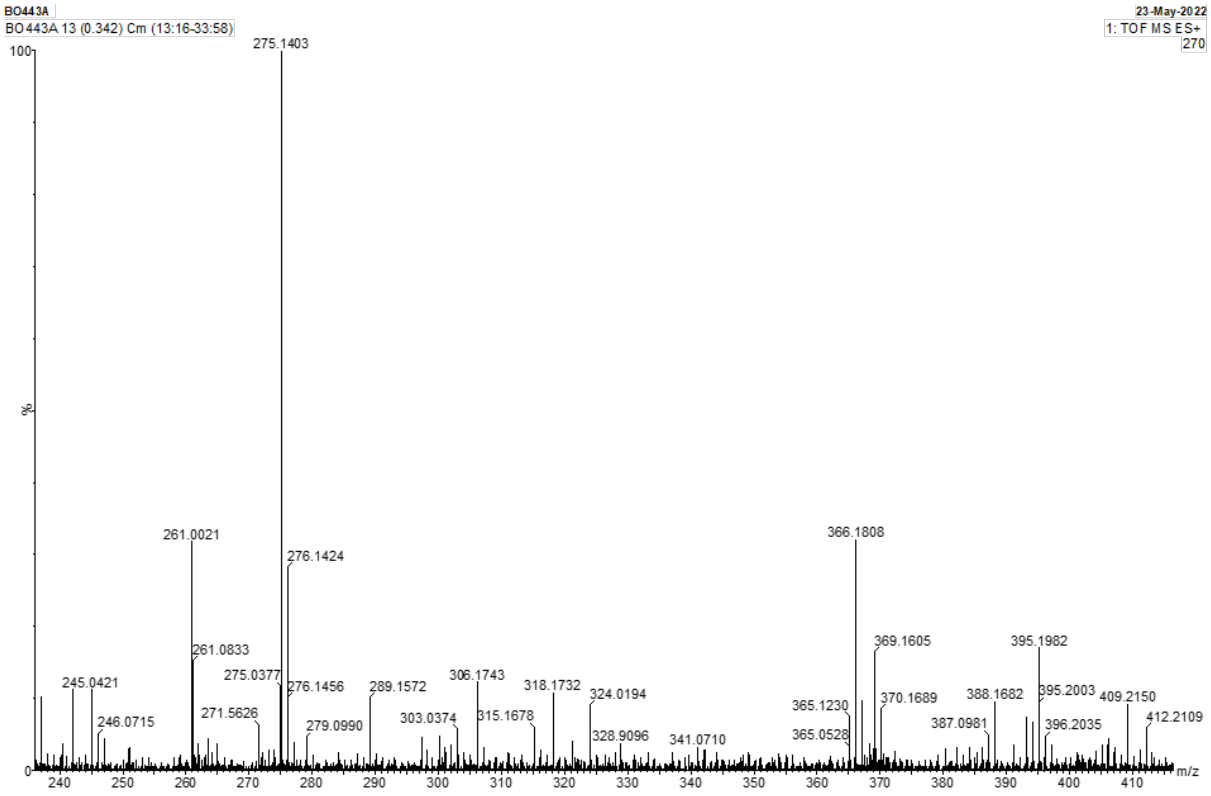

Figure 8.199 ES-TOF+ MS of **34**.

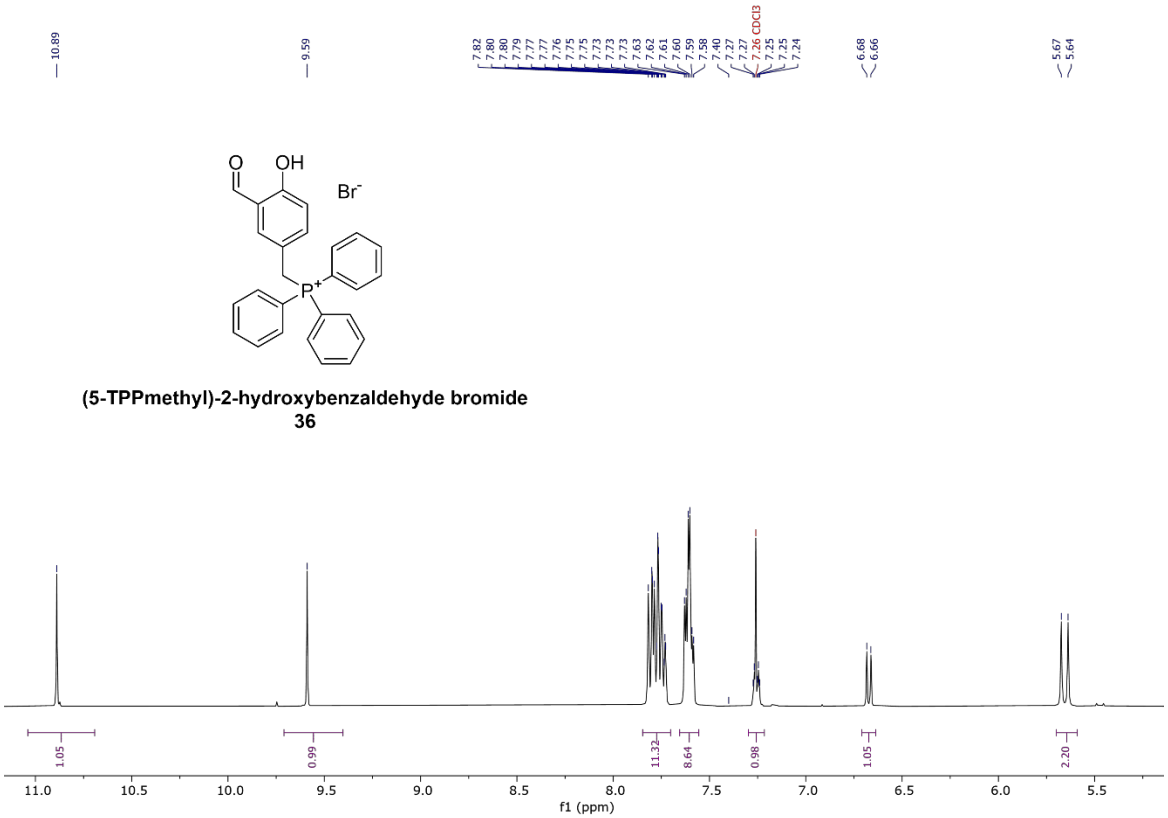

Figure 8.200 ^{1}H NMR spectrum of **36** ($CDCl_3$, 400 MHz, 298 K).

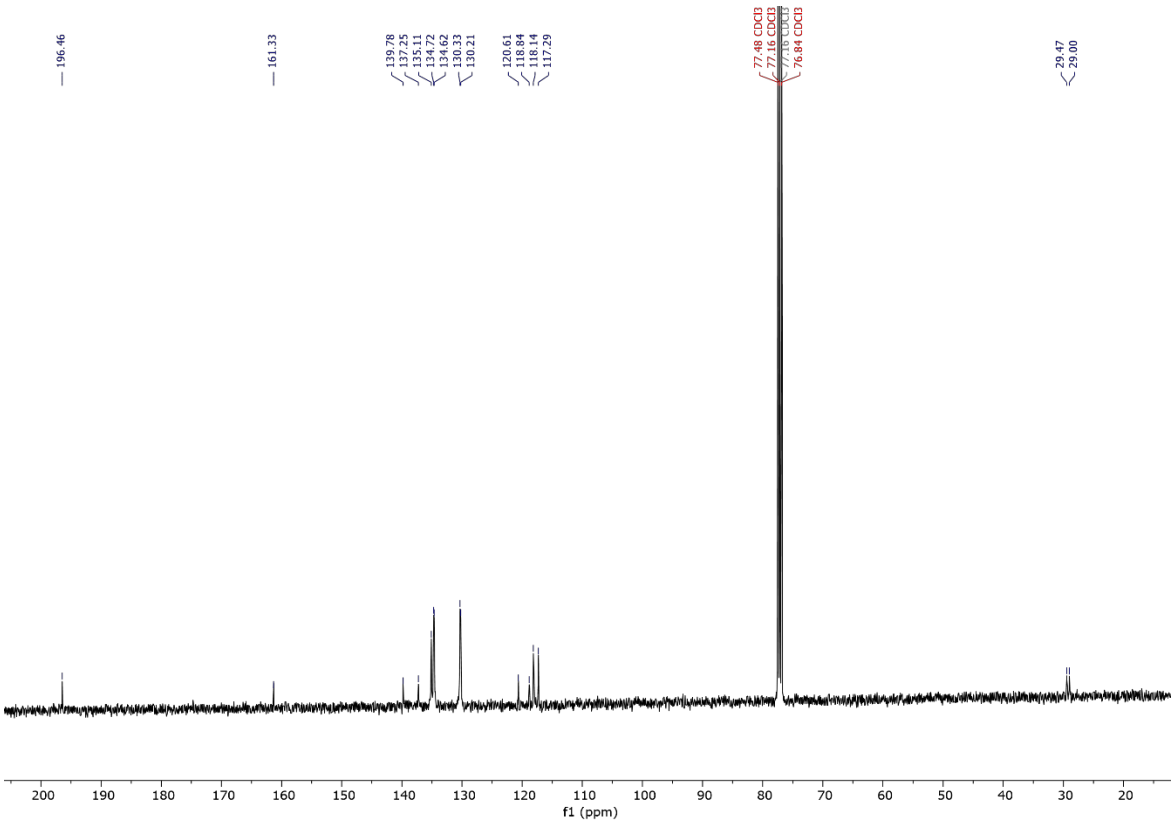

Figure 8.201 $^{13}C\{^{1}H\}$ NMR spectrum of **36** ($CDCl_3$, 101 MHz, 298 K).

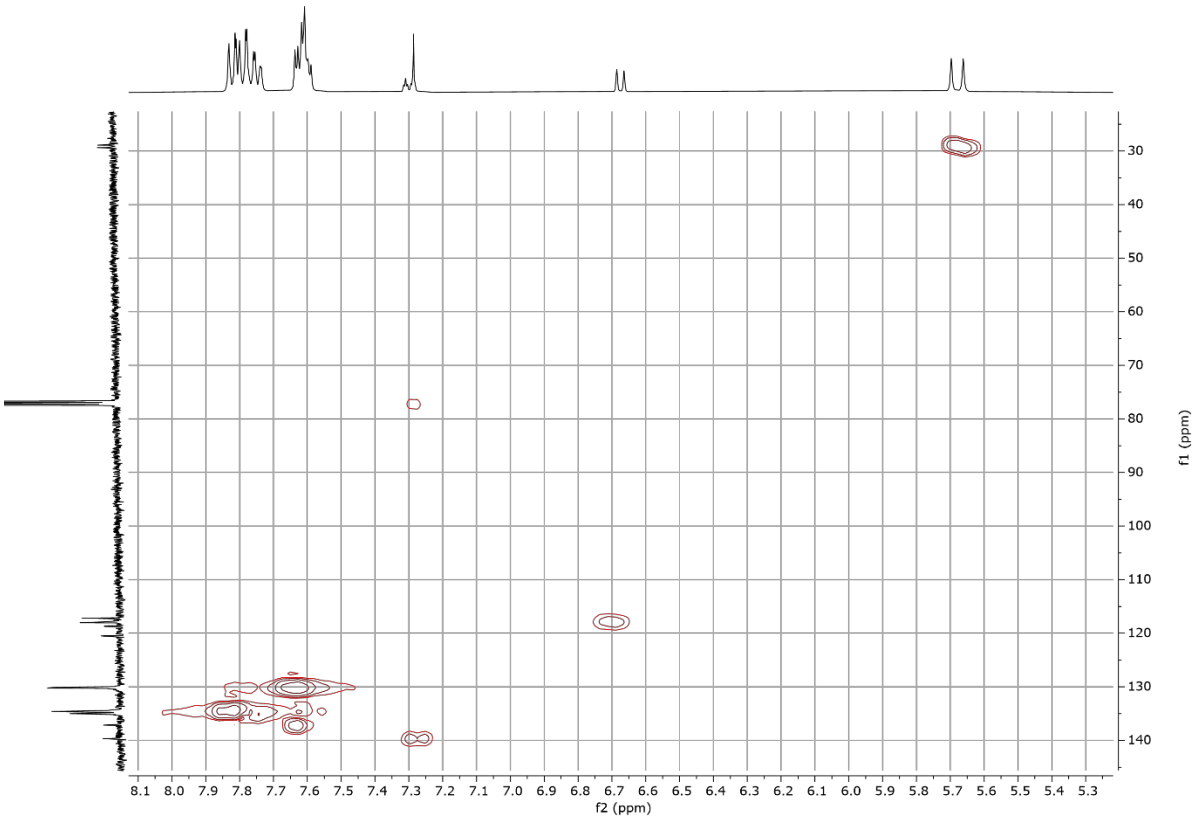

Figure 8.202 HMQC NMR spectrum of **36** ($CDCl_3$, 298 K).

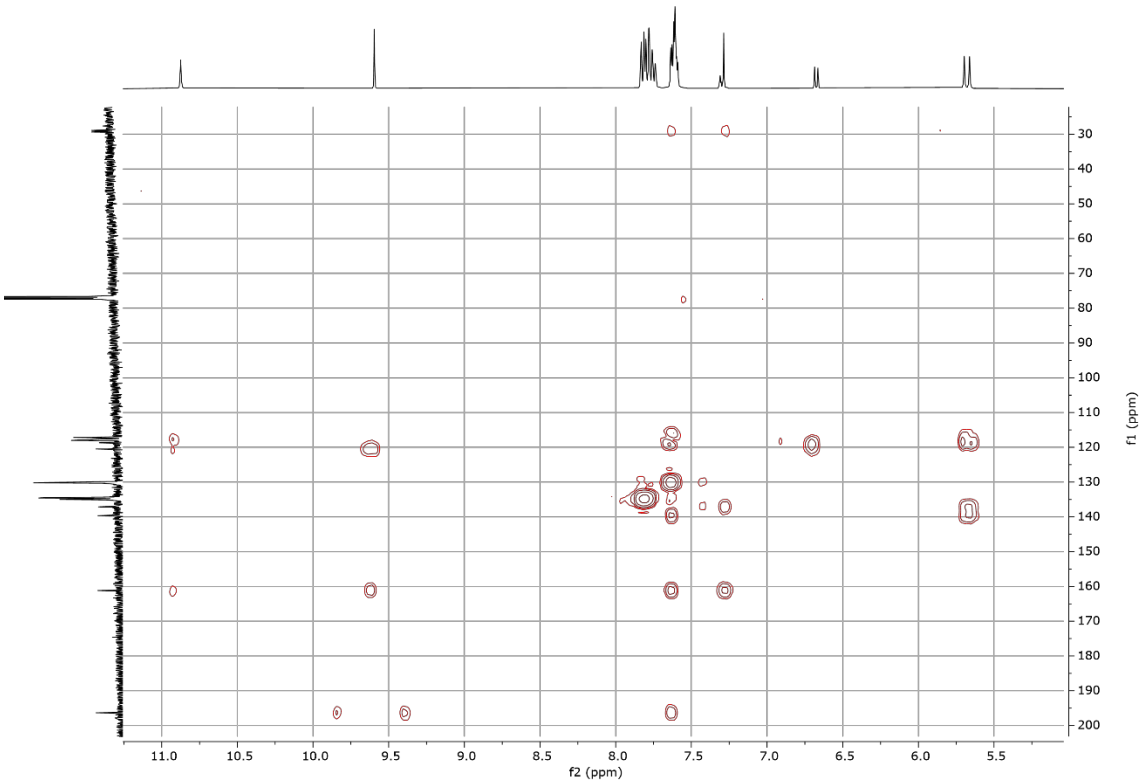

Figure 8.203 HMBC NMR spectrum of **36** ($CDCl_3$, 298 K).

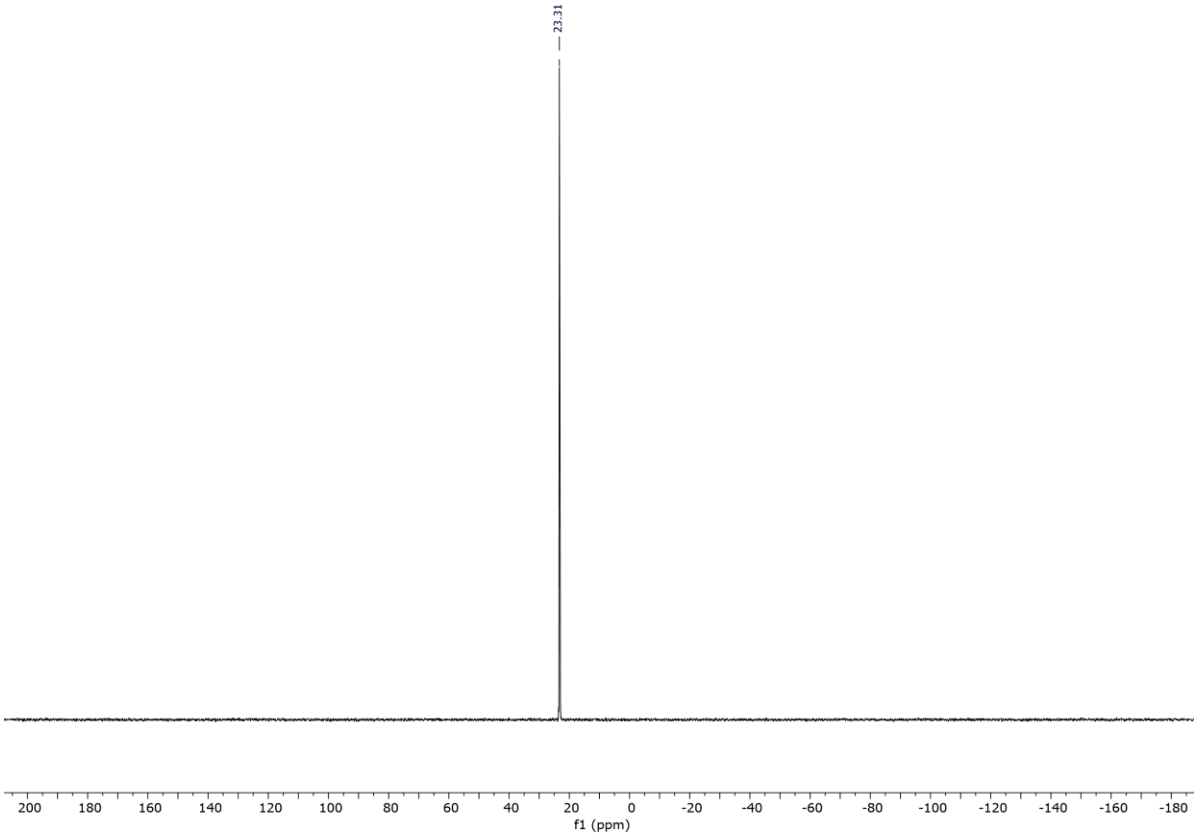

Figure 8.204 $^{31}P\{^{1}H\}$ NMR spectrum of **36** ($CDCl_3$, 162 MHz, 298 K).

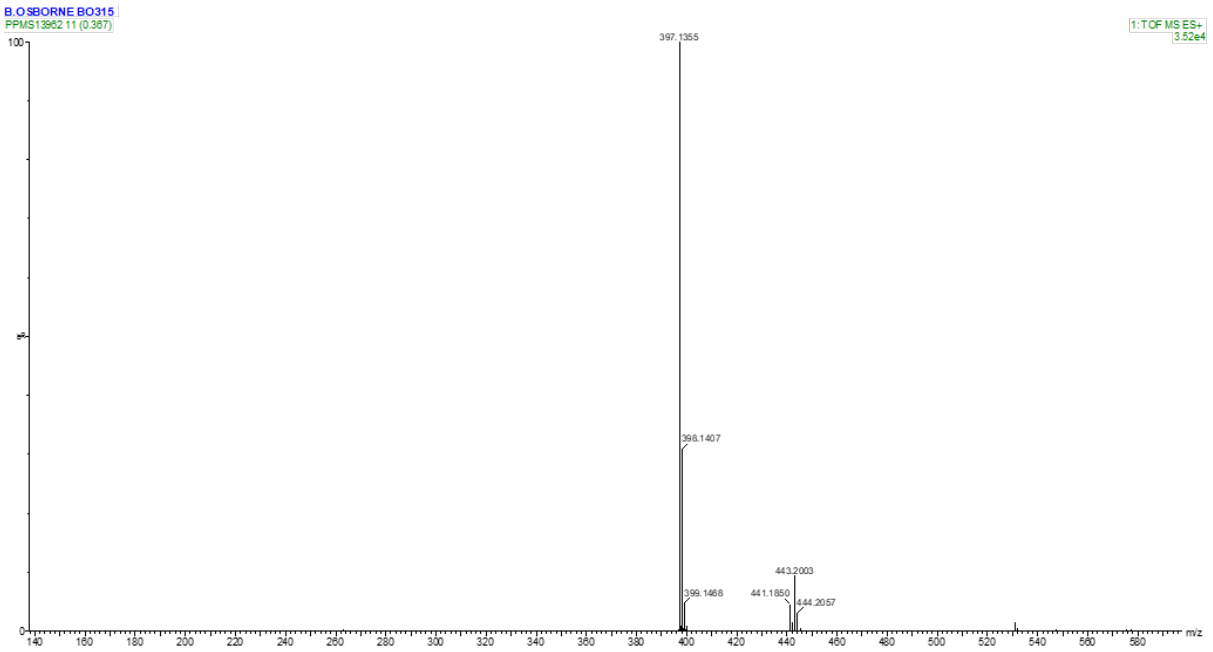

Figure 8.205 ES-TOF+ MS of **36**.

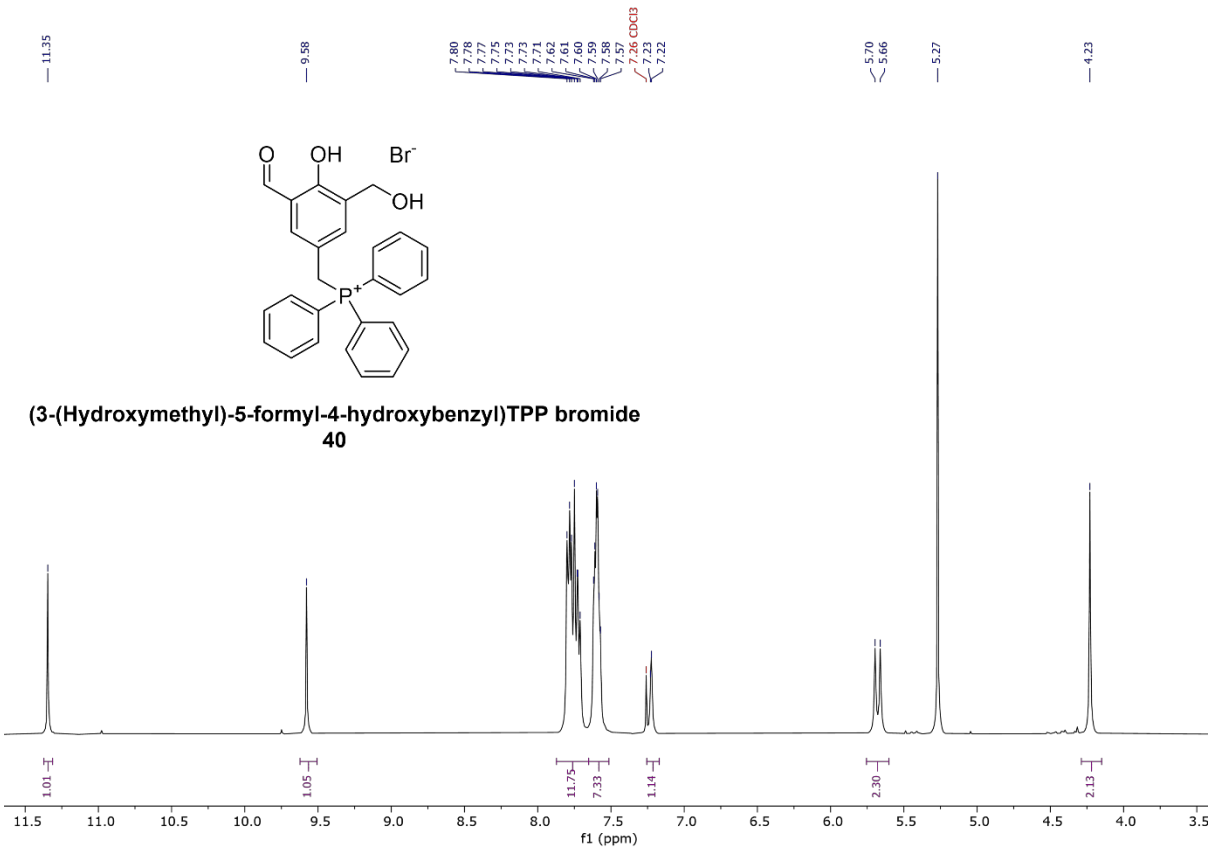

Figure 8.206 ^{1}H NMR spectrum of **40** ($CDCl_3$, 400 MHz, 298 K).

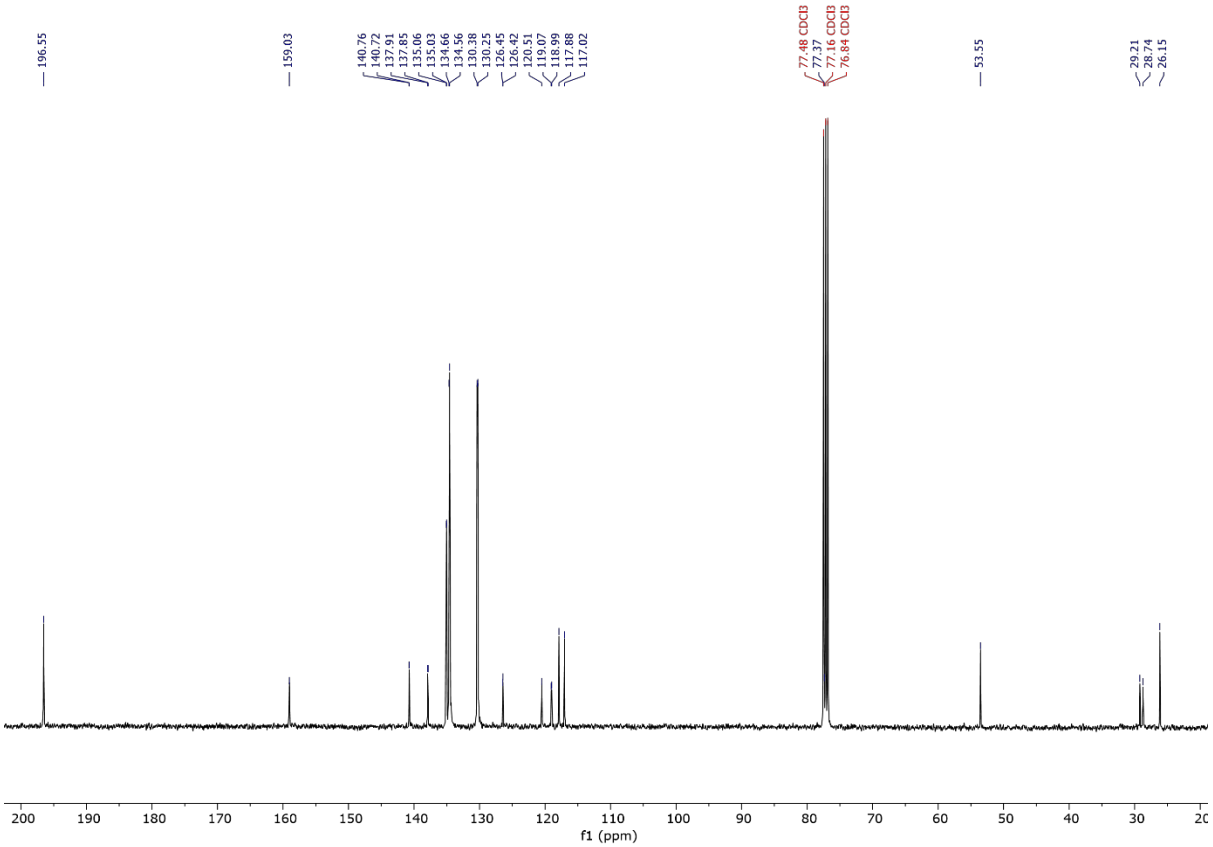

Figure 8.207 $^{13}C\{^{1}H\}$ NMR spectrum of **40** ($CDCl_3$, 101 MHz, 298 K).

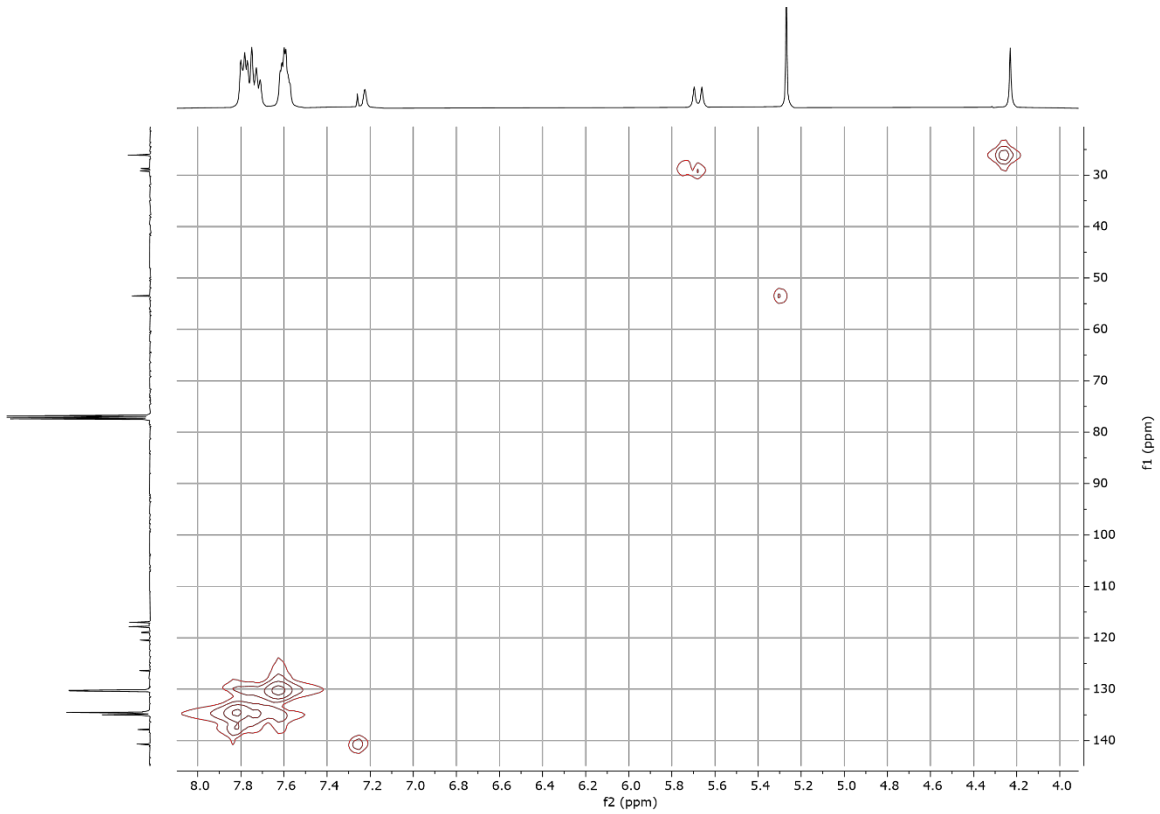

Figure 8.208 HMQC NMR spectrum of **40** ($CDCl_3$, 298 K).

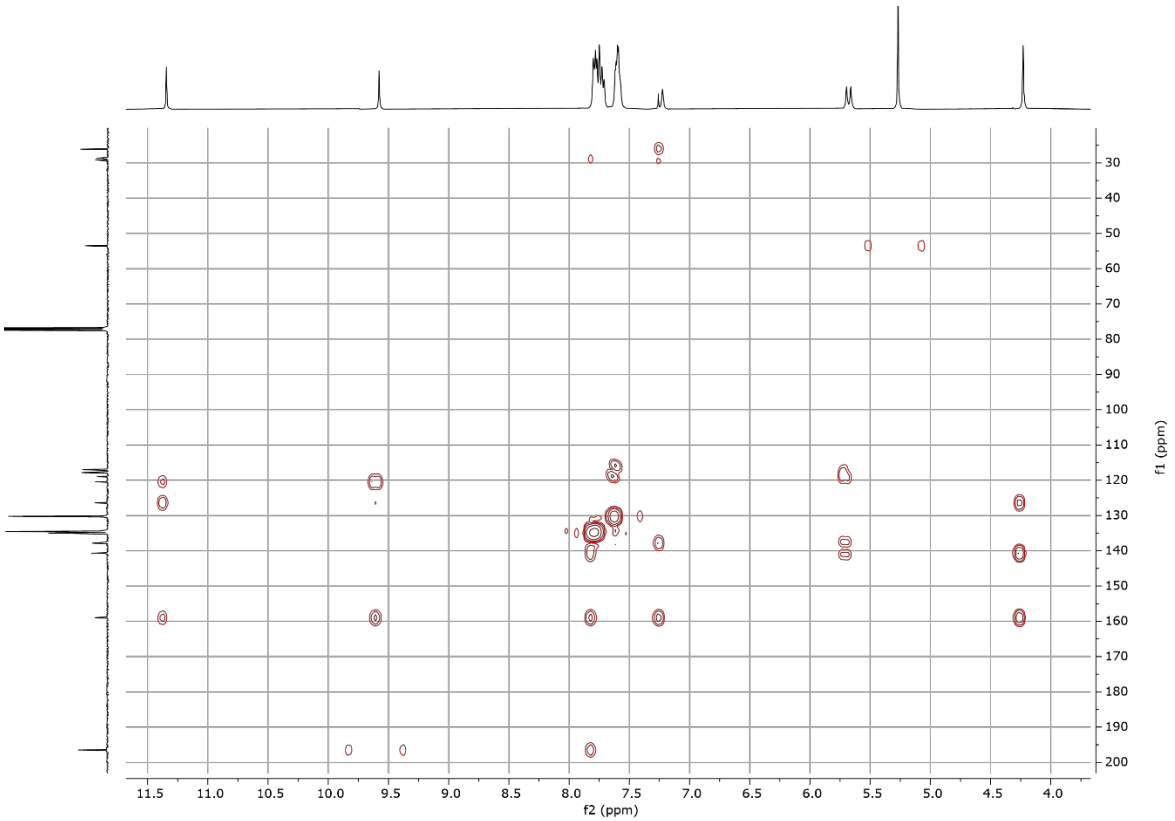

Figure 8.209 HMBC NMR spectrum of **40** ($CDCl_3$, 298 K).

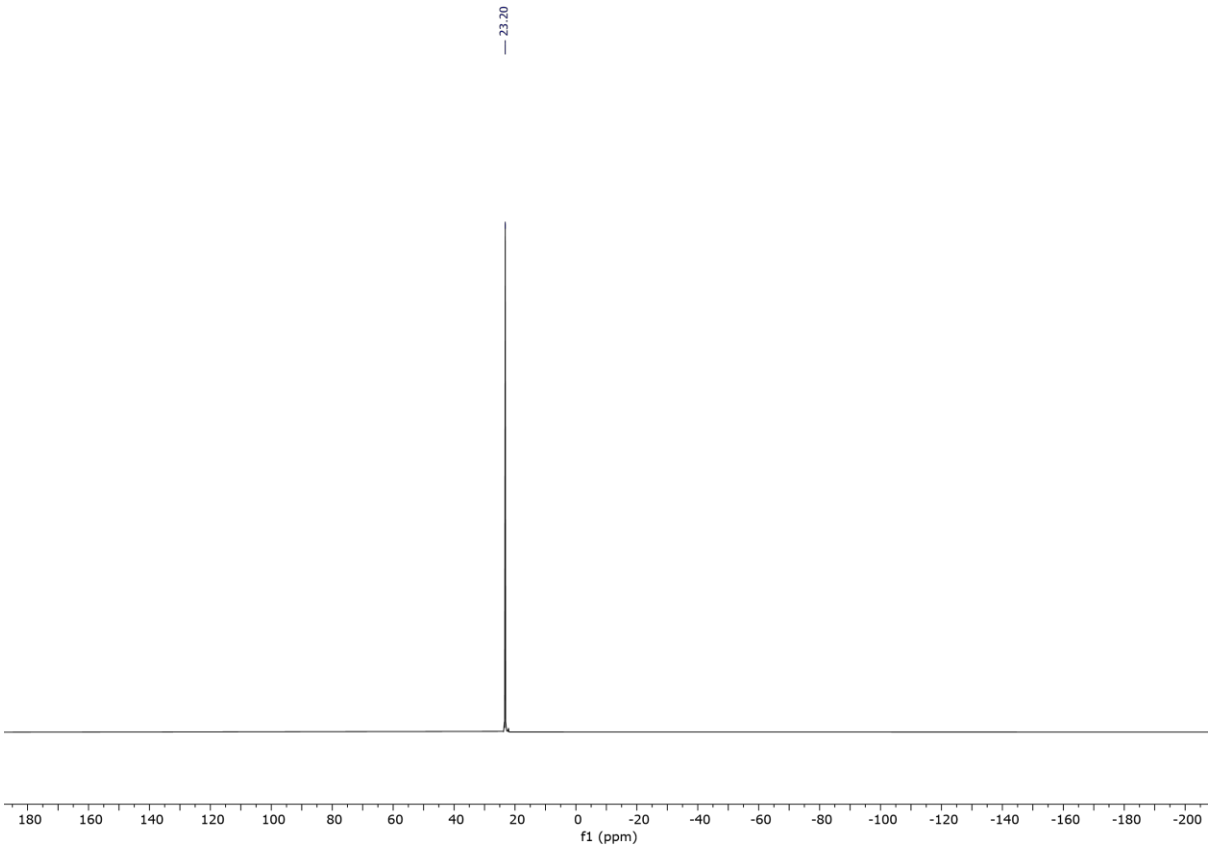

Figure 8.210 $^{31}P\{^{1}H\}$ NMR spectrum of **40** ($CDCl_3$, 162 MHz, 298 K).

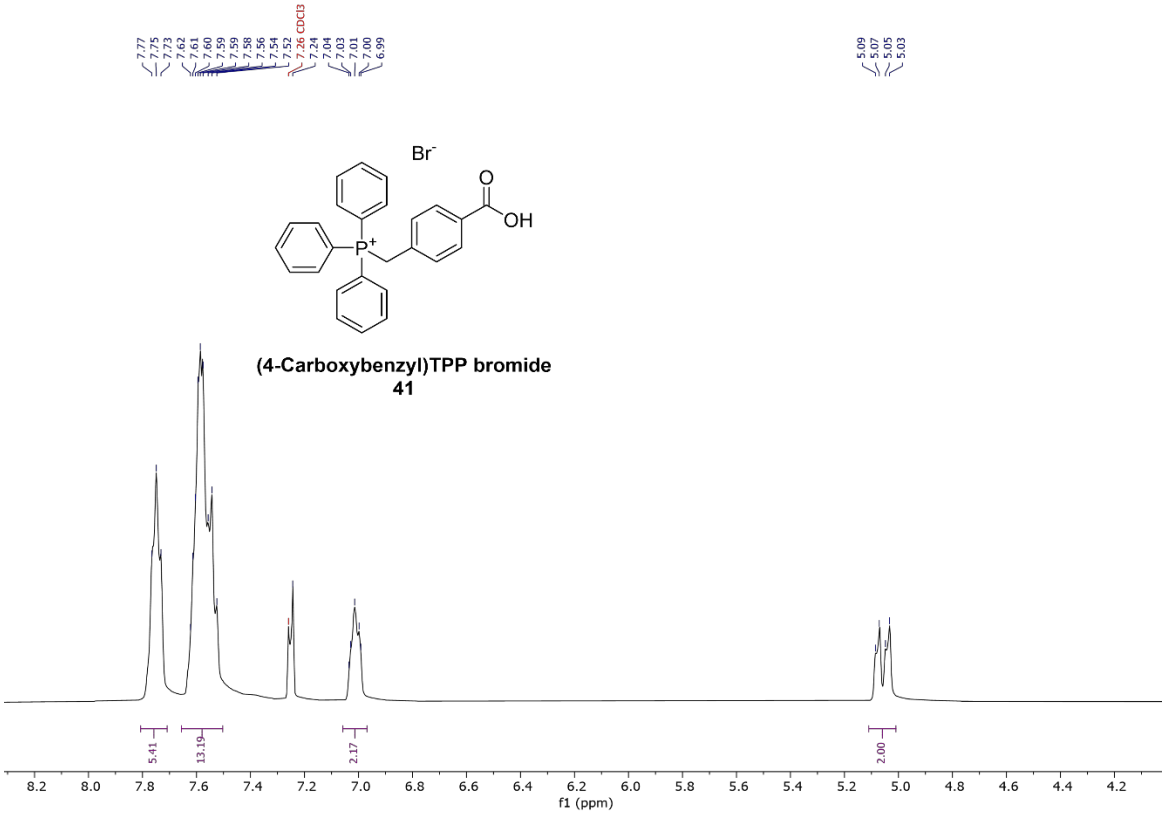

Figure 8.211 ^{1}H NMR spectrum of **41** ($CDCl_3$, 400 MHz, 298 K).

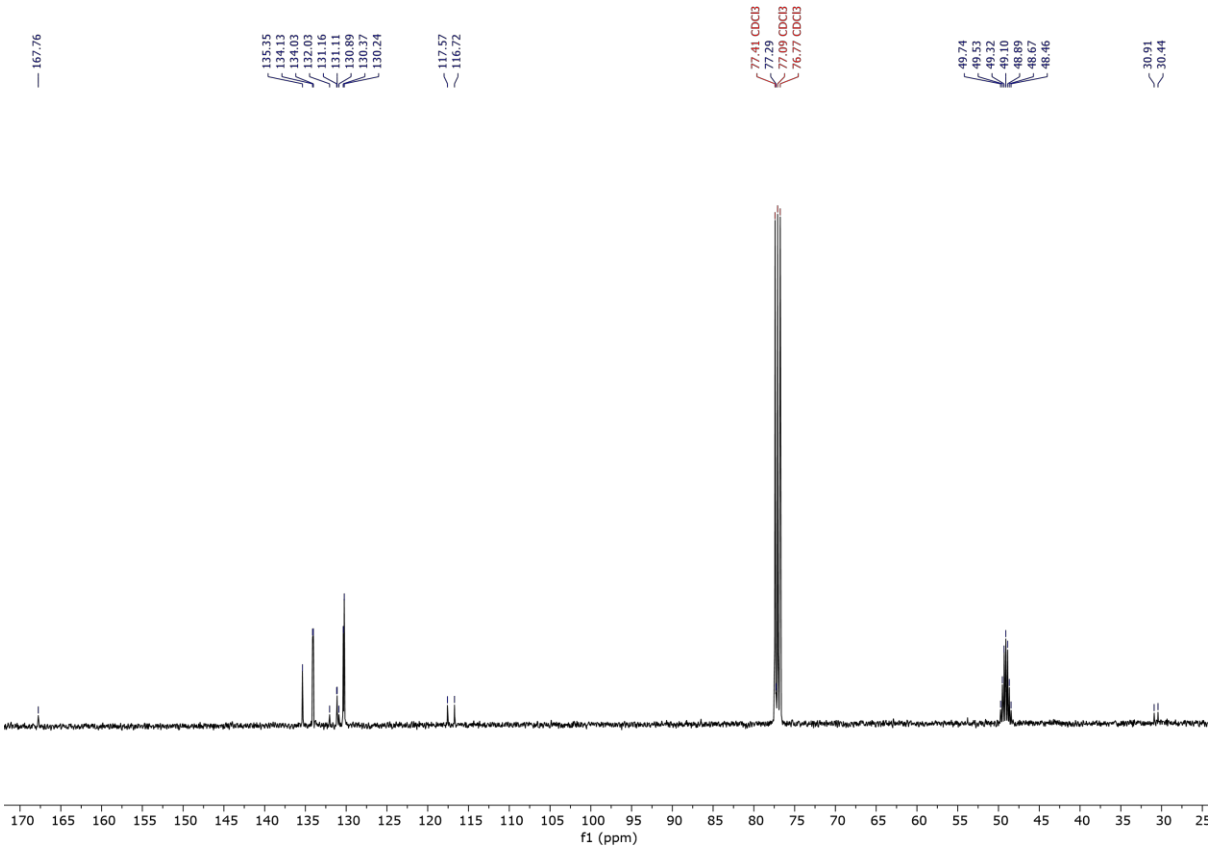

Figure 8.212 $^{13}C\{^{1}H\}$ NMR spectrum of **41** ($CDCl_3$, 101 MHz, 298 K).

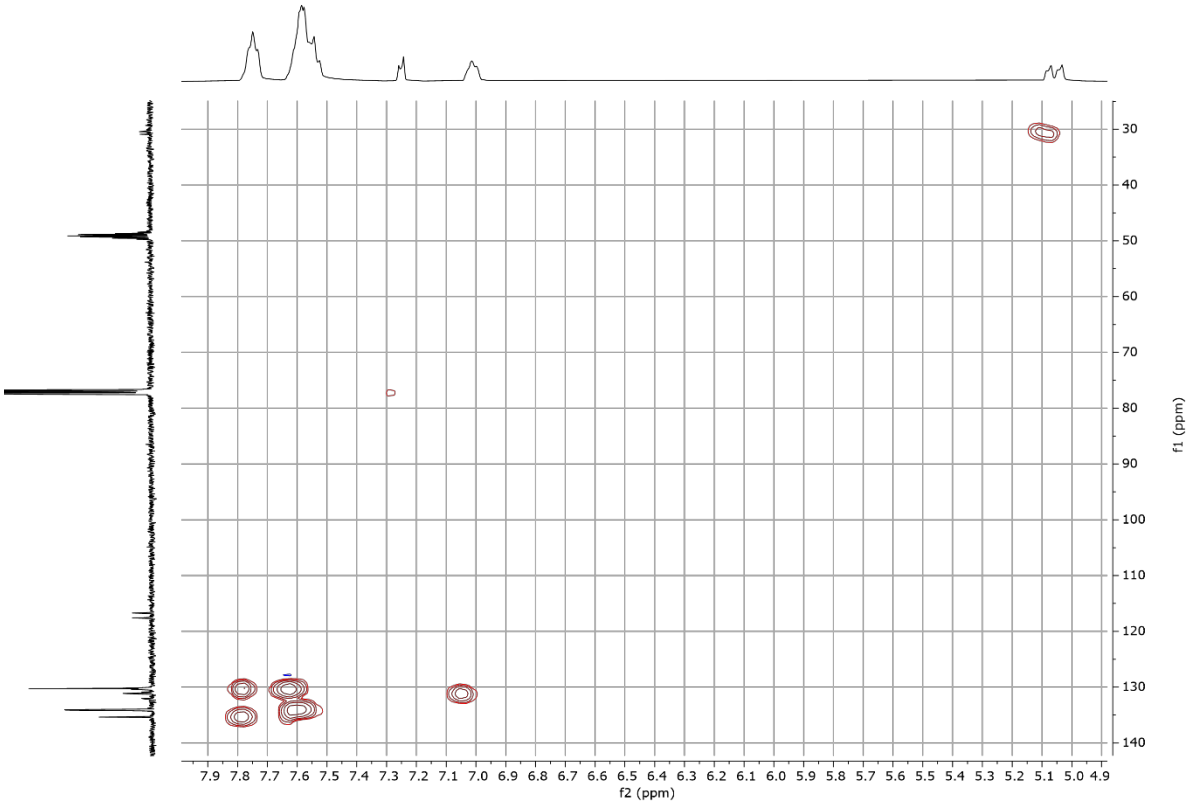

Figure 8.213 HMQC NMR spectrum of **41** ($CDCl_3$, 298 K).

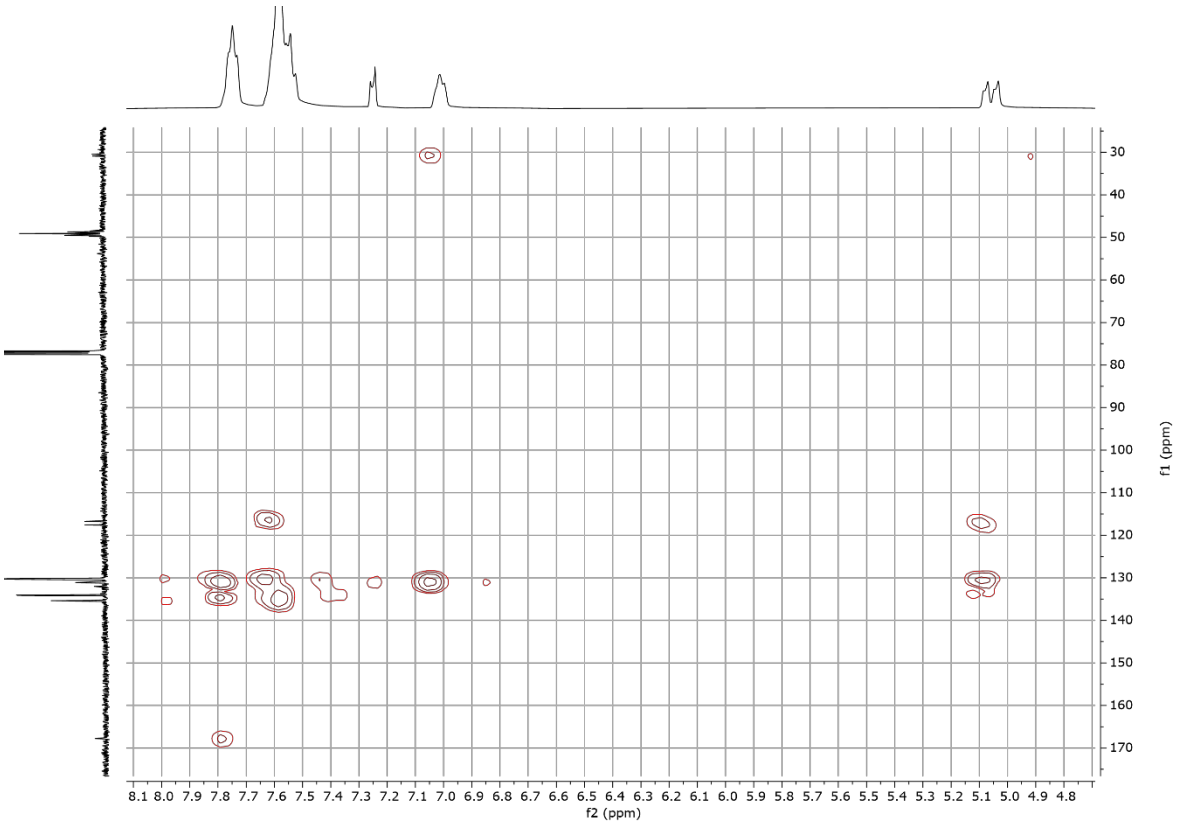

Figure 8.214 HMBC NMR spectrum of **41** ($CDCl_3$, 298 K).

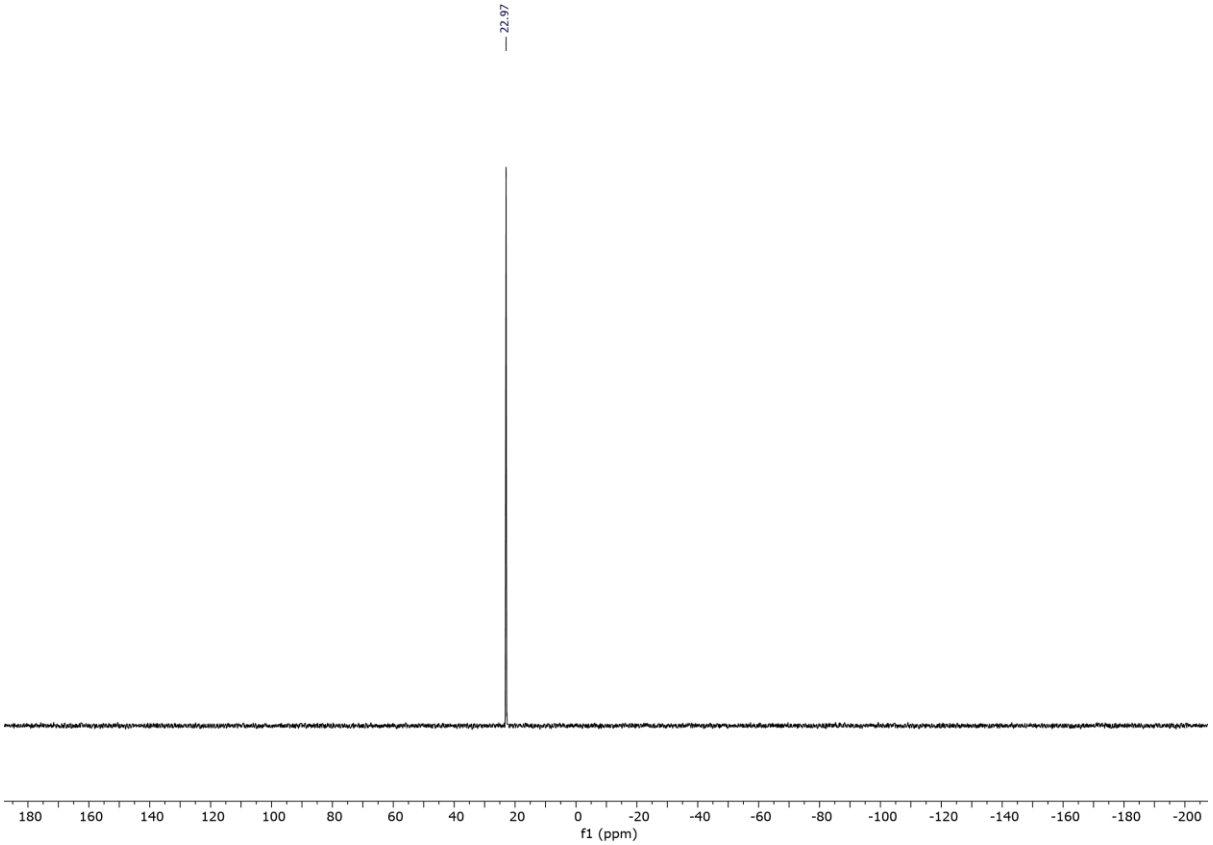

Figure 8.215 $^{31}P\{^{1}H\}$ NMR spectrum of **41** ($CDCl_3$, 162 MHz, 298 K).

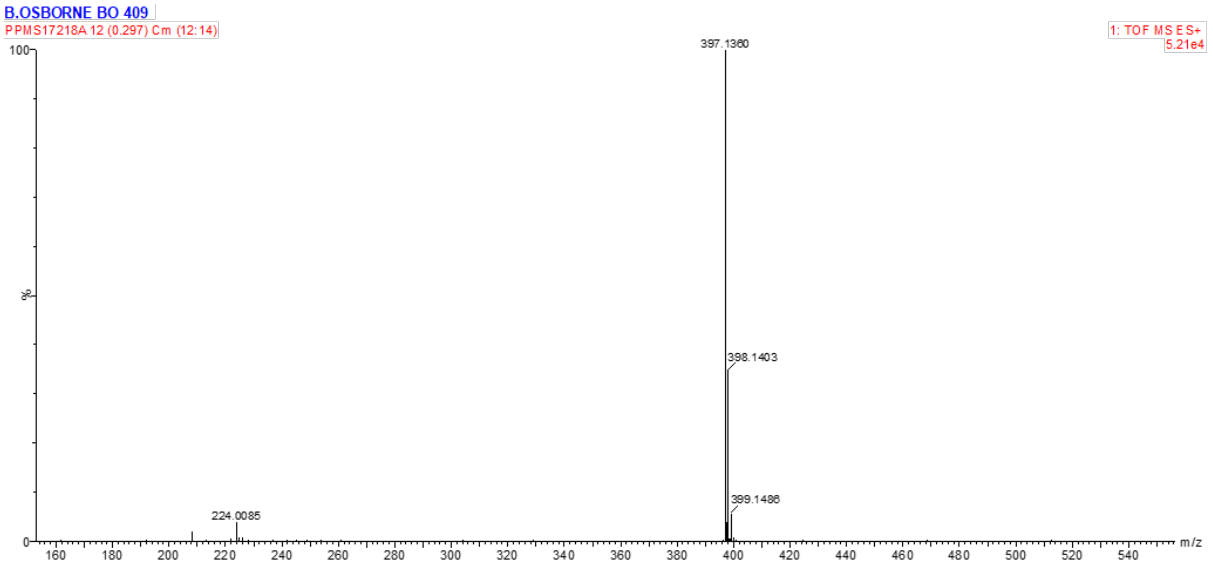

Figure 8.216 ES-TOF+ MS of **41**.

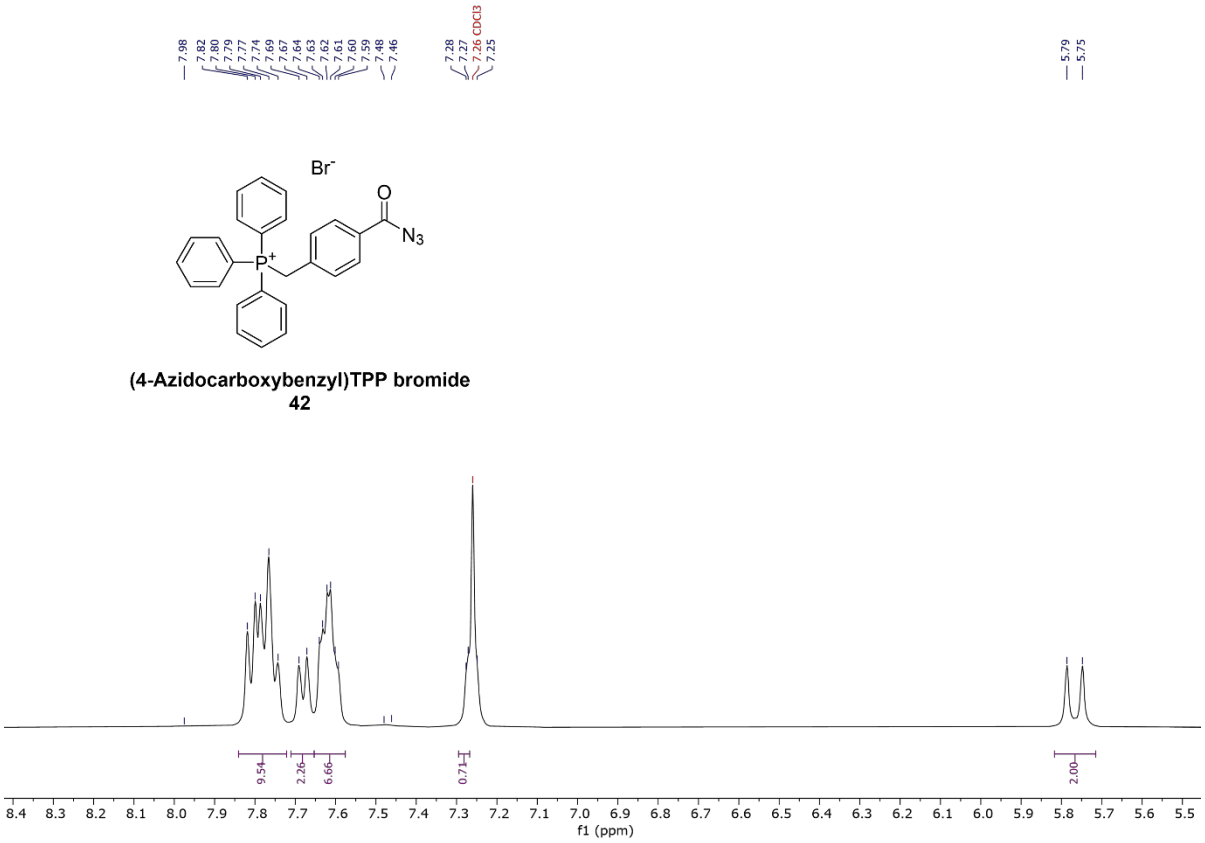

Figure 8.217 ^{1}H NMR spectrum of **42** ($CDCl_3$, 400 MHz, 298 K).

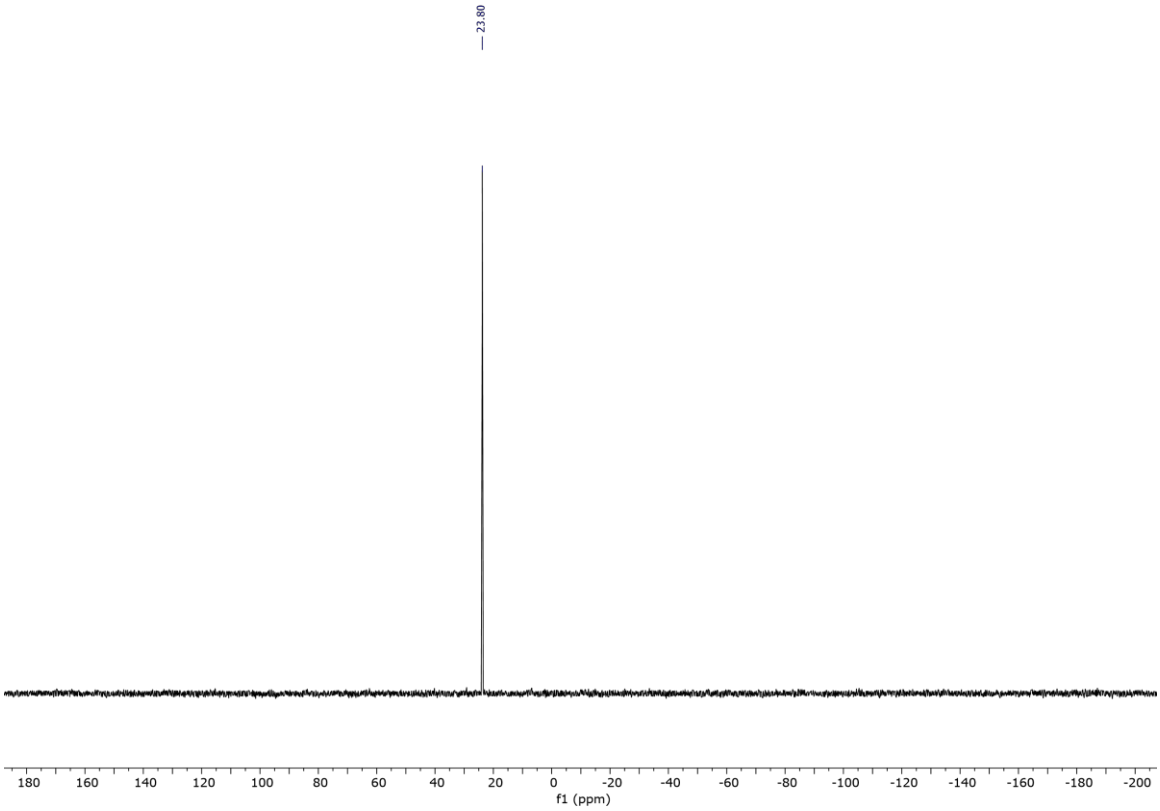

Figure 8.218 $^{31}P\{^{1}H\}$ NMR spectrum of **42** ($CDCl_3$, 162 MHz, 298 K).

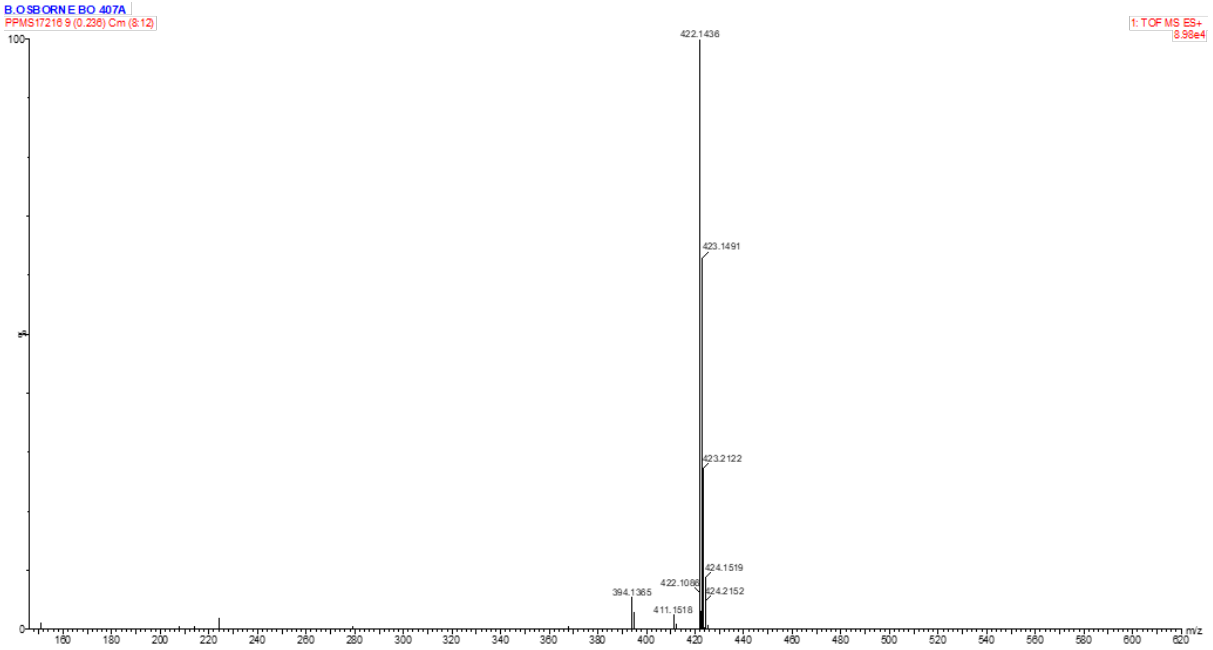

Figure 8.219 ES-TOF+ MS of **42**.

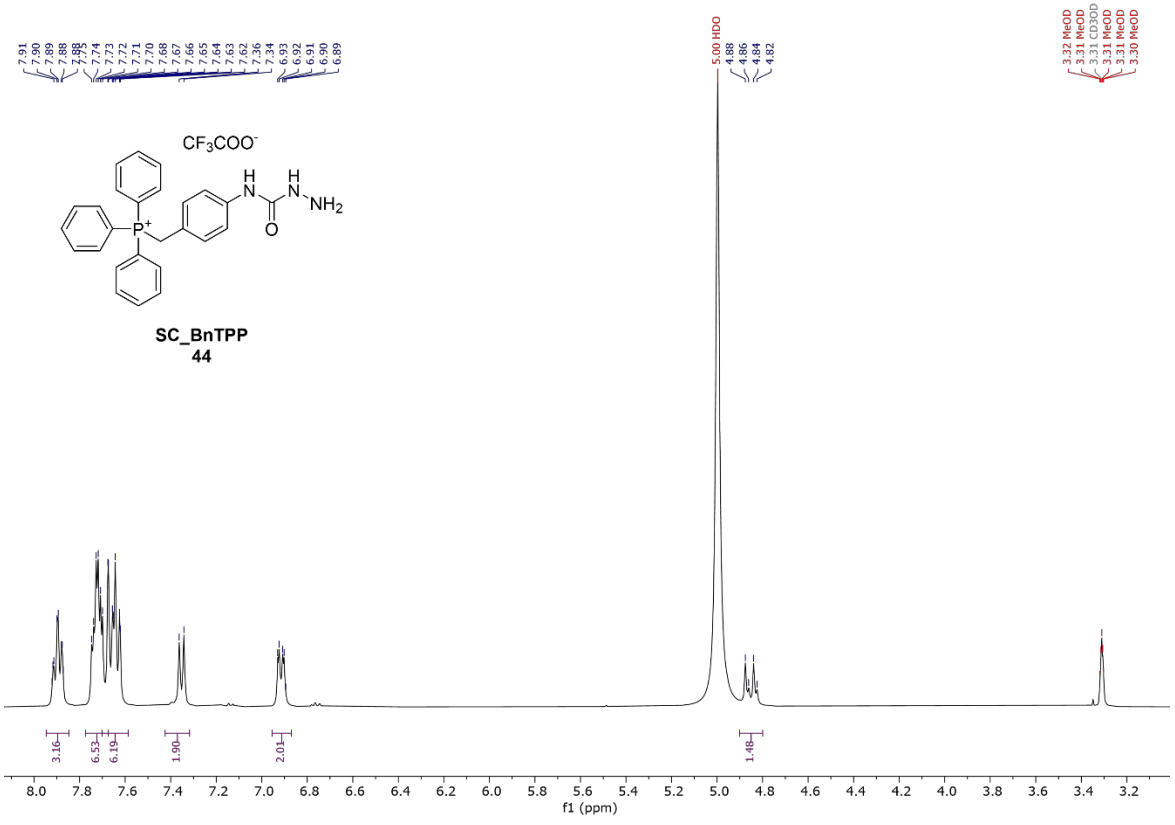

Figure 8.220 ^{1}H NMR spectrum of **44** (CD_3OD, 400 MHz, 298 K).

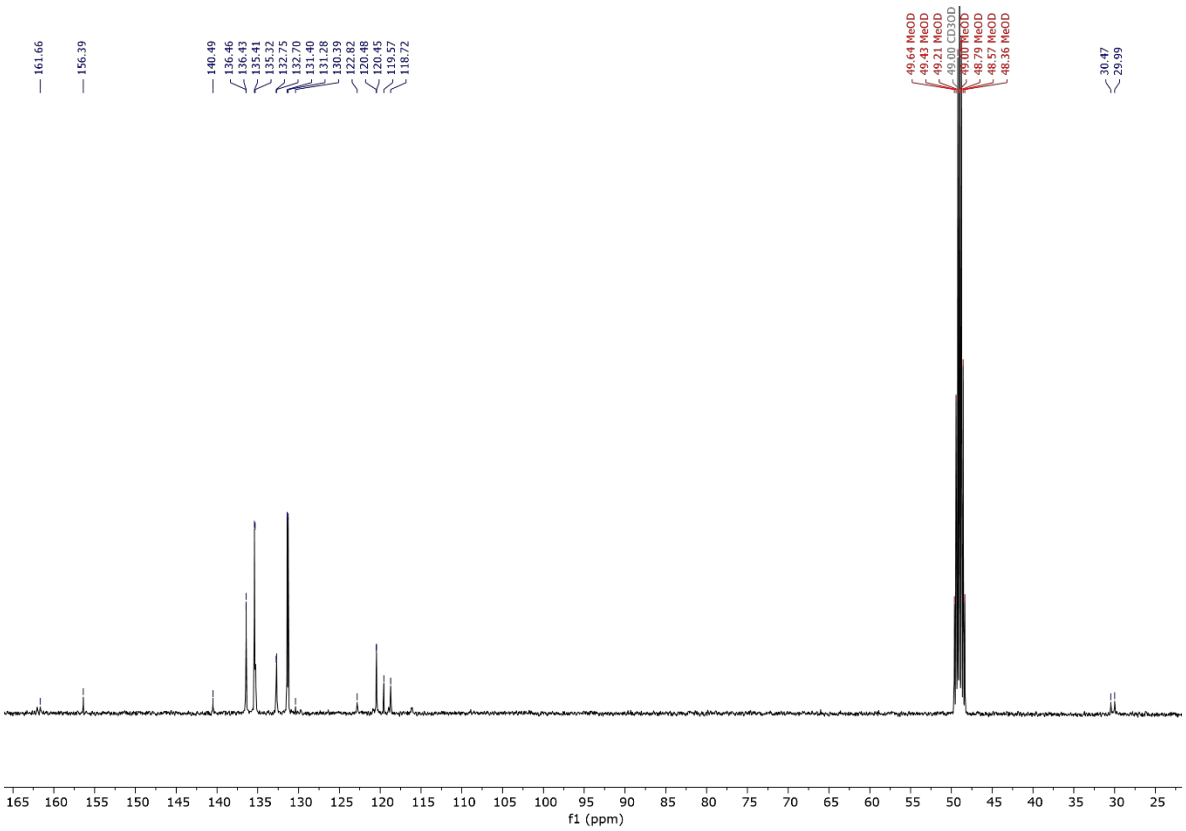

Figure 8.221 $^{13}C\{^{1}H\}$ NMR spectrum of **44** (CD_3OD, 101 MHz, 298 K).

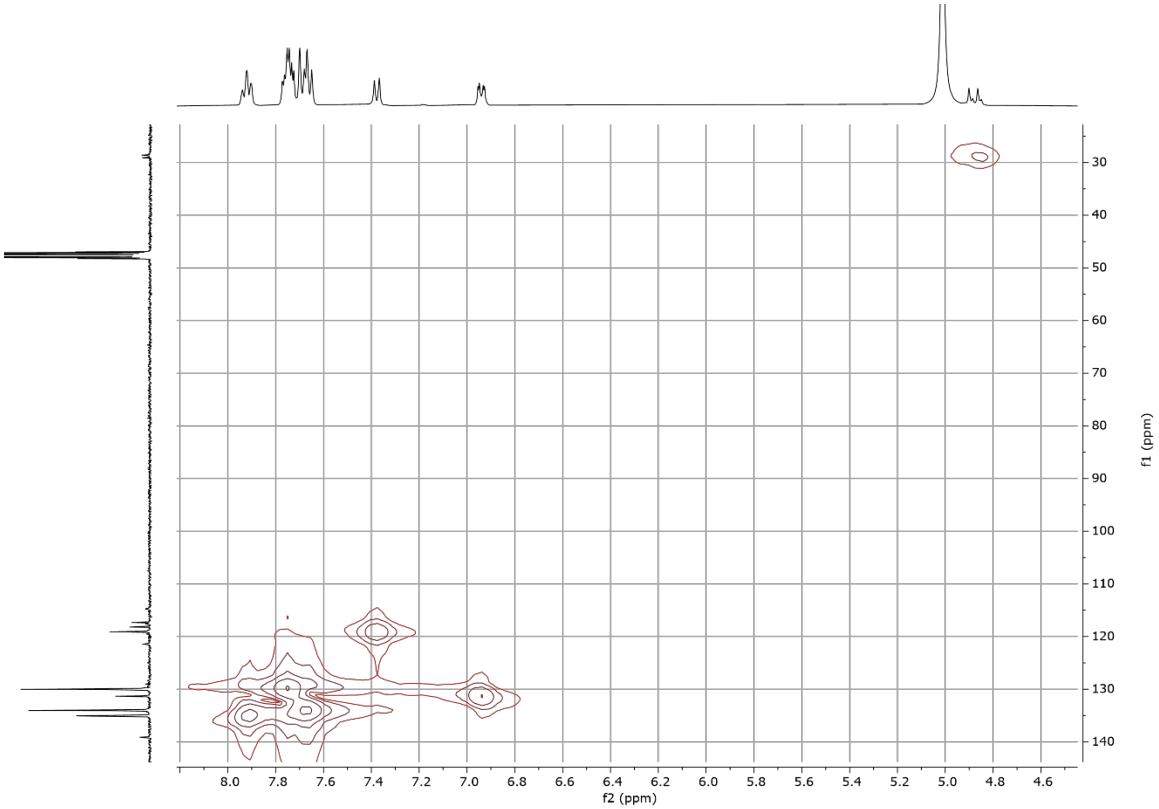

Figure 8.222 HMQC NMR spectrum of **44** (CD_3OD, 298 K).

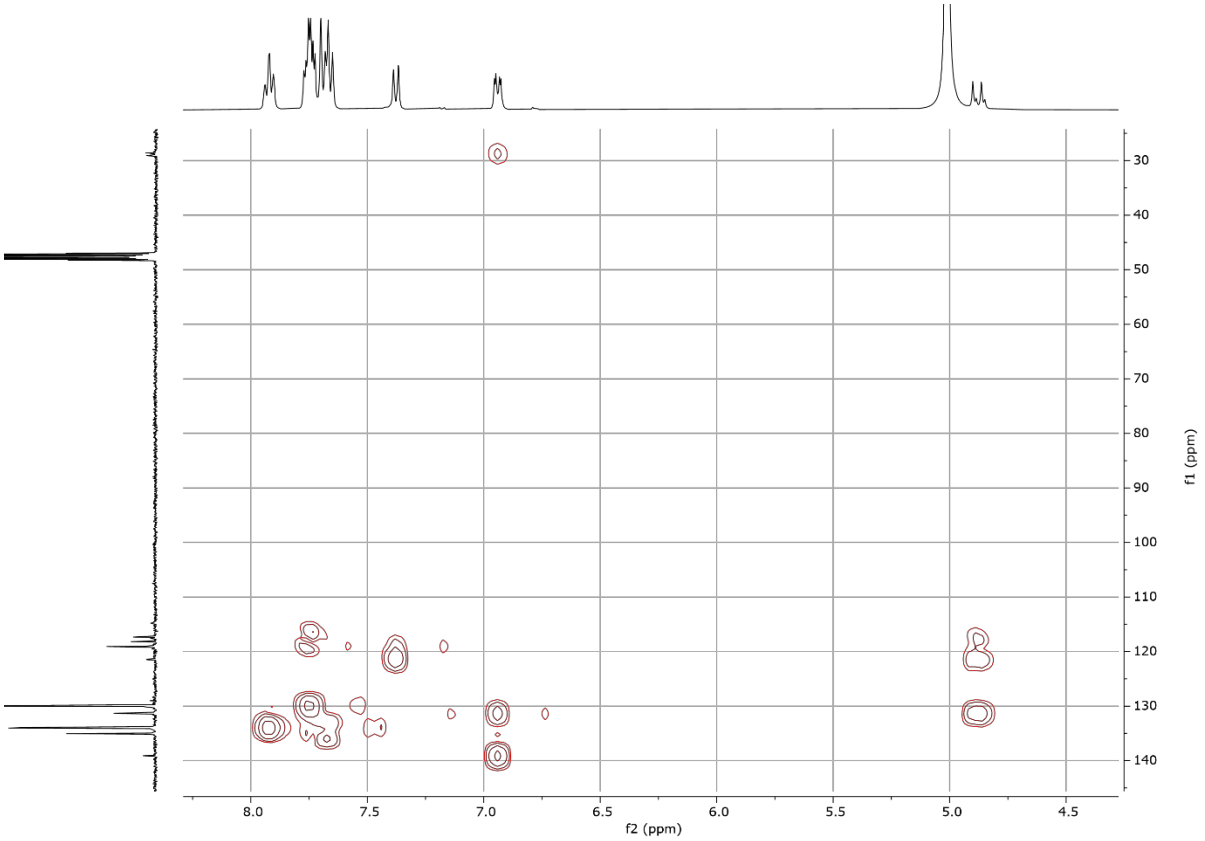

Figure 8.223 HMBC NMR spectrum of **44** (CD_3OD, 298 K).

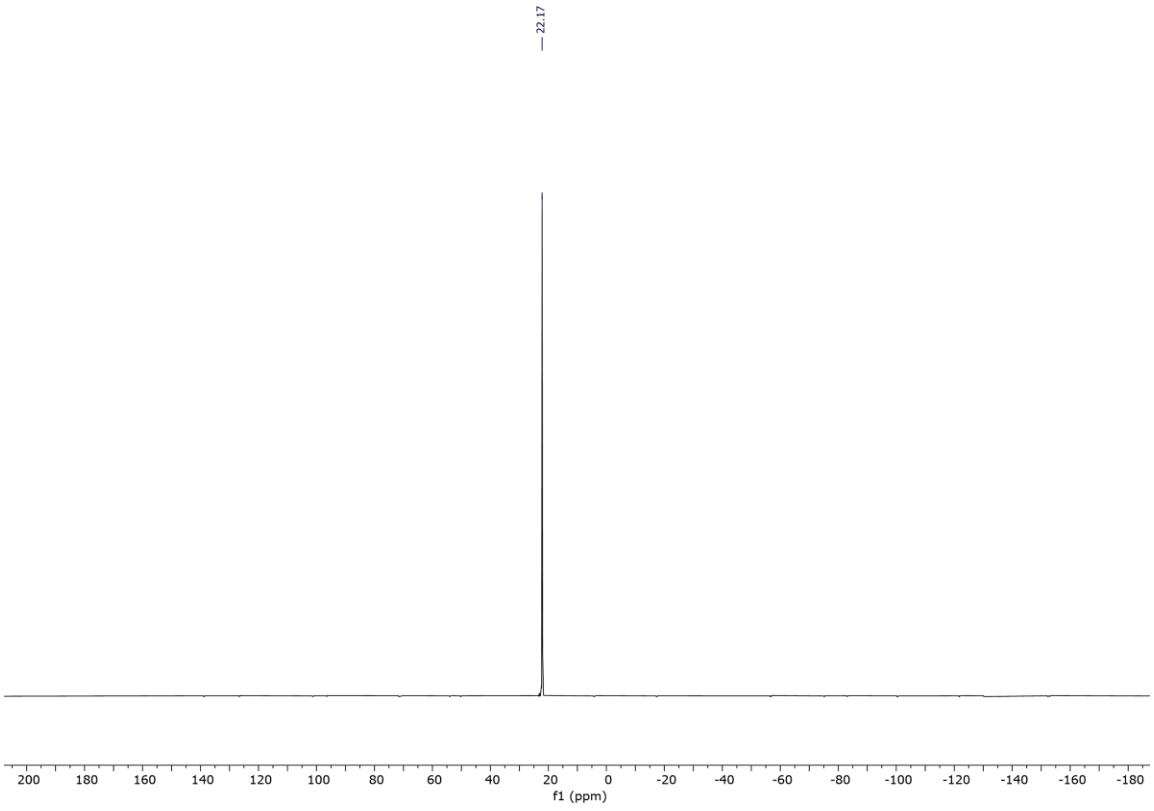

Figure 8.224 $^{31}P\{^{1}H\}$ NMR spectrum of **44** (CD_3OD, 162 MHz, 298 K).

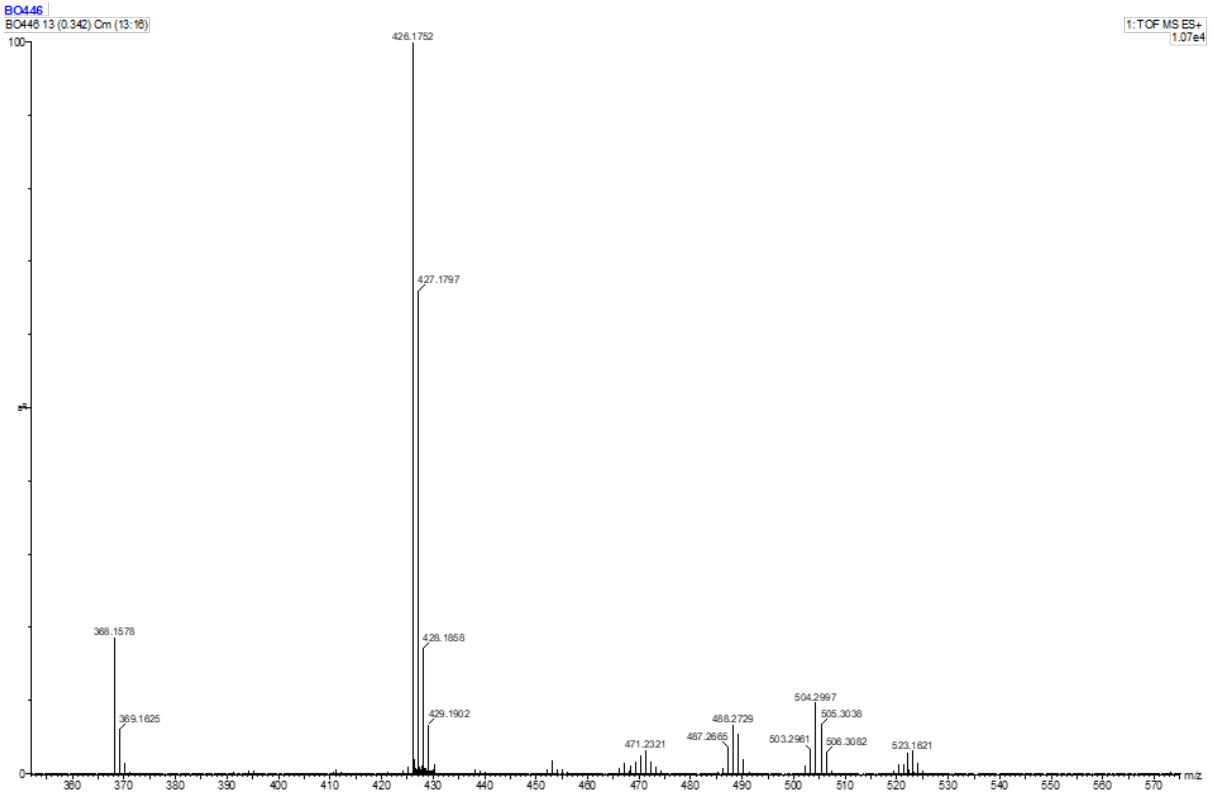

Figure 8.225 ES-TOF+ MS of **44**.

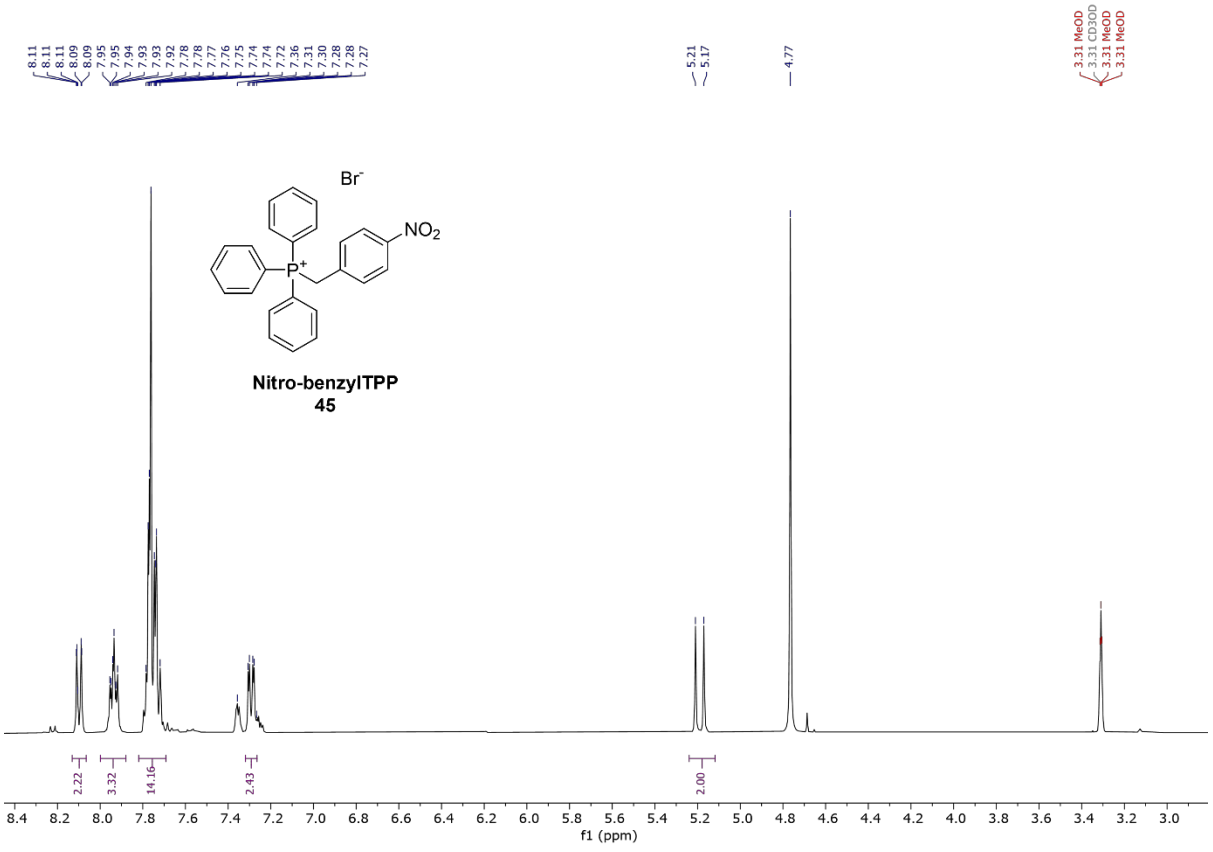

Figure 8.226 ^{1}H NMR spectrum of **45** (CD_3OD, 400 MHz, 298 K).

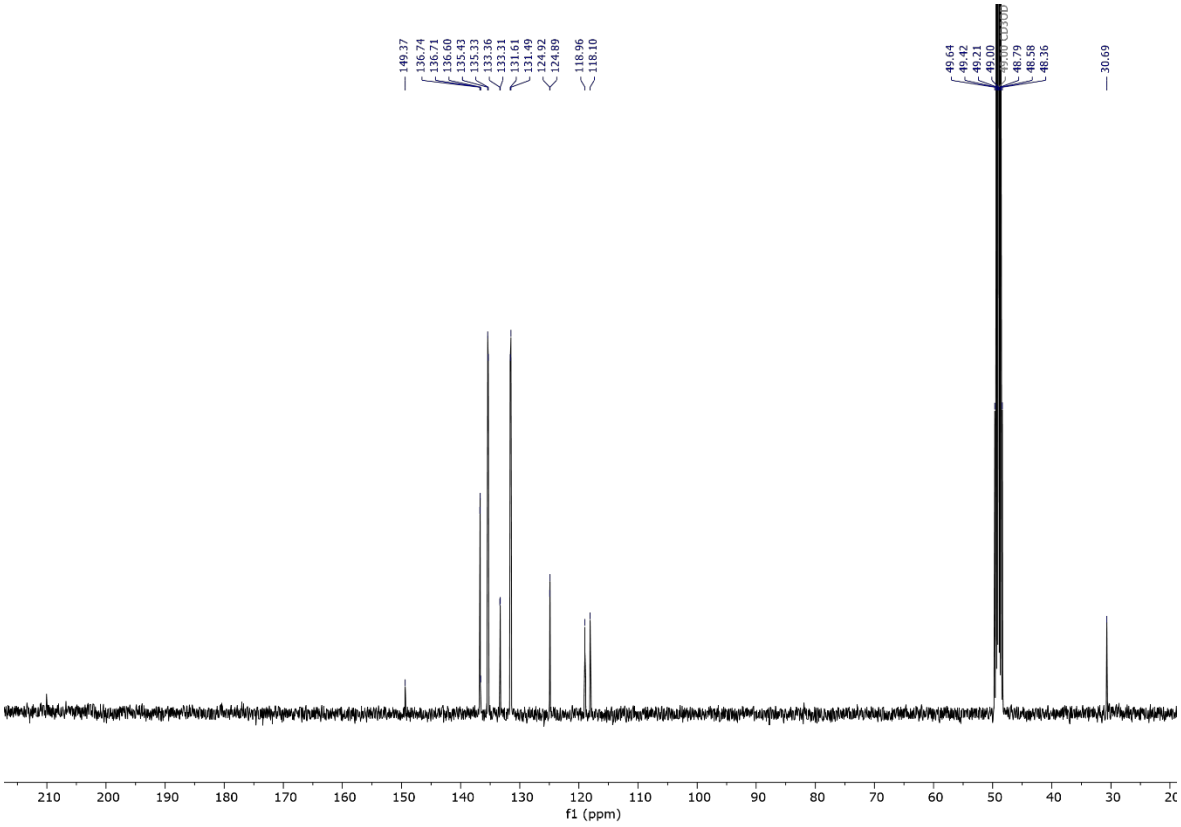

Figure 8.227 $^{13}C\{^{1}H\}$ NMR spectrum of **45** (CD_3OD, 101 MHz, 298 K).

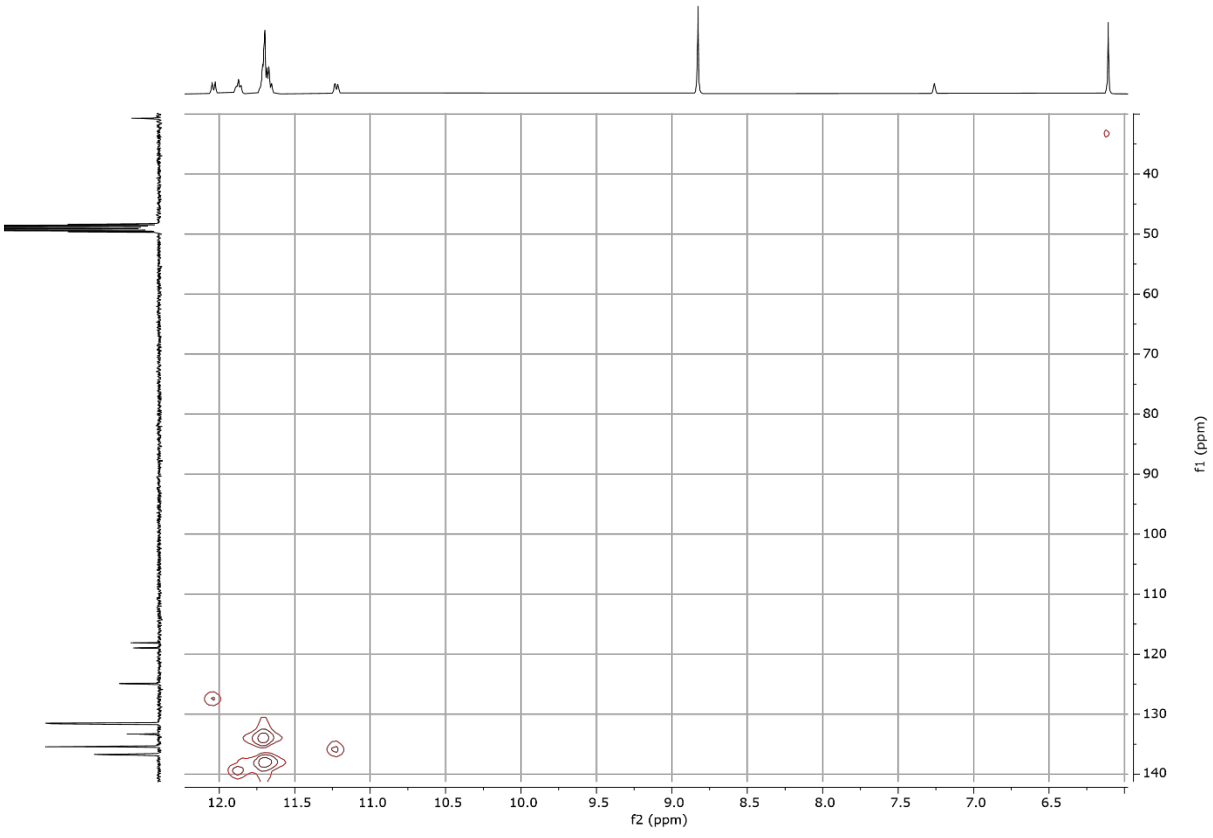

Figure 8.228 HMQC NMR spectrum of **45** (CD_3OD, 298 K).

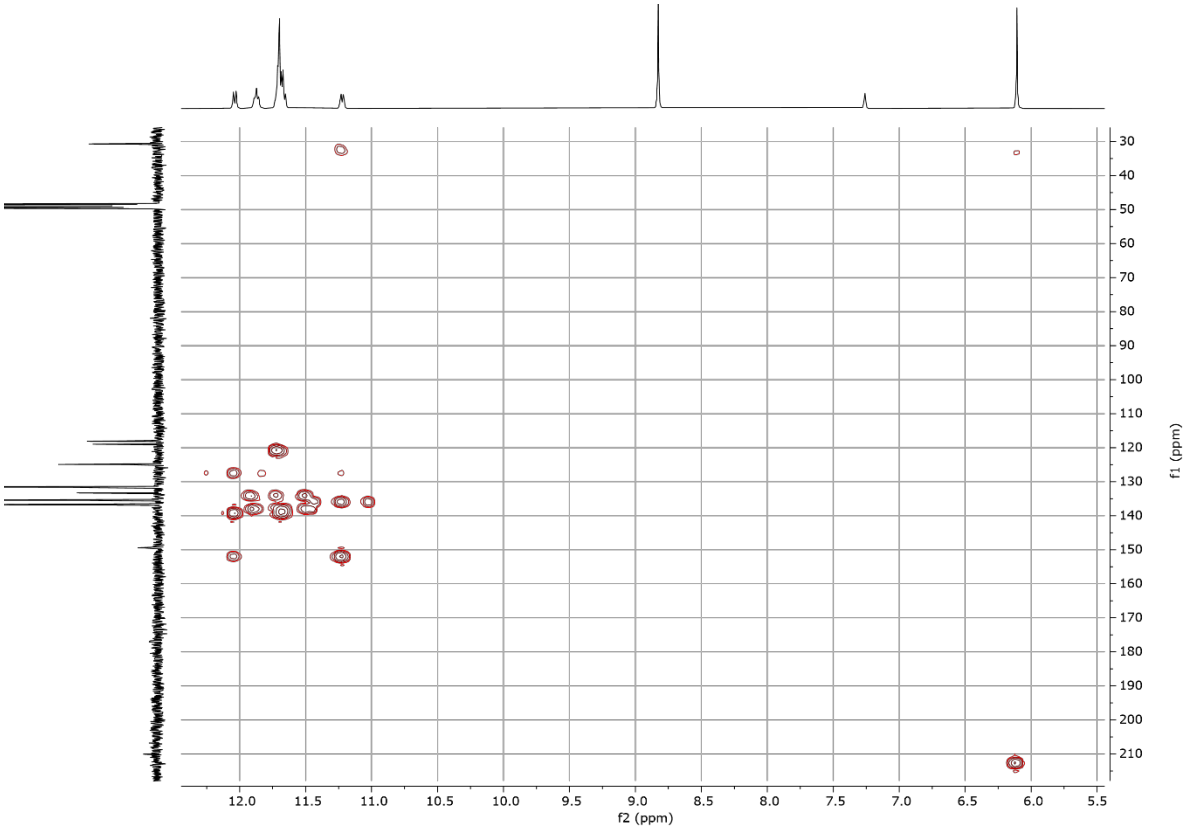

Figure 8.229 HMBC NMR spectrum of **45** (CD_3OD, 298 K).

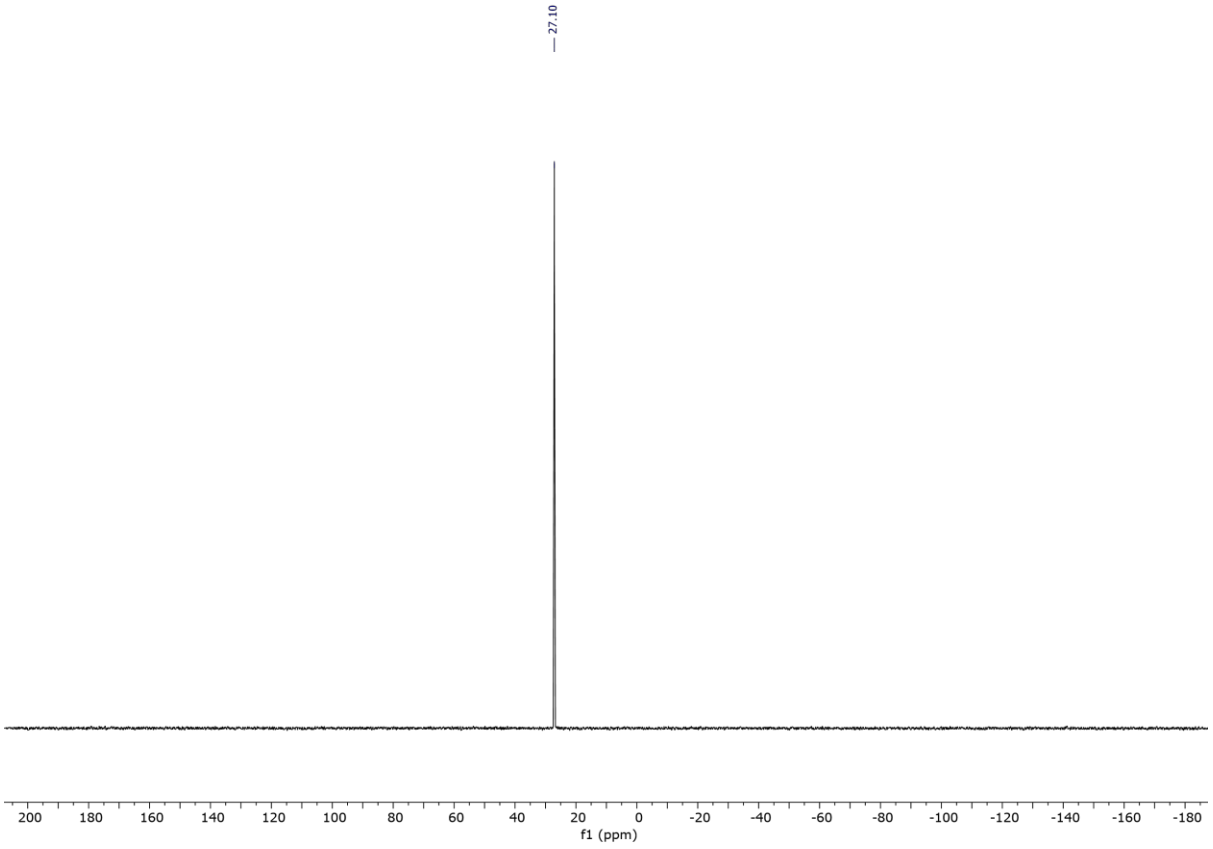

Figure 8.230 $^{31}P\{^1H\}$ NMR spectrum of **45** (CD_3OD, 162 MHz, 298 K).

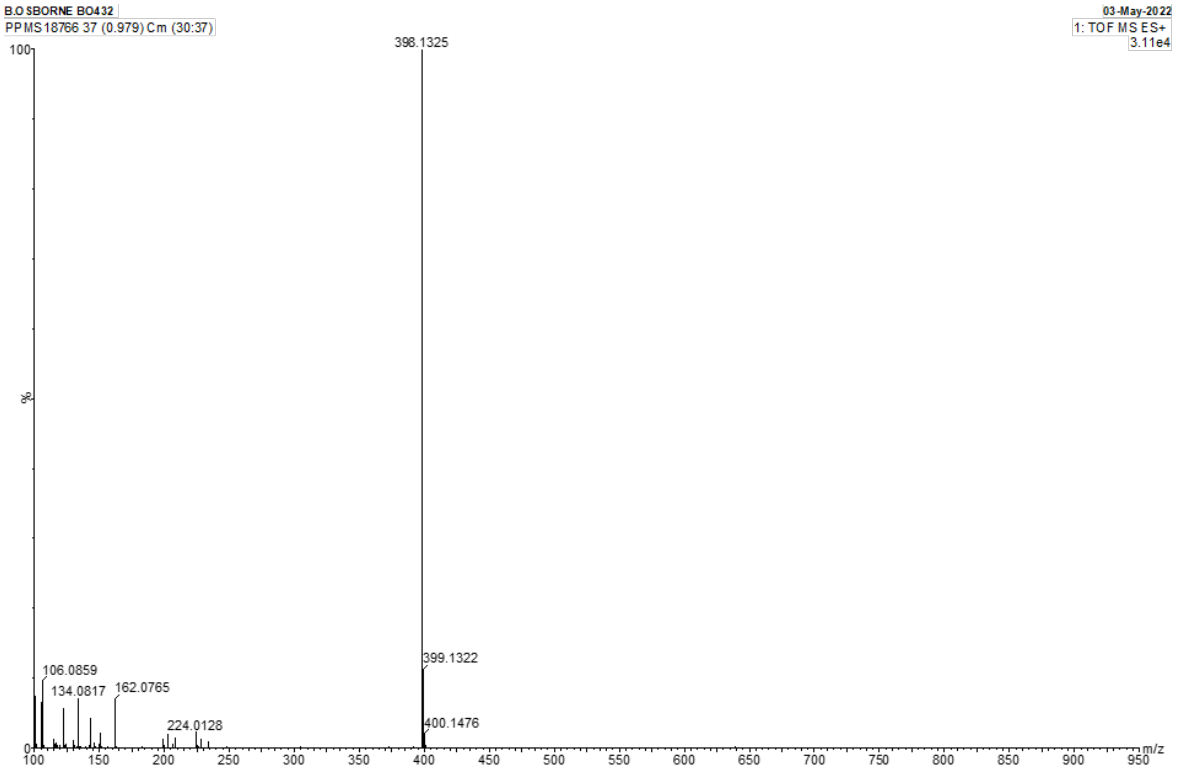

Figure 8.231 ES-TOF+ MS of **45**.

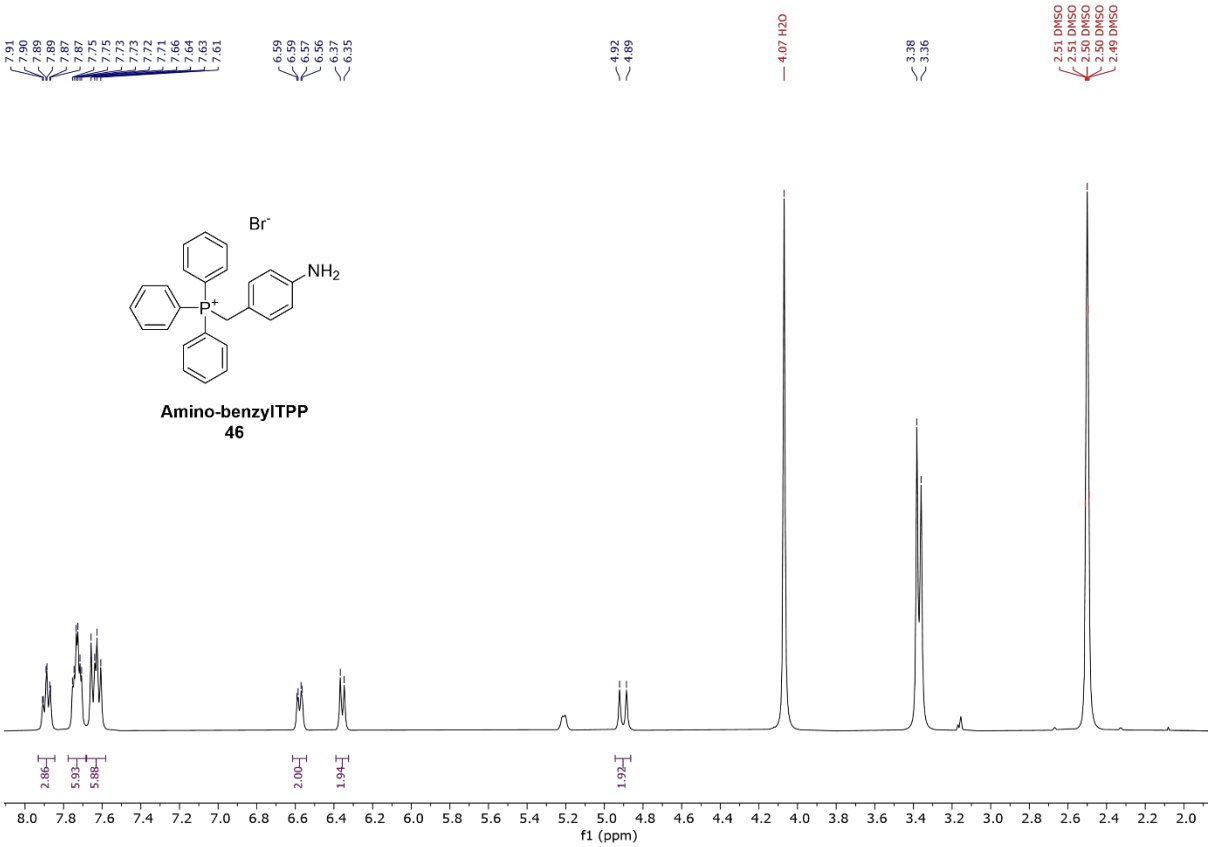

Figure 8.232 ^{1}H NMR spectrum of **46** (DMSO-d_6, 400 MHz, 298 K).

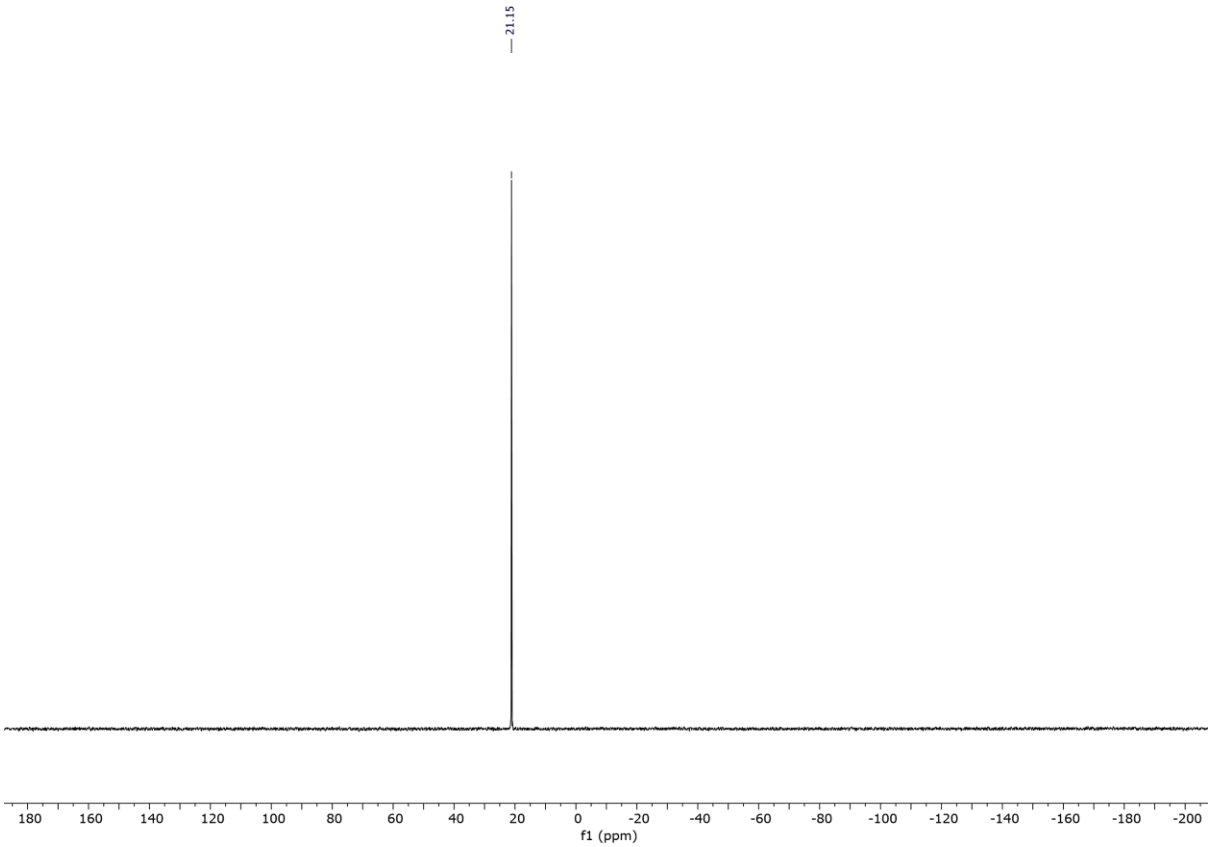

Figure 8.233 $^{31}P\{^{1}H\}$ NMR spectrum of **46** (DMSO-d_6, 162 MHz, 298 K).

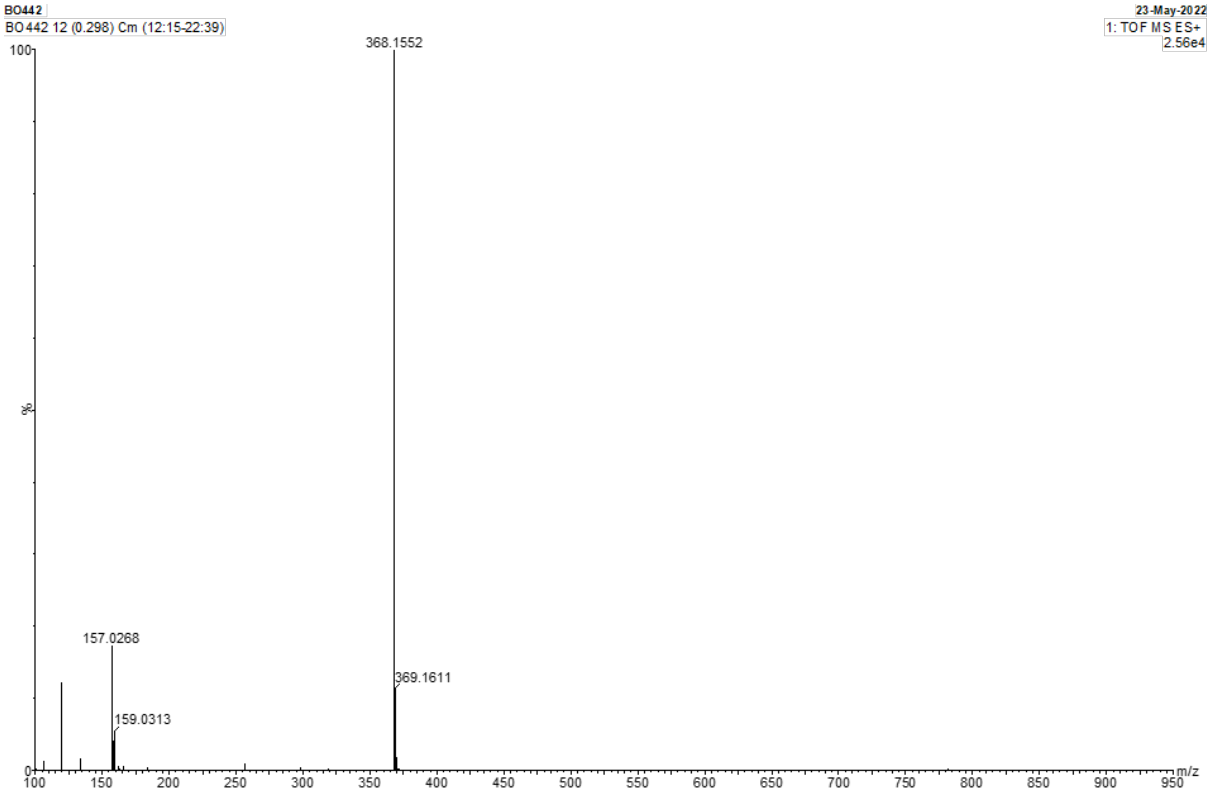

Figure 8.234 ES-TOF+ MS of **46**.

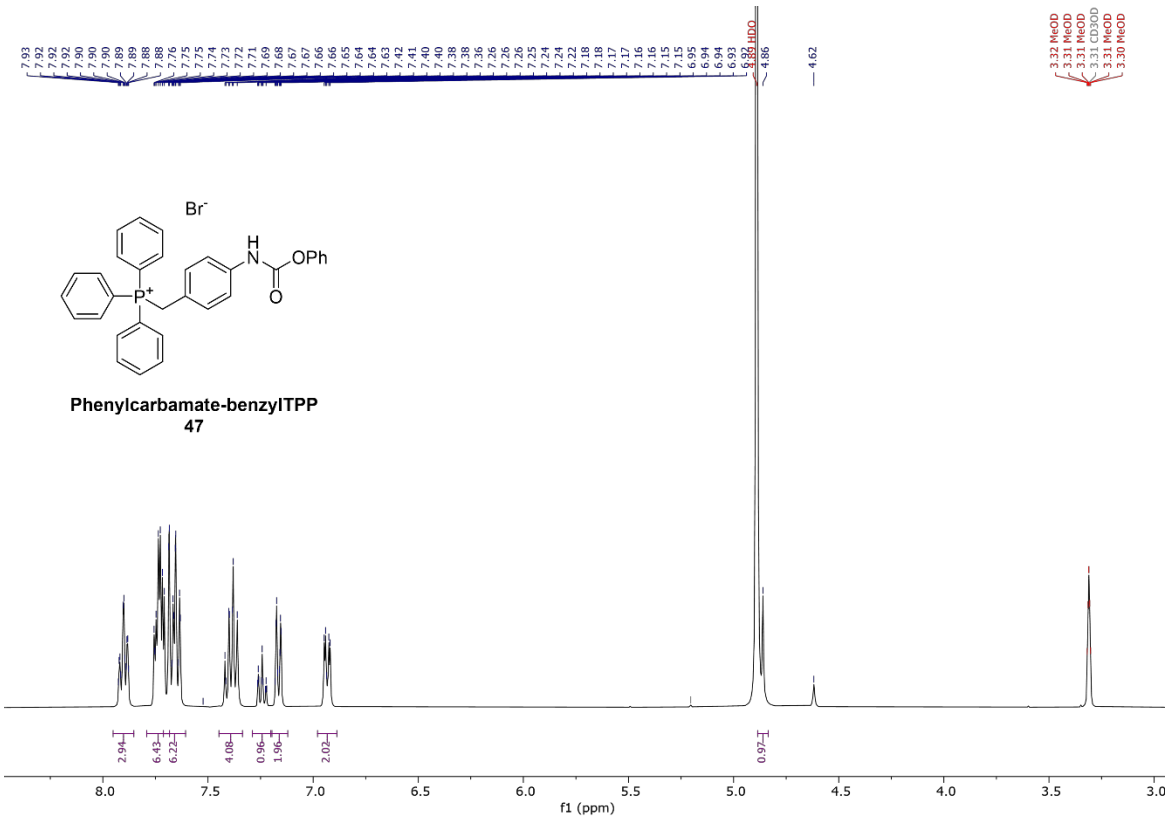

Figure 8.235 ^{1}H NMR spectrum of **47** (CD_3OD, 400 MHz, 298 K).

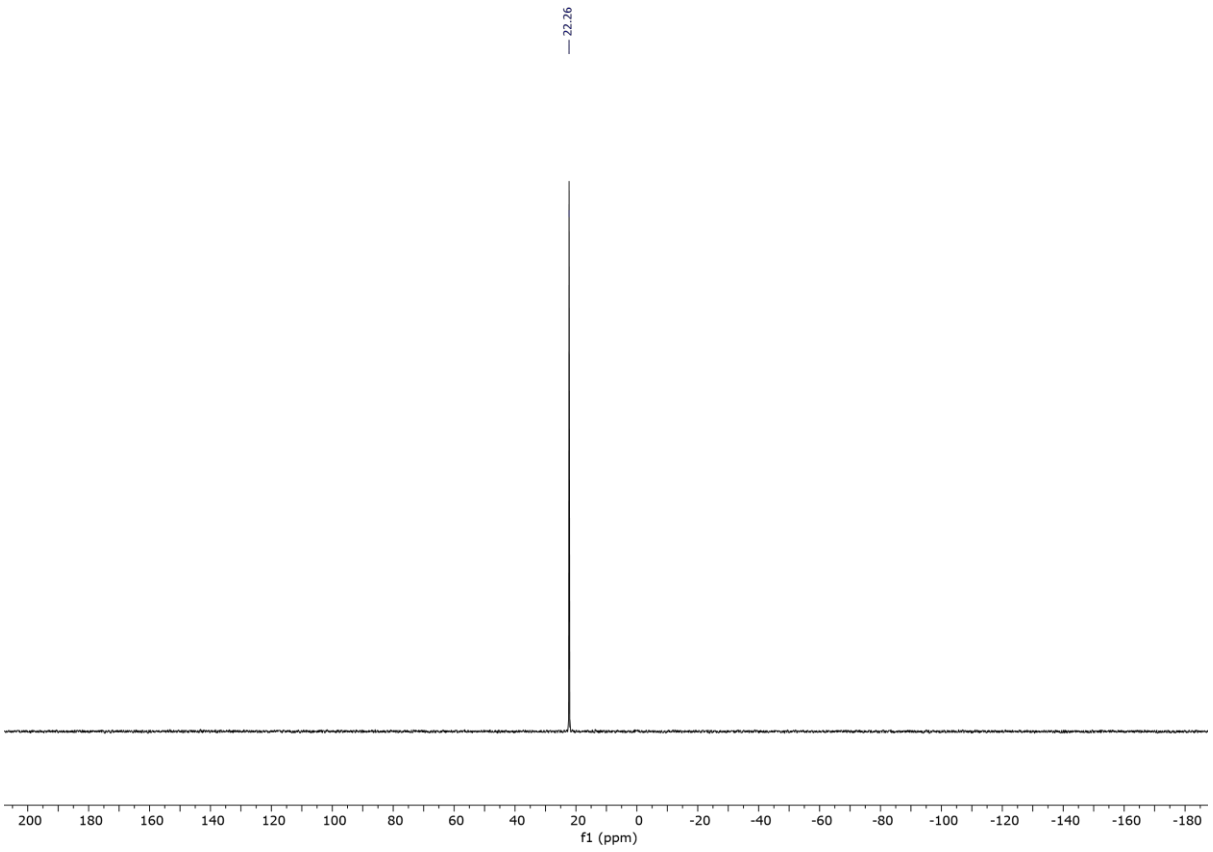

Figure 8.236 $^{31}P\{^{1}H\}$ NMR spectrum of **47** (CD_3OD, 162 MHz, 298 K).

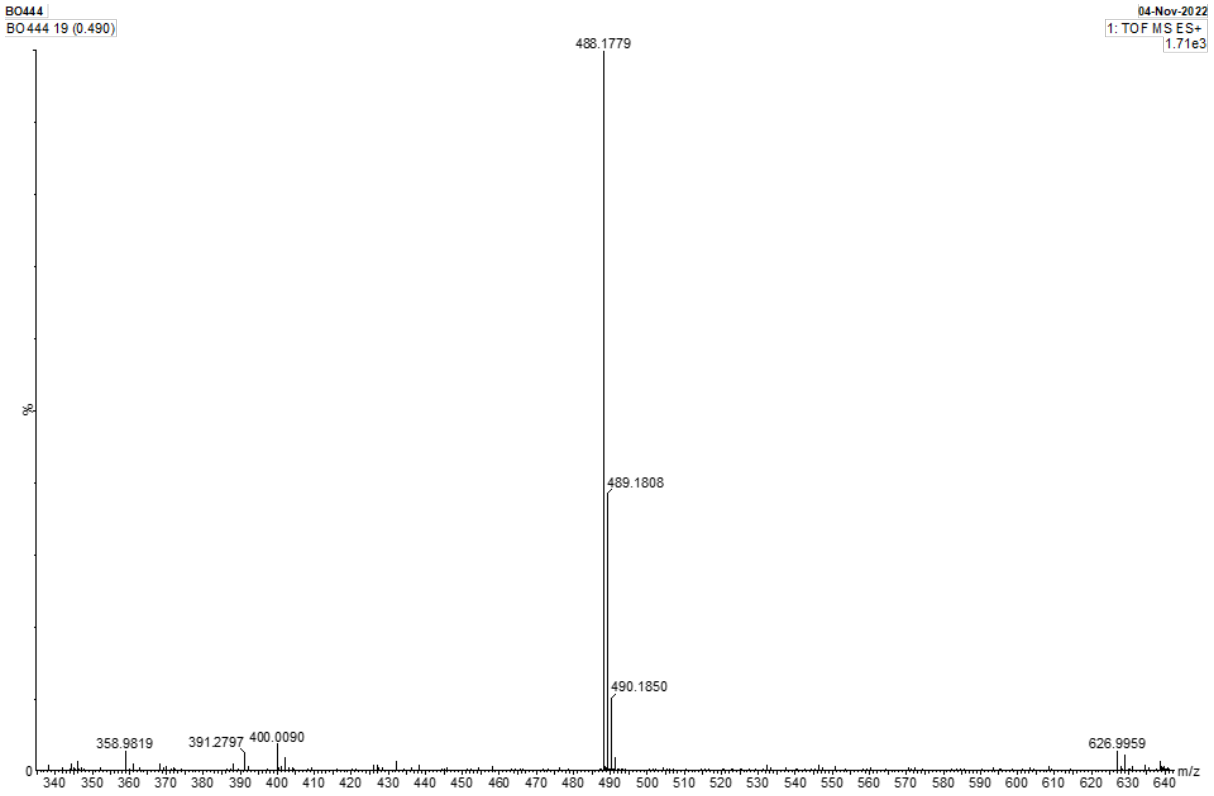

Figure 8.237 ES-TOF+ MS of **47**.

8.3 DFT Experimental Data

8.3.1 Geometry Optimisation Confirmation – Ga-NODAGA-xy-TXP

```
         Item               Value     Threshold  Converged?
Maximum Force            0.000054      0.000450     YES
RMS     Force            0.000007      0.000300     YES
Maximum Displacement     0.000394      0.001800     YES
RMS     Displacement     0.000069      0.001200     YES
Predicted change in Energy=-1.238836D-09
Optimization completed.
   -- Stationary point found.
```

Vibrational Frequency Analysis to Confirm Absence of Imaginary Frequencies:

	Mode #	Frequency	Infrared
1	1	14.19	2.4525
2	2	18.11	0.7611
3	3	21.26	0.3955
4	4	21.84	0.7019
5	5	24.18	2.5757
6	6	25.13	0.4365
7	7	29.28	2.3595
8	8	31.67	0.1787
9	9	32.46	0.1271
10	10	34.63	0.6491

8.3.2 Geometry Optimisation Confirmation – Ga-DO2A-(xy-TXP)$_2$

```
         Item               Value     Threshold  Converged?
Maximum Force            0.000002      0.000450     YES
RMS     Force            0.000000      0.000300     YES
Maximum Displacement     0.000500      0.001800     YES
RMS     Displacement     0.000087      0.001200     YES
Predicted change in Energy=-7.875922D-10
Optimization completed.
   -- Stationary point found.
```

Vibrational Frequency Analysis to Confirm Absence of Imaginary Frequencies:

	Mode #	Frequency	Infrared
1	1	4.64	0.1138
2	2	6.50	0.0344
3	3	7.87	0.2451
4	4	12.08	0.0074
5	5	14.11	0.1492
6	6	15.47	0.1042
7	7	16.21	0.1283
8	8	18.03	0.1975
9	9	21.64	0.3210
10	10	22.42	0.4514

8.3.3 Cartesian Coordinates of Optimised Ga-DO2A-(xy-TXP)$_2$ Structure

Ga 22.57631 2.19878 8.44649
P 31.61788 3.63614 7.39867
O 22.68863 0.92365 9.29718
O 23.06225 -0.65194 10.92648
O 22.05388 2.12338 7.01068
O 21.23039 2.58198 4.91104
N 24.9246 2.50614 8.29046
N 23.27079 3.04914 10.68038
N 20.7628 3.4859 9.28079
N 22.95619 4.50758 7.58206
C 25.53721 2.65906 9.68475
C 24.69369 3.56017 10.62866
C 22.31274 4.07844 11.23968
C 20.87357 3.71183 10.78939
C 20.67116 4.83592 8.55523
C 22.04987 5.49572 8.28236
C 24.40703 4.93352 7.64506
C 25.30737 3.69184 7.40443
C 23.20835 1.7824 11.51595
C 22.98756 0.54126 10.56544
C 22.52818 4.34862 6.13227
C 21.85244 2.93388 5.92959
C 25.47474 1.21744 7.6431
C 26.98687 1.24873 7.37831
C 27.47726 1.63673 6.11662
C 28.85254 1.79326 5.90381
C 29.76285 1.57074 6.95465
C 29.28001 1.10134 8.19157
C 27.90604 0.93872 8.39935

C 31.24416 1.90456 6.78163
C 30.98193 4.87847 6.20987
C 29.60832 4.92676 5.92154
C 29.11239 5.87944 5.01244
C 30.01609 6.77356 4.40831
C 31.39579 6.73419 4.6923
C 31.87544 5.77567 5.60451
C 33.4306 3.82353 7.57262
C 33.94926 4.52987 8.66798
C 35.3418 4.69187 8.80055
C 36.18496 4.13829 7.81866
C 35.67142 3.43207 6.71258
C 34.27812 3.27709 6.59432
C 30.80821 3.83646 9.0328
C 29.0803 4.8146 10.43876
C 29.51038 3.99009 11.49468
C 30.59118 3.09866 11.34291
C 31.24066 3.02645 10.09745
C 29.74476 4.73435 9.19979
H 26.56275 3.06433 9.61673
H 25.59495 1.65015 10.12331
H 25.1641 3.54848 11.63055
H 24.67384 4.60094 10.27925
H 22.6083 5.07117 10.87467
H 22.34335 4.10417 12.3453
H 20.58201 2.76611 11.27068
H 20.16864 4.49918 11.11325
H 20.0386 5.53468 9.13262
H 20.17618 4.64756 7.58892
H 21.88403 6.39999 7.66578
H 22.53804 5.81167 9.21392
H 23.41004 4.40858 5.4729
H 21.82473 5.14475 5.83324
H 26.778 1.83826 5.29659
H 29.21883 2.11796 4.9228
H 29.98034 0.87987 9.0045
H 27.54832 0.58221 9.37172
H 24.60061 5.38252 8.62882
H 24.6417 5.69481 6.87739
H 25.20942 0.38851 8.32123
H 24.92565 1.08862 6.69459
H 31.54575 1.86331 5.72492
H 31.88327 1.22207 7.36209
H 28.91207 4.22185 6.38609
H 29.6384 7.51699 3.69542
H 32.94717 5.73348 5.83309
H 25.18902 3.36087 6.36044
H 26.36492 3.97041 7.56212
H 33.27993 4.95576 9.42511
H 37.27084 4.26089 7.91573

H 33.86983 2.7343 5.73362
H 28.99071 4.04078 12.45951
H 32.07629 2.32795 9.96945
H 29.41631 5.37473 8.37389
H 22.36252 1.83533 12.22123
H 24.13239 1.64352 12.10281
C 19.35871 1.33568 9.52271
C 19.77046 0.27658 8.68704
C 19.70928 -1.04706 9.13234
C 19.22286 -1.35046 10.42184
C 18.80124 -0.29795 11.24955
C 18.86503 1.03035 10.80293
H 20.12929 0.49081 7.67293
H 20.03038 -1.85984 8.47008
H 18.4104 -0.49188 12.25122
H 18.50293 1.8313 11.45847
C 19.41248 2.78082 9.01099
H 18.6029 3.38178 9.46572
H 19.27997 2.78065 7.91632
C 31.06416 2.2308 12.51375
H 30.23277 2.02324 13.2012
H 31.47583 1.27931 12.14973
H 31.85402 2.75298 13.07714
C 27.92158 5.79963 10.62741
H 27.24585 5.4548 11.42168
H 28.30891 6.79082 10.91234
H 27.3528 5.91214 9.69388
C 35.91789 5.48115 9.98103
H 36.95284 5.17392 10.18355
H 35.91656 6.55902 9.75276
H 35.31266 5.32324 10.88465
C 36.61225 2.82003 5.66919
H 36.10895 2.73229 4.69665
H 37.51394 3.43713 5.55292
H 36.92556 1.81254 5.98665
C 27.6099 5.94256 4.71697
H 27.18637 4.93035 4.64816
H 27.08711 6.47569 5.52697
H 27.42174 6.47503 3.77512
C 32.35821 7.73346 4.04124
H 32.42655 8.64699 4.65345
H 33.36521 7.30274 3.95512
H 32.00199 8.01788 3.04153
P 18.66806 -3.29599 12.52522
C 19.14474 -2.84297 10.78843
C 18.96006 -5.10347 12.6899
C 19.37306 -5.61605 13.9294
C 19.58534 -6.99843 14.08314
C 19.37341 -7.84469 12.97734
C 18.96057 -7.33976 11.73002

C 18.75364 -5.95371 11.59181
C 16.87992 -2.96849 12.79906
C 16.45163 -1.81396 13.47109
C 15.07539 -1.57323 13.64701
C 14.15222 -2.50643 13.13976
C 14.57293 -3.67135 12.46815
C 15.95138 -3.89746 12.30171
C 19.69852 -2.42268 13.75878
C 20.95567 -1.9214 13.38156
C 21.78079 -1.30716 14.33983
C 21.31779 -1.20424 15.66851
C 20.06326 -1.7073 16.05601
C 19.25216 -2.32973 15.08588
H 20.11366 -3.33059 10.59355
H 18.40151 -3.33133 10.13696
H 19.54318 -4.94692 14.78096
H 19.54182 -8.92294 13.08892
H 18.4419 -5.56092 10.61768
H 17.17124 -1.09178 13.87267
H 13.07855 -2.32219 13.2693
H 16.28749 -4.80491 11.78646
H 21.30866 -1.99802 12.34687
H 21.95572 -0.72097 16.41893
H 18.27597 -2.73237 15.38106
C 23.16459 -0.78559 13.94196
H 23.24692 -0.73837 12.84077
H 23.33551 0.21176 14.37115
H 23.94409 -1.45813 14.33202
C 19.57412 -1.60242 17.50448
H 19.47953 -2.60525 17.94894
H 20.27792 -1.01535 18.10897
H 18.58533 -1.1213 17.54205
C 20.01687 -7.57061 15.43771
H 19.13108 -7.85587 16.02761
H 20.63777 -8.46641 15.29888
H 20.58462 -6.82489 16.01089
C 18.71483 -8.2771 10.54271
H 17.64808 -8.54737 10.48831
H 18.99102 -7.78762 9.59833
H 19.29827 -9.20128 10.65231
C 14.6054 -0.32422 14.40028
H 15.24587 0.53627 14.16046
H 13.56653 -0.08255 14.1384
H 14.65732 -0.49559 15.48736
C 13.55169 -4.69 11.95067
H 13.95353 -5.23881 11.08796
H 13.3115 -5.41948 12.7407
H 12.62043 -4.18728 11.65518

8.3.4 Cartesian Coordinates of Optimised Ga-NODAGA-xy-TXP Structure

P 7.03089 3.62599 -2.39091
C 3.99196 8.2422 -5.98412
C 5.15117 7.65454 -5.15669
C 6.05443 6.74373 -5.73483
C 6.95567 6.02982 -4.93417
C 6.95578 6.20133 -3.53598
C 6.10276 7.16558 -2.96503
C 5.21253 7.88572 -3.76797
C 7.82114 5.30474 -2.65081
C 8.19524 2.55238 -1.46798
C 7.70623 1.76849 -0.4117
C 8.57971 0.92439 0.29873
C 9.93768 0.88592 -0.07343
C 10.43713 1.66904 -1.13149
C 9.55105 2.50984 -1.83199
C 6.65802 2.89942 -4.03191
C 5.50162 3.33337 -4.70182
C 5.20056 2.83102 -5.98035
C 6.07378 1.89095 -6.56108
C 7.23089 1.44514 -5.89342
C 7.52081 1.96185 -4.61592
C 5.44138 3.76453 -1.49417
C 5.18152 4.8551 -0.65325
C 3.92541 4.96749 -0.02639
C 2.96326 3.9599 -0.22667
C 3.23579 2.83616 -1.03431
C 4.4828 2.75162 -1.67892
H 6.03193 6.56729 -6.81685
H 7.64059 5.30897 -5.39574
H 6.12065 7.34317 -1.88428
H 4.53228 8.61108 -3.30682
H 3.75286 9.27364 -5.67135
H 4.23751 8.23218 -7.06118
H 7.98397 5.7453 -1.65628
H 8.8005 5.11201 -3.11359
H 6.6464 1.81155 -0.13279
H 10.62394 0.22985 0.47617
H 9.93852 3.12119 -2.65547
H 4.82511 4.05974 -4.23628
H 5.84563 1.4938 -7.5579
H 8.41821 1.62139 -4.08596
H 5.93991 5.62486 -0.4782
H 1.96984 4.06688 0.25942
H 4.69785 1.89639 -2.33037
Ga -0.9993 3.68526 0.23849
O -0.32036 3.19085 -1.46712
O 0.24106 3.7672 -3.6262

O -1.59112 2.32364 0.62419
O -2.94101 0.46445 0.76561
O 0.34963 4.39224 0.92819
O 1.41147 5.37203 2.72878
N -2.03875 5.32142 1.65662
N -1.20099 5.72671 -0.99459
N -3.34374 3.91646 -0.47052
C -2.00583 6.75341 1.15982
C -1.01902 6.89244 -0.03778
C 0.01321 5.59231 -1.9093
C -0.02202 4.08971 -2.44298
C -2.50734 5.89627 -1.76869
C -3.32839 4.57521 -1.82683
C -3.7395 2.4616 -0.5353
C -2.72622 1.62722 0.36495
C -4.18393 4.68151 0.53819
C -3.4441 4.83391 1.90651
C -1.08291 5.12776 2.8055
C 0.3651 4.9779 2.16488
H -1.69347 7.44105 1.96631
H -3.01959 7.04432 0.84747
H 0.02098 6.85949 0.32332
H -1.18555 7.86314 -0.53981
H 0.88136 5.65555 -1.2274
H -2.31384 6.22983 -2.80019
H -3.10201 6.68031 -1.27727
H -4.34644 4.79868 -2.20077
H -2.84421 3.86969 -2.52199
H -4.77895 2.29715 -0.20142
H -3.64549 2.10754 -1.57621
H -4.41139 5.67611 0.12553
H -5.14567 4.16742 0.71387
H -3.36645 3.85087 2.40086
H -4.01896 5.51844 2.55974
H -1.10292 5.96111 3.53155
H -1.34632 4.18827 3.3233
C 0.19712 6.67486 -3.01055
H 0.21159 7.67392 -2.54572
H -0.62707 6.64902 -3.73802
C 1.53312 6.4407 -3.7642
H 1.41776 5.58905 -4.45142
H 2.3271 6.176 -3.0434
O 1.83092 8.88855 -4.14457
N 2.7559 7.40825 -5.75173
H 3.01161 6.39147 -5.78007
C 2.0282 7.71643 -4.52354
C 3.58943 6.18293 0.84345
H 3.19089 6.99371 0.2131
H 2.82075 5.90806 1.59179
H 4.48844 6.55943 1.34987

C 2.18857 1.72879 -1.19428
H 2.18181 1.09169 -0.29629
H 1.17735 2.17621 -1.3163
H 2.42408 1.09702 -2.06049
C 8.05293 0.04491 1.43784
H 7.74452 -0.93765 1.04612
H 8.83382 -0.1182 2.19335
H 7.18118 0.51153 1.91676
C 11.92304 1.63351 -1.5051
H 12.38072 0.68876 -1.18196
H 12.0523 1.74217 -2.5911
H 12.45756 2.46181 -1.0131
C 3.96064 3.33056 -6.7292
H 3.14082 3.53607 -6.0265
H 4.19437 4.26442 -7.2654
H 3.62481 2.58722 -7.46481
C 8.15 0.39628 -6.52897
H 9.19338 0.55998 -6.22554
H 7.85388 -0.61403 -6.20402
H 8.08405 0.43692 -7.62476

8.3.5 Calculated Energies from Optimised Structures of Ga-NODAGA-xy-TXP and Ga-DO2A-(xy-TXP)$_2$

	E(SCF) (kJ mol^{-1})	ZPE (kJ mol^{-1})
Ga-NODAGA-xy-TXP	-12542376.47	2781.75
Ga-DO2A-(xy-TXP)$_2$	-15759969.50	4306.88

8.3.6 Selected Bond Lengths:

Complexes/Bond distances	Ga-O$_{acetic}$ (Å)	Ga-O$_{glutaric}$ (Å)	Ga-N$_{glycinic}$ (Å)	Ga-N$_{benzylamino}$ (Å)	Ga-N$_{glutaric}$ (Å)
Ga-DO2A-(xy-TXP)$_2$	1.537, 1.530	N/A	2.489, 2.494	2.373, 2.375	N/A
Ga-NODAGA-xy-TXP	1.534, 1.672	1.901	2.402, 2.460	N/A	2.393